



**Newcastle
University**

**Redox Chemistry of Polyoxometalates and
Applications in Energy Storage**

Kate Ann Phipps

A thesis submitted in partial fulfilment of the
requirements for the award of

Doctor of Philosophy

School of Natural and Environmental Sciences
(Chemistry)

Newcastle University

Newcastle upon Tyne, UK

April 2020

For my parents,
Dawn and Gordon Phipps.

Acknowledgements

Abstract

The first part of this thesis describes investigations into the multi-electron reduction of $(TBA)_3[PMo_{12}O_{40}]$ and $(TBA)_3[V_{13}O_{34}]$ and interactions between the reduced anions $[PMo_{12}O_{40}]^{(3+n)-}$ and M^{2+} and M^{3+} cations in non-aqueous solvents. Systematic stepwise reduction of $(TBA)_3[PMo_{12}O_{40}]$ with various reducing agents ($Na|Hg$, $Li|Hg$, KC_8 and $K^+PhCN^{-\bullet}$) in non-aqueous solvents (MeCN, propylene carbonate and PhCN) was monitored by NMR and FTIR spectroscopy. The different reducing agents produced differing results and this is thought to be due to interactions with solvent. Evidence for the formation of “super-reduced” $(TBA)_3[PMo_{12}O_{40}M_{24}]$ (where $M = Na$ or Li) was obtained for the first time (via chemical reduction and not in a Li-ion battery set-up), broad resonances were present in both solid state and solution ^{31}P NMR spectra. Systematic stepwise reduction of $(TBA)_3[V_{13}O_{34}]$ with $M|Hg$ amalgam ($M = Na$ or Li) was also monitored by NMR and FTIR spectroscopy. Products from these reactions have been isolated but not all of them can be confidently assigned structures. The capped reduced compounds; $(TBA)_3[PMo_{12}O_{40}Sb_2]$ and $(TBA)_3[PMo_{12}O_{40}\{M(dmsO)_x\}_n]$ ($M = Bi^{3+}$, $n = 2$ and $x = 4$, $M = Zn^{2+}$, $n = 1$ and $x = 2$) were successfully prepared, isolated and characterised by NMR spectroscopy, FTIR spectroscopy, cyclic voltammetry and crystallography.

In the second part of this thesis, investigations into the use of the polyoxovanadate $Na_6V_{10}O_{28}.nH_2O$ as a supercapacitor cathode material are described. The decavanadate was synthesised by three different methods and was characterised by NMR and FTIR spectroscopy, TGA, CV and SEM. The electrode performance was optimised using powder processing, the results of which were monitored by SEM imaging, and by varying the electrode slurry composition. Decavanadate-containing electrodes were electrochemically characterised by three-electrode experiments, with an optimised electrode achieving a specific capacitance of 225 F.g^{-1} . An asymmetric hybrid supercapacitor using activated carbon electrical double layer electrode and decavanadate faradaic electrode was also investigated and it exhibited an energy density of 14 W.h.kg^{-1} with a power density of 356 W.kg^{-1} .

Acknowledgements

Firstly I would like to thank my supervisor; Dr John Errington for his continued support and guidance throughout this project. His guidance in the lab and teaching me all I know about air-sensitive chemistry and techniques was invaluable. As well as his patience during my write-up. I would also like to express my gratitude for providing me with the opportunity to interact with the wider POM community as well as travel to Japan as part of the EPSRC-JSPS Core-to-Core Collaboration in Advanced Materials International Network on Polyoxometalate Science for Advanced Energy Materials; an unique experience!

I would also like to thank my second supervisor Professor Keith Scott for his guidance and support.

I would like to give my gratitude to Professor Walter Klemperer for four years of unwavering support, guidance and motivation. He pushed me to fully understand every aspect of the project and helped me with relevant reading materials, as well as teaching me that you can never be too thorough. The project would not have progressed as well as it did without his invaluable input. I would also like to thank him for his patience and thoroughness during my write-up.

I would also like to thank the following people:

Dr Jochen Friedl for his guidance and support with the fundamentals of electrochemistry and energy storage materials.

The Stimming group for allowing me access to a potentiostat.

Dr Mohamed Mamlouk and Dr Ravikumar for their assistance and advice.

Dr Corinne Wills and Professor William McFarlane for their assistance with NMR spectroscopy.

Maggie White for assistance with PXRD.

Dr Karen Johnston and Abbey Haworth from Durham University for their help with running my samples for solid-state NMR spectroscopy.

Dr Paul Waddell for X-ray crystallography.

Acknowledgements

Dr Kathryn White, Tracey Davey and Ross Laws for training me to use the SEM and their support throughout.

The Gibson group for assisting me with TGA and UV-Vis spectroscopy.

Gary Day and John Corner from the mechanical workshop, Chris Burrow and Geoff Reah from the electrical workshop, Tom Steward from stores and Robyn Hare from glassblowing.

The chemistry office staff past and present; Kate Kirkpatrick, Joanne Lakey, Kate Gorman, Claire Nicoll, Justina Heslop, Gayle Thompson, Brian Shields, Alison Walker and Pippa Wood.

SNES IT department – Mark Garner and Allan Parkin.

Retsch for allowing me to visit them and use the HEBM.

Kuraray for sending me samples of activated carbon.

I would like to acknowledge Newcastle University School of Chemistry for funding my project.

I would like to thank current and past members of the Errington research group; Dr Lan Feng, Dr Daniel Lebbie, Dr Thompson Izuagie, Cansu Ylidiz and Franscesa Stals as well as past MChem students. I would also like to thank Tina Tran, Dr Tom Backhouse and Phillip Layford for their friendships and support.

Special thanks to my family and friends for their continued support and encouragement and getting me through the last four years.

Table of Contents

Dedication	i
Abstract	iii
Acknowledgements	v
Table of Contents	vii
Abbreviations	xiii
List of Figures	xvii
List of Tables	xxix
Chapter 1 Introduction	1
1.1 Introduction	3
1.2 Aims	4
1.3 Thesis Organisation	4
1.4 Background to Study	5
1.4.1 Keggin Structure	5
1.4.2 POM Synthesis	7
1.4.3 Electrochemical Studies	7
1.4.4 Chemical Reduction	22
1.4.5 Applications	24
1.5 References	27
Chapter 2 Chemical Reduction of Polyoxometalates	33
2.1 Introduction to POM Redox Chemistry	35
2.2 Reductions with Metal Mercury Amalgams	36
2.2.1 The Reaction Between $(TBA)_3[PMo_{12}O_{40}]$ and $Na Hg$ Amalgam in MeCN	37
2.2.2 The Reaction Between $(TBA)_3[PMo_{12}O_{40}]$ and $Na Hg$ Amalgam in PC	41

Table of Contents

2.2.3 The Reaction Between (TBA) ₃ [PMo ₁₂ O ₄₀] and Na Hg Amalgam in PhCN	48
2.2.4 The Reaction Between (TBA) ₃ [PMo ₁₂ O ₄₀] and Li Hg Amalgam in MeCN	50
2.2.5 The Reaction Between (TBA) ₃ [PMo ₁₂ O ₄₀] and Li Hg Amalgam in PC	52
2.2.6 The Reaction Between (TBA) ₃ [V ₁₃ O ₃₄] and Na Hg Amalgam in MeCN	66
2.2.7 The Reaction Between (TBA) ₃ [V ₁₃ O ₃₄] and Na Hg Amalgam in PC	69
2.2.8 The Reaction Between (TBA) ₃ [V ₁₃ O ₃₄] and Li Hg Amalgam in MeCN	71
2.2.9 The Reaction Between (TBA) ₃ [V ₁₃ O ₃₄] and Li Hg Amalgam in PC	74
2.3 Other Reducing Agents	76
2.3.1 The Reaction Between (TBA) ₃ [PMo ₁₂ O ₄₀] and KC ₈ in MeCN	76
2.3.2 The Reaction Between (TBA) ₃ [PMo ₁₂ O ₄₀] and K ⁺ PhCN [•]	78
2.4 Discussion	80
2.5 Conclusions and Future Work	89
2.5.1 Conclusions	89
2.5.2 Future Work	90
2.6 References	91
Chapter 3 Addition of Capping M²⁺ and M³⁺ cations to reduced (TBA)₃[PMo₁₂O₄₀]	93
3.1 Introduction	95
3.2 Reduced (TBA) ₃ [PMo ₁₂ O ₄₀] Capped with M ²⁺ /M ³⁺	96
3.2.1 M = Sb(III)	96
3.2.2 M = Bi(III)	101
3.2.3 M = Zn(II)	103
3.3 Discussion	108
3.4 Conclusions	112
3.5 References	114

Chapter 4 Na₆V₁₀O₂₈ Containing Supercapacitor	115
4.1 Background	117
4.1.1 Electrical Energy Storage Devices	117
4.2 Materials and Methods	124
4.2.1 Characterisation Methods of Na ₆ V ₁₀ O ₂₈ . <i>n</i> H ₂ O	124
4.2.2 Processing of V ₁₀	125
4.2.3 Preparation of Electrodes	127
4.2.4 Electrochemical Characterisation of Electrodes	129
4.3 Optimisation and Performance of the Decavanadate Cathode	135
4.3.1 Decavanadate Synthesis and Characterisation	135
4.3.2 Temperature Stability	139
4.3.3 Processing of Decavanadate	142
4.3.4 Electrode Preparation	144
4.3.5 CP with Dwell Period Experiments	153
4.3.6 Two-electrode Experiments	154
4.4 Discussion	158
4.4.1 Introduction	158
4.4.2 Optimisation of the Decavanadate Electrode Capacitance	158
4.4.3 Polyoxometalate Hybrid Supercapacitors	160
4.4.4 Polyoxometalate Containing Batteries	162
4.5 Outlook	165
4.6 References	168

Table of Contents

Chapter 5 Experimental	173
5.1 Characterisation Techniques	175
5.1.1 NMR Spectroscopy	175
5.1.2 FTIR Spectroscopy	175
5.1.3 UV-Vis Spectroscopy	175
5.1.4 X-Ray Powder Diffraction	175
5.1.5 Single Crystal X-Ray Diffraction	176
5.1.6 Thermogravimetric Analysis	176
5.1.7 Scanning Electron Microscopy	176
5.1.8 Solution Cyclic Voltammetry	176
5.1.9 Solid State Electrochemistry	176
5.2 Chapter 2	177
5.2.1 Materials	177
5.2.2 Synthesis	178
5.3 Chapter 3	195
5.3.1 Materials	195
5.3.2 Synthesis	196
5.4 Chapter 4	198
5.4.1 Materials	198
5.4.2 Synthesis	199
5.4.3 V ₁₀ Processing	200
5.4.4 Working Electrode Preparation	201
5.5 References	204

Table of Contents

A1 Appendix	205
A1.1 Crystal Data for (TBA) ₂ [PMo ₁₂ O ₄₀ Sb ₂]	207
A1.2 Crystal Data for (TBA) ₃ [PMo ₁₂ O ₄₀ Sb ₂]	210
A1.3 Crystal Data for (TBA) ₃ [PMo ₁₂ O ₄₀ {Bi(dmso) ₄ } ₂]	232
A1.4 Crystal Data for (TBA) ₃ [PMo ₁₂ O ₄₀ {Zn(dmso) ₂ }]	238

Abbreviations

Å –	Angstrom
AC –	Activated carbon
CE –	Counter electrode
CP –	Chronopotentiometry
C_{sp} –	Specific capacitance
CV –	Cyclic voltammetry
DEC –	Diethyl carbonate
DMC –	Dimethyl carbonate
DMSO –	Dimethyl sulfoxide
EC –	Ethylene carbonate
EDLC –	Electrical Double Layer Capacitor
EMC –	Ethyl methyl carbonate
FTIR –	Fourier-Transform Infrared
fw hm	Full width at half maximum
GC –	Glassy carbon
GCD –	Galvanostatic charge discharge
HEBM –	High energy ball mill
hr –	Hour
Hz –	Hertz
I –	Current
min –	Minute
MSE –	Mercury-mercurous sulfate electrode
NHE –	Normal hydrogen electrode

Abbreviations

NMP –	N-methylpyrrolidone
NMR –	Nuclear magnetic resonance
o/n –	Overnight
PC –	Propylene carbonate
PEEK –	Polyether ether ketone
PEFC –	Polymer electrolyte fuel cell
POM –	Polyoxometalate
PMo ₁₂ –	(TBA) ₃ [PMo ₁₂ O ₄₀]
PMo ₁₂ Bi ₂ –	(TBA) ₃ [PMo ₁₂ O ₄₀ {Bi(dmso) ₄ } ₂]
PMo ₁₂ Li ₂ –	(TBA) ₃ [PMo ₁₂ O ₄₀ Li ₂]
PMo ₁₂ Li ₆ –	(TBA) ₃ [PMo ₁₂ O ₄₀ Li ₆]
PMo ₁₂ Na ₂ –	(TBA) ₃ [PMo ₁₂ O ₄₀ Na ₂]
PMo ₁₂ Na ₆ –	(TBA) ₃ [PMo ₁₂ O ₄₀ Na ₆]
PMo ₁₂ Sb ₂ –	(TBA) ₃ [PMo ₁₂ O ₄₀ Sb ₂]
PMo ₁₂ Zn –	(TBA) ₃ [PMo ₁₂ O ₄₀ {Zn(dmso) ₂ }]
ppm –	Parts per million
PTFE –	Polytetrafluoroethylene
PVDF –	Poly(vinylidene) fluoride
PXRD –	Powder X-Ray Diffraction
RE –	Reference electrode
RT –	Room temperature
SC –	Supercapacitor
SCE –	Standard calomel electrode
SEM –	Scanning electron microscopy

Super P –	Carbon black Super P
SWCNT	Single walled carbon nanotubes
t –	Time
TBA –	Tetra n-butylammonium
TBAP –	Tetra n-butylammonium perchlorate
TGA –	Thermogravimetric analysis
THF –	Tetrahydrofuran
UV-Vis –	Ultraviolet and visible spectroscopy
V ₁₀ –	Na ₆ V ₁₀ O ₂₈ . <i>n</i> H ₂ O
WE –	Working electrode
XAFS –	X-Ray absorption fine structure

List of Figures

Figure 1.1: Ball-and-stick representations of $[M_6O_{19}]^{n-}$ Lindqvist structure (A), $[XM_{12}O_{40}]^{n-}$ Keggin structure (B) and $[X_2M_{18}O_{64}]^{n-}$ Wells-Dawson structure (C).	5
Figure 1.2: Baker-Figgis isomers of $[PM_{12}O_{40}]^{3-}$, M = Mo or W.	6
Figure 1.3: CV of a 1 mM solution of $H_4SiW_{12}O_{40}$ in 0.5 M H_2SO_4 (aq), glassy carbon WE, SCE RE, Pt CE, 100 mV/s scan rate. Curve 1 is background current in the absence of $H_4SiW_{12}O_{40}$ and curve 2 is the first voltammetric run in the presence of $H_4SiW_{12}O_{40}$. After ref ¹⁶	8
Figure 1.4: The reduction peak potentials in the CV of 1 mM $H_4SiW_{12}O_{40}$ in 0.1 M $LiClO_4$ in water solution, with increasing $HClO_4$ concentration. After ref ²²	10
Figure 1.5: The reduction peak potentials in the CV of 1 mM $K_4SiW_{12}O_{40}$ in 0.1 M $LiClO_4$ in DMF solution, with increasing $HClO_4$ concentration. After ref ²²	11
Figure 1.6: The reduction peak potentials in the CV of 1 mM $H_4SiW_{12}O_{40}$ in 0.1 M $LiClO_4$ in DMF solution, with increasing $HClO_4$ concentration. After ref ²²	11
Figure 1.7: The reduction peak potentials in the CV of 1 mM $K_4SiW_{12}O_{40}$ in 0.1 M $LiClO_4$ in various solvents. After ref ²⁵	12
Figure 1.8: CV of a 0.5 mM solution of $(TBA)_4[SiMo_{12}O_{40}]$ in MeCN containing TBAP + $LiClO_4$, GC WE, Pt CE, Ag/Ag ⁺ RE, 50 mV/s scan rate. Where the ionic strength = 0.10. $[Li^+]/ mM$: (a) 0; (b) 1.0; (c) 5.0; (d) 50; (e) 100. After ref ²⁶	12
Figure 1.9: CV of a solution of 0.3 mM (a) β -(TBA) ₃ [PW ₁₂ O ₄₀] and (b) α -(TBA) ₃ [PW ₁₂ O ₄₀] in 95% (v/v) MeCN + water containing 0.1 M TBAP + 3 mM CF_3SO_3H . Ag/Ag ⁺ RE, Pt CE, GC WE, 100 mV/s scan rate. After ref ³⁰	14
Figure 1.10: The reduction peak potentials in the CV of 1 mM $H_3PW_{12}O_{40}$ in aqueous solution with increasing concentrations of $HClO_4$. After ref ²²	15
Figure 1.11: The reduction peak potentials in the CV of 1 mM $H_3PW_{12}O_{40}$ in DMF with increasing concentrations of $HClO_4$. After ref ²²	16
Figure 1.12: CV of 0.5 mM $(TBA)_3[PMo_{12}O_{40}]$ in $TBAClO_4$ in MeCN, Ag/Ag ⁺ RE, GC WE, Pt CE, 1 mV/s scan rate. After ref ²⁶	16
Figure 1.13: The scheme for the reduction of the metatungstate anion, after ref ³⁹	20
Figure 2.1: Molecular orbital diagram of $\{M(O)L_5\}$ complexes with C_{4v} symmetry. After ref ¹	35

List of Figures

Figure 2.2: Ball-and-stick representation of the anion $[\text{PMo}_{12}\text{O}_{40}]^{3-}$	37
Figure 2.3: $^{31}\text{P}\{^1\text{H}\}$ NMR spectra from reactions between n mole-equivalents of $\text{Na} \text{Hg}$ amalgam and PMo_{12} in MeCN.	39
Figure 2.4: $^{31}\text{P}\{^1\text{H}\}$ NMR spectra of the reaction between PMo_{12} and one-mole equivalent of $\text{Na} \text{Hg}$ amalgam (A), and with the calculated amount of $\text{Na} \text{Hg}$ amalgam added to form all one-electron reduced PMo_{12} (B).	39
Figure 2.5: FTIR spectra of solids isolated from reactions between n mole-equivalents of $\text{Na} \text{Hg}$ amalgam and PMo_{12} in MeCN.	40
Figure 2.6: $^{31}\text{P}\{^1\text{H}\}$ NMR spectra from reactions between n mole-equivalents of $\text{Na} \text{Hg}$ amalgam and PMo_{12} in PC.	42
Figure 2.7: Solid-state ^{31}P NMR spectra for the reaction between PMo_{12} and n mole-equivalents of $\text{Na} \text{Hg}$ amalgam in PC.	43
Figure 2.8: Solid-state ^{23}Na NMR spectra for the reaction between PMo_{12} and n mole-equivalents of $\text{Na} \text{Hg}$ amalgam in PC.	44
Figure 2.9: FTIR spectra of isolated solids from the reaction of n mole-equivalents of $\text{Na} \text{Hg}$ amalgam and PMo_{12} in PC.	45
Figure 2.10: The UV-Vis spectra of reactions between PMo_{12} and n mole-equivalents of $\text{Na} \text{Hg}$ in PC, $c = 0.25$ mM, $l = 1$ cm.	46
Figure 2.11: The UV-Vis spectra of reactions between PMo_{12} and n mole-equivalents of $\text{Na} \text{Hg}$ in PC, $c = 0.25$ mM, $l = 1$ cm.	47
Figure 2.12: The UV-Vis spectra of reactions between PMo_{12} and n mole-equivalents of $\text{Na} \text{Hg}$ in PC, $c = 0.25$ mM, $l = 1$ cm.	47
Figure 2.13: Plot of molar extinction coefficient (ϵ) against the number of mole-equivalents (n) of $\text{Na} \text{Hg}$ amalgam added to PMo_{12}	48
Figure 2.14: $^{31}\text{P}\{^1\text{H}\}$ NMR spectra for the reactions between PMo_{12} and n mole-equivalents of $\text{Na} \text{Hg}$ amalgam in PhCN.	49
Figure 2.15: $^{31}\text{P}\{^1\text{H}\}$ NMR spectra for the reactions between PMo_{12} and n mole-equivalents of $\text{Li} \text{Hg}$ amalgam in MeCN.	51
Figure 2.16: FTIR spectra for the products isolated from the reactions between PMo_{12} and n mole-equivalents of $\text{Li} \text{Hg}$ amalgam in MeCN.	52

Figure 2.17: $^{31}\text{P}\{^1\text{H}\}$ NMR spectra for the reactions between PMo_{12} and n mole-equivalents of $\text{Li} \text{Hg}$ amalgam in PC.	54
Figure 2.18: $^{31}\text{P}\{^1\text{H}\}$ NMR spectra for the reactions between PMo_{12} and n mole-equivalents of $\text{Li} \text{Hg}$ amalgam in PC.	54
Figure 2.19: Solid-state ^{31}P NMR spectra for solids isolated from the reactions between PMo_{12} and n mole-equivalents of $\text{Li} \text{Hg}$ amalgam in PC.	55
Figure 2.20: Solid-state ^7Li NMR spectra for solids isolated from the reactions between PMo_{12} and n mole-equivalents of $\text{Li} \text{Hg}$ amalgam in PC.	56
Figure 2.21: FTIR spectra of solids isolated from the reactions between PMo_{12} and n mole-equivalents of $\text{Li} \text{Hg}$ amalgam in PC.	57
Figure 2.22: UV-Vis spectra for the reactions between PMo_{12} and n equivalents of $\text{Li} \text{Hg}$ amalgam in PC, $c = 0.25 \text{ mM}$, $l = 1 \text{ cm}$	58
Figure 2.23: UV-Vis spectra for the reactions between PMo_{12} and n equivalents of $\text{Li} \text{Hg}$ amalgam in PC, $c = 0.25 \text{ mM}$, $l = 1 \text{ cm}$	59
Figure 2.24: UV-Vis spectra for the reactions between PMo_{12} and n equivalents of $\text{Li} \text{Hg}$ amalgam in PC, $c = 0.25 \text{ mM}$, $l = 1 \text{ cm}$	59
Figure 2.25: Plot of molar extinction coefficient (ϵ) against the number of mole-equivalents (n) of $\text{Li} \text{Hg}$ amalgam added to PMo_{12}	60
Figure 2.26: Cyclic voltammograms of solids isolated from the reactions between PMo_{12} and 0 mole-equivalents of $\text{Li} \text{Hg}$ amalgam. 1 mM POM in 100 mM (TBA)(BF ₄) in MeCN, from +1.0 V to -2.0 V vs Ag wire, 100 mV/s scan rate, GC WE, Pt wire CE, Ag wire RE.	60
Figure 2.27: Cyclic voltammograms of solids isolated from the reactions between PMo_{12} and 1 mole-equivalents of $\text{Li} \text{Hg}$ amalgam. 1 mM POM in 100 mM (TBA)(BF ₄) in MeCN, from +1.0 V to -2.0 V vs Ag wire, 100 mV/s scan rate, GC WE, Pt wire CE, Ag wire RE.	61
Figure 2.28: Cyclic voltammograms of solids isolated from the reactions between PMo_{12} and 2 mole-equivalents of $\text{Li} \text{Hg}$ amalgam. 1 mM POM in 100 mM (TBA)(BF ₄) in MeCN, from +1.0 V to -2.0 V vs Ag wire, 100 mV/s scan rate, GC WE, Pt wire CE, Ag wire RE.	61
Figure 2.29: Cyclic voltammograms of solids isolated from the reactions between PMo_{12} and 3 mole-equivalents of $\text{Li} \text{Hg}$ amalgam. 1 mM POM in 100 mM (TBA)(BF ₄)	

List of Figures

in MeCN, from +1.0 V to –2.0 V vs Ag wire, 100 mV/s scan rate, GC WE, Pt wire CE, Ag wire RE.	62
Figure 2.30: Cyclic voltammograms of solids isolated from the reactions between PMo_{12} and 4 mole-equivalents of Li Hg amalgam. 1 mM POM in 100 mM (TBA)(BF ₄) in MeCN, from +1.0 V to –2.0 V vs Ag wire, 100 mV/s scan rate, GC WE, Pt wire CE, Ag wire RE.	62
Figure 2.31: Cyclic voltammograms of solids isolated from the reactions between PMo_{12} and 5 mole-equivalents of Li Hg amalgam. 1 mM POM in 100 mM (TBA)(BF ₄) in MeCN, from +1.0 V to –2.0 V vs Ag wire, 100 mV/s scan rate, GC WE, Pt wire CE, Ag wire RE.	63
Figure 2.32: Cyclic voltammograms of solids isolated from the reactions between PMo_{12} and 6 mole-equivalents of Li Hg amalgam. 1 mM POM in 100 mM (TBA)(BF ₄) in MeCN, from +1.0 V to –2.0 V vs Ag wire, 100 mV/s scan rate, GC WE, Pt wire CE, Ag wire RE.	63
Figure 2.33: Cyclic voltammograms of solids isolated from the reactions between PMo_{12} and 8 mole-equivalents of Li Hg amalgam. 1 mM POM in 100 mM (TBA)(BF ₄) in MeCN, from +1.0 V to –2.0 V vs Ag wire, 100 mV/s scan rate, GC WE, Pt wire CE, Ag wire RE.	64
Figure 2.34: Cyclic voltammograms of solids isolated from the reactions between PMo_{12} and 10 mole-equivalents of Li Hg amalgam. 1 mM POM in 100 mM (TBA)(BF ₄) in MeCN, from +1.0 V to –2.0 V vs Ag wire, 100 mV/s scan rate, GC WE, Pt wire CE, Ag wire RE.	64
Figure 2.35: Cyclic voltammograms of solids isolated from the reactions between PMo_{12} and n mole-equivalents of Li Hg amalgam (n is an odd number). 1 mM POM in 100 mM (TBA)(BF ₄) in MeCN, from +1.0 V to –2.0 V vs Ag wire, 100 mV/s scan rate, GC WE, Pt wire CE, Ag wire RE.	65
Figure 2.36: Cyclic voltammograms of solids isolated from the reactions between PMo_{12} and n mole-equivalents of Li Hg amalgam (n is an even number). 1 mM POM in 100 mM (TBA)(BF ₄) in MeCN, from +1.0 V to –2.0 V vs Ag wire, 100 mV/s scan rate, GC WE, Pt wire CE, Ag wire RE.	65
Figure 2.37: Plot of the potential difference between the first reduction peak (E_p) when $n = 0$ (n_0) and the first reduction peak when $n = 1-10$ in the cyclic voltammogram of solids isolated from the reactions between n mole-equivalents of Li Hg amalgam and PMo_{12}	66

Figure 2.38: Ball-and-stick model of the anion, $[V_{13}O_{34}]^{3-}$ (A) and ball-and-stick model with the four vanadium environments indicated by the different colour atoms (B). ...	66
Figure 2.39: $^{51}V\{^1H\}$ NMR spectra for the reactions between V_{13} and n mole-equivalents of $Na Hg$ amalgam in MeCN.	68
Figure 2.40: FTIR spectra for solids isolated from the reactions between V_{13} and n mole-equivalents of $Na Hg$ amalgam in MeCN.	69
Figure 2.41: $^{51}V\{^1H\}$ NMR spectra for the reactions between V_{13} and n mole-equivalents of $Na Hg$ amalgam in PC.	70
Figure 2.42: FTIR spectra for the solids isolated from the reactions between V_{13} and n mole-equivalents of $Na Hg$ amalgam in PC.	71
Figure 2.43: $^{51}V\{^1H\}$ NMR spectra for the reactions between V_{13} and n mole-equivalents of $Li Hg$ amalgam in MeCN.	72
Figure 2.44: FTIR spectra of the solids isolated from the reactions between V_{13} and n mole-equivalents of $Li Hg$ amalgam in MeCN.	73
Figure 2.45: $^{51}V\{^1H\}$ NMR spectra for the reactions between V_{13} and n mole-equivalents of $Li Hg$ in PC.	75
Figure 2.46: FTIR spectra of solids isolated from the reactions between V_{13} and n mole-equivalents of $Li Hg$ in PC.	76
Figure 2.47: The preparation of KC_8 , adapted from ref ¹⁹	77
Figure 2.48: $^{31}P\{^1H\}$ NMR spectra from the reactions between PMo_{12} and n mole-equivalents of KC_8 in MeCN.	78
Figure 2.49: $^{31}P\{^1H\}$ NMR spectra from the reactions between PMo_{12} and n mole-equivalents of $K^+PhCN^- \bullet$ in PhCN.	80
Figure 2.50: $^{31}P\{^1H\}$ NMR spectra of reactions between PMo_{12} and different reducing agents, (A) one mole-equivalent, (B) two mole-equivalents, (C) three mole-equivalents and (D) four mole-equivalents, with peaks relative to fully oxidised PMo_{12}	81
Figure 2.51: $^{31}P\{^1H\}$ NMR spectra of reactions between PMo_{12} and different reducing agents, (A) five mole-equivalents, (B) six mole-equivalents, (C) twelve mole-equivalents and (D) twenty-four mole-equivalents, with peaks relative to fully oxidised PMo_{12}	82

List of Figures

Figure 2.52: Solid-state ^{31}P NMR of solids isolated from reactions in PC between PMo_{12} and (A) one mole-equivalent of $\text{Na} \text{Hg}$ amalgam, (B) one mole-equivalent $\text{Li} \text{Hg}$ amalgam, (C) two mole-equivalents of $\text{Na} \text{Hg}$ amalgam (D) two mole-equivalents of $\text{Li} \text{Hg}$ amalgam, (E) twenty-four mole-equivalents of $\text{Na} \text{Hg}$ amalgam and (F) twenty-four mole-equivalents of $\text{Li} \text{Hg}$ amalgam.	83
Figure 2.53: FTIR spectra of solids isolated from the reactions between PMo_{12} and different reducing agents, (A) one mole-equivalents, (B) two mole-equivalents, (C) three mole-equivalents and (D) four mole-equivalents.	84
Figure 2.54: FTIR spectra of solids isolated from the reactions between PMo_{12} and different reducing agents, (A) five mole-equivalents, (B) six mole-equivalents, (C) twelve mole-equivalents and (D) twenty-four mole-equivalents.	85
Figure 2.55: UV-Vis spectra for the solids isolated from the reactions between PMo_{12} and $\text{Na} \text{Hg}$ amalgam, or $\text{Li} \text{Hg}$ amalgam in PC.	85
Figure 2.56: UV-Vis spectra for the solids isolated from the reactions between PMo_{12} and $\text{Na} \text{Hg}$ amalgam, or $\text{Li} \text{Hg}$ amalgam in PC.	86
Figure 2.57: UV-Vis spectra for the solids isolated from the reactions between PMo_{12} and $\text{Na} \text{Hg}$ amalgam, or $\text{Li} \text{Hg}$ amalgam in PC.	86
Figure 2.58: Plot of molar extinction coefficient (ϵ) against the number of mole-equivalents (n) of $\text{Li} \text{Hg}$ amalgam, or $\text{Na} \text{Hg}$ amalgam added to PMo_{12}	87
Figure 2.59: $^{51}\text{V}\{^1\text{H}\}$ NMR spectra of the reaction between V_{13} and different reducing agents (A) one mole-equivalent, (B) two mole-equivalents, (C) three mole-equivalents and (D) four mole-equivalents.	88
Figure 2.60: $^{51}\text{V}\{^1\text{H}\}$ NMR spectra of the reaction between V_{13} and different reducing agents (A) five mole-equivalents, (B) six mole-equivalents and (C) thirteen mole-equivalents.	89
Figure 3.1: Ball-and-stick representation of the anion $[\text{PMo}_{12}\text{O}_{40}\text{Sb}_2]^{3-}$	96
Figure 3.2: Ball-and-stick model of disordered $[\text{PMo}_{12}\text{O}_{40}\text{Sb}_2]^{2-}$ (A) and ordered (B).	97
Figure 3.3: $^{31}\text{P}\{^1\text{H}\}$ NMR spectra of PMo_{12} (A), $(\text{TBA})_3[\text{PMo}_{12}\text{O}_{40}\text{Na}_6]$ (B), crystals isolated from attempt 1 (C) and crystals isolated from attempt 2 (D).	98
Figure 3.4: The extended structure of $[\text{PMo}_{12}\text{O}_{40}\text{Sb}_2]^{3-}$	98

Figure 3.5: FTIR spectra of PMo_{12} (yellow line), crystals isolated from attempt 1 (green line) and crystals isolated from attempt 2 (red line).	99
Figure 3.6: CV of 1 mM PMo_{12} (black line) and 1 mM $\text{PMo}_{12}\text{Sb}_2$ (red line) in 100 mM (TBA)(BF ₄) MeCN, Ag wire RE, Pt CE, GC WE, from +1.0 V to -2.0 V vs Ag wire, 100 mV/s scan rate.	100
Figure 3.7: Ball-and-stick representation of the anion $[\text{PMo}_{12}\text{O}_{40}\{\text{Bi}(\text{dmso})_4\}_2]^{3-}$	101
Figure 3.8: ³¹ P{ ¹ H} NMR spectra of PMo_{12} (A), the reaction mixture of PMo_{12} + two mole-equivalents of Bi stirred o/n (B), the reaction mixture of PMo_{12} + two mole-equivalents of Bi stirred for a further 5 hours (C) and isolated crystals of $\text{PMo}_{12}\text{Bi}_2$ (D).	102
Figure 3.9: FTIR spectra of PMo_{12} (yellow line) and isolated crystals of $\text{PMo}_{12}\text{Bi}_2$ (green line).	102
Figure 3.10: CV of 1 mM PMo_{12} (black line) and 1 mM $\text{PMo}_{12}\text{Bi}_2$ (green line) in 100 mM (TBA)(BF ₄) MeCN, Ag wire RE, Pt CE, GC WE, from +1.0 V to -2.0 V vs Ag wire, 100 mV/s scan rate.	103
Figure 3.11: Ball-and-stick representation of the anion $[\text{PMo}_{12}\text{O}_{40}\{\text{Zn}(\text{dmso})_2\}]^{3-}$. .	104
Figure 3.12: ³¹ P{ ¹ H} NMR spectra of PMo_{12} (A), the reaction mixture of PMo_{12} and one mole-equivalent of Zn (B), the reaction mixture of PMo_{12} + two mole-equivalents of Zn (C), crystals from one mole-equivalent of Zn to get PMo_{12}Zn (D) and crystals from two mole-equivalents of Zn to get PMo_{12}Zn (E) (ppm and line widths Hz are labelled next to peaks).	105
Figure 3.13: ³¹ P{ ¹ H} NMR spectra of the reaction between PMo_{12} and (A) one mole-equivalent of Zn, (B) one-mole equivalent of Zn, (C) two-mole equivalents of Zn, and (D) four mole-equivalents of Zn (ppm and line widths Hz are labelled next to peaks).	106
Figure 3.14: FTIR spectra of PMo_{12} (yellow line), crystallised products from PMo_{12} + one mole-equivalent of Zn (purple line) and crystallised products from PMo_{12} + two mole-equivalents of Zn (brown line).	107
Figure 3.15: CV of 1 mM PMo_{12} (black line) and 1 mM PMo_{12}Zn (purple line) in 100 mM (TBA)(BF ₄) MeCN, Ag wire RE, Pt CE, GC WE, from +0.6 V to -2.0 V vs Ag wire, 100 mV/s scan rate.	107
Figure 3.16: ³¹ P{ ¹ H} NMR spectra of six-electron reduced species of PMo_{12} ; (TBA) ₃ [$\text{PMo}_{12}\text{O}_{40}\text{Na}_6$] (A), (TBA) ₃ [$\text{PMo}_{12}\text{O}_{40}\text{Li}_6$] (B), $\text{PMo}_{12}\text{Sb}_2$ (C) and $\text{PMo}_{12}\text{Bi}_2$ (D).	108

List of Figures

Figure 3.17: FTIR spectra of six-electron reduced species of PMo_{12} ; $\text{PMo}_{12}\text{Na}_6$ (red line), $\text{PMo}_{12}\text{Li}_6$ (green line), $\text{PMo}_{12}\text{Sb}_2$ (turquoise line) and $\text{PMo}_{12}\text{Bi}_2$ (purple line). 109
Figure 3.18: CV of six-electron reduced species of PMo_{12} , 1 mM solutions of the POMs in 100 mM (TBA)(BF ₄) MeCN, Ag wire RE, Pt CE, GC WE, 100 mV/s scan rate, from +1.0 V to -2.0 V vs Ag wire; $\text{PMo}_{12}\text{Li}_6$ (green line), $\text{PMo}_{12}\text{Sb}_2$ (turquoise line) and $\text{PMo}_{12}\text{Bi}_2$ (purple line). 109
Figure 3.19: $^{31}\text{P}\{^1\text{H}\}$ NMR spectra of two-electron reduced PMo_{12} , $\text{PMo}_{12}\text{Na}_2$ (A), $\text{PMo}_{12}\text{Li}_2$ (B) and PMo_{12}Zn (C). 110
Figure 3.20: Ball-and-stick model of the disordered anion, $[\text{PMo}_{12}\text{O}_{40}\text{Na}_2]^{3-}$. 111
Figure 3.21: FTIR spectra of two-electron reduced PMo_{12} , $\text{PMo}_{12}\text{Na}_2$ (red line), $\text{PMo}_{12}\text{Li}_2$ (green line) and PMo_{12}Zn (blue line). 111
Figure 3.22: CV of two-electron reduced species of PMo_{12} , 1 mM solutions of the POMs in 100 mM (TBA)(BF ₄) MeCN, Ag wire RE, Pt CE, GC WE, 100 mV/s scan rate; $\text{PMo}_{12}\text{Li}_2$ (green line) from +1.0 V to -2.0 V vs Ag wire and PMo_{12}Zn (blue line) from +0.6 V to -2.0 V vs Ag wire. 112
Figure 4.1: Schematic Ragone plot of electrical energy storage devices. ⁴ 118
Figure 4.2: The different mechanisms of capacitive energy storage; double-layer capacitance develops at electrodes comprising carbon particles (A) or porous carbon (B). The double layer shown here arises from adsorption of negative ions from the electrolyte on the positively charged electrode. Pseudocapacitive mechanisms include redox pseudocapacitance (C) as occurs in hydrous RuO ₂ , and intercalation pseudocapacitance (D) where Li ⁺ ions are inserted into the host material. Electrochemical characteristics distinguish capacitor and battery materials. CV distinguishes a capacitor material where the response to a linear change in potential is a constant current (E), as compared to a battery material, which exhibits faradaic redox peaks (F). Galvanostatic discharge behaviour (where Q is charge) for a MnO ₂ pseudocapacitor is linear for both bulk and nanoscale material (G), but a LiCoO ₂ nanoscale material exhibits a linear response while the bulk material shows a voltage plateau (H). After ref ⁵ . 119
Figure 4.3: Diagram of a charged parallel plate capacitor. 119
Figure 4.4: Diagram showing a LiCoO ₂ /Graphite Li-ion battery during charging. ⁹ 120
Figure 4.5: Diagram illustrating an EDLC during charging. ¹⁰ 121

Figure 4.6: Schematic representation of the cyclic voltammograms of a symmetric MnO ₂ /MnO ₂ (A) and asymmetric AC/MnO ₂ electrodes (B) showing the expanded voltage window obtained in the asymmetric case. After ref ¹⁶	123
Figure 4.7: Photo of sonication probe in a test tube containing 50 mg of V ₁₀ and 10 mL of anti-solvent (A) and a schematic showing the complete experimental set up for sonoprecipitation (B).	126
Figure 4.8: A schematic showing the set up for sonofragmentation.	126
Figure 4.9: A schematic showing the ball mill set up using a vortex mixer, test tube and ball bearings.	127
Figure 4.10: Schematic of slurry and electrode preparation.	128
Figure 4.11: Three-electrode experiment set up.	129
Figure 4.12: Three-electrode CV experiment; at 100 mV.s ⁻¹ scan rate, 1 M H ₂ SO ₄ electrolyte, SCE RE, Pt wire CE, with AC WE (electrical double layer), with the oxidation and reduction direction labelled, after ref ³⁶	130
Figure 4.13: Schematic diagram showing a CV and potential profile for how the area under a CV curve is integrated to substitute into Equation 6.1. After ref ³⁷	130
Figure 4.14: Three-electrode CP experiment at 6 A.g ⁻¹ current density, 1 M H ₂ SO ₄ electrolyte, SCE RE, Pt wire CE, AC WE, oxidation and reduction curves and IR drop labelled. After ref ³⁶	131
Figure 4.15: Diagram illustrating a CP dwell period experiment, IR drops indicated by double headed arrows. After ref ³⁸	132
Figure 4.16: Schematic showing the two-electrode set up for an asymmetric supercapacitor.	133
Figure 4.17: Photo of an EL-Cell.	133
Figure 4.18: Ball and stick model of [V ₁₀ O ₂₈] ⁶⁻ , with the three different vanadium environments labelled as V1, V2 and V3.	135
Figure 4.19: ⁵¹ V{ ¹ H} NMR spectra in D ₂ O of V ₁₀ -A Johnson and Murmann, V ₁₀ -B Yerra, V ₁₀ -C Chen EtOH, V ₁₀ -D Chen acetone. All samples were prepared using 10 mg of solid and 0.5 mL of solvent.	136
Figure 4.20: FTIR spectra of V ₁₀ -A Johnson and Murmann, V ₁₀ -B Yerra, V ₁₀ -C Chen EtOH, V ₁₀ -D Chen acetone.	137

List of Figures

Figure 4.21: SEM images of V ₁₀ ; (A) V ₁₀ -A, (B) V ₁₀ -B, (C) V ₁₀ -C, (D) V ₁₀ -D. The scale bar (bottom left) is 5 μ m for all four images.	138
Figure 4.22: Solution CV of 1 mM V ₁₀ in pH 5 0.4 M CH ₃ COONa/H ⁺ buffer, 10 mV.s ⁻¹ scan rate, from 0.60 V to -0.20, 3 cycles.	138
Figure 4.23: TGA of V ₁₀ -A between 30 – 530 °C, heated at a rate of 10.0 °C per minute.	139
Figure 4.24: PXRD pattern of V ₁₀ -A.	139
Figure 4.25: ⁵¹ V{ ¹ H} NMR spectra in D ₂ O of V ₁₀ dried at different temperatures; (A) RT in air, (B) 80 °C, (C) 120 °C, (D) 200 °C under N ₂ . All samples were prepared using 10 mg of solid and 0.5 mL of solvent. There was insoluble material present in samples C and D.	140
Figure 4.26: FTIR spectra of V ₁₀ dried at different temperatures; RT in air, 80 °C, 120 °C, 200 °C under N ₂	141
Figure 4.27: Diagram demonstrating that when you go from a big crystal to smaller ones the portion of crystallite accessible electrochemically gets bigger.	142
Figure 4.28: SEM images of (A) V ₁₀ -B, (B) V ₁₀ -B sonoprecipitation, (C) V ₁₀ -C, (D) V ₁₀ -C sonoprecipitation, (E) V ₁₀ -D and (F) V ₁₀ -D sonoprecipitation.	143
Figure 4.29: SEM images of (A) V ₁₀ -C dried 80 °C, (B) V ₁₀ -C dried 80 °C and ground, (C) V ₁₀ -C dried 80 °C and sonicated, (D) V ₁₀ -C dried 80 °C, ground and sonicated, (E) V ₁₀ -C dried 80 °C, ground, sonicated and ball milled o/n, (F) V ₁₀ -A dried 80 °C and HEBM 61 minutes. Scale bar for A-D 2 μ m, and E and F 5 μ m.	144
Figure 4.30: The second cycles of 5 mV.s ⁻¹ CV of Q3 0.8 mg V ₁₀ , R1 2.2 mg V ₁₀ , S2 1.1 mg V ₁₀ and U2 0.7 mg V ₁₀ . Scanned from 0.7 V to -1.0 V.	146
Figure 4.31: Third cycle of 0.5 A.g ⁻¹ CP of Q3 0.8 mg V ₁₀ , R1 2.2 mg V ₁₀ , S2 1.1 mg V ₁₀ and U2 0.7 mg V ₁₀	146
Figure 4.32: Bar chart summarising the C _{sp} for CV and CP for each series.	147
Figure 4.33: Schematic to show how the thickness of current collector effects the slurry uptake.	147
Figure 4.34: Second cycles of 5 mV.s ⁻¹ CV of AR3 1.4 mg V ₁₀ and AL2 1.3 mg V ₁₀ . Scanned from 0.7 V to -1.0 V.	148
Figure 4.35: Third cycle of 0.5 A.g ⁻¹ CP of AR3 1.4 mg V ₁₀ and AL2 1.3 mg V ₁₀ . ..	148

Figure 4.36: Bar chart summarising the C_{sp} for CV and CP for Series AR and AL.	149
Figure 4.37: Illustration of different loadings of slurry on current collectors.	150
Figure 4.38: Second cycles of 5 mV.s^{-1} CV of AU2 0.7 mg V ₁₀ , AL3 1.1 mg V ₁₀ and AK1 1.8 mg V ₁₀ , AH4 2.2 mg V ₁₀ . Scanned from 0.7 V to -1.0 V.	151
Figure 4.39: Third cycle of 0.5 A.g^{-1} CP of AU2 0.7 mg V ₁₀ , AL3 1.1 mg V ₁₀ and AK1 1.8 mg V ₁₀ , AH4 2.2 mg V ₁₀ .	151
Figure 4.40: C_{sp} calculated from 5 mV.s^{-1} CV plotted against the mass of V ₁₀ on the electrodes.	152
Figure 4.41: C_{sp} calculated from the third cycle of 0.5 A.g^{-1} CP plotted against the mass of V ₁₀ on the electrodes.	153
Figure 4.42: AK1 electrode 1.8 mg V ₁₀ , dwell experiment: 0 A initially for 5 s, 0.5 A.g^{-1} oxidised up to +0.7 V, 0 A held for 60 s, 0.5 A.g^{-1} reduced to -1.0 V, 0 A held for 60 s then, repeated a further four times. IR drop is labelled.	154
Figure 4.43: Three-electrode experiments, 5 mV.s^{-1} CV for V ₁₀ electrode and AC electrode. Pt CE, Ag/AgNO ₃ RE, 1 M LiClO ₄ in PC electrolyte. Scanned from 0.7 V to -1.0 V.	155
Figure 4.44: The third cycles of 1.0 A.g^{-1} GCD at different voltage ranges for an asymmetric supercapacitor.	156
Figure 4.45: The five cycles of 1.0 A.g^{-1} GCD at 3.0 V voltage range for an asymmetric supercapacitor.	156
Figure 4.46: C_{sp} calculated for an asymmetric supercapacitor calculated from the third cycle of 1.0 A.g^{-1} GCD at voltage ranges 1.0-3.0 V.	157
Figure 4.47: Ragone plot for an asymmetric supercapacitor calculated from the third cycle of 1.0 A.g^{-1} GCD at voltage ranges 1.0-3.0 V.	158
Figure 4.48: Expanded view of the dwell period chronopotentiometry experiment.	160
Figure 4.49: Ragone plot adapted from ref ⁵⁹ .	161
Figure 4.50: SEM images of Chen et al. Na ₆ V ₁₀ O ₂₈ .nH ₂ O ⁴³ (a) and Na ₆ V ₁₀ O ₂₈ .nH ₂ O prepared under the same synthetic conditions described by Chen et al. (b).	162
Figure 4.51: The first galvanostatic charge discharge curves of m-KM (microsized KMV), n-KMV (nanoparticulate KMV) and n/m-KMV (1:1 mixture of nanoparticulate	

List of Figures

and mircosized KMV) with the corresponding current densities labelled, adapted from ref ⁶⁶	165
Figure 5.1: Control panel of sonication probe.	201

List of Tables

Table 1.1: Summary of literature electrochemical data for $[\text{SiW}_{12}\text{O}_{40}]^{4-}$	9
Table 1.2: Summary of literature electrochemical data for $[\text{SiMo}_{12}\text{O}_{40}]^{4-}$	13
Table 1.3: Summary of literature electrochemical data for $[\text{PW}_{12}\text{O}_{40}]^{3-}$	14
Table 1.4: Summary of literature electrochemical data for $[\text{PMo}_{12}\text{O}_{40}]^{3-}$	17
Table 1.5: Summary of literature electrochemical data for a variety of Keggin-type POMs.	19
Table 1.6: Table summarising reduced POMs both non-capped and capped. Abbreviations: Synth. = Synthetic, HT = hydrothermal, pz = pyrazine, RT = room temperature, TBA = tetra-n-butylammonium, bpmb = 1,4-bis(pyrazol-1-ylmethyl)benzene, 2-btz = 1-benzyl-1H-(1,2,4)triazole, phen = phenanthroline, NPr ₄ = tetrapropylammonium, bix = 1,4-bis(imidazole-1-ylmethyl)benzene.	23
Table 2.1: Peaks in the $^{31}\text{P}\{^1\text{H}\}$ NMR spectra from reactions between n mole-equivalents of $\text{Na} \text{Hg}$ amalgam and PMo_{12} in MeCN (major peak is in bold for when there is more than one peak present).	38
Table 2.2: Bands in the FTIR spectra of solids isolated from reactions between n mole-equivalents of $\text{Na} \text{Hg}$ amalgam and PMo_{12} in MeCN.	40
Table 2.3: Peaks in $^{31}\text{P}\{^1\text{H}\}$ NMR spectra from reactions between n mole-equivalents of $\text{Na} \text{Hg}$ amalgam and PMo_{12} in PC (major peak is in bold for when there is more than one peak present).	42
Table 2.4: Peaks in the solid-state ^{31}P NMR spectra for the reaction between PMo_{12} and n mole-equivalents of $\text{Na} \text{Hg}$ amalgam in PC.	43
Table 2.5: Peaks in the solid-state ^{23}Na NMR spectra for the reaction between PMo_{12} and n mole-equivalents of $\text{Na} \text{Hg}$ amalgam in PC.	43
Table 2.6: Bands in the FTIR spectra of solids isolated from the reaction between n mole-equivalents of $\text{Na} \text{Hg}$ amalgam and PMo_{12} in PC. t=terminal and b=bridging.	45
Table 2.7: The λ_{max} and molar absorption coefficient (ϵ) values for the UV-Vis spectra of reactions between PMo_{12} and n mole-equivalents of $\text{Na} \text{Hg}$ in PC, $c = 0.25\text{ mM}$, $l = 1\text{ cm}$	46

List of Tables

Table 2.8: Peaks in the $^{31}\text{P}\{^1\text{H}\}$ NMR spectra for the reactions between PMo_{12} and n mole-equivalents of $\text{Na} \text{Hg}$ amalgam in PhCN (major peak is in bold for when there is more than one peak present).	49
Table 2.9: Peaks in $^{31}\text{P}\{^1\text{H}\}$ NMR spectra for the reactions between PMo_{12} and n mole-equivalents of $\text{Li} \text{Hg}$ amalgam in MeCN (major peak is in bold for when there is more than one peak present).	50
Table 2.10: Bands in the FTIR spectra for the products isolated from the reactions between PMo_{12} and n mole-equivalents of $\text{Li} \text{Hg}$ amalgam in MeCN	51
Table 2.11: Peaks in the $^{31}\text{P}\{^1\text{H}\}$ NMR spectra for the reactions between PMo_{12} and n mole-equivalents of $\text{Li} \text{Hg}$ amalgam in PC (major peak is in bold for when there is more than one peak present).	53
Table 2.12: Peaks in the solid-state ^{31}P NMR spectra for solids isolated from the reactions between PMo_{12} and n mole-equivalents of $\text{Li} \text{Hg}$ amalgam in PC	55
Table 2.13: Peaks in the solid-state ^{7}Li NMR spectra for solids isolated from the reactions between PMo_{12} and n mole-equivalents of $\text{Li} \text{Hg}$ amalgam in PC	56
Table 2.14: Bands in the FTIR spectra of solids isolated from the reactions between PMo_{12} and n mole-equivalents of $\text{Li} \text{Hg}$ amalgam in PC	57
Table 2.15: The λ_{max} and molar absorption coefficient (ϵ) values for the UV-Vis spectra of reactions between PMo_{12} and n mole-equivalents of $\text{Li} \text{Hg}$ in PC , $c = 0.25$ mM, $l = 1$ cm.	58
Table 2.16: Peaks in the $^{51}\text{V}\{^1\text{H}\}$ NMR spectra for the reactions between V_{13} and n mole-equivalents of $\text{Na} \text{Hg}$ amalgam in MeCN	67
Table 2.17: Bands in the FTIR spectra for solids isolated from the reactions between V_{13} and n equivalents of $\text{Na} \text{Hg}$ amalgam in MeCN	68
Table 2.18: Peaks in the $^{51}\text{V}\{^1\text{H}\}$ NMR spectra for the reactions between V_{13} and n mole-equivalents of $\text{Na} \text{Hg}$ amalgam in PC	70
Table 2.19: Bands in the FTIR spectra for the solids isolated from the reactions between V_{13} and n mole-equivalents of $\text{Na} \text{Hg}$ amalgam in PC	71
Table 2.20: Peaks in $^{51}\text{V}\{^1\text{H}\}$ NMR spectra for the reactions between V_{13} and n mole-equivalents of $\text{Li} \text{Hg}$ amalgam in MeCN	72
Table 2.21: Bands in the FTIR spectra of the solids isolated from the reactions between V_{13} and n mole-equivalents of $\text{Li} \text{Hg}$ amalgam in MeCN	73

Table 2.22: Peaks in $^{51}\text{V}\{^1\text{H}\}$ NMR spectra for the reaction between V_{13} and n mole-equivalents of $\text{Li} \text{Hg}$ in PC.	74
Table 2.23: Bands in the FTIR spectra of solids isolated from the reactions between V_{13} and n mole-equivalents of $\text{Li} \text{Hg}$ in PC.	75
Table 2.24: Peaks in $^{31}\text{P}\{^1\text{H}\}$ NMR spectra from the reactions between PMo_{12} and n mole-equivalents of KC_8 in MeCN.	78
Table 2.25: Peaks in $^{31}\text{P}\{^1\text{H}\}$ NMR spectra from the reactions between PMo_{12} and n mole-equivalents of $\text{K}^+\text{PhCN}^- \bullet$ in PhCN.	79
Table 4.1: Peaks in the $^{51}\text{V}\{^1\text{H}\}$ NMR spectra for the four V_{10} preparations.	136
Table 4.2: Bands in the FTIR spectra of the four V_{10} preparations.	137
Table 4.3: Summary of all current collectors investigated as part of the electrode preparation study. ^a manufactured by Spectracarb TM , ^b manufactured by Toray TM	145
Table 4.4: Table summarising the C_{sp} for CV and CP for each series.	147
Table 4.5: Summary of C_{sp} for CV and CP for Series AR and AL.	149
Table 4.6: Summary of the C_{sp} for the different slurry loadings.	152
Table 4.7: Coulombic efficiency calculated for the five charge/discharge cycles at 1.0 A.g ⁻¹ for 3.0 V window.	157
Table 4.8: Results for asymmetric supercapacitor calculated from the third cycle of 1.0 A.g ⁻¹ GCD at voltage ranges 1.0-3.0 V.	157
Table 4.9: Literature results of POM containing batteries.	163
Table 5.1: Materials used in Chapter 2 and their suppliers.	177
Table 5.2: Solvents and their specific drying agents for use in stills and ampoules.	178
Table 5.3: The reactions between PMo_{12} and n mole-equivalents of $\text{Na} \text{Hg}$ amalgam in MeCN.	179
Table 5.4: Peaks in $^{31}\text{P}\{^1\text{H}\}$ NMR spectra for the reactions between PMo_{12} and n mole-equivalents of $\text{Na} \text{Hg}$ amalgam in MeCN.	179
Table 5.5: Bands in FTIR spectra for solids isolated from the reactions between PMo_{12} and n mole-equivalents of $\text{Na} \text{Hg}$ amalgam in MeCN.	180

List of Tables

Table 5.6: The reactions between PMo_{12} and n mole-equivalents of $\text{Na} \text{Hg}$ amalgam in PC.	180
Table 5.7: Peaks in $^{31}\text{P}\{^1\text{H}\}$ NMR spectra for the reactions between PMo_{12} and n mole-equivalents of $\text{Na} \text{Hg}$ amalgam in PC.	181
Table 5.8: Peaks in the ^{31}P MAS NMR spectra for the reactions between PMo_{12} and n mole-equivalents of $\text{Na} \text{Hg}$ amalgam in PC. Abbreviations: D1 = recycle delay, P1 = pulse speed, RG = receiver gain, NS = number of scans.	181
Table 5.9: Peaks in the ^{23}Na MAS NMR spectra for the reactions between PMo_{12} and n mole-equivalents of $\text{Na} \text{Hg}$ amalgam in PC. Abbreviations: D1 = recycle delay, P1 = pulse speed, RG = receiver gain, NS = number of scans.	181
Table 5.10: Bands in FTIR spectra for solids isolated from the reactions between PMo_{12} and n mole-equivalents of $\text{Na} \text{Hg}$ amalgam in PC.	182
Table 5.11: The reactions between PMo_{12} and n mole-equivalents of $\text{Na} \text{Hg}$ amalgam in PhCN.	182
Table 5.12: Peaks in the $^{31}\text{P}\{^1\text{H}\}$ NMR spectra for the reactions between PMo_{12} and n mole-equivalents of $\text{Na} \text{Hg}$ amalgam in PhCN.	183
Table 5.13: The reactions between PMo_{12} and n mole-equivalents of $\text{Li} \text{Hg}$ amalgam in MeCN.	183
Table 5.14: Peaks in $^{31}\text{P}\{^1\text{H}\}$ NMR spectra for the reactions between PMo_{12} and n mole-equivalents of $\text{Li} \text{Hg}$ amalgam in MeCN.	183
Table 5.15: Bands in the FTIR spectra for solids isolated from the reactions between PMo_{12} and n mole-equivalents of $\text{Li} \text{Hg}$ amalgam in MeCN.	184
Table 5.16: The reactions between PMo_{12} and n mole-equivalents of $\text{Li} \text{Hg}$ amalgam in PC.	184
Table 5.17: Peaks in the $^{31}\text{P}\{^1\text{H}\}$ NMR spectra for the reactions between PMo_{12} and n mole-equivalents of $\text{Li} \text{Hg}$ amalgam in PC.	185
Table 5.18: Peaks in the ^{31}P MAS NMR spectra for solids isolated from the reactions between PMo_{12} and n mole-equivalents of $\text{Li} \text{Hg}$ amalgam in PC. Abbreviations: D1 = recycle delay, P1 = pulse speed, RG = receiver gain, NS = number of scans.	185
Table 5.19: Peaks in the ^7Li MAS NMR spectra for solids isolated from the reactions between PMo_{12} and n mole-equivalents of $\text{Li} \text{Hg}$ amalgam in PC. Abbreviations: D1 = recycle delay, P1 = pulse speed, RG = receiver gain, NS = number of scans.	185

Table 5.20: Bands in the FTIR spectra for solids isolated from the reactions between PMo ₁₂ and <i>n</i> mole-equivalents of Li Hg amalgam in PC.	186
Table 5.21: The reactions between (TBA) ₃ [V ₁₃ O ₃₄] and <i>n</i> mole-equivalents of Na Hg in MeCN.	188
Table 5.22: Peaks in the ⁵¹ V{ ¹ H} NMR spectra for the reactions between (TBA) ₃ [V ₁₃ O ₃₄] and <i>n</i> mole-equivalents of Na Hg in MeCN.	188
Table 5.23: Bands in the FTIR spectra for solids isolated from the reactions between (TBA) ₃ [V ₁₃ O ₃₄] and <i>n</i> mole-equivalents of Na Hg in MeCN.	189
Table 5.24: The reactions between (TBA) ₃ [V ₁₃ O ₃₄] and <i>n</i> mole-equivalents of Na Hg in PC.	189
Table 5.25: Peaks in the ⁵¹ V{ ¹ H} NMR spectra for the reactions between (TBA) ₃ [V ₁₃ O ₃₄] and <i>n</i> mole-equivalents of Na Hg in PC.	190
Table 5.26: Bands in the FTIR spectra for solids isolated from the reactions between (TBA) ₃ [V ₁₃ O ₃₄] and <i>n</i> mole-equivalents of Na Hg in PC.	190
Table 5.27: The reactions between (TBA) ₃ [V ₁₃ O ₃₄] and <i>n</i> mole-equivalents of Li Hg in MeCN.	191
Table 5.28: Peaks in the ⁵¹ V{ ¹ H} NMR spectra for the reactions between (TBA) ₃ [V ₁₃ O ₃₄] and <i>n</i> mole-equivalents of Li Hg in MeCN.	191
Table 5.29: Bands in the FTIR spectra for solids isolated from the reactions between (TBA) ₃ [V ₁₃ O ₃₄] and <i>n</i> mole-equivalents of Li Hg in MeCN.	192
Table 5.30: The reactions between (TBA) ₃ [V ₁₃ O ₃₄] and <i>n</i> mole-equivalents of Li Hg in PC.	192
Table 5.31: Peaks in the ⁵¹ V{ ¹ H} NMR spectra for the reactions between (TBA) ₃ [V ₁₃ O ₃₄] and <i>n</i> mole-equivalents of Li Hg in PC.	193
Table 5.32: Bands in the FTIR spectra for solids isolated from the reactions between (TBA) ₃ [V ₁₃ O ₃₄] and <i>n</i> mole-equivalents of Li Hg in PC.	193
Table 5.33: The reactions between (TBA) ₃ [PMo ₁₂ O ₄₀] and <i>n</i> mole-equivalents of KC ₈ in MeCN.	194
Table 5.34: Peaks in the ³¹ P{ ¹ H} NMR spectra for the reactions between (TBA) ₃ [PMo ₁₂ O ₄₀] and <i>n</i> mole-equivalents of KC ₈ in MeCN.	194

List of Tables

Table 5.35: The reactions between $(TBA)_3[PMo_{12}O_{40}]$ and n mole-equivalents of $K^+PhCN^- \bullet$ in PhCN.	195
Table 5.36: Peaks in the $^{31}P\{^1H\}$ NMR spectra for the reactions between $(TBA)_3[PMo_{12}O_{40}]$ and n mole-equivalents of $K^+PhCN^- \bullet$	195
Table 5.37: Materials used in Chapter 3 and their suppliers.	195
Table 5.38: Materials used in Chapter 4 and their suppliers.	198
Table 5.39: Current collectors.	199
Table A1.1: Crystal data and structure refinement for $(TBA)_2[PMo_{12}O_{40}Sb_2]$	207
Table A1.2: Fractional Atomic Coordinates ($\times 10^4$) and Equivalent Isotropic Displacement Parameters ($\text{\AA}^2 \times 10^3$). U_{eq} is defined as 1/3 of the trace of the orthogonalised U_{ij} tensor, for $(TBA)_2[PMo_{12}O_{40}Sb_2]$	207
Table A1.3: Anisotropic Displacement Parameters ($\text{\AA}^2 \times 10^3$). The Anisotropic displacement factor exponent takes the form: $-2\pi^2[h^2a^*{}^2U_{11} + 2hka^*b^*U_{12} + \dots]$, for $(TBA)_2[PMo_{12}O_{40}Sb_2]$	208
Table A1.4: Bond lengths for $(TBA)_2[PMo_{12}O_{40}Sb_2]$	208
Table A1.5: Bond Angles for $(TBA)_2[PMo_{12}O_{40}Sb_2]$	208
Table A1.6: Hydrogen Atom Coordinates ($\text{\AA} \times 10^4$) and Isotropic Displacement Parameters ($\text{\AA}^2 \times 10^3$) for $(TBA)_2[PMo_{12}O_{40}Sb_2]$	210
Table A1.7: Atomic Occupancy for $(TBA)_2[PMo_{12}O_{40}Sb_2]$	210
Table A1.8: Crystal data and structure refinement for $(TBA)_3[PMo_{12}O_{40}Sb_2]$	210
Table A1.9: Fractional Atomic Coordinates ($\times 10^4$) and Equivalent Isotropic Displacement Parameters ($\text{\AA}^2 \times 10^3$). U_{eq} is defined as 1/3 of the trace of the orthogonalised U_{ij} tensor, for $(TBA)_3[PMo_{12}O_{40}Sb_2]$	211
Table A1.10: Anisotropic Displacement Parameters ($\text{\AA}^2 \times 10^3$). The Anisotropic displacement factor exponent takes the form: $-2\pi^2[h^2a^*{}^2U_{11} + 2hka^*b^*U_{12} + \dots]$, for $(TBA)_3[PMo_{12}O_{40}Sb_2]$	214
Table A1.11: Bond Lengths for $(TBA)_3[PMo_{12}O_{40}Sb_2]$	218
Table A1.12: Bond Angles for $(TBA)_3[PMo_{12}O_{40}Sb_2]$	220

Table A1.13: Hydrogen Atom Coordinates ($\text{\AA} \times 10^4$) and Isotropic Displacement Parameters ($\text{\AA}^2 \times 10^3$) for $(\text{TBA})_3[\text{PMo}_{12}\text{O}_{40}\text{Sb}_2]$	227
Table A1.14: Atomic Occupancy for $(\text{TBA})_3[\text{PMo}_{12}\text{O}_{40}\text{Sb}_2]$	230
Table A1.15: Crystal data and structure refinement for $(\text{TBA})_3[\text{PMo}_{12}\text{O}_{40}\{\text{Bi}(\text{dmso})_4\}_2]$	232
Table A1.16: Fractional Atomic Coordinates ($\times 10^4$) and Equivalent Isotropic Displacement Parameters ($\text{\AA}^2 \times 10^3$). U_{eq} is defined as 1/3 of the trace of the orthogonalised U_{IJ} tensor, for $(\text{TBA})_3[\text{PMo}_{12}\text{O}_{40}\{\text{Bi}(\text{dmso})_4\}_2]$	232
Table A1.17: Anisotropic Displacement Parameters ($\text{\AA}^2 \times 10^3$). The Anisotropic displacement factor exponent takes the form: $-2\pi^2[h^2a^*{}^2U_{11}+2hka^*b^*U_{12}+\dots]$, for $(\text{TBA})_3[\text{PMo}_{12}\text{O}_{40}\{\text{Bi}(\text{dmso})_4\}_2]$	233
Table A1.18: Bond Lengths for $(\text{TBA})_3[\text{PMo}_{12}\text{O}_{40}\{\text{Bi}(\text{dmso})_4\}_2]$	234
Table A1.19: Bond Angles for $(\text{TBA})_3[\text{PMo}_{12}\text{O}_{40}\{\text{Bi}(\text{dmso})_4\}_2]$	235
Table A1.20: Torsion Angles for $(\text{TBA})_3[\text{PMo}_{12}\text{O}_{40}\{\text{Bi}(\text{dmso})_4\}_2]$	236
Table A1.21: Hydrogen Atom Coordinates ($\text{\AA} \times 10^4$) and Isotropic Displacement Parameters ($\text{\AA}^2 \times 10^3$) for $(\text{TBA})_3[\text{PMo}_{12}\text{O}_{40}\{\text{Bi}(\text{dmso})_4\}_2]$	237
Table A1.22: Atomic Occupancy for $(\text{TBA})_3[\text{PMo}_{12}\text{O}_{40}\{\text{Bi}(\text{dmso})_4\}_2]$	238
Table A1.23: Solvent masks information for $(\text{TBA})_3[\text{PMo}_{12}\text{O}_{40}\{\text{Bi}(\text{dmso})_4\}_2]$	238
Table A1.24: Crystal data and structure refinement for $(\text{TBA})_3[\text{PMo}_{12}\text{O}_{40}\{\text{Zn}(\text{dmso})_2\}]$	238
Table A1.25: Fractional Atomic Coordinates ($\times 10^4$) and Equivalent Isotropic Displacement Parameters ($\text{\AA}^2 \times 10^3$). U_{eq} is defined as 1/3 of the trace of the orthogonalised U_{IJ} tensor, for $(\text{TBA})_3[\text{PMo}_{12}\text{O}_{40}\{\text{Zn}(\text{dmso})_2\}]$	239
Table A1.26: Anisotropic Displacement Parameters ($\text{\AA}^2 \times 10^3$). The Anisotropic displacement factor exponent takes the form: $-2\pi^2[h^2a^*{}^2U_{11}+2hka^*b^*U_{12}+\dots]$ for $(\text{TBA})_3[\text{PMo}_{12}\text{O}_{40}\{\text{Zn}(\text{dmso})_2\}]$	243
Table A1.27: Bond Lengths for $(\text{TBA})_3[\text{PMo}_{12}\text{O}_{40}\{\text{Zn}(\text{dmso})_2\}]$	248
Table A1.28: Bond Angles for $(\text{TBA})_3[\text{PMo}_{12}\text{O}_{40}\{\text{Zn}(\text{dmso})_2\}]$	250

List of Tables

Table A1.29: Hydrogen Atom Coordinates ($\text{\AA} \times 10^4$) and Isotropic Displacement Parameters ($\text{\AA}^2 \times 10^3$) for $(\text{TBA})_3[\text{PMo}_{12}\text{O}_{40}\{\text{Zn}(\text{dmso})_2\}]$	257
Table A1.30: Atomic Occupancy for $(\text{TBA})_3[\text{PMo}_{12}\text{O}_{40}\{\text{Zn}(\text{dmso})_2\}]$	262

Chapter 1

Introduction

Chapter 1 Introduction

1.1. Introduction

Electron-rich polyoxometalates (POMs) may be formed by the addition of multiple electrons to the fully oxidised POMs, which increases their electron density and in turn their basicity.¹ The resulting reduced POMs can be stabilised by protonation or by the addition of electrophiles such as metal ions (M^{n+}) as capping groups.¹ The phosphomolybdate Keggin-type POMs have been found to have more positive reduction potentials than the phosphotungstates, and $[PMo_{12}O_{40}]^{3-}$ has been found to be a versatile electron acceptor.² POM reduction has been studied extensively using electrochemical techniques,² but not as much research has been undertaken for the chemical reduction of POMs and in particular the preparation of capped reduced POM species.¹ The majority of characterised examples have been obtained from uncontrolled hydrothermal methods.³⁻⁵ Errington *et al.* developed a rational method in which the degree of reduction and the stoichiometry of the reactions may be controlled in the synthesis of target compounds.⁶ This study focuses on the controlled preparation and characterisation of a series of capped reduced POMs.

The ability of POMs to reversibly accept multiple electrons has been exploited for energy storage applications and in 2012 Awaga *et al.* investigated the use of the TBA salt of $[PMo_{12}O_{40}]^{3-}$ as the active material in the cathode of a lithium-ion battery.⁷ In-situ XAFS was used to probe the battery electrode and they proposed that the POM could reversibly accept twenty-four electrons during charging and discharging of the battery. This raised the question of whether or not the “super-reduced” state of $[PMo_{12}O_{40}]^{3-}$ could be isolated via chemical reduction. The characterisation of the isolated reduced species prepared in several solvents are investigated.

In the past several years there has been a lot of interest in developing supercapacitors for use as energy storage devices.^{8, 9} This is because supercapacitors have higher energy density than conventional capacitors and higher power density than batteries.^{8, 9} Transition metal oxides are promising electrode materials for supercapacitors, but RuO_2 is expensive so is not suitable for widespread use. POMs share many properties with transition metal oxides, including their redox properties, which makes them potential candidates for use in energy storage as an alternative to RuO_2 . In 1998 Yamada and Goodenough investigated

Chapter 1 Introduction

the Keggin-type POM, phosphomolybdic acid, $H_3[PMo_{12}O_{40}]$ as electrode material for an asymmetric supercapacitor, which also used a RuO_2 electrode. They found that the energy density was lower than for a symmetric RuO_2 device, however the energy per unit cost was higher.¹⁰ In 2014 Chen *et al.* investigated the isopolyanion $Na_6V_{10}O_{28}$ as a material in supercapacitor electrodes, and found that the electrode had high specific capacitance and, when part of a device, high power density.¹¹

1.2. Aims

The first part of this thesis addresses POM reduction with associated capping by metal cations. The aims of this part of the project were:

1. To explore the chemical reduction of POMs in non-aqueous solvents and compare with literature reports of electrochemical experiments
2. To characterise products of $[PMo_{12}O_{40}]^{3-}$ “super-reduction”
3. To synthesise and characterise capped reduced POMs

The second part of this thesis describes investigations into the use of $Na_6V_{10}O_{28} \cdot nH_2O$ in supercapacitor electrodes. The aims were:

4. To optimise the specific capacitance of decavanadate cathodes
5. To investigate the energy density and power density of an asymmetric supercapacitor

1.3. Thesis Organisation

This thesis is divided in to 5 chapters in two separate parts. Part 1 concerns the reduction of polyoxometalates and contains Chapters 2 and 3. Part 2 focuses on the use of $Na_6V_{10}O_{28}$ in supercapacitors and contains Chapter 4. Experimental details for Chapters 2, 3 and 4 are given in Chapter 5.

Part 1: Chapter 2 discusses the results from various reduction reactions of POMs. Chapter 3 focuses on the capping of reduced $(TBA)_3[PMo_{12}O_{40}]$.

Part 2: Chapter 4 describes $Na_6V_{10}O_{28}$ containing supercapacitors. This Chapter introduces the background of energy storage devices and POMs in energy storage, as well as the materials, methods and the various characterisation techniques

employed in the research. An overview of the results from the sample preparation and electrochemical characterisation are also described and discussed.

1.4. Background to Study

Polyoxometalates (POMs) are a class of metal oxides, the most common structure types are named after those who discovered them; e.g. Lindqvist, Keggin and Wells-Dawson.¹² The Lindqvist structure (Figure 1.1A) is a hexametalate POM with the general formula, $[M_6O_{19}]^{n-}$, there are many examples of Lindqvist POMs including where M = Mo, W, Nb and Ta, as well as mixed-metal derivatives e.g. $[V_2W_4O_{19}]^{4-}$ and $[Nb_3W_3O_{19}]^{5-}$.¹² The heteropolyanion Keggin structure (Figure 1.1B) has the general formula $[XM_{12}O_{40}]^{n-}$, where X is P, Si, As or Ge and M is Mo, W, V, Ta, Nb, or mixtures of these transition metals.¹² The Keggin structure is able to form lacunary polyanions by the loss of one or more metal atoms to give $[XM_{11}O_{39}]^{n-}$ or $[XM_9O_{34}]^{n-}$. Wells-Dawson POMs form by the dimerisation of the latter lacunary polyanions, thus they have the general formula $[X_2M_{18}O_{64}]^{n-}$ (Figure 1.1C).¹²

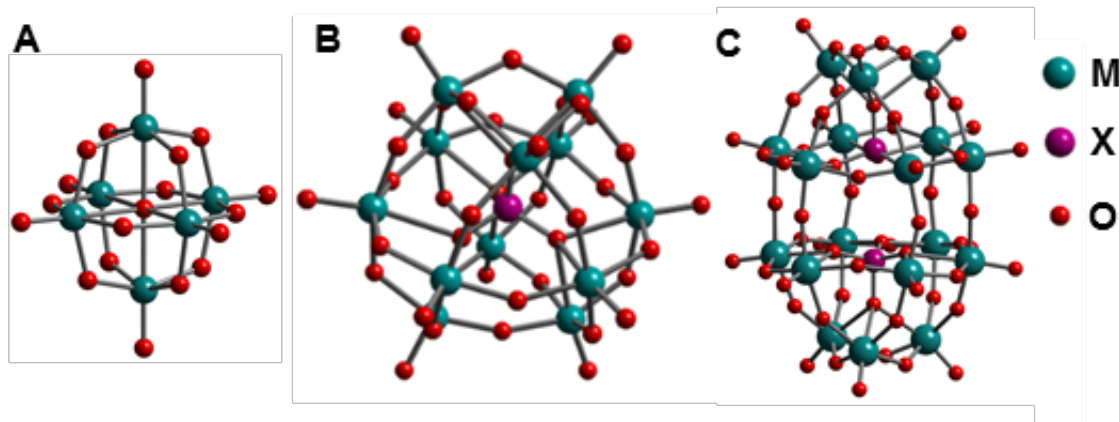


Figure 1.1 Ball-and-stick representations of $[M_6O_{19}]^{n-}$ Lindqvist structure (A), $[XM_{12}O_{40}]^{n-}$ Keggin structure (B) and $[X_2M_{18}O_{64}]^{n-}$ Wells-Dawson structure (C).

1.4.1 Keggin Structure

The Keggin structure has been briefly described above and this section will go into more detail, as the Keggin-type POM is of greater focus throughout this thesis. The heteropolyanion Keggin structure consists of the general formula $[XM_{12}O_{40}]^{n-}$. The heteroatom in the centre of the Keggin structure is bonded to four oxygen atoms to form $[XO_4]^{n-}$, and this tetrahedron is bonded to twelve MO_6 octahedron units. The MO_6 octahedral units form four triads with the formula $[M_3O_{13}]$, these four triads surround the central heteroatom to give the general formula $[M_{12}O_{36}][XO_4]$. The

Chapter 1 Introduction

Keggin structure forms isomers, as discovered by Baker and Figgis, by the rotation of one or more of the triads by 60° as shown in Figure 1.2, there are five known isomers; α , β , γ , δ and ε .¹³

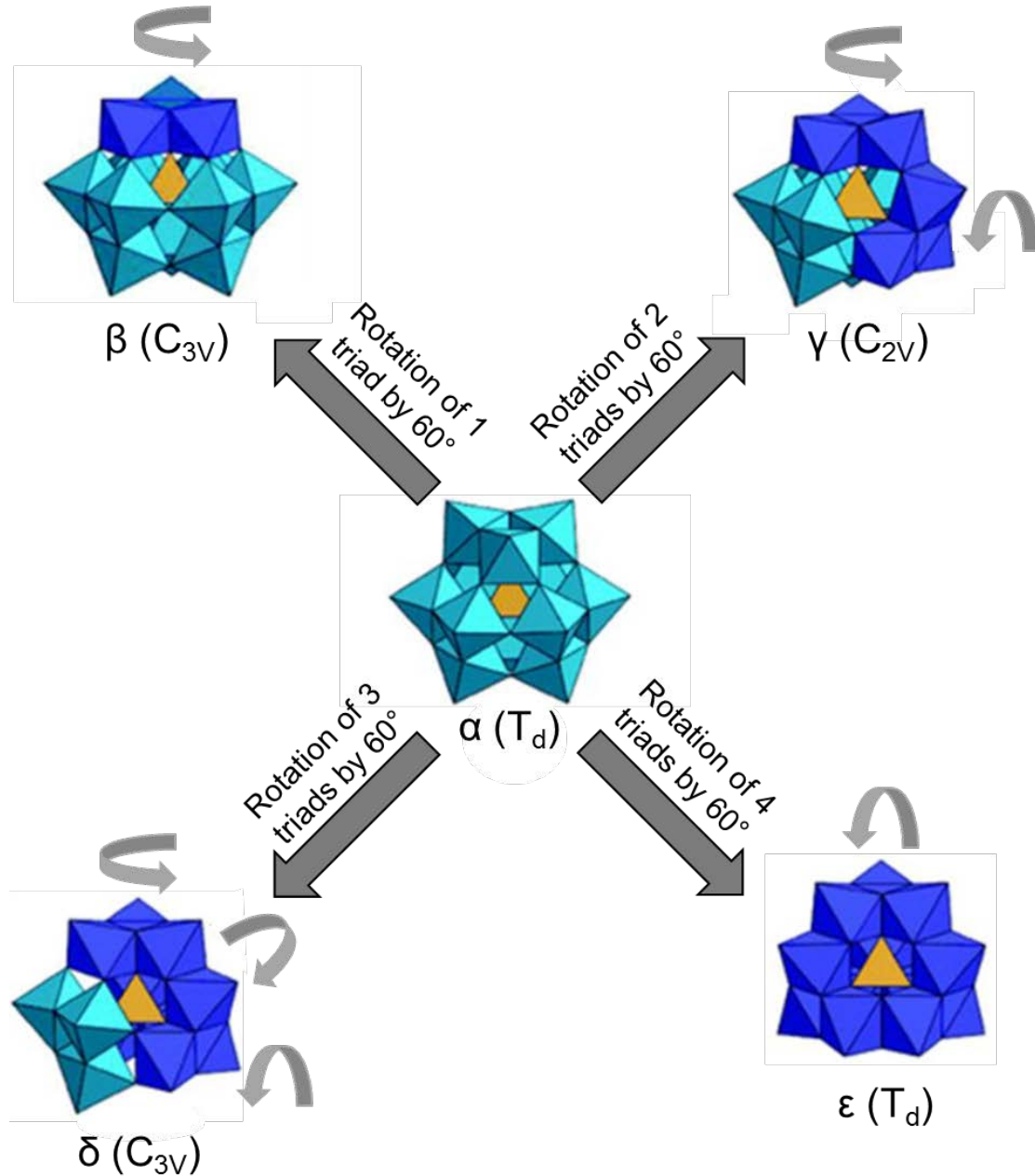
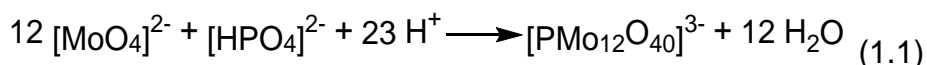


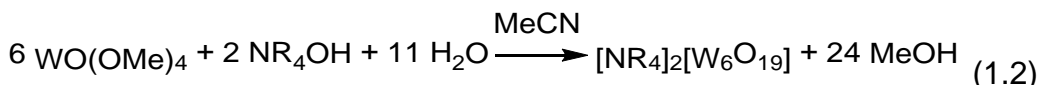
Figure 1.2 Baker-Figgis isomers of $[PM_{12}O_{40}]^{3-}$, $M = Mo$ or W .

1.4.2 POM Synthesis

POMs can be synthesised following both aqueous and non-aqueous procedures and the more common aqueous methods usually involve the acidification of simple oxoanions as shown in Equation 1.1.¹²



There are examples of the synthesis of POMs in non-aqueous solvents, for example the Lindqvist type POM, $[\text{W}_6\text{O}_{19}]^{2-}$ can be synthesised in acetonitrile, using an organic base and hydrolysing the metal oxoalkokide as shown in Equation 1.2.¹⁴



The reactivity of POMs can be studied in both aqueous and non-aqueous conditions depending on the counter cation and the nature and sensitivity of the products.

1.4.3 Electrochemical Studies

POMs have interesting redox properties as they have many stable redox states, which can be tuned by changing the heteroatom, and/or the metal addenda atoms. They can also undergo multiple reversible electron transfers with little change to their structures.²

POMs containing metals with a single terminal M=O are generally readily reduced and reduction can be studied by electrochemical methods, particularly cyclic voltammetry (CV) and before the development of CV, polarography. There is extensive literature concerning the electrochemical properties of POMs, including three detailed reviews. An initial review of the electrochemical study of POMs using polarography was presented by Souchay in 1965,¹⁵ which discussed the electrochemical properties of a range of isopolyanions and heteropolyanions. A later review by Sadakane and Steckhan reviewed the electrochemical properties of heteropolyanion POMs, Keggin- and Dawson-type, with regard to their use as electrocatalysts.² A more recent review by Gumerova and Rompel discussed in detail the electron-rich isopolyanion and heteropolyanion POMs, Lindqvist-, Keggin- and Dawson-type, as well as many others.¹ This literature review will focus on

Keggin-type POMs. The electrolyte composition (aqueous or organic), the presence of acid, and the nature of cation, heteroatoms and addenda atoms all have significant effects on the electrochemistry of Keggin-type POMs.

1.4.3.1 $[\text{SiW}_{12}\text{O}_{40}]^{4-}$

An example of a CV of $\text{H}_4\text{SiW}_{12}\text{O}_{40}$ is shown in Figure 1.3 and a summary of electrochemical data for $[\text{SiW}_{12}\text{O}_{40}]^{4-}$ from the literature is contained in Table 1.1.

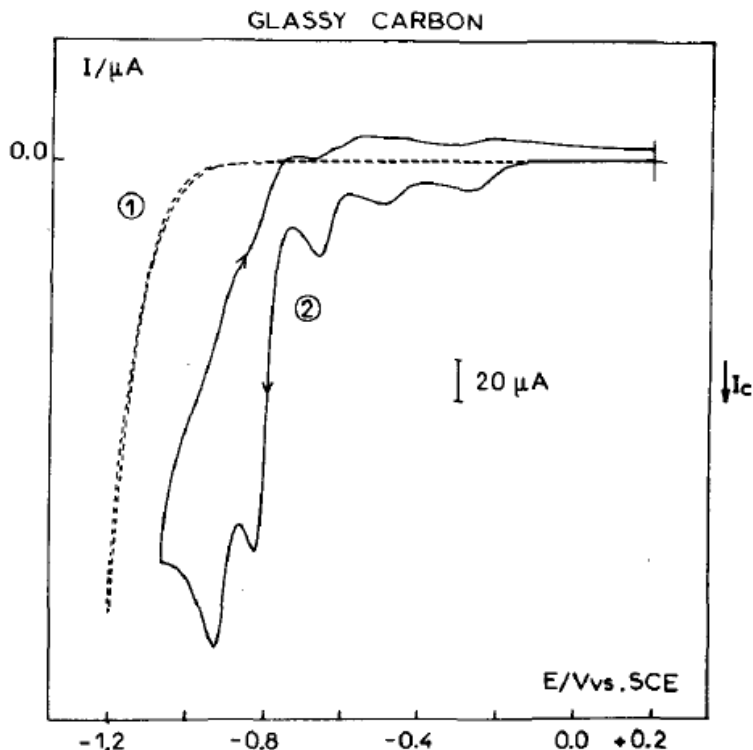


Figure 1.3 CV of a 1 mM solution of $\text{H}_4\text{SiW}_{12}\text{O}_{40}$ in 0.5 M H_2SO_4 (aq), glassy carbon WE, SCE RE, Pt CE, 100 mV/s scan rate. Curve 1 is background current in the absence of $\text{H}_4\text{SiW}_{12}\text{O}_{40}$ and curve 2 is the first voltammetric run in the presence of $\text{H}_4\text{SiW}_{12}\text{O}_{40}$. After ref ¹⁶.

Year ^{REF}	POM	Electrochemical method	Electrochemistry data	
			Reduction peak/ V	# electrons
1966 ¹⁷	K ₄ SiW ₁₂	Polarography, 0.5 mM POM in 1 M H ₂ SO ₄ (aq), SCE RE	-0.228, -0.433	1:1
1967 ¹⁸	H ₄ SiW ₁₂	Polarography, 0.5 M HCl (aq), Dropping mercury electrode	-0.240, -0.480, -0.600	1:1:2
1971 ^{19, 20}	H ₄ SiW ₁₂	Polarography, Acid	-0.265, -0.490, -0.655, -0.830, -0.930	1:1:2:8:12
1985 ¹⁶	H ₄ SiW ₁₂	CV, 1 mM POM in 0.5 M H ₂ SO ₄ (aq), SCE RE, Pt CE, GC WE, 100 mV/s	-0.265, -0.490, -0.655, -0.830, -0.930	1:1:2:8:12
1987 ²¹	H ₄ SiW ₁₂	CV, 1 mM POM in 1 M HClO ₄ (aq), SCE RE, Pt CE, GC WE, 100 mV/s	-0.220, -0.420, -0.580, -0.740, -0.850	1:1:2:8:12
1987 ²¹	K ₄ SiW ₁₂	CV, 1 mM POM in DMF + 0.1 M LiClO ₄ , SCE RE, Pt CE, GC WE, 100 mV/s	-0.840, -1.060, -1.320, -1.780, -1.890	1:1:1.4
1987 ²²	H ₄ SiW ₁₂	CV, 1 mM POM in 0.1 M DMF, SCE RE, Pt gauze CE, GC WE, 100 mV/s	-0.660, -0.815, -1.065	

Table 1.1 Summary of literature electrochemical data for [SiW₁₂O₄₀]⁴⁻.

In 1967 Souchay *et al.* investigated the electrochemical properties of H₄[SiW₁₂O₄₀] (H₄SiW₁₂) in 0.5 M HCl using polarography.¹⁸ The polarography shows three reduction waves with a ratio of 1:1:2 electrons. Controlled potential electrolysis (CPE) allowed the isolation of one- and two-electron reduced H₄SiW₁₂, but the isolation of four-electron reduced H₄SiW₁₂ was not possible due to the instability of the compound in acid.¹⁸ In 1971, Hervé investigated H₄SiW₁₂ in acidic aqueous solution using polarography and identified five redox waves in the approximate ratio of 1:1:2:8:12 electron transfer steps.^{19, 20}

Keita and Nadjo have investigated extensively the electrochemistry of [SiW₁₂O₄₀]⁴⁻ as both the acid and potassium salt with varying electrolyte compositions, in both aqueous and organic solvents. In 1985, they measured the CV of H₄SiW₁₂ in 0.5 M H₂SO₄ and found five reduction waves in agreement with results from polarography, where the first three waves were reversible and the last two waves were irreversible.

Chapter 1 Introduction

¹⁶ In 1987, Keita and Nadjo investigated $\text{H}_4\text{SiW}_{12}$ and $\text{K}_4[\text{SiW}_{12}\text{O}_{40}]$ ($\text{K}_4\text{SiW}_{12}$) in water and DMF.²²⁻²⁴ The CV of $\text{H}_4\text{SiW}_{12}$ in water with increasing concentrations of HClO_4 , from 1 M HClO_4 to 5 M HClO_4 was investigated and the effects on the reduction peak potentials for the five peaks are shown in Figure 1.4. The concentration increase from 1 M to 5 M HClO_4 shows that the first reduction peak moves to more negative potentials and the other four peaks move to less negative potentials. After the addition of 4 M HClO_4 the first two redox waves begin to merge. As the concentration of HClO_4 is increased further to 6 and 7 M, the first two redox waves have completely merged and the peak potential is slightly more negative than the first redox wave in 1 M HClO_4 .

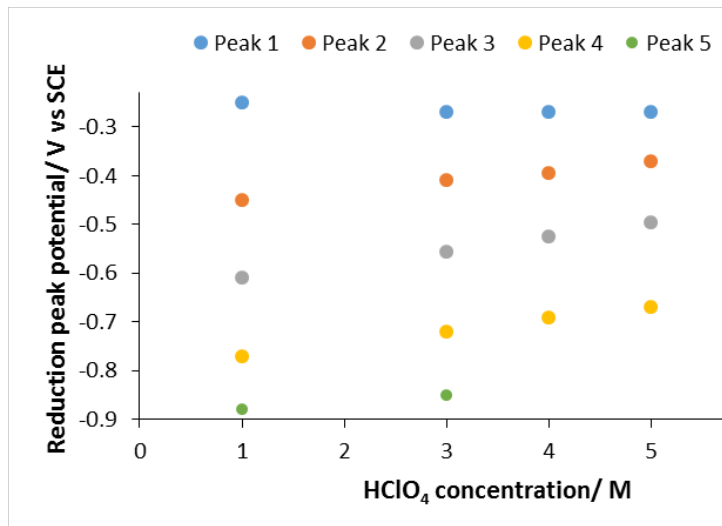


Figure 1.4 The reduction peak potentials in the CV of 1 mM $\text{H}_4\text{SiW}_{12}\text{O}_{40}$ in 0.1 M LiClO_4 in water solution, with increasing HClO_4 concentration. After ref²².

The CVs of $\text{H}_4\text{SiW}_{12}$ and $\text{K}_4\text{SiW}_{12}$ in 0.1 M LiClO_4 in DMF show that, upon addition of HClO_4 to the $\text{K}_4\text{SiW}_{12}$ solution an extra redox wave appears at a more positive potential than the first redox wave in the absence of acid.²² The peaks merge and become multi-electron with more H^+ . Figure 1.5 shows that as the concentration of HClO_4 added to the $\text{K}_4\text{SiW}_{12}$ solution increases, the potential of the first three reduction peaks shift to less negative potentials.

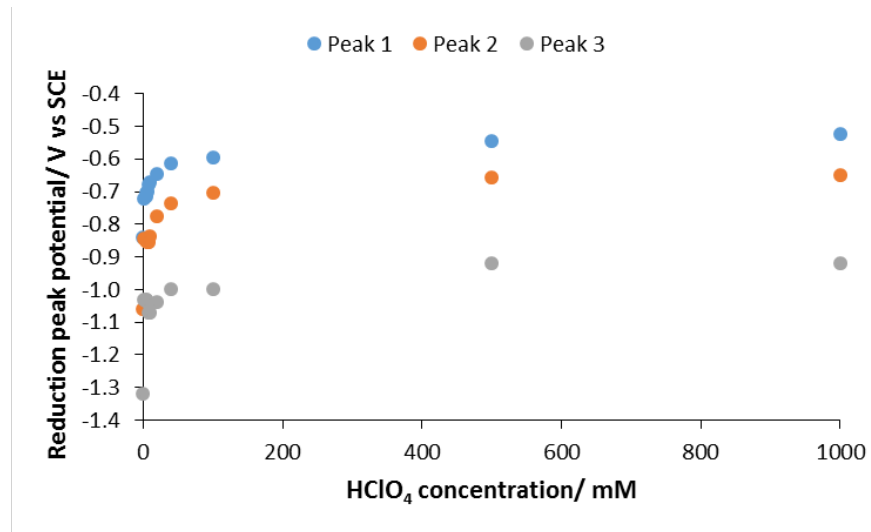


Figure 1.5 The reduction peak potentials in the CV of 1 mM $\text{K}_4\text{SiW}_{12}\text{O}_{40}$ in 0.1 M LiClO_4 in DMF solution, with increasing HClO_4 concentration. After ref ²².

The CV of $\text{H}_4\text{SiW}_{12}$ in DMF with increasing concentration of HClO_4 showed that the potential of the first three reduction waves are shifted to less negative potentials, as shown in Figure 1.6. ²²

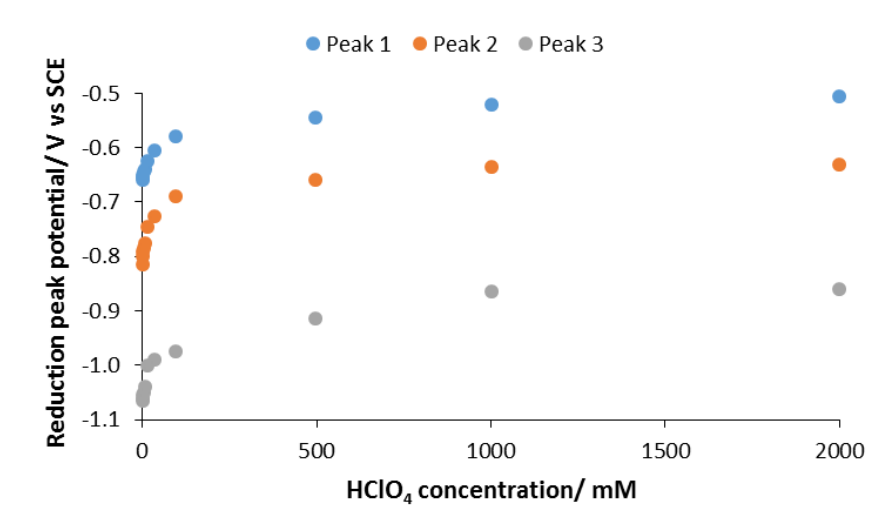


Figure 1.6 The reduction peak potentials in the CV of 1 mM $\text{H}_4\text{SiW}_{12}\text{O}_{40}$ in 0.1 M LiClO_4 in DMF solution, with increasing HClO_4 concentration. After ref ²².

In 1988, Keita and Nadjo investigated $\text{K}_4\text{SiW}_{12}$ in 0.1 M LiClO_4 in varying solvents as shown in Figure 1.7. ²⁵ They found that the potential of the first reduction peak was the most negative in DMF and the least negative in water (+ 1 M HClO_4).

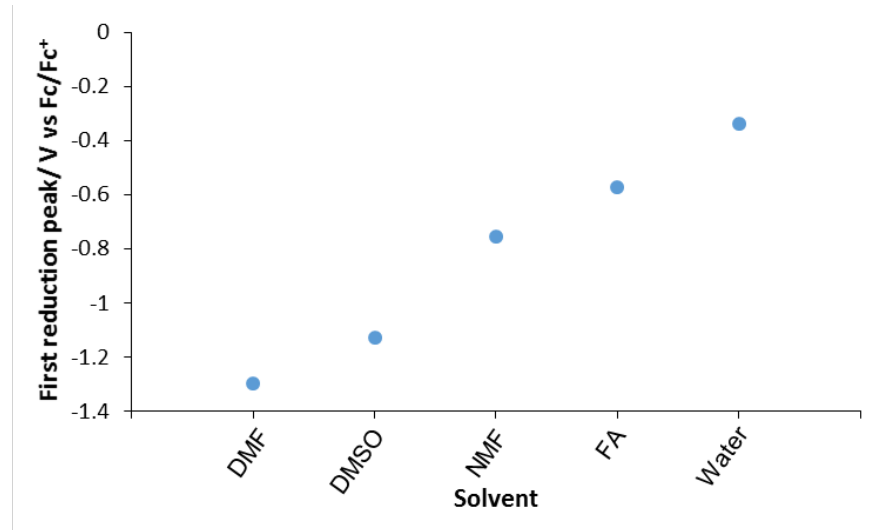


Figure 1.7 The reduction peak potentials in the CV of 1 mM $\text{K}_4\text{SiW}_{12}\text{O}_{40}$ in 0.1 M LiClO_4 in various solvents. After ref ²⁵.

1.4.3.2 $[\text{SiMo}_{12}\text{O}_{40}]^{4-}$

An example of a CV of $(\text{TBA})_4[\text{SiMo}_{12}\text{O}_{40}]$ is shown in Figure 1.8 and a summary of electrochemical data for $[\text{SiMo}_{12}\text{O}_{40}]^{4-}$ from the literature is contained in Table 1.2.

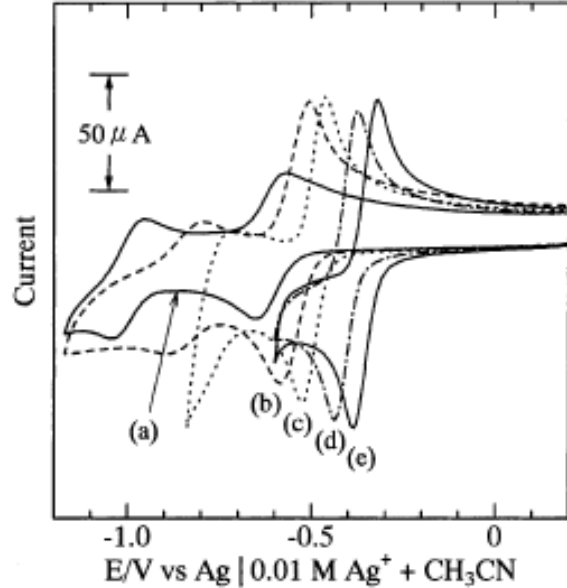


Figure 1.8 CV of a 0.5 mM solution of $(\text{TBA})_4[\text{SiMo}_{12}\text{O}_{40}]$ in MeCN containing TBAP + LiClO_4 , GC WE, Pt CE, Ag/Ag^+ RE, 50 mV/s scan rate. Where the ionic strength = 0.10. $[\text{Li}^+]$ / mM: (a) 0; (b) 1.0; (c) 5.0; (d) 50; (e) 100. After ref ²⁶.

Year ^{REF}	POM	Electrochemical method	Electrochemistry data	
			Reduction peak/ V	# electrons
1967 ¹⁸	α -H ₄ SiMo ₁₂	Polarography, 0.5 M HCl, Pt electrode	0.29, 0.15, -0.03	2:2:2
1967 ¹⁸	β -H ₄ SiMo ₁₂	Polarography, 0.5 M HCl, Pt electrode	0.40, 0.34, -0.10	2:2:2
1983 ²⁷	A-H ₄ SiMo ₁₂	Polarography, 0.5 M HClO ₄ 1:1 water-1,4-dioxane, Pt electrode	0.29, 0.18, -0.06	2:2:2
1983 ²⁷	β -H ₄ SiMo ₁₂	Polarography, 0.5 M HClO ₄ 1:1 water-1,4-dioxane, Pt electrode	0.39, 0.295, -0.01	2:2:2
2000 ²⁶	(TBA) ₄ SiMo ₁₂	CV, 0.5 mM POM in TBAP MeCN, GC WE, Pt CE, Ag/Ag ⁺ RE, 50 mV/s	-0.65, -1.00	1:1

Table 1.2 Summary of literature electrochemical data for [SiMo₁₂O₄₀]⁴⁻.

The first polarography studies of H₄SiMo₁₂ showed three waves, which equated to two electrons each.¹⁸ In 1974 Launay *et al.*²⁸ investigated the electrochemical properties of POMs using CPE, α -H₄SiMo₁₂ and β -H₄SiMo₁₂. Launay *et al.* found evidence of zero-, two- and four-electron reduced H₄SiMo₁₂ in acidic media, whereas six-electron reduced required pH 4.8. They were also able to see H₄SiMo₁₂ reduced by an odd number of electrons; one-, three- and five-electron reduced species in basic media. The five-electron reduced species was only observed in the presence of LiOH.²⁸ The β -isomer was reduced at higher potentials in 0.5 M HCl in 1:1 water-alcohol, the hydro-alcoholic medium stabilises the β -isomer. Tsigdinos and Hallada studied the stability of the β -isomer of H₄SiMo₁₂ using polarography.²⁹ They found that the β -isomer was stabilised in aqueous solutions containing 50% (v/v) of methanol, ethanol, isopropanol, acetone, ether and 1,4-dioxane.

The electrochemistry of (TBA)₄SiMo₁₂ in MeCN and acetone with H⁺, Li⁺ and Na⁺ cations present in the solution was investigated by Himeno *et al.*²⁶ The CV of (TBA)₄SiMo₁₂ in the presence of Na⁺ or Li⁺ led to the conversion of two one-electron waves to one two-electron wave, which was shifted to a more positive potential.

1.4.3.3 $[\text{PW}_{12}\text{O}_{40}]^{3-}$

Examples of CV of $(\text{TBA})_3[\text{PW}_{12}\text{O}_{40}]$ is shown in Figure 1.9 and a summary of electrochemical data for $[\text{PW}_{12}\text{O}_{40}]^{3-}$ from the literature is contained in Table 1.3.

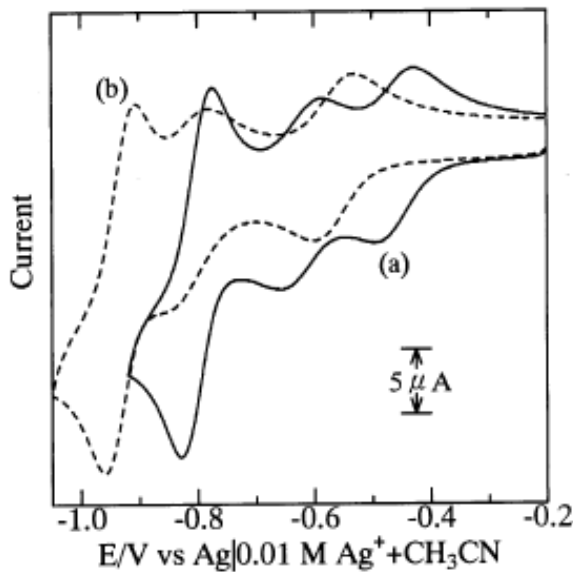


Figure 1.9 CV of a solution of 0.3 mM (a) β -(TBA)₃[PW₁₂O₄₀] and (b) α -(TBA)₃[PW₁₂O₄₀] in 95% (v/v) MeCN + water containing 0.1 M TBAP + 3 mM CF₃SO₃H. Ag/Ag⁺ RE, Pt CE, GC WE, 100 mV/s scan rate. After ref ³⁰.

Year ^{REF}	POM	Electrochemical method	Electrochemistry data	
			Reduction peak/ V	# electrons
1966 ¹⁷	K ₃ PW ₁₂	Polarography, 0.5 mM POM in 1 M H ₂ SO ₄ (aq), SCE RE	-0.023, -0.266	1:1:2
1987 ²²	H ₃ PW ₁₂	CV, 1 mM POM in 1 M HClO ₄ (aq), SCE RE, Pt CE, GC WE, 100 mV/s	-0.020, -0.275, -0.590, -0.775, -0.850	1:1:2
1999 ³⁰	α -(TBA) ₃ PW ₁₂	CV, 0.3 mM POM in 0.1 M TBAP in MeCN, Ag/Ag ⁺ RE, Pt CE, GC WE, 100 mV/s	-0.60, -1.13, -1.83, -2.30	1:1:1:1
1999 ³⁰	β -(TBA) ₃ PW ₁₂	CV, 0.3 mM POM in 0.1 M TBAP in MeCN, Ag/Ag ⁺ RE, Pt CE, GC WE, 100 mV/s	-0.50, -1.07, -1.70, -2.20	1:1:1:1

Table 1.3 Summary of literature electrochemical data for $[\text{PW}_{12}\text{O}_{40}]^{3-}$.

In 1960 Kennedy investigated the polarography of $\text{H}_3[\text{PW}_{12}\text{O}_{40}]$ (H_3PW_{12}) in 0.1 M H_2SO_4 , three reduction waves were present in the ratio of 1:1:2.³¹ Kennedy found that the first reduction wave corresponded to the transfer of two electrons by investigating CPE. In 1966 the polarography of $\text{K}_3\text{PW}_{12}\text{O}_{40}$ (K_3PW_{12}) was investigated by Pope and Varga. They found three waves in the ratio of 1:1:2, they found that even at pH 1.3 K_3PW_{12} was stable, as the polarography remained nearly unchanged. Keita *et al.*²² investigated the electrochemistry of 1 mM H_3PW_{12} in water with increasing concentrations of HClO_4 , as shown in Figure 1.10. In 1 M HClO_4 the CV of H_3PW_{12} contained five well defined waves, the first three correspond to two one-electron processes and one two-electron process and the other two are irreversible waves corresponding to more than two electrons. With increasing HClO_4 concentration the first two waves are shifted to more negative potentials and the other three waves shift to more positive potentials.

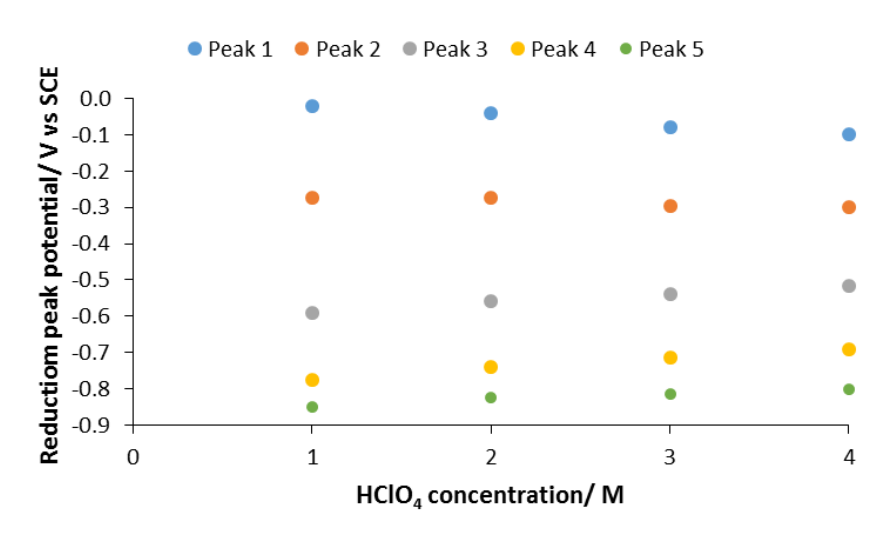


Figure 1.10 The reduction peak potentials in the CV of 1 mM $\text{H}_3\text{PW}_{12}\text{O}_{40}$ in aqueous solution with increasing concentration of HClO_4 . After ref²².

Keita and Nadjo investigated the CV of 1 mM H_3PW_{12} in the organic solvent, DMF with increasing concentrations of HClO_4 added.²² They found that as the concentration of HClO_4 increased, the reduction peaks moved to less negative potentials, as shown in Figure 1.11.

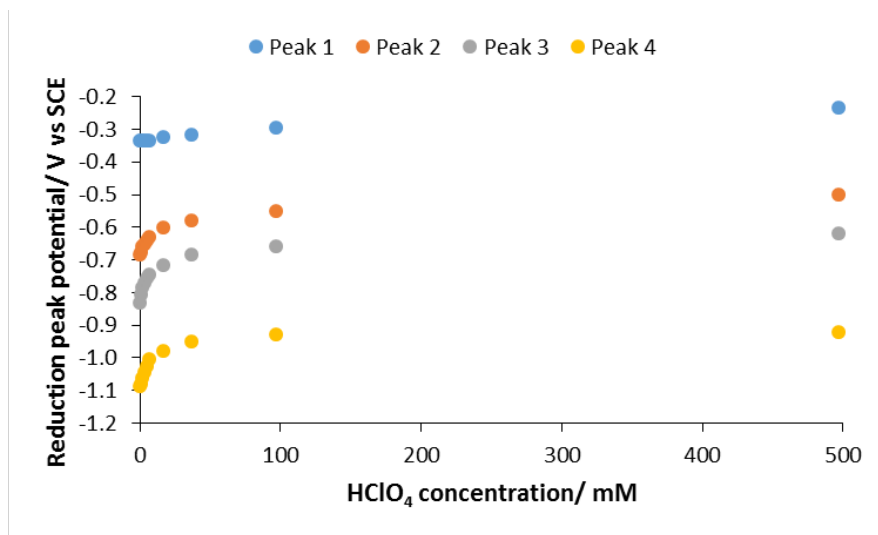


Figure 1.11 The reduction peak potentials in the CV of 1 mM $\text{H}_3\text{PW}_{12}\text{O}_{40}$ in DMF with increasing concentrations of HClO_4 . After ref ²².

In 1999 Himeno *et al.* investigated the effect of the presence of acid on the CV of MeCN solutions of α - and β -isomers of $(\text{TBA})_3\text{PW}_{12}$.³⁰ They found that in the presence of low concentrations of acid the CV still contained three redox waves in the ratio of 1:1:2. When the concentration of $\text{CF}_3\text{SO}_3\text{H}$ was increased to 3 mM two two-electron reduction waves were present and another wave that the number of electrons was not calculated.

1.4.3.4 $[\text{PMo}_{12}\text{O}_{40}]^{3-}$

An example of a CV of $(\text{TBA})_3[\text{PMo}_{12}\text{O}_{40}]$ is shown in Figure 1.12 and a summary of electrochemical data for $[\text{PMo}_{12}\text{O}_{40}]^{3-}$ from the literature is contained in Table 1.4.

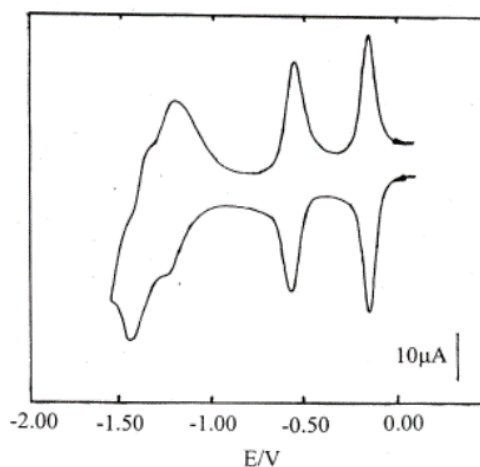


Figure 1.12 CV of 0.5 mM $(\text{TBA})_3[\text{PMo}_{12}\text{O}_{40}]$ in TBAClO_4 in MeCN, Ag/Ag^+ RE, GC WE, Pt CE, 1 mV/s scan rate. After ref ²⁶.

Year ^{REF}	POM	Electrochemical method	Electrochemistry data	
			Reduction peak/ V	# electrons
1974 ²⁹	H ₃ PMo ₁₂	CV, 1 mM POM in 0.5 M H ₂ SO ₄ (1:1 Water-dioxane), rotating Pt disc WE, SCE RE, Pt CE, 100 mV/s	0.28, 0.15, -0.10, -0.23	
1989 ³²	α-H ₃ PMo ₁₂	CV, 0.16 mM POM in 80% (v/v) MeCN, 0.1 M HCl, GC WE, SCE RE, Pt CE, 100 mV/s	0.27, 0.16, -0.08, -0.25	2:2:2:4
1989 ³²	β-(TBA) ₃ PMo ₁₂	CV, 0.17 mM POM in 80% (v/v) MeCN, 0.1 M HCl, GC WE, SCE RE, Pt CE, 100 mV/s	0.38, 0.28, -0.12, -0.27	2:2:2:4
1994 ³³	(TBA) ₃ PMo ₁₂	CV, 0.5 mM POM in 0.05 M TBACIO ₄ in MeCN, Ag/Ag ⁺ RE, GC WE, Pt CE, 100 mV/s	-0.20, -0.63, -1.36	1:1:1
1998 ³⁴	(TBA) ₃ PMo ₁₂	CV, 0.5 mM POM in 0.1 M TBACIO ₄ in MeCN, Ag/Ag ⁺ RE, Pt WE, Pt CE, 60 mV/s	-0.70, -1.00, -1.40, -1.85	1:1:1:1
2000 ²⁶	(TBA) ₃ PMo ₁₂	CV, 0.5 mM POM in TBACIO ₄ in Acetone, Ag/Ag ⁺ RE, GC WE, Pt CE	-0.70, -1.00, -1.40, -1.85	1:1:1:1
2000 ²⁶	(TBA) ₃ PMo ₁₂	CV, 0.5 mM POM in TBACIO ₄ in MeCN, Ag/Ag ⁺ RE, GC WE, Pt CE	-0.20, -0.60, -0.90, -1.38	1:1:1:1

Table 1.4 Summary of literature electrochemical data for [PMo₁₂O₄₀]³⁻.

Chapter 1 Introduction

In 1974 Tsigdinos *et al.*²⁹ investigated the polarography and CV of 1 mM H₃PMo₁₂ in 0.5 M H₂SO₄ (1:1 Water-dioxane), the CV contained four redox waves, the first three are reversible, they suggest that the redox waves correspond to two-electron transfer steps. In 1982 Tanaka *et al.*³⁵ investigated the effect of the percentage of 1,4-dioxane in aqueous solutions on the CV of H₃PMo₁₂. They found that the reduction wave shifts to more positive potential as the percentage of 1,4-dioxane decreased. In 1989 Himeno *et al.*³² studied the CV characterisation of α - and β -PMo₁₂ in mixed aqueous organic solutions and they found that the β -isomer was only stable in organic solutions and that it transformed to the α -isomer in aqueous solvents.

In 1994 Maeda *et al.*³³ investigated the CV of α - and β -isomers of (TBA)₃[PMo₁₂O₄₀] ((TBA)₃PMo₁₂), they found that in both acetone and MeCN the mid-point potentials for the α -isomer were more negative than for the β -isomer. In 1998 Sun *et al.* investigated the spectroelectrochemical properties of (TBA)₃PMo₁₂ in MeCN. The CV of (TBA)₃PMo₁₂ contained four reversible one-electron redox waves.³⁴

The CV of (TBA)₃PMo₁₂ in MeCN and acetone with the addition of Li⁺ and Na⁺ cations was investigated by Himeno *et al.*²⁶ The presence of Li⁺ in acetone and MeCN, led to the formation of a fourth wave in between the original first and second waves. With increasing [Li⁺] the new wave grows as the second wave shrinks, until only the new wave is present, and at very high [Li⁺] the new wave and the first wave merge to form a two-electron wave. The addition of Na⁺ to an acetone solution of (TBA)₃PMo₁₂ led to a similar effect on the cyclic voltammogram as the addition of Li⁺. The addition of Na⁺ to (TBA)₃PMo₁₂ in MeCN, did not lead to the formation of two-electron waves in the CV, however it did cause the potential of the second and third one-electron waves to shift to more positive potentials.

1.4.3.5 Others

A summary of electrochemical data for a variety of POMs from the literature is contained in Table 1.5.

Year ^{REF}	POM	Electrochemical method	Electrochemistry data	
			Reduction peak/ V	# electrons
1966 ¹⁷	FeW ₁₂	Polarography, 0.5 mM POM in 1 M H ₂ SO ₄ (aq), SCE RE	-0.349, -0.577	1
1966 ¹⁷	CoW ₁₂	Polarography, 0.5 mM POM in 1 M H ₂ SO ₄ (aq), SCE RE	-0.510, -0.714	1:1
1966 ¹⁷	H ₂ W ₁₂	Polarography, 0.5 mM POM in 1 M H ₂ SO ₄ (aq), SCE RE	-0.581, -0.730	
2001 ³⁶	SMo ₁₂	CV, 2 mM POM in 0.1 M NH ₄ ClO ₄ CH ₂ Cl ₂ , Ag/AgCl RE, Pt wire CE, GC WE, 10 mV/s	0.00, -0.45, -1.20, 1.70	
2008 ³⁷	CoMo ₁₂	CV, 1 mM POM, 2 M H ₂ SO ₄ (aq), Ag/AgCl RE, Pt CE, GC WE, 50 mV/s	0.900 (Co), 0.367, 0.257	
2008 ³⁷	CoW ₁₂	CV, 1 mM POM, 2 M H ₂ SO ₄ (aq), Ag/AgCl RE, Pt CE, GC WE, 50 mV/s	0.914 (Co), -0.235, -0.345	
2008 ³⁷	NiMo ₁₂	CV, 1 mM POM, pH 0.5 H ₂ SO ₄ (aq), Ag/AgCl RE, Pt CE, GC WE, 50 mV/s	0.339, 0.214	
2010 ³⁸	ZnW ₁₂	CV, 0.5 mM POM, 0.1 M (TBA)ClO ₄ MeCN + 10 mM CF ₃ SO ₃ H, Ag/Ag ⁺ RE, GC WE, Pt CE	-0.50	4

Table 1.5 Summary of literature electrochemical data for a variety of Keggin-type POMs.

In 1966, Pope and Varga investigated the electrochemistry of $[XW_{12}O_{40}]^{n-}$ where X = P and n = 3, X = Si and n = 4, X = Fe^{III} and n = 5 and X = Co^{II} and n = 6.¹⁷ They studied the Keggin POMs by redox titrations and polarography. They found that in acidic solutions the POMs were reduced by one electron without the addition of a proton, until the overall charge of the species reached 6⁻. The addition of further electrons was accompanied by the addition of a proton to then balance the charge at

Chapter 1 Introduction

6-. They also found that with increasing overall charge on the POM, the reduction potential of the first redox wave shifted to more negative potentials.

In 1974 Launay investigated the reduction of the metatungstate anion, $[\text{H}_2\text{W}_{12}\text{O}_{40}]^{6-}$ by polarography with up to thirty-two electrons added to the POM, as shown in Figure 1.13. ³⁹

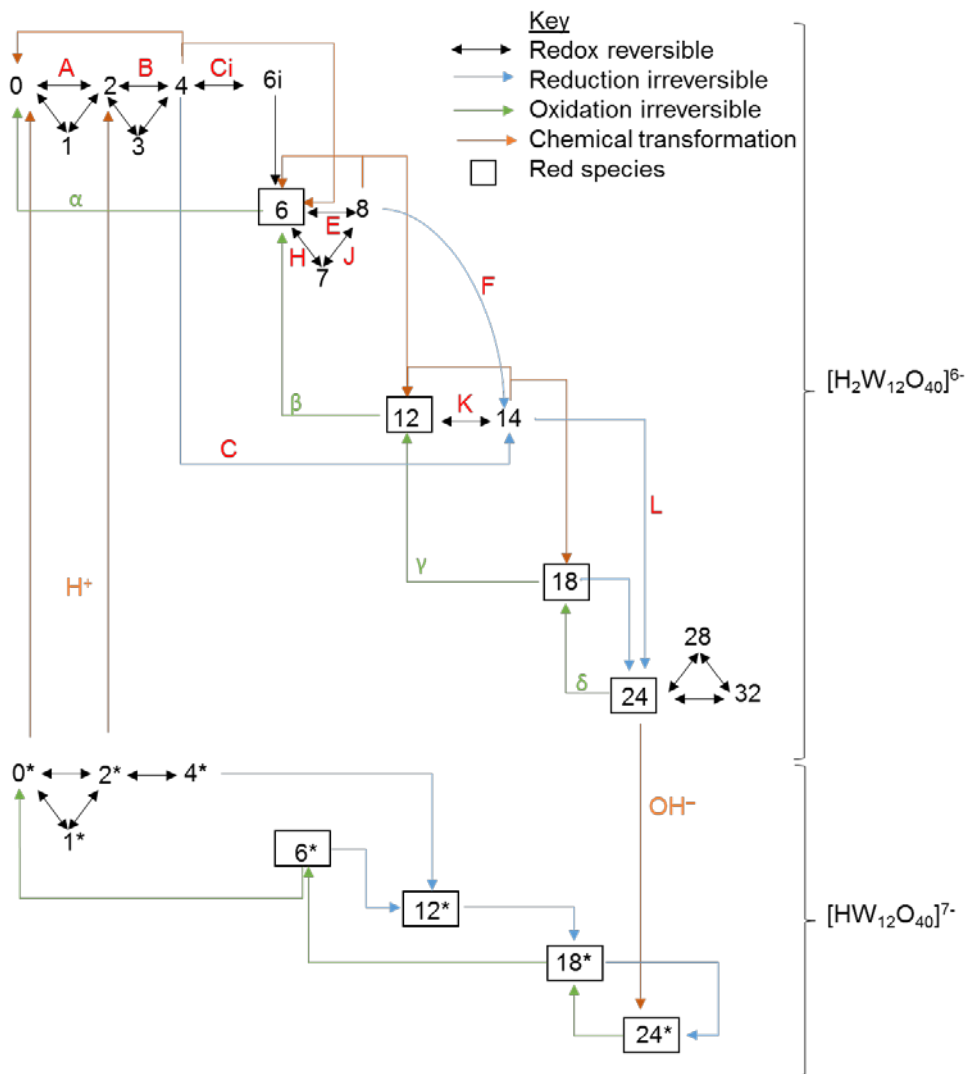


Figure 1.13 The scheme for the reduction of the metatungstate anion, after ref ³⁹.

In 1975 Pope *et al.* investigated the polarography of a series of Keggin POMs; $[\text{PZW}_{11}\text{O}_{40}]^{n-}$ ($\text{Z} = \text{V}^{IV}, \text{Mo}^V$), $[\text{XV}^{IV}\text{W}_{11}\text{O}_{40}]^{n-}$ ($\text{X} = \text{P}, \text{Si}, \text{Ge}, \text{B}, \text{H}_2, \text{Zn}$) and $[\text{XV}^{IV}\text{Mo}_{11}\text{O}_{40}]^{n-}$ ($\text{X} = \text{P}, \text{Si}$). They found that with increasing charge on the POM anion the first electron reduction potential shifted to a more negative potential. ⁴⁰

In 1994 Maeda *et al.* investigated several polyoxomolybdates with varying heteroatoms, $[XMo_{12}O_{40}]^{n-}$ (where X = S and n = 2, X = P, As, V and n = 3, X = Si, Ge and n = 4). ³³ They found that there was an 80 mV difference in the first redox wave between the α - and β -isomers, where X = P, As, Si and Ge, the β -isomer redox wave being at the more positive potential. They also found the same relationship as Pope *et al.*, ⁴⁰ that with increasing charge on the POM, the first redox wave shifts to a more negative potential. They also found that on addition of acid to all the POM solutions the one-electron waves were transformed in to two-electron waves.

In 1995 Maeda *et al.* ⁴¹ investigated the one-electron redox potentials of a range of Keggin-type POMs. They investigated the effect on the cyclic voltammograms of the overall charge of the POM anion in several solvents; α - $[XMo_{12}O_{40}]^{n-}$ (where X = S and n = 2, X = P, As, V and n = 3, X = Si, Ge and n = 4), β - $[XMo_{12}O_{40}]^{n-}$ (X = P, As and n = 3, X = Si, Ge and n = 4) and α - $[XW_{12}O_{40}]^{n-}$ (X = P and n = 3, X = Si and n = 4). They found that with increasing charge on the POM anion, the first and second one-electron redox waves were shifted to more negative potentials, this was the case in several solvents including; acetone, MeCN, 1,2-DCE, dmso, nitrobenzene and PC. The first and second one-electron redox waves in the cyclic voltammograms of α -PMo₁₂ and α -SiMo₁₂ were shifted to more positive potentials with increasing concentration of TBACIO₄ in the electrolyte, from 0.02 M to 0.20 M.

Vu *et al.* investigated the electrochemistry of $[NHex_4]_2[SMo_{12}O_{40}]$, they observed four reversible one-electron reductions in DCM. They were able to isolate one-electron reduced $[SMo_{12}O_{40}]^{3-}$ by bulk electrolysis at -0.1 V and adding $[NBu_4]^+$ or $[NPr_4]^+$. The isolation of two-electron reduced $[SMo_{12}O_{40}]^{4-}$ was achieved by bulk electrolysis at -0.5 V and then the addition of $[NPr_4]^+$. ³⁶

In 2002 Himeno and Takamoto investigated the cyclic voltammograms of $[XW_{12}O_{40}]^{n-}$ and $[XMo_{12}O_{40}]^{n-}$ (X = P, Ge; n = 3, 4). ⁴² They found that with the addition of H^+ , Li^+ and Na^+ , the one-electron redox waves were converted to two-electron waves, and this occurred more easily for the Mo addenda POMs with the same ionic charge as the W addenda POMs, this is because the Mo addenda POMs have greater basicity. They also investigated the mono-vanadium mixed addenda POMs; $[SVW_{11}O_{40}]^{3-}$ and $[PVW_{11}O_{40}]^{4-}$ and they found that the one-electron redox wave that corresponds to

Chapter 1 Introduction

the V^V/V^{IV} redox couple occurs at a more positive potential than the redox wave corresponding to the W^{VI}/W^V redox couple in the non-mixed addenda POMs.⁴²

The CV of CoMo₁₂, CoW₁₂ and NiMo₁₂ were investigated by Gao *et al.* They found that the Co^{III}/Co^{II} process was visible in the CV and the redox waves corresponding to Mo were in a similar position to SiMo₁₂.³⁷

In 2010 Nakajima *et al.* investigated the cyclic voltammogram of [ZnW₁₂O₄₀]⁶⁻ (ZnW₁₂) and they found that unlike Keggin-type POMs with lower ionic charge, the CV of ZnW₁₂ contained a redox wave that corresponded to a four-electron process in acidified MeCN.³⁸

In 2010 Mbomekalle *et al.* investigated the effect of the heteroatom size on the CV of [XW₁₂O₄₀]ⁿ⁻, where X = B(III), Al(III), Ga(III), Si(IV), Ge(IV), P(V) and As(V). They found that as X got smaller, when X is in the same group, the reduction potential of the first redox wave became more negative, i.e. the POM became harder to reduce,⁴³ the trend within the groups was as follows; B>Al>Ga, Si>Ge and P>As. They investigated this effect by using DFT calculations and found that as X got smaller the electrostatic repulsion of the central [XO₄]ⁿ⁻ unit got larger, the value of electrostatic repulsion calculated for when X = B was the highest.

1.4.4 Chemical Reduction

There are many examples in the literature of the preparation of reduced non-capped and capped Keggin-type POMs with one, two, four, five, six and eight electrons added to the POM, by uncontrolled hydrothermal synthesis, electrolysis and controlled synthesis. Hydrothermal synthesis involves heating an aqueous solution to above the boiling point of water in a sealed system, this offers very little control over the products of the reaction. Electrolysis entails the electrochemical reduction of the POM with subsequent addition of a suitable counter cation in order to isolate the reduced species. Controlled synthesis of reduced POMs involves addition of a known amount of reductant to the POM in order to produce a target product. Some examples of reduced non-capped Keggin-type POMs are; [K₂Ag₁₅(5-o-tolyl-1H-tetrazole)₁₀(H₂O)₂][H(PMo^VMo^{VI}₁₁O₄₀)₂],⁴⁴ α -(TBA)₃[S^{VI}Mo^VMo^{VI}₁₁O₄₀],³⁶ α -[Cu⁴(bpmb)₄][PW^VW^{VI}₁₁O₄₀] and α -NaH₆[PW^V₄W^{VI}₈O₄₀].4H₂O.^{45, 46} Some examples of reduced capped POMs are the mono-capped

α -(TBA)₃[PMo₁₂O₄₀{Co^{II}(MeCN)₂}],⁶ the di-capped α -(NMe₄)₅[SiMo^V₄Mo^{VI}₈(Mo^{VI}O₂)₂]
and the tetra-capped ϵ -(TBA)₃[H₂PMo^V₈Mo^{VI}₄O₄₀Zn₄][C₇H₆(CO₂)₂]₂.^{5, 47, 48} Table 1.6 gives a summary of non-capped and capped reduced Keggin-type POMs, indicating the number of electrons that have been added to the POM and the synthetic conditions.

POM formula	# of e ⁻	Synth. conditions	Ref.
Non-capped reduced POMs			
[K ₂ Ag ₁₅ (5-o-tolyl-1H-tetrazole) ₁₀ (H ₂ O) ₂][H(PMo ^V Mo ^{VI} ₁₁ O ₄₀) ₂]	1	HT	44
[Cu ^I (pz) _{1.5}] ₄ [PMo ^V Mo ^{VI} ₁₁ O ₄₀]pz.2H ₂ O	1	HT	49
[Cu ^I ₃ (pz) ₃ Cl][Cu ^I ₂ (pz) ₃ (H ₂ O)][PMo ^V Mo ^{VI} ₁₁ O ₄₀]	1	HT	49
[Ni(H ₂ O) ₆][H ₃ PMo ^V Mo ^{VI} ₁₁ O ₄₀] ₂ .30H ₂ O	1	RT	50
α -(TBA) ₃ [S ^{VI} Mo ^V Mo ^{VI} ₁₁ O ₄₀]	1	electrolysis	36
α -[Cu ^I ₄ (bpmb) ₄][PW ^V W ^{VI} ₁₁ O ₄₀]	1	HT	45
[Ag ₄ (2-btz) ₄ (HPMo ^V ₂ Mo ^{VI} ₁₀ O ₄₀)]	2	HT	51
[Ni(phen) ₂ (H ₂ O) ₂](H ₃ O)[PMo ^V ₂ Mo ^{VI} ₁₀ O ₄₀].4H ₂ O	2	HT	52
α -[(NPr) ₄] ₄ [S ^{VI} Mo ^V ₂ Mo ^{VI} ₁₀ O ₄₀]	2	electrolysis	36
β -[Ca _{0.5} H ₆ PMo ^V ₄ Mo ^{VI} ₈ O ₄₀].18H ₂ O	4	electrolysis	53
α -NaH ₆ [PW ^V ₄ W ^{VI} ₈ O ₄₀].4H ₂ O	4	HT	46
Mono-capped reduced POM			
α -(TBA) ₃ [PMo ₁₂ O ₄₀ {Co ^{II} (MeCN) ₂ }]	2	controlled	6
Di-capped reduced POMs			
α -[HMn ^{II} (bix) ₄][PMo ^{VI} ₈ V ^{VI} ₄ O ₄₀ (V ^{VI} O) ₂]	2	HT	54
α -(NMe ₄) ₅ [SiMo ^V ₄ Mo ^{VI} ₈ (Mo ^{VI} O ₂) ₂]	4	HT	5
α -(C ₂ N ₂ H ₉) ₂ [PMo ^V ₅ Mo ^{VI} ₇ Sb ^{III} ₂ O ₄₀].2H ₂ O	5	HT	55
α -(TBA) ₃ [PMo ₁₂ O ₄₀ (V ^{IV} O) ₂]	6	controlled	6
α -(TBA) ₃ [PMo ₁₂ O ₄₀ Sb ^{III} ₂]	6	controlled	6
α -(NEt ₃ H) ₅ [PMo ^V ₆ Mo ^{VI} ₆ O ₄₀ (V ^{IV} O) ₂]	8	HT	3
Tetra-capped reduced POM			
ϵ -(TBA) ₃ [H ₂ PMo ^V ₈ Mo ^{VI} ₄ O ₄₀ Zn ₄][C ₇ H ₆ (CO ₂) ₂] ₂	8	HT	47, 48

Table 1.6 Table summarising reduced POMs both non-capped and capped. Abbreviations: Synth. = Synthetic, HT = hydrothermal, pz = pyrazine, RT = room temperature, TBA = tetra-*n*-butylammonium, bpmb = 1,4-bis(pyrazol-1-ylmethyl)benzene, 2-btz = 1-benzyl-1H-(1,2,4)triazole, phen = phenanthroline, NPr₄ = tetrapropylammonium, bix= 1,4-bis(imidazole-1-ylmethyl)benzene.

1.4.5 Applications

The versatile redox properties of POMs has led to their use for a wide variety of applications such as; medicine,⁵⁶⁻⁵⁸ catalysis,^{2, 21, 22, 59-61} and energy storage devices.^{7, 10, 62-101}

The antiviral activities of POMs has been reported extensively,⁵⁶ and the Keggin-type POMs; $\text{Na}_6[\text{H}_2\text{W}_{12}\text{O}_{40}]$,^{57, 58} $\text{K}_5[\text{BW}_{12}\text{O}_{40}]$,⁵⁷ $\text{H}_6[\text{ZnW}_{12}\text{O}_{40}]$ and $[(\text{DMA})_2\text{H}]_3[\text{PMo}_{12}\text{O}_{40}]$ were found to be effective against HIV.^{57, 58}

The Keggin-type POMs have shown promise for catalytic applications;² SiW_{12} and SiMo_{12} have been investigated as electrocatalysts for the hydrogen evolution reaction and chlorate ion reduction respectively, due to the activity of their reduced species.^{21, 22, 59} Phosphotungstic acid has also shown promise as a photocatalyst when co-assembled with graphene oxide nanosheets.⁶¹

The ability of POMs to reversibly accept multiple electrons has led to extensive research into their use in energy storage devices such as; fuel cells,⁶²⁻⁶⁷ redox flow batteries,⁶⁸⁻⁷⁰ Li-ion batteries,^{7, 71-80} Na-ion batteries,⁸¹⁻⁸⁴ and supercapacitors (SCs).^{10, 85-101}

POMs have been incorporated into fuel cells in a wide range of ways such as; electrolyte membranes, electrolyte solutions, electrode supports and catalyst layers.⁶² A composite membrane consisting of polybenzimidazole and phosphotungstic acid absorbed on to SiO_2 has been investigated by Staiti *et al.*⁶³ They found that the membrane was thermally stable up to 400 °C, a specific conductivity of 3 mS.cm⁻¹ at 100% RH and 100 °C, and stable proton conductivity of 1.42 mS.cm⁻¹ at 150 °C. Composite membranes containing partially sulfonated polyether ether ketone (PEEK) polymer and the hydrated forms of heteropolyacids (phosphotungstic acid, sodium salt of PW_{12} and phosphomolybdic acid) incorporated in their solid form were reported by Zaidi *et al.*⁶⁴ The membranes were found to have high conductivity, mechanically strong, good flexibility and less expensive than the commercially available membranes. In 2016 Matsui *et al.* investigated $\text{H}_{3+x}\text{PV}_x\text{Mo}_{12-x}\text{O}_{40}$ ($x = 0, 2, 3$) as catholyte and redox mediator for oxygen reduction in polymer electrolyte fuel cell (PEFC).⁶⁵ They found that for $\text{H}_6\text{PV}_3\text{Mo}_9\text{O}_{40}$ the fuel cell performed the best and the reoxidation rate of this catholyte was the fastest. In 2017 Gunn *et al.* investigated

$H_6PV_3Mo_9O_{40}$ as catholyte in a PEFC with a chemically regenerative redox cathode, they found that the system achieved a power density of 0.37 W.cm^{-2} at a current density of 0.8 A.cm^{-1} , though this is lower than what is achieved by conventional fuel cells, the system is Pt free.⁶⁶ In 2018 Ward *et al.* investigated PEFCs containing catholytes containing $H_6PV_3Mo_9O_{40}$, $H_7PV_4Mo_8O_{40}$, $Na_3H_3PV_3Mo_9O_{40}$ and $Na_4H_3PV_4Mo_8O_{40}$.⁶⁷

Pratt *et al.* have investigated several different POMs in redox flow batteries, such as; $[SiV^{IV}_3W^{VI}_9O_{40}]^{7-}$, $[PV^{IV}_3W^{VI}_9O_{40}]^{9-}$ and $[(SiFe_3W_9(OH)_3O_{34})_2(OH)_3]^{11-}$.⁶⁸⁻⁷⁰

POMs and organic molecule composite materials have been incorporated in to Li-ion battery electrodes; $[PMo_{12}O_{40}]^{3-}$ with polyaniline,⁷¹ $[PV_2Mo_{10}O_{40}]^{5-}$ and polydopamine.⁷² POMs have also been combined with carbon materials for Li-ion battery electrodes; $[SiW_{11}O_{39}[O(Si(CH_2)_3NHCOOCH_2C_{16}H_9)_2]]^{4-}$ and single walled carbon nanotubes (SWCNT),⁷³ $[PVMo_{11}O_{40}]^{4-}$ and SWCNT,⁷⁴ and $[P_2Mo_{18}O_{60}]^{6-}$ grafted on to graphene oxide.⁷⁵ Several crystalline POM salts have been incorporated in to Li-ion batteries; $Li_6[V_{10}O_{28}]$,⁷⁶ $(TBA)_3[PMo_{12}O_{40}]$,⁷⁷ $K_7[NiV_{13}O_{38}]$,⁷⁸ $K_7[MnV_{13}O_{38}]$,⁷⁹ $Li_7[V_{15}O_{38}(CO_3)]$,⁷⁹ $K_4Na_2[V_{10}O_{28}]$ and $Mg_2(NH_4)_2[V_{10}O_{28}]$.⁸⁰

Several crystalline POM salts have been investigated as materials for the anode and the cathode in Na-ion batteries; two examples for each will hence forth be described. In 2015 Hartung *et al.* investigated $Na_6V_{10}O_{28} \cdot 16H_2O$ as anode material in a Na-ion battery, they found that it achieved a stable discharge capacity of 276 mA.h.g^{-1} at a current density of 20 mA.g^{-1} .⁸¹ In 2017 Liu *et al.* investigated $Na_2H_8[MnV_{13}O_{38}]$ coated in graphene sheets as cathode material in a Na-ion battery, they found that it exhibited a high specific capacity of 190 mA.h.g^{-1} at a discharge rate of $0.1C$.⁸² In 2018 Lin *et al.* investigated $Na_7[H_2PV_{14}O_{42}]$ as anode material in a Na-ion battery, they found that it achieved a high, reversible specific capacity of 322 mA.h.g^{-1} at a current density of 25 mA.g^{-1} .⁸³ In 2018 Chen *et al.* investigated $Li_7V_{15}O_{36}(CO_3)$ as cathode material in a Na-ion battery, they found that it achieved a reversible specific capacity of 240 mA.h.g^{-1} at a current density of 50 mA.g^{-1} .⁸⁴

Keggin-type POMs $[PMo_{12}O_{40}]^{3-}$ and $[PW_{12}O_{40}]^{3-}$ have been investigated in several SCs; combined with various carbons, binders and current collectors.^{10, 85-99} $H_3PMo_{12}O_{40}$ was the first crystalline POM studied as a SC component by Yamada

Chapter 1 Introduction

and Goodenough in 1998, the $\text{H}_3\text{PMo}_{12}\text{O}_{40} \cdot n\text{H}_2\text{O}/\text{Nafion } 117/\text{H}_x\text{RuO}_{2 \cdot n}\text{H}_2\text{O}$ SC achieved a specific capacitance of 112 F.g^{-1} and energy density of 36 J.g^{-1} with a 0.8 V voltage window.¹⁰ The best results have been achieved for $[\text{PW}_{12}\text{O}_{40}]^{3-}$ with AC or reduced graphene oxide, these combinations afford the highest capacitance and stability.^{98, 99} The Wells-Dawson POM $[\text{P}_2\text{Mo}_{18}\text{O}_{62}]^{6-}$ has also been used in SCs, however it exhibits poorer stability than the Keggin-type POMs.^{100, 101}

This study focused on the incorporation of crystalline POM salts in energy storage devices.

1.5. References

1. N. I. Gumerova and A. Rompel, *Nat. Rev. Chem.*, 2018, **2**, 0112.
2. M. Sadakane and E. Steckhan, *Chem. Rev.*, 1998, **98**, 219.
3. Q. Chen and C. L. Hill, *Inorg. Chem.*, 1996, **35**, 2403.
4. Y. Xu, H.-G. Zhu, H. Cai and X.-Z. You, *Chem. Commun.*, 1999, 787.
5. A. Dolbecq, E. Cadot, D. Eisner and F. Sécheresse, *Inorg. Chem.*, 1999, **38**, 4217.
6. R. Bakri, A. Booth, G. Harle, P. S. Middleton, C. Wills, W. Clegg, R. W. Harrington and R. J. Errington, *Chem. Commun.*, 2012, **48**, 2779.
7. H. Wang, S. Hamanaka, Y. Nishimoto, S. Irle, T. Yokoyama, H. Yoshikawa and K. Awaga, *J. Am. Chem. Soc.*, 2012, **134**, 4918.
8. C. Zhong, Y. Deng, W. Hu, J. Qiao, L. Zhang and J. Zhang, *Chem. Soc. Rev.*, 2015, **44**, 7484.
9. P. Simon and Y. Gogotsi, *Nat. Mater.*, 2008, **7**, 845.
10. A. Yamada and J. B. Goodenough, *J. Electrochem. Soc.*, 1998, **145**, 737.
11. H.-Y. Chen, G. Wee, R. Al-Oweini, J. Friedl, K. S. Tan, Y. Wang, C. L. Wong, U. Kortz, U. Stimming and M. Srinivasan, *ChemPhysChem*, 2014, **15**, 2162.
12. M. T. Pope, *Heteropoly and isopoly oxometalates*, Springer-Verlag, Berlin, 1983.
13. L. C. W. Baker and J. S. Figgis, *J. Am. Chem. Soc.*, 1970, **92**, 3794.
14. K. F. Jahr, J. Fuchs and R. Oberhauser, *Chem. Ber.*, 1968, **101**, 477.
15. P. Souchay, *Talanta*, 1965, **12**, 1187.
16. B. Keita and L. Nadjo, *J. Electroanal. Chem. Interfacial Electrochem.*, 1985, **191**, 441.
17. M. T. Pope and G. M. J. Varga, *Inorg. Chem.*, 1966, **5**, 1249.
18. P. Souchay, R. Massart and G. Hervé, *Rev. Polarogr.*, 1967, **14**, 270.
19. G. Hervé, *Ann. Chim.*, 1971, **6**, 219.
20. G. Hervé, *Ann. Chim.*, 1971, **6**, 287.

Chapter 1 Introduction

21. B. Keita and L. Nadjo, *J. Electroanal. Chem. Interfacial Electrochem.*, 1987, **217**, 287.
22. B. Keita and L. Nadjo, *J. Electroanal. Chem. Interfacial Electrochem.*, 1987, **227**, 77.
23. B. Keita and L. Nadjo, *J. Electroanal. Chem. Interfacial Electrochem.*, 1987, **219**, 355.
24. B. Keita and L. Nadjo, *J. Electroanal. Chem. Interfacial Electrochem.*, 1987, **217**, 287.
25. B. Keita, D. Bouaziz and L. Nadjo, *J. Electrochem. Soc.*, 1988, **135**, 87.
26. S. Himeno, M. Takamoto and T. Ueda, *J. Electroanal. Chem.*, 2000, **485**, 49.
27. C. Rocchicciolli-Deltcheff, M. Fournier, R. Franck and R. Thouvenot, *Inorg. Chem.*, 1983, **22**, 207.
28. J. P. Launay, R. Massart and P. Souchay, *J. less-common MET.*, 1974, **36**, 139.
29. G. A. Tsigdinos and C. J. Hallada, *J. less-common met.*, 1974, **36**, 79.
30. S. Himeno, M. Takamoto and T. Ueda, *J. Electroanal. Chem.*, 1999, **465**, 129.
31. J. H. Kennedy, *J. Am. Chem. Soc.*, 1960, **82**, 2701.
32. S. Himeno, T. Osakai and A. Saito, *Bull. Chem. Soc. Jpn.*, 1989, **62**, 1335.
33. K. Maeda, S. Himeno, T. Osakai, A. Saito and T. Hori, *J. Electroanal. Chem. Interfacial Electrochem.*, 1994, **364**, 149.
34. H. R. Sun, S. Y. Zhang, J. Q. Xu, G. Y. Yang and T. S. Shi, *J. Electroanal. Chem.*, 1998, **455**, 57.
35. N. Tanaka, K. Unoura and E. Itabashi, *Inorg. Chem.*, 1982, **21**, 1662.
36. T. Vu, A. M. Bond, D. C. R. Hockless, B. Moubaraki, K. S. Murray, G. Lazarev and A. G. Wedd, *Inorg. Chem.*, 2001, **40**, 65.
37. G.-G. Gao, L. Xu, W.-J. Wang, X.-S. Qu, H. Liu and Y.-Y. Yang, *Inorg. Chem.*, 2008, **47**, 2325.
38. K. Nakajima, K. Eda and S. Himeno, *Inorg. Chem.*, 2010, **49**, 5212.
39. J. P. Launay, *J. Inorg. Nucl. Chem.*, 1976, **38**, 807.

40. J. J. Altenau, M. T. Pope, R. A. Prados and H. So, *Inorg. Chem.*, 1975, **14**, 417.
41. K. Maeda, H. Katano, T. Osakai, S. Himeno and A. Saito, *J. Electroanal. Chem.*, 1995, **389**, 167.
42. S. Himeno and M. Takamoto, *J. Electroanal. Chem.*, 2002, **528**, 170.
43. I. M. Mbomekalle, X. Lopez, J. M. Poblet, F. Secheresse, B. Keita and L. Nadjo, *Inorg. Chem.*, 2010, **49**, 7001.
44. A.-X. Tian, X. Hou, J. Ying, G.-C. Liu, Y. Yang, Y.-L. Ning, T.-J. Li and X.-L. Wang, *RSC Advances*, 2015, **5**, 53757.
45. C. Zhao, H. Ma, H. Pang, Y. Yu, S. Li, T. Yu and Z. Zhang, *Z. Naturforsch. B*, 2015, **70**, 547.
46. Z. Wang, S. Gao, L. Xu, E. Shen and E. Wang, *Polyhedron*, 1996, **15**, 1383.
47. B.-X. Dong, L. Chen, S.-Y. Zhang, Y.-C. Wu, H. Tian, J. Ge, L. Song, Y.-L. Teng and W.-L. Liu, *J. Cluster Sci.*, 2015, **26**, 1595.
48. B.-X. Dong, Y.-C. Wu, H. Tian, C.-B. Liu, W.-L. Liu and Y.-L. Teng, *J. Cluster Sci.*, 2016, **27**, 361.
49. M.-L. Qi, K. Yu, Z.-H. Su, C.-X. Wang, C.-M. Wang, B.-B. Zhou and C.-C. Zhu, *Dalton Trans.*, 2013, **42**, 7586.
50. Q.-Z. Zhang, C.-Z. Lu, W.-B. Yang, C.-D. Wu, Y.-Q. Yu, Y. Yan, J.-H. Liu and X. He, *J. Cluster Sci.*, 2003, **14**, 381.
51. A.-X. Tian, Y.-L. Ning, J. Ying, G.-C. Liu, X. Hou, T.-J. Li and X.-L. Wang, *CrystEngComm*, 2015, **17**, 5569.
52. L. Dai, Y. Ma, E. Wang, Y. Lu, X. Xu and X. Bai, *Transition Met. Chem.*, 2006, **31**, 340.
53. J. N. Barrows, G. B. Jameson and M. T. Pope, *J. Am. Chem. Soc.*, 1985, **107**, 1771.
54. Y. Ding, J.-X. Meng, W.-L. Chen and E.-B. Wang, *CrystEngComm*, 2011, **13**, 2687.
55. Q.-B. Zhang, Y.-K. Lu, Y.-B. Liu, J. Lu, M.-H. Bi, J.-H. Yu, T.-G. Wang, J.-Q. Xu and J. Liu, *Inorg. Chem. Commun.*, 2006, **9**, 544.

Chapter 1 Introduction

56. J. T. Rhule, C. L. Hill and D. A. Judd, *Chem. Rev.*, 1998, **98**, 327.
57. C. L. Hill, M. Hartnup, M. Faraj, M. Weeks, C. M. Prosser-McCartha, R. B. Brown, Jr., M. Kadkhodayan, J.-P. Sommadossi and R. F. Schinazi, *Polyoxometalates as inorganic anti-HIV compounds. Structure-activity relationships.*, Pergamon Press, Inc., New York, 1990.
58. Y. Inouye, Y. Fujimoto, M. Sugiyama, T. Yoshida and T. Yamase, *Biol. Pharm. Bull.*, 1995, **18**, 996.
59. S. Dong, X. Xi and M. Tian, *J. Electroanal. Chem.*, 1995, **385**, 227.
60. Z. Zhang, Q. Lin, S.-T. Zheng, X. Bu and P. Feng, *Chem. Commun.*, 2011, **47**, 3918.
61. H. Lv, Y. V. Geletii, C. Zhao, J. W. Vickers, G. Zhu, Z. Luo, J. Song, T. Lian, D. G. Musaev and C. L. Hill, *Chem. Soc. Rev.*, 2012, **41**, 7572.
62. M. Kourasi, R. G. A. Wills, A. A. Shah and F. C. Walsh, *Electrochim. Acta*, 2014, **127**, 454.
63. P. Staiti, M. Minutoli and S. Hocevar, *J. Power Sources*, 2000, **90**, 231.
64. S. M. J. Zaidi, S. D. Mikhailenko, G. P. Robertson, M. D. Guiver and S. Kaliaguine, *J. Membr. Sci.*, 2000, **173**, 17.
65. T. Matsui, E. Morikawa, S. Nakada, T. Okanishi, H. Muroyama, Y. Hirao, T. Takahashi and K. Eguchi, *ACS Appl. Mater. Interfaces*, 2016, **8**, 18119.
66. N. L. O. Gunn, D. B. Ward, C. Menelaou, M. A. Herbert and T. J. Davies, *J. Power Sources*, 2017, **348**, 107.
67. D. B. Ward, N. L. O. Gunn, N. Uwigena and T. J. Davies, *J. Power Sources*, 2018, **375**, 68.
68. H. D. Pratt III, N. S. Hudak, X. Fang and T. M. Anderson, *J. Power Sources*, 2013, **236**, 259.
69. H. D. Pratt III and T. M. Anderson, *Dalton Trans.*, 2013, **42**, 15650.
70. H. D. Pratt III, W. R. Pratt, X. Fang, N. S. Hudak and T. M. Anderson, *Electrochim. Acta*, 2014, **138**, 210.
71. H. Yang, T. Song, L. Liu, A. Devadoss, F. Xia, H. Han, H. Park, W. Sigmund, K. Kwon and U. Paik, *J. Phys. Chem. C*, 2013, **117**, 17376.

72. Y. H. Ding, J. Peng, S. U. Khan and Y. Yuan, *Chem. Eur. J.*, 2017, **23**, 10338.
73. D. Ma, L. Liang, W. Chen, H. Liu and Y.-F. Song, *Adv. Funct. Mater.*, 2013, **23**, 6100.
74. J. Hu, Y. Ji, W. Chen, C. Streb and Y.-F. Song, *Energy Environ. Sci.*, 2016, **9**, 1095.
75. J. Hu, H. Diao, W. Luo and Y.-F. Song, *Chem. Eur. J.*, 2017, **23**, 8729.
76. A. Xie, C.-A. Ma, L. Wang and Y. Chu, *Electrochim. Acta*, 2007, **52**, 2945.
77. E. Ni, S. Uematsu, Z. Quan and N. Sonoyama, *J. Nanopart. Res.*, 2013, **15**, 1732.
78. E. Ni, S. Uematsu and N. Sonoyama, *Solid State Ionics*, 2014, **268**, 222.
79. J. J. Chen, M. D. Symes, S. C. Fan, M. S. Zheng, H. N. Miras, Q. F. Dong and L. Cronin, *Adv. Mater.*, 2015, **27**, 4649.
80. S. Lu, Y. Lv, W. Ma, X. Lei, R. Zhang, H. Liu and X. Liu, *Inorg. Chem. Front.*, 2017, **4**, 2012.
81. S. Hartung, N. Bucher, H.-Y. Chen, R. Al-Oweini, S. Sreejith, P. Borah, Z. Yanli, U. Kortz, U. Stimming, H. E. Hoster and M. Srinivasan, *J. Power Sources*, 2015, **288**, 270.
82. J. Liu, Z. Chen, S. Chen, B. Zhang, J. Wang, H. Wang, B. Tian, M. Chen, X. Fan, Y. Huang, T. C. Sum, J. Lin and Z. X. Shen, *ACS Nano*, 2017, **11**, 6911.
83. C.-C. Lin, W.-H. Lin, S.-C. Huang, C.-W. Hu, T.-Y. Chen, C.-T. Hsu, H. Yang, A. Haider, Z. Lin, U. Kortz, U. Stimming and H.-Y. Chen, *Adv. Mater. Interfaces*, 2018, **5**, 1800491.
84. J.-J. Chen, J.-C. Ye, X.-G. Zhang, M. D. Symes, S.-C. Fan, D.-L. Long, M.-S. Zheng, D.-Y. Wu, L. Cronin and Q.-F. Dong, *Adv. Energy Mater.*, 2018, **8**, 1701021.
85. P. Gómez-Romero, M. Chojak, K. Cuentas-Gallegos, J. A. Asensio, P. J. Kulesza, N. Casañ-Pastor and M. Lira-Cantú, *Electrochem. Commun.*, 2003, **5**, 149.
86. V. Ruiz, J. Suárez-Guevara and P. Gomez-Romero, *Electrochem. Commun.*, 2012, **24**, 35.

Chapter 1 Introduction

87. M. Genovese and K. Lian, *Electrochim. Commun.*, 2014, **43**, 60.
88. M. Yang and B. G. Choi, *Carbon Lett.*, 2016, **18**, 84.
89. H. Tang, Z. Wan, M. Pan and S. P. Jiang, *Electrochim. Commun.*, 2007, **9**, 2003.
90. M. Yang, S. B. Hong, J. H. Yoon, D. S. Kim, S. W. Jeong, D. E. Yoo, T. J. Lee, K. G. Lee, S. J. Lee and B. G. Choi, *ACS Appl. Mater. Interfaces*, 2016, **8**, 22220.
91. M. Yang, B. G. Choi, S. C. Jung, Y.-K. Han, Y. S. Huh and S. B. Lee, *Adv. Funct. Mater.*, 2014, **24**, 7301.
92. J. Suarez-Guevara, V. Ruiz and P. Gomez-Romero, *Phys. Chem. Chem. Phys.*, 2014, **16**, 20411.
93. C. Hu, E. Zhao, N. Nitta, A. Magasinski, G. Berdichevsky and G. Yushin, *J. Power Sources*, 2016, **326**, 569.
94. Z. Cui, C. X. Guo, W. Yuan and C. M. Li, *Phys. Chem. Chem. Phys.*, 2012, **14**, 12823.
95. J. Vaillant, M. Lira-Cantu, K. Cuentas-Gallegos, N. Casañ-Pastor and P. Gómez-Romero, *Prog. Solid State Chem.*, 2006, **34**, 147.
96. D. P. Dubal, N. R. Chodankar, A. Vinu, D.-H. Kim and P. Gomez-Romero, *ChemSusChem*, 2017, **10**, 2742.
97. M. Genovese and K. Lian, *J. Mater. Chem. A*, 2017, **5**, 3939.
98. R. Li, C. He, L. Cheng, G. Lin, G. Wang, D. Shi, R. K.-Y. Li and Y. Yang, *Compos. B: Eng.*, 2017, **121**, 75.
99. J. Suárez-Guevara, V. Ruiz and P. Gomez-Romero, *J. Mater. Chem. A*, 2014, **2**, 1014.
100. S. Chinnathambi and M. Ammam, *J. Power Sources*, 2015, **284**, 524.
101. A. Mu, J. Li, W. Chen, X. Sang, Z. Su and E. Wang, *Inorg. Chem. Commun.*, 2015, **55**, 149.

Chapter 2

Chemical Reduction of Polyoxometalates

Chapter 2 Chemical Reduction of Polyoxometalates

2.1 Introduction to POM Redox Chemistry

The reversible reduction of POMs is associated mostly with those containing addenda atoms with single terminal M=O bonds. Keggin-type POMs, as described in Chapter 1 are an example of this. The Mo atoms in $[\text{PMo}_{12}\text{O}_{40}]^{3-}$ occupy 'octahedral' sites that are analogous to $\{\text{M(O)O}_5\}$, mono-oxo complexes. The symmetry of Mo in $[\text{PMo}_{12}\text{O}_{40}]^{3-}$, approximates to C_{4v} and the d-orbitals are transformed as a_1 (z^2), b_1 (x^2-y^2), b_2 (xy) and e (xz, yz).¹

The molecular orbital diagram of $\{\text{M(O)O}_5\}$ complexes is shown in Figure 2.1. The metal based a_1 (z^2) and b_1 (x^2-y^2) orbitals are anti-bonding σ orbitals. The b_2 orbital is a non-bonding orbital and the e orbitals are anti-bonding π orbitals. The presence of the non-bonding orbital (b_2) essentially a d_{xy} orbital, which can accept up to two electrons, leads to the reversible redox properties of the Keggin-type POMs and explains the minimal effect to the metal-ligand bond orders.¹ The ligand-based orbitals; $3a_1 + b_1 + e$ and e are occupied with ligand electrons. For fully oxidised POMs the metal will have an electron configuration of d^0 , e.g. Mo^{6+} or W^{6+} , and therefore the metal-based orbitals will be unoccupied.

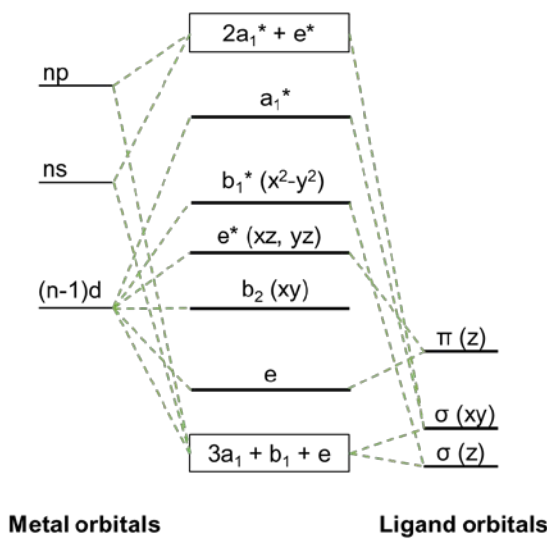


Figure 2.1 Molecular orbital diagram of $\{\text{M(O)O}_5\}$ complexes with C_{4v} symmetry. After ref¹.

The species obtained by the reduction of Keggin-type POMs are often called heteropoly blues. This is due to the colour change obtained upon the reduction of these POMs, to a dark blue colour. The dark blue colour is due to inter-valence charge transfer in mixed oxidation state compounds. Heteropoly blues have been

prepared by many POM researchers including Strickland,² Pope,³ Kazansky and Himeno.^{4,5}

The reduction of phosphomolybdic acid, $H_3[PMo_{12}O_{40}]$ with hydrazine in water-dioxane solution and the subsequent isolation of the reduced POMs as TBA salts was investigated by Canioni in 2010.⁶ They isolated two- and four-electron reduced α - $[PMo_{12}O_{40}]^{3-}$ and found that the four-electron reduced α -species isomerised and formed the β -species in acidic medium. The reduction of $H_3[PMo_{12}O_{40}]$ with hydrazine was also investigated by Maksimovskaya in 2013.⁷ They observed resonances in the $^{31}P\{^1H\}$ NMR spectra for the POM reduced by zero, one, two and four electrons. However they were unable to obtain clean step-wise reductions.

The “super-reduction” of PMo_{12} within a Li-ion battery was investigated by Awaga *et al.*⁸ From XAFS studies they inferred to the reversible addition of twenty-four electrons to PMo_{12} and referred to this as super-reduction, as each Mo atom in PMo_{12} was reduced by two electrons.⁸

The reduction of $(TBA)_3[PMo_{12}O_{40}]$ (PMo_{12}) and $(TBA)_3[V_{13}O_{34}]$ (V_{13}) with $Na|Hg$ amalgam and $Li|Hg$ amalgam is investigated in this Chapter. The reduction of PMo_{12} with KC_8 and $K^+PhCN^{•-}$ is also investigated. These reductions were all followed by NMR spectroscopy; some by FTIR spectroscopy, UV-Vis spectroscopy and CV.

2.2 Reductions with Metal Mercury Amalgams

This section is a continuation of work published in *Chem. Commun.* by the RJE group, where the reduction of PMo_{12} with up to six mole-equivalents of $Na|Hg$ amalgam in MeCN has been studied.⁹ The number of electrons accepted by PMo_{12} has yet to be fully rationalised. This is the first time the ‘super-reduction’ of PMo_{12} has been studied and products isolated, and the reduction of PMo_{12} with $Na|Hg$ amalgam has been investigated in propylene carbonate (PC) and PhCN. This is also the first time the RJE group has studied reductions using $Li|Hg$ amalgam in detail. Preliminary investigations of the reduction of PMo_{12} with $Li|Hg$ amalgam have been undertaken by the group previously, but there were problems with regard to the solubility of Li in Hg. For this study the weight percentage of Li in $Li|Hg$ amalgam was 0.03 wt.% to ensure the full solvation of the Li.¹⁰ $Li|Hg$ amalgam was chosen because of the previous study conducted by Awaga *et al.* on PMo_{12} in a Li-ion

battery cathode.⁸ The Mo K-edge XANES spectra were used to calculate the average valence of Mo, they found that all 12 Mo⁶⁺ ions in PMo₁₂ were reduced to Mo⁴⁺ when the battery was discharged.⁸ PC was also chosen as a solvent as it is commonly used as an electrolyte solvent for energy storage devices.^{11, 12, 13} Na|Hg and Li|Hg amalgams were also investigated as reducing agents for V₁₃ in both MeCN and PC. Hill *et al.* found that V₁₃ has the most positive reduction potential of the vanadate POMs.¹⁴

2.2.1 The Reaction Between (TBA)₃[PMo₁₂O₄₀] and Na|Hg Amalgam in MeCN

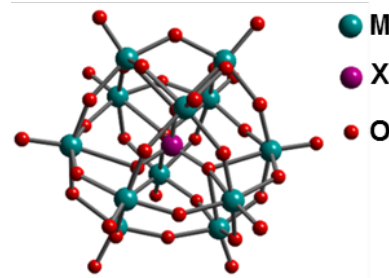
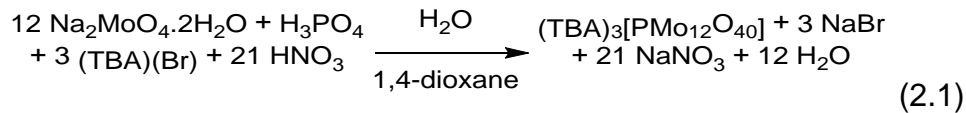


Figure 2.2 Ball-and-stick representation of the anion [PMo₁₂O₄₀]³⁻.

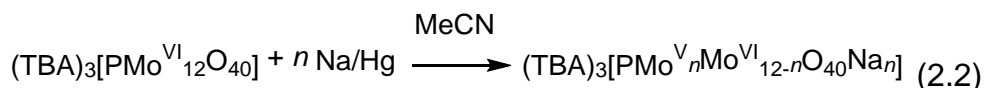


(TBA)₃[PMo₁₂O₄₀] (PMo₁₂) was prepared following a literature procedure as shown in Equation 2.1, to give yellow crystals.¹⁵ The ³¹P{¹H} NMR spectrum contained one peak at -3.8 ppm in CD₃CN, -3.7 ppm in PC and -3.0 ppm in PhCN (with reference to 85% aqueous H₃PO₄). The ball-and-stick representation of the anion [PMo₁₂O₄₀]³⁻ is shown in Figure 2.2.

The reduction of PMo₁₂ with Na|Hg amalgam in MeCN as shown in Equation 2.2 has been followed by ³¹P{¹H} NMR and FTIR spectroscopy. The solution of PMo₁₂ changes from yellow to dark green on the addition of one mole-equivalent of Na|Hg amalgam. The addition of two mole-equivalents of Na|Hg amalgam gives a dark blue reaction solution, i.e. a heteropoly blue. Kazansky suggests that on the addition of one electron to PMo₁₂, the electron will be delocalised over all 12 Mo atoms.⁴ The addition of electrons leads to inter-valence charge transfer which effects the shift in the NMR resonance and the effect on the Mo-O-Mo bands in the FTIR spectra, which will be discussed further below. On the addition of two electrons to PMo₁₂, the

Chapter 2 Chemical Reduction of Polyoxometalates

electrons can form a spin bipolaron and the coupled electrons move around the twelve Mo atoms in a pair.



The peaks in the $^{31}\text{P}\{^1\text{H}\}$ NMR spectra of the reduction of PMo_{12} with increasing amounts of Na/Hg amalgam are listed in Table 2.1 and shown in Figure 2.3. The addition of one mole-equivalent of Na/Hg amalgam shifts the resonance downfield from -3.8 to 0.0 ppm. The addition of two mole-equivalents of Na/Hg amalgam shifts the resonance upfield, and this pattern continues as more Na/Hg amalgam is added. For an odd number of mole-equivalents, the resonance is shifted downfield and when an even number of mole-equivalents is added the resonance is shifted upfield. For one to five mole-equivalents of Na/Hg amalgam, there is a major peak in the $^{31}\text{P}\{^1\text{H}\}$ NMR spectrum but for six mole-equivalents there are four peaks, two of which are quite similar in size, so it is difficult to deduce which resonance should be assigned to six electron reduced PMo_{12} . The shift in the NMR resonances could be due to the formation of spin bipolarons on the addition of an even number of electrons to PMo_{12} .

<i>n</i>	$\delta_{\text{P}} / \text{ppm}$
0	-3.8
1	0.0
2	-7.0
3	-2.7, -6.3, -7.0
4	-2.7, -6.9
5	-3.1, -6.1
6	-2.5, -3.1, -3.9, -4.6

Table 2.1 Peaks in the $^{31}\text{P}\{^1\text{H}\}$ NMR spectra from reactions between n mole-equivalents of Na/Hg amalgam and PMo_{12} in MeCN (major peak is in bold for when there is more than one peak present).

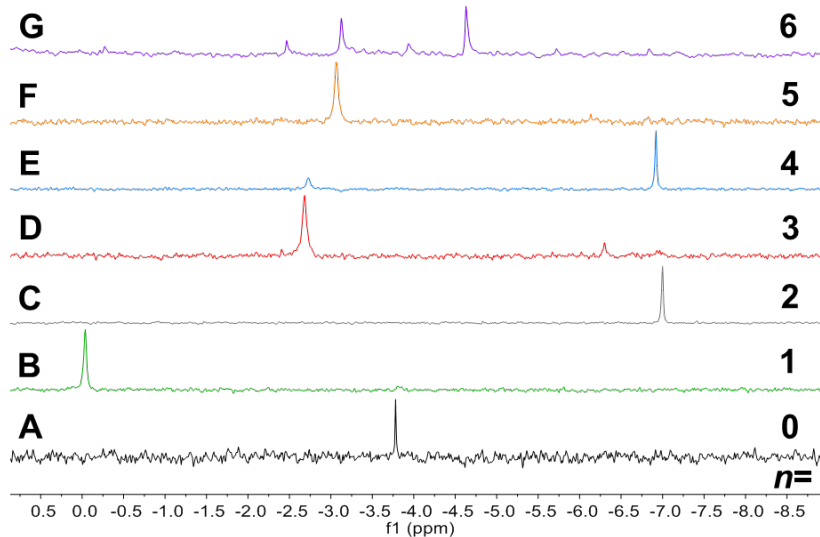


Figure 2.3 $^{31}\text{P}\{^1\text{H}\}$ NMR spectra from reactions between n mole-equivalents of $\text{Na}|\text{Hg}$ amalgam and PMo_{12} in MeCN.

There have been issues with the accurate determination of the number of mole-equivalents of amalgam used in the reactions, this is due to errors in accurately weighing out the Na that is dissolved in Hg. This was evident in the attempts to synthesise one electron reduced PMo_{12} , as a small percentage of fully-oxidised PMo_{12} was present in the $^{31}\text{P}\{^1\text{H}\}$ NMR spectrum of the reaction mixture (Figure 2.4A). The integration of the two peaks in the $^{31}\text{P}\{^1\text{H}\}$ NMR spectrum enabled the recalculation of the wt.% of Na in the amalgam, so the amount of $\text{Na}|\text{Hg}$ amalgam added to PMo_{12} could be more accurate for two to six mole-equivalents.

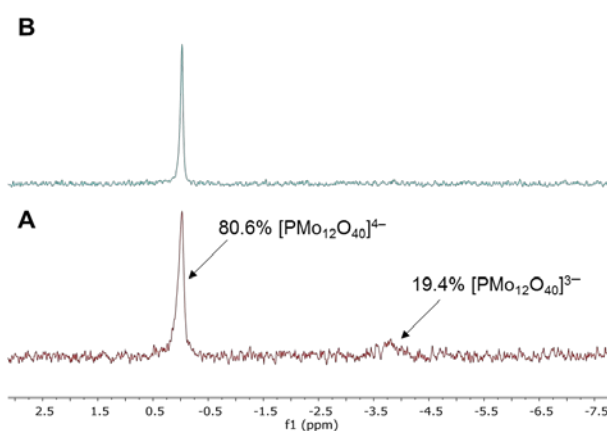


Figure 2.4 $^{31}\text{P}\{^1\text{H}\}$ NMR spectra of the reaction between PMo_{12} and one-mole equivalent of $\text{Na}|\text{Hg}$ amalgam (A), and with the calculated amount of $\text{Na}|\text{Hg}$ amalgam added to form all one-electron reduced PMo_{12} (B).

The bands in the FTIR spectra of solid products isolated from the addition of $\text{Na}|\text{Hg}$ to PMo_{12} in MeCN are listed in Table 2.2 and shown in Figure 2.5. The $\nu(\text{P-O})$ band

decreases in intensity as more electrons are added to PMo_{12} . The band at 874 cm^{-1} in the FTIR spectrum of fully oxidised PMo_{12} disappears on the addition of $\text{Na}|\text{Hg}$ amalgam. The $\nu(\text{Mo}-\text{O}_t)$ band shifts to lower wavenumber with increasing amounts of $\text{Na}|\text{Hg}$ amalgam. The $\nu(\text{Mo}-\text{O}_b\text{-Mo})$ bands are also shifted to lower wavenumbers with increasing amounts of $\text{Na}|\text{Hg}$ amalgam, the bands have become broader and less defined. Eguchi *et al.* witnessed a similar effect to the bands in the IR spectra obtained upon the reduction of the potassium salt of $[\text{PMo}_{12}\text{O}_{40}]^{3-}$ with H_2 in a closed system at $350\text{-}400 \text{ }^\circ\text{C}$.¹⁶

<i>n</i>	Wavenumber/ cm^{-1}			
	P-O	Mo-O_t	Mo-O_b-Mo	
0	1060.0	950.4	873.8, 785.4, 615.7, 499.5, 462.4	
1	1056.5, 1027.4	938.0	768.3, 592.4, 494.7	
2	1056.2	935.7	748.7, 590.3, 486.9	
3	1056.4	936.2	749.1, 590.5, 487.3	
4	1056.5	935.6	744.8, 590.0, 484.1	
5	1056.5	937.1	751.2, 590.4, 493.0	
6	1056.4	938.2	732.3, 590.4, 489.5	

Table 2.2 Bands in the FTIR spectra of solids isolated from reactions between n mole-equivalents of $\text{Na}|\text{Hg}$ amalgam and PMo_{12} in MeCN.

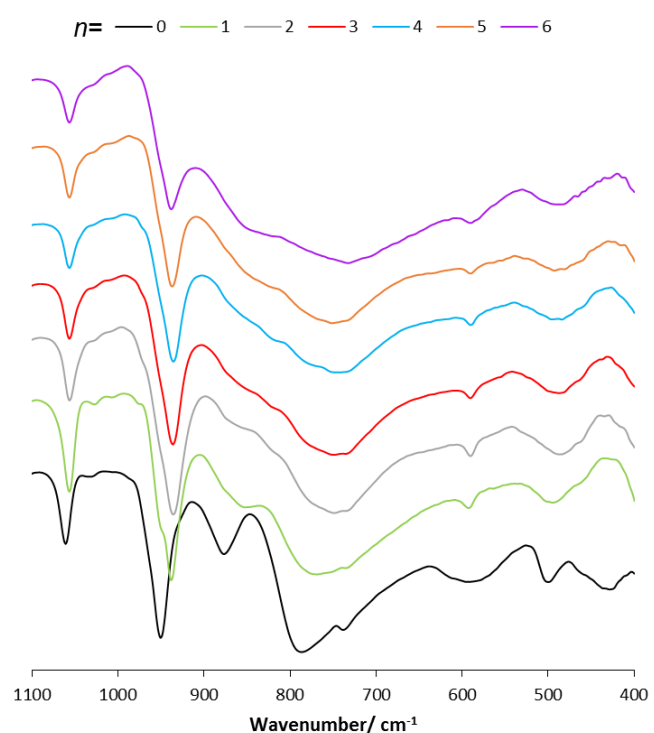
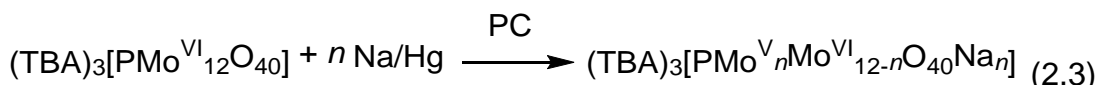


Figure 2.5 FTIR spectra of solids isolated from reactions between n mole-equivalents of $\text{Na}|\text{Hg}$ amalgam and PMo_{12} in MeCN.

2.2.2 The Reaction Between $(TBA)_3[PMo_{12}O_{40}]$ and $Na|Hg$ Amalgam in PC

The reaction between PMo_{12} and $Na|Hg$ amalgam in PC is shown in Equation 2.3.

The reaction was followed by $^{31}P\{^1H\}$ NMR, FTIR and UV-Vis spectroscopy. The colour changes observed were similar to those in the reaction between PMo_{12} and $Na|Hg$ in MeCN; one mole-equivalent (dark green) and two to ten mole-equivalents (dark blue). In PC the amount of $Na|Hg$ amalgam added was increased further and the colours of the reaction solutions after the addition of twelve and twenty-four mole-equivalents of $Na|Hg$ amalgam were dark brown.



The peaks in the $^{31}P\{^1H\}$ NMR spectra of the reaction of PMo_{12} with increasing amounts of $Na|Hg$ amalgam are listed in Table 2.3 and the resonances are shown in Figure 2.6. The addition of one mole-equivalent of $Na|Hg$ amalgam shifts the resonance downfield from -3.7 to 0.2 ppm, the addition of two mole-equivalents of $Na|Hg$ amalgam shifts the peak upfield to -6.6 ppm. The peaks when two and three mole-equivalents of $Na|Hg$ amalgam added have very similar chemical shifts. The broad peak for when five mole-equivalents of $Na|Hg$ amalgam are added is shifted downfield, the peak is shifted further downfield than for when the same number of mole-equivalents of $Na|Hg$ are added to PMo_{12} in MeCN. The $^{31}P\{^1H\}$ NMR spectra for when four and six mole-equivalents of $Na|Hg$ amalgam are added to PMo_{12} are shown in Figure 2.6E and G, there is more than one species present and the peaks are broad, this is indicative of electron and/or cation exchange between the multiple species that are present. The $^{31}P\{^1H\}$ NMR spectrum for the reaction between PMo_{12} and twelve mole-equivalents of $Na|Hg$ amalgam contains one resonance that is shifted upfield and when twenty-four mole-equivalents of $Na|Hg$ amalgam are added there are no peaks. The non-observance of peaks could possibly be due to the poor solubility of PMo_{12} reduced by twenty-four electrons.

<i>n</i>	δ_P ppm
0	-3.7
1	0.2
2	-6.6
3	-6.7
4	-2.7, -3.3, -5.8
5	0.1
6	-2.7, -3.7 , -5.5, -6.1
12	-6.5
24	No peaks

Table 2.3 Peaks in $^{31}P\{^1H\}$ NMR spectra from reactions between *n* mole-equivalents of Na|Hg amalgam and PMo_{12} in PC (major peak is in bold for when there is more than one peak present).

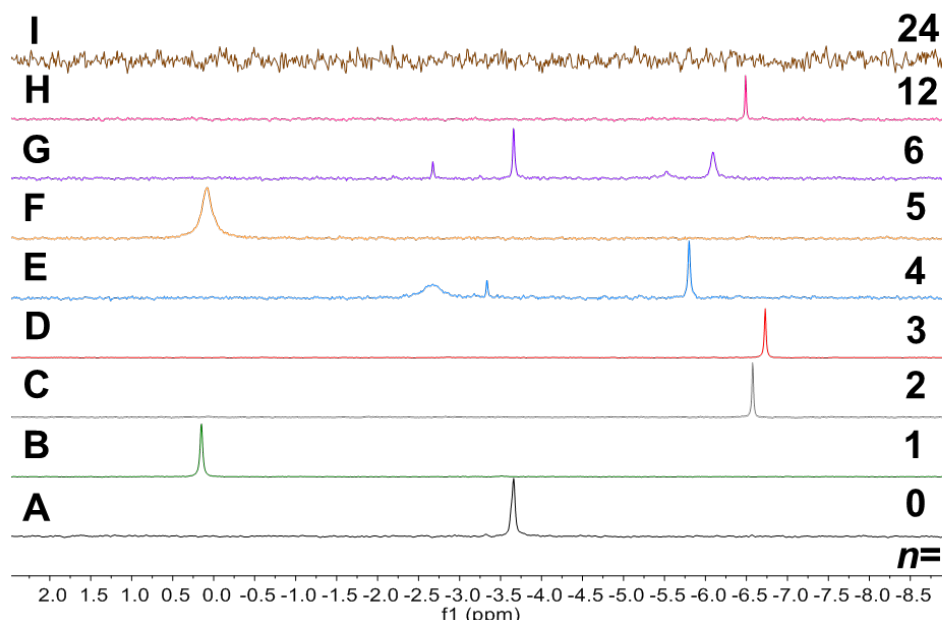


Figure 2.6 $^{31}P\{^1H\}$ NMR spectra from reactions between *n* mole-equivalents of Na|Hg amalgam and PMo_{12} in PC.

The peaks in the solid-state ^{31}P NMR spectra are listed in Table 2.4 and shown in Figure 2.7 for solids isolated from the reaction between PMo_{12} and *n* mole-equivalents of Na|Hg amalgam in PC. Spectra are yet to be recorded for *n* = 3, 4, 5, 6 and 12 mole-equivalents of Na|Hg amalgam. The resonances in the solid-state NMR spectra of the isolated solids are in similar positions to the resonances in the solution NMR. The peak for fully oxidised PMo_{12} is split in to two, possibly due to a solid-state effect. The peak in the spectrum of the solid isolated from the reaction between PMo_{12} and twenty-four mole-equivalents of Na|Hg amalgam is very broad.

<i>n</i>	$\delta_{\text{P}}/\text{ppm}$
0	-3.4, -3.6
1	0.1
2	-0.1, -6.8
24	8.4

Table 2.4 Peaks in the solid-state ^{31}P NMR spectra for the reaction between PMo_{12} and *n* mole-equivalents of $\text{Na}|\text{Hg}$ amalgam in PC.

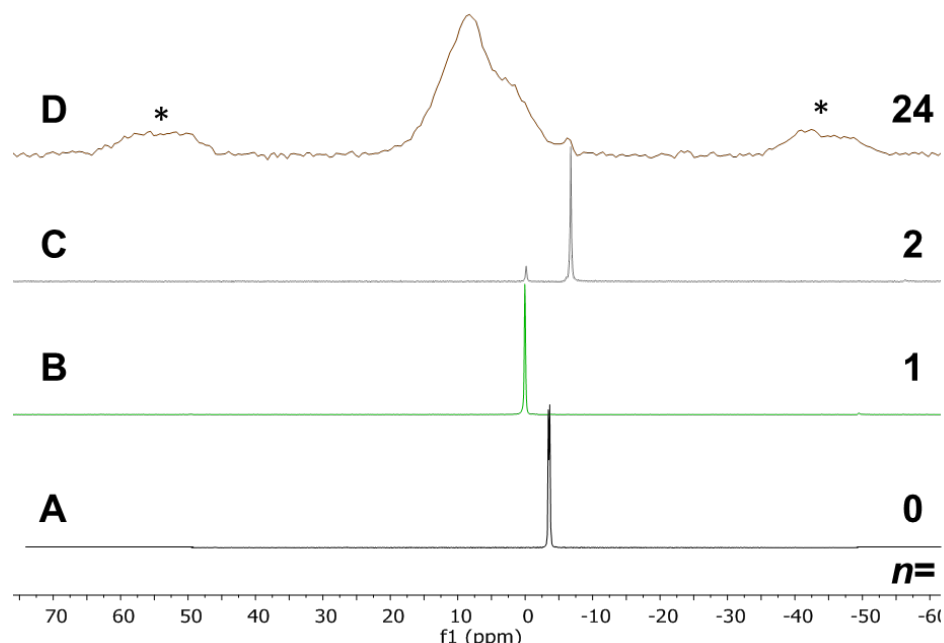


Figure 2.7 Solid-state ^{31}P NMR spectra for the reaction between PMo_{12} and *n* mole-equivalents of $\text{Na}|\text{Hg}$ amalgam in PC.

The peaks in the solid-state ^{23}Na NMR spectra are listed in Table 2.5 and shown in Figure 2.8 for the reaction between PMo_{12} and *n* mole-equivalents of $\text{Na}|\text{Hg}$ amalgam in PC.

<i>n</i>	$\delta_{\text{Na}}/\text{ppm}$
1	6.8, -3.4, -10.9, -11.6, -22.0
2	-13.8, -21.4
24	-7.7

Table 2.5 Peaks in the solid-state ^{23}Na NMR spectra for the reaction between PMo_{12} and *n* mole-equivalents of $\text{Na}|\text{Hg}$ amalgam in PC.

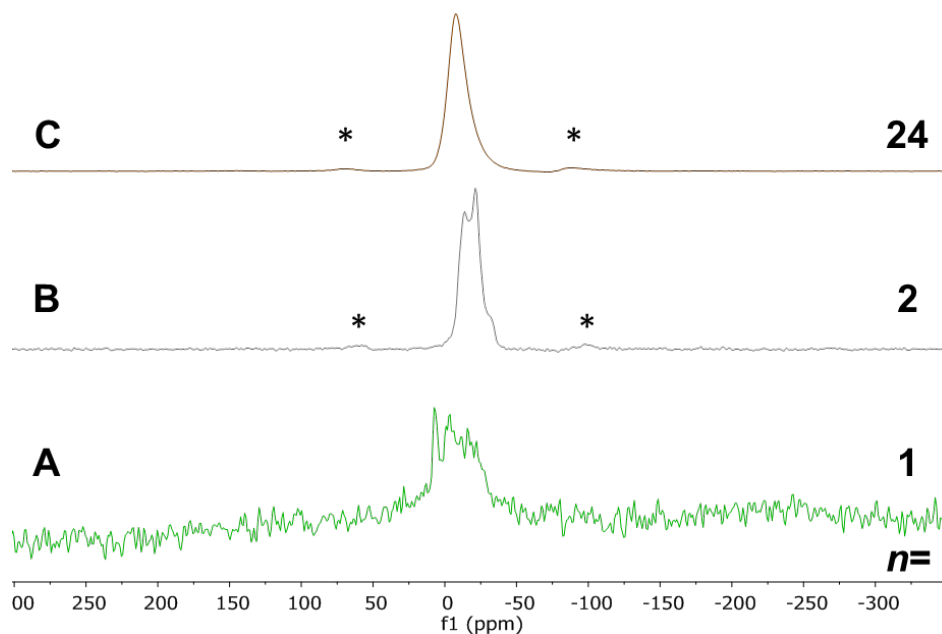


Figure 2.8 Solid-state ^{23}Na NMR spectra for the reaction between PMo_{12} and n mole-equivalents of $\text{Na}|\text{Hg}$ amalgam in PC.

The bands in the FTIR spectra of solids isolated from the addition of n mole-equivalents of $\text{Na}|\text{Hg}$ amalgam to PMo_{12} in PC are listed in Table 2.6 and shown in Figure 2.9. The band at 874 cm^{-1} in the FTIR spectrum of fully oxidised PMo_{12} is still present when one mole-equivalent of $\text{Na}|\text{Hg}$ amalgam is added but disappears on the addition of more $\text{Na}|\text{Hg}$ amalgam. The $\nu(\text{P}-\text{O})$ band starts to broaden and decrease in intensity as the mole-equivalents of $\text{Na}|\text{Hg}$ amalgam added increases, up to four equivalents. For five mole-equivalents of $\text{Na}|\text{Hg}$ amalgam and greater, the $\nu(\text{P}-\text{O})$ band is much broader, although this could be due to overlap with bands from PC, which has several strong bands between 1000 and 1200 cm^{-1} .¹⁷ The $\nu(\text{Mo}-\text{O})$ terminal band shifts to lower wavenumber with increasing mole-equivalents of $\text{Na}|\text{Hg}$ amalgam. The $\nu(\text{Mo}-\text{O}-\text{Mo})$ bridging bands are similarly shifted to lower wavenumbers with the addition of $\text{Na}|\text{Hg}$ amalgam and become broader and less well defined. On the addition of twelve and twenty-four mole-equivalents of $\text{Na}|\text{Hg}$ amalgam the intensity of the $\nu(\text{Mo}-\text{O}-\text{Mo})$ bridging bands had decreased significantly.

n	Wavenumber/ cm^{-1}		
	P-O	Mo-O _t	Mo-O _b -Mo
0	1060.0	950.4	873.8, 785.4, 615.7, 499.5, 462.4
1	1057.0	953.1	873.7, 779.2, 584.1, 500.1, 429.9
2	1054.2	938.0	749.8, 715.3, 590.6, 490.8
3	1052.4	940.8	767.3, 708.6, 591.5, 490.6, 445.1
4	1055.4	934.9	742.0, 709.6, 589.0, 481.1
5	1054.1	936.8	751.5, 710.5, 590.3, 491.8
6	1046.3	931.4	775.6, 736.5, 706.5, 624.2, 587.2, 514.5, 462.2, 437.6
12	1047.0	934.7	821.9, 775.1, 742.0, 709.6, 612.4, 481.1, 408.9
24	1045.0	937.7	852.3, 818.7, 775.4, 708.6, 618.2, 575.1, 486.0

Table 2.6 Bands in the FTIR spectra of solids isolated from the reaction between n mole-equivalents of Na|Hg amalgam and PMo_{12} in PC. t= terminal and b= bridging.

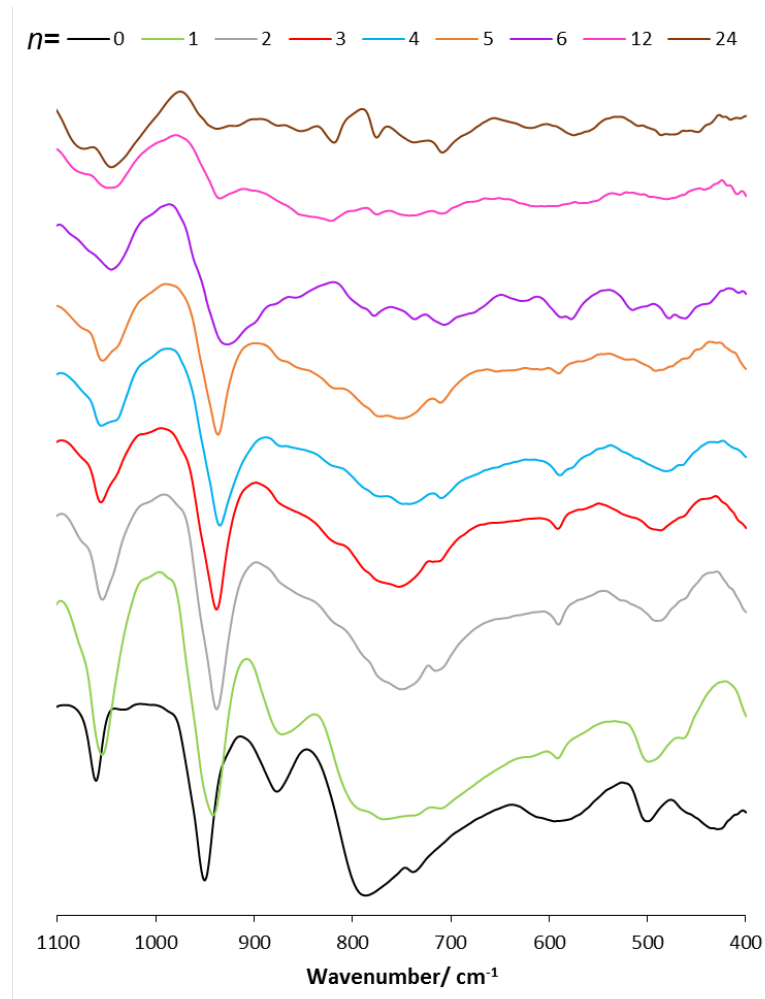


Figure 2.9 FTIR spectra of isolated solids from the reaction of n mole-equivalents of Na|Hg amalgam and PMo_{12} in PC.

The UV-Vis spectra of the reactions between PMo_{12} and n mole-equivalents of $\text{Na}|\text{Hg}$ amalgam ($n = 0\text{-}6$) in PC are shown in Figure 2.10 and the λ_{max} and molar absorption coefficient values are listed in Table 2.7. It shows that the absorbance spectrum changes from zero to one and then two to six mole-equivalents of $\text{Na}|\text{Hg}$ amalgam. The spectrum for one mole-equivalent of $\text{Na}|\text{Hg}$ amalgam contains two very broad absorption peaks, at λ_{max} 570 and 827 nm. The spectra for two to six mole equivalents of $\text{Na}|\text{Hg}$ amalgam contain two absorptions at λ_{max} between 540 and 559 nm, and between 720 and 733 nm.

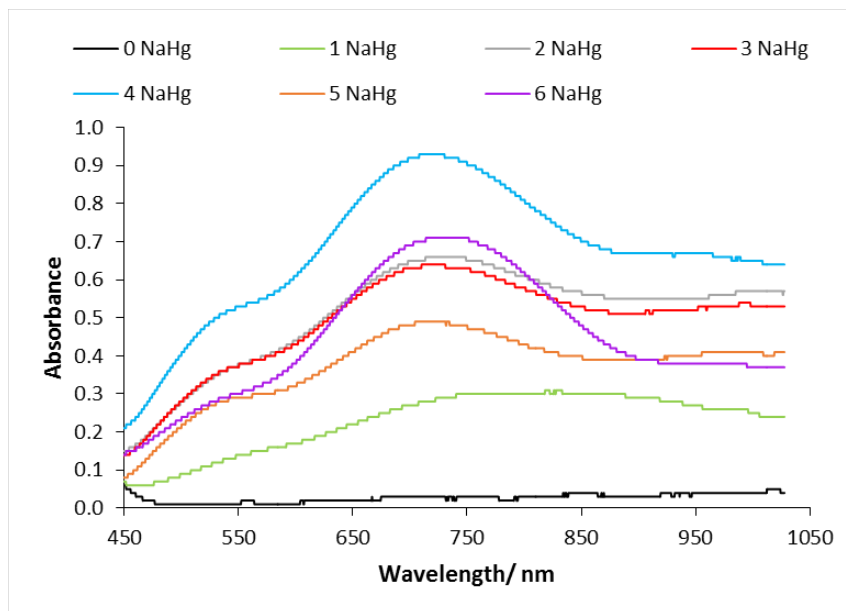


Figure 2.10 The UV-Vis spectra of reactions between PMo_{12} and n mole-equivalents of $\text{Na}|\text{Hg}$ in PC, $c = 0.25 \text{ mM}$, $l = 1 \text{ cm}$.

n	$\lambda_{\text{max}1}/\text{nm}$	$\epsilon/\text{M}^{-1}.\text{cm}^{-1}$	$\lambda_{\text{max}2}/\text{nm}$	$\epsilon/\text{M}^{-1}.\text{cm}^{-1}$
0	854	120		
1	570	600	827	1200
2	559	1520	733	2640
3	546	1480	723	2560
4	546	2080	720	3720
5	553	1160	720	1960
6	540	1160	729	2840

Table 2.7 The λ_{max} and molar absorption coefficient (ϵ) values for the UV-Vis spectra of reactions between PMo_{12} and n mole-equivalents of $\text{Na}|\text{Hg}$ in PC, $c = 0.25 \text{ mM}$, $l = 1 \text{ cm}$.

The UV-Vis spectra of the reactions between PMo_{12} and an odd number of mole-equivalents of $\text{Na}|\text{Hg}$ amalgam are shown in Figure 2.11. The absorbance spectrum for one mole-equivalent of $\text{Na}|\text{Hg}$ is significantly different from the absorbance spectra for three and five mole-equivalents of $\text{Na}|\text{Hg}$.

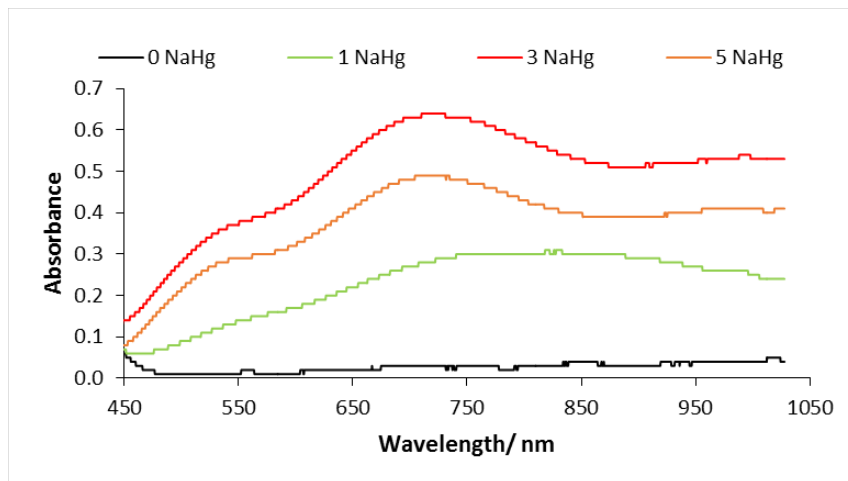


Figure 2.11 The UV-Vis spectra of reactions between PMo_{12} and n mole-equivalents of $\text{Na}|\text{Hg}$ in PC, $c = 0.25 \text{ mM}$, $l = 1 \text{ cm}$.

The UV-Vis spectra of the reactions between PMo_{12} and an even number of mole-equivalents of $\text{Na}|\text{Hg}$ amalgam is shown in Figure 2.12. They show that the absorbance increases when $2 < 6 < 4$ mole-equivalents of $\text{Na}|\text{Hg}$ amalgam is added to PMo_{12} , with the greatest absorbance for 4 equivalents of $\text{Na}|\text{Hg}$ amalgam.

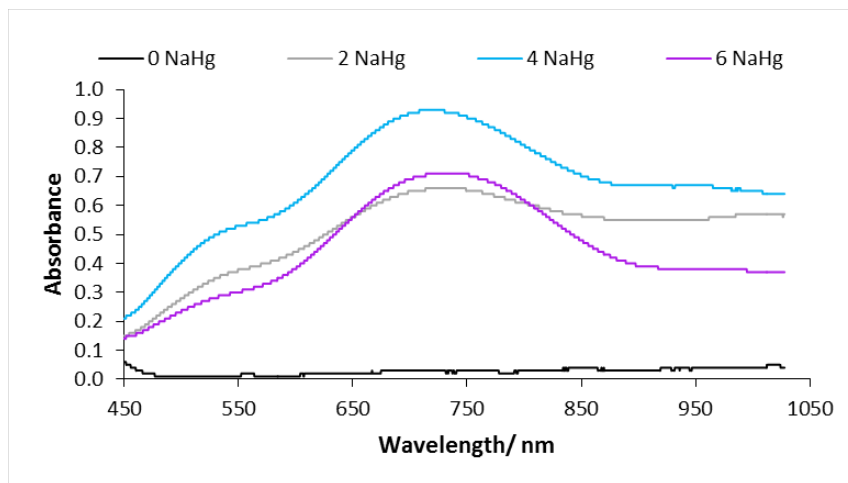


Figure 2.12 The UV-Vis spectra of reactions between PMo_{12} and n mole-equivalents of $\text{Na}|\text{Hg}$ in PC, $c = 0.25 \text{ mM}$, $l = 1 \text{ cm}$.

The molar extinction coefficient ($\epsilon / \text{M}^{-1} \cdot \text{cm}^{-1}$) was calculated from the UV-Vis spectra as n equivalents of $\text{Na}|\text{Hg}$ were added to PMo_{12} using the Beer-Lambert Law

(Equation 2.4), where A is the absorbance, c is the concentration of the solution (M) and l is the pathlength (cm). ϵ is plotted against n equivalents of Na|Hg amalgam in Figure 2.13. When n is an odd number ϵ is lower than for when n is an even number, and is highest for when $n = 4$. The difference in ϵ could be due to stability issues, it is possible that when an odd number of electrons are added to PMo_{12} it is less stable than for when an even number of electrons are added, and therefore PMo_{12} is oxidising before the UV-Vis measurement is taken. This problem could be rectified by carrying out the UV-Vis measurements inside a glovebox but this facility was not available.

$$A = \epsilon cl \quad (2.4)$$

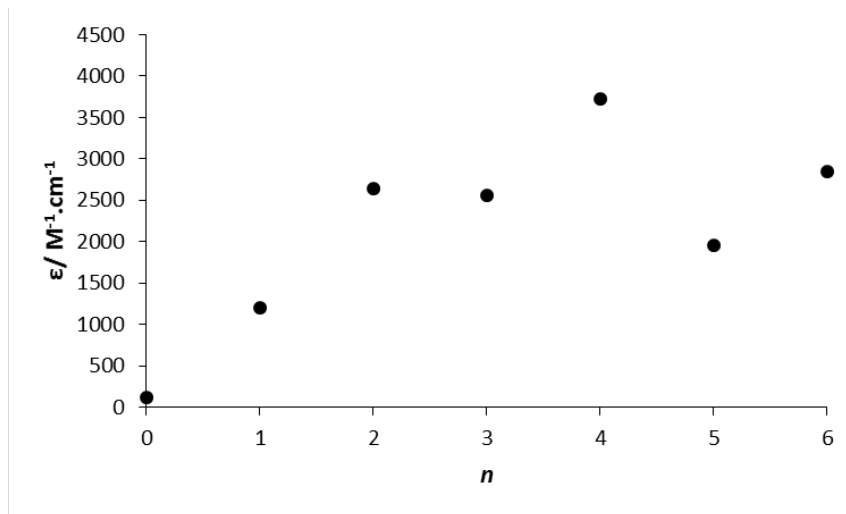


Figure 2.13 Plot of molar extinction coefficient (ϵ) against the number of mole-equivalents (n) of Na|Hg amalgam added to PMo_{12} .

2.2.3 The Reaction Between $(\text{TBA})_3[\text{PMo}_{12}\text{O}_{40}]$ and Na|Hg Amalgam in PhCN

The reaction between PMo_{12} and n mole-equivalents of Na|Hg amalgam in PhCN is shown in Equation 2.5. The reaction was followed by $^{31}\text{P}\{^1\text{H}\}$ NMR spectroscopy. The reaction between PMo_{12} and Na|Hg in PhCN was investigated in order to compare the results with the reaction between PMo_{12} and K^+PhCN^- , which will be discussed in Section 2.3.2.

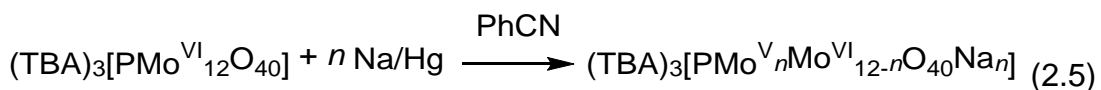


Table 2.8 lists the peaks in the $^{31}\text{P}\{^1\text{H}\}$ NMR spectra and Figure 2.14 shows $^{31}\text{P}\{^1\text{H}\}$ NMR spectra for comparisons. The resonances in the NMR spectra follow a similar

trend as seen previously for zero, one and two mole-equivalents of Na|Hg amalgam. However, for three to six mole-equivalents of Na|Hg amalgam there is little change in the chemical shift of the major peak, which is different to what was seen for reduction with Na|Hg amalgam in MeCN and PC, where the resonances alternated between downfield and upfield for odd and even numbers of equivalents added to PMo_{12} . This might be due to non-innocent PhCN; i.e. the PhCN is consuming electrons and forming PhCN radical anion or alternatively impure/wet solvent is causing oxidation of products formed.

n	$\delta_{\text{P}}/\text{ppm}$
0	-3.0
1	1.6 , -2.6, -5.6
2	1.1, -5.8
3	-0.7, -5.8
4	-6.1
5	-1.6, -4.7, -5.9
6	-5.8

Table 2.8 Peaks in the ${}^{31}\text{P}\{{}^1\text{H}\}$ NMR spectra for the reactions between PMo_{12} and n mole-equivalents of Na|Hg amalgam in PhCN (major peak is in bold for when there is more than one peak present).

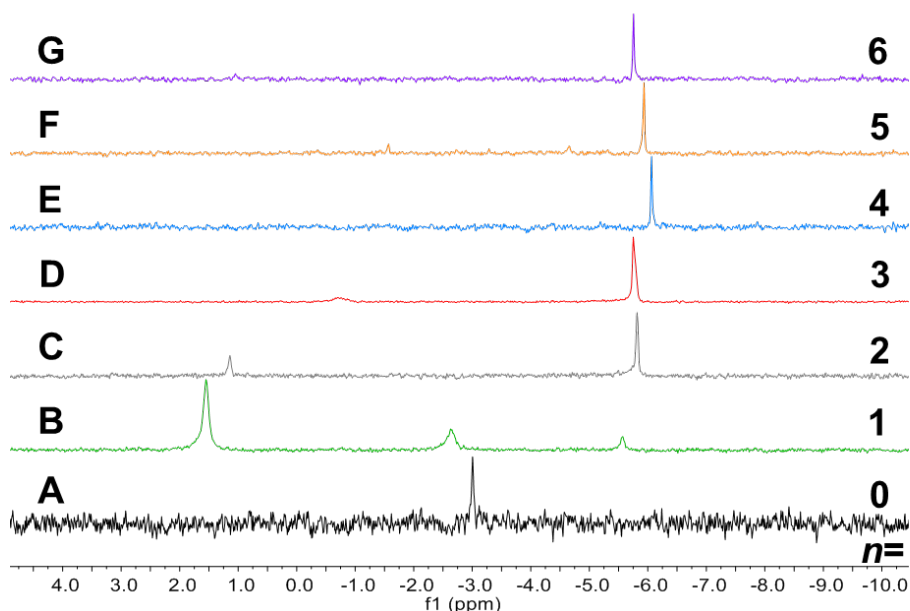
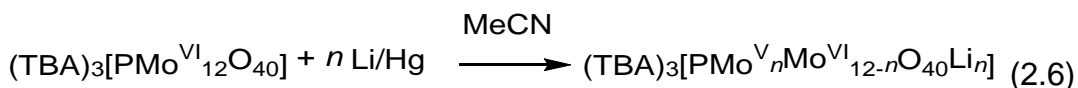


Figure 2.14 ${}^{31}\text{P}\{{}^1\text{H}\}$ NMR spectra for the reactions between PMo_{12} and n mole-equivalents of Na|Hg amalgam in PhCN.

2.2.4 The Reaction Between $(TBA)_3[PMo_{12}O_{40}]$ and $Li|Hg$ Amalgam in MeCN

The reaction between PMo_{12} and n mole-equivalents of $Li|Hg$ amalgam in MeCN is shown in Equation 2.6. The reaction was followed by $^{31}P\{^1H\}$ NMR and FTIR spectroscopy.



The peaks in the $^{31}P\{^1H\}$ NMR spectra of the reaction between PMo_{12} and increasing mole-equivalents of $Li|Hg$ amalgam are listed in Table 2.9 and the resonances are shown in Figure 2.15. The addition of one-mole-equivalent of $Li|Hg$ shifts the resonance downfield from -3.8 to -0.1 ppm. The addition of two mole-equivalents of $Li|Hg$ shifted the peak upfield to -7.0 ppm, and the main peaks after the addition of four and six mole-equivalents of $Li|Hg$ are also upfield. The $^{31}P\{^1H\}$ NMR spectrum for the reaction between PMo_{12} and twelve mole-equivalents of $Li|Hg$ amalgam contained one resonance that is shifted downfield to 9.7 ppm and when twenty-four mole-equivalents of $Li|Hg$ amalgam were added a very broad peak at -2.4 ppm was observed with a line width of 109 Hz. The broadness of the peak could possibly be due to aggregation of PMo_{12} reduced by twenty-four electrons, as the larger aggregated species tumble more slowly in solution, increasing the correlation time and thereby broadening the lines.¹⁸ The line broadening is not due to errors as the errors in relation to the peak widths are ± 0.2 Hz for the sharper peaks and ± 100 Hz for the much broader peaks.

n	δ_P/ ppm
0	-3.8
1	-0.1
2	-7.0
4	-2.3, -5.9 , -6.9
6	-2.3, -5.9, -6.9
12	9.7 , 1.1, -2.5, -5.4
24	-2.4

Table 2.9 Peaks in $^{31}P\{^1H\}$ NMR spectra for the reactions between PMo_{12} and n mole-equivalents of $Li|Hg$ amalgam in MeCN (major peak is in bold for when there is more than one peak present).

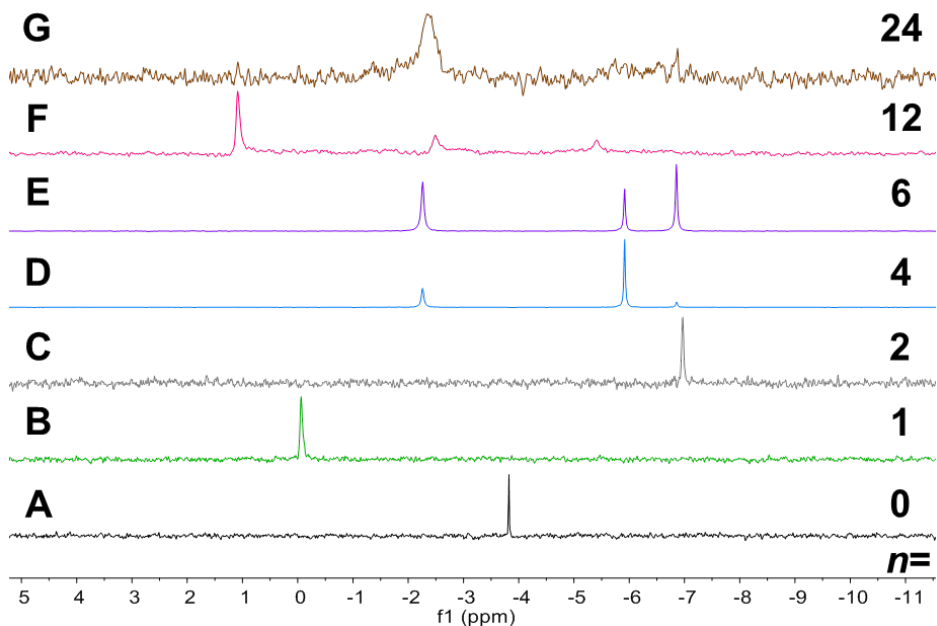


Figure 2.15 $^{31}\text{P}\{^1\text{H}\}$ NMR spectra for the reactions between PMo_{12} and n mole-equivalents of $\text{Li}|\text{Hg}$ amalgam in MeCN.

The bands in the FTIR spectra of solids isolated from the addition of n mole-equivalents of $\text{Li}|\text{Hg}$ amalgam to PMo_{12} in MeCN are listed in Table 2.10 and shown in Figure 2.16. The FTIR spectra follow a similar trend to that observed for products from the reaction between PMo_{12} and $\text{Na}|\text{Hg}$, i.e. the $\nu(\text{P}-\text{O})$ and $\nu(\text{Mo}-\text{O}_t)$ bands shift to lower wavenumbers and decrease in intensity. The $\nu(\text{P}-\text{O})$ band is barely visible for when $n = 24$. The $\nu(\text{Mo}-\text{O}_b\text{-Mo})$ bands also shift to lower wavenumbers and are less well defined. The increase in the wavenumber for the first $\nu(\text{Mo}-\text{O}_b\text{-Mo})$ band in the spectra of solids isolated from the reaction between PMo_{12} and twelve and twenty-four mole-equivalents of $\text{Li}|\text{Hg}$ amalgam could be indicative of a new mode.

n	Bands in FTIR/ cm^{-1}		
	P-O	Mo-O _t	Mo-O _b -Mo
1	1056.6	937.7	851.4, 765.2, 590.7, 497.6
2	1057.5	934.4	746.3, 590.8, 486.9
4	1057.3	937.5	790.0, 735.1, 591.2, 468.6
6	1057.4	936.6	748.4, 591.2, 485.2
12	1056.1	936.5	806.5, 629.0, 620.9, 459.7
24	1032.2	929.1	817.0, 733.7

Table 2.10 Bands in the FTIR spectra for the products isolated from the reactions between PMo_{12} and n mole-equivalents of $\text{Li}|\text{Hg}$ amalgam in MeCN.

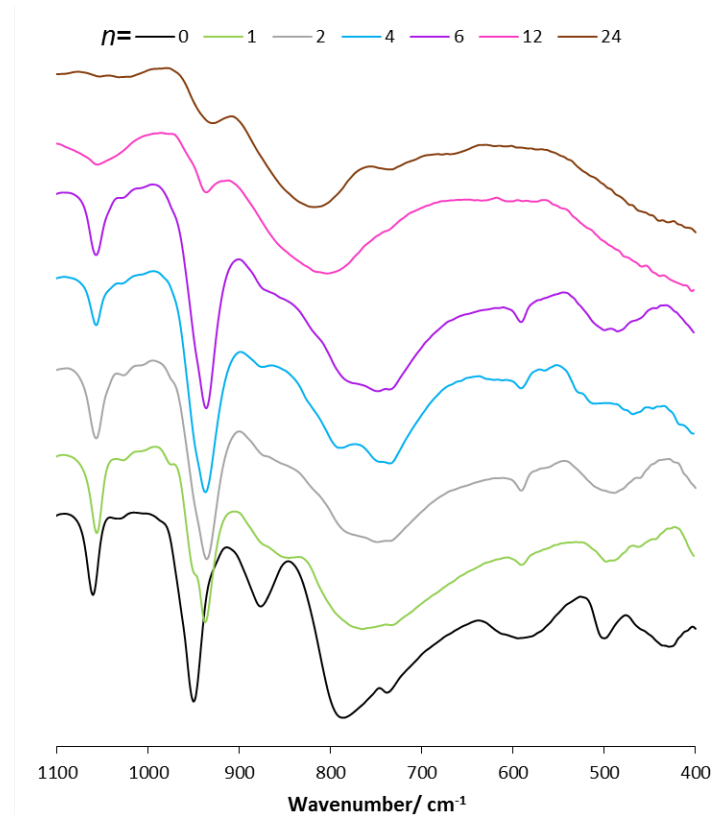


Figure 2.16 FTIR spectra for the products isolated from the reactions between PMo_{12} and n mole-equivalents of $\text{Li}|\text{Hg}$ amalgam in MeCN.

2.2.5 The Reaction Between $(\text{TBA})_3[\text{PMo}_{12}\text{O}_{40}]$ and $\text{Li}|\text{Hg}$ Amalgam in PC

The reaction between PMo_{12} and n mole-equivalents of $\text{Li}|\text{Hg}$ amalgam in PC is shown in Equation 2.7. The reaction was followed by $^{31}\text{P}\{^1\text{H}\}$ NMR (solution and solid-state), FTIR and UV-Vis spectroscopy. CV on solutions of isolated products.



The peaks in the $^{31}\text{P}\{^1\text{H}\}$ NMR spectra of the reaction between PMo_{12} and increasing mole-equivalents of $\text{Li}|\text{Hg}$ amalgam in PC are listed in Table 2.11 and the resonances are shown in Figures 2.17 and 2.18. The addition of one mole equivalent of $\text{Li}|\text{Hg}$ amalgam shifts the resonance downfield from -3.7 to $+0.1$ ppm. The addition of two mole-equivalents of $\text{Li}|\text{Hg}$ amalgam shifts the peak upfield to -6.7 ppm. The main peak when three to six mole-equivalents of $\text{Li}|\text{Hg}$ amalgam are added is also upfield. The $^{31}\text{P}\{^1\text{H}\}$ NMR spectra for the products after addition of eight and ten mole-equivalents of $\text{Li}|\text{Hg}$ amalgam are similar, and a broad peak at ca. -4.4 ppm is present, that is also apparent for the spectrum after addition of

twelve mole-equivalents of Li|Hg amalgam. The $^{31}\text{P}\{^1\text{H}\}$ NMR spectrum for the reaction mixture after the addition of twelve mole-equivalents of Li|Hg amalgam contains two broad resonances at +15.5 and -5.0 ppm and one sharper resonance at -1.2 ppm. After the addition of twenty-four equivalents of Li|Hg amalgam to PMo_{12} , the NMR spectrum contained one very broad peak between -20 and +20 ppm, with fwhm line width of 3189 Hz. The broadness of the peak could possibly be due to aggregation of PMo_{12} reduced by twenty-four electrons and the decrease in solubility. The line broadening is not due to errors as the errors in relation to the peak widths are ± 0.2 Hz for the sharper peaks and ± 100 Hz for the much broader peaks.

<i>n</i>	$\delta_{\text{P}}/\text{ppm}$
0	-3.7
1	0.1 , -3.6
2	-0.1, -6.7
3	-2.3, -5.8, -6.7
4	-0.1, -6.7
5	-2.3, -5.8 , -6.7
6	-2.2, -5.8 , -6.8
8	2.1, -0.8 , -4.4
10	2.3 , -0.8, -4.3
12	15.5 , -1.2, -5.0
24	+20 to -20

Table 2.11 Peaks in the $^{31}\text{P}\{^1\text{H}\}$ NMR spectra for the reactions between PMo_{12} and *n* mole-equivalents of Li|Hg amalgam in PC (major peak is in bold for when there is more than one peak present).

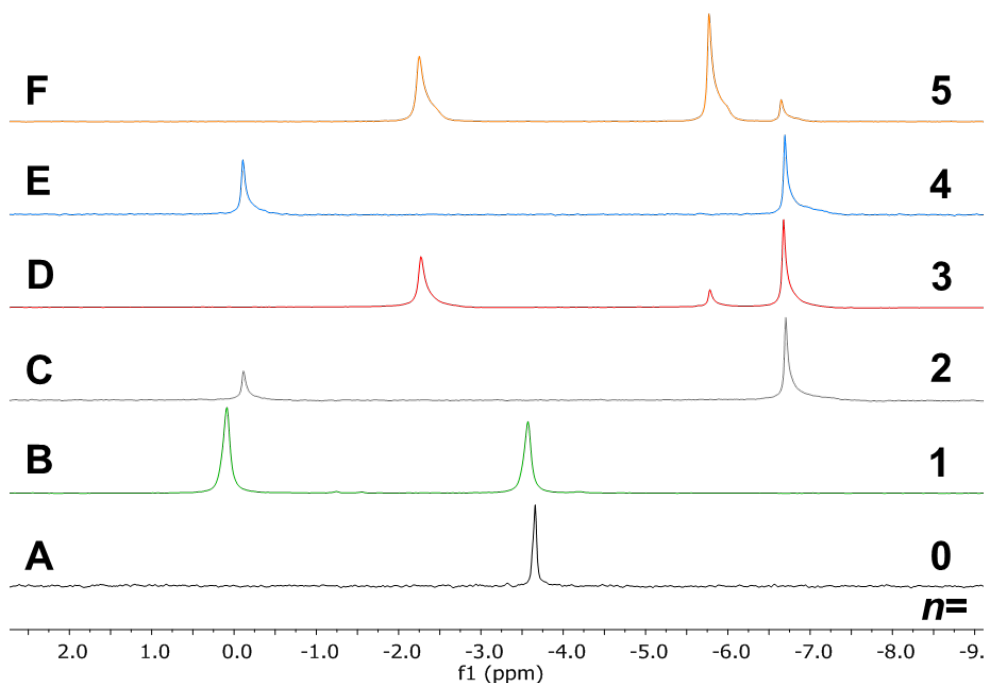


Figure 2.17 $^{31}\text{P}\{^1\text{H}\}$ NMR spectra for the reactions between PMo_{12} and n mole-equivalents of $\text{Li}|\text{Hg}$ amalgam in PC.

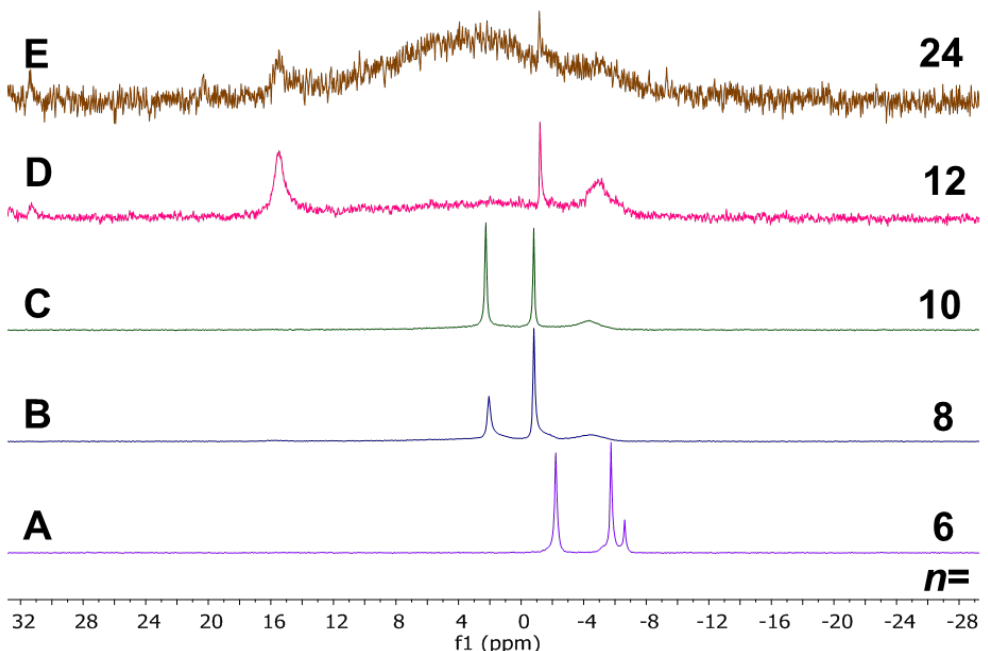


Figure 2.18 $^{31}\text{P}\{^1\text{H}\}$ NMR spectra for the reactions between PMo_{12} and n mole-equivalents of $\text{Li}|\text{Hg}$ amalgam in PC.

The peaks in the solid-state ^{31}P NMR spectra of solids isolated from the reaction between PMo_{12} and n mole-equivalents of $\text{Li}|\text{Hg}$ amalgam are listed in Table 2.12 and shown in Figure 2.19. Spectra are yet to be recorded for $n = 3, 4, 5, 6, 8$ and 10 mole-equivalents of $\text{Li}|\text{Hg}$ amalgam. The peaks in the spectra for the isolated solids

are in similar positions to the solution NMR spectra. The linewidth of the peak (2432 Hz) in the solid-state spectrum of twenty-four mole-equivalents of Li|Hg amalgam is similar to the linewidth of the peak in the solution NMR. The broader line widths in solid-state could be due to disorder and the reduction in symmetry.

<i>n</i>	δ_P / ppm
0	-3.4, -3.6
1	-0.1
2	0.1, -6.6, -7.3
12	0.0, -6.6, -6.8, -7.6
24	5.7

Table 2.12 Peaks in the solid-state ^{31}P NMR spectra for solids isolated from the reactions between PMo_{12} and *n* mole-equivalents of Li|Hg amalgam in PC.

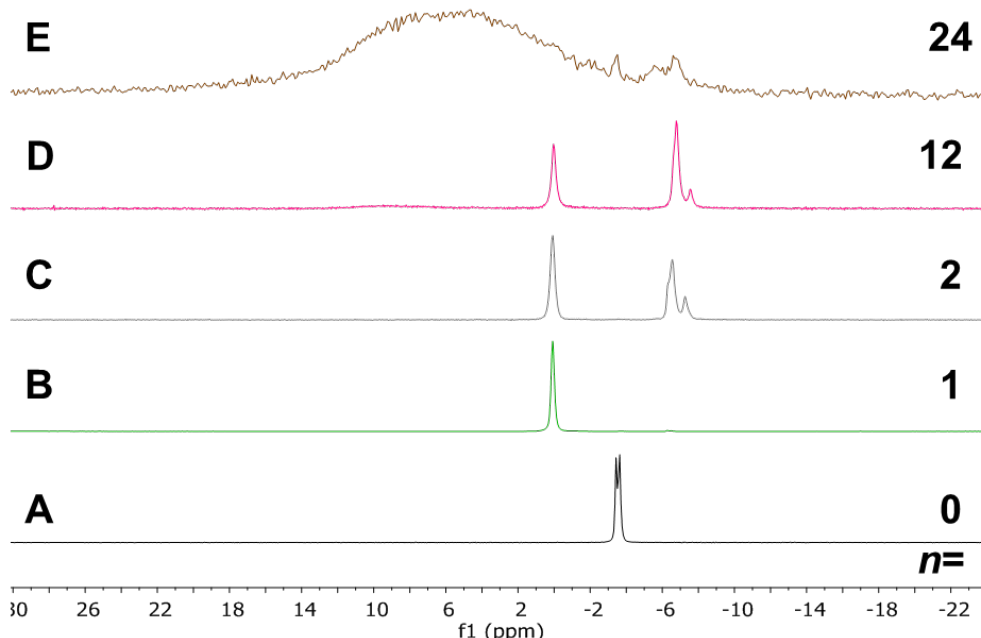


Figure 2.19 Solid-state ^{31}P NMR spectra for solids isolated from the reactions between PMo_{12} and *n* mole-equivalents of Li|Hg amalgam in PC.

The peaks in the solid-state ^7Li NMR spectra for the reaction between PMo_{12} and *n* mole-equivalents of Li|Hg amalgam are listed in Table 2.13 and shown in Figure 2.20. As the number of mole-equivalents of Li|Hg amalgam increases the linewidth of the peaks increase.

<i>n</i>	$\delta_{\text{Li}}/\text{ppm}$
1	-1.7
2	-0.6
12	-0.6
24	-0.2

Table 2.13 Peaks in the solid-state ^7Li NMR spectra for solids isolated from the reactions between PMo_{12} and *n* mole-equivalents of $\text{Li}|\text{Hg}$ amalgam in PC.

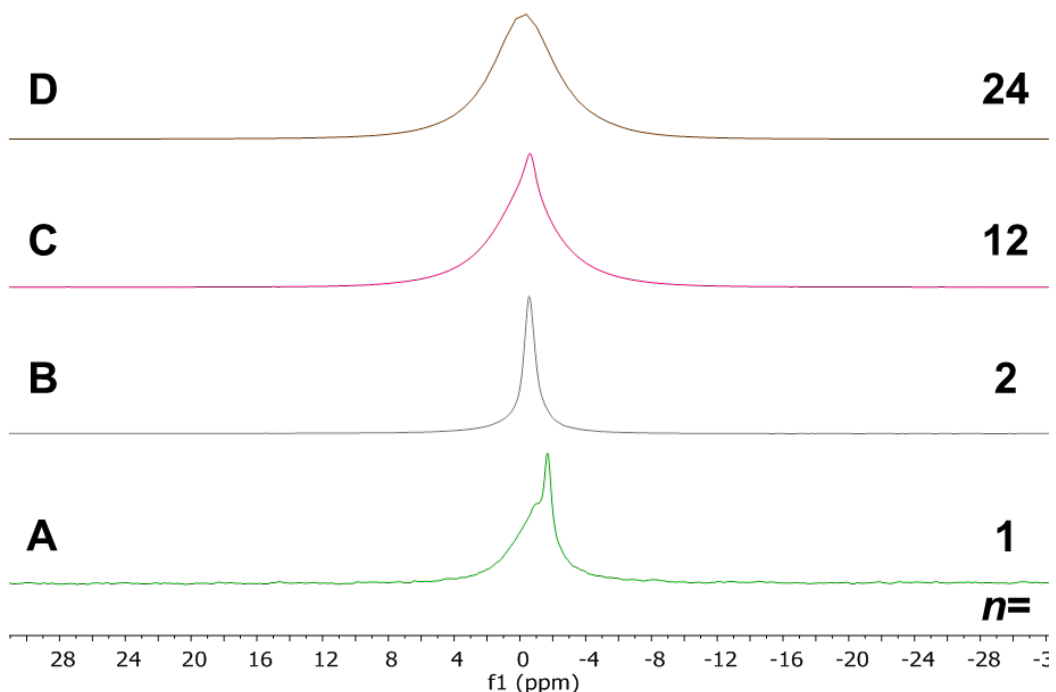


Figure 2.20 Solid-state ^7Li NMR spectra for solids isolated from the reactions between PMo_{12} and *n* mole-equivalents of $\text{Li}|\text{Hg}$ amalgam in PC.

The bands in the FTIR spectra of solids isolated from the addition of *n* mole-equivalents of $\text{Li}|\text{Hg}$ amalgam to PMo_{12} in PC are listed in Table 2.14 and shown in Figure 2.21. As the amount of $\text{Li}|\text{Hg}$ amalgam added to PMo_{12} increases from zero to six equivalents, the $\nu(\text{P}-\text{O})$ band decreases in intensity and is shifted to lower wavenumber. The $\nu(\text{P}-\text{O})$ band then starts to increase in intensity between eight and twenty-four mole-equivalents of $\text{Li}|\text{Hg}$ amalgam, although this could be due to residual PC in the solid. The $\nu(\text{Mo}-\text{O}_t)$ band is shifted to lower wavenumber as the amount of $\text{Li}|\text{Hg}$ amalgam added increases. The $\nu(\text{Mo}-\text{O}_b-\text{Mo})$ bands also shift to lower wavenumbers and decrease in intensity.

<i>n</i>	Bands in FTIR/ cm ⁻¹		
	P-O	Mo-O _t	Mo-O _b -Mo
0	1060.0	950.4	873.8, 785.4, 615.7, 499.5, 462.4
1	1059.8	945.8	874.6, 783.4, 591.0, 462.2, 496.9
2	1055.2	942.3	742.8, 716.1, 591.0, 491.2
3	1057.3	939.9	765.1, 592.0, 488.3, 428.1
4	1057.1	940.6	782.9, 591.6, 493.0, 423.0, 444.1
5	1055.5	939.3	772.8, 591.4, 480.1, 443.7, 430.6, 464.8
6	1057.6	938.1	779.9, 752.5, 591.1
8	1052.0	937.3	773.1, 591.0
10	1048.2	934.0	733.4, 588.0, 427.3
12	1051.4	932.8	869.6, 778.3, 730.7, 586.1
24	1044.4	939.3	868.8, 775.5, 707.2

Table 2.14 Bands in the FTIR spectra of solids isolated from the reactions between PMo_{12} and *n* mole-equivalents of Li|Hg amalgam in PC.

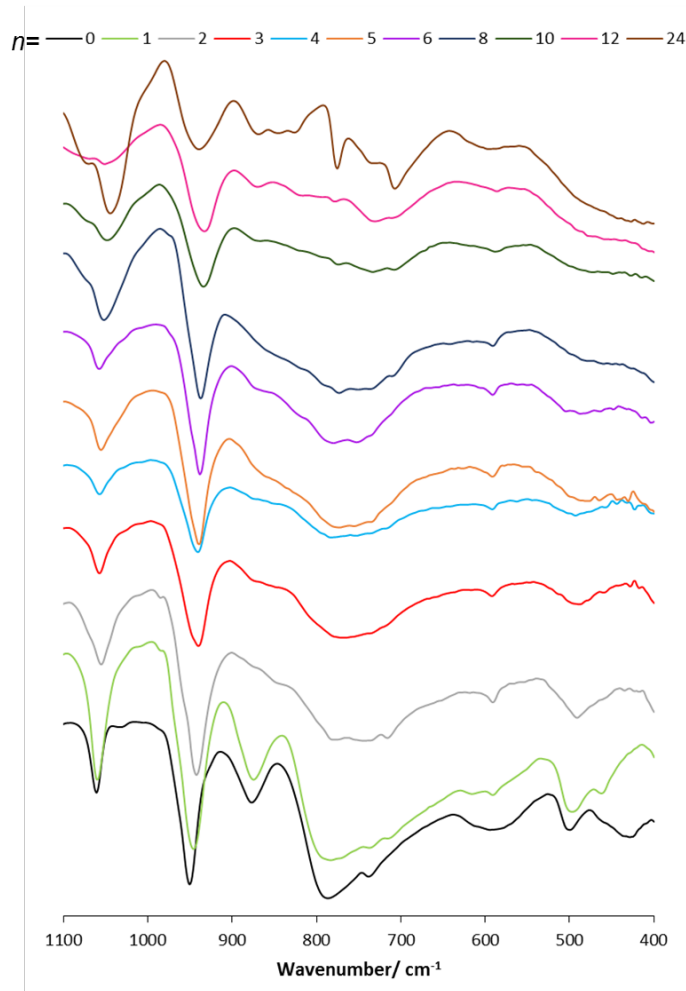


Figure 2.21 FTIR spectra of solids isolated from the reactions between PMo_{12} and *n* mole-equivalents of Li|Hg amalgam in PC.

Chapter 2 Chemical Reduction of Polyoxometalates

The UV-Vis spectra of the products isolated from reactions between PMo_{12} and n mole-equivalents of $\text{Li}|\text{Hg}$ amalgam ($n = 0\text{-}6, 8, 10$) in PC are shown in Figure 2.22 and λ_{max} and molar absorption coefficient values are listed in Table 2.15. It shows that the absorbance spectrum changes from zero to one and then two to ten mole-equivalents of $\text{Li}|\text{Hg}$ amalgam. The spectrum for one mole-equivalent of $\text{Li}|\text{Hg}$ amalgam contains two very broad absorption peaks, at λ_{max} 584 and 826 nm. For two to six, eight and ten mole-equivalents of $\text{Li}|\text{Hg}$ amalgam, there are two better defined absorption peaks at λ_{max} between 551 and 566 nm, and between 704 and 725 nm.

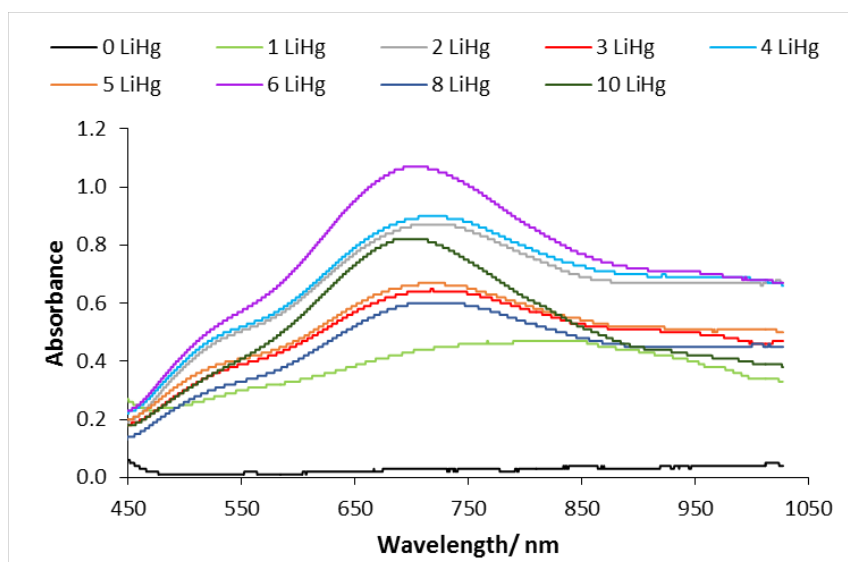


Figure 2.22 UV-Vis spectra for the reactions between PMo_{12} and n equivalents of $\text{Li}|\text{Hg}$ amalgam in PC, $c = 0.25 \text{ mM}$, $l = 1 \text{ cm}$.

n	$\lambda_{\text{max}1}/\text{nm}$	$\epsilon/\text{M}^{-1}.\text{cm}^{-1}$	$\lambda_{\text{max}2}/\text{nm}$	$\epsilon/\text{M}^{-1}.\text{cm}^{-1}$
0	854	120		
1	584	1240	826	1880
2	561	2080	723	3480
3	561	1600	725	2560
4	557	2120	720	3600
5	566	1680	720	2680
6	551	2280	704	4280
8	561	1360	723	2400
10	557	1680	701	3280

Table 2.15 The λ_{max} and molar absorption coefficient (ϵ) values for the UV-Vis spectra of reactions between PMo_{12} and n mole-equivalents of $\text{Li}|\text{Hg}$ in PC, $c = 0.25 \text{ mM}$, $l = 1 \text{ cm}$.

The UV-Vis spectra of the products isolated from the reactions between PMo_{12} and n mole-equivalents of $\text{Li}|\text{Hg}$ amalgam, where n is an odd number are shown in Figure 2.23, it shows that the absorbance profile for one mole-equivalent of $\text{Li}|\text{Hg}$ amalgam is significantly different to the absorbance profile for three and five equivalents of $\text{Li}|\text{Hg}$ amalgam.

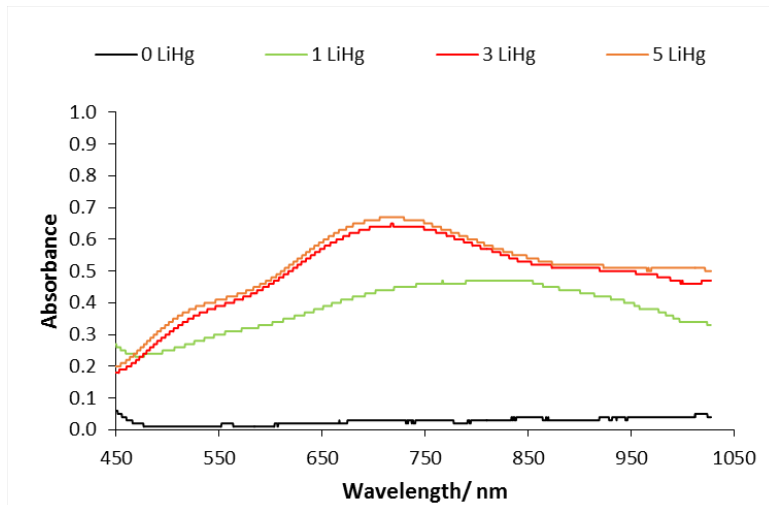


Figure 2.23 UV-Vis spectra for the reactions between PMo_{12} and n equivalents of $\text{Li}|\text{Hg}$ amalgam in PC, $c = 0.25 \text{ mM}$, $l = 1 \text{ cm}$.

The UV-Vis spectra of the products isolated from the reactions between PMo_{12} and n mole-equivalents of $\text{Li}|\text{Hg}$ amalgam, where n is an even number are shown in Figure 2.24, it shows that there is an increase in absorbance as more $\text{Li}|\text{Hg}$ amalgam is added to PMo_{12} up to $n = 6$, then for when $n = 8$ and 10 the absorbance decreases in intensity.

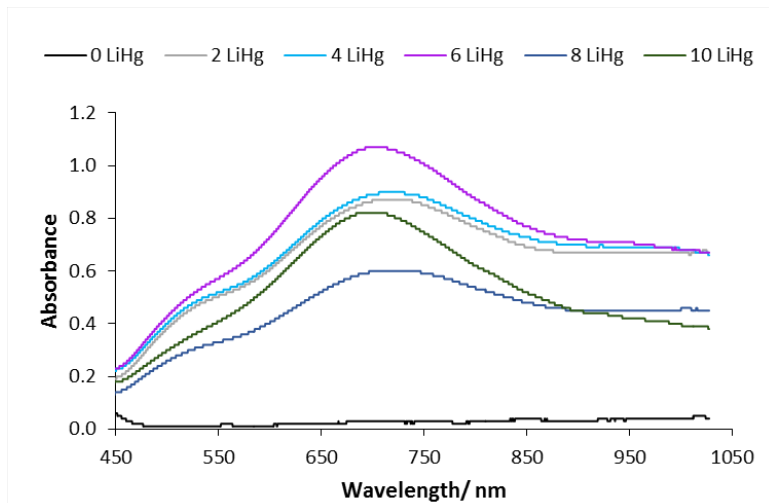


Figure 2.24 UV-Vis spectra for the reactions between PMo_{12} and n equivalents of $\text{Li}|\text{Hg}$ amalgam in PC, $c = 0.25 \text{ mM}$, $l = 1 \text{ cm}$.

The molar extinction coefficient ($\epsilon / M^{-1} \cdot \text{cm}^{-1}$) was calculated from the UV-Vis spectra using Equation 2.1 and was plotted against n in Figure 2.25. When n is an odd number ϵ is lower than for when n is an even number, and is highest for when $n = 6$. The difference in ϵ could be due to stability issues, it is possible that when an odd number of electrons are added to PMo_{12} it is less stable than for when an even number of electrons are added and therefore PMo_{12} could be oxidising before the UV-Vis measurement is taken.

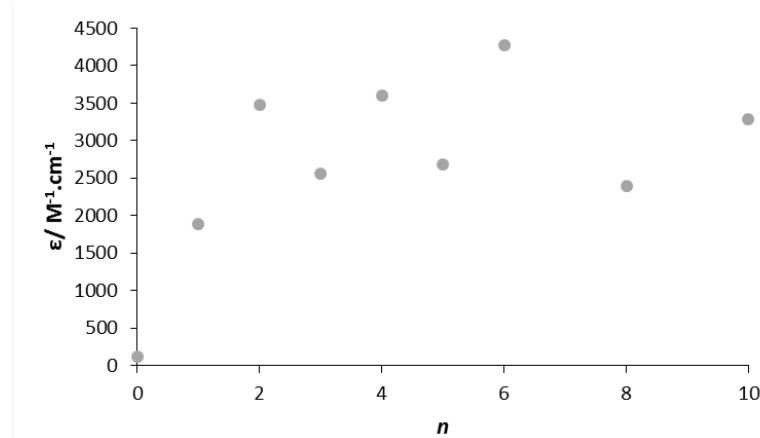


Figure 2.25 Plot of molar extinction coefficient (ϵ) against the number of mole-equivalents (n) of $\text{Li}|\text{Hg}$ amalgam added to PMo_{12} .

The cyclic voltammograms of products isolated after treatment of PMo_{12} with increasing amounts of $\text{Li}|\text{Hg}$ amalgam are shown Figure 2.26-2.34. They show that as the number of mole-equivalents of $\text{Li}|\text{Hg}$ amalgam increases the redox waves are shifted.

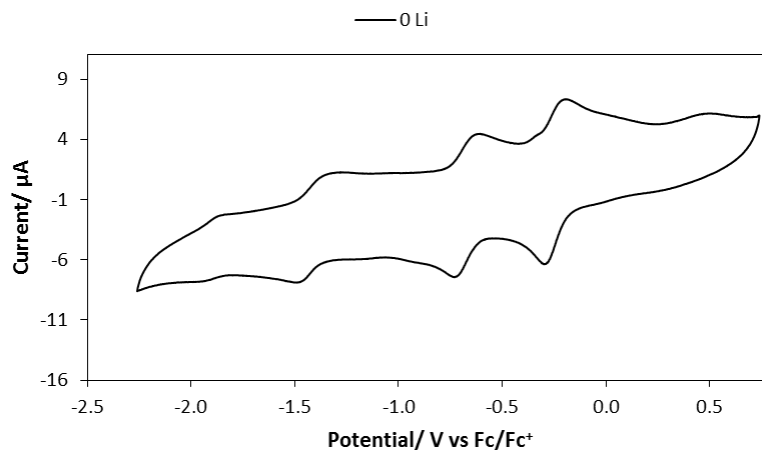


Figure 2.26 Cyclic voltammogram of solid isolated from the reactions between PMo_{12} and 0 mole-equivalents of $\text{Li}|\text{Hg}$ amalgam. 1 mM POM in 100 mM (TBA)(BF₄) in MeCN, from +1.0 V to -2.0 V vs Ag wire, 100 mV/s scan rate, GC WE, Pt wire CE, Ag wire RE.

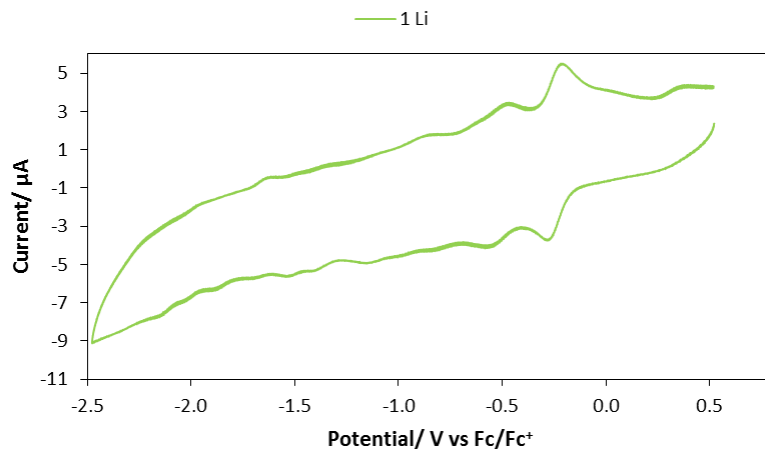


Figure 2.27 Cyclic voltammogram of solid isolated from the reactions between PMo_{12} and 1 mole-equivalents of $\text{Li}|\text{Hg}$ amalgam. 1 mM POM in 100 mM (TBA)(BF₄) in MeCN, from +1.0 V to -2.0 V vs Ag wire, 100 mV/s scan rate, GC WE, Pt wire CE, Ag wire RE.

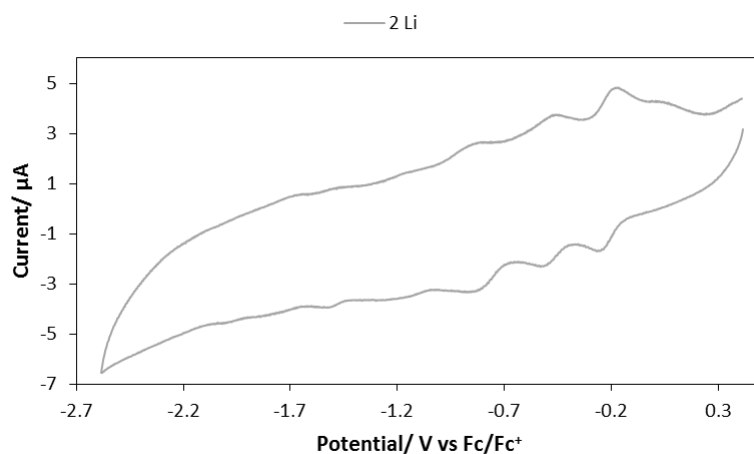


Figure 2.28 Cyclic voltammogram of solid isolated from the reactions between PMo_{12} and 2 mole-equivalents of $\text{Li}|\text{Hg}$ amalgam. 1 mM POM in 100 mM (TBA)(BF₄) in MeCN, from +1.0 V to -2.0 V vs Ag wire, 100 mV/s scan rate, GC WE, Pt wire CE, Ag wire RE.

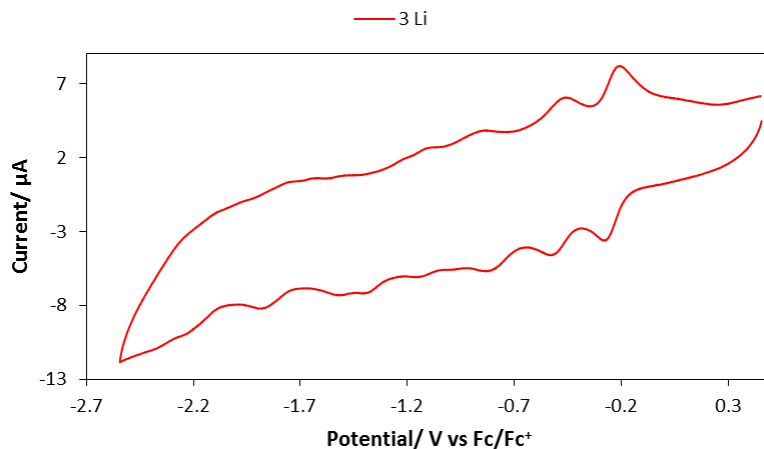


Figure 2.29 Cyclic voltammogram of solid isolated from the reactions between PMo_{12} and 3 mole-equivalents of $\text{Li}|\text{Hg}$ amalgam. 1 mM POM in 100 mM (TBA)(BF₄) in MeCN, from +1.0 V to -2.0 V vs Ag wire, 100 mV/s scan rate, GC WE, Pt wire CE, Ag wire RE.

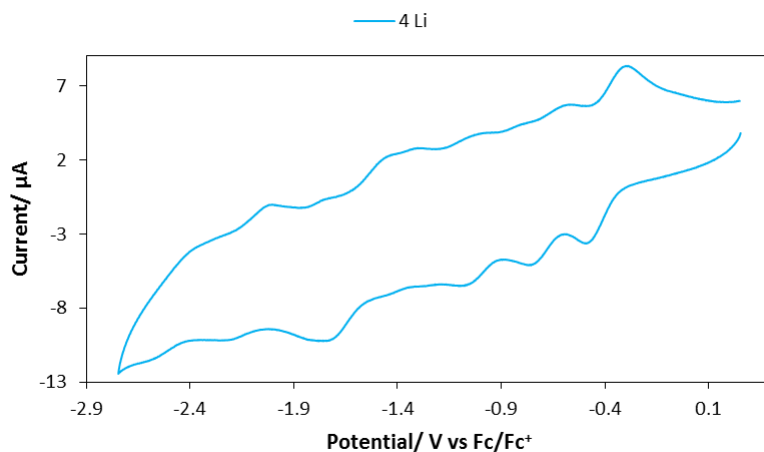


Figure 2.30 Cyclic voltammogram of solid isolated from the reactions between PMo_{12} and 4 mole-equivalents of $\text{Li}|\text{Hg}$ amalgam. 1 mM POM in 100 mM (TBA)(BF₄) in MeCN, from +1.0 V to -2.0 V vs Ag wire, 100 mV/s scan rate, GC WE, Pt wire CE, Ag wire RE.

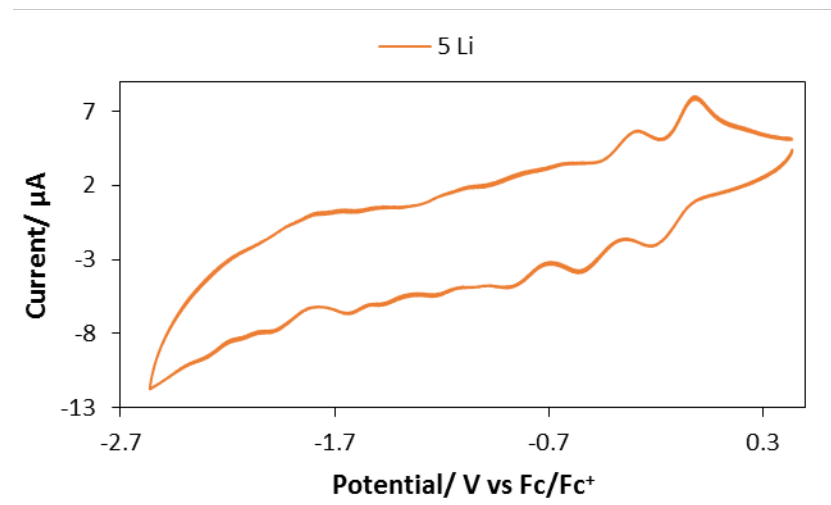


Figure 2.31 Cyclic voltammogram of solid isolated from the reactions between PMo_{12} and 5 mole-equivalents of $\text{Li}|\text{Hg}$ amalgam. 1 mM POM in 100 mM (TBA)(BF₄) in MeCN, from +1.0 V to -2.0 V vs Ag wire, 100 mV/s scan rate, GC WE, Pt wire CE, Ag wire RE.

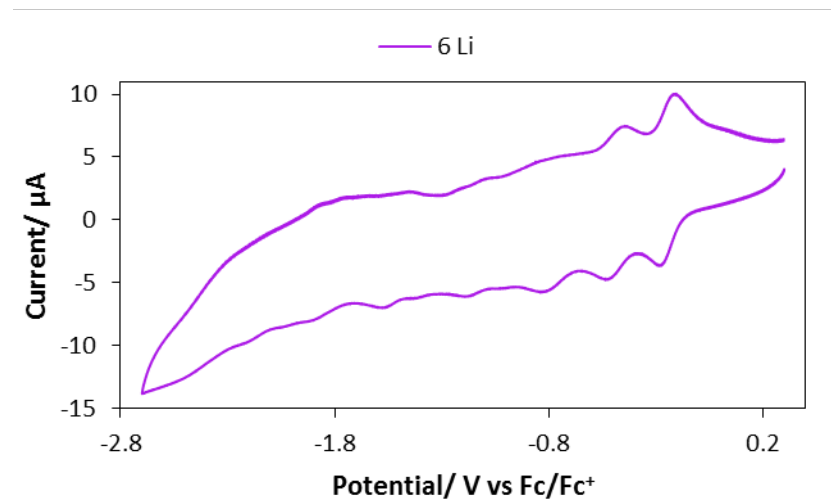


Figure 2.32 Cyclic voltammogram of solid isolated from the reactions between PMo_{12} and 6 mole-equivalents of $\text{Li}|\text{Hg}$ amalgam. 1 mM POM in 100 mM (TBA)(BF₄) in MeCN, from +1.0 V to -2.0 V vs Ag wire, 100 mV/s scan rate, GC WE, Pt wire CE, Ag wire RE.

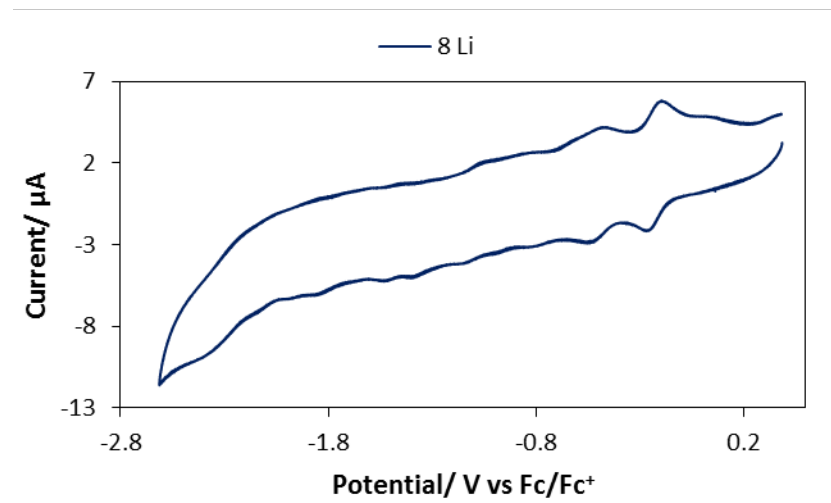


Figure 2.33 Cyclic voltammogram of solid isolated from the reactions between PMo_{12} and 8 mole-equivalents of $\text{Li}|\text{Hg}$ amalgam. 1 mM POM in 100 mM (TBA)(BF₄) in MeCN, from +1.0 V to -2.0 V vs Ag wire, 100 mV/s scan rate, GC WE, Pt wire CE, Ag wire RE.

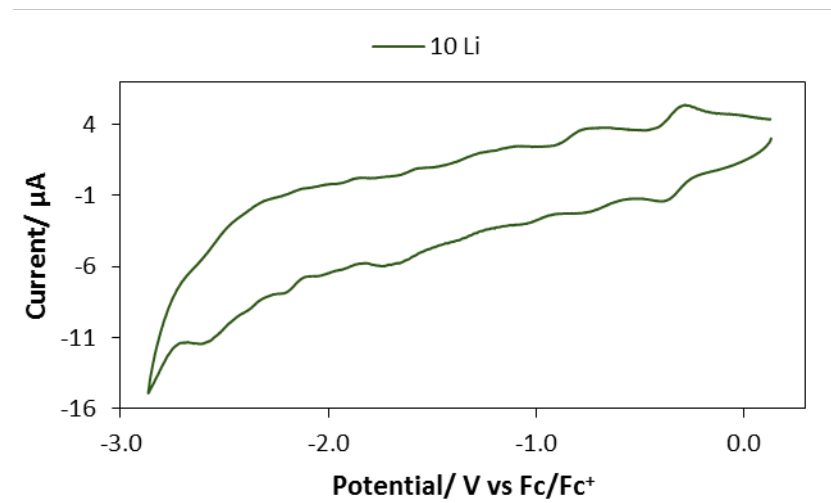


Figure 2.34 Cyclic voltammogram of solid isolated from the reactions between PMo_{12} and 10 mole-equivalents of $\text{Li}|\text{Hg}$ amalgam. 1 mM POM in 100 mM (TBA)(BF₄) in MeCN, from +1.0 V to -2.0 V vs Ag wire, 100 mV/s scan rate, GC WE, Pt wire CE, Ag wire RE.

The cyclic voltammograms of products isolated after treatment of PMo_{12} with an odd number of mole-equivalents of $\text{Li}|\text{Hg}$ amalgam are shown Figure 2.35 and it shows that as the amount of $\text{Li}|\text{Hg}$ amalgam increases the first redox wave shifts to more positive potential, suggesting that reduced PMo_{12} is easier to reduce further. The potential of the first redox wave for one and three mole-equivalents of $\text{Li}|\text{Hg}$ amalgam is very similar.

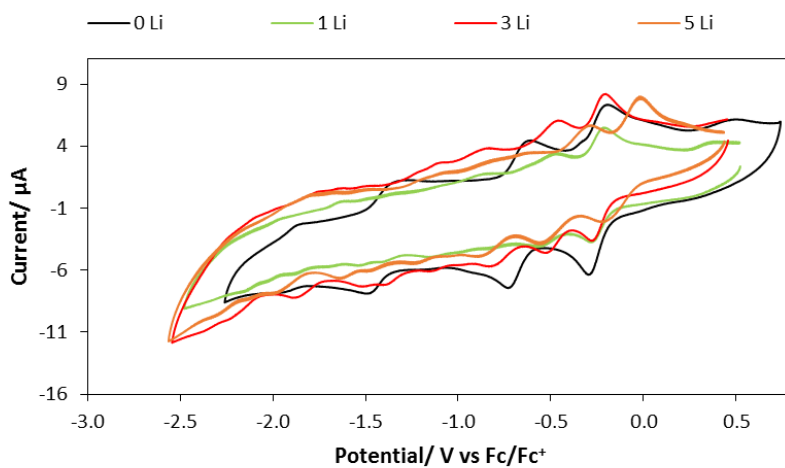


Figure 2.35 Cyclic voltammograms of solids isolated from the reactions between PMo_{12} and n mole-equivalents of $\text{Li}|\text{Hg}$ amalgam (n is an odd number). 1 mM POM in 100 mM (TBA)(BF₄) in MeCN, from +1.0 V to -2.0 V vs Ag wire, 100 mV/s scan rate, GC WE, Pt wire CE, Ag wire RE.

The cyclic voltammograms of products isolated after treatment of PMo_{12} with an even number of mole-equivalents of $\text{Li}|\text{Hg}$ amalgam are shown Figure 2.36 and it shows there is no real trend. From zero to two mole-equivalents the potential of the first redox wave shifts to a more positive potential, from two to four mole-equivalents the potential shifts to a potential more negative than zero, for six and eight mole equivalents it shifts to a more positive potential and then it shifts to more negative potentials for ten mole-equivalents.

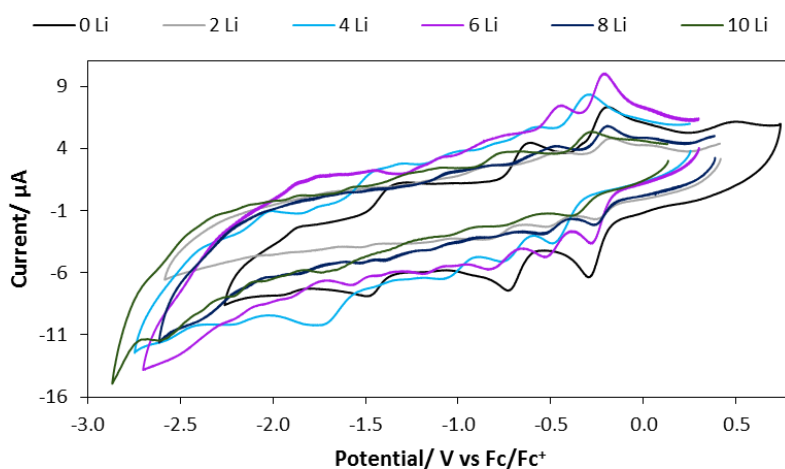


Figure 2.36 Cyclic voltammograms of solids isolated from the reactions between PMo_{12} and n mole-equivalents of $\text{Li}|\text{Hg}$ amalgam (n is an even number). 1 mM POM in 100 mM (TBA)(BF₄) in MeCN, from +1.0 V to -2.0 V vs Ag wire, 100 mV/s scan rate, GC WE, Pt wire CE, Ag wire RE.

Figure 2.37 is a plot of the potential difference between the first reduction peak (E_p) when $n = 0$ and the first reduction peak when $n = 1 - 10$ in the cyclic voltammograms

vs the mole-equivalents of Li|Hg added to PMo_{12} (n), it shows that the E_p increases from $n = 1$ to $n = 2$, E_p then decreases from $n = 3$ to $n = 4$. E_p is the most positively shifted for when $n = 5$ and the most negatively shifted for when $n = 4$.

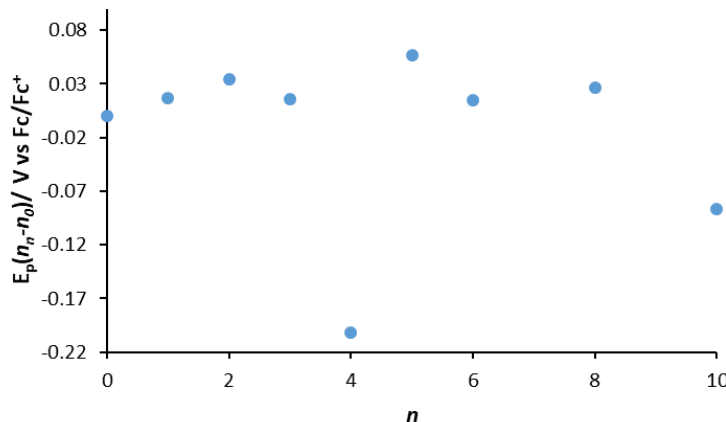


Figure 2.37 Plot of the potential difference between the first reduction peak (E_p) when $n = 0$ (n_0) and the first reduction peak when $n = 1-10$ in the cyclic voltammogram of solids isolated from the reactions between n mole-equivalents of Li|Hg amalgam and PMo_{12} .

2.2.6 The Reaction Between $(\text{TBA})_3[\text{V}_{13}\text{O}_{34}]$ and $\text{Na}|\text{Hg}$ Amalgam in MeCN

$(\text{TBA})_3[\text{V}_{13}\text{O}_{34}]$ (V_{13}) was prepared according to Equation 2.8, a previously reported procedure,¹⁹ with a slight modification in that the heating of the solution during recrystallization was more vigorous. The yield of this preparation was 93%. The $^{51}\text{V}\{^1\text{H}\}$ NMR spectrum of the orange crystals contained four peaks at -331.3 , -451.0 , -496.4 , -500.2 ppm, which integrated to 1:3:3:6, which is consistent with the structure of the anion shown in Figure 2.38B. Hill *et al.* found that V_{13} has the most positive reduction potential of the vanadate POMs.¹⁴

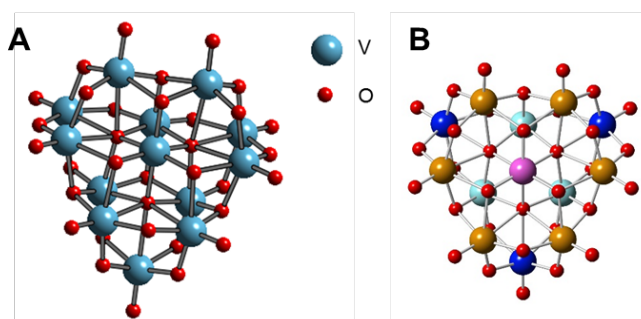
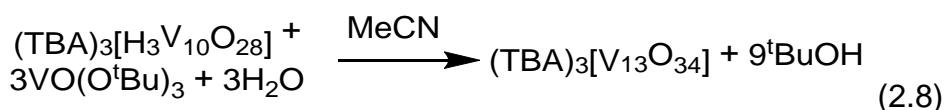
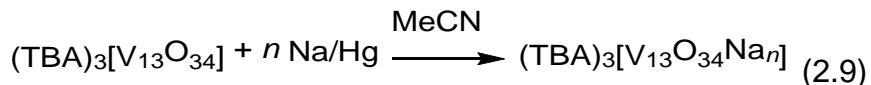


Figure 2.38 Ball-and-stick model of the anion, $[\text{V}_{13}\text{O}_{34}]^{3-}$ (A) and ball-and-stick model with the four vanadium environments indicated by the different colour atoms (B).

The reduction of V_{13} was investigated by adding increasing amounts of 0.35 wt.% $Na|Hg$ amalgam to a V_{13} solution in MeCN, as shown in Equation 2.9.



The results from the initial $^{51}V\{^1H\}$ NMR spectra of the reaction mixtures are listed in Table 2.16 and are shown in Figure 2.39. For the 1:1 reaction mixture (Fig. 2.39B) there were two extra peaks at -226.7 and -293.0 ppm compared to that of the fully oxidized $(TBA)_3[V_{13}O_{34}]$ (Figure. 2.39A). The peaks can possibly be assigned to two-electron reduced $[V_{13}O_{34}]^{5-}$. The relative intensities of (all four peaks assigned to $(TBA)_3[V_{13}O_{34}]$): (both peaks assigned to two-electron reduced $[V_{13}O_{34}]^{5-}$) were calculated to be approximately 1:1 which would agree with the suggested reaction in Equation 2.10.



For the 1:2 reaction mixture (Figure 2.39C) and the 1:3 reaction mixture (Figure 2.39D) the only peaks present are what were assigned to the two-electron reduced species. For the 1:4 reaction (Figure 2.39E), 1:5 reaction mixture (Figure 2.39F) and 1:6 reaction mixture (Figure 2.39G) no new resonances could be resolved, possibly due to paramagnetic broadening. Several new resonances were observed in the spectrum of 1:13 reaction mixture (Figure 2.39H).

<i>n</i>	$\delta v/\text{ppm}$
0	$-331.2, -450.6, -495.9, -499.7$
1	$-226.7, -293.0, -330.8, -450.6, -496.1, -499.9$
2	$-230.7, -300.8$
3	$-229.7, -302.8, -500.3$
4	-229.5
5	-239.0
6	-227.5
13	$-496.7, -501.1, -518.3, -523.2, -528.2, -544.9, -552.2, -569.1$

Table 2.16 Peaks in the $^{51}V\{^1H\}$ NMR spectra for the reactions between V_{13} and n mole-equivalents of $Na|Hg$ amalgam in MeCN.

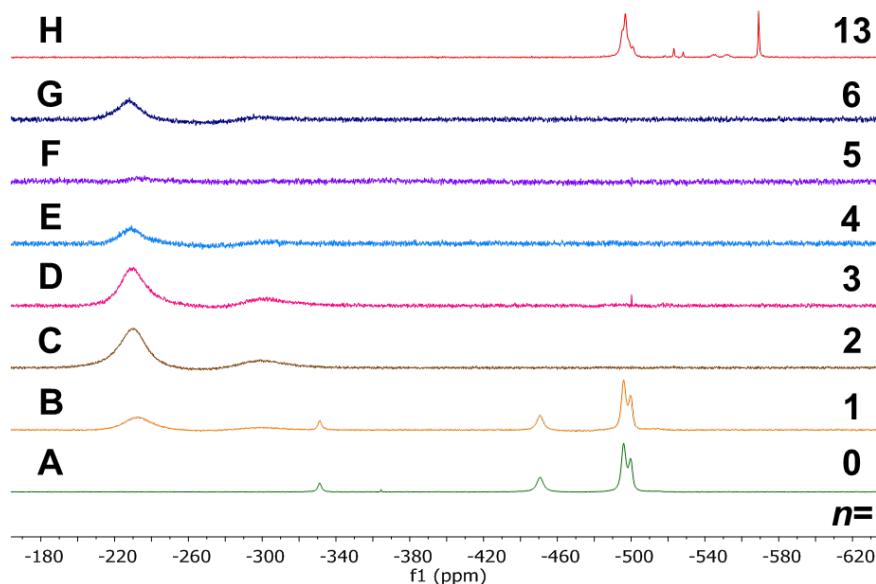


Figure 2.39 $^{51}\text{V}\{^1\text{H}\}$ NMR spectra for the reactions between V_{13} and n mole-equivalents of $\text{Na}|\text{Hg}$ amalgam in MeCN.

The bands in the FTIR spectra of solids isolated from the addition of n mole-equivalents of $\text{Na}|\text{Hg}$ to V_{13} in MeCN are listed in Table 2.17 and shown in Figure 2.40, where $n = 0\text{--}6$ and 13. As n increases, the $\nu(\text{V}-\text{O}_t)$ band shifts to lower wavenumber until $n = 13$, at which point the $\nu(\text{V}-\text{O}_t)$ band shifts to higher wavenumber and is less intense. The $\nu(\text{V}-\text{O}_b\text{-V})$ bands also shifts to lower wavenumber and the intensity decreases as the amount of $\text{Na}|\text{Hg}$ amalgam increases.

n	Bands in FTIR/ cm^{-1}	
	$\text{V}-\text{O}_t$	$\text{V}-\text{O}_b\text{-V}$
0	1062.2, 963.6	881.2, 835.5, 800.3, 764.6, 715.7, 599.8, 548.5, 505.8, 488.5, 440.4
1	1064.5, 974.4	851.0, 815.1, 753.7, 586.6, 558.2, 515.5, 445.4
2	1069.6, 987.4, 970.1	850.3, 820.3, 749.2, 587.1, 555.4, 524.4, 433.1
3	987.2, 969.0	850.4, 816.6, 751.6, 590.2, 555.8, 522.6, 436.2
4	1066.1, 1027.1, 986.4, 967.5	850.6, 817.2, 741.3, 587.7, 555.1, 524.3, 428.4, 408.9
5	1065.8, 1031.1, 962.5	884.8, 808.4, 737.1, 585.8, 553.0, 533.0, 533.4, 508.3, 432.0, 414.9
6	1067.3, 1027.4, 965.8	852.4, 813.2, 737.4, 587.3, 527.6, 427.0
13	1047.1	894.3, 643.8, 558.1, 440.8, 426.6

Table 2.17 Bands in the FTIR spectra for solids isolated from the reactions between V_{13} and n equivalents of $\text{Na}|\text{Hg}$ amalgam in MeCN.

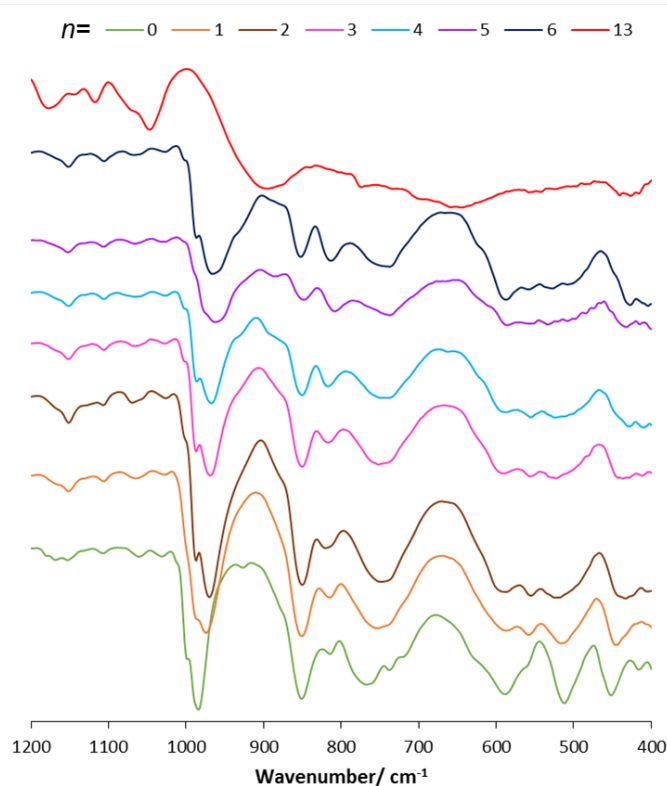
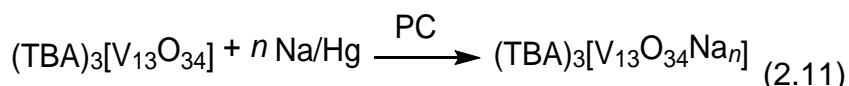


Figure 2.40 FTIR spectra for solids isolated from the reactions between V_{13} and n mole-equivalents of $Na | Hg$ amalgam in MeCN.

2.2.7 The Reaction Between $(TBA)_3[V_{13}O_{34}]$ and $Na | Hg$ Amalgam in PC

The reduction of V_{13} with varying amounts of 0.35 wt.% $Na | Hg$ amalgam in PC as shown in Equation 2.11 and was followed by $^{51}V\{^1H\}$ NMR and FTIR spectroscopy.



The peaks in the $^{51}V\{^1H\}$ NMR spectra of the reaction mixtures after the addition of n mole-equivalents of $Na | Hg$ amalgam to V_{13} are listed in Table 2.18 and are shown in Figure 2.41. On the addition of one and two mole-equivalents of $Na | Hg$ amalgam to V_{13} (Figure 2.41 and C) there are two species present in the NMR spectra, possibly due to fully oxidised and two-electron reduced V_{13} . The peak for the fully oxidised anion is broadened upon the addition of electrons. On the addition of three mole-equivalents of $Na | Hg$ amalgam to V_{13} (Figure 2.41D) the NMR spectrum contains a new peak at +4.9 ppm and an upfield shifted broad peak at -502.1 ppm. After the addition of four mole-equivalents (Figure 2.41E) the NMR spectrum contains a resonance in a similar position to the upfield shifted broad peak for three mole-equivalents that has split into several peaks and the downfield peak has grew. After

the addition of five mole-equivalents (Figure 2.41F) the downfield shifted peak has grown further and there is a sharp peak upfield. After the addition of six mole-equivalents of $\text{Na}|\text{Hg}$ amalgam the downfield peak has shrunk and the upfield peak has grew, after the addition of thirteen mole-equivalents there is only the upfield peak. The broadening of peaks in the NMR could be due to paramagnetism.

n	δ_V/ppm
0	-331.2, -450.6, -495.9, -499.7
1	-224.1, -297.8, -485.9, -517.5
2	-24.5, -219.3, -284.4, -494.4
3	4.9, -502.1
4	-10.1, -498.6, -513.2, -577.0
5	-12.8, -494.9, -496.9, -499.3
6	-10.3, -495.2, -497.2, -499.5
13	-496.4, -518.8, -523.6

Table 2.18 Peaks in the $^{51}\text{V}\{^1\text{H}\}$ NMR spectra for the reactions between V_{13} and n mole-equivalents of $\text{Na}|\text{Hg}$ amalgam in PC.

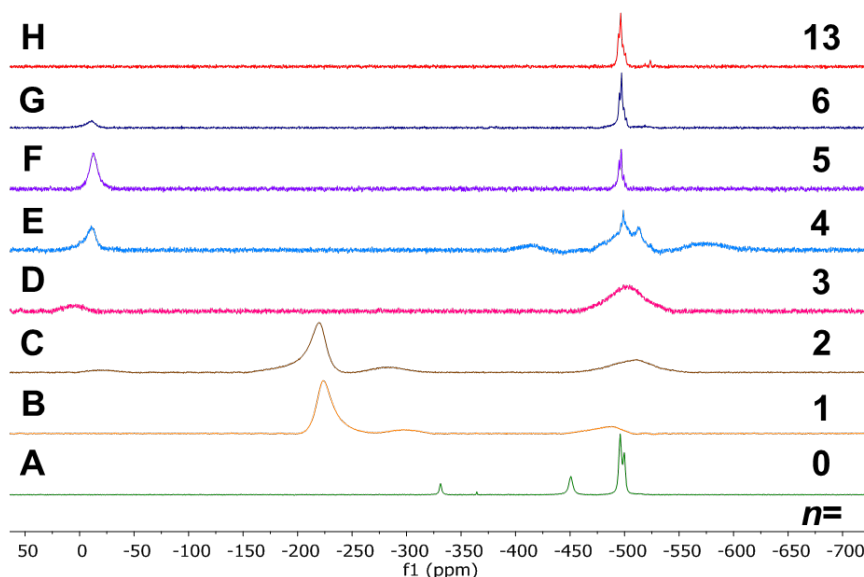


Figure 2.41 $^{51}\text{V}\{^1\text{H}\}$ NMR spectra for the reactions between V_{13} and n mole-equivalents of $\text{Na}|\text{Hg}$ amalgam in PC.

The bands in the FTIR spectra of solids isolated from reactions between n mole-equivalents of $\text{Na}|\text{Hg}$ and V_{13} in PC are listed in Table 2.19 and spectra are shown in Figure 2.42. As n increases the $\nu(\text{V}-\text{O}_t)$ band shifts to lower wavenumber until $n = 13$, at which point the $\nu(\text{V}-\text{O}_t)$ band shifts to higher wavenumber and is less intense. The $\nu(\text{V}-\text{O}_b-\text{V})$ bands also shift to lower wavenumber and the intensity decreases with increasing amounts of $\text{Na}|\text{Hg}$ amalgam.

n	Bands in FTIR/ cm^{-1}	
	V-O _t	V-O _b -V
0	1062.2, 963.6	881.2, 835.5, 800.3, 764.6, 715.7, 599.8, 548.5, 505.9, 488.5, 440.4
1	1051.3, 988.4, 971.8	850.3, 815.0, 753.0, 588.6, 556.3, 526.6, 426.1
2	1048.6, 987.2, 964.4	850.7, 816.4, 739.0, 592.3, 533.3, 427.0, 408.6
3	1046.4, 948.1, 922.4	890.9, 797.5, 737.1, 661.6, 584.0, 541.0, 424.1
4	1047.4, 953.2, 924.3	887.3, 833.1, 685.8, 655.3, 524.1, 448.1
5	1044.8, 948.7	809.7, 738.3, 585.7, 565.6, 541.3
6	1044.7, 943.0	807.3, 736.9, 562.8, 410.7
13	1057.9, 940.4	879.3, 810.7, 739.3, 564.6, 441.1, 409.8

Table 2.19 Bands in the FTIR spectra for the solids isolated from the reactions between V_{13} and n mole-equivalents of $\text{Na}|\text{Hg}$ amalgam in PC.

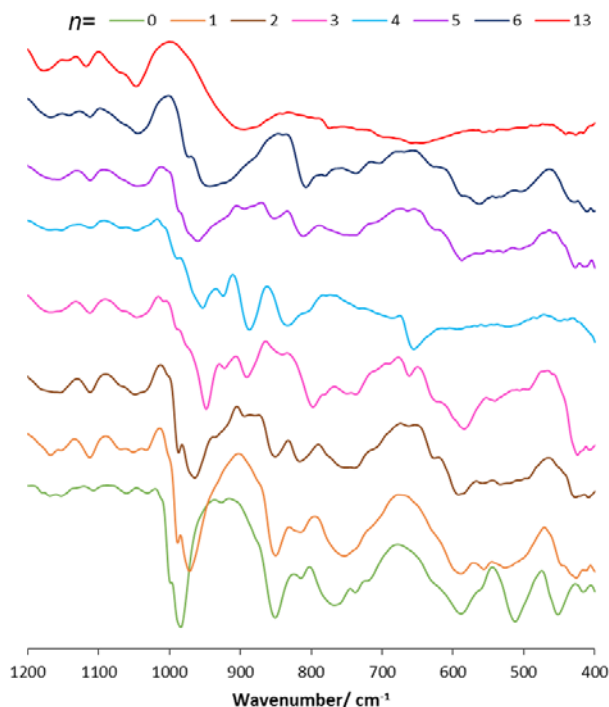
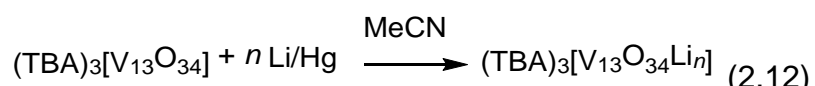


Figure 2.42 FTIR spectra for the solids isolated from the reactions between V_{13} and n mole-equivalents of $\text{Na}|\text{Hg}$ amalgam in PC.

2.2.8 The Reaction Between $(\text{TBA})_3[\text{V}_{13}\text{O}_{34}]$ and $\text{Li}|\text{Hg}$ Amalgam in MeCN

V_{13} has also been reacted with 0.03 wt.% $\text{Li}|\text{Hg}$ amalgam in MeCN (Equation 2.12).



The peaks in the $^{51}\text{V}\{^1\text{H}\}$ NMR spectra obtained upon addition of n mole-equivalents of $\text{Li}|\text{Hg}$ to V_{13} are listed in Table 2.20 and the $^{51}\text{V}\{^1\text{H}\}$ NMR spectra are shown in Figure 2.43. After the addition of one mole-equivalent of $\text{Li}|\text{Hg}$ amalgam, there is still

a small amount of fully oxidised V_{13} and two broad peaks downfield at -232.2 and -306.3 ppm. After the addition of two mole-equivalents of $Li|Hg$ amalgam, the spectrum contained downfield shifted broad peaks. A new broad peak at -33.2 ppm is apparent in the spectrum after the addition of three mole-equivalents of $Li|Hg$ amalgam, this peak is also present in the spectrum obtained after the addition of four mole-equivalents. After the addition of five, six and thirteen mole-equivalents of $Li|Hg$ amalgam the spectra obtained contain a broad peak that is upfield shifted, *ca.* -570 ppm, the broadening of peaks in the NMR could be due to paramagnetism.

n	δ_V / ppm
0	$-331.2, -364.4, -450.6, -495.9, -499.7$
1	$-232.2, -306.3, -450.0, -485.8, -495.7, -499.5$
2	$-179.1, -225.0, -291.4, -480.7, -510.5$
3	$-30.5, -225.5, -290.6, -500.0$
4	-33.2
5	$-530.7, -568.4, -613.0$
6	-545.2
13	-565.5

Table 2.20 Peaks in $^{51}V\{^1H\}$ NMR spectra for the reactions between V_{13} and n mole-equivalents of $Li|Hg$ amalgam in MeCN.

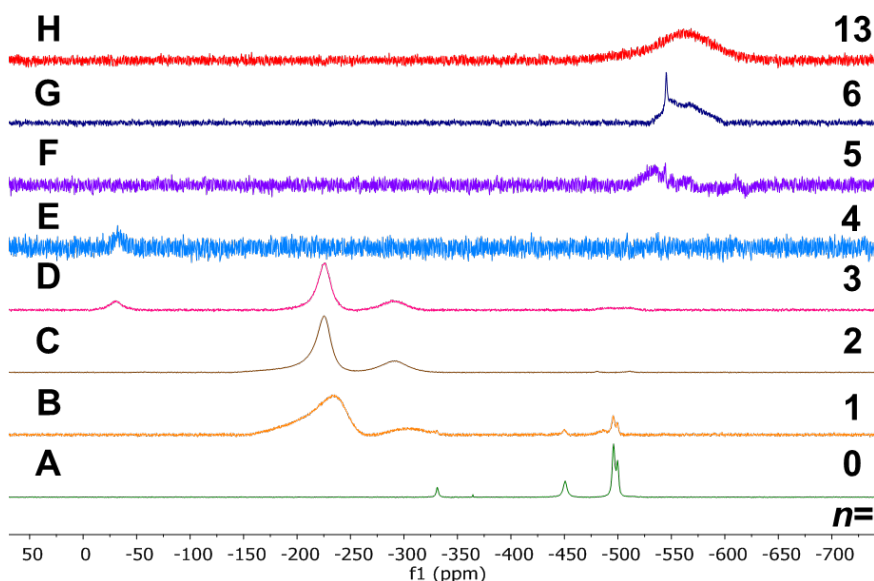


Figure 2.43 $^{51}V\{^1H\}$ NMR spectra for the reactions between V_{13} and n mole-equivalents of $Li|Hg$ amalgam in MeCN.

The bands in the FTIR spectra of solids isolated from reaction between n mole-equivalents of $Li|Hg$ amalgam and V_{13} in MeCN are listed in Table 2.21 and spectra

are shown in Figure 2.44. As n increases the $\nu(V-O_t)$ band shifts to lower wavenumber, until $n = 13$, at which point the $\nu(V-O_t)$ band shifts to higher wavenumber and is less intense. The $\nu(V-O_t)$ band also splits into two when $n = 3-6$. The $\nu(V-O_b-V)$ also shifts to lower wavenumber and the intensity decreases as the amounts of Li|Hg amalgam increases.

n	Bands in FTIR/ cm^{-1}	
	$V-O_t$	$V-O_b-V$
0	1062.2, 963.6	881.2, 835.5, 800.3, 764.6, 715.7, 599.8, 548.5, 505.8, 488.5, 440.4
1	1066.3, 974.3	850.8, 815.6, 753.1, 557.4, 512.3, 442.8, 417.3
2	1064.9, 986.9, 971.8	850.9, 816.2, 751.1, 556.0, 514.4, 435.0
3	1066.0, 1026.6, 976.2, 943.5, 892.2	855.4, 814.4, 739.0, 575.8, 529.0, 496.6, 463.5, 432.3
4	1065.9, 1028.3, 974.8, 942.5	812.3, 764.3, 735.9, 630.2, 563.9, 529.5, 495.6
5	1065.9, 1028.4, 974.7, 941.1	811.8, 766.5, 735.0, 631.1, 563.1, 528.1, 495.3, 434.7
6	1066.9, 974.7, 941.2	811.1, 735.2, 629.8, 565.4, 530.3, 495.2, 423.6, 412.2
13	1059.1, 1029.2	875.1, 812.2, 735.4

Table 2.21 Bands in the FTIR spectra of the solids isolated from the reactions between V_{13} and n mole-equivalents of Li|Hg amalgam in MeCN.

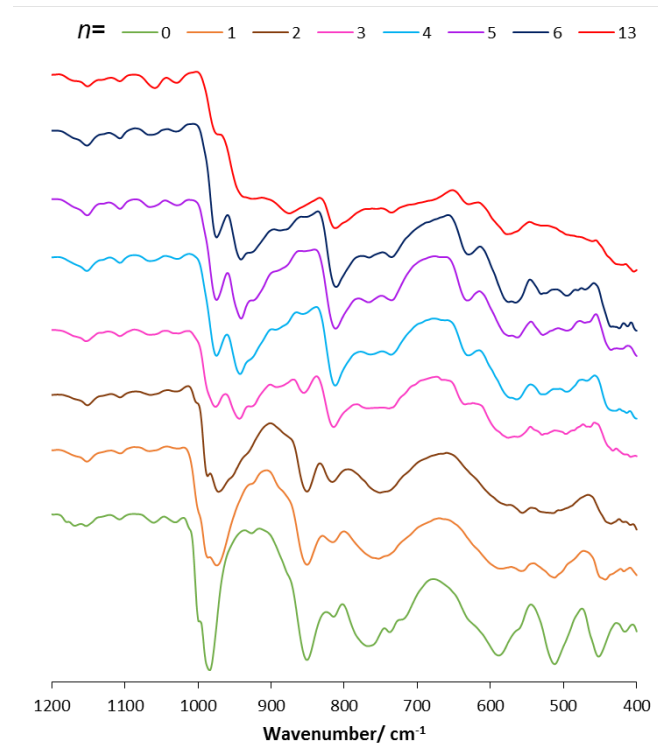
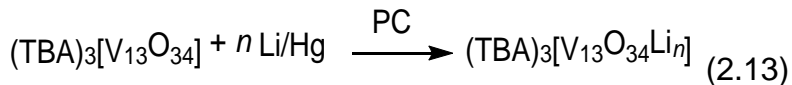


Figure 2.44 FTIR spectra of the solids isolated from the reactions between V_{13} and n mole-equivalents of Li|Hg amalgam in MeCN.

2.2.9 The Reaction Between $(TBA)_3[V_{13}O_{34}]$ and $Li|Hg$ Amalgam in PC

V_{13} was reduced with 0.03 wt.% $Li|Hg$ amalgam in PC as shown in Equation 2.13.



The peaks in the $^{51}V\{^1H\}$ NMR spectra upon the addition of n mole-equivalents of $Li|Hg$ to V_{13} are listed in Table 2.22 and $^{51}V\{^1H\}$ NMR spectra are shown in Figure 2.45. After the addition of one mole-equivalent of $Li|Hg$ the peaks in the NMR spectra are shifted downfield. Similar resonances are observed for $n = 1-3$ equivalents of $Li|Hg$. A broad peak that is downfield shifted, at ca. -30 ppm, is apparent in the spectrum for when $n = 2-4$ equivalents of $Li|Hg$, the peak grows as the amount of $Li|Hg$ amalgam increases. A new broad peak at ca. -500 ppm is present in the spectrum obtained from the addition of four mole-equivalents, and this peak grows as the mole-equivalents is increased further from four to thirteen. The broadening of peaks in the NMR could be due to paramagnetism.

n	$\delta\nu/\text{ppm}$
0	$-331.2, -364.4, -450.6, -495.9, -499.7$
1	$-57.1, -232.6, -297.6, -395.5, -428.6, -505.1, -524.4$
2	$-54.4, -225.5, -291.4, -506.1$
3	$-29.4, -225.7, -292.6, -509.1$
4	$-29.1, -225.7, -290.6, -495.2$
5	$-27.1, -494.1, -511.5, -519.3, -523.7$
6	$-395.6, -496.8, -518.9, -523.8$
13	-524.2

Table 2.22 Peaks in $^{51}V\{^1H\}$ NMR spectra for the reaction between V_{13} and n mole-equivalents of $Li|Hg$ in PC.

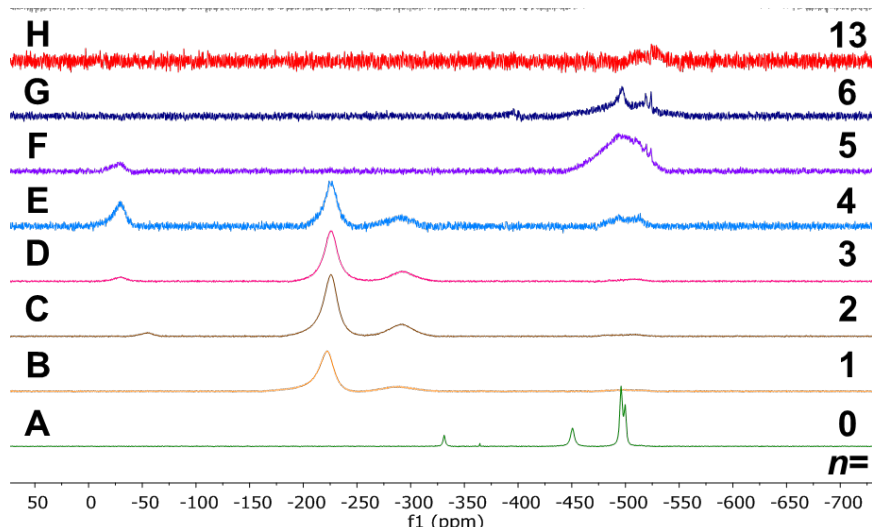


Figure 2.45 $^{51}\text{V}\{^1\text{H}\}$ NMR spectra for the reactions between V_{13} and n mole-equivalents of $\text{Li}|\text{Hg}$ in PC.

The bands in the FTIR spectra of solids isolated from the reactions between n mole-equivalents of $\text{Li}|\text{Hg}$ and V_{13} in PC are listed in Table 2.23 and spectra are shown in Figure 2.46. As n increases the $\nu(\text{V}-\text{O}_t)$ band shifts to lower wavenumber and decreases in intensity. The $\nu(\text{V}-\text{O}_b-\text{V})$ bands also shift to lower wavenumber and the intensity decreases with increasing amounts of $\text{Li}|\text{Hg}$.

n	Bands in FTIR/ cm^{-1}	
	$\text{V}-\text{O}_t$	$\text{V}-\text{O}_b-\text{V}$
0	1062.2, 963.6	881.2, 835.5, 800.3, 764.6, 715.7, 599.8, 548.5, 505.8, 488.5, 440.4
1	1050.9, 987.5, 970.6	850.5, 814.9, 753.8, 590.6, 556.6, 521.7, 431.6
2	1048.7, 987.6, 971.1	851.3, 816.5, 750.1, 555.6, 523.5, 425.8
3	1046.2, 973.1, 945.5	853.7, 814.9, 757.4, 578.3, 526.9, 422.4, 411.2
4	1067.0, 975.5, 942.5	856.5, 813.8, 738.5, 632.8, 566.1, 531.7, 495.5, 466.8, 418.8
5	1061.6, 977.0, 936.1	814.9, 578.4, 533.3
6	1032.4, 977.0	933.2, 814.2, 574.5, 533.4, 424.4
13	1046.3, 977.5, 937.8	873.1, 812.5, 778.6, 737.4, 632.3, 569.8, 495.8, 437.9

Table 2.23 Bands in the FTIR spectra of solids isolated from the reactions between V_{13} and n mole-equivalents of $\text{Li}|\text{Hg}$ in PC.

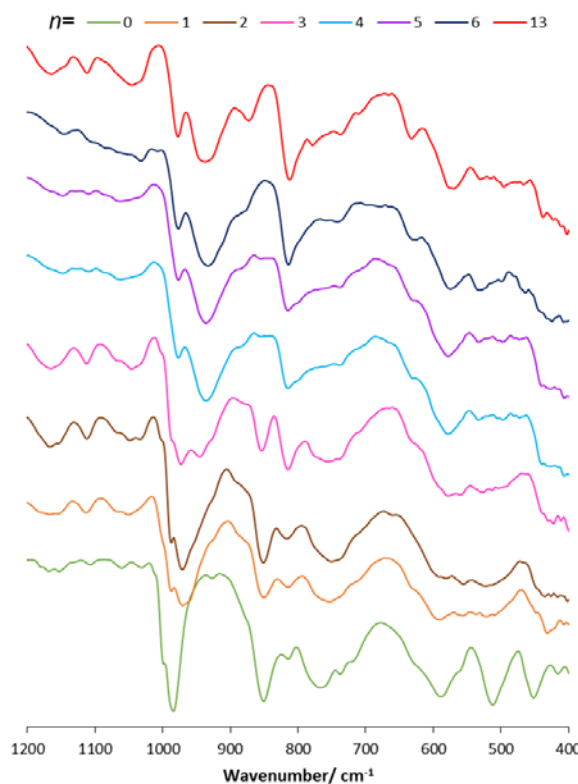


Figure 2.46 FTIR spectra of solids isolated from the reactions between V_{13} and n mole-equivalents of $\text{Li}|\text{Hg}$ in PC.

2.3 Other Reducing Agents

KC_8 and K^+PhCN^- were explored as alternative reducing agents to metal mercury amalgams for the reduction of PMo_{12} , this was to try and move away from using toxic Hg . KC_8 is a lot easier to store and easier to handle with regards to weighing out the materials accurately in an air/moisture-free environment. A stock solution of K^+PhCN^- is also easier to measure out than weighing amalgams. It was hoped that since it is easier to weigh out KC_8 and measure K^+PhCN^- that this would improve the accuracy of the stoichiometry of reducing agent added to PMo_{12} . The clean-up following the use of K^+PhCN^- and KC_8 is also more straightforward than metal mercury amalgams.

2.3.1 The Reaction Between $(\text{TBA})_3[\text{PMo}_{12}\text{O}_{40}]$ and KC_8 in MeCN

KC_8 is an example of a graphite intercalation compound, with the alkali metal, potassium ion as an interlayer guest between the negatively charged graphite sheets.²⁰ KC_8 has been used as a reducing agent in organic synthesis, for example in the reduction of substituted naphthalenes and polycyclic hydrocarbons.²¹⁻²³

KC_8 was formed by first drying graphite under vacuum with heating, then adding K metal which was vaporised by heating to high temperatures, this then formed KC_8 and the colour of the graphite flakes changed from black to bronze as shown in Figure 2.47.²⁰ The electrons and K^+ that are trapped in the graphite are able to migrate to the POM when KC_8 is suspended in a solution of PMo_{12} .

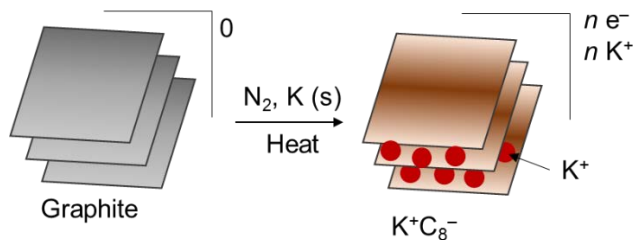
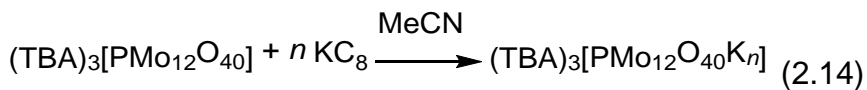


Figure 2.47 The preparation of KC_8 , adapted from ref²⁰.

The reaction between PMo_{12} and n mole-equivalents of KC_8 (Equation 2.14) was monitored by $^{31}\text{P}\{^1\text{H}\}$ NMR spectroscopy. The colour changes to the POM solution on the addition of KC_8 are similar to what has been seen previously for both $\text{Na}|\text{Hg}$ and $\text{Li}|\text{Hg}$ amalgams; when $n = 0$ the solution is yellow, when $n = 1$ the solution is green and when $n = 2-10$ the solution is dark blue.



The peaks in the $^{31}\text{P}\{^1\text{H}\}$ NMR spectra are listed in Table 2.24 and spectra are shown in Figure 2.48. The addition of one mole-equivalent of KC_8 to PMo_{12} shifts the resonance in the NMR spectrum downfield from -3.8 to 0.0 ppm, the PMo_{12} has been fully reduced by one-electron as only one resonance is present in the spectrum, which is assigned to $[\text{PMo}_{12}\text{O}_{40}]^{4-}$. After the addition of two mole-equivalents of KC_8 , the resonance in the NMR is shifted upfield to -6.8 ppm and this is assigned to $[\text{PMo}_{12}\text{O}_{40}]^{5-}$, on the addition of a further three to five mole-equivalents of KC_8 the peak in the NMR spectra stays in the same position. After the addition of six mole-equivalents of KC_8 there are three species in the NMR spectrum, with a major peak at -6.8 ppm. The spectra obtained after the addition of seven and eight mole-equivalents of KC_8 also contain multiple peaks. The spectrum obtained after the addition of nine mole-equivalents of KC_8 contains one peak at -5.8 ppm and the spectrum for ten mole-equivalents contains no peaks. The lack of peaks could be

due to a solubility issue, as it is likely that upon the addition of increasing amounts of K to PMo_{12} , the reduced products will become less soluble.

n	$\delta_{\text{P}}/\text{ppm}$
0	-3.8
1	0.0
2	-6.8
3	-6.8
4	-6.8
5	-6.8
6	-4.0, -5.8, -6.8
7	-4.1, -5.9, -6.8
8	0.0, -4.1, -5.9, -6.8
9	-5.8
10	No peaks

Table 2.24 Peaks in $^{31}\text{P}\{^1\text{H}\}$ NMR spectra from the reactions between PMo_{12} and n mole-equivalents of KC_8 in MeCN.

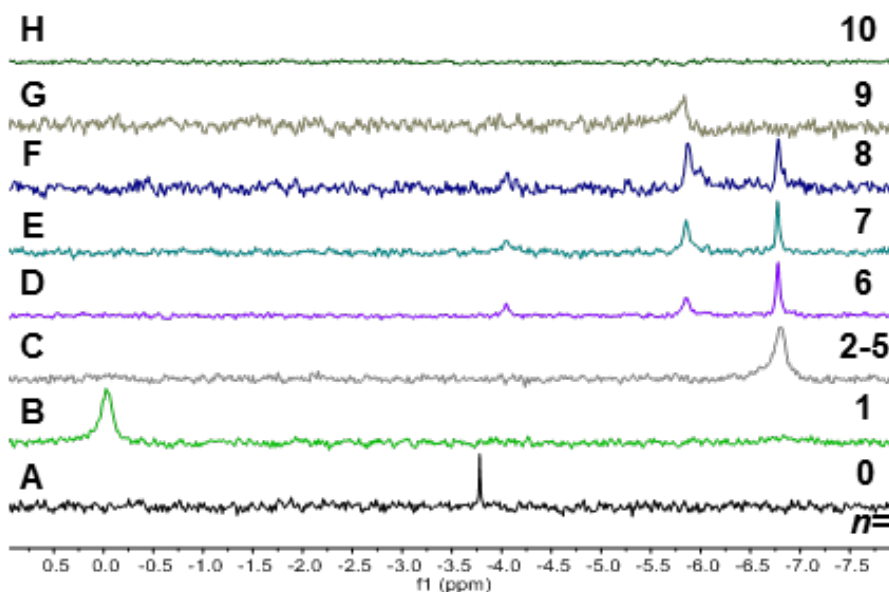


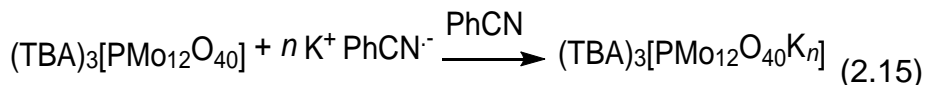
Figure 2.48 $^{31}\text{P}\{^1\text{H}\}$ NMR spectra from the reactions between PMo_{12} and n mole-equivalents of KC_8 in MeCN.

2.3.2 The Reaction Between $(\text{TBA})_3[\text{PMo}_{12}\text{O}_{40}]$ and $\text{K}^+\text{PhCN}^{\bullet-}$

The potassium benzonitrile radical anion ($\text{K}^+\text{PhCN}^{\bullet-}$) was investigated as a reducing agent for the reduction of PMo_{12} with the hope of improving reaction stoichiometry, since a known amount of K metal is dissolved in a known amount of PhCN, therefore the concentration of K in the stock solution was easily calculated assuming no decomposition due to hydrolysis or oxidation.

$\text{K}^+\text{PhCN}^{\bullet-}$ was formed by adding K metal to benzonitrile and heating the solution until all K dissolved, to give a deep red solution, indicative that the $\text{PhCN}^{\bullet-}$ radical anion had formed. The radical anion is able to form due to the low reduction potential of PhCN.²⁰

The reaction between PMo_{12} and the radical anion $\text{K}^+\text{PhCN}^{\bullet-}$ (Equation 2.15) was monitored by $^{31}\text{P}\{^1\text{H}\}$ NMR.



The peaks in the $^{31}\text{P}\{^1\text{H}\}$ NMR spectra are listed in Table 2.25 and spectra are shown in Figure 2.49. After the addition of one mole-equivalent of $\text{K}^+\text{PhCN}^{\bullet-}$ the peak in the NMR spectrum is shifted downfield. The NMR resonance is shifted further upfield to 1.2 ppm upon the addition of two mole-equivalents of $\text{K}^+\text{PhCN}^{\bullet-}$ to PMo_{12} ; this is in a different position to two-electron reduced PMo_{12} obtained with $\text{Na}|\text{Hg}$ amalgam, $\text{Li}|\text{Hg}$ amalgam and KC_8 . After the addition of four mole-equivalents of $\text{K}^+\text{PhCN}^{\bullet-}$ two peaks were present in the NMR spectrum, 0.3 and –6.4 ppm in a 1:1 ratio. Only one peak was observed in the NMR spectrum after the addition of six mole-equivalents of $\text{K}^+\text{PhCN}^{\bullet-}$ to PMo_{12} at –6.9 ppm.

<i>n</i>	$\delta_{\text{P}}/\text{ppm}$
0	–3.0
1	0.4
2	1.2
4	0.3, –6.4
6	–6.9

Table 2.25 Peaks in $^{31}\text{P}\{^1\text{H}\}$ NMR spectra from the reactions between PMo_{12} and *n* mole-equivalents of $\text{K}^+\text{PhCN}^{\bullet-}$ in PhCN.

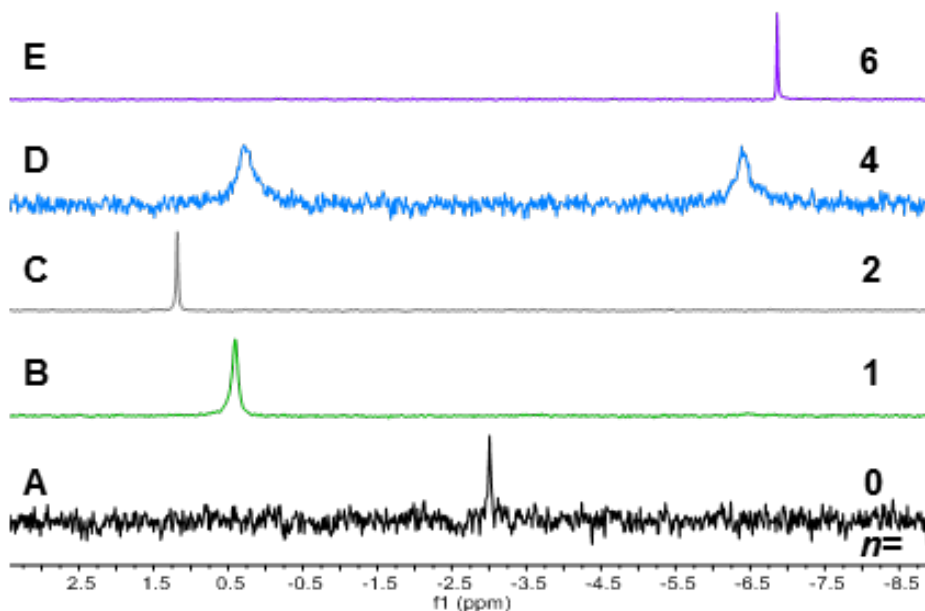


Figure 2.49 $^{31}\text{P}\{^1\text{H}\}$ NMR spectra from the reactions between PMo_{12} and n mole-equivalents of $\text{K}^+\text{PhCN}^\bullet$ in PhCN.

2.4 Discussion

The $^{31}\text{P}\{^1\text{H}\}$ NMR spectra of the reactions between PMo_{12} and different reducing agents are compared in Figure 2.50 and 2.51, with the peaks relative to the peak for fully oxidised PMo_{12} set to 0 ppm. Figure 2.50A compares the resonances in the $^{31}\text{P}\{^1\text{H}\}$ NMR spectra for the reaction between PMo_{12} and one mole-equivalent of reducing agent, for all reducing agents except $\text{Li}|\text{Hg}$ amalgam in PC, the main peak in the spectrum is downfield shifted. For $\text{Li}|\text{Hg}$ amalgam in PC there are two peaks in *ca.* 1:1 ratio. Figure 2.50B compares the resonances in the $^{31}\text{P}\{^1\text{H}\}$ NMR spectra for the reaction between PMo_{12} and two mole-equivalents of reducing agent, for all reducing agents except $\text{K}^+\text{PhCN}^\bullet$, the main peak in the spectrum is upfield shifted. There is a possibility that $\text{K}^+\text{PhCN}^\bullet$ was not as concentrated as calculated, therefore the stoichiometry in the reactions were incorrect. Figure 2.50C compares the resonances in the $^{31}\text{P}\{^1\text{H}\}$ NMR spectra for the reaction between PMo_{12} and three mole-equivalents of reducing agent, for all reducing agents except $\text{Na}|\text{Hg}$ amalgam in MeCN, the main peak in the spectrum is upfield shifted. Figure 2.50D compares the resonances in the $^{31}\text{P}\{^1\text{H}\}$ NMR spectra for the reaction between PMo_{12} and four mole-equivalents of reducing agent, the spectra for three of the reducing agents contains two species, two three species and two one species. The spectra for the majority of the reducing agents indicate the presence of more than one species.

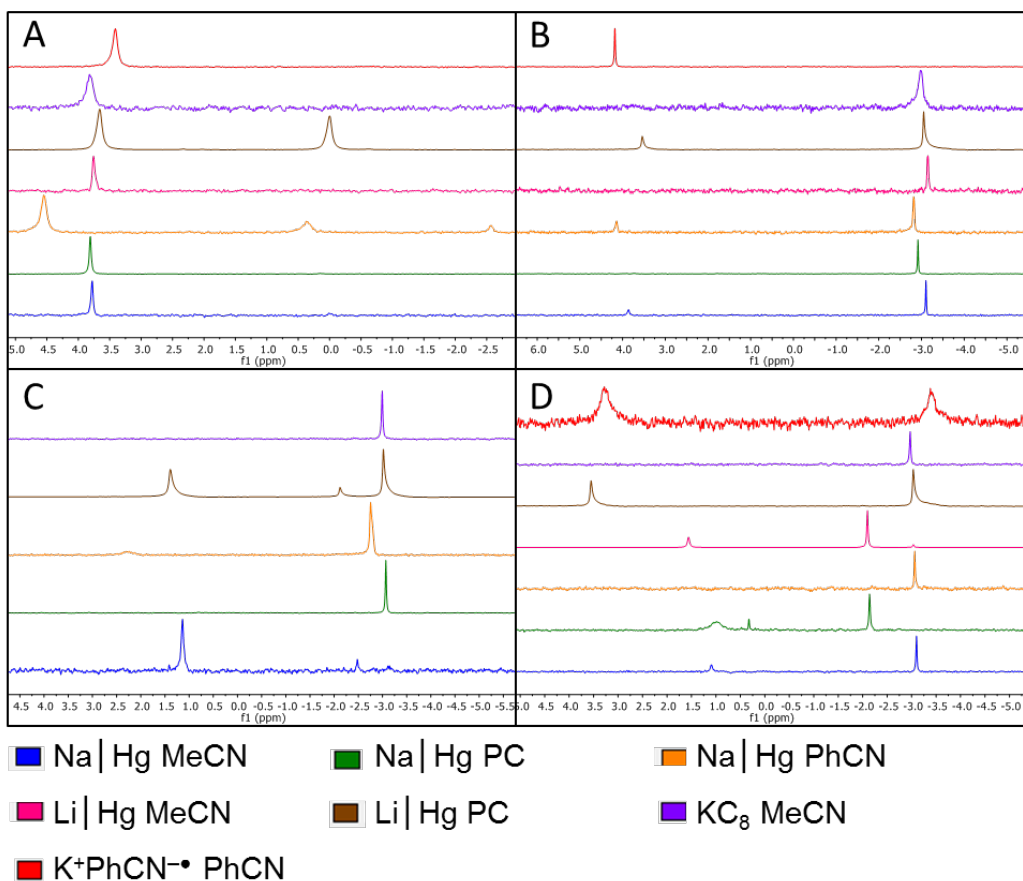


Figure 2.50 $^{31}\text{P}\{^1\text{H}\}$ NMR spectra of reactions between PMo_{12} and different reducing agents, (A) one mole-equivalents, (B) two mole-equivalents, (C) three mole-equivalents and (D) four mole-equivalents, with peaks relative to fully oxidised PMo_{12} .

Figure 2.51A compares the resonances in the $^{31}\text{P}\{^1\text{H}\}$ NMR spectra for when five mole-equivalents of reducing agent has been added to PMo_{12} , it shows a mixed result as the spectra for Na|Hg amalgam in MeCN and PC the main peak is downfield, whereas for Na|Hg amalgam in PhCN, Li|Hg amalgam in PC and KC₈ in MeCN the main peak in the spectra is upfield shifted. Figure 2.51B compares the resonances in the $^{31}\text{P}\{^1\text{H}\}$ NMR spectra for when six mole-equivalents of reducing agent has been added to PMo_{12} , it shows a mixed result as the spectra for all the reducing agents contain multiple species, except for $\text{K}^+\text{PhCN}^{-\bullet}$, which only has one resonance in the NMR spectra. This suggests that as the number of electrons added to PMo_{12} increases, the likelihood of multiple species forming in solution is stronger. Figure 2.51C compares the resonances in the $^{31}\text{P}\{^1\text{H}\}$ NMR spectra for when twelve mole-equivalents of reducing agent has been added to PMo_{12} , it also shows a mixed result as the spectra contain multiple species at different ppm. The resonance in the spectrum obtained for the reaction between Na|Hg amalgam and PMo_{12} in PC

shows one sharp peak, whereas the reaction between Li|Hg amalgam and PMo_{12} in MeCN contains three relatively broad peaks. The reaction between Li|Hg amalgam and PMo_{12} in PC contains three peaks, two very broad and one less broad, with one of the peaks shifted downfield. Figure 2.51D compares the resonances in the $^{31}\text{P}\{^1\text{H}\}$ NMR spectra for when twenty-four mole-equivalents of reducing agent has been added to PMo_{12} , three very different spectra are obtained.

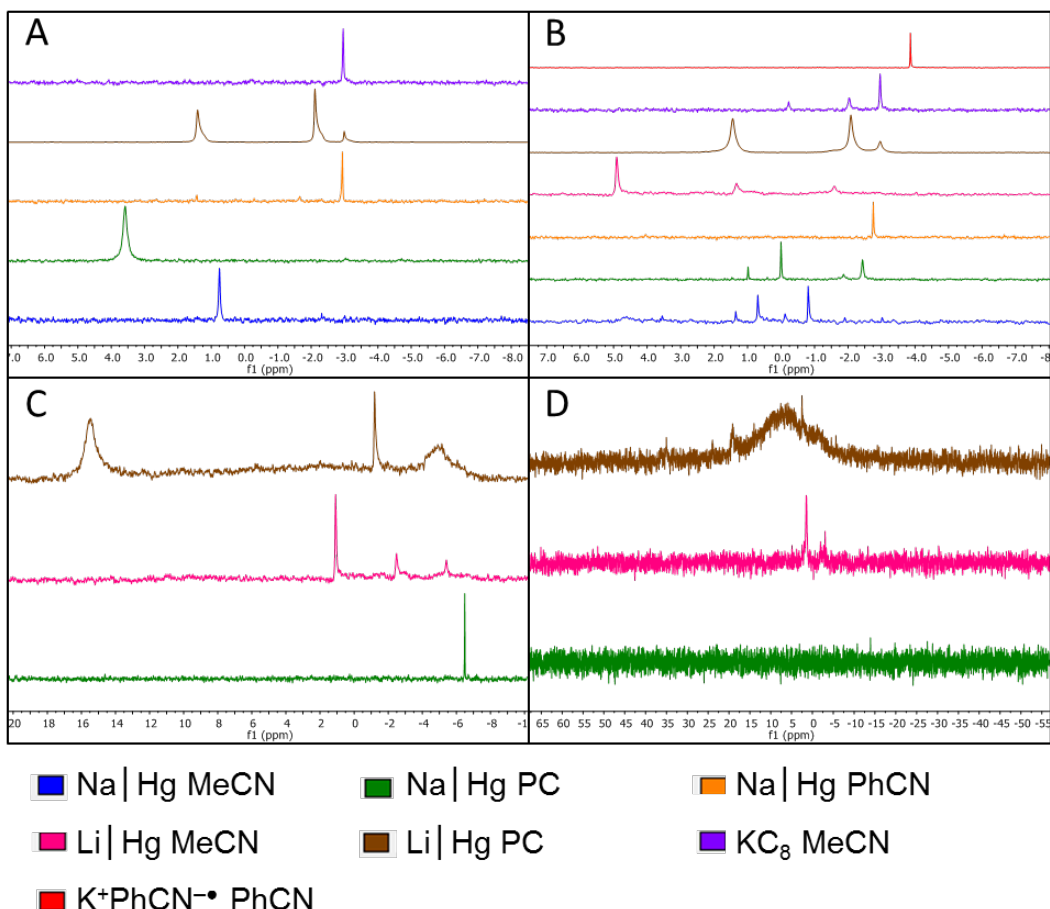


Figure 2.51 $^{31}\text{P}\{^1\text{H}\}$ NMR spectra of reactions between PMo_{12} and different reducing agents, (A) five mole-equivalents, (B) six mole-equivalents, (C) twelve mole-equivalents and (D) twenty-four mole-equivalents, with peaks relative to fully oxidised PMo_{12} .

The solid-state ^{31}P NMR spectra of solids isolated from reactions between PMo_{12} and one, two, and twenty-four mole-equivalents of either Na|Hg amalgam or Li|Hg amalgam in PC are shown in Figure 2.52. It shows that the NMR spectra for the solids isolated from reactions with one and twenty-four mole-equivalents of Na|Hg amalgam and Li|Hg amalgam are very similar. The spectra for solids isolated from reactions with two mole-equivalents are different in that the spectrum for Li|Hg amalgam contains more one-electron reduced PMo_{12} , and the peak corresponding to

two-electron reduced PMo_{12} is split in two. The peaks in the solid-state spectra are in similar positions to the peaks in the solution-state NMR spectra.

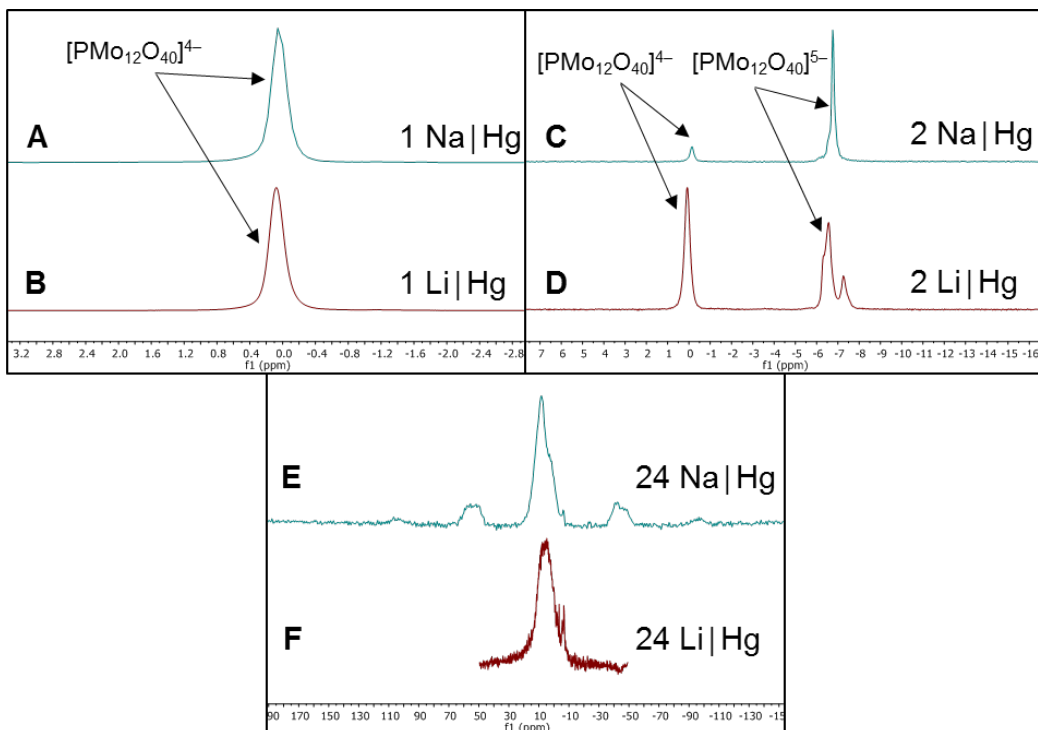


Figure 2.52 Solid-state ^{31}P NMR of solids isolated from reactions in PC between PMo_{12} and (A) one mole-equivalent of $\text{Na}|\text{Hg}$ amalgam, (B) one mole-equivalent $\text{Li}|\text{Hg}$ amalgam, (C) two mole-equivalents of $\text{Na}|\text{Hg}$ amalgam (D) two mole-equivalents of $\text{Li}|\text{Hg}$ amalgam, (E) twenty-four mole-equivalents of $\text{Na}|\text{Hg}$ amalgam and (F) twenty-four mole-equivalents of $\text{Li}|\text{Hg}$ amalgam.

The effect on the FTIR spectra of the solids isolated from the reactions between PMo_{12} and n mole-equivalents of $\text{Na}|\text{Hg}$ amalgam and $\text{Li}|\text{Hg}$ amalgam in MeCN and PC are compared in Figures 2.53 and 2.54. The spectra of the solids isolated from the reactions between PMo_{12} and one mole-equivalent of reducing agent (Figure 2.53A) show that the reactions in MeCN a similar spectrum is obtained and reactions in PC the spectrum obtained is the same; in MeCN the first $\nu(\text{Mo-O}_\text{b}-\text{Mo})$ band is less intense. The spectra of the solids isolated from the reactions between PMo_{12} and two, three and four mole-equivalents of reducing agent (Figure 2.53B-D) are the same for the respective amounts of reducing agent.

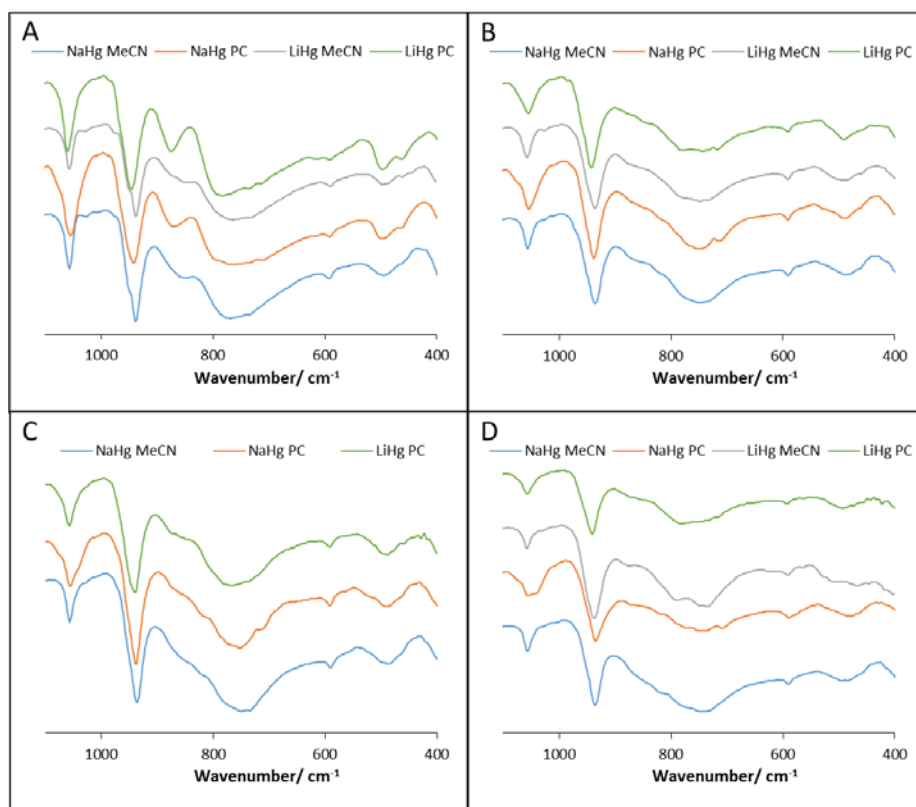


Figure 2.53 FTIR spectra of solids isolated from the reactions between PMo_{12} and different reducing agents, (A) one mole-equivalents, (B) two mole-equivalents, (C) three mole-equivalents and (D) four mole-equivalents.

The spectra of the solids isolated from the reactions between PMo_{12} and five, six, twelve and twenty-four mole-equivalents of reducing agent (Figure 2.54A-D) show that the reactions in PC produce spectra that are dramatically different to the solids isolated from the reactions in MeCN. This could be due to residual PC in the isolated solids that may be associated with the cations.

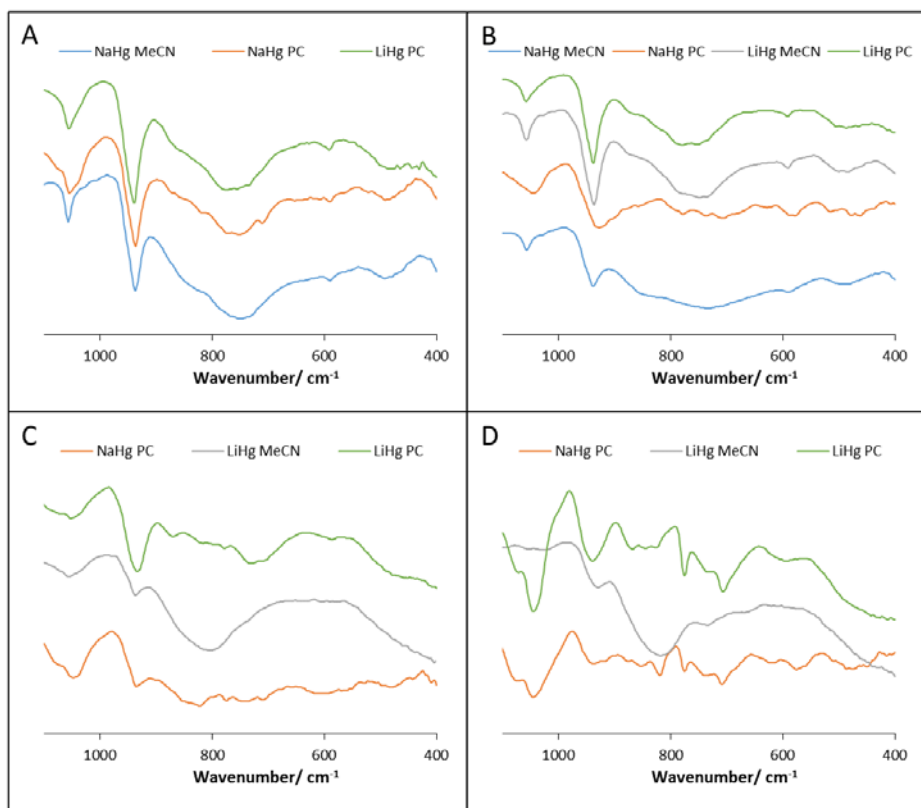


Figure 2.54 FTIR spectra of solids isolated from the reactions between PMo_{12} and different reducing agents, (A) five mole-equivalents, (B) six mole-equivalents, (C) twelve mole-equivalents and (D) twenty-four mole-equivalents.

The UV-Vis spectra are compared in Figure 2.55, where dashed lines represent the spectra of solids isolated from reactions with $\text{Na}|\text{Hg}$ amalgam and solid lines represent the spectra of solids isolated from reactions with $\text{Li}|\text{Hg}$ amalgam.

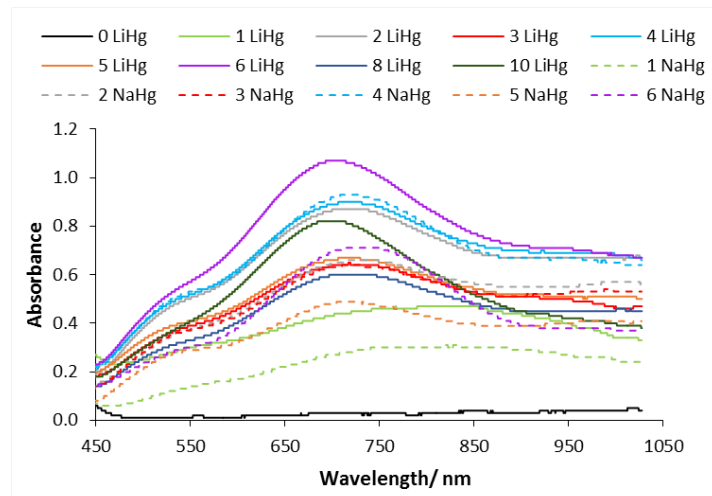


Figure 2.55 UV-Vis spectra for the solids isolated from the reactions between PMo_{12} and $\text{Na}|\text{Hg}$ amalgam, or $\text{Li}|\text{Hg}$ amalgam in PC.

Chapter 2 Chemical Reduction of Polyoxometalates

The UV-Vis spectra in Figure 2.56 show that the solids isolated from the reactions between PMo_{12} and $\text{Li}|\text{Hg}$ amalgam have higher absorbance than the solids isolated from the reactions with the same mole-equivalents of $\text{Na}|\text{Hg}$ amalgam.

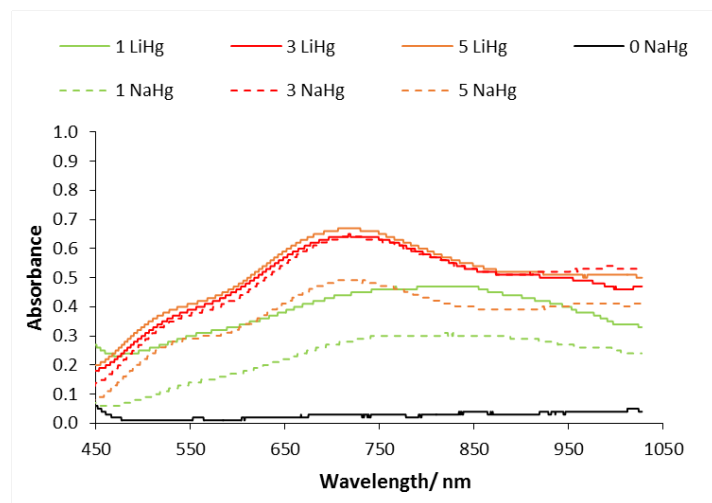


Figure 2.56 UV-Vis spectra for the solids isolated from the reactions between PMo_{12} and $\text{Na}|\text{Hg}$ amalgam, or $\text{Li}|\text{Hg}$ amalgam in PC.

The UV-Vis spectra in Figure 2.57 show that the solids isolated from the reactions between PMo_{12} and $\text{Li}|\text{Hg}$ amalgam have higher absorbance than the solids isolated from the reactions with the same mole-equivalents of $\text{Na}|\text{Hg}$ amalgam, except for four mole-equivalents where the absorbance for $\text{Na}|\text{Hg}$ amalgam is slightly higher than for $\text{Li}|\text{Hg}$ amalgam.

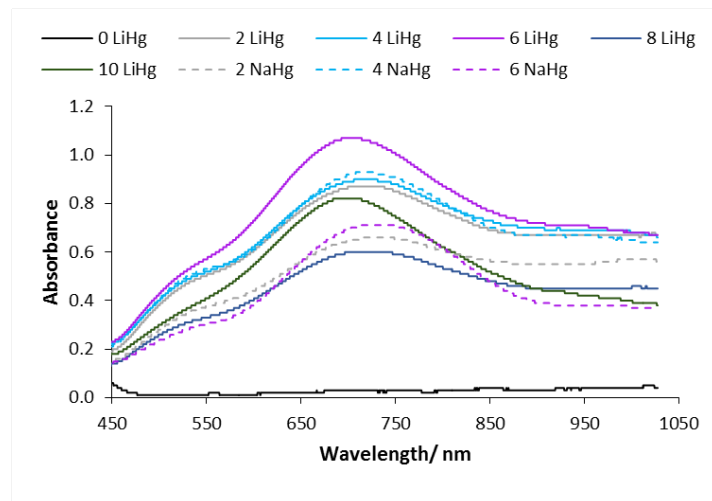


Figure 2.57 UV-Vis spectra for the solids isolated from the reactions between PMo_{12} and $\text{Na}|\text{Hg}$ amalgam, or $\text{Li}|\text{Hg}$ amalgam in PC.

The scatter plot comparing the values of ϵ for the isolated solids of the reaction between Na|Hg amalgam and PMo_{12} and Li|Hg amalgam and PMo_{12} in PC is shown in Figure 2.58. It shows that for zero to two mole-equivalents of M|Hg amalgam (M = Na or Li) the value of ϵ obtained increases linearly. The value of ϵ obtained is identical for three mole-equivalents and nearly the same for four mole-equivalents of Na|Hg and Li|Hg amalgam. It also shows there is an alternating pattern for when n is odd and even, up to when $n = 6$ for M|Hg amalgam (M = Na or Li). It also shows that ϵ is greater for solids isolated from the reactions with Li|Hg than Na|Hg amalgam, this could be because the Li^+ salts are more soluble than Na^+ salts.

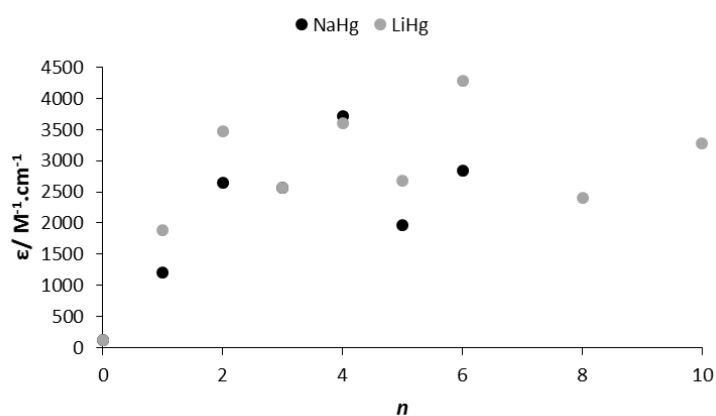


Figure 2.58 Plot of molar extinction coefficient (ϵ) against the number of mole-equivalents (n) of Li|Hg amalgam, or Na|Hg amalgam added to PMo_{12} .

The redox waves in the CV of solids isolated from the reactions between PMo_{12} and Li|Hg amalgam shift as electrons are added to the POM. After the addition of one mole-equivalent of Li|Hg amalgam the potential of the first redox wave shifts to a more positive potential when compared to the CV of fully oxidised PMo_{12} , which is the expected results as when more electrons are added to the POM the addition of further electrons should be easier. The first redox wave continues to shift to a more positive potential after the addition of two mole-equivalents of Li|Hg amalgam, this is similar to the shift of the redox waves to more positive potentials in the CV of $\text{H}_3\text{PW}_{12}\text{O}_{40}$ in DMF with increasing amounts of acid, investigated by Keita and Nadio.²⁴ After the addition of further amounts of Li|Hg amalgam the trend is no longer the same.

$^{51}\text{V}\{^1\text{H}\}$ NMR spectra comparing the reactions of V_{13} with different reducing agents are shown in Figures 2.59 and 2.60. Figure 2.59A compares the resonances in the $^{51}\text{V}\{^1\text{H}\}$ NMR spectra after the addition of one mole-equivalent of reducing agent and shows that similar spectra are obtained for $\text{Na}|\text{Hg}$ and $\text{Li}|\text{Hg}$ amalgam in MeCN. A similar spectrum is also obtained after the addition of one mole-equivalent of $\text{Na}|\text{Hg}$ and $\text{Li}|\text{Hg}$ amalgam in PC. This suggests that the reactivity between one mole-equivalent of reducing agent and V_{13} in MeCN or PC is similar. Figure 2.59B compares the resonances in the $^{51}\text{V}\{^1\text{H}\}$ NMR spectra after the addition of two mole-equivalents of reducing agent and it shows that three of the spectra are very similar. The spectrum obtained after the addition of two mole-equivalents of $\text{Na}|\text{Hg}$ amalgam in PC has an extra peak upfield in comparison to the other spectra. Figure 2.59C compares the resonances in the $^{51}\text{V}\{^1\text{H}\}$ NMR spectra after the addition of three mole-equivalents of reducing agent and it shows that again the spectrum obtained for $\text{Na}|\text{Hg}$ amalgam in PC is significantly different to the other three. This suggests that reactivity between V_{13} and $\text{Na}|\text{Hg}$ amalgam in PC is different. Figure 2.59D compares the resonances in the $^{51}\text{V}\{^1\text{H}\}$ NMR spectra after the addition of four mole-equivalents of reducing agent and it shows that the spectra obtained for the different reducing agents are all different.

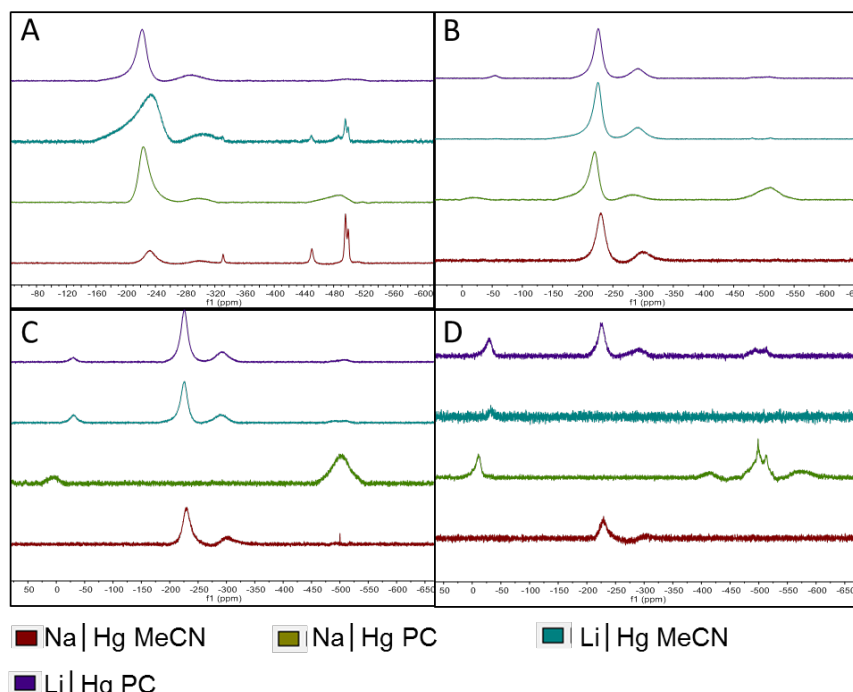


Figure 2.59 $^{51}\text{V}\{^1\text{H}\}$ NMR spectra of the reaction between V_{13} and different reducing agents (A) one mole-equivalent, (B) two mole-equivalents, (C) three mole-equivalents and (D) four mole-equivalents.

Figure 2.60 compares the resonances in $^{51}\text{V}\{^1\text{H}\}$ NMR spectra obtained after the addition of five, six and thirteen mole-equivalents of reducing agents to V_{13} and it shows for all three amounts of $\text{Li}|\text{Hg}$ amalgam the spectra obtained are similar in both solvents. This suggests that reactivity between V_{13} and $\text{Li}|\text{Hg}$ amalgam in MeCN and PC is similar.

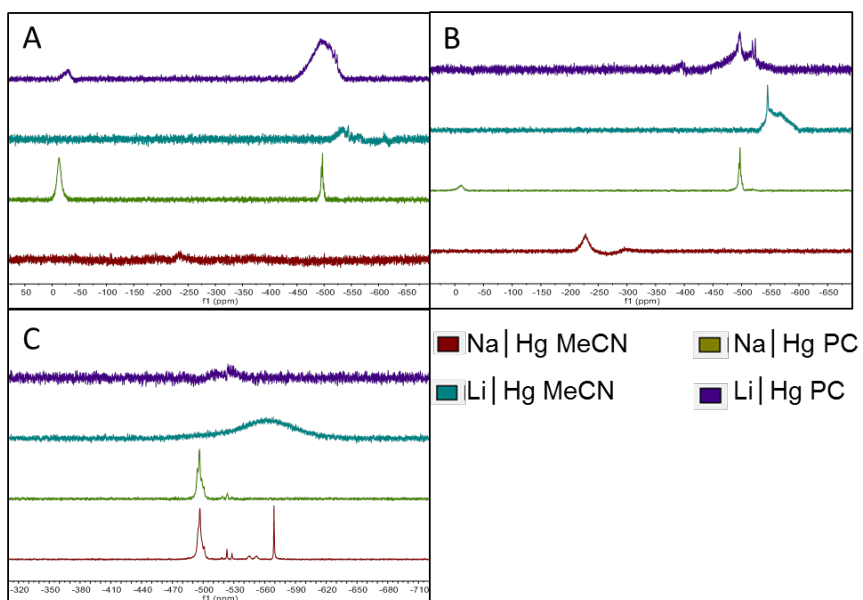


Figure 2.60 $^{51}\text{V}\{^1\text{H}\}$ NMR spectra of the reactions between V_{13} and different reducing agents (A) five mole-equivalents, (B) six mole-equivalents and (C) thirteen mole-equivalents.

The effect on the bands in the FTIR of solids isolated from the reactions between V_{13} and different reducing agents follow the same trends i.e. the $\nu(\text{V}-\text{O}_t)$ band decreases in intensity and is splits in two and the $\nu(\text{V}-\text{O}_b-\text{V})$ bands shift to lower wavenumbers and become less well defined as the amount of reducing agent increases, this is due to lower symmetry as electrons and cations are added to V_{13} . In the spectra of the solids isolated from the reactions between V_{13} and thirteen mole-equivalents of reducing agent ($\text{Na}|\text{Hg}$ in MeCN and PC and $\text{Li}|\text{Hg}$ in PC) new vibrations are formed at ca. 1200 cm^{-1} . The new vibrations in the spectra of solids isolated from PC could be due to the incorporation of PC into the products by binding to the cations.

2.5 Conclusions and Future Work

2.5.1 Conclusions

The reduction of PMo_{12} with different reducing agents was investigated, the NMR spectra suggest that the concentration of the reducing agent wasn't always accurate. The FTIR spectra suggest that at higher amounts of reducing agent (five, six, twelve

and twenty-four mole-equivalents) PC is reduced/decomposed or incorporated into the product by binding to the cations as there is a significant difference in the spectra obtained of solids isolated from reactions in MeCN compared to PC. The UV-Vis spectra of the solids isolated from reactions between PMo_{12} and $\text{Na}|\text{Hg}$ and $\text{Li}|\text{Hg}$ amalgam in PC contain two absorbance bands and ϵ is greater for solids isolated from the reactions with $\text{Li}|\text{Hg}$ than $\text{Na}|\text{Hg}$ amalgam, this could be because the Li^+ salts are more soluble than Na^+ salts.

The similar NMR and FTIR spectra obtained from the reactions between V_{13} and $\text{Li}|\text{Hg}$ amalgam in both MeCN and PC, suggest that similar products are formed in both solvents. Spectra obtained from the reactions between V_{13} and $\text{Na}|\text{Hg}$ amalgam in both MeCN and PC, suggest that different species are formed in the different solvents and that speciation is different from reductions with $\text{Li}|\text{Hg}$ amalgam.

2.5.2 Future Work

In order to investigate the reductions of PMo_{12} and V_{13} further, there are several techniques that can contribute to understanding and quantifying the degree of reduction of solids obtained from the reduction reactions. Electron paramagnetic resonance (EPR) spectroscopy is a technique used to characterise species with unpaired electrons. Redox titrations of reduced PMo_{12} and V_{13} with a suitable oxidising agent in order to quantify the degree of reduction is required. Once the degree of reduction has been quantified of the solids isolated from the reactions between PMo_{12} and $\text{Li}|\text{Hg}$ amalgam, the repeat of cyclic voltammetry measurements is required.

Solid state ^{31}P and ^7Li or ^{23}Na NMR is required of the remaining solids isolated from the reductions of PMo_{12} with $\text{Na}|\text{Hg}$ and $\text{Li}|\text{Hg}$ amalgam.

Cyclic voltammetry of the solids isolated from reactions between PMo_{12} and $\text{Na}|\text{Hg}$ amalgam is required in order to compare with the cyclic voltammetry obtained for the solids isolated from reactions between PMo_{12} and $\text{Li}|\text{Hg}$ amalgam.

Further characterisation of the solids isolated from the reductions of V_{13} with $\text{Na}|\text{Hg}$ and $\text{Li}|\text{Hg}$ amalgam by solid-state ^{51}V and ^7Li or ^{23}Na NMR spectroscopy, UV-Vis spectroscopy and cyclic voltammetry is required.

2.6 References

1. M. T. Pope, in *Polyoxometalate Molecular Science*, eds. J. J. Borras-Almenar, E. Coronado, A. Muller and M. T. Pope, Kluwer Academic Publishers, Dordrecht, The Netherlands, First edn., 2003, ch. 1, pp. 3-31.
2. J. D. H. Strickland, *J. Am. Chem. Soc.*, 1952, **74**, 868.
3. M. T. Pope and G. M. Varga, *Inorg. Chem.*, 1966, **5**, 1249.
4. L. P. Kazansky, *Chem. Phys. Lett.*, 1996, **258**, 248.
5. S. Himeno, M. Takamoto and T. Ueda, *J. Electroanal. Chem.*, 1999, **465**, 129.
6. R. Canioni, PhD, Versailles Saint-Quentin-en-Yvelines University, 2010.
7. R. I. Maksimovskaya, *Polyhedron*, 2013, **65**, 54.
8. H. Wang, S. Hamanaka, Y. Nishimoto, S. Irle, T. Yokoyama, H. Yoshikawa and K. Awaga, *J. Am. Chem. Soc.*, 2012, **134**, 4918.
9. R. Bakri, A. Booth, G. Harle, P. S. Middleton, C. Wills, W. Clegg, R. W. Harrington and R. J. Errington, *Chem. Commun.*, 2012, **48**, 2779.
10. in *Metals in Mercury*, eds. C. Hirayama, Z. Galus and C. Guminski, Pergamon, Amsterdam, First edn., 1986, pp. 1-54.
11. H.-Y. Chen, G. Wee, R. Al-Oweini, J. Friedl, K. S. Tan, Y. Wang, C. L. Wong, U. Kortz, U. Stimming and M. Srinivasan, *ChemPhysChem*, 2014, **15**, 2162.
12. J. Liu, Z. Chen, S. Chen, B. Zhang, J. Wang, H. Wang, B. Tian, M. Chen, X. Fan, Y. Huang, T. C. Sum, J. Lin and Z. X. Shen, *ACS Nano*, 2017, **11**, 6911.
13. S. Hartung, N. Bucher, H.-Y. Chen, R. Al-Oweini, S. Sreejith, P. Borah, Z. Yanli, U. Kortz, U. Stimming, H. E. Hoster and M. Srinivasan, *J. Power Sources*, 2015, **288**, 270.
14. D. Hou, K. S. Hagen and C. L. Hill, *J. Am. Chem. Soc.*, 1992, **114**, 5864.
15. C. Sanchez, J. Livage, J. P. Launay, M. Fournier and Y. Jeannin, *J. Am. Chem. Soc.*, 1982, **104**, 3194.
16. K. Eguchi, Y. Toyozawa, N. Yamazoe and T. Seiyama, *J. Catal.*, 1983, **83**, 32.
17. D. Battisti, G. A. Nazri, B. Klassen and R. Aroca, *J. Phys. Chem.*, 1993, **97**, 5826.
18. C. J. Besecker, W. G. Klemperer, D. J. Maltbie and D. A. Wright, *Inorg. Chem.*, 1985, **24**, 1027.
19. R. Bakri, PhD Thesis, Newcastle University, 1998.
20. P. Vecera, J. Holzwarth, K. F. Edelthalhammer, U. Mundloch, H. Peterlik, F. Hauke and A. Hirsch, *Nat. Commun.*, 2016, **7**, 12411.

Chapter 2 Chemical Reduction of Polyoxometalates

21. A. Weitz and M. Rabinovitz, *Synth. Met.*, 1995, **74**, 201.
22. I. S. Weitz and M. Rabinovitz, *J. Chem. Soc., Perkin Trans. 1*, 1993, DOI: 10.1039/P19930000117, 117.
23. B. Lacave-Goffin, L. Hevesi and J. Devaux, *J. Chem. Soc., Chem. Commun.*, 1995, DOI: 10.1039/C39950000769, 769.
24. B. Keita and L. Nadjo, *J. Electroanal. Chem. Interfacial Electrochem.*, 1987, **227**, 77.

Chapter 3

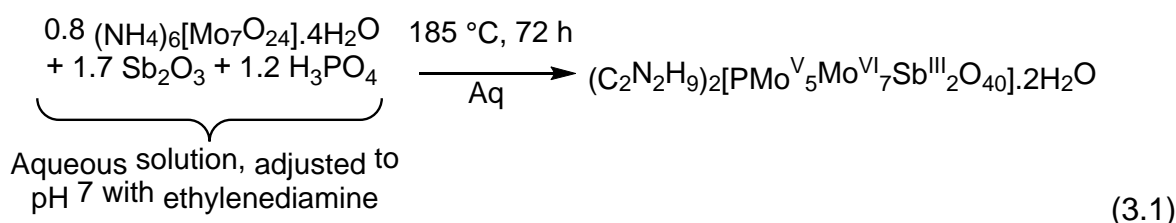
Addition of Capping M²⁺ and M³⁺ Cations to Reduced (TBA)₃[PMo₁₂O₄₀]

Chapter 3 Addition of Capping M^{2+} and M^{3+} Cations to Reduced $(TBA)_3[PMo_{12}O_{40}]$

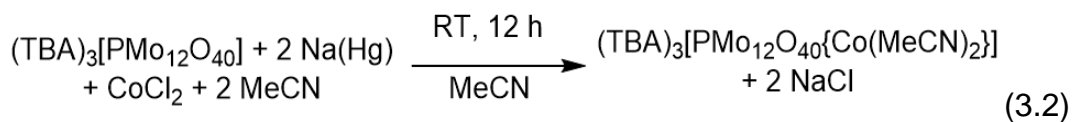
3.1 Introduction

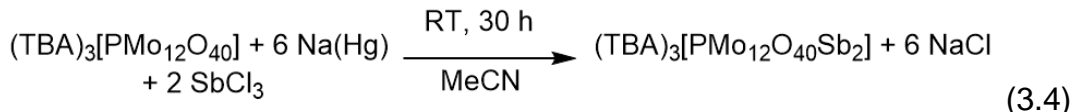
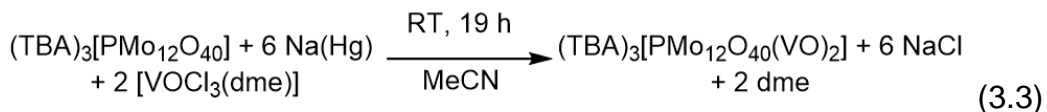
The addition of M^{n+} ions to reduced POMs is an important feature of this chemistry as the capping cations can stabilise reduced POMs and thereby facilitate the uptake of multiple electrons.

In the literature reduced capped Keggin POMs have mostly been obtained in uncontrolled hydrothermal reactions as briefly described in Section 1.4.4.^{1, 2} The previously reported di-capped antimony containing Keggin-type POM, $(C_2N_2H_9)_2[PMo^V_5Mo^{VI}_7Sb^{III}_2O_{40}].2H_2O$ was prepared via uncontrolled hydrothermal synthesis in an autoclave, as shown in Equation 3.1.³ The product was isolated as a crystalline solid by cooling the solution in the autoclave to RT with a yield of 58% and the solid-state structure showed a 1-D sinusoidal chain of $[PMo_{12}Sb_2]$ anions linked through Sb–O inter-molecular interactions.



Previous work from the RJE group established the controlled reduction and capping of PMo_{12} with Co, V and Sb.⁴ The strategy involved first reducing the PMo_{12} cluster with $Na|Hg$ amalgam and then adding the corresponding metal salt, as shown in Equations 3.2, 3.3 and 3.4. Crystals of $(TBA)_3[PMo_{12}O_{40}\{Co(MeCN)_2\}]$ and $(TBA)_3[PMo_{12}O_{40}(VO)_2]$ were isolated by recrystallisation from MeCN-Et₂O at –20 °C. Crystals of $(TBA)_3[PMo_{12}O_{40}Sb_2]$ were isolated by the diffusion of ether into a concentrated MeCN solution of the POM.





This chapter describes an extension of the initial work on reduction assembly by capping PMo₁₂ with Sb as well as Bi and Zn, and the characterisation of the reduced products.

3.2 Reduced (TBA)₃[PMo₁₂O₄₀] Capped with M²⁺/M³⁺.

3.2.1 M = Sb(III)

The RJE Group have previously synthesised (TBA)₃[PMo₁₂O₄₀Sb₂] (PMo₁₂Sb₂) via the reaction in Equation 3.4.⁴ The ball-and-stick model for this compound is shown in Figure 3.1. It shows the Sb ions occupying two mutually *trans* tetragonal sites in the PMo₁₂ cluster. The two Sb atoms in the cluster are assigned a +3 oxidation state from bond valence sum (BVS) analysis,^{5,6} which means the PMo₁₂ core has been reduced by six electrons. BVS analysis is a structure analysis technique that determines an estimation of bond valence from bond lengths, by comparing to known compounds.

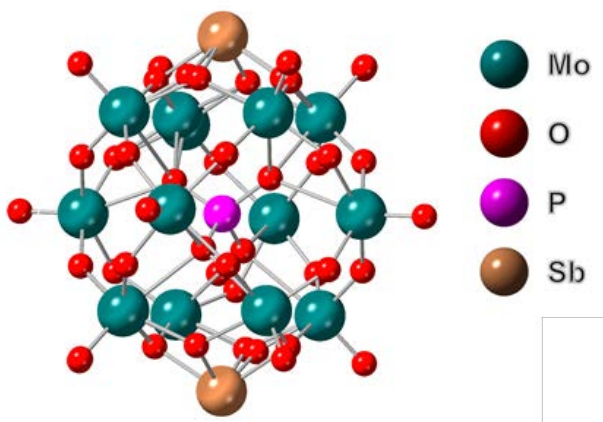


Figure 3.1 Ball-and-stick representation of the anion [PMo₁₂O₄₀Sb₂]³⁻.

The synthesis of PMo₁₂Sb₂ was repeated using the reaction shown in Equation 3.4. Crystals were obtained by cooling a concentrated MeCN solution of PMo₁₂Sb₂ to -20 °C. However, unlike the crystal structure obtained previously, in this crystal structure the two Sb(III) ions were disordered over six tetragonal sites, as shown in the ball-

and-stick diagram in Figure 3.2A and only two TBA cations were found in the crystal structure, this suggests a different degree of reduction, i.e. $[\text{PMo}_{12}\text{O}_{40}\text{Sb}^{\text{III}}_2]^{2-}$, where the POM core is apparently a five-electron reduced species. This led to a second attempt at repeating the previously published synthesis, following the same procedure as attempt 1 and this time the crystal structure obtained was the same as the structure published in the literature.

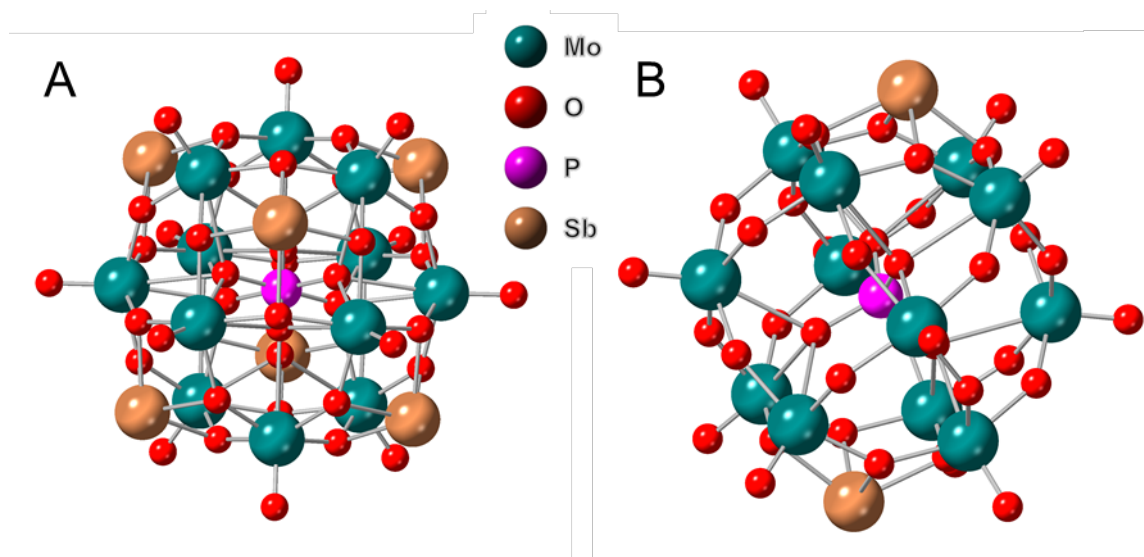


Figure 3.2 Ball-and-stick model of disordered $[\text{PMo}_{12}\text{O}_{40}\text{Sb}_2]^{2-}$ (A) and ordered (B).

The $^{31}\text{P}\{^1\text{H}\}$ NMR spectra for the two reactions are shown in Figure 3.3. The resonance shifts upfield from the fully oxidised PMo_{12} after addition of six electrons from $\text{Na}|\text{Hg}$ and the resonance then shifts slightly downfield after the addition of two mole-equivalents of SbCl_3 . Each step of the reaction proceeds cleanly as there is only one species present in each of the NMR spectra. The resonance in the NMR spectra of crystals isolated from attempt 1 and attempt 2 are the same, suggesting the same product is formed. The peaks in the NMR spectra for the isolated products (Figure 3.3C and D) are fairly broad (13 Hz), this could be due to the formation of aggregates by the interaction of Sb with O atoms on a neighbouring molecule in concentrated solutions, which can be seen in the extended structures in Figure 3.4. The extended structures shown in Figure 3.4 emphasise the aligned orientation of the POM and the intermolecular interactions between the anions in solid-state.

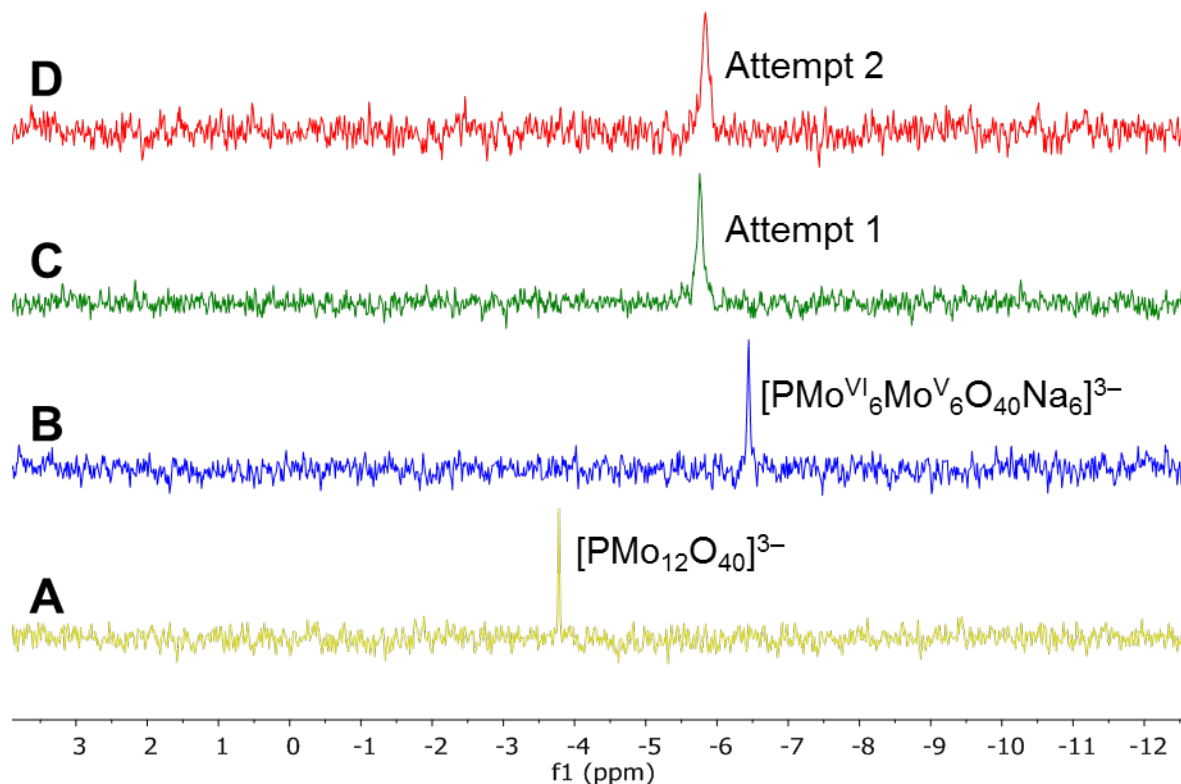


Figure 3.3 $^{31}P\{^1H\}$ NMR spectra of PMo_{12} (A), $(TBA)_3[PMo_{12}O_{40}Na_6]$ (B), crystals isolated from attempt 1 (C) and crystals isolated from attempt 2 (D).

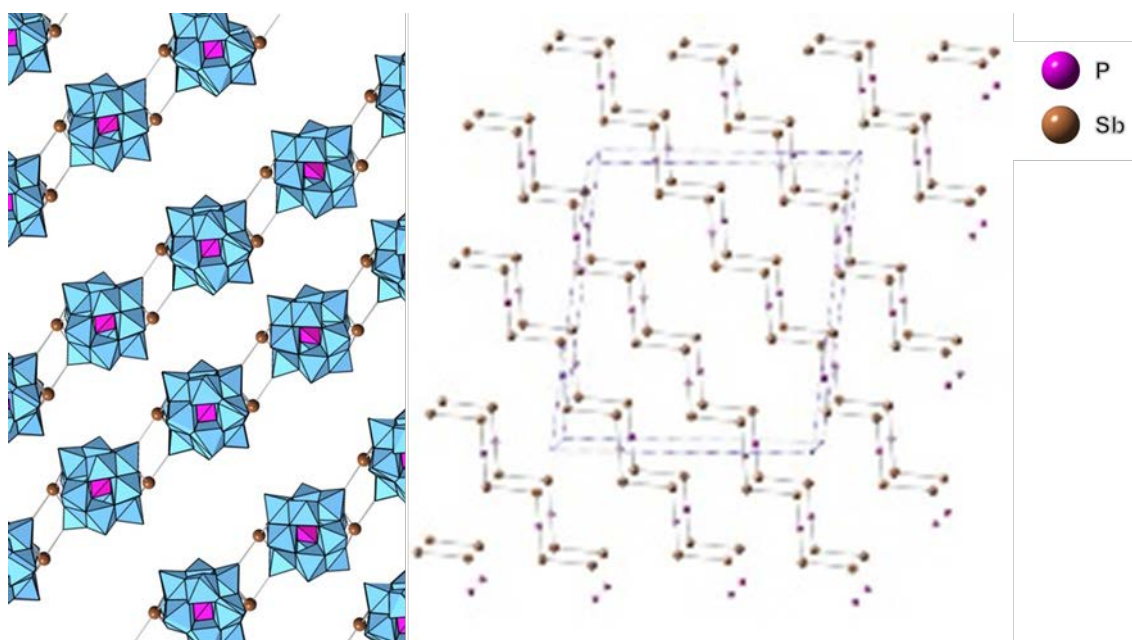


Figure 3.4 The extended structure of $[PMo_{12}O_{40}Sb_2]^{3-}$.

The FTIR spectra for crystals isolated from attempts 1 and 2 to prepare $\text{PMo}_{12}\text{Sb}_2$, are shown in Figure 3.5, alongside the spectrum of PMo_{12} for comparison. The spectra for the isolated crystals are similar and both are distinctly different from that of fully oxidised PMo_{12} . The $\nu(\text{P-O})$ band at $\sim 1050 \text{ cm}^{-1}$ for the reduced capped species is much less intense and split into two in comparison to the $\nu(\text{P-O})$ band in PMo_{12} , the changes are due to the reduction of the symmetry of the capped species from T_d . The $\nu(\text{Mo-O}_t)$ band for the reduced capped species has a shoulder whereas the same band in the fully oxidised PMo_{12} spectrum does not. The $\nu(\text{Mo-O}_b\text{-Mo})$ bands are less intense and split in comparison to the bands in the PMo_{12} spectrum, the bridging bands are effected most when bonded to Sb. Fournier *et al.* reported that the formation of a spin bipolaron in two-electron reduced phosphomolybdic acid ($\text{H}_3\text{PMo}_{12}\text{O}_{40}$) led to the broadening and reduction in intensity of the $\nu(\text{Mo-O}_b\text{-Mo})$ bands, this was caused by the coupling of the spin bipolaron to the vibrations of the bridging bands, this is a similar effect to what is seen for the FTIR spectra of $\text{PMo}_{12}\text{Sb}_2$.⁷

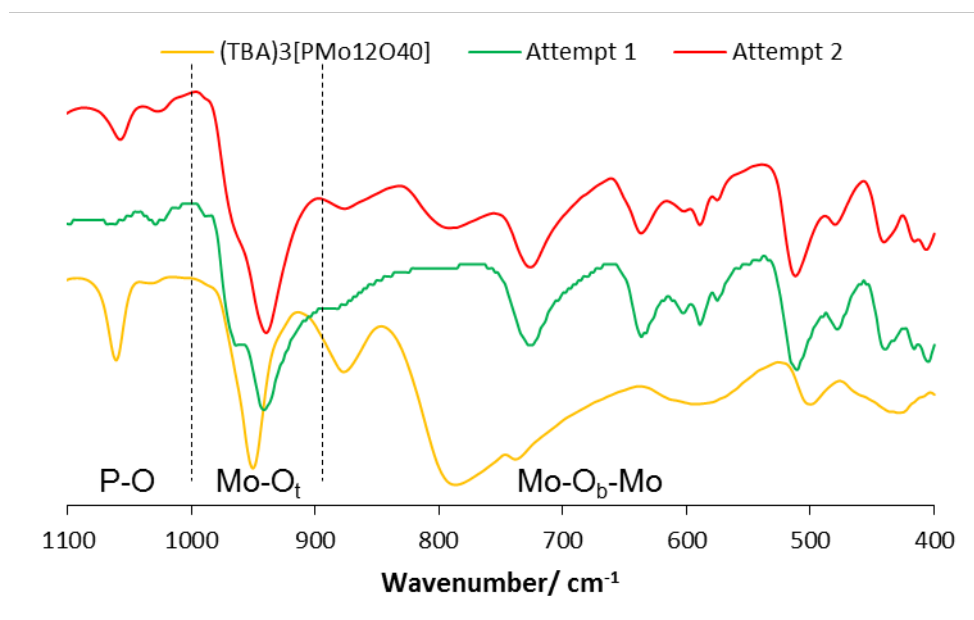


Figure 3.5 FTIR spectra of PMo_{12} (yellow line), crystals isolated from attempt 1 (green line) and crystals isolated from attempt 2 (red line).

The similarities of the resonances in the $^{31}\text{P}\{^1\text{H}\}$ NMR spectra and the FTIR spectra of the isolated crystals from attempts 1 and 2 to prepare $\text{PMo}_{12}\text{Sb}_2$ suggest that the oxidation of the crystals from attempt 1 to $(\text{TBA})_2[\text{PMo}_{12}\text{O}_{40}\text{Sb}_2]$ occurred during crystal growth, a possible cause of oxidation is the exposure of the crystallisation process to air, and a 'rogue' crystal was selected. It is likely that

(TBA)₂[PMo₁₂O₄₀Sb₂] is less soluble than (TBA)₃[PMo₁₂O₄₀Sb₂] and therefore formed crystals first and the majority of the species in solution could have been

(TBA)₃[PMo₁₂O₄₀Sb₂] The ³¹P{¹H} NMR spectrum of PMo₁₂ reduced with five mole-equivalents of Na is shown in Figure 2.3 in Chapter 2, and this shows the resonance is downfield shifted (−3.1 ppm) when compared to the resonance obtained for the six-electron reduced species PMo₁₂Sb₂ and PMo₁₂Na₆ in Figure 3.3.

The CV of 1 mM PMo₁₂Sb₂ (crystals isolated from attempt 2) in a 100 mM (TBA)(BF₄) in MeCN electrolyte solution was measured (Figure 3.6). This CV was then compared to the CV of the fully oxidised PMo₁₂ using the same concentrations and electrolyte solution. On the addition of Sb to the POM the potentials at which the electron transfer steps occur are shifted to more negative potentials and there is a new redox peak at −0.29 V vs Fc/Fc⁺. The shift to more negative potentials is due to the addition of electrons into the POM core, as it means it is more difficult to reduce the POM. The first redox wave in the CV of PMo₁₂Sb₂ could be a stripping wave and indicative of surface reactions on the GC WE.

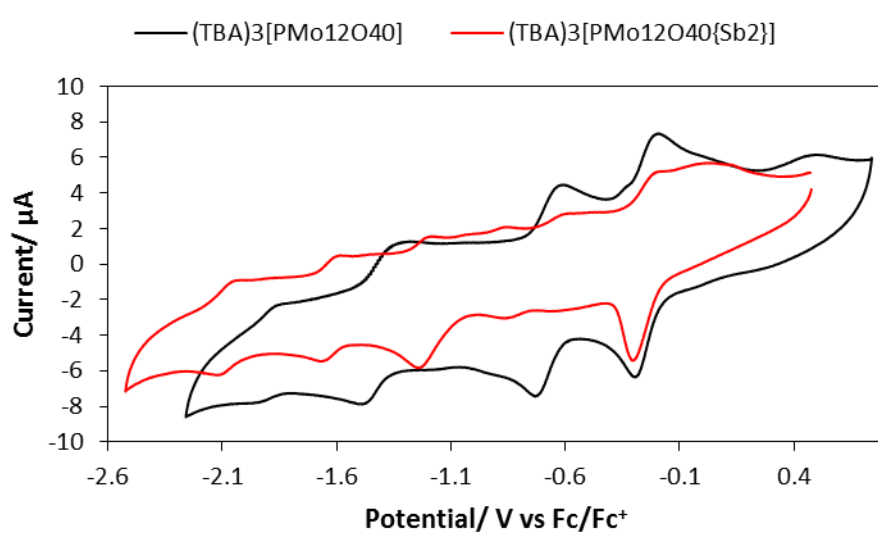


Figure 3.6 CV of 1 mM PMo₁₂ (black line) and 1 mM PMo₁₂Sb₂ (red line) in 100 mM (TBA)(BF₄) MeCN, Ag wire RE, Pt CE, GC WE, from +1.0 V to −2.0 V vs Ag wire, 100 mV/s scan rate.

3.2.2 M = Bi(III)

The di-capped $(TBA)_3[PMo_{12}O_{40}\{Bi(dmso)_4\}_2]$ ($PMo_{12}Bi_2$) species was synthesised according to the reaction shown in Equation 3.5. PMo_{12} was dissolved in DMSO and heated with then two mole-equivalents of Bi metal at 60 °C overnight. In this case, elemental Bi is used as the reducing agent. Crystals of $PMo_{12}Bi_2$ were obtained by diffusing ether into the POM solution, and a ball-and-stick model of the anion structure is shown in Figure 3.7. The Bi atoms in the structure were assigned +3 oxidation state by using BVS analysis.^{5, 6}

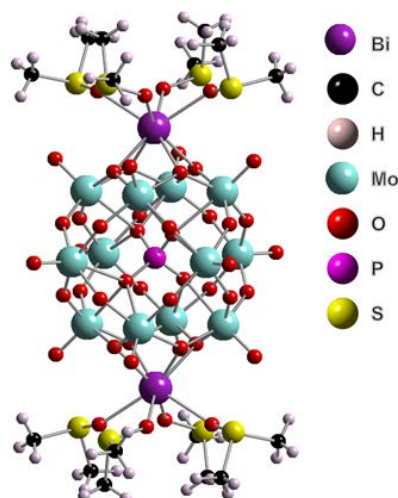
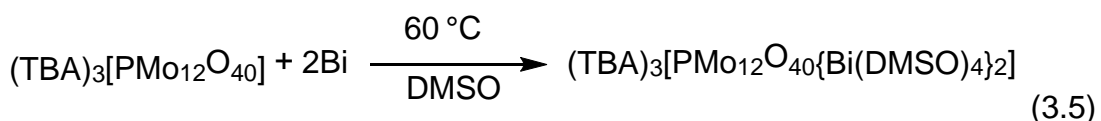


Figure 3.7 Ball-and-stick representation of the anion $[PMo_{12}O_{40}\{Bi(dmso)_4\}_2]^{3-}$.

The $^{31}\text{P}\{^1\text{H}\}$ NMR spectra from the reaction between PMo_{12} and two mole-equivalents of Bi are shown in Figure 3.8 and it shows that in the reaction solutions (Figures 3.8B and C) there is evidence for other species or intermediates as well as the structurally characterised species $PMo_{12}Bi_2$ which is assigned to the resonance at -0.3 ppm.

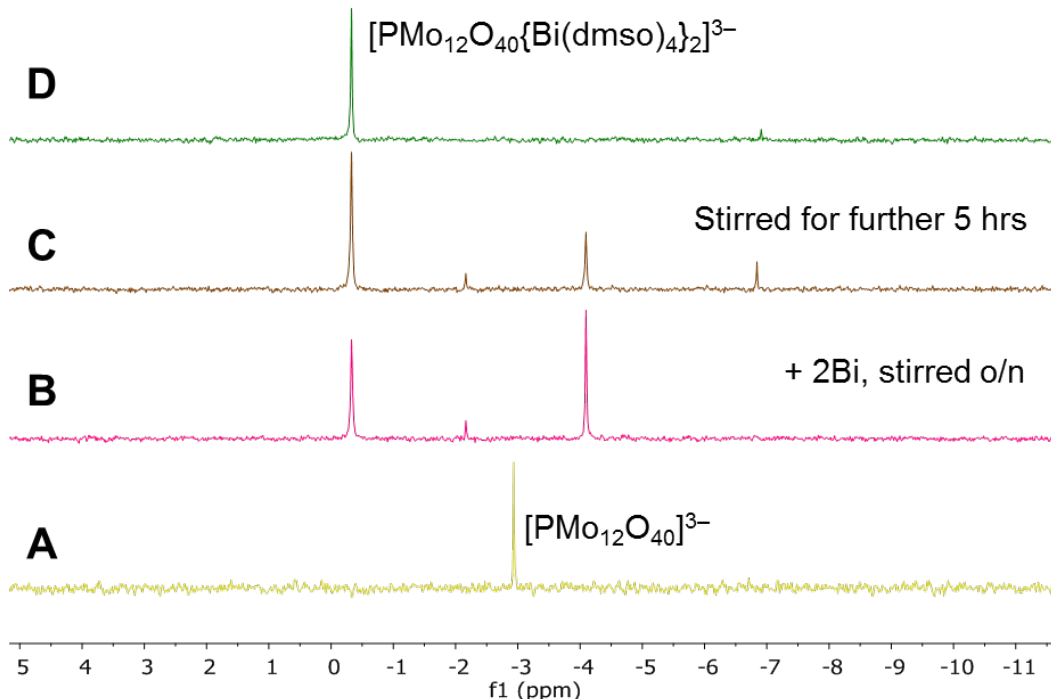


Figure 3.8 $^{31}P\{^1H\}$ NMR spectra of PMo_{12} (A), the reaction mixture of PMo_{12} + two mole-equivalents of Bi stirred overnight (B), the reaction mixture of PMo_{12} + two mole-equivalents of Bi stirred for a further 5 hours (C) and isolated crystals of $PMo_{12}Bi_2$ (D).

The FTIR spectra in Figure 3.9 show that when PMo_{12} is capped with two Bi atoms, the $\nu(P-O)$ band is less intense and is shifted to slightly lower wavenumber. The $\nu(Mo-O_t)$ band has broadened and shifted to slightly lower wavenumber. The $\nu(Mo-O_b-Mo)$ bands have broadened and decreased in intensity, this suggests the formation of spin bipolarons which have coupled to the bridging bond vibrations.⁷ The FTIR spectrum of $PMo_{12}Bi_2$ contains bands for dmsO.

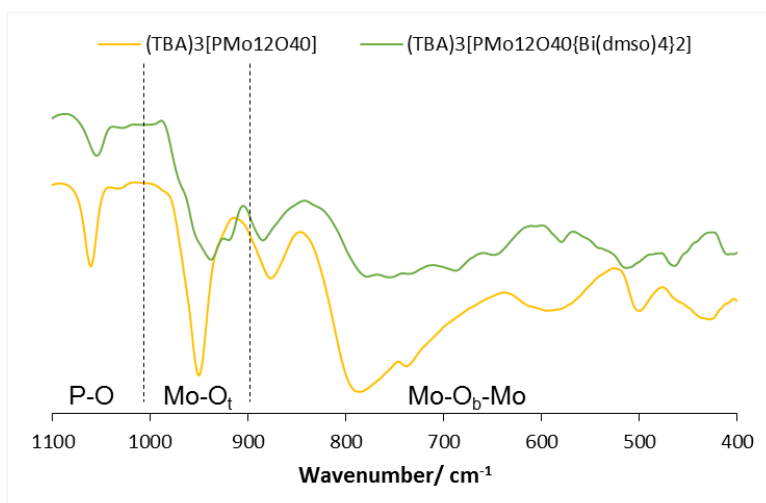


Figure 3.9 FTIR spectra of PMo_{12} (yellow line) and isolated crystals of $PMo_{12}Bi_2$ (green line).

The cyclic voltammograms of 1 mM $\text{PMo}_{12}\text{Bi}_2$ and PMo_{12} in a 100 mM (TBA)(BF₄) in MeCN electrolyte solution are compared in Figure 3.10 and it shows that the electron transfer steps in the CV of $\text{PMo}_{12}\text{Bi}_2$ are shifted to slightly more positive potentials than PMo_{12} . There are several extra redox peaks on both the oxidation and reduction waves for $\text{PMo}_{12}\text{Bi}_2$ as indicated by the arrows in Figure 3.10.

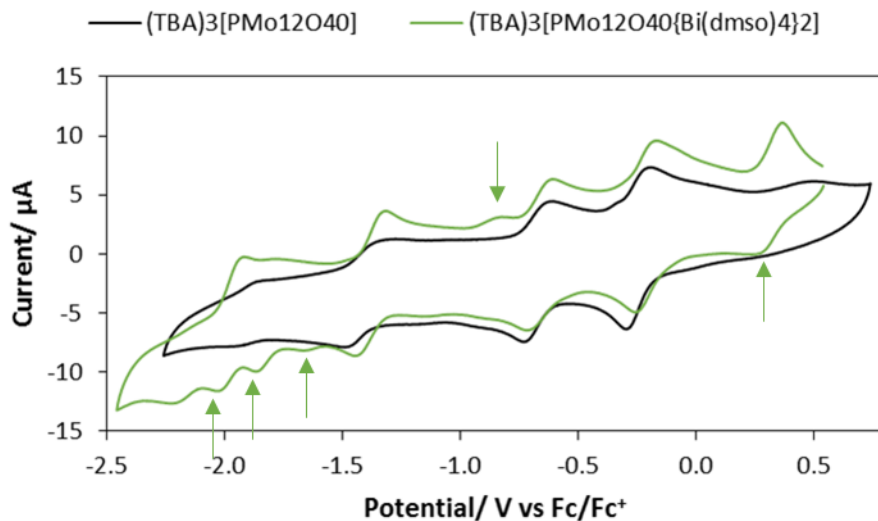
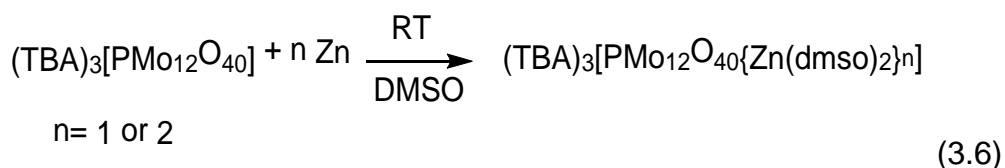


Figure 3.10 CV of 1 mM PMo_{12} (black line) and 1 mM $\text{PMo}_{12}\text{Bi}_2$ (green line) in 100 mM (TBA)(BF₄) MeCN, Ag wire RE, Pt CE, GC WE, from +1.0 V to -2.0 V vs Ag wire, 100 mV/s scan rate.

3.2.3 M = Zn(II)

PMo_{12} was reduced with one and two mole-equivalents of Zn metal in DMSO as shown in Equation 3.6. The products were precipitated by the addition of ether and the dark blue solid was dissolved in the minimum amount of MeCN. Crystals of $(\text{TBA})_3[\text{PMo}_{12}\text{O}_{40}\{\text{Zn}(\text{dmso})_2\}]$ (PMo_{12}Zn) were obtained by diffusing ether into the concentrated MeCN solution. Attempts to synthesise the di-capped species only gave crystals of the mono-capped POM as characterised by X-ray crystallography. A ball-and-stick representation of $[\text{PMo}_{12}\text{O}_{40}\{\text{Zn}(\text{dmso})_2\}]^{3-}$ is shown in Figure 3.11. The Zn atom can be assigned a +2 oxidation state by using BVS analysis.^{5, 6}



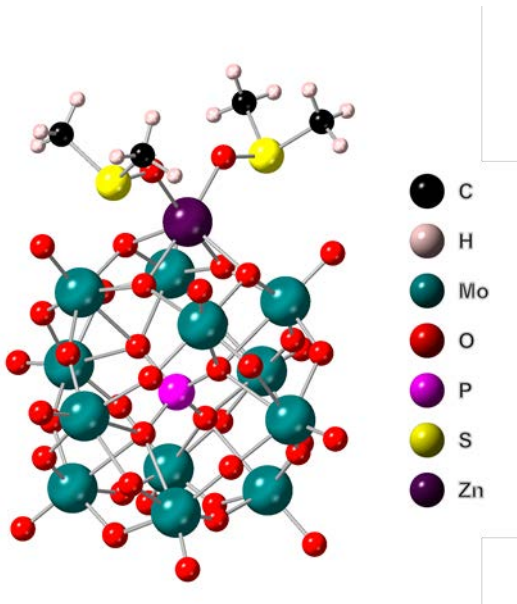


Figure 3.11 Ball-and-stick representation of the anion $[PMo_{12}O_{40}\{Zn(dmsO)_2\}]^{3-}$.

$^{31}P\{^1H\}$ NMR spectra (Figure 3.12) show that when PMo_{12} is reacted with one or two equivalents of Zn, three species are present in the reaction solutions in a ratio of 1: 0.2: 0.6 and 0.4: 0.4: 1.0 respectively, with no peak corresponding to the fully oxidised PMo_{12} . A dark blue crude solid was precipitated and then dissolved in minimum amount of MeCN. Vapour diffusion of ether gave crystals, which gave a spectrum containing a peak at -8.1 ppm and X-ray structure characterisation showed the mono-capped anion. The species at -0.2 and -6.9 ppm have not been successfully crystallised. The broadness of the line widths indicated next to the peaks in Figure 3.12B and C suggest that the species at -0.2 and -8.1 in the reaction mixtures may be undergoing rapid self-exchange or association/dissociation of Zn^{2+} . The fact that the isolated crystals of $PMo_{12}Zn$ give an upfield sharp peak, which broadens in the presence of the low field species supports the proposal that electron or cation exchange is occurring. The species at -0.2 ppm could be assigned to PMo_{12} reduced by one-electron and since the reaction mixture for one-mole equivalent of Zn contains 56% of this species, this suggests that this species is formed faster than the structurally characterised species at -8.1 ppm. This could be investigated further by adding fully oxidised PMo_{12} to a solution of the crystallised species and monitoring the mixture by NMR. Variable temperature NMR experiments could be used to investigate the reaction kinetics, as at high temperatures the rate of exchange of electrons/ cations would increase, which would affect linewidths.

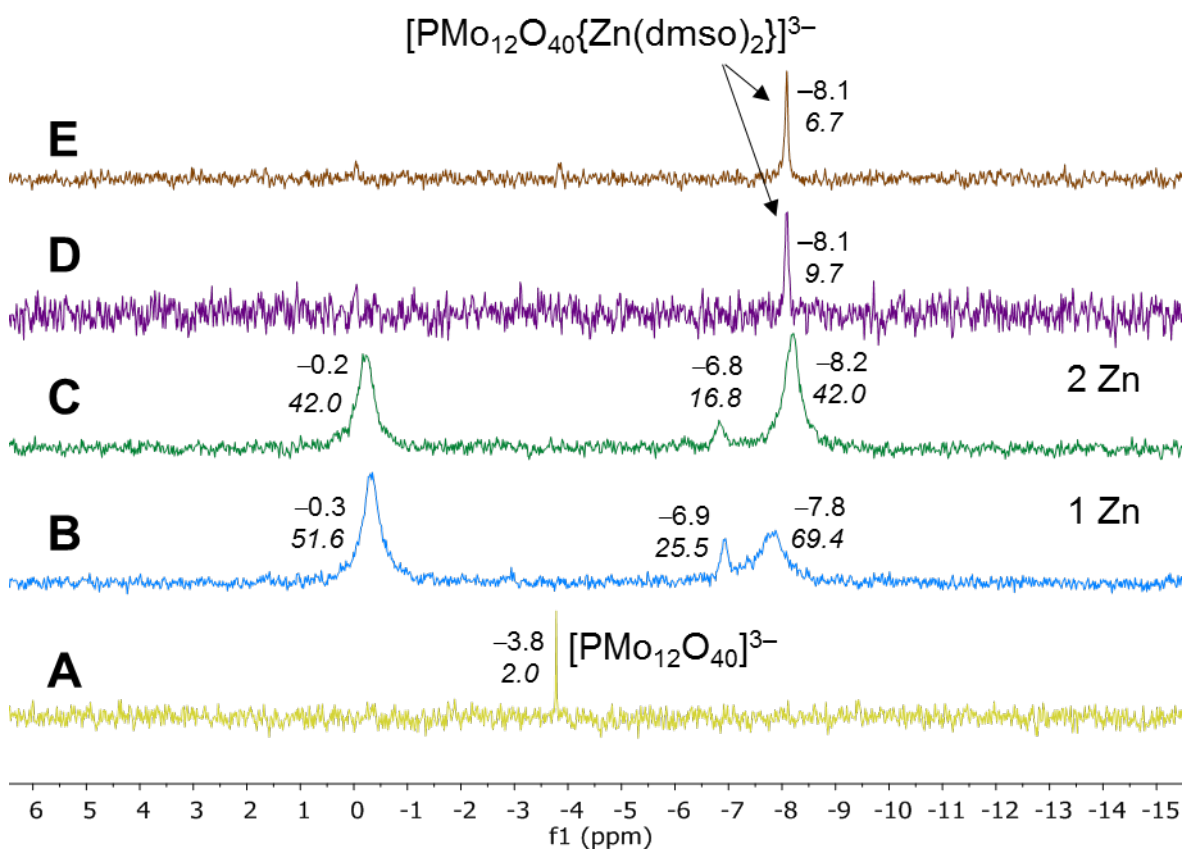


Figure 3.12 $^{31}\text{P}\{^1\text{H}\}$ NMR spectra of PMo_{12} (A), the reaction mixture of PMo_{12} and one mole-equivalent of Zn (B), the reaction mixture of PMo_{12} and two mole-equivalents of Zn (C), crystals from one mole-equivalent of Zn to get PMo_{12}Zn (D) and crystals from two mole-equivalents of Zn to get PMo_{12}Zn (E) (ppm and *line widths* Hz are labelled next to peaks).

The RJE group have previously attempted to prepare the mono- and tetra-capped Zn-PMo_{12} species, the NMR spectra for the reaction mixtures obtained are shown in Figure 3.13B and D respectively. The spectrum obtained from the previous attempt to synthesise PMo_{12}Zn is similar to the spectrum obtained in this study (Figure 3.13A), however there is a smaller amount of the species that we have assigned to -0.3 ppm, one-electron reduced PMo_{12} . The attempt to synthesise $[\text{PMo}_{12}\text{O}_{40}\{\text{Zn}(\text{dmso})_2\}_4]^{3-}$ did not yield any crystals, but the NMR spectrum contained a major peak at -4.3 ppm, which was not present in the reaction mixtures when one or two mole-equivalents of Zn were added to PMo_{12} , which suggests a new species was formed.

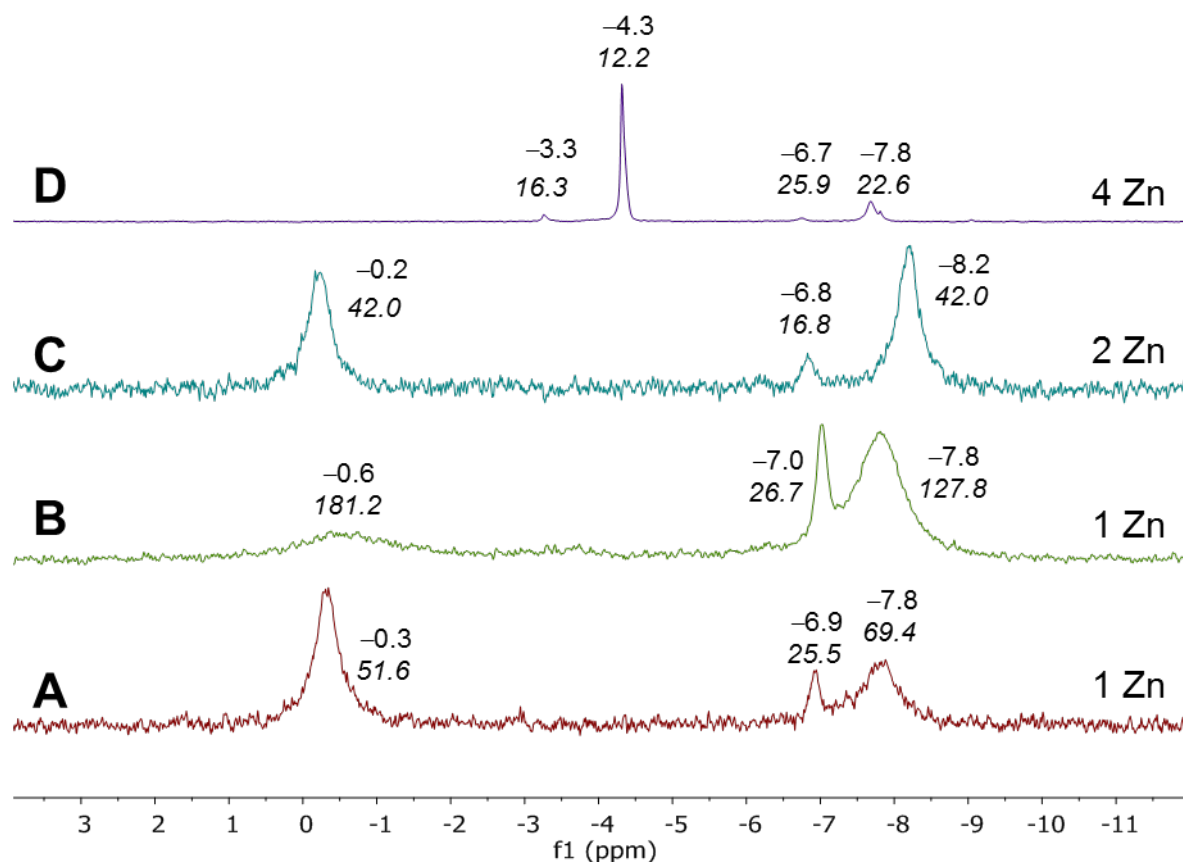


Figure 3.13 $^{31}\text{P}\{\text{H}\}$ NMR spectra of the reaction between PMo₁₂ and (A) one mole-equivalent of Zn, (B) one-mole equivalent of Zn, (C) two-mole equivalents of Zn, and (D) four mole-equivalents of Zn (ppm and *line widths* Hz are labelled next to peaks).

The FTIR spectra for the crystallised products obtained from reactions involving the addition of one and two mole-equivalents of Zn to PMo₁₂ are identical (Figure 3.14). It shows that the spectrum of PMo₁₂Zn is different to the spectrum for fully oxidised PMo₁₂. The $\nu(\text{P-O})$ band at 1050 cm^{-1} for PMo₁₂ is split into two at 1053 and 1033 cm^{-1} , and is much less intense for the Zn-capped species. Both the $\nu(\text{Mo-O}_\text{t})$ and $\nu(\text{Mo-O}_\text{b}-\text{Mo})$ bands are shifted to lower wavenumbers upon reduction and are also reduced in intensity, this could be for the same reasons as previously discussed for PMo₁₂Sb₂ and PMo₁₂Bi₂, the formation of a spin bipolaron on the addition of two electrons to the POM which couples to the vibrations of the bridging bonds.⁷

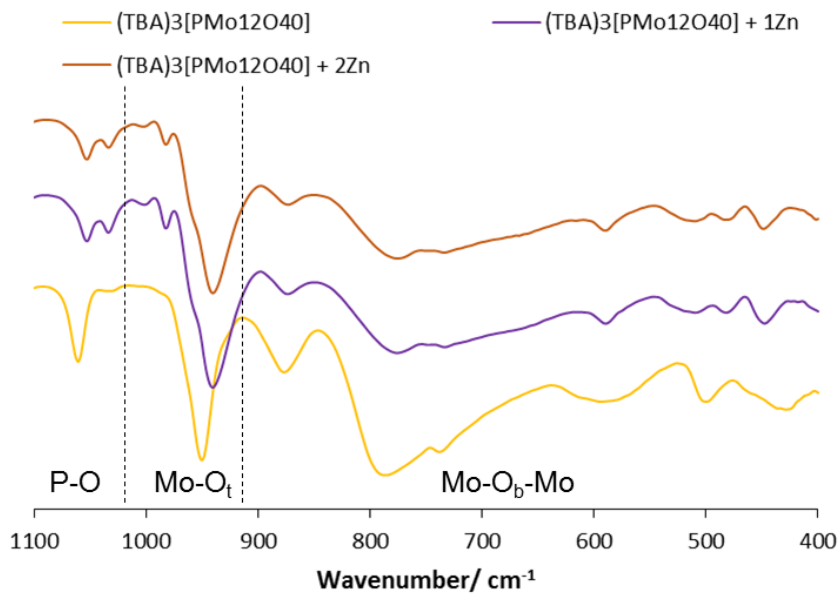


Figure 3.14 FTIR spectra of PMo_{12} (yellow line), crystallised products from PMo_{12} + one mole-equivalent of Zn (purple line) and crystallised products from PMo_{12} + two mole-equivalents of Zn (brown line).

The CV of 1 mM PMo_{12}Zn in a 100 mM (TBA)(BF₄) in MeCN electrolyte solution was measured (Figure 3.15) and compared with fully oxidised PMo_{12} . For the Zn-capped species, the three electron transfer steps with the lowest potential have reduced intensity and the electron transfer step with the most positive potential has significantly increased in intensity, possibly a multi-electron step. There is also an extra peak in the oxidation wave at ca. -3.79 V vs Fc/Fc⁺.

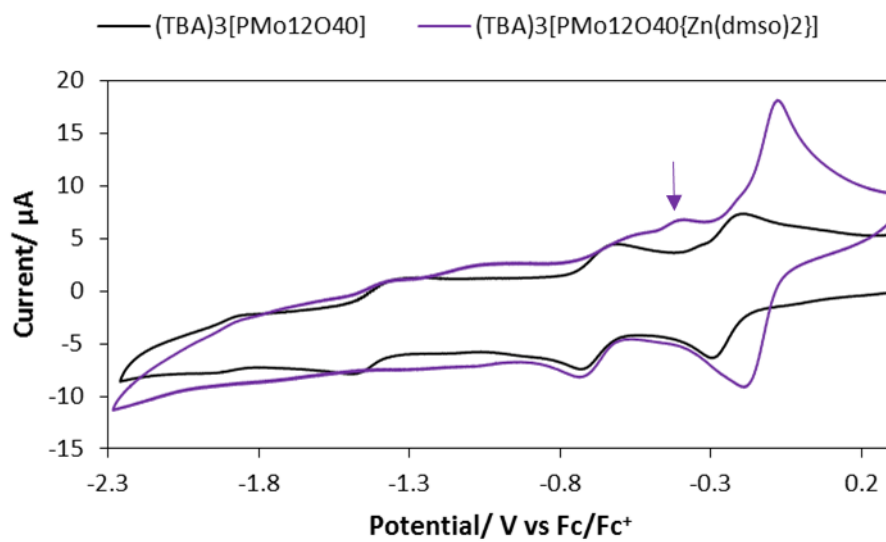


Figure 3.15 CV of 1 mM PMo_{12} (black line) and 1 mM PMo_{12}Zn (purple line) in 100 mM (TBA)(BF₄) MeCN, Ag wire RE, Pt CE, GC WE, from +0.6 V to -2.0 V vs Ag wire, 100 mV/s scan rate.

3.3 Discussion

The $^{31}\text{P}\{^1\text{H}\}$ NMR spectra of the species obtained when PMo₁₂ is reduced by six electrons is shown in Figure 3.16 and it shows that for the four different six-electron reduced species, the resonances in the NMR spectra have different chemical shifts. A dramatic shift of the chemical shift in the $^{31}\text{P}\{^1\text{H}\}$ NMR spectra of PMo₁₂ capped with paramagnetic Co^{II}, shows that the magnetic environment of P is influenced by the capping group, as seen by Errington *et al.*⁴

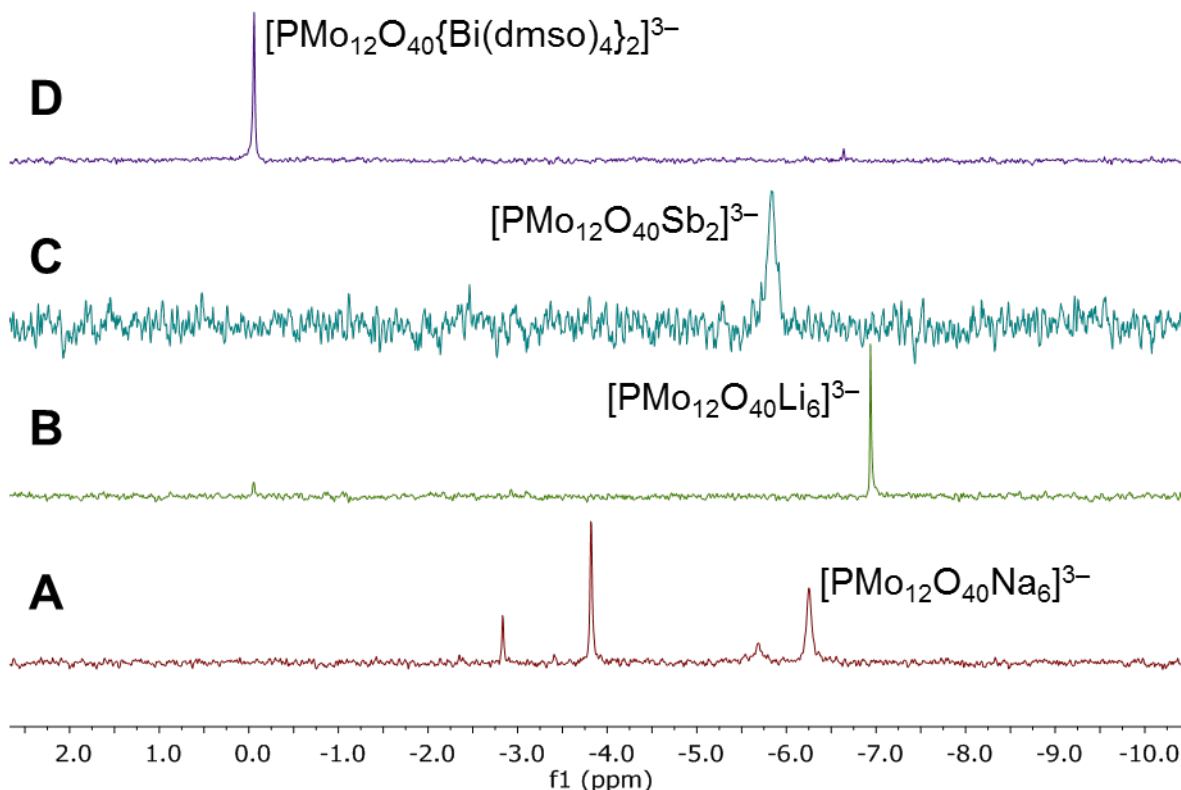


Figure 3.16 $^{31}\text{P}\{^1\text{H}\}$ NMR spectra of six-electron reduced species of PMo₁₂; (TBA)₃[PMo₁₂O₄₀Na₆] (A), (TBA)₃[PMo₁₂O₄₀Li₆] (B), PMo₁₂Sb₂ (C) and PMo₁₂Bi₂ (D).

The FTIR spectra for the solids obtained when PMo₁₂ is reduced by six electrons are shown in Figure 3.17 and it shows that the spectra obtained for (TBA)₃[PMo₁₂O₄₀Na₆] (PMo₁₂Na₆) and (TBA)₃[PMo₁₂O₄₀Li₆] (PMo₁₂Li₆) are quite similar whereas the spectra of PMo₁₂Sb₂ and PMo₁₂Bi₂ are different from the Na/Li species and from each other. The $\nu(\text{Mo-O}_\text{b}-\text{Mo})$ bands in the reduced capped species will be affected by the bonding of Sb or Bi. The spectrum of PMo₁₂Bi₂ is different from PMo₁₂Sb₂ due to overlap with bands from dmso. Computational calculations are required to rationalise the reasons for the differences.

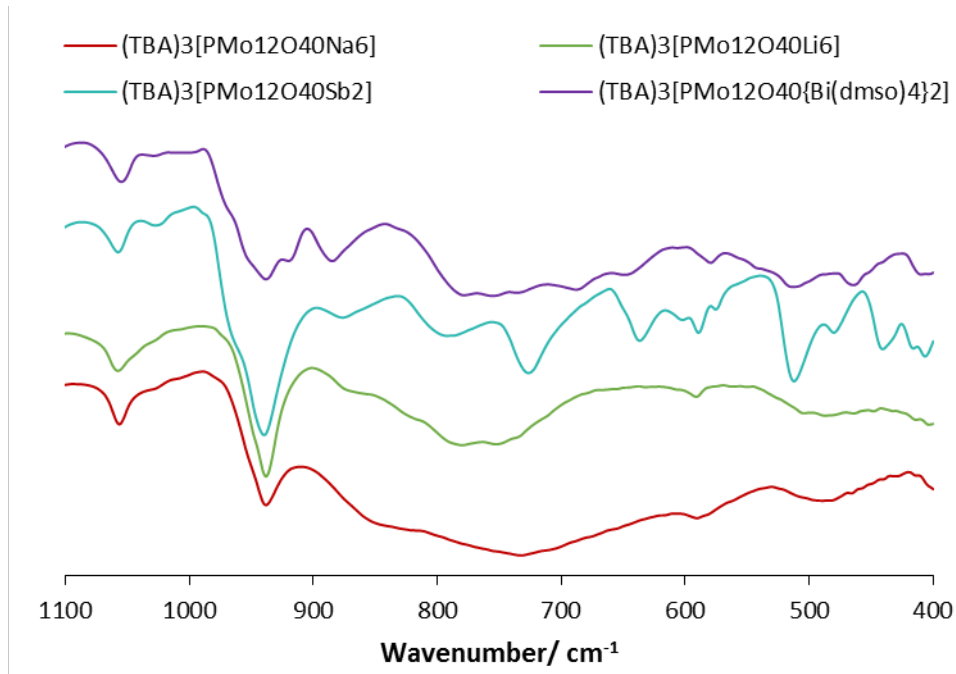


Figure 3.17 FTIR spectra of six-electron reduced species of PMo_{12} ; $\text{PMo}_{12}\text{Na}_6$ (red line), $\text{PMo}_{12}\text{Li}_6$ (green line), $\text{PMo}_{12}\text{Sb}_2$ (turquoise line) and $\text{PMo}_{12}\text{Bi}_2$ (purple line).

The CV of the six-electron reduced capped species; $\text{PMo}_{12}\text{Sb}_2$ and $\text{PMo}_{12}\text{Bi}_2$ are compared with $\text{PMo}_{12}\text{Li}_6$ in Figure 3.18. The redox waves in the CV of the reduced capped species are better defined than for $\text{PMo}_{12}\text{Li}_6$. The CV of $\text{PMo}_{12}\text{Bi}_2$ is significantly different, it contains a redox wave at a positive potential.

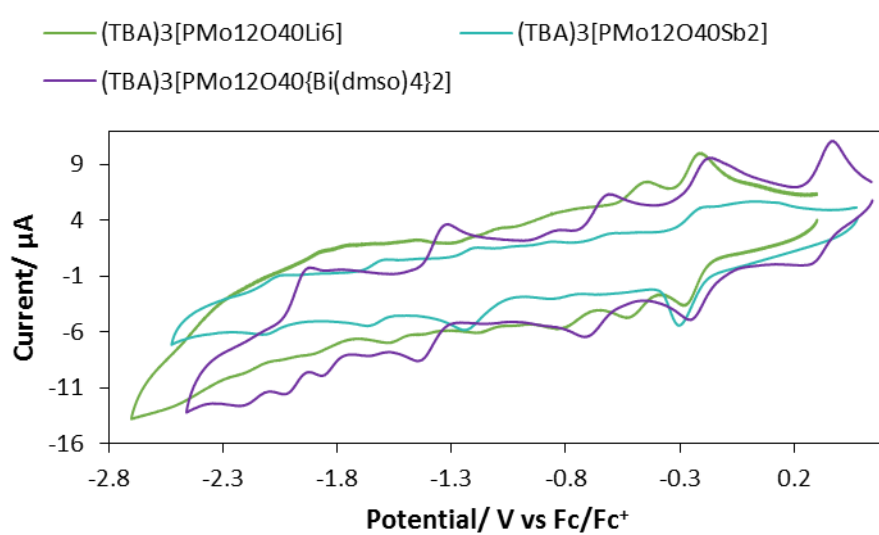


Figure 3.18 CV of six-electron reduced species of PMo_{12} , 1 mM solutions of the POMs in 100 mM (TBA)(BF₄) MeCN, Ag wire RE, Pt CE, GC WE, 100 mV/s scan rate, from +1.0 V to -2.0 V vs Ag wire; $\text{PMo}_{12}\text{Li}_6$ (green line), $\text{PMo}_{12}\text{Sb}_2$ (turquoise line) and $\text{PMo}_{12}\text{Bi}_2$ (purple line).

The $^{31}\text{P}\{^1\text{H}\}$ NMR spectra of two-electron reduced PMo₁₂ are shown in Figure 3.19, it compares the spectra of (TBA)₃[PMo₁₂O₄₀Na₂] (PMo₁₂Na₂), (TBA)₃[PMo₁₂O₄₀Li₂] (PMo₁₂Li₂) and PMo₁₂Zn and it shows that the resonances for each species are in very similar positions, between -6 and -8 ppm. A disordered crystal structure (Figure 3.20) determination for PMo₁₂Na₂ was obtained and although not of high quality, the structure showed that the Na⁺ interacts with the tetragonal sites in the solid state.

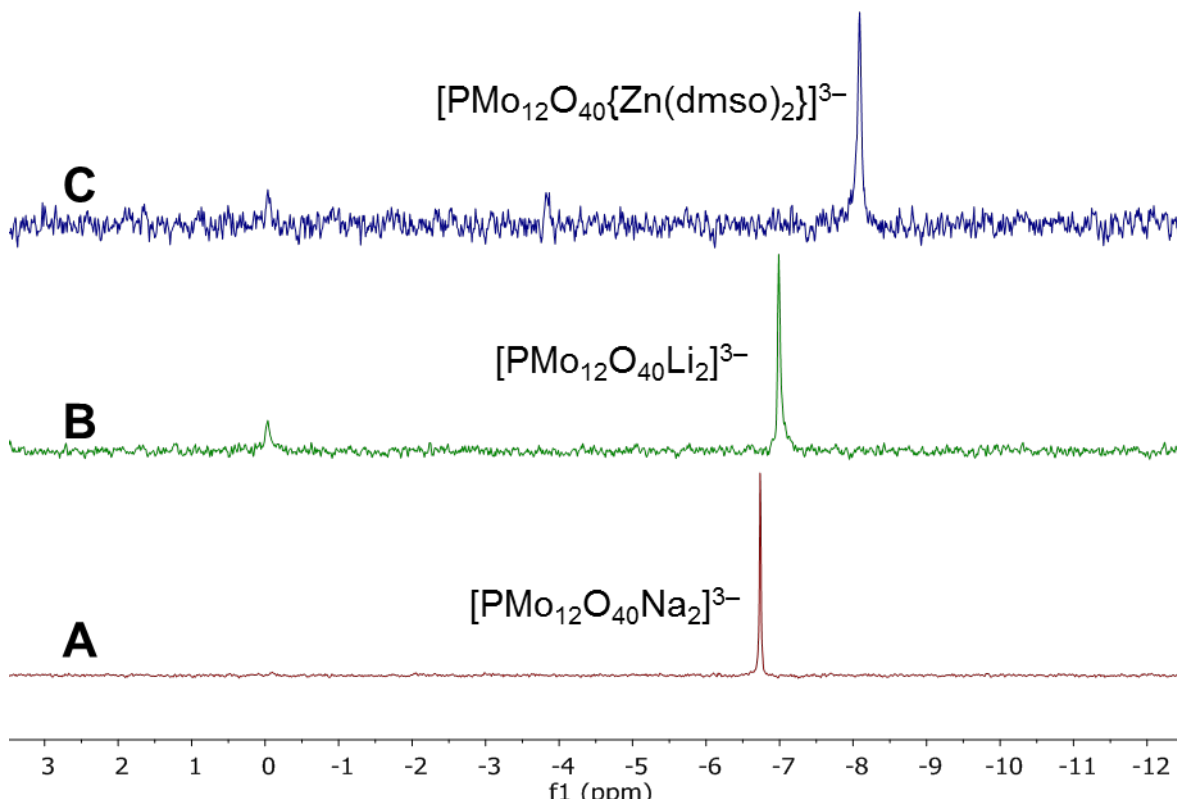


Figure 3.19 $^{31}\text{P}\{^1\text{H}\}$ NMR spectra of two-electron reduced PMo₁₂, PMo₁₂Na₂ (A), PMo₁₂Li₂ (B) and PMo₁₂Zn (C).

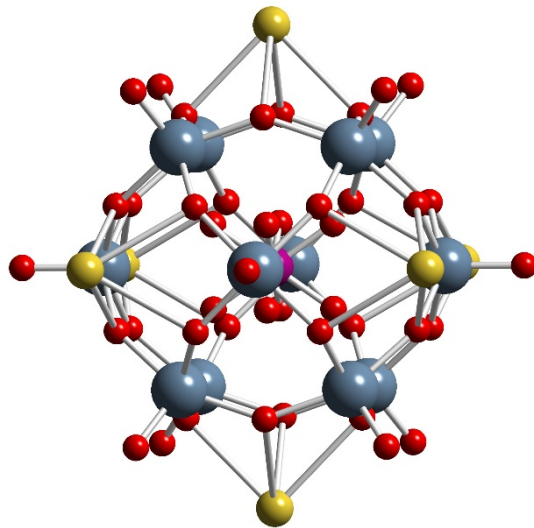


Figure 3.20 Ball-and-stick representation of the disordered anion, $[\text{PMo}_{12}\text{O}_{40}\text{Na}_2]^{3-}$.

The FTIR spectra of two-electron reduced PMo_{12} shown in Figure 3.21 are quite similar, except that the $\nu(\text{P}-\text{O})$ band for the species capped with Zn is split into two and is reduced in intensity. The $\nu(\text{Mo}-\text{O}_\text{b}-\text{Mo})$ bands in the spectrum of $\text{PMo}_{12}\text{Na}_2$ are the broadest, $\text{PMo}_{12}\text{Li}_2$ the $\nu(\text{Mo}-\text{O}_\text{b}-\text{Mo})$ bands are less broad and $\nu(\text{Mo}-\text{O}_\text{b}-\text{Mo})$ bands in the spectrum of PMo_{12}Zn are better defined.

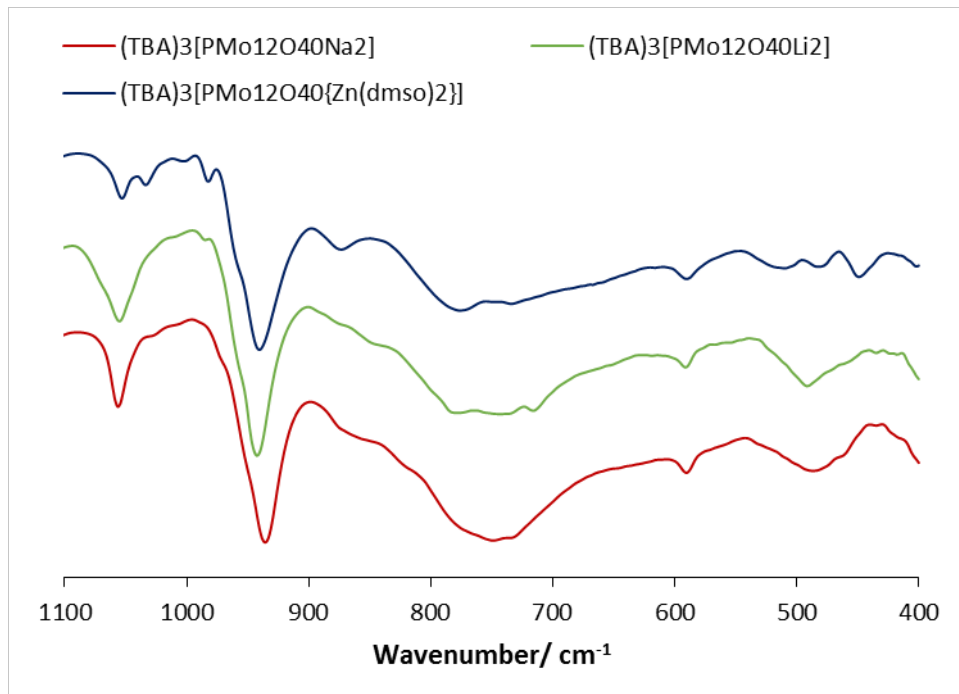


Figure 3.21 FTIR spectra of two-electron reduced PMo_{12} , $\text{PMo}_{12}\text{Na}_2$ (red line), $\text{PMo}_{12}\text{Li}_2$ (green line) and PMo_{12}Zn (blue line).

The cyclic voltammograms of $\text{PMo}_{12}\text{Li}_2$ and the two-electron reduced capped species PMo_{12}Zn are compared in Figure 3.22. The redox waves in the CV of the Zn

mono-capped species are less well defined than those for $PMo_{12}Li_2$. The first redox wave for $PMo_{12}Zn$ is much more intense and could be due to multiple electron transfers.

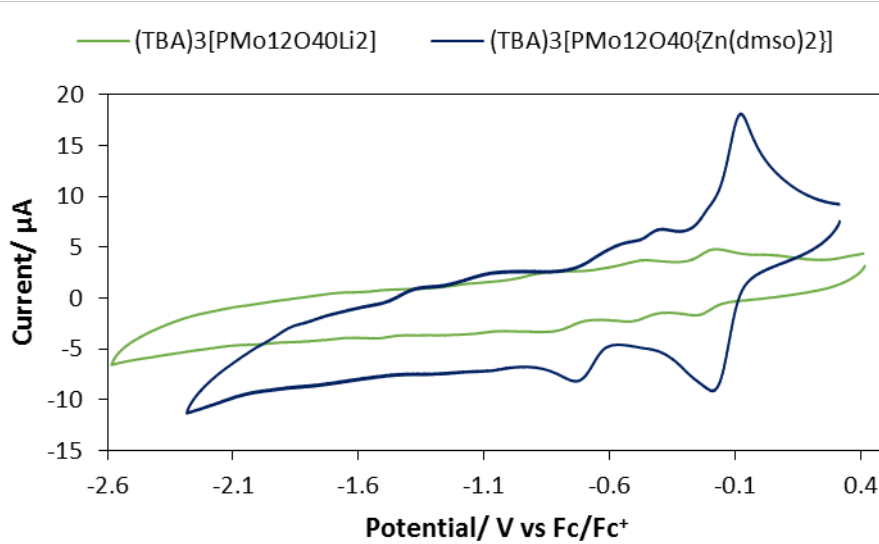


Figure 3.22 CV of two-electron reduced species of PMo_{12} , 1 mM solutions of the POMs in 100 mM $(TBA)(BF_4)^-$ MeCN, Ag wire RE, Pt CE, GC WE, 100 mV/s scan rate; $PMo_{12}Li_2$ (green line) from +1.0 V to -2.0 V vs Ag wire and $PMo_{12}Zn$ (blue line) from +0.6 V to -2.0 V vs Ag wire.

3.4 Conclusions

Di-capped $(TBA)_3[PMo_{12}O_{40}Sb_2]$ and $(TBA)_3[PMo_{12}O_{40}\{Bi(dmso)4\}_2]$ and mono-capped $(TBA)_3[PMo_{12}O_{40}\{Zn(dmso)2\}]$ have been successfully prepared and characterised by NMR, FTIR spectroscopy and CV. X-ray crystallography proves that the capping electrophiles all bond to tetragonal faces on the PMo_{12} structure. FTIR spectroscopy suggests that spin bipolarons are formed in all three capped reduced species due to the broadening of the $\nu(Mo-O_b-Mo)$ bands. The cyclic voltammograms of the reduced capped species are all different. The electron-transfer steps in the CV of $PMo_{12}Sb_2$ are negatively shifted in comparison to fully oxidised PMo_{12} which suggests it is harder to reduce the Sb-capped species. The electron-transfer steps in the CV of $PMo_{12}Bi_2$ are slightly positively shifted which suggests it is easier to reduce the Bi-capped species. The electron-transfer steps in the CV of $PMo_{12}Zn$ are at similar potentials to the fully oxidised PMo_{12} , however the first redox wave corresponds to a multi-electron process.

More work is required in order to understand why two crystal structures have been obtained in the attempted preparation of $(TBA)_3[PMo_{12}O_{40}Sb_2]$. The deliberate

oxidation of crystals of six-electron reduced $(TBA)_3[PMo_{12}O_{40}Sb_2]$ could be attempted to see if five-electron reduced $(TBA)_2[PMo_{12}O_{40}Sb_2]$ is obtained and the reaction monitored by NMR spectroscopy and X-ray crystallography.

Dielectric measurements of $(TBA)_3[PMo_{12}O_{40}\{Bi(dmsO)_4\}_2]$ and the aligned structure of $(TBA)_3[PMo_{12}O_{40}Sb_2]$ are being investigated by co-workers in Japan.⁸

Further characterisation of the capped compounds by solid-state NMR spectroscopy, UV-Vis spectroscopy, and elemental analysis is required.

To expand on this research, continued work with M^{2+}/M^{3+} ions is required, which should include Fe, Mg and Al. Further work to devise a preparation of di-capped $(TBA)_3[PMo_{12}O_{40}\{Zn(dmsO)_2\}_2]$, or establish an understanding as to why it does not form.

3.5 References

1. A. Dolbecq, E. Cadot, D. Eisner and F. Sécheresse, *Inorg. Chem.*, 1999, **38**, 4217.
2. Q. Chen and C. L. Hill, *Inorg. Chem.*, 1996, **35**, 2403.
3. Q.-B. Zhang, Y.-K. Lu, Y.-B. Liu, J. Lu, M.-H. Bi, J.-H. Yu, T.-G. Wang, J.-Q. Xu and J. Liu, *Inorg. Chem. Commun.*, 2006, **9**, 544.
4. R. Bakri, A. Booth, G. Harle, P. S. Middleton, C. Wills, W. Clegg, R. W. Harrington and R. J. Errington, *Chem. Commun.*, 2012, **48**, 2779.
5. I. D. Brown and D. Altermatt, *Acta Crystallogr. B*, 1985, **41**, 244.
6. N. E. Brese and M. O'Keeffe, *Acta Crystallogr. B*, 1991, **47**, 192.
7. M. Fournier, C. Rocchiccioli-Deltcheff and L. P. Kazansky, *Chem. Phys. Lett.*, 1994, **223**, 297.
8. I. Nakamura, R. Tsunashima, S. Nishihara, K. Inoue and T. Akutagawa, *Chem. Commun.*, 2017, **53**, 6824.

Chapter 4

Na₆V₁₀O₂₈ Containing Supercapacitor

Chapter 4. $\text{Na}_6\text{V}_{10}\text{O}_{28}$ Containing Supercapacitor

4.1 Background

The development of electrical energy storage devices is important due to the increasing requirement of environmentally friendly generation and storage of electrical energy, such as wind and solar power. The storage of electrical energy in a rechargeable battery, such as a Li-ion battery, is already used in commercial applications. Everyday items such as mobile phones and laptops use Li-ion battery technology. However, a significant improvement in performance is required for use in applications which require storage of larger amounts of energy, such as hybrid electric vehicles.¹ The development of supercapacitor (SC) technology is a growing research area with many applications. SCs can be used as back-up energy sources for clocks and toys. They can also be used as uninterrupted power supply during a power cut to bridge the gap between the power cut and the back-up generator coming in to play, especially in hospitals and banks to maintain crucial services. Wider applications of batteries and SCs will require great improvements in their energy and power densities and the components of these electrical energy storage devices must be optimised.² The use of batteries and SCs alongside each other could also address this issue, as batteries can supply high energy density while SCs provide high power density.

4.1.1 Electrical Energy Storage Devices

The performance of electrical energy storage devices is measured by the energy and power released upon discharge.³ Electrical energy (E) is measured by integrating current (I) and voltage (V) over time and is conventionally reported in terms of Watt-hours. Power (P), the rate at which energy is released, is therefore reported in Watts. Since all real devices have internal resistance (R) the voltage measured for a device depends on the current flowing such that $V = V_0 - IR$, where V_0 is the potential measured when $I = 0$. Here, R includes both internal and other resistances in the circuit. Both energy and power are scaled to device size, usually by mass in kilograms, where mass is either the mass of the entire device or the mass of the energy-storing materials involved. The latter convention is followed in this thesis.

The relative performance for four major types of electrical energy storage devices are shown in Figure 4.1, a simplified Ragone plot.⁴ Three devices are relevant to the

present thesis: capacitors, batteries and SCs. Of these three, batteries offer the best performance in terms of (gravimetric) energy density but the worst in terms of (gravimetric) power density; the opposite is true for capacitors. SCs offer a compromise between the two.

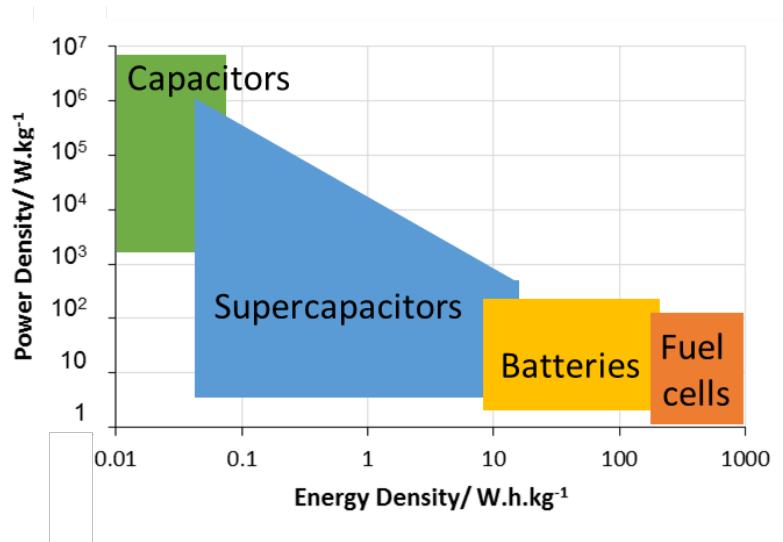


Figure 4.1 Schematic Ragone plot of electrical energy storage devices.⁴

There is some confusion in the literature between batteries and SCs with regards to how data is reported, whether as capacity or capacitance as discussed by Simon *et al.*⁵ Figure 4.2 compares the different mechanisms of energy storage and the electrochemical properties to help distinguish between the different forms of energy storage devices.⁵ Usually batteries are described by their capacity in terms of ampere hours and SCs are described by their capacitance in terms of farads. However, the confusion begins when SCs display similar electrochemical characteristics as batteries for example the galvanostatic discharge curve is non-linear similar to the red line in Figure 4.2H. The shape of the CV and galvanostatic charge-discharge curve should be taken into consideration before labelling a material capacitive or battery-like. Polyoxometalate-containing SCs published in the literature judge the performance by calculating capacitance in terms of farads.⁶

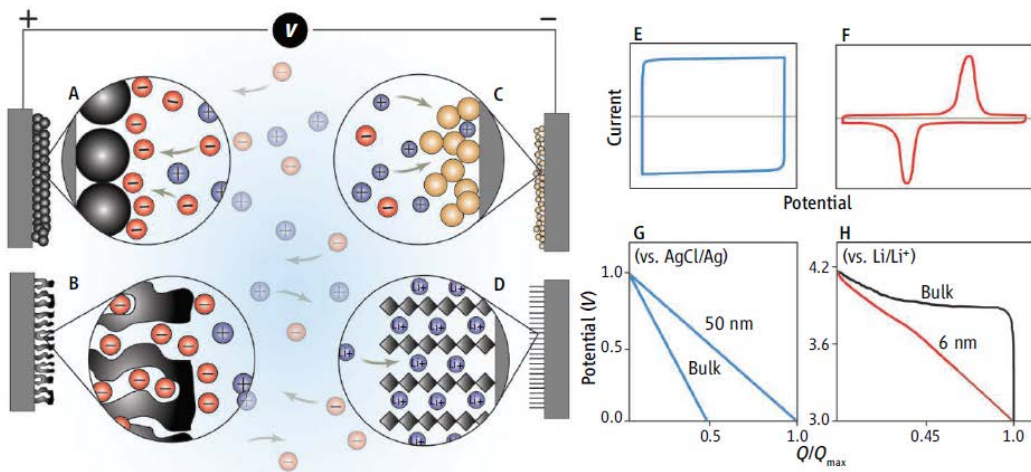


Figure 4.2 The different mechanisms of capacitive energy storage; double-layer capacitance develops at electrodes comprising carbon particles (A) or porous carbon (B). The double layer shown here arises from adsorption of negative ions from the electrolyte on the positively charged electrode. Pseudocapacitive mechanisms include redox pseudocapacitance (C) as occurs in hydrous RuO_2 , and intercalation pseudocapacitance (D) where Li^+ ions are inserted into the host material. Electrochemical characteristics distinguish capacitor and battery materials. CV distinguishes a capacitor material where the response to a linear change in potential is a constant current (E), as compared to a battery material, which exhibits faradaic redox peaks (F). Galvanostatic discharge behaviour (where Q is charge) for a MnO_2 pseudocapacitor is linear for both bulk and nanoscale material (G), but a LiCoO_2 nanoscale material exhibits a linear response while the bulk material shows a voltage plateau (H). After ref ⁵.

4.1.1.1 Capacitors

In capacitors, charge is stored electrostatically on the surface of metal electrodes as illustrated in Figure 4.3 for a parallel plate capacitor. Here, the charge built up on the electrodes is stabilised by opposing charge accumulated on the surface of the dielectric through polarisation. Capacitors are characterised by high power since dielectrics can discharge very rapidly. Their energy density is low, however, because charge is restricted to the surface of the electrodes and dielectric.

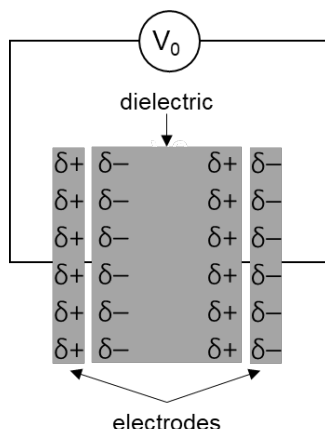


Figure 4.3 Diagram of a charged parallel plate capacitor.

In capacitors, the amount of charge stored is proportional to the potential applied, that is, $Q = CV$ where C is the capacitance.⁷ As a result, the current flowing upon discharge of a capacitor, $I = \frac{dQ}{dt}$, is therefore $C\frac{dV}{dt}$. The energy released, obtained by integrating $V.C\frac{dV}{dt}$ over time is therefore $\frac{1}{2}CV^2$ or $\frac{1}{2}QV$.

4.1.1.2 Batteries

In batteries, electrical energy is stored faradaically, that is by oxidation-reduction reactions (electron transfer). A typical battery is shown in Figure 4.4, where discharge involves reduction of the LiCoO_2 cathode and oxidation of the lithiated graphite electrode. The separator serves to prevent an electric short-circuit between the electrodes yet allow flow of ions in the electrolyte between the cathode and the anode. Since the redox reaction involves phase changes, the potential (V_0) between the electrodes is independent of charge (Q) in the battery's operating potential window, and the maximum possible energy released upon discharge is V_0Q_0 , assuming no internal resistance.⁸ Here, Q_0 is the capacity of the battery, the amount of charge stored before discharge. Since charge is stored in the bulk of battery electrodes, not just the surface, Q_0 is relatively high, leading to high energy density. Power is low relative to capacitors, however, since discharge involves relatively slow charge transfer, both ion diffusion in the electrolyte as well as ion and electron diffusion in the electrodes. In battery research the gravimetric specific capacity of a battery has the units mA.h.g^{-1} .

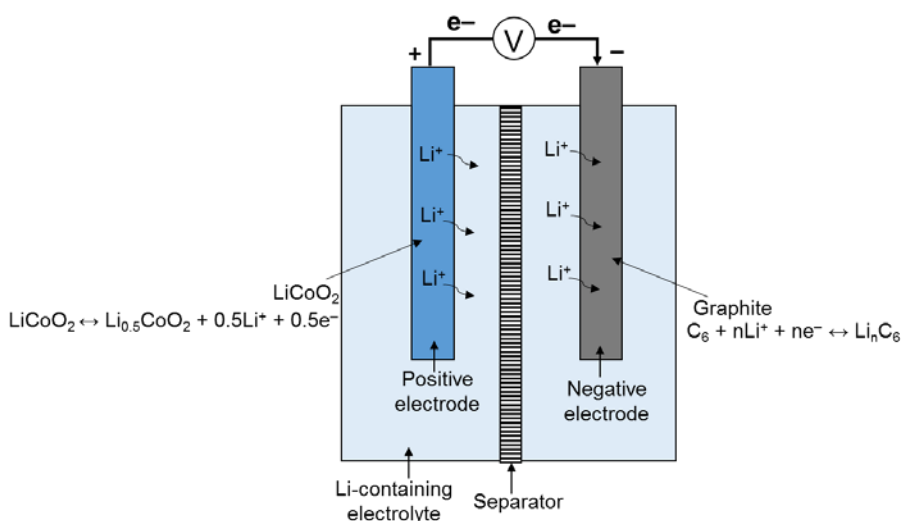


Figure 4.4 Diagram showing a LiCoO_2 /Graphite Li-ion battery during charging.⁹

4.1.1.3 Supercapacitors (SCs)

SCs are also known as ultracapacitors or electrochemical capacitors. They are classified as capacitive devices since like capacitors their potential is a linear or approximately linear function of stored charge.⁸ Unlike capacitors, however, charge storage involves charge transfer, not only polarisation. Three types of capacitor have been developed: electrical double layer capacitors, pseudocapacitors, and hybrid SCs. Typically in the case of SCs the performance is calculated from specific capacitance, which has the units F.g⁻¹.

4.1.1.3A Electrical Double Layer Capacitors (EDLCs)

An EDLC is illustrated schematically in Figure 4.5.¹⁰ Here, conducting electrodes are immersed in an electrolyte and a separator is provided to prevent electric short-cuts. Charge is stored at the surface of the electrodes in the form of electrical double layers at the electrode surfaces: charge storage is electrostatic, not faradaic. Large amounts of charge can be stored because the double layer is not restricted to the electrode surfaces and the electrodes can have high surface areas. As a result they can store more charge than capacitors but less charge than batteries since charge is not stored in the bulk of the electrodes, so their energy content is intermediate between capacitors and batteries. In a similar fashion, their power is intermediate between capacitors because discharge involves charge transfer, but charge transfer only through the electrolyte, not through the bulk of the electrodes.

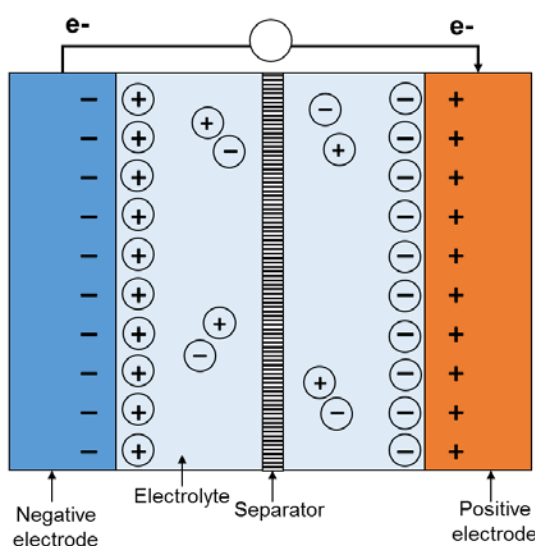


Figure 4.5 Diagram illustrating an EDLC during charging.¹⁰

4.1.1.3B Pseudocapacitors

Pseudocapacitors are defined here as SCs where charge in both electrodes is stored faradaically, as in batteries, but charge storage is restricted to redox sites at or near electrode surfaces.¹¹ Charge transfer is therefore relatively rapid since ion and electron diffusion occurs over only very short distances. This can be achieved by using extremely porous electrode materials like amorphous ruthenium dioxide hydrates which have very high surface area or using nanoparticle electrodes having very high surface to volume ratios. In both cases, capacitive behaviour has been observed.^{9, 11}

4.1.1.3C Asymmetric Supercapacitors

Asymmetric SCs or hybrid SCs utilise one electrostatic and one faradaic electrode.¹² Examples include lithium ion capacitors,¹³ which use (faradaic) lithiated graphite anodes and (electrostatic) activated carbon cathodes, and activated carbon/ MnO_2 SCs.¹⁴ Asymmetric SCs can combine the advantages of electrostatic and faradaic devices.

The distinction between symmetric and asymmetric SCs may be understood by representing the device capacitance (C) as an anode capacitance (C_a) and a cathode capacitance (C_c) in series: $\frac{1}{C} = \frac{1}{C_a} + \frac{1}{C_c}$.¹⁵ Since, $C = \frac{Q}{V}$ in a capacitive electrode; $\frac{V}{Q} = \frac{V_a}{Q_a} + \frac{V_c}{Q_c}$ and since $Q = Q_a = Q_c$, the voltage window of the asymmetric capacitor is the sum of the two electrode voltage windows. Since $E \sim CV^2$, energy density is enhanced. A good example of this effect is illustrated in Figure 4.6, where the voltage windows for a symmetric and an asymmetric device are compared.¹⁶

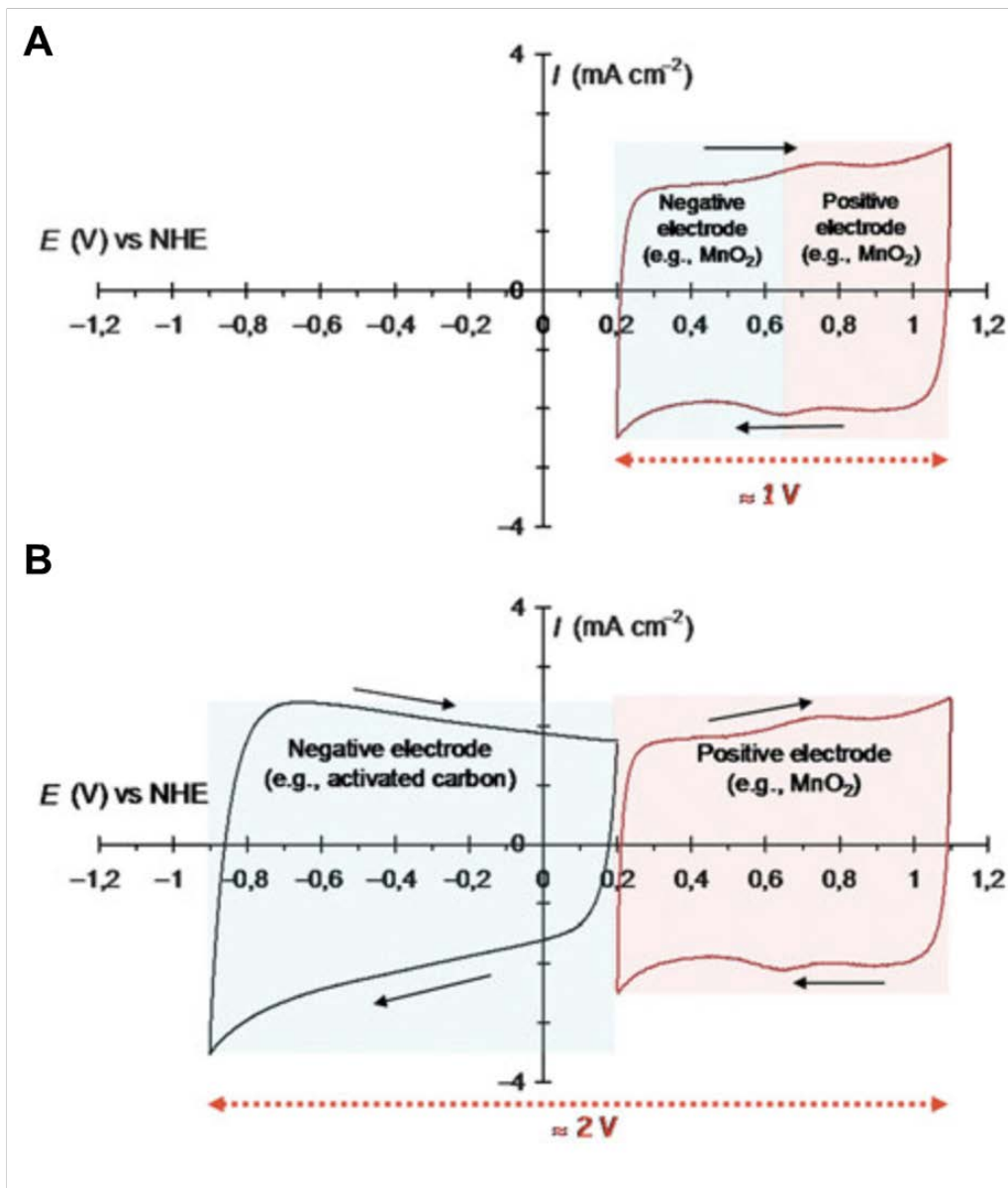


Figure 4.6 Schematic representation of the cyclic voltammograms for two different configurations of aqueous-based SCs for; a symmetric SC $\text{MnO}_2/\text{MnO}_2$ electrodes in $0.5 \text{ M K}_2\text{SO}_4$ (A) and asymmetric SC AC/ MnO_2 electrodes in $0.5 \text{ M K}_2\text{SO}_4$ (B); showing the expanded voltage window obtained in the asymmetric case. After ref ¹⁶.

4.1.1.4 Lifetime of Electrical Energy Storage Devices

The above paragraphs have focused on the energy and power ratings of electrical energy storage devices as the key figures of merit. Equally important, however, is device lifetime: devices whose energy and power ratings degrades upon repeated charge-discharge cycling are of limited practical importance. Lifetime can in principle be tested in real time, but given the long time-spans involved, this is unviable.¹⁷

Alternative methods have therefore been proposed for estimating lifetime.

The simplest method is evaluation of coulombic efficiency (CE), also known as faradaic efficiency.^{17, 18} This is the ratio of charge released upon discharge to the charge delivered during the previous charging. Since irreversible processes lead to reductions of CE below 100%, low CE implies low lifetime. However, since viable devices may require thousands of charge-discharge cycles, high CE does not guarantee long lifetime.

4.1.1.5 Solid State Polyoxometalate Electrical Energy Storage Devices

Solid state electrochemistry of POMs was first reported for silicotungstic acid ($\text{H}_4\text{SiW}_{12}\text{O}_{40}$) in 1991,¹⁹ and many publications on this topic have appeared since then. The first incorporation of POMs in electrical energy storage devices was reported in 1998,⁶ with the fabrication of a hybrid ruthenium oxide/ phosphomolybdic acid ($\text{H}_3\text{PMo}_{12}\text{O}_{40}$) SC. Subsequently, numerous reports describing battery and SC applications have been published, and reports relevant to the present study are summarised in Section 4.5 for purposes of comparison.

4.2 Material and Methods

4.2.1 Characterisation Methods of $\text{Na}_6\text{V}_{10}\text{O}_{28} \cdot n\text{H}_2\text{O}$

The polyoxovanadate, $\text{Na}_6\text{V}_{10}\text{O}_{28} \cdot n\text{H}_2\text{O}$ (V_{10}) used in this study has been thoroughly characterised using several different techniques. These techniques have included nuclear magnetic resonance (NMR) spectroscopy, Fourier-transform infrared (FTIR) spectroscopy, powder X-ray diffraction (PXRD), scanning electron microscopy (SEM), thermogravimetric analysis (TGA) and solution electrochemistry. The techniques are complementary to each other and help to confidently assign what has been prepared.

4.2.1.1 Nuclear Magnetic Resonance Spectroscopy

Nuclear magnetic resonance (NMR) spectroscopy is a fundamental technique that can be used to identify POMs containing spin-active nuclei and establish purity.²⁰ POMs have characteristic peaks in their NMR spectrum, which can make them easily identifiable. To identify V_{10} , $^{51}\text{V}\{^1\text{H}\}$ NMR is recorded.²⁰

4.2.1.2 Fourier-transform Infrared Spectroscopy

Absorptions in Fourier-transform infrared (FTIR) spectroscopy occur when the frequency of the IR radiation resonates with a molecular bond vibration in the species, notably if the molecular dipole moment is affected by the excitation of the

molecular bond vibration. Bands in FTIR relevant to POMs appear in the region 1000-400 cm⁻¹ due to metal-oxygen vibrations. The fingerprint region is unique to each POM.²¹

4.2.1.3 Powder X-Ray Diffraction

Powder X-Ray diffraction (PXRD) patterns are unique to the crystal structure of a material.²² PXRD provides information on the lattice parameters and lattice type as well as phase identification.²²

4.2.1.4 Scanning Electron Microscopy

Scanning electron microscopy (SEM) is a technique that allows the morphology of a sample to be identified and an idea of the size of crystallites in a sample.²³ SEM was an important technique used in this project to assess the effects of powder processing on the size of V₁₀ crystallites.

4.2.1.5 Thermogravimetric Analysis

Thermogravimetric analysis (TGA) is a technique that measures mass changes of a sample upon heating from water loss and/or decomposition. The sample is placed in a crucible on a microbalance in an enclosed furnace and the temperature is increased at a rate of 10 °C per minute up to a certain temperature, under a flow of nitrogen and the changing mass of the sample is recorded.²⁴ The change in mass means that the degree of hydration can be determined.

4.2.1.6 Solution Electrochemistry

Cyclic voltammetry (CV) is an electrochemical technique, where at a pre-determined scan rate the potential of the working electrode (WE) is swept between two potentials, P1 and P2, and then the direction is reversed. The current response is recorded.²⁵ CV can be used to electrochemically characterise POMs in both aqueous and non-aqueous solutions. The number and the potential of redox waves in the CV tend to be characteristic to each POM.²⁶

4.2.2 Processing of V₁₀

4.2.2.1 Sonoprecipitation

The use of a sonication probe during the addition of a solution to an anti-solvent has been seen to produce smaller crystals.²⁷ Figure 4.7A shows a sonication probe in a test tube containing V₁₀ solution. Figure 4.7B shows the complete experimental set

up for sonoprecipitation where an aqueous V_{10} solution is added to a sonicated anti-solvent from a syringe.

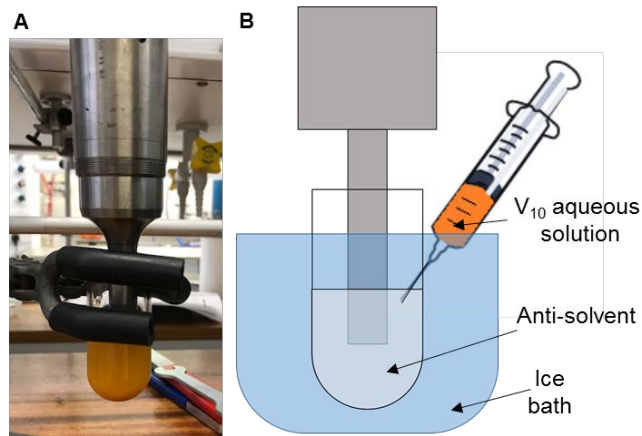


Figure 4.7 Photo of sonication probe in a test tube containing 50 mg V_{10} and 10 mL of anti-solvent (A), and a schematic showing the complete experimental set up for sonoprecipitaion (B).

4.2.2.2 Grinding

The V_{10} solid was ground using a pestle and mortar after drying in an oven at 80 °C overnight (o/n) to remove anti-solvent and water, in order to decrease the size of the particles and homogenise the sample.

4.2.2.3 Sonofragmentation

Figure 4.8 shows the set up for sonofragmentation, whereby V_{10} was suspended in anti-solvent and then sonicated in attempts to break larger crystallites into smaller ones. The literature contains various examples of sonication being used for this purpose.^{28, 29, 30}

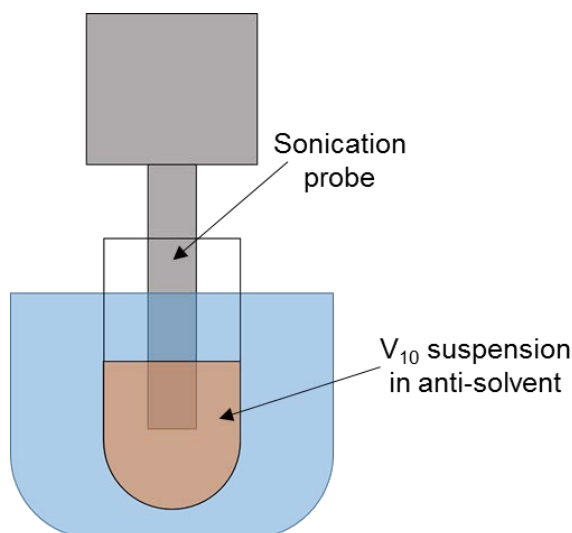


Figure 4.8 A schematic showing the set up for sonofragmentation.

4.2.2.4 Ball Mill

A ball mill was constructed from a plastic test tube, two 5 mm stainless steel ball bearings and a vortex mixer as shown in Figure 4.9.³¹ The ball mill was used to mechanically break up the V₁₀ crystallites.

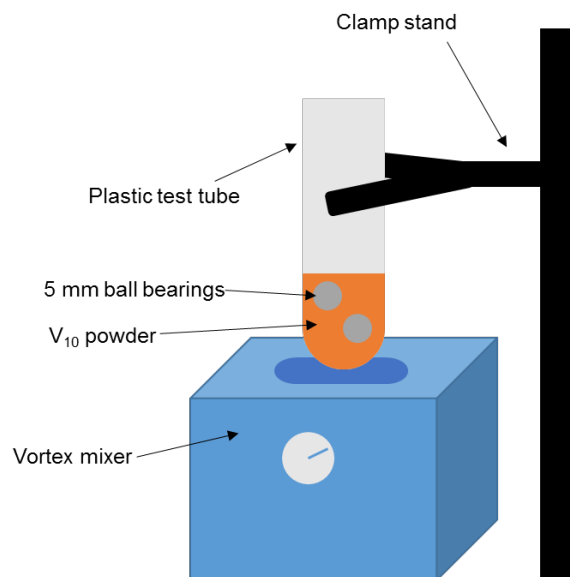


Figure 4.9 A schematic showing the ball mill set up using a vortex mixer, test tube and ball bearings.

4.2.2.5 HEBM

A high energy ball mill, HEBM (Retsch E_{max}) was then used to see if the higher energy and longer milling time would produce smaller particles.³² The HEBM used rotated jars containing V₁₀ at a speed of 2000 rpm with cooling to prevent overheating. The use of a HEBM was expected to dramatically reduce particle size and increase the homogeneity of the sample.

4.2.3 Preparation of Electrodes

The standard protocol for V₁₀ containing electrode preparation is shown in Figure 4.10.³³ V₁₀ was dried o/n at 80 °C and ground using a pestle and mortar for 15 mins (followed by further powder processing for several series) and then ground together with carbon using a pestle and mortar for 15 mins. The homogeneous powder was then transferred into a vial, PVDF and NMP (ca. 3 mL) added to make a slurry, and the slurry was then stirred o/n. The weight percentage composition of the slurry was: V₁₀ 75%, super P 15% and PVDF 10%. For activated carbon (AC) electrodes, the weight percentage composition of the slurry was: AC 88% and PVDF 12%. The AC was first ground using a pestle and mortar for 15 mins and then combined in a vial with NMP and PVDF and stirred o/n. The slurry was then coated using a spatula on

to an $1 \times 1 \text{ cm}^2$ area of a $3 \times 1 \text{ cm}^2$ pre-weighed current collector for three-electrode testing or on to an 18 mm diameter (area of 2.54 cm^2) pre-weighed disk for two-electrode testing, the electrodes were then dried in an oven set to 80°C o/n.

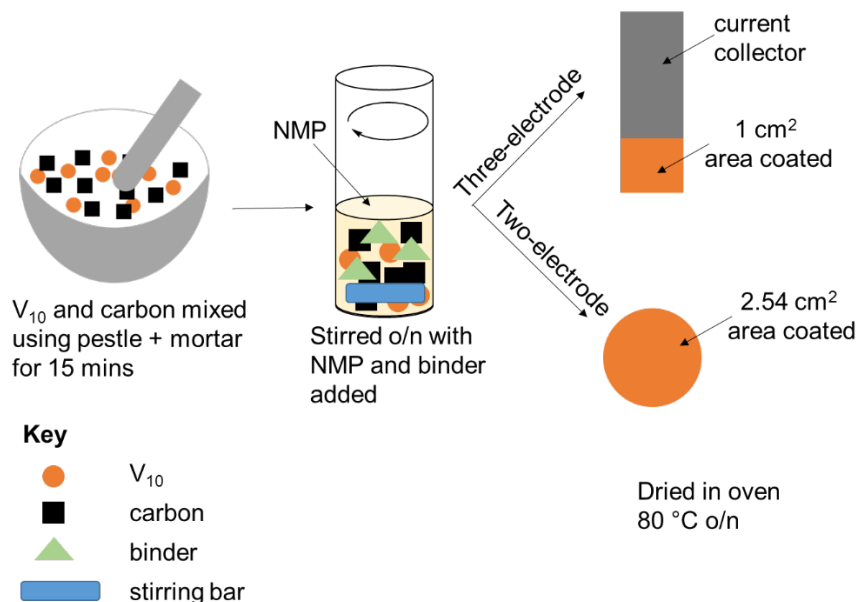


Figure 4.10 Schematic of slurry and electrode preparation.

The different components of the slurry are all important in their own way and all have different purposes. The slurry is coated on to the current collector and it is important that there is good contact between them, as the current collector transfers current from the potentiostat to the electrode materials. The current collector is connected to the potentiostat using a crocodile clip. The V_{10} in the slurry is an insulator therefore conductive carbon is essential as it acts as a pathway for the electrons through the sample.^{6, 34} The carbon additive also helps to reduce internal resistance.¹⁰ The binder holds together the active material and carbon in the slurry and binds the slurry to the current collector, it also prevents the degradation of the electrode.³⁵ The solvent is added to make a smooth homogeneous slurry, it needs to disperse the carbon well, dissolve the binder and not the active material and evaporate upon drying of the electrodes.

The amount of V_{10} coated on to an electrode was calculated by weighing the blank electrode and then the coated electrode after drying o/n and calculating the difference. This mass is then multiplied by the fraction of V_{10} in the slurry (0.75); assuming all NMP has evaporated. An electrode that is coated with 1.4 mg of slurry

contains 1.1 mg V₁₀. The amount of AC on an electrode was calculated using the relevant weight percent ratio of AC in the slurry used.

4.2.4 Electrochemical Characterisation of Electrodes

Electrochemical characterisation of V₁₀ electrodes has been investigated using both a three-electrode and a two-electrode system.

4.2.4.1 Three-electrode Set Up

The set up for three-electrode experiments is shown in Figure 4.11. The cell consists of a Pt counter electrode (CE), Ag/AgNO₃ non-aqueous reference electrode (RE) and the V₁₀ containing working electrode (WE) with a nitrogen bubbler and 1 M LiClO₄ in propylene carbonate (PC) electrolyte solution. The WE and CE are attached to the potentiostat connectors using smaller crocodile clips. The cell is degassed using N₂ for 10 mins before each measurement.

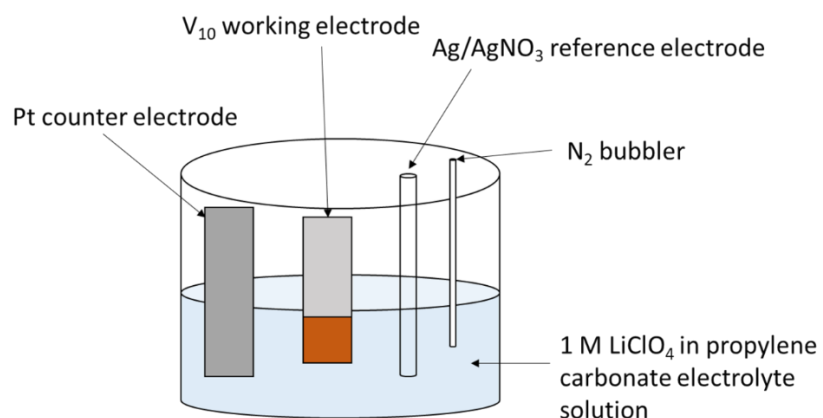


Figure 4.11 Three-electrode experiment set up.

CV and chronopotentiometry (CP) can be explored in a three-electrode set up. CV has been described previously in Section 4.2.1.6 for POMs in solutions, in this case we are investigating the solid-state properties of the POM on the electrode, but the principles are the same, an example is shown in Figure 4.12.³⁶

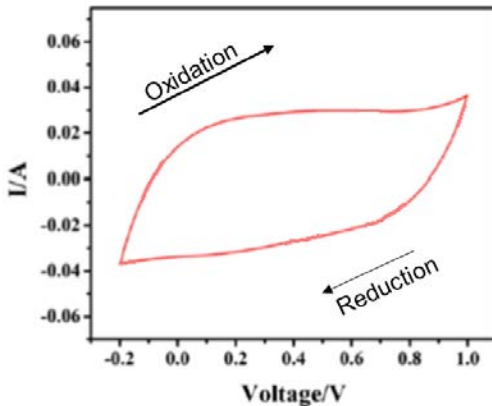


Figure 4.12 Three-electrode CV experiment; 100 mV.s^{-1} scan rate, $1 \text{ M H}_2\text{SO}_4$ electrolyte, SCE RE, Pt wire CE, AC WE (electrical double layer), with the oxidation and reduction direction labelled. After ref³⁶.

C_{sp} in F.g^{-1} can be calculated from the CV curves by using Equation 4.1. Figure 4.12 is a plot of a CV, the CV has been plotted differently to the CV in Figure 4.13.³⁷ In Figure 4.13 the CV is the blue line plotted with time on the x-axis and measured current on y2-axis, the black line is a potential profile with applied potential plotted on the y1-axis. The CV is plotted this way to make integrating under the reduction curve easier, as shown by the shaded area, to get the total charge from under the second reduction curve and are plugged in to Equation 4.1, where $\int i \Delta t$ is the integration under the reduction curve (A.s), ΔU is voltage range (V), m is mass of V_{10} (g) and Q is charge (C).³⁷

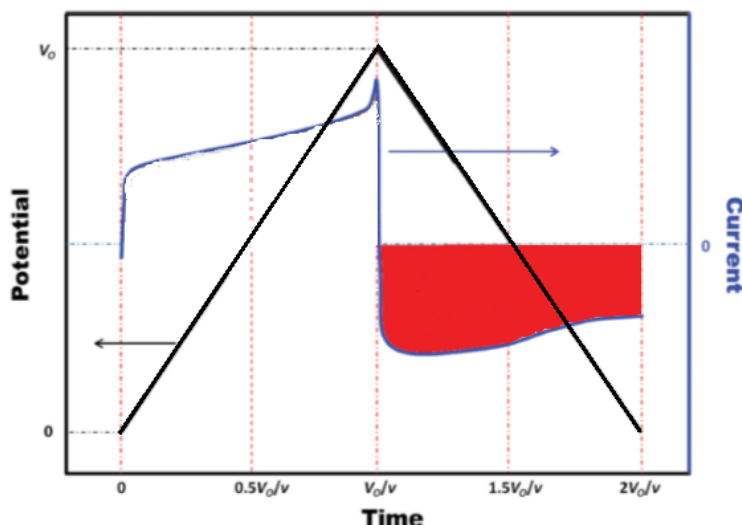


Figure 4.13 Schematic diagram showing a CV and potential profile for how the area under a CV is integrated to substitute into Equation 4.1. After ref³⁷.

$$C_{sp} = \frac{\int i \Delta t}{\Delta U \times m} = \frac{Q}{\Delta U \times m} \quad (4.1)$$

The value for Q calculated from Equation 4.1 can also be substituted into Equation 4.2 in order to calculate the ratio of moles of electrons to moles of V_{10} on the electrode, where Q is charge (C) and F is the Faraday constant.

$$\text{Ratio of moles of electrons to moles of } V_{10} = \frac{Q}{F} \div \frac{\text{mass } V_{10}}{\text{MW } V_{10}} \quad (4.2)$$

CP can also be used to calculate the three parameters mentioned above in a three-electrode system. CP from a three-electrode set up is shown in Figure 4.14. CP is where a constant current is applied to the WE and the change in potential is recorded over time. 2 IR is labelled on the CP, where IR is the potential drop due to Ohmic resistance in the electrode and the electrolyte. The reason the IR drop is equal to 2 IR is that there is a drop in the measured potential (in the positive direction) with regards to the oxidation and a drop in the measured potential (in the negative direction) with regards to the reduction curve. The IR drop can be seen clearer in a dwell period experiment which will be shown later.

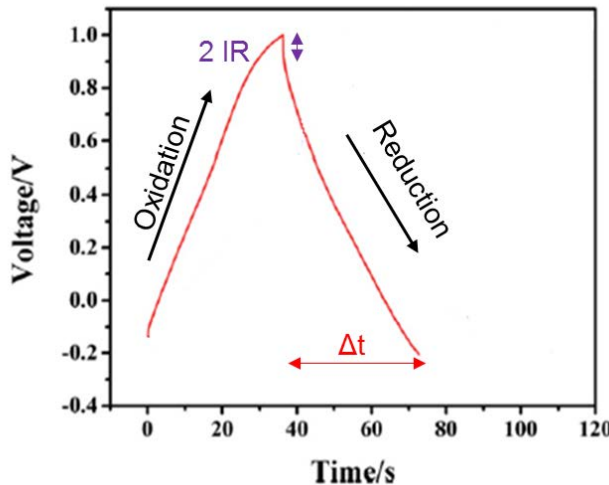


Figure 4.14 Three-electrode CP experiment at 6 A.g^{-1} current density, $1 \text{ M H}_2\text{SO}_4$ electrolyte, SCE RE, Pt wire CE, AC WE, oxidation and reduction curves and IR drop labelled. After ref ³⁶.

C_{sp} can be calculated for CP using Equation 4.3 where i is the applied current (A), Δt is the time taken for the reduction for the third cycle (s), ΔU is the potential range (V) and m is mass of V_{10} on the electrode (g).

$$C_{sp} = \frac{i \times \Delta t}{\Delta U \times m} \quad (4.3)$$

A CP dwell period experiment is shown in Figure 4.15.³⁸ The SC tested was a symmetrical carbon-based SC. The dwell period experiment was carried out in order to see the IR drop. The IR drop can be seen before and after the current is switched off and then back on again, this is indicated in Figure 4.15 using double headed arrows.

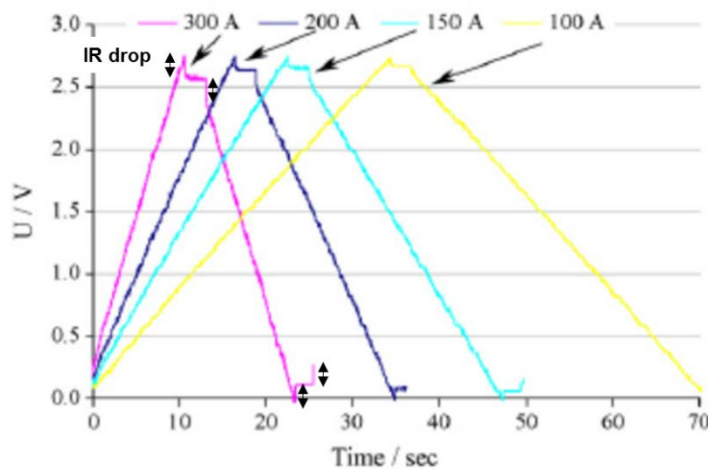


Figure 4.15 Diagram illustrating a CP dwell period experiment, IR drops indicated by double headed arrows. After ref³⁸.

The CP dwell period experiment shown in Figure 4.15 are results for two-electrode experiments and the experiments undertaken in this study were measured on a three-electrode set up but the diagram is still valid.

4.2.4.2 Two-electrode Set Up

A full SC device is tested using a two-electrode set up. The experimental set up for an asymmetric SC is shown in Figure 4.16. The cell contains an anode and a cathode (both 2.54 cm² discs); which are different for an asymmetric device; with an electrolyte-soaked glass fibre separator in between and these are housed within an ECC-Std manufactured by EL-cell as shown in Figure 4.17. In the case of this study, the asymmetric SC contains a POM containing electrode and an AC electrode.

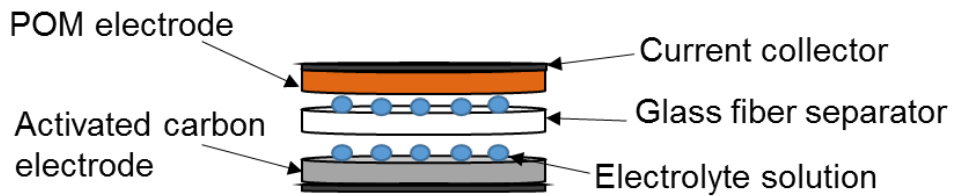


Figure 4.16 Schematic showing the two-electrode set up for an asymmetric supercapacitor.



Figure 4.17 Photo of an EL-Cell.

For a two-electrode system CV and Galvanostatic constant current charge-discharge (GCD) curves are measured. GCD is the charging and discharging of the cell at a constant current, where charging involves the movement of electrons away from cathode and towards the anode and discharging involves the opposite scenario.³⁹

The experimental capacitance (C_{exptl}) of a SC device can be calculated from CV using Equation 4.4, integrating under the discharge curve. This equation is identical to the calculation of capacitance for a three-electrode system. C_{exptl} refers to the capacitance of the two electrodes in series in the full device as explained in Equation 4.5, where C_1 and C_2 are the capacitance of electrodes 1 and 2. To calculate C_{sp} of one electrode, the value for C_{exptl} is plugged in to Equation 4.6, where m is the mass of active material on one electrode.

$$C_{\text{exptl}} = \frac{\int i \Delta t}{\Delta U} \quad (4.4)$$

$$\frac{1}{C_{\text{exptl}}} = \frac{1}{C_1} + \frac{1}{C_2}, \text{ where } C_1 = C_2 = C, \text{ therefore } \frac{1}{C_{\text{exptl}}} = \frac{2}{C}, C = 2C_{\text{exptl}} \quad (4.5)$$

$$C_{sp} = \frac{2C_{exptl}}{m} \quad (4.6)$$

C_{exptl} for GCD is calculated using Equation 4.7, which is then substituted in to Equation 4.6 to calculate C_{sp} .

$$C_{exptl} = \frac{i \times \Delta t}{\Delta U} \quad (4.7)$$

For an asymmetric SC it is important to mass balance the electrodes so that both electrodes store an equal amount of charge. In order to do so, three-electrode experiments are measured for both electrodes and the charge is then calculated for each electrode. The series of equations in Equation 4.8 are then used to determine the mass balance, where Q_1 is the charge stored at electrode 1, C_1 is the capacitance of electrode 1, V_1 is the voltage range of electrode 1, m_1 is the mass of active material on electrode 1, C_{sp1} is the specific capacitance of electrode 1. Subscript 2 indicates that the values to insert in to the equation are for electrode 2.

$$\begin{aligned} Q_1 &= Q_2 \\ Q_1 &= C_1 \times V_1 = C_{sp1} \times m_1 \times V_1 \\ Q_2 &= C_2 \times V_2 = C_{sp2} \times m_2 \times V_2 \\ C_{sp1} \times m_1 \times V_1 &= C_{sp2} \times m_2 \times V_2 \\ \rightarrow \frac{m_1}{m_2} &= \frac{C_{sp2} \times V_2}{C_{sp1} \times V_1} \end{aligned} \quad (4.8)$$

Gravimetric energy density is the amount of energy that can be stored by a SC per unit weight, it has the units W.h.kg⁻¹.³⁷ Energy density can be calculated from Equation 4.9, where M is the total mass of active material (on both the anode and the cathode). The calculation of energy density using the mass of both the anode and cathode means that comparisons can be made with devices in the literature.⁴⁰

$$E = \frac{1}{2} \frac{C_{exptl}}{M} \Delta U^2 \quad (4.9)$$

Gravimetric power density can be calculated from Equation 4.10, this describes how fast a SC can discharge the stored energy per unit weight; it has the units W.kg⁻¹.³⁷

$$P = \frac{E}{\Delta t} \quad (4.10)$$

4.3 Optimisation and Performance of the Decavanadate Cathode

4.3.1 Decavanadate Synthesis and Characterisation

Three different methods to synthesise $\text{Na}_6\text{V}_{10}\text{O}_{28}\cdot n\text{H}_2\text{O}$ (V_{10}) have been explored for this work; those described in papers by Johnson and Murmann,⁴¹ Yerra *et al.*⁴² and Chen *et al.*⁴³ The Johnson and Murmann preparation of V_{10} acidified an aqueous solution of Na_3VO_4 , the product is then recrystallised from water and isolated on a filter paper.⁴¹ V_{10} prepared by this method will be referred to as **V₁₀-A** from this point onwards. Yerra *et al.* acidified an aqueous solution of NaVO_3 and the V_{10} is precipitated using MeCN.⁴² V_{10} prepared by this method will be referred to as **V₁₀-B** from now on. Chen *et al.*⁴³ used a method by Domaille *et al.*⁴⁴ to acidify an aqueous solution of NaVO_3 and then Chen *et al.* go on to isolate the V_{10} by the addition of EtOH.⁴³ V_{10} prepared following this method will be referred to as **V₁₀-C**. We also modified the Chen *et al.* preparation by precipitating with acetone. V_{10} prepared via this method will be referred to as **V₁₀-D**. The decavanadate samples in each case were air dried before characterisation.

The V_{10} from each method has been characterised by NMR spectroscopy, FTIR spectroscopy and SEM. Figure 4.18 shows the ball-and-stick model of $[\text{V}_{10}\text{O}_{28}]^{6-}$ with the three different vanadium environments labelled.

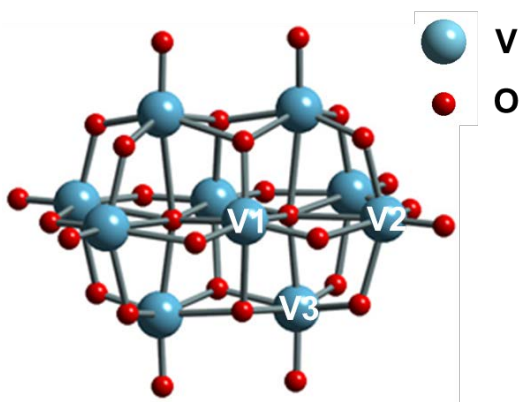


Figure 4.18 Ball and stick model of $[\text{V}_{10}\text{O}_{28}]^{6-}$, with the three different vanadium environments labelled as V1, V2 and V3.

Figure 4.19 shows the $^{51}\text{V}\{{}^1\text{H}\}$ NMR spectra for all four preparations. The peaks which correspond to the three different vanadium environments in V_{10} are labelled as

V1, V2 and V3 and these correspond to the labels in the ball-and-stick model of V_{10} (Figure 4.17). ⁴⁵ V_{10} -A produces V_{10} with the smallest amount of side products. The resonances in the ${}^{51}\text{V}\{{}^1\text{H}\}$ NMR spectra can be assigned to the side products; I1 $[\text{VO}_4]^{3-}$, I2 $[\text{V}_2\text{O}_7]^{4-}$ and I3 $[\text{V}_4\text{O}_{12}]^{4-}$ and there is a fourth impurity in V_{10} -B, I4 $[\text{V}_5\text{O}_{15}]^{5-}$. ²⁰ Table 4.1 lists the peaks in the ${}^{51}\text{V}\{{}^1\text{H}\}$ NMR spectra for each V_{10} preparation.

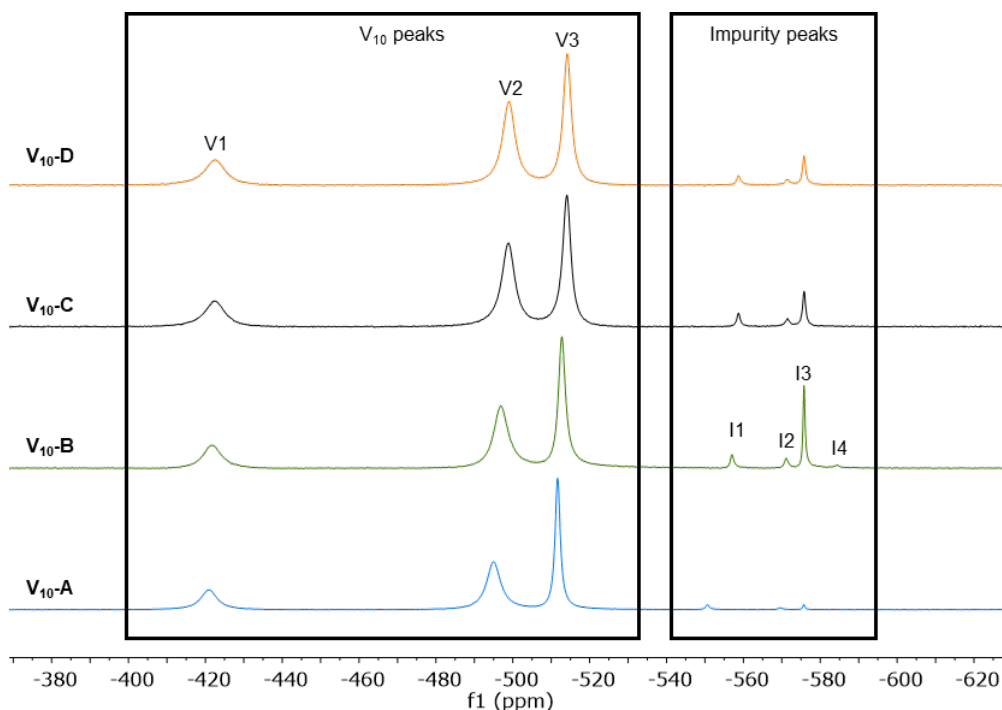


Figure 4.19 ${}^{51}\text{V}\{{}^1\text{H}\}$ NMR spectra in D_2O of V_{10} -A Johnson and Murmann, V_{10} -B Yerra, V_{10} -C Chen EtOH, V_{10} -D Chen acetone. All samples were prepared using 10 mg of solid and 0.5 mL of solvent.

V_{10} prep	δv / ppm					
V_{10} -A	-420.9	-495.0	-511.7	-550.7	-569.6	-575.7
V_{10} -B	-421.8	-496.9	-512.8	-557.1	-571.2	-575.8
V_{10} -C	-422.8	-498.8	-514.1	-558.7	-571.5	-575.8
V_{10} -D	-422.5	-499.0	-514.2	-558.8	-571.5	-575.8

Table 4.1 Peaks in the ${}^{51}\text{V}\{{}^1\text{H}\}$ NMR spectra for the four V_{10} preparations.

The FTIR spectra for all four preparations are shown in Figure 4.20. The bands in the FTIR are listed in Table 4.2. The $\nu(\text{V}-\text{O}_t)$ band 973-977 and 949 cm^{-1} and $\nu(\text{V}-\text{O}_b-\text{V})$ bridging bands at 813-817 and $734-740\text{ cm}^{-1}$ are in close agreement with the literature. ⁴⁶ The FTIR for all four preparations are very similar except V_{10} -C and V_{10} -D have an extra extremely weak band at ca. 1025 cm^{-1} . Unlike the NMR spectra the bands due to impurities cannot be identified in FTIR spectra, since the impurities are only a small percentage of the samples.

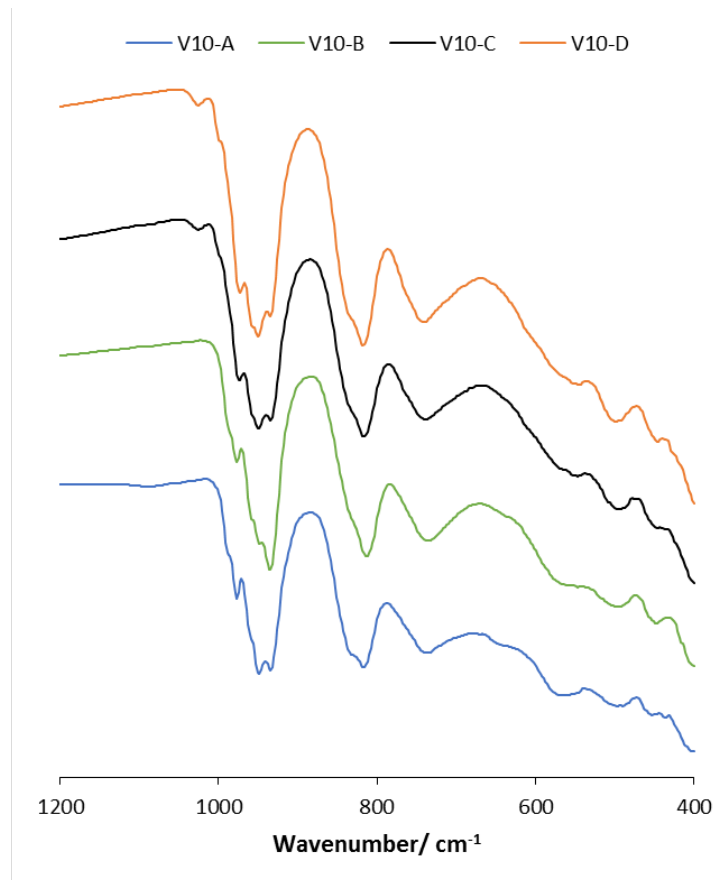


Figure 4.20 FTIR spectra of V₁₀-A Johnson and Murmann, V₁₀-B Yerra, V₁₀-C Chen EtOH, V₁₀-D Chen acetone.

V ₁₀ prep	Bands in FTIR/ cm ⁻¹							
V ₁₀ -A	1625.4		977.3	949.1	934.4	816.7	735.0	559.6
V ₁₀ -B	1625.1		977.2		935.1	813.1	736.4	493.2 447.2
V ₁₀ -C	1623.5	1025.4	974.1	949.4		816.2	739.3	492.8
V ₁₀ -D	1624.1	1025.9	973.1	949.9		817.1	740.9	499.3

Table 4.2 Bands in the FTIR spectra of the four V₁₀ preparations.

The SEM images of V₁₀ prepared following the four different methods described above are shown in Figure 4.21. Figure 4.21A is a SEM image of V₁₀-A, it shows a large cracked crystal with smaller crystallites. Figure 4.21B is a SEM image of V₁₀-B, it shows a large variety in size of crystallites, some large crystals and some a lot smaller. Figure 4.21C and D correspond to V₁₀-C and V₁₀-D the SEM images for these show crystal that are very similar.

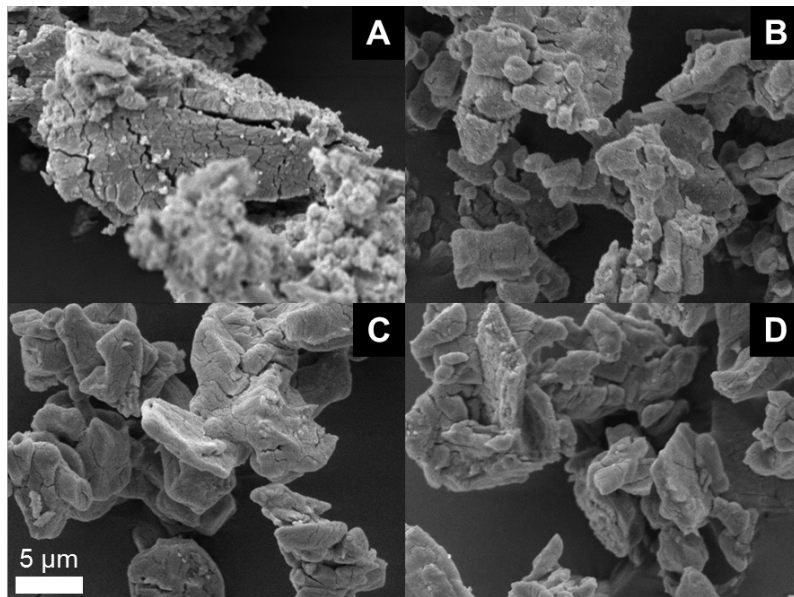


Figure 4.21 SEM images of V_{10} ; (A) V_{10} -A, (B) V_{10} -B, (C) V_{10} -C, (D) V_{10} -D. The scale bar (bottom left) is $5\text{ }\mu\text{m}$ for all four images.

The characterisation of the four different preparations of V_{10} show that V_{10} -A is the most suitable to use due to the presence of fewer impurities in the NMR spectrum and the smaller crystallites in the SEM show promise that even smaller crystallites can be achieved on further processing. The crystallites size is important as the V_{10} will be used in a SC electrode and the smaller the crystals the larger there surface area will be. V_{10} -A has been characterised further by solution CV, TGA and PXRD.

The solution CV of V_{10} -A is shown in Figure 4.22, it reproduces literature results reported under the same conditions and experimental parameters.⁴⁷

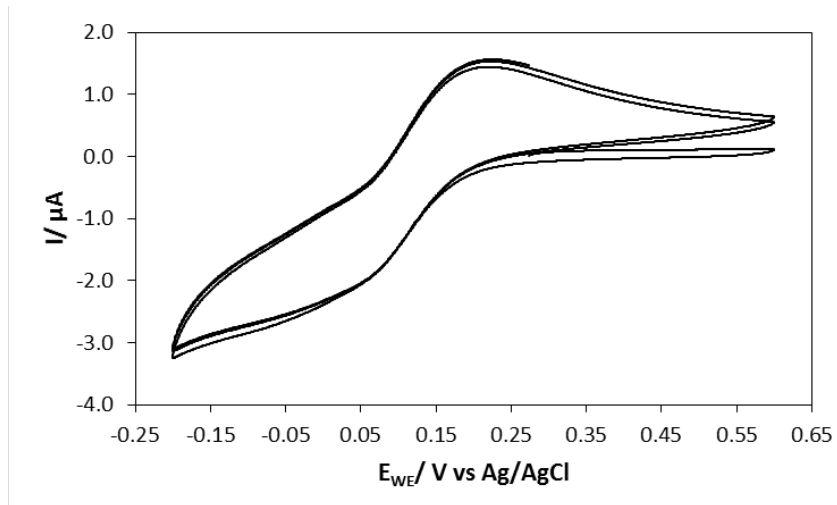


Figure 4.22 Solution CV of 1 mM V_{10} in pH 5 0.4 M $\text{CH}_3\text{COONa}/\text{H}^+$ buffer, 10 mV.s^{-1} scan rate, from 0.60 V to -0.20 V, 3 cycles.

From the TGA (Figure 4.23) there is a weight loss of 11%, and this gives V₁₀-A the formula Na₆V₁₀O₂₈.8H₂O. The weight loss by V₁₀-A is due to water of crystallisation.

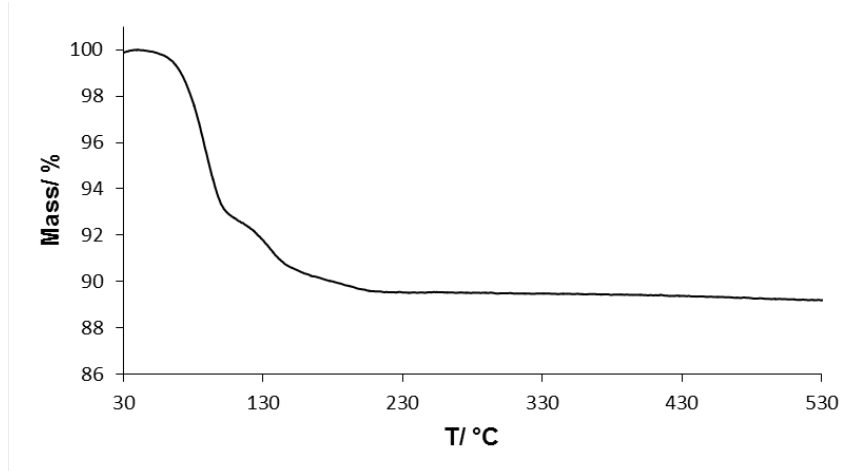


Figure 4.23 TGA of V₁₀-A between 30 – 530 °C, heated at a rate of 10.0 °C per minute.

V₁₀-A is a new phase that has not been reported in the literature. The PXRD pattern of V₁₀-A is shown in Figure 4.24. Only the higher hydrates of V₁₀ have been reported and characterised by PXRD; Na₆V₁₀O₂₈.*n*H₂O where *n* = 12,⁴⁸ 18,⁴⁹ 24,⁵⁰ 26.⁵¹

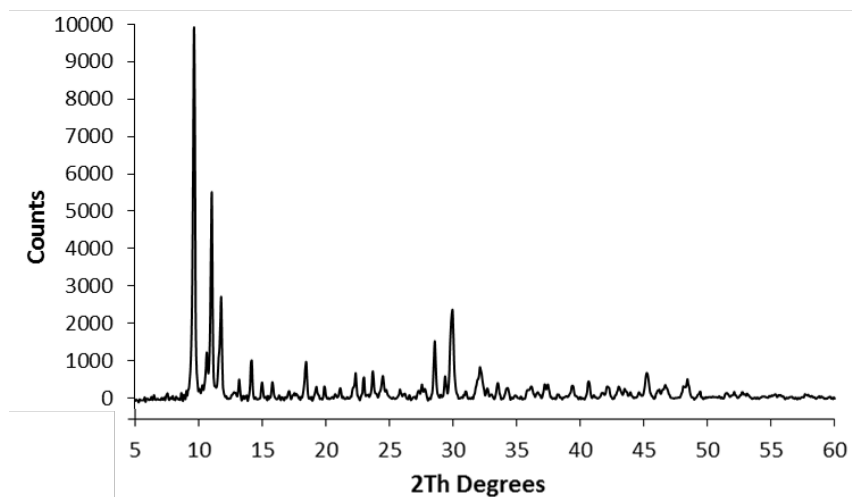


Figure 4.24 PXRD pattern of V₁₀-A.

4.3.2 Temperature Stability

For the purpose of electrochemistry experiments V₁₀ was heated at 80 °C after precipitation in order to remove water and the anti-solvent and then again once it is part of the electrode slurry as described in Section 4.2.3. The stability of V₁₀ was monitored at different temperatures under nitrogen in order to determine if V₁₀ decomposed on heating. V₁₀ was dried at RT in air and at 80, 120 and 200 °C under N₂ for 12 hrs. The resulting V₁₀ from the drying experiment was then characterised

by $^{51}\text{V}\{^1\text{H}\}$ NMR and FTIR spectroscopy. Streb *et al.* carried out a similar study on the Li salt of $[\text{V}_{10}\text{O}_{28}]^{6-}$ and found that the vanadate POM decomposes when heated to temperatures of 120 °C and above, and the products of heating were characterised by PXRD, TGA, Raman spectroscopy and CV.⁵²

Figure 4.25 shows the $^{51}\text{V}\{^1\text{H}\}$ NMR spectra of the water soluble material from the samples obtained from the treatment of V_{10} at different drying temperatures. The relative intensities of the resonances in the NMR spectra change as the temperature is increased, the amount of impurities increases as the temperature increases and there is only a very small amount of V_{10} present after drying at 200 °C. The resonances in the $^{51}\text{V}\{^1\text{H}\}$ NMR spectra are assigned to I1 $[\text{VO}_4]^{3-}$, I2 $[\text{V}_2\text{O}_7]^{4-}$ and I3 $[\text{V}_4\text{O}_{12}]^{4-}$.²⁰ The formation of these impurities can be rationalised by the formation of V_2O_5 , which is insoluble in water, as shown in Equation 4.11. The NMR samples of V_{10} dried at 120 and 200 °C contained insoluble dark brown material presumed to be V_2O_5 .

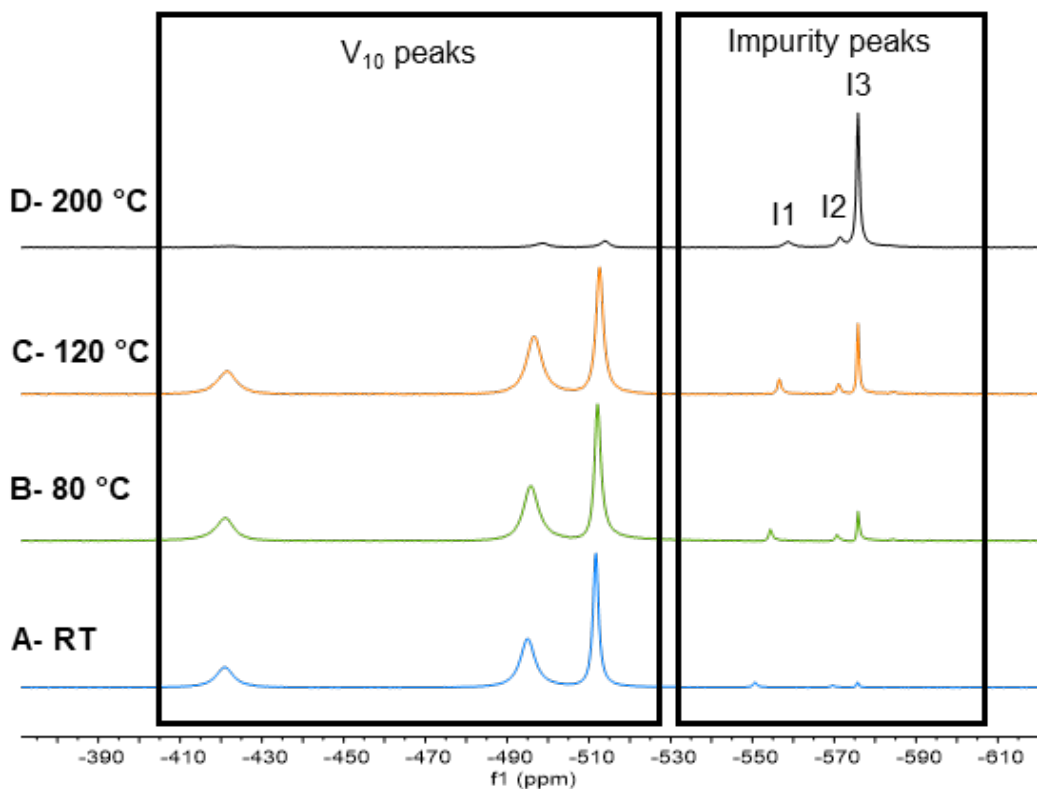


Figure 4.25 $^{51}\text{V}\{^1\text{H}\}$ NMR spectra in D_2O of V_{10} dried at different temperatures; (A) RT in air, (B) 80 °C, (C) 120 °C, (D) 200 °C under N_2 . All samples were prepared using 10 mg of solid and 0.5 mL of solvent. There was insoluble material present in samples C and D.

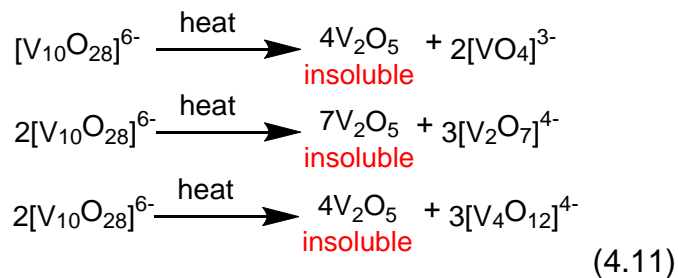


Figure 4.26 shows FTIR spectra from the same drying experiment. The FTIR spectra of V_{10} dried in air at RT, at 80 °C and at 120 °C under N_2 (Figure 4.26A-C) are quite similar but the FTIR spectrum of V_{10} dried at 200 °C under N_2 (Figure 4.26D) is quite different, it clearly indicates decomposition like in the NMR spectra.

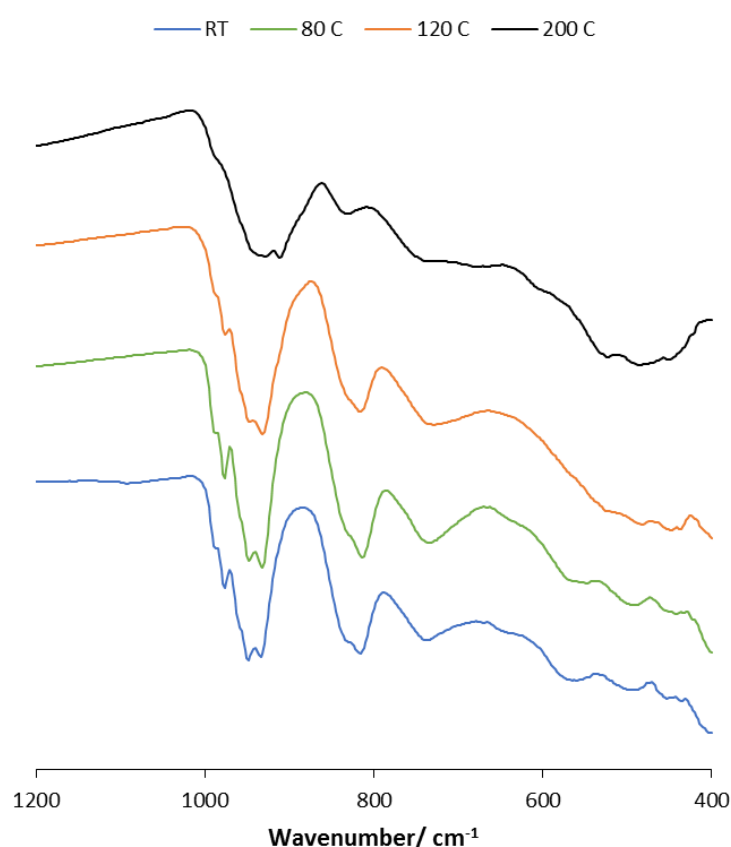


Figure 4.26 FTIR spectra of V_{10} dried at different temperatures; RT in air, 80 °C, 120 °C, 200 °C under N_2 .

The investigation of temperature stability suggests that drying V_{10} at 80 °C after precipitation and once it is part of the slurry should not change the composition of V_{10} significantly. From the TGA (Figure 4.23) at 80 °C, there is roughly a weight loss of 5% which corresponds to 4 H_2O , and from the formula of $\text{Na}_6V_{10}\text{O}_{28} \cdot 8\text{H}_2\text{O}$ there is 50% of the water remaining.

4.3.3 Processing of Decavanadate

V_{10} has been processed several different ways as described in Section 4.2.2, sonoprecipitation and powder processing; mainly grinding, sonofragmentation, ball mill and high energy ball mill (HEBM). The aim was to achieve smaller crystallites, because it was hoped that incorporating smaller crystallites into the electrode slurries, a higher volume fraction of the V_{10} would be electrochemically accessible in a SC electrode. This is illustrated in Figure 4.27, as the crystal gets smaller the ratio of the portion of surface available electrochemically (yellow) to the inner crystal (orange) gets bigger.

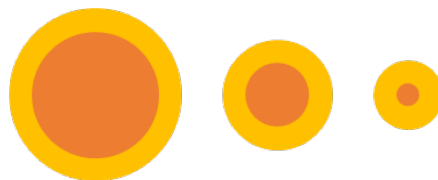


Figure 4.27 Diagram demonstrating the increasing portion of crystallite accessible electrochemically with reduction in crystallite size.

4.3.3.1 Sonoprecipitation

The precipitations in the Yerra *et al.*⁴² and Chen *et al.*⁴³ preparations have been modified by sonoprecipitation as described in Section 4.2.2. This was in an effort to achieve smaller crystallites.⁵³ The SEM images in Figure 4.28A-D show that when sonoprecipitation is used the crystallite sizes are smaller. Figure 4.28E and F show that the bigger crystals have cracked but not as big of an effect as the other two preparations.

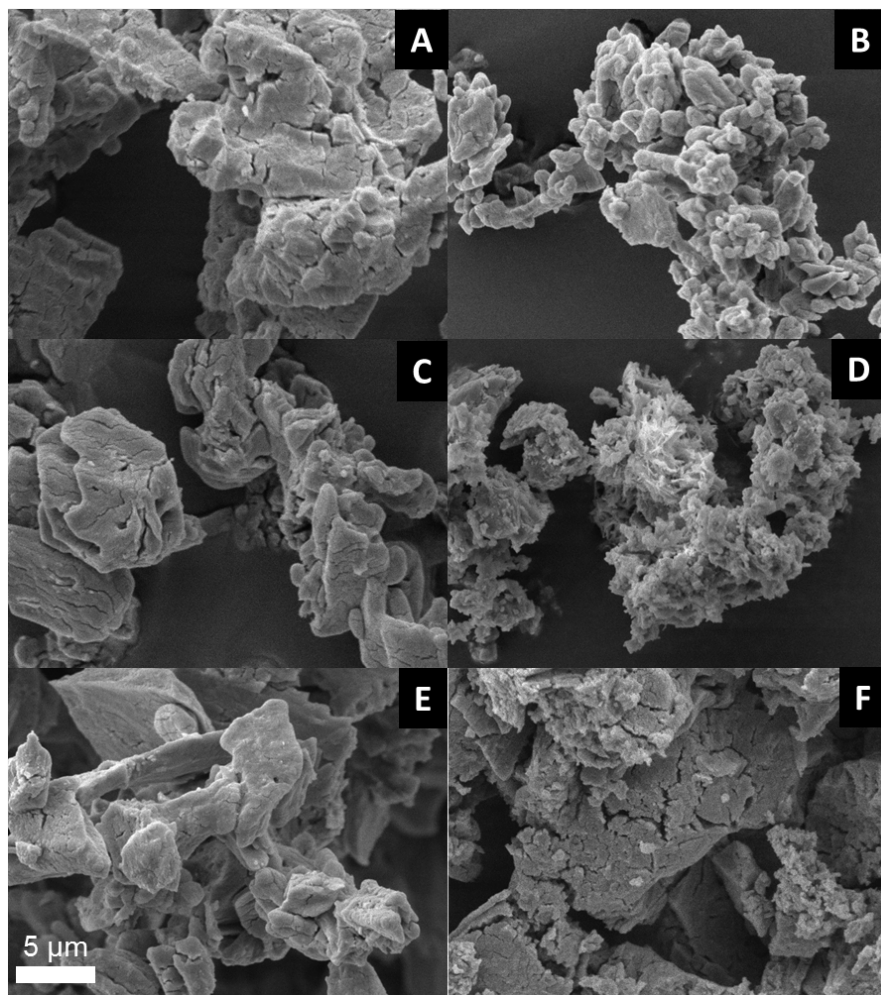


Figure 4.28 SEM images of (A) V_{10} -B, (B) V_{10} -B sonoprecipitation, (C) V_{10} -C, (D) V_{10} -C sonoprecipitation, (E) V_{10} -D and (F) V_{10} -D sonoprecipitation.

4.3.3.2 Powder Processing

V_{10} powder which has been prepared via one of the four methods described in Section 4.3.1 can be processed further in an attempt to achieve smaller crystallites. The progress of V_{10} processing is shown in the SEM images in Figure 4.29. Firstly V_{10} -C is dried o/n at 80 °C (Figure 4.29A), this shows a large crystal approximately 10 x 10 μm in size, with some cracks on the surface. This V_{10} has then been ground for 15 mins using a pestle and mortar (Figure 4.29B), the crystals are now slightly smaller (6 x 4 μm) with much smaller crystallites (1 x 1 μm) on the surface. Figure 4.29C shows V_{10} -C that has been dried at 80 °C o/n and sonofragmented in EtOH as described in Section 4.2.2, the SEM shows an aggregate that is approximately 10 x 12 μm in size, possibly bigger as some may be out of the image. The aggregate is made up of much smaller crystals, some as small as 0.5 x 0.5 μm . Figure 4.29D shows V_{10} -C that has been dried at 80 °C o/n, ground for 15 mins using a pestle and

mortar then sonofragmented in EtOH. The SEM shows similar to Figure 4.29C, an aggregate of slightly smaller crystallites, some as small as $0.3 \times 0.3 \mu\text{m}$. Figure 4.29E shows $\text{V}_{10}\text{-C}$ that has been dried at 80°C o/n, ground for 15 mins using a pestle and mortar, sonofragmented in EtOH and ball milled o/n, the SEM is similar to Figure 4.29C and D, some of the crystals that make up the aggregate are even smaller $0.1 \times 0.1 \mu\text{m}$ in size. $\text{V}_{10}\text{-A}$ dried at 80°C o/n and then HEBM for 61 mins is shown in Figure 4.29F, it shows some very small crystallites ($0.1 \times 0.1 \mu\text{m}$) and some small crystal aggregates ($2 \times 2 \mu\text{m}$) and some much bigger ones.

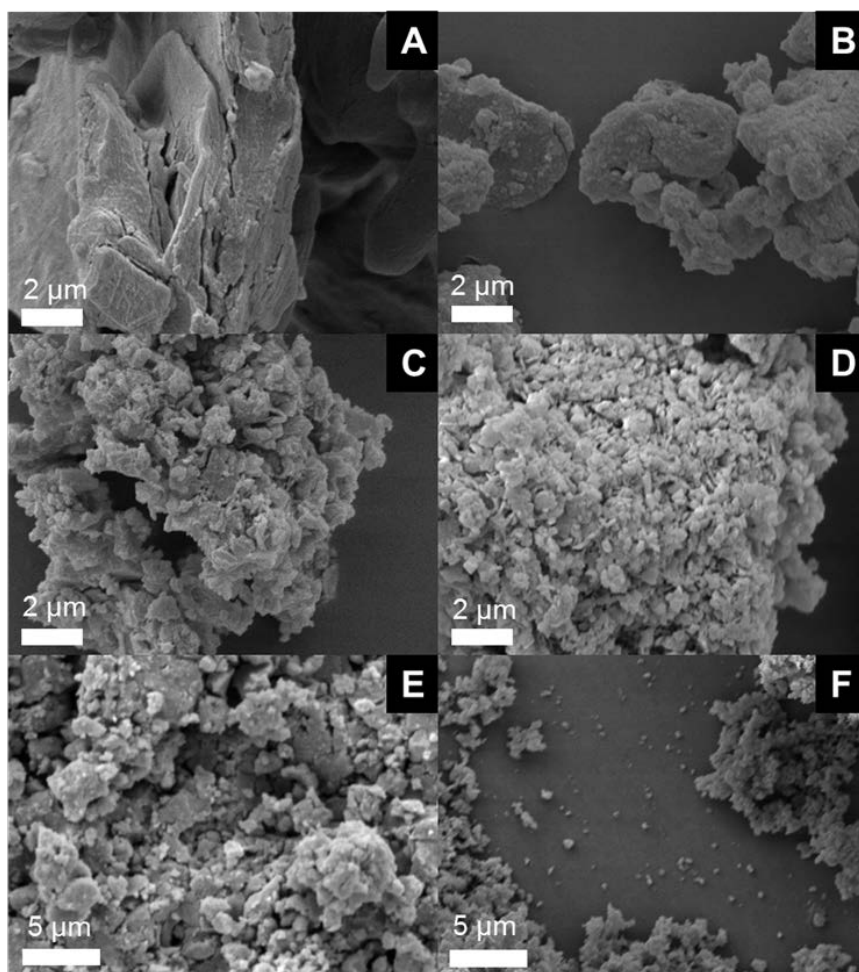


Figure 4.29 SEM images of (A) $\text{V}_{10}\text{-C}$ dried 80°C , (B) $\text{V}_{10}\text{-C}$ dried 80°C and ground, (C) $\text{V}_{10}\text{-C}$ dried 80°C and sonicated, (D) $\text{V}_{10}\text{-C}$ dried 80°C , ground and sonicated, (E) $\text{V}_{10}\text{-C}$ dried 80°C , ground, sonicated and ball milled o/n, (F) $\text{V}_{10}\text{-A}$ dried 80°C and HEBM 61 minutes. Scale bar for A-D $2 \mu\text{m}$, and E and F $5 \mu\text{m}$.

4.3.4 Electrode Preparation

Many components used in the electrode preparation as discussed in Section 4.2.3, have been investigated in order to optimise the performance of SC electrodes.

These components include; current collector, conducting carbon, binder and solvent.

In addition to the components, slurry loading has also been investigated. The electrodes investigated in this section have all been comprised in a three-electrode set up.

4.3.4.1 Current Collector

Four different current collectors have been explored; three carbon fiber papers manufactured by Spectracarb™ and one carbon fiber paper manufactured by Toray™. The Spectracarb™ papers differ in thickness and 2050A and 2050L differ in the temperature at which they are carbonised, L being at a lower unspecified temperature. The properties of the current collectors are summarised in Table 4.3. The current collectors were investigated to see how the varying properties would affect the performance of electrodes.

Current collector	Thickness/ mm	Density/ g.cm ⁻³	Series
2050A-0550 ^a	0.127	0.50	Q
2050A-0850 ^a	0.203	0.50	R
2050L-0850 ^a	0.203	0.50	S
TGP-H-030 ^b	0.110	0.40	U

Table 4.3 Summary of all current collectors investigated as part of the electrode preparation study.

^a manufactured by Spectracarb™, ^b manufactured by Toray™.

The electrodes for Series Q, R, S and U were prepared using **V₁₀-C** that was dried in an oven overnight at 80 °C, ground for 15 mins using a pestle and mortar, sonofragmented in EtOH, dried in an oven at 80 °C overnight and then ball milled for 5 mins. The slurry and electrodes were then prepared following the standard procedure as described in Section 4.2.3.

CV at 5 mV.s⁻¹ scan rate are shown in Figure 4.30, they show that the best CV is for S2 and R1 as the most current was detected.

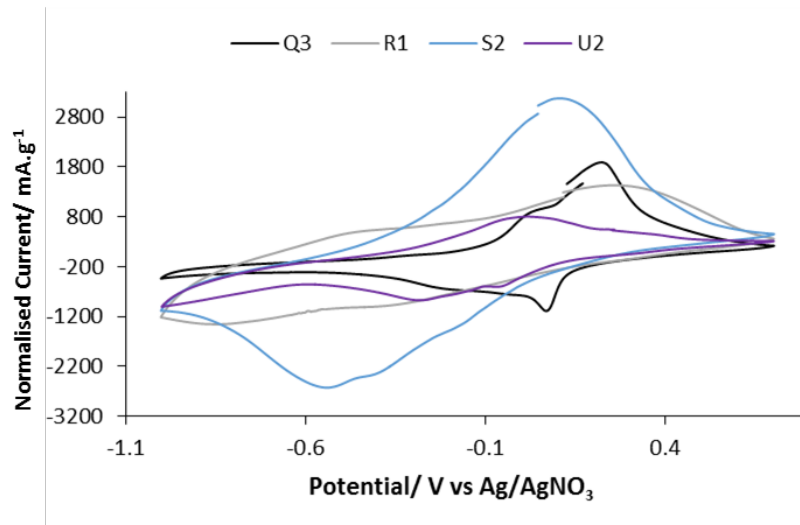


Figure 4.30 The second cycles of 5 mV.s^{-1} CV of Q3 0.8 mg V_{10} , R1 2.2 mg V_{10} , S2 1.1 mg V_{10} and U2 0.7 mg V_{10} . Scanned from 0.7 V to -1.0 V .

CP measured at 0.5 A.g^{-1} current density are shown in Figure 4.31, they show that the best result was achieved for S2 and R1, in agreement with the results from CV.

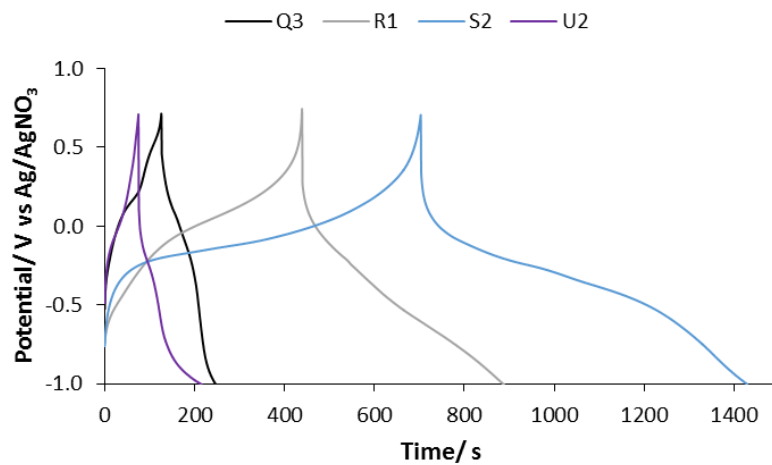


Figure 4.31 Third cycle of 0.5 A.g^{-1} CP of Q3 0.8 mg V_{10} , R1 2.2 mg V_{10} , S2 1.1 mg V_{10} and U2 0.7 mg V_{10} .

The C_{sp} calculated from CV and CP are listed in Table 4.4 and shown in the bar chart in Figure 4.32. The highest C_{sp} achieved from both CV and CP was by series R and S. The current collectors used for series R and S were of the same thickness and thicker than the other two current collectors that were investigated. It is thought that with a thicker current collector the slurry can penetrate further into the material as illustrated in Figure 4.33, providing better contact between the material and the current collector.

Current collector	Series	CV/ F.g ⁻¹	CP/ F.g ⁻¹
2050A-0550	Q	88	32
2050A-0850	R	149	148
2050L-0850	S	228	248
TGP-H-030	U	94	31

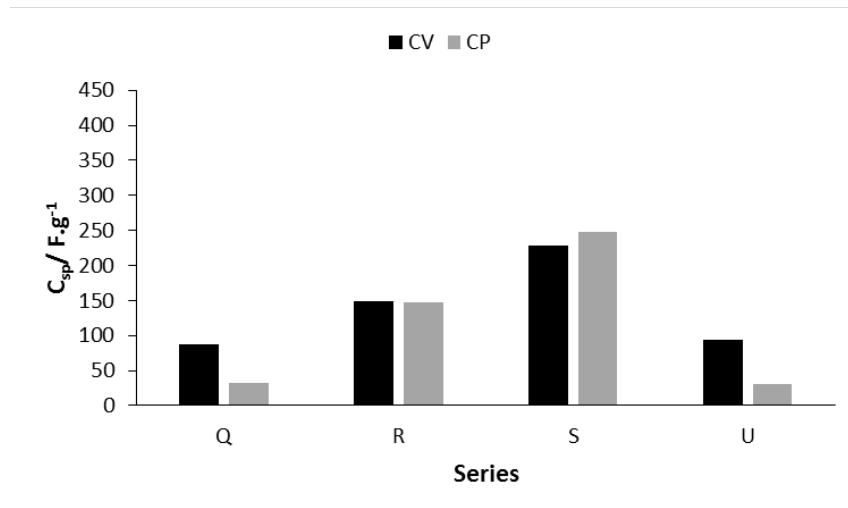
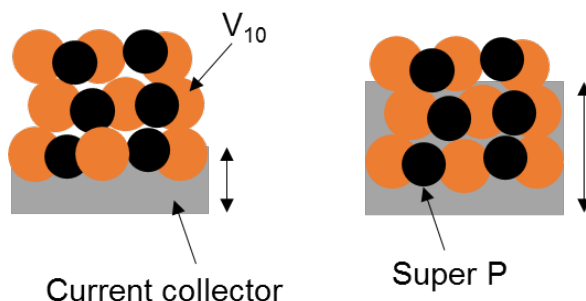
Table 4.4 Table summarising the C_{sp} for CV and CP for each series.Figure 4.32 Bar chart summarising the C_{sp} for CV and CP for each series.

Figure 4.33 Schematic to show how the thickness of current collector effects the slurry uptake.

4.3.4.2 Conducting Carbon

Two different kinds of conducting carbon have been investigated as a component in the slurry for preparing V_{10} containing electrodes; Denka black and Super P. Denka black is a type of acetylene black and Super P is a type of furnace black. Denka black contains fewer impurities, higher conductivity and higher dispersibility in comparison to Super P due to the different manufacturing methods.⁵⁴

The slurries used in these experiments were prepared using $V_{10}\text{-C}$ dried at 80 °C o/n in an oven, ground, and sonofragmented in EtOH then dried at 80 °C o/n in oven and

then combined in the slurry with the conducting carbon following the standard protocol described in Section 4.2.3.

The CV (Figure 4.34) and CP (Figure 4.35) for electrodes containing Denka black (Series AR) and Super P (Series AL) are shown below. They show that current produced by AL2 is much higher than that of AR3 which leads to a C_{sp} that is much higher. The CP of AL2 is also much more symmetrical than the CP of AR3.

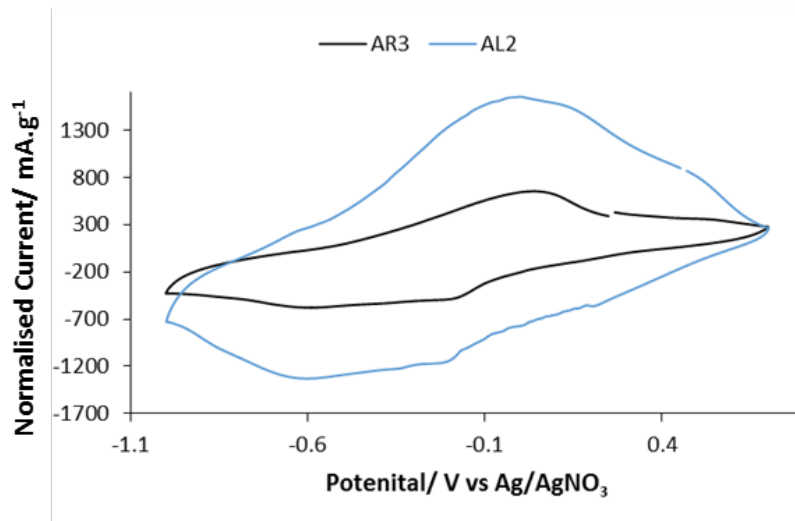


Figure 4.34 Second cycles of 5 mV.s^{-1} CV of AR3 1.4 mg V_{10} and AL2 1.3 mg V_{10} . Scanned from 0.7 V to -1.0 V .

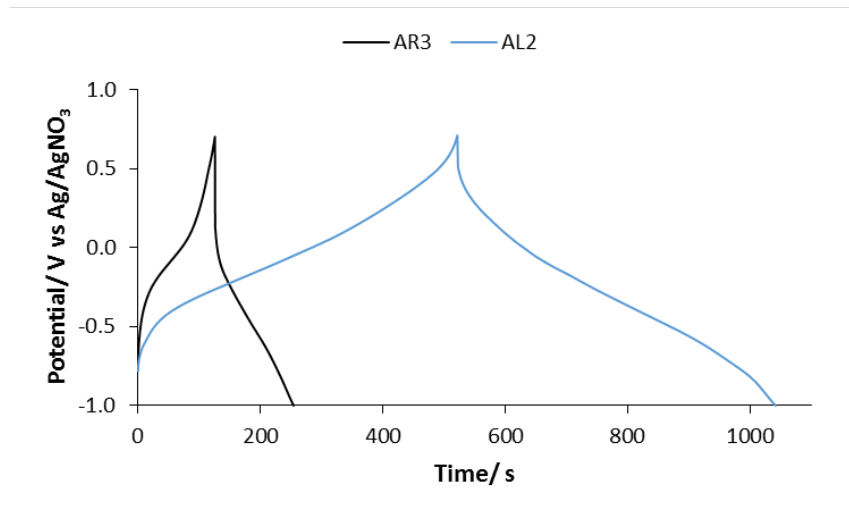
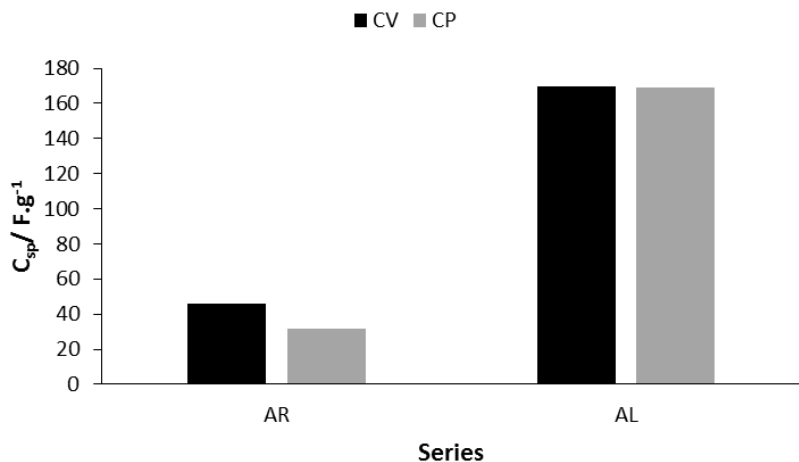


Figure 4.35 Third cycle of 0.5 A.g^{-1} CP of AR3 1.4 mg V_{10} and AL2 1.3 mg V_{10} .

The results from Denka black and Super P containing electrodes are listed in Table 4.5 and shown in Figure 4.36. They show that the electrodes made using Super P had higher C_{sp} for both CV and CP.

Conducting carbon	Series	$C_{sp} \text{ CV/ F.g}^{-1}$	$C_{sp} \text{ CP/ F.g}^{-1}$
Denka black	AR	46	32
Super P	AL	170	169

Table 4.5 Summary of C_{sp} for CV and CP for Series AR and AL.Figure 4.36 Bar chart summarising the C_{sp} for CV and CP for Series AR and AL.

4.3.4.3 Solvent in Slurry

NMP is a standard solvent used as a mixing agent in the preparation of slurries for electrode coating, this is because carbon black disperses well and the binder is soluble in NMP.⁵⁵ However NMP has a very high boiling point 202 °C, therefore heating the electrode o/n is required to remove all the solvent. THF was investigated since it has a lower boiling point (66 °C) and therefore the electrodes could be dried at a lower temperature. The lower boiling point caused problems during electrode preparation, as when coating the electrodes with the slurry the THF was evaporating before the electrodes could be coated smoothly, so the electrodes were unevenly coated and therefore unusable.

4.3.4.4 Binder

The binders investigated were PVDF and PTFE, as they are both commonly used as binders in the preparation of electrodes.^{43, 56, 6} PVDF is soluble in NMP, the solvent selected to be used in Section 4.3.4.3. PTFE was not compatible with the other ingredients used to make the slurries for this project. The PTFE caused the carbon black to stick together and form clumps, which meant the carbon did not disperse homogeneously in the NMP and therefore made a poor slurry. The electrodes made using PTFE in the slurry were not tested. To investigate the use of PTFE further a different solvent would need to be used, Yamada and Goodenough used a range of

solvents to construct their PTFE containing electrodes, which included MeOH , EtOH , toluene and acetone.⁶

4.3.4.5 Loading

The amount of slurry deposited on to the current collector has been investigated, this was due to the hypothesis that the smaller the amount of material on the current collector, the thinner the layer of material would be and therefore increased contact of all the V_{10} and Super P with the current collector as illustrated in Figure 4.37.

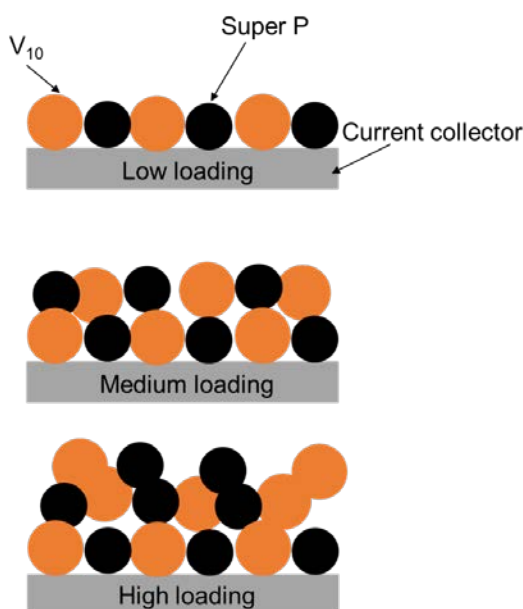


Figure 4.37 Illustration of different loadings of slurry on current collectors.

The V_{10} used in each slurry for the four different series was powder processed as described below; (1) Series AH - **$\text{V}_{10}\text{-C}$** dried at $80\text{ }^\circ\text{C}$ o/n in an oven, ground for 15 mins in pestle and mortar, sonofragmented in EtOH then dried at $80\text{ }^\circ\text{C}$ o/n in an oven and then ball milled for 5 mins. The V_{10} was then sonicated with Super P for 10 mins in EtOH , dried in oven o/n at $80\text{ }^\circ\text{C}$. (2) Series AK - **$\text{V}_{10}\text{-C}$** dried at $80\text{ }^\circ\text{C}$ o/n in an oven, ground for 15 mins in pestle and mortar, sonofragmented in EtOH then dried at $80\text{ }^\circ\text{C}$ o/n in an oven and then ball milled for 5 mins. (3) Series AL - **$\text{V}_{10}\text{-C}$** dried at $80\text{ }^\circ\text{C}$ o/n in an oven, ground for 15 mins in pestle and mortar, sonofragmented in EtOH then dried at $80\text{ }^\circ\text{C}$ o/n in an oven and then ball milled o/n. The V_{10} was then sonicated with Super P for 10 mins in EtOH , dried in an oven o/n at $80\text{ }^\circ\text{C}$ (4) Series AU - **$\text{V}_{10}\text{-A}$** ball milled using HEBM at Retsch for 60 min, separated from alcohol dispersant by centrifuging for 60 min at 6500 rpm, dried in air

and then dried in an oven at 80 °C o/n. The slurries and electrodes were then prepared following the standard protocol described in Section 4.2.3.

Figures 4.38 and 4.39 show the CV and CP from this investigation. The CV demonstrates that the most current was detected for AU2, therefore a high C_{sp} was achieved. The current decreases as there is more material on the electrode.

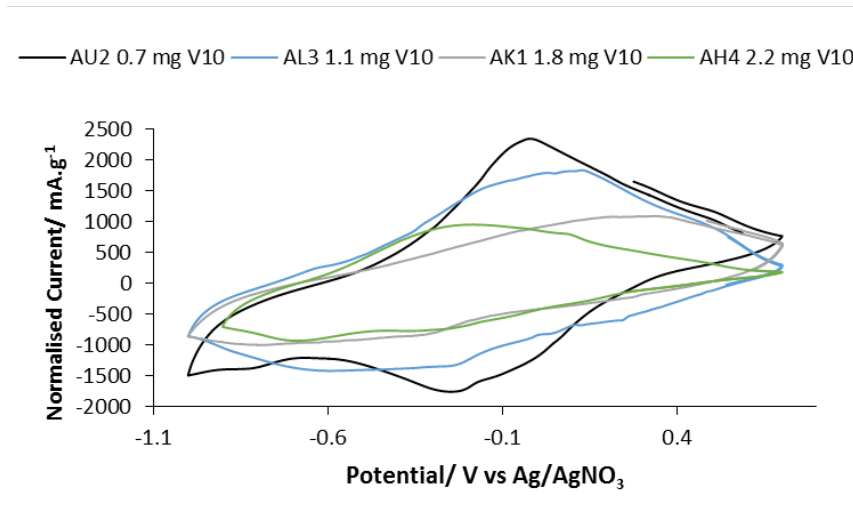


Figure 4.38 Second cycles of 5 mV.s⁻¹ CV of AU2 0.7 mg V₁₀, AL3 1.1 mg V₁₀ and AK1 1.8 mg V₁₀, AH4 2.2 mg V₁₀. Scanned from 0.7 V to -1.0 V.

The CP in Figure 4.39 shows that at lower loading of material on the electrode, the reduction takes longer and in turn a higher C_{sp} is achieved.

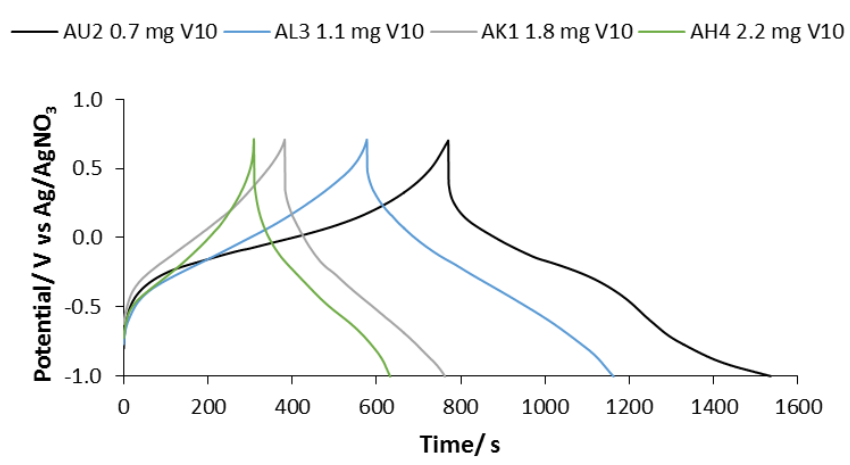


Figure 4.39 Third cycle of 0.5 A.g⁻¹ CP of AU2 0.7 mg V₁₀, AL3 1.1 mg V₁₀ and AK1 1.8 mg V₁₀, AH4 2.2 mg V₁₀.

Chapter 4 $\text{Na}_6\text{V}_{10}\text{O}_{28}$ Containing Supercapacitor

A summary of the results from the various loadings is listed in Table 4.6 and shown in Figures 4.40 and 4.41, they show that for a low loading (Series AU) the highest C_{sp} is achieved for both CV and CP.

V_{10} loading/ mg	Series	C_{sp} CV/ F.g^{-1}	C_{sp} CP/ F.g^{-1}
0.7	AU	178	225
1.1	AL	171	172
1.8	AK	111	111
2.2	AH	98	95

Table 4.6 Summary of the C_{sp} for the different slurry loadings.

The scatter graph for C_{sp} calculated from CV (Figure 4.40) and C_{sp} calculated from CP (4.41) are shown below, they show that there is a relationship between the amount of material on the electrodes and the C_{sp} achieved, the lower the amount of material the higher the C_{sp} achieved. The results show that the optimum loading was ca. 1 mg.cm^{-2} . This result was independent of the powder processing of V_{10} , as the loading of material on the electrode had a bigger effect on the outcome of C_{sp} than the details of the powder processing of V_{10} .

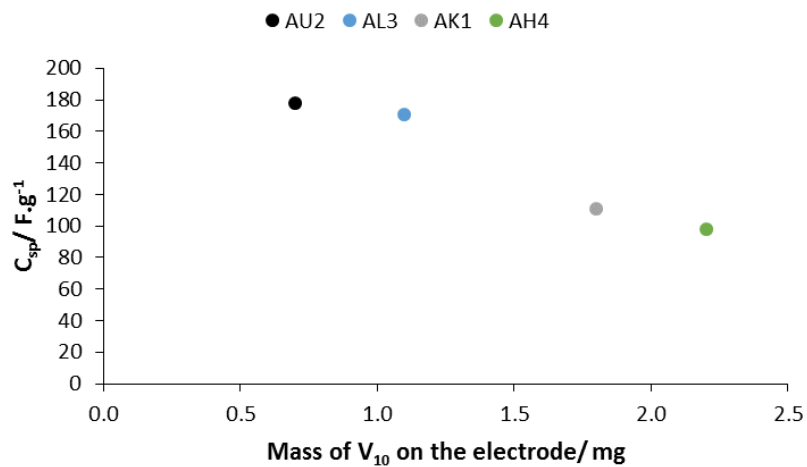


Figure 4.40 C_{sp} calculated from 5 mV.s^{-1} CV plotted against the mass of V_{10} on the electrodes.

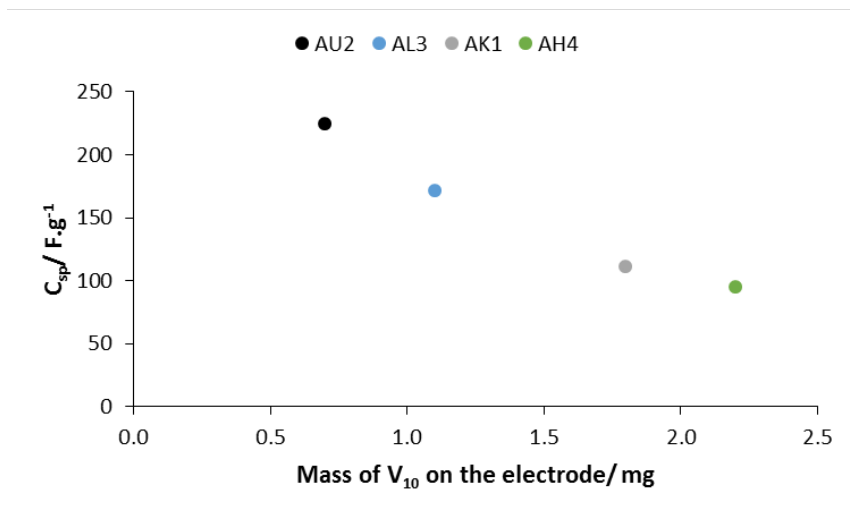


Figure 4.41 C_{sp} calculated from the third cycle of 0.5 A.g^{-1} CP plotted against the mass of V_{10} on the electrodes.

Attempts were made to achieve an even better performance by using even lower loadings of V_{10} on the electrode (μg range), but when this was attempted the electrochemistry of the current collector dominated the electrochemistry of V_{10} .⁵⁷

4.3.5 CP with Dwell Period Experiment

Dwell period experiments have been explained in Section 4.2.4. A CP dwell period experiment for a three-electrode set up is shown in Figure 4.42. The dwell period experiment was carried out to see if the electrodes were fully oxidised and if the potential would drop once the current was set to 0 A. The current was initially held at 0 A for 5 secs before oxidising the electrode, once the electrode was oxidised up to 0.7 V, the current was then held at 0 A for 60 s and this was repeated after the reduction cycle. From the graph you can see that after each oxidation cycle the voltage drops when the current is switched to 0 A, which suggests that the electrode is not fully oxidised at +0.7 V. The current also rises when the current is held at 0 A after the reduction cycle, this suggests the electrode is not fully reduced at -1.0 V. The results from the dwell period experiment suggest that there is poor electron and ion transfer within the electrode.

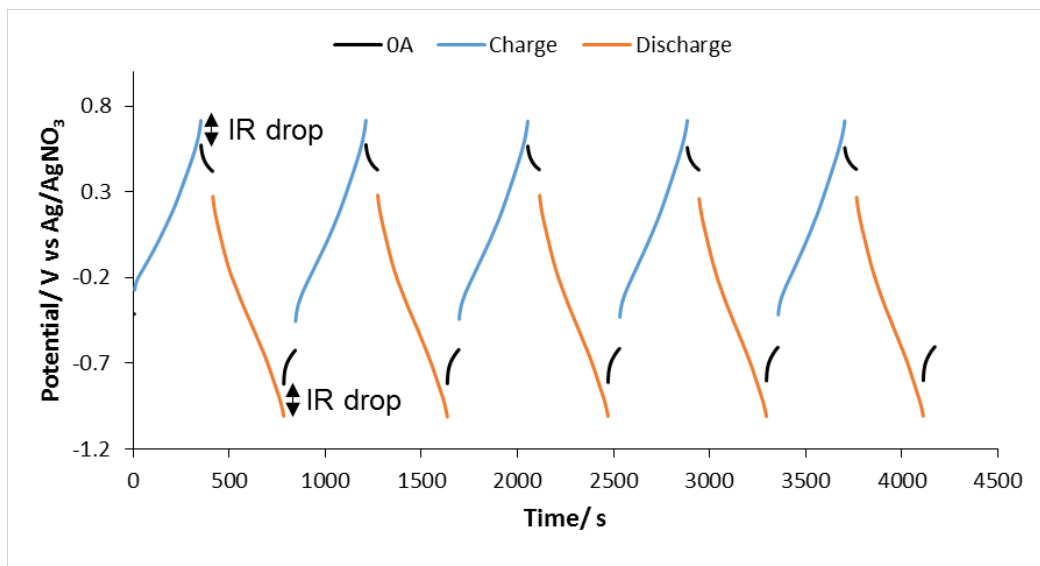


Figure 4.42 AK1 electrode 1.8 mg V_{10} , dwell experiment: 0 A initially for 5 s, 0.5 A.g^{-1} oxidised up to $+0.7 \text{ V}$, 0 A held for 60 s, 0.5 A.g^{-1} reduced to -1.0 V , 0 A held for 60 s then, repeated a further four times. IR drop is labelled.

The slurry used for electrode AK1 has already been described in Section 4.3.4.5.

4.3.6 Two-electrode Experiments

Electrodes have been investigated in a two-electrode set up so that the properties of a SC device could be evaluated. An asymmetric hybrid SC has been investigated, where the V_{10} electrode is faradaic and the AC electrode is an electrical double layer.

4.3.6.1 Asymmetric Supercapacitor

In order to investigate an asymmetric SC the first step is to balance the mass of the active materials on the cathode and the anode using three-electrode experiments, as previously explained in Section 4.2.4. The electrodes for the three-electrode experiments are prepared using the same slurry and current collector as the two-electrode experiments. The V_{10} electrode used in the asymmetric SC was prepared using the optimised conditions that were discovered in Section 4.3.4. The mass of V_{10} on the electrode was ca. 1 mg.cm^{-2} and the current collector used was the thickest, spectracarb 2050A-1550.

The slurry for the V_{10} electrode was composed of **V₁₀-A**, which was ball milled using HEBM at Retsch for 60 min, separated from alcohol dispersant by centrifuging for 60 min at 6500 rpm, dried in air and then dried in an oven at $80 \text{ }^\circ\text{C}$ o/n. The slurry and electrodes were then prepared following the standard protocol described in Section 4.2.3. The slurry for the AC electrodes was prepared following the standard protocol

as described in Section 4.2.3. The V_{10} electrode for the three-electrode experiment contained 1.2 mg of V_{10} and the AC electrode contained 1.7 mg of AC.

The second cycles of the CV from the mass balancing experiments are shown in Figure 4.43. The C_{sp} calculated for the V_{10} electrode was 108 F.g^{-1} and the C_{sp} calculated for the AC electrode was 92 F.g^{-1} . Using Equation 4.8, the mass balance is 1.2, i.e. multiply the mass of V_{10} by a factor of 1.2.

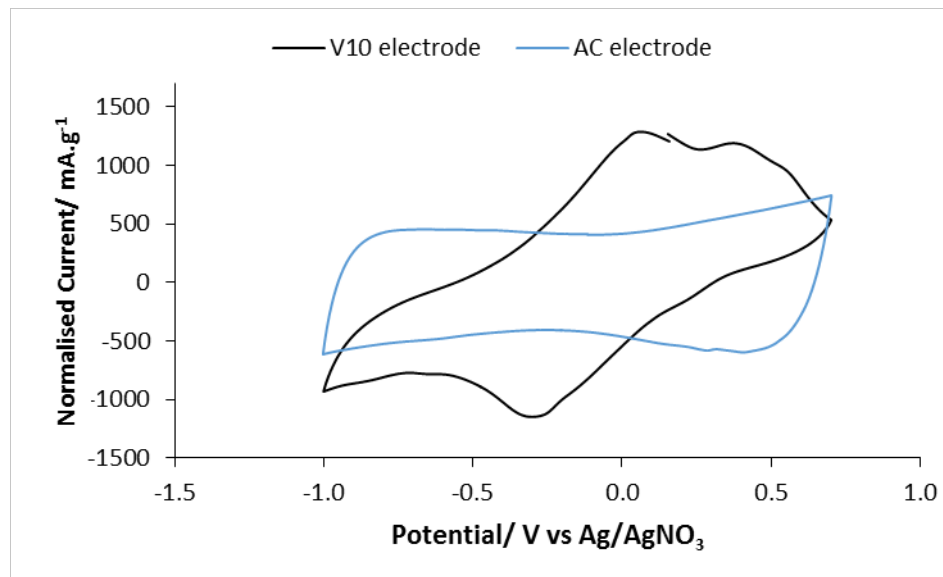


Figure 4.43 Three-electrode experiments, 5 mV.s^{-1} CV for V_{10} electrode and AC electrode. Pt CE, Ag/AgNO_3 RE, 1 M LiClO_4 in PC electrolyte. Scanned from 0.7 V to -1.0 V .

For two electrode experiments, several 2.54 cm^2 current collector discs were coated with either the V_{10} slurry or the AC slurry, this was in an attempt to obtain the correct V_{10} to AC ratio. The V_{10} electrode contained 2.7 mg V_{10} (1.1 mg.cm^{-2}) and the AC electrode contained 3.5 mg AC. The ratio of V_{10} to AC is 1.3, which was the closest to 1.2 of all the electrodes coated.

The results from the asymmetric two-electrode device experiments are shown below. The third cycle of the 1.0 A.g^{-1} GCD from an asymmetric SC with varying voltage ranges are shown in Figure 4.44.

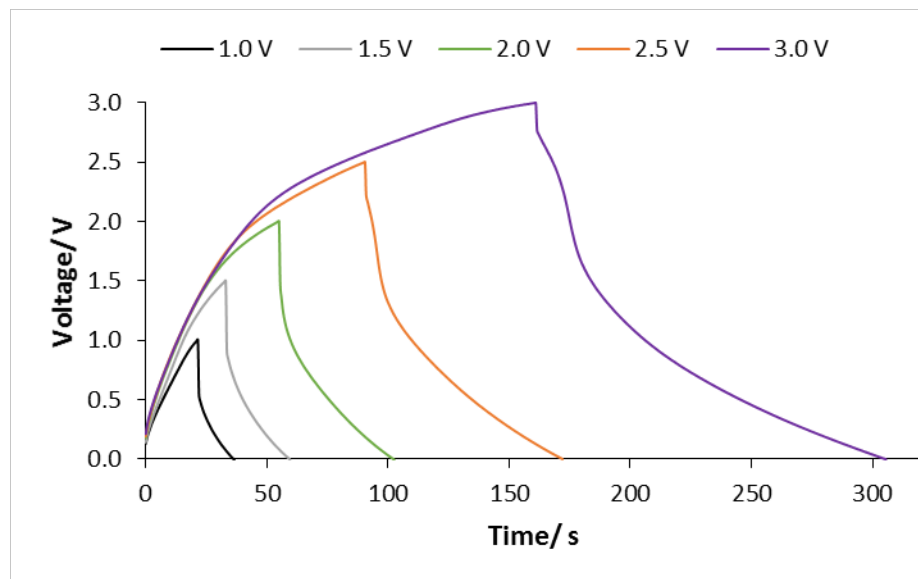


Figure 4.44 The third cycles of 1.0 A.g^{-1} GCD at different voltage ranges for an asymmetric supercapacitor.

The five cycles of 1.0 A.g^{-1} GCD at 3.0 V voltage range for an asymmetric SC are shown in Figure 4.45. It shows that the first cycle is slightly different, then the other four are very similar. It also shows that irreversible processes could be occurring as after five cycles the amount of charge stored/released on charge and discharge is not identical, this is referred to as the coulombic efficiency. The values of coulombic efficiency for the five cycles are listed in Table 4.7.

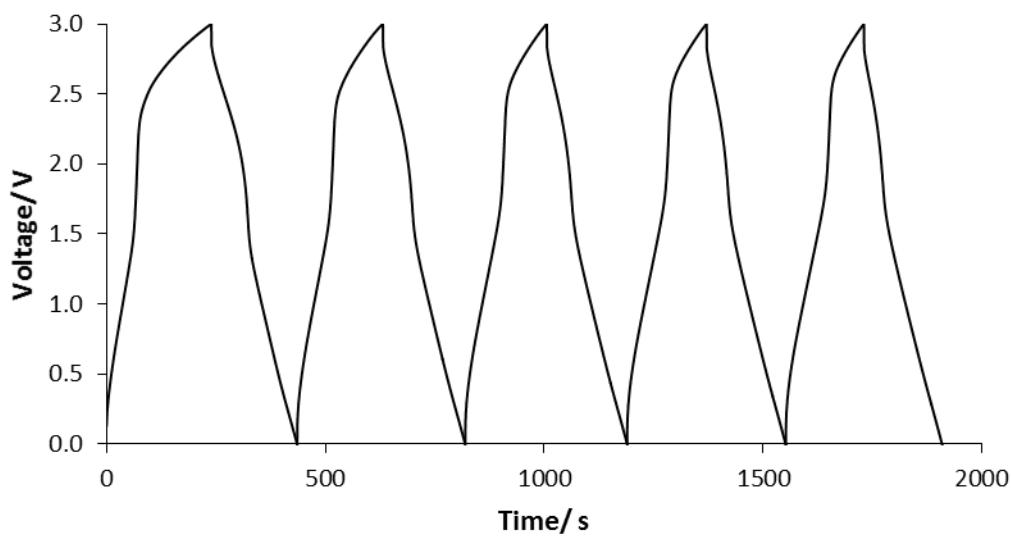


Figure 4.45 The five cycles of 1.0 A.g^{-1} GCD at 3.0 V voltage range for an asymmetric supercapacitor.

Cycle	Coulombic Efficiency/ %
1	71
2	87
3	90
4	91
5	92

Table 4.7 Coulombic efficiency calculated for the five charge/discharge cycles at 1.0 A.g^{-1} for 3.0 V window.

The values for C_{exptl} , C_{sp} , power density and energy density calculated for the asymmetric SC device are listed in Table 4.8. The values for C_{sp} are plotted against the voltage range in Figure 4.46, it shows that as the voltage range increases the C_{sp} increases. The Ragone plot for the values for power and energy density is shown in Figure 4.47, it shows that with increasing voltage range the power density and energy density increases. The highest values obtained for power density (356.3 W.kg^{-1}) and energy density (14.3 W.h.kg^{-1}) were for the asymmetric supercapacitor GCD measurements at a 3.0 V voltage range.

V range/ V	$C_{\text{sp}}/ \text{F.g}^{-1}$	$P/ \text{W.kg}^{-1}$	$E/ \text{W.h.kg}^{-1}$
1.0	30.0	85.2	0.4
1.5	35.3	140.9	1.0
2.0	47.5	205.5	2.7
2.5	65.2	287.3	6.5
3.0	96.3	356.3	14.3

Table 4.8 Results for asymmetric supercapacitor calculated from the third cycle of 1.0 A.g^{-1} GCD at voltage ranges 1.0-3.0 V.

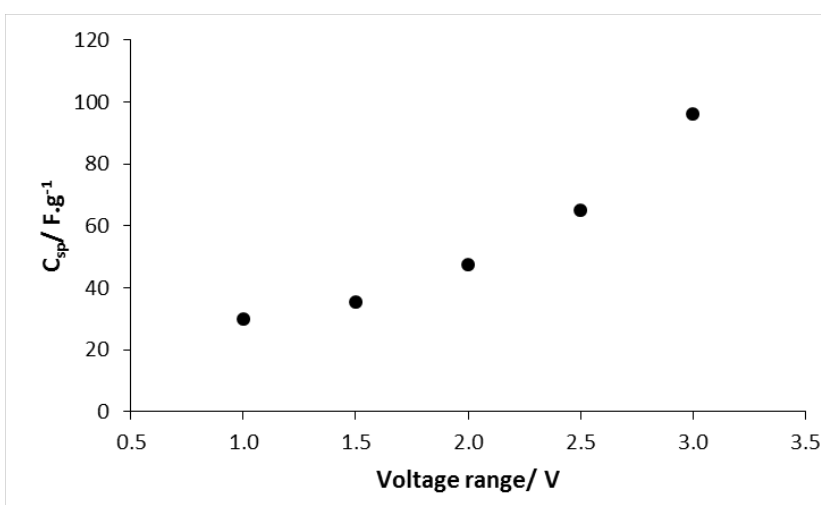


Figure 4.46 C_{sp} calculated for an asymmetric supercapacitor calculated from the third cycle of 1.0 A.g^{-1} GCD at voltage ranges 1.0-3.0 V.

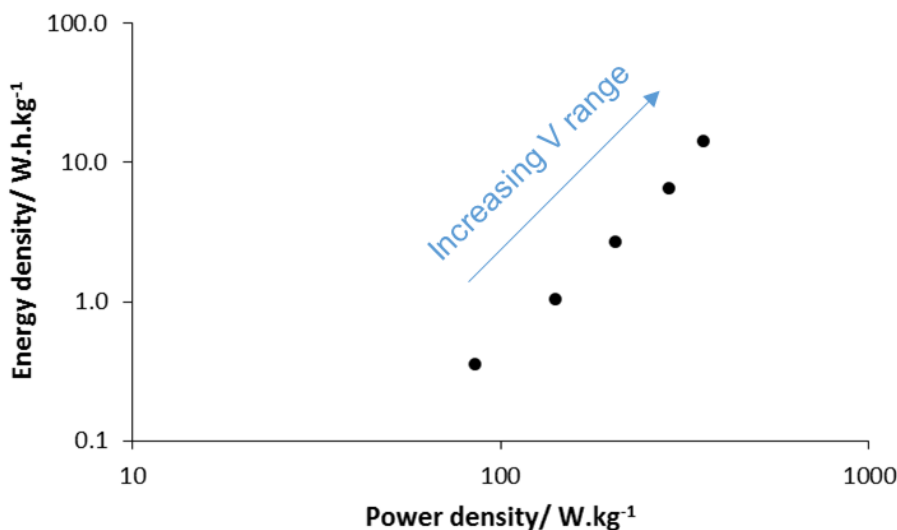


Figure 4.47 Ragone plot for an asymmetric supercapacitor calculated from the third cycle of 1.0 A.g^{-1} GCD at voltage ranges $1.0\text{--}3.0 \text{ V}$.

4.4 Discussion

4.4.1 Introduction

In this section the results of V_{10} electrode optimisation and preliminary SC testing are presented. The performance of the V_{10} SC is compared with that of other POM electrical energy storage devices, suggestions are made for future development. Throughout this section, comparisons of performance with other devices will be restricted to those employing analogous active materials i.e. purely inorganic POM salts and standard electrode preparation protocols.³³

4.4.2 Optimisation of the Decavanadate Electrode Capacitance

Several different methods were tested in an effort to prepare pure sodium decavanadate samples, and the procedure optimised by Johnson and Murmann provided the purest material according to ^{51}V solution NMR spectroscopy.⁴¹ Unfortunately, all of the methods involve preparation in an aqueous environment, and as a result, sodium decavanadate is presently known only as hydrates. Complete dehydration to anhydrous $\text{Na}_6\text{V}_{10}\text{O}_{28}$ would provide the optimum electrode material, since water is electrochemically active and leads to deleterious irreversible electrode processes. Decavanadate could be completely dehydrated thermally, but under those conditions the decavanadate ion was found to decompose completely. Drying at 80°C provided material that was 94% pure according to ^{51}V solution NMR spectroscopy. This material proved to be the octahydrate, $\text{Na}_6\text{V}_{10}\text{O}_{28} \cdot 8\text{H}_2\text{O}$.

Considerable effort was devoted to minimising the V_{10} crystallite size in order to maximise the specific surface area and hopefully obtain pseudocapacitive electrode material. Several methods were explored, including sonoprecipitation, sonofragmentation, grinding, ball milling, and high energy ball milling. High energy ball milling proved most effective, yielding ca. 100 nm particle size. Efforts to reproduce the preparation of ca. 25 nm particles reported by Yerra *et al.* were unsuccessful.⁴²

A variety of current collectors, conducting carbons, slurry solvents, and binders were examined in an effort to maximise the specific capacitance of V_{10} electrodes. Optimum performance was obtained using 0.203 mm thick carbon fiber paper, super P conductive carbon, NMP solvent, and PVDF binder. Some loadings used were found to yield higher specific capacitance, and a loading of 1 mg.cm⁻² yielded about 200 F.g⁻¹ according to chronopotentiometry using 0.5 A.g⁻¹ current and $\Delta V = 1.7$ V. Lower loadings were not considered for purely practical reasons, given that the mass of the current collector should not greatly exceed the mass of the active material. Also, significantly higher currents were not considered due to the high IR drop, and significantly lower currents were not considered since SC devices need to be charged and discharged at high currents.

The specific capacitance of ca. 200 F.g⁻¹ was not optimal but nonetheless suitable, for the following reasons. Although the decavanadate ion $V_{10}O_{28}^{6-}$ contains only V^{V} centres, its V^{IV} analogue is known in the form of the organic derivative $[V^{IV}V_{10}O_{16}\{(OCH_2)_3CCH_2CH_3\}_4]^{4-}$, where all the vanadium centres are in +4 oxidation state.⁵⁸ This can be conceptually viewed as $\{V_{10}O_{28}^{16-}\}\{(CH_2)_3CCH_2CH_3^{3+}\}_4$ i.e. alkylated ten-electron reduced $V_{10}O_{28}^{6-}$. If all of the vanadium centres in a decavanadate electrode are to be reduced to V^{IV} , a specific capacitance of 515 F.g⁻¹ would be obtained. The observed capacitance of about 200 F.g⁻¹ indicates that only about 40% of the vanadium centres have been reduced, corresponding to the reduction of four of the ten decavanadate centres on average.

The fact that the theoretical capacitance has not been attained is most easily understood by examining the results of the CP experiments performed with a dwell period at zero current inserted between charging, and discharging periods (See Figure 4.42). As shown in an expanded view of the dwell period, Figure 4.48, three

potential drops are observed, two IR drops at the beginning and end of the dwell period and a third potential drop during the dwell period. Since only a fraction of the V^{IV} centres have been oxidised to V^{V} at the end of the charging period, the potential drops during the dwell period as V^{V} centres near the current collector are replaced by V^{IV} centres through electron/ion diffusion. Two plausible mechanisms come to mind. First, diffusion could be occurring within crystallites as electrons from V^{IV} centres in the interior diffuse to the surface. Inter-crystallite diffusion presents a second possible mechanism.

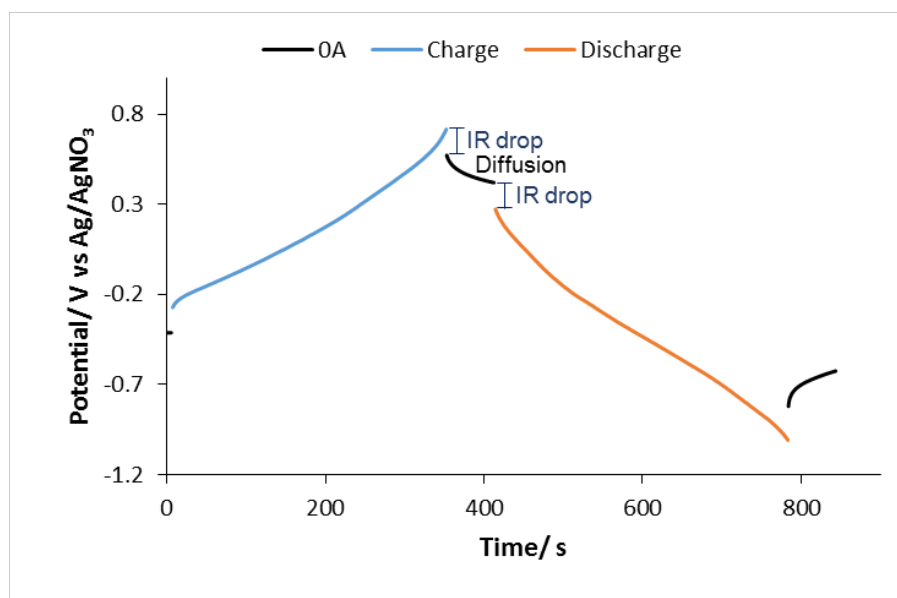


Figure 4.48 Expanded view of the dwell period chronopotentiometry experiment.

Since decavanadate crystallites are not conductive, electron transfer between crystallites is poor despite the presence of conducting carbon particles. As a result, crystallites near the current collector have a higher percentage of V^{V} than those further away. During the dwell time, diffusion of electrons and electrolyte ions through the matrix lowers the percentage of V^{V} crystallites near the current collector. This could explain the higher specific capacitance observed for thicker carbon fiber paper current collectors and lower loadings.

4.4.3 Polyoxometalate Hybrid Supercapacitors

Three POM hybrid SCs have been studied to date: (1) Yamada and Goodenough's $\text{H}_3\text{PMo}_{12}\text{O}_{40} \cdot n\text{H}_2\text{O}/\text{H}_x\text{RuO}_{2} \cdot n\text{H}_2\text{O}$ device,⁶ (2) an $\text{Na}_6\text{V}_{10}\text{O}_{28}/$ active carbon device reported by Chen *et al.*,⁴³ and (3) the present $\text{Na}_6\text{V}_{10}\text{O}_{28} \cdot 4\text{H}_2\text{O}/$ active carbon SC. At 138 mA.g^{-1} discharge rate, Yamada and Goodenough obtained a very high energy

density of 56 W.h.kg^{-1} but only modest power density (55 W.kg^{-1}) relative to performance standards plotted in Figure 4.49. At 694 mA.g^{-1} discharge rate, 279 W.kg^{-1} power was observed with only slightly lower energy, 45 W.h.kg^{-1} . Comparable results were obtained in the present study without the use of RuO_2 : maximum energy density of 14 W.h.kg^{-1} at 1.0 A.g^{-1} with a 3.0 V window and 356 W.kg^{-1} power density. However, the $\text{H}_3\text{PMo}_{12}\text{O}_{40}.n\text{H}_2\text{O}$ device, was far more stable, maintaining good performance after 30 charge/discharge cycles while the $\text{Na}_6\text{V}_{10}\text{O}_{28.4}\text{H}_2\text{O}$ device showed moderate coulombic efficiency during the first five cycles (See Section 4.3.6).

The instability of the vanadate system is most likely due to water electrolysis given the large potential window. The phosphomolybdate system operated in an aqueous environment using a much lower, 0.8 V window.

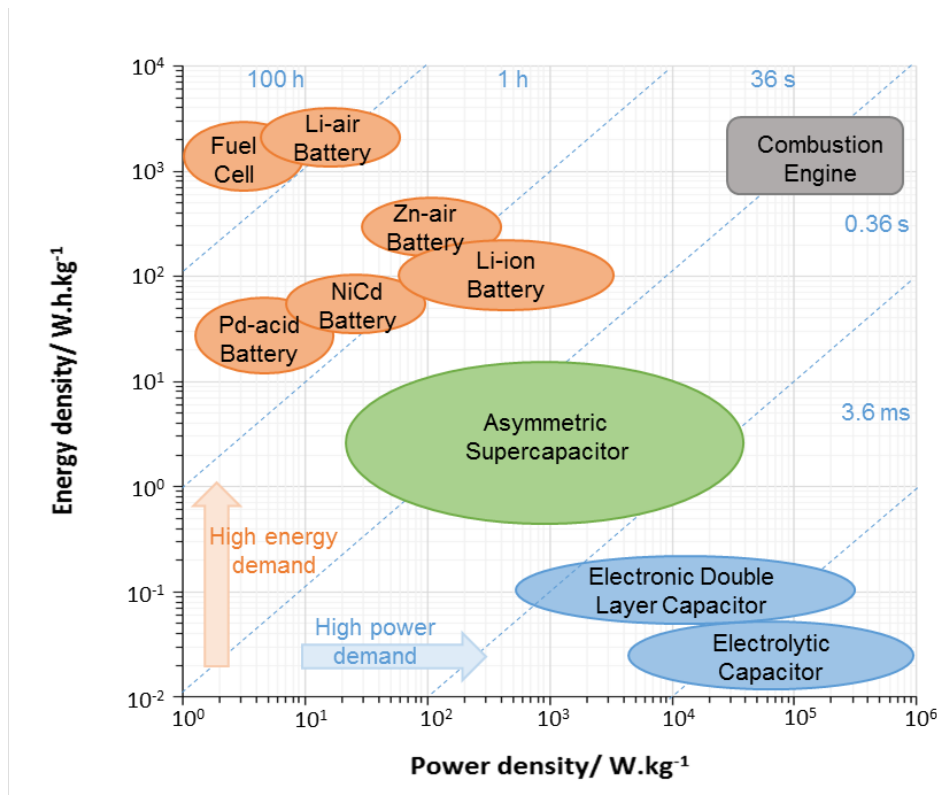


Figure 4.49 Ragone plot adapted from ref ⁵⁹.

The $\text{Na}_6\text{V}_{10}\text{O}_{28}$ /active carbon SC reported by Chen *et al.* showed remarkable performance with 22 W.h.kg^{-1} and 6238 W.kg^{-1} at 10 A.g^{-1} .⁴³ The discrepancy between these results and the results of the present study can be accounted for by comparing scanning electron micrographs of the “ $\text{Na}_6\text{V}_{10}\text{O}_{28}$ ” electrode material

(Figure 4.50a) and micrographs of $\text{Na}_6\text{V}_{10}\text{O}_{28}\text{.}n\text{H}_2\text{O}$ (Figure 4.49b) prepared under the same synthetic conditions described by Chen *et al.*: rod-like morphology was not observed.⁴³ Professor Ulrich Kortz finally provided a sample of the material used in the “ $\text{Na}_6\text{V}_{10}\text{O}_{28}$ ” electrode described by Chen *et al.*,⁴³ and this material proved to be largely insoluble in water, although $^{51}\text{V}\{^1\text{H}\}$ NMR spectra obtained after aqueous extraction did reveal the presence of some decavanadate. Given that V_2O_5 can have rod-like morphology,^{60, 61} the active electrode material studied by Chen *et al.*⁴³ was most likely V_2O_5 , a material whose electrochemistry has been studied extensively.^{61, 62}

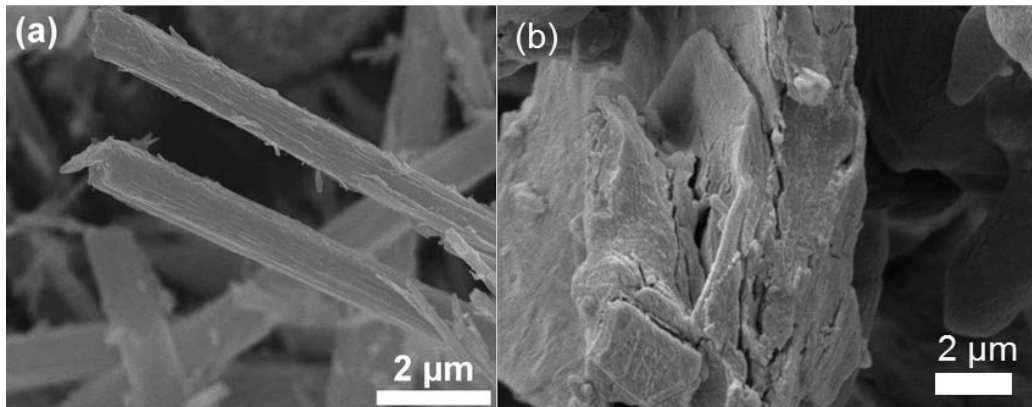


Figure 4.50 SEM images of Chen *et al.* $\text{Na}_6\text{V}_{10}\text{O}_{28}\text{.}n\text{H}_2\text{O}$ ⁴³ (a) and $\text{Na}_6\text{V}_{10}\text{O}_{28}\text{.}n\text{H}_2\text{O}$ prepared under the same synthetic conditions described by Chen *et al.* (b).

4.4.4 Polyoxometalate Batteries

Polyoxometalate electrical energy storage devices have been classified in the literature according to the anode materials employed. In the case of EDL (active carbon) or pseudocapacitive ($\text{RuO}_2\text{.}n\text{H}_2\text{O}$) electrode, the device is classified as a SC. In the case of Li or Na anode, the device is classified as a battery on the assumption that charge in and on cathode is stored primarily in the bulk.⁸ At rapid charge/discharge rate, however, charge may be stored primarily at the cathode surface qualifying it as a capacitor electrode.⁸ The distinction between battery and SC can therefore become blurred. If the performance of a device is evaluated in terms of energy and power, the distinction between a high energy capacitor and a high power battery is of no practical consequence. The focus of this section is therefore on the performance of POM batteries at high discharge rate.

Eleven POM batteries have been discussed in the literature that incorporate simple inorganic POM salts in an activated carbon/ binder matrix and provide charge/

discharge rates that for estimates of energy and power (see Table 4.9). Several of these can be discounted. First, Anjass *et al.* have demonstrated that dehydration of $\text{Li}_6\text{V}_{10}\text{O}_{28} \cdot 16\text{H}_2\text{O}$ at 200 °C yielded significant amounts of LiV_3O_8 according to PXRD analysis.⁵² Since the “ $\text{Li}_6[\text{V}_{10}\text{O}_{28}]$ ” described in reference 64 (Table 4.9 entry 1) was annealed at 240 °C, the cathode material is most likely contaminated. Second, Wang *et al.* have shown that $\text{Li}_7[\text{V}_{15}\text{O}_{36}(\text{CO}_3)]$ is converted to $\gamma\text{-LiV}_2\text{O}_5$ by annealing at 200 °C.⁶³ Since the “ $\text{Li}_7[\text{V}_{15}\text{O}_{36}(\text{CO}_3)]$ ” studied in Table 4.9 entries 4, 9 and 10 was annealed at 200 °C, the identity of this cathode material must also be called into question. Finally SEM images of the “ $\text{Na}_6\text{V}_{10}\text{O}_{28} \cdot 16\text{H}_2\text{O}$ ” powder shown in reference 67 (Table 4.9 entry 5) identify this material as the same material used in reference 43 (see Figure 4.50a) and therefore largely insoluble material, presumably V_2O_5 (see Section 4.4.3).

	Year ^{REF}	Cathode composition	Anode composition	Electrolyte
1	2007 ⁶⁴	$\text{Li}_6[\text{V}_{10}\text{O}_{28}]$, acetylene black, PVDF, 70:20:10	Li metal	1 M LiPF_6 in 1:1 EC-DMC
2	2013 ⁶⁵	$\text{K}_7[\text{NiV}_{13}\text{O}_{38}]$, acetylene black, PVDF 32:64:4	Li metal	1 M LiPF_6 in 7:3 EC-DEC
3	2014 ⁶⁶	$\text{K}_7[\text{MnV}_{13}\text{O}_{38}]$, acetylene black, PVDF, 48:48:4	Li metal	1 M LiPF_6 in 7:3 EC-DEC
4	2015 ⁵⁶	$\text{Li}_7[\text{V}_{15}\text{O}_{36}(\text{CO}_3)]$, acetylene black, PVDF, 70:20:10	Li metal	1 M LiPF_6 in 1:1:1 EC-DMC-EMC
5	2015 ⁶⁷	$\text{Na}_6[\text{V}_{10}\text{O}_{28}]$, acetylene black, PVDF, 60:20:20	Na metal	1 M NaClO_4 in 1:1 EC-PC
6	2017 ⁶⁸	$\text{K}_4\text{Na}_2[\text{V}_{10}\text{O}_{28}]$, acetylene black, PTFE, 60:30:10	Li metal	1 M LiPF_6 in 1:1 EC-DMC
7	2017 ⁶⁸	$\text{Mg}_2(\text{NH}_4)_2[\text{V}_{10}\text{O}_{28}]$, acetylene black, PTFE, 60:30:10	Li metal	1 M LiPF_6 in 1:1 EC-DMC
8	2017 ⁶⁹	$\text{Na}_2\text{H}_8[\text{MnV}_{13}\text{O}_{38}]$, acetylene black, PVDF, 70:20:10	Na metal	1 M NaClO_4 in 1:1 PC-EC
9	2018 ⁷⁰	$\text{Li}_7[\text{V}_{15}\text{O}_{36}(\text{CO}_3)]$, acetylene black, PVDF, 70:20:10	$\text{Li}_7[\text{V}_{15}\text{O}_{36}(\text{CO}_3)]$, acetylene black, PVDF, 70:20:10	1 M LiPF_6 in 1:1:1 EC-DMC-EMC
10	2018 ⁷⁰	$\text{Li}_7[\text{V}_{15}\text{O}_{36}(\text{CO}_3)]$, acetylene black, PVDF, 70:20:10	Na metal	1 M NaClO_4 in 49:49:2 EC-DEC-fluorinated EC
11	2018 ⁷¹	$\text{Na}_7[\text{H}_2\text{PV}_{14}\text{O}_{42}]$, carbon black, PVDF 70:20:10	Na metal	1 M NaClO_4 in 1:1 PC-EC

Table 4.9 Literature results of POM containing batteries.

Of the eleven studies listed in Table 4.9, only six cannot be discounted: studies of three mixed-metal triskaidecavanadate salts (Table 4.9 entries 2, 3 and 8), two studies of decavanadate salts (Table 4.9 entries 6 and 7), and one phosphovanadate study (Table 4.9 entry 11). Unfortunately, the performance of these batteries are unknown i.e. energy density and power density were not reported in any of the studies. However, some idea of their performance can be estimated when galvanostatic discharge curves are available.

The $\text{K}_7[\text{MnV}_{13}\text{O}_{38}]$ (KMV) device (Table 4.9 entry 3) provides a good example of how estimates can be made. The charge discharge curves reported are reproduced in Figure 4.50. The discharge curve measured for nanoparticulate KMV (n-KMV), at 167 mA.g^{-1} is quite linear, and therefore the area under the curve will provide a good estimate of energy, $E_s \approx \frac{1}{2} Q(\Delta V)$, where the capacity Q was reported as 225 mA.h.g^{-1} . Reading from the graph in Figure 4.51, the voltage window of the discharge is ca. 1.5 V and $E_s \approx 169 \text{ W.h.kg}^{-1}$ and given the discharge rate of 167 mA.g^{-1} , P_s is calculated to be 125 W.kg^{-1} . Consulting the Ragone plot in Figure 4.49, these are reasonable values for a battery. However, this battery exhibits a voltage drop of ca. 1.2 V between charge and discharge (indicated on the graph with the red double headed arrow), a value comparable with the voltage window (1.5 V). In other words, relatively high power could be obtained but only by using an unrealistically high current density, leading to very high polarisation. A large potential drop was also obtained at the much lower current density of 17 mA.g^{-1} (indicated on the graph with the green double headed arrow). A similar situation was observed for the devices reported in references 66 and 69. (Table 4.9 entries 3 and 8).

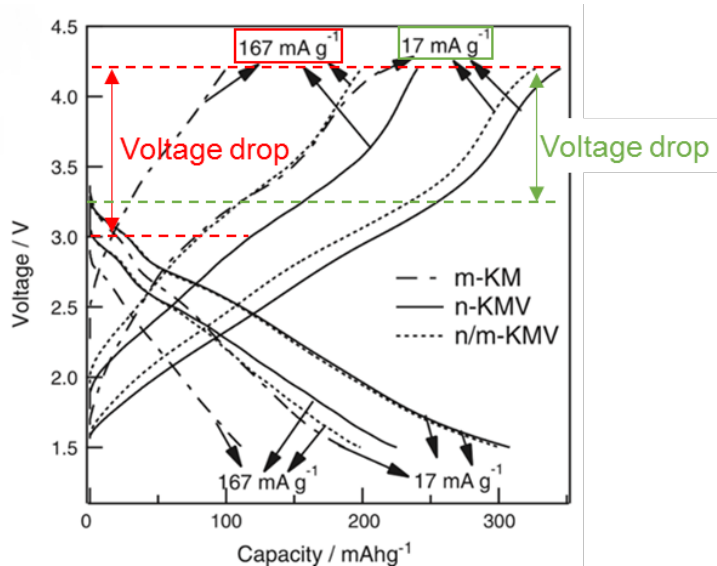


Figure 4.51 The first galvanostatic charge discharge curves of m-KM (microsized KMV), n-KMV (nanoparticulate KMV) and n/m-KMV (1:1 mixture of nanoparticulate and mircosized KMV) with the corresponding current densities labelled, adapted from ref ⁶⁶.

An approximately linear discharge curve was also observed for the magnesium ammonium decavanadate battery described in reference 68 (Table 4.9 entry 7). Here, a capacity of 198.8 mA.h.g⁻¹ was observed at 50 mA.g⁻¹ over a ca. 1.75 V window, implying $E_s \approx 174 \text{ W.h.kg}^{-1}$ and $P_s \approx 44 \text{ W.kg}^{-1}$. But here again, an unrealistically high potential drop of ca. 1 V was observed between charge and discharge.

Discharge curves measured at a lower current of 25 mA.g⁻¹ were provided for the phosphovanadate battery reported in reference 71 (Table 4.9 entry 11). As expected, a far lower IR drop was observed, and although the discharge curves were quite non-linear, energy in the 300-400 W.h.kg⁻¹ range and power in the 25-50 W.kg⁻¹ range can be estimated at a 25 mA.g⁻¹ discharge.

To summarise, POM batteries can provide significantly greater energy density than POM SCs but with significantly lower power density, as expected.

4.5 Outlook

Two questions remain to be further addressed upon conclusion of the research associated with this thesis. Firstly, are POMs the true active materials in POM-based energy storage devices or are they merely precursors? Secondly, how may the performance of POM-based devices be improved to the point where they are viable in a practical sense?

Degradation of crystalline POM salts used in energy storage devices can occur either during electrode preparation or during charge-discharge cycling. All of the POMs listed in Table 4.9 (Section 4.4.4) were prepared as hydrated salts, and when dehydration occurred, it occurred upon thermal dehydration prior to electrode preparation. Although degradation was avoided in the present research by limiting the dehydration temperature, the resulting materials still contained water. This problem could be circumvented either by working in an aqueous environment,⁶ or by recrystallisation from the solvent employed as the electrolyte or another non-aqueous solvent. For example, $\text{Na}_6\text{V}_{10}\text{O}_{28} \cdot 8\text{H}_2\text{O}$ is reasonably soluble in propylene carbonate and could presumably be recrystallised in that solvent to form a propylene carbonate solvate. The question of degradation during charge-discharge cycling is far more difficult to detect since the initially crystalline POM has been shown to lose crystallinity in the devices examined to date and PXRD is not applicable.⁵⁹ FTIR spectroscopy does not require crystalline samples and has been successfully applied in at least one case to show that at least some $[\text{MnV}_{13}\text{O}_{38}]^{10-}$ active material survives one charge-discharge cycle.⁶⁹ It would be useful to record FTIR on the V_{10} salts before and after several charge-discharge cycles, this would require extracting the V_{10} from the slurry or recording FTIR spectra on the V_{10} within the slurry and subtracting out the other components. Long term stability testing would also be a useful indicator of POM and/or electrode degradation, in this study only five charge-discharge cycles were recorded for each electrode due to time constraints; hundreds or even thousands of cycles would be necessary to fully investigate POM and/or electrode stability.

Both the energy and power performance of the decavanadate SC leave much room for improvement. These could be enhanced in the present system through optimisation of the current density and voltage window. More generally, however, other POMs may be more suitable than the decavanadate anion. Compounds such as $\text{K}_7\text{MnV}_{13}\text{O}_{38}$ can be crystallised as nanocrystals with well-defined morphology such that higher specific surface area are obtained.⁶⁶ Also, several porous POM salts are known, and these might provide for rapid cation diffusion during charge-discharge cycling.⁷² Other possible POMs to investigate are $\text{Na}_7\text{H}_2[\text{PV}_{14}\text{O}_{42}]$, $\text{H}_3\text{PW}_{12}\text{O}_{40}$, $\text{H}_4\text{SiW}_{12}\text{O}_{40}$, $\text{H}_3\text{PMo}_{12}\text{O}_{40}$ and $\text{H}_4\text{SiMo}_{12}\text{O}_{40}$. In order to fully optimise the SC device it is necessary to fully investigate all the different variables further. For

example; a wider variety of conductive carbon, binder, solvent, ratio of materials in the slurry, electrolyte composition. In order to consider the SC as a real device there would need to be a significant scale-up, ca. 10 mg.cm⁻² of active material on the electrodes, as well as to take into account all components when calculating specific capacity, energy density and power density, not just the active materials but the separator, electrolyte, current collectors, binder and carbon too.⁷³ Finally, the issue of rapid electron transport should be considered. Given that all known POM salts are insulators, they join the class of other important insulating oxides such as MnO₂ that must rely on nanostructured active materials for achieving high power ratings.⁵⁷

4.6 References

1. J. B. Goodenough and K.-S. Park, *J. Am. Chem. Soc.*, 2013, **135**, 1167.
2. B. D. McCloskey, *J. Phys. Chem. Lett.*, 2015, **6**, 3592.
3. V. S. Bagotsky, A. M. Skundin and Y. M. Volkovich, *Batteries, Fuel Cells, and Supercapacitors*, John Wiley & Sons, Hoboken, New Jersey, First edn., 2015.
4. R. B. Marichi, V. Sahu, R. K. Sharma and G. Singh, *Efficient, Sustainable, and Clean Energy Storage in Supercapacitors Using Biomass-Derived Carbon Materials*, Springer International Publishing, Cham, 2017.
5. P. Simon, Y. Gogotsi and B. Dunn, *Science*, 2014, **343**, 1210.
6. A. Yamada and J. B. Goodenough, *J. Electrochem. Soc.*, 1998, **145**, 737.
7. P. A. Tipler, *Physics for Scientists and Engineers*, Worth Publishers, Inc., New York, Third edn., 1991.
8. J. B. Goodenough, H. Y. Lee and V. Manivannan, *Mat. Res. Soc. Symp. Proc.*, 1999, **548**, 655.
9. M. Okubo, E. Hosono, J. Kim, M. Enomoto, N. Kojima, T. Kudo, H. Zhou and I. Honma, *J. Am. Chem. Soc.*, 2007, **129**, 7444.
10. A. Yu, V. Chabot and J. Zhang, *Electrochemical supercapacitors for energy storage and delivery: Fundamentals and applications*, CRC Press, Boca Raton, First edn., 2013.
11. V. Augustyn, P. Simon and B. Dunn, *Energy Environ. Sci.*, 2014, **7**, 1597.
12. P. Kurzweil, *Electrochemical Hybrid Capacitors*, Elsevier B. V., 2009.
13. S. R. Sivakkumar and A. G. Pandolfo, *Electrochim. Acta*, 2012, **65**, 280.
14. T. Brousse, P.-L. Taberna, O. Crosnier, R. Dugas, P. Guillemet, Y. Scudeller, Y. Zhou, F. Favier, D. Bélanger and P. Simon, *J. Power Sources*, 2007, **173**, 633.
15. B. E. Conway, *Electrochemical Supercapacitors: Scientific fundamentals and technological applications*, Springer Science New York, First edn., 1999.
16. J. W. Long, D. Bélanger, T. Brousse, W. Sugimoto, M. B. Sassin and O. Crosnier, *MRS Bull.*, 2011, **36**, 513.
17. A. J. Smith, J. C. Burns, S. Trussler and J. R. Dahn, *J. Electrochem. Soc.*, 2010, **157**, A196.
18. J. R. Dahn, J. C. Burns and D. A. Stevens, *Electrochem. Soc. Interface*, 2016, **25**, 75.

19. P. J. Kulesza, L. R. Faulkner, J. Chen and W. G. Klemperer, *J. Am. Chem. Soc.*, 1991, **113**, 379.
20. L. Pettersson, B. Hedman, I. Andersson and N. Ingri, *Chem. Scr.*, 1983, **22**, 254.
21. H. R. Sun, S. Y. Zhang, J. Q. Xu, G. Y. Yang and T. S. Shi, *J. Electroanal. Chem.*, 1998, **455**, 57.
22. B. D. Cullity and S. R. Stock, *Elements of X-ray Diffraction*, Prentice Hall, New York, Third edn., 2001.
23. A. Ul-Hamid, *A beginners' guide to scanning electron microscopy*, Springer, Cham, Gewerbestrasse 11, 6330 Cham, Switzerland, First edn., 2018.
24. W. M. Groenewoud, *Characterisation of Polymers by Thermal Analysis*, Elsevier Science B.V., Amsterdam, 2001.
25. A. J. Bard and L. R. Faulkner, *Electrochemical Methods: Fundamentals and Applications*, John Wiley & Sons Ltd, 2001.
26. G. A. Tsigdinos and C. J. Hallada, *J. less-common met.*, 1974, **36**, 79.
27. M. D. Luque de Castro and F. Priego-Capote, *Ultrason. Sonochem.*, 2007, **14**, 717.
28. J. R. Sander, B. W. Zeiger and K. S. Suslick, *Ultrason. Sonochem.*, 2014, **21**, 1908.
29. B. W. Zeiger and K. S. Suslick, *J. Am. Chem. Soc.*, 2011, **133**, 14530.
30. S. K. Bhangu and M. Ashokkumar, *Top Curr. Chem.*, 2016, **374**, 56.
31. J. Stojakovic, B. S. Farris and L. R. MacGillivray, *Chem. Commun.*, 2012, **48**, 7958.
32. M. Dindarsafa, A. Khataee, B. Kaymak, B. Vahid, A. Karimi and A. Rahmani, *Ultrason. Sonochem.*, 2017, **34**, 389.
33. C. Cao, X. Yuan, S. Zhao, Y. Wu and T. van Ree, *Assembly Processes for Lithium-Ion Batteries* CRC Press, Boca Raton, 2015.
34. A. G. Pandolfo and A. F. Hollenkamp, *J. Power Sources*, 2006, **157**, 11.
35. J. Chen, J. Liu, Y. Qi, T. Sun and X. Li, *J. Electrochem. Soc.*, 2013, **160**, A1502.
36. A. Mu, J. Li, W. Chen, X. Sang, Z. Su and E. Wang, *Inorg. Chem. Commun.*, 2015, **55**, 149.
37. S. Zhang and N. Pan, *Adv. Energy Mater.*, 2015, **5**, 1401401.

38. M. Arulepp, J. Leis, M. Lätt, F. Miller, K. Rumma, E. Lust and A. F. Burke, *J. Power Sources*, 2006, **162**, 1460.
39. M. Winter and R. J. Brodd, *Chem. Rev.*, 2004, **104**, 4245.
40. F. Beguin, V. Presser, A. Balducci and E. Frackowiak, *Adv. Mater.*, 2014, **26**, 2219.
41. G. K. Johnson and R. K. Murmann, *Inorg. Synth.*, 1979, **19**, 142.
42. S. Yerra, B. K. Tripuramallu and S. K. Das, *Polyhedron*, 2014, **81**, 147.
43. H.-Y. Chen, G. Wee, R. Al-Oweini, J. Friedl, K. S. Tan, Y. Wang, C. L. Wong, U. Kortz, U. Stimming and M. Srinivasan, *ChemPhysChem*, 2014, **15**, 2162.
44. P. J. Domaille, *J. Am. Chem. Soc.*, 1984, **106**, 7677.
45. C. J. Besecker, W. G. Klemperer, D. J. Maltbie and D. A. Wright, *Inorg. Chem.*, 1985, **24**, 1027.
46. K. F. Juhr, J. Fuchs and R. Oherhauser, *Chem. Ber.*, 1968, **101**, 482.
47. U. Lee, H. C. Joo, K. M. Park, S. S. Mal, U. Kortz, B. Keita and L. Nadjo, *Angew. Chem. Int. Ed. Engl.*, 2008, **47**, 793.
48. J.-N. Xu, G.-Y. Yang, H.-R. Sun, T.-G. Wang, J.-Q. Xu and Q.-J. Wu, *Jiegou Huaxue*, 1996, **15**, x19.
49. A. Durif, M. T. Averbuch-Pouchot and J. C. Guitel, *Acta Cryst.*, 1980, **B36**, 680.
50. H.-X. Guo and Z.-L. Yao, *Acta Cryst. C*, 2007, **63**, i51.
51. J. Nilsson, E. Nordlander, U. Behrens and D. Rehder, *Acta Cryst. E*, 2010, **66**, i30.
52. M. H. Anjass, M. Deisböck, S. Greiner, M. Fichtner and C. Streb, *Chem. Electro. Chem.*, 2019, **6**, 398.
53. V. S. Nalajala and V. S. Moholkar, *Ultrason. Sonochem.*, 2011, **18**, 345.
54. M. E. Spahr, *Carbon-Conductive Additives for Lithium-Ion Batteries*, 2009.
55. A. Basch, R. Horn and J. O. Besenhard, *Colloids and Surfaces A: Physicochem. Eng. Aspects*, 2005, **253**, 155.
56. J. J. Chen, M. D. Symes, S. C. Fan, M. S. Zheng, H. N. Miras, Q. F. Dong and L. Cronin, *Adv. Mater.*, 2015, **27**, 4649.
57. Y. Hu, Y. Wu and J. Wang, *Adv. Mater.*, 2018, **30**, 1802569.
58. M. I. Khan, Q. Chen, D. P. Goshorn and J. Zubieta, *Inorg. Chem.*, 1993, **32**, 672.

59. Y. Shao, M. F. El-Kady, J. Sun, Y. Li, Q. Zhang, M. Zhu, H. Wang, B. Dunn and R. B. Kaner, *Chem. Rev.*, 2018, **118**, 9233.
60. J. Livage and J. Lemerle, *Ann. Rev. Mater. Sci.*, 1982, **12**, 103.
61. N. A. Chernova, M. Roppolo, A. C. Dillon and M. S. Whittingham, *J. Mater. Chem.*, 2009, **19**, 2526.
62. D. McNulty, D. N. Buckley and C. O'Dwyer, *J. Power Sources*, 2014, **267**, 831.
63. H. Wang, J. Isobe, T. Shimizu, D. Matsumura, T. Ina and H. Yoshikawa, *J. Power Sources*, 2017, **360**, 150.
64. A. Xie, C.-A. Ma, L. Wang and Y. Chu, *Electrochim. Acta*, 2007, **52**, 2945.
65. E. Ni, S. Uematsu, Z. Quan and N. Sonoyama, *J. Nanopart. Res.*, 2013, **15**, 1732.
66. E. Ni, S. Uematsu and N. Sonoyama, *Solid State Ionics*, 2014, **268**, 222.
67. S. Hartung, N. Bucher, H.-Y. Chen, R. Al-Oweini, S. Sreejith, P. Borah, Z. Yanli, U. Kortz, U. Stimming, H. E. Hoster and M. Srinivasan, *J. Power Sources*, 2015, **288**, 270.
68. S. Lu, Y. Lv, W. Ma, X. Lei, R. Zhang, H. Liu and X. Liu, *Inorg. Chem. Front.*, 2017, **4**, 2012.
69. J. Liu, Z. Chen, S. Chen, B. Zhang, J. Wang, H. Wang, B. Tian, M. Chen, X. Fan, Y. Huang, T. C. Sum, J. Lin and Z. X. Shen, *ACS Nano*, 2017, **11**, 6911.
70. J.-J. Chen, J.-C. Ye, X.-G. Zhang, M. D. Symes, S.-C. Fan, D.-L. Long, M.-S. Zheng, D.-Y. Wu, L. Cronin and Q.-F. Dong, *Adv. Energy Mater.*, 2018, **8**, 1701021.
71. C.-C. Lin, W.-H. Lin, S.-C. Huang, C.-W. Hu, T.-Y. Chen, C.-T. Hsu, H. Yang, A. Haider, Z. Lin, U. Kortz, U. Stimming and H.-Y. Chen, *Adv. Mater. Interfaces*, 2018, **5**, 1800491.
72. S. Uchida, *Struct. Bond.*, 2018, **176**, 65.
73. Y. Gogotsi and P. Simon, *Science*, 2011, **334**, 917.

Chapter 5

Experimental

Chapter 5 Experimental

5.1 Characterisation Techniques

5.1.1 NMR Spectroscopy

$^{31}\text{P}\{^1\text{H}\}$ NMR spectra were recorded on a Bruker Avance spectrometer at a magnetic field of 7.05 Tesla and a frequency of 121.495 MHz, using a 10.40 μs pulse. Some spectra were obtained using a Bruker Avance spectrometer at a magnetic field of 11.7 Tesla. Chemical shifts are quoted in ppm relative to external 85% H_3PO_4 . Dry deuterated solvents were used to obtain the spectra lock.

$^{51}\text{V}\{^1\text{H}\}$ NMR spectra were recorded on a Bruker Avance spectrometer at a magnetic field of 7.05 Tesla and a frequency of 78.90 MHz, using a 9.20 μs pulse. Chemical shifts are quoted in ppm relative to external VOCl_3 90% in C_6D_6 . Deuterium oxide (99%) was used to obtain the spectra lock. The NMR samples were a concentration of 10 mg in 0.5 mL solvent, unless otherwise stated.

MAS NMR spectra were recorded on a Bruker Avance spectrometer at a magnetic field of 11.7 Tesla with MAS 10 kHz. ^7Li with a frequency of 194.20 MHz, ^{23}Na with a frequency of 132.18 MHz and ^{31}P with a frequency of 202.28 MHz. 1 M $\text{LiCl}(\text{aq})$ was used as the standard for ^7Li MAS NMR. 0.1 M $\text{NaCl}(\text{aq})$ was used as the standard for ^{23}Na MAS NMR. TMS was used as a standard for ^{31}P MAS NMR.

Errors: ± 0.2 Hz for sharp peaks, line widths (fwhm) of ca. 10 Hz and ± 100 Hz for the broader peaks, line widths (fwhm) of ca. 1000 Hz.

5.1.2 FTIR Spectroscopy

Infrared spectra were recorded using the Platinum ATR module on a Bruker Alpha spectrometer (4000 – 400 cm^{-1}) with a resolution of 3 cm^{-1} . IR spectra were recorded for solid samples which were obtained after vacuum drying for at least 6 hr.

5.1.3 UV-Vis Spectroscopy

UV-Vis spectra were recorded on an Ocean Optics USB2000+ spectrometer using an Ocean Optics tungsten-halogen bulb. All solutions measured were 0.25 mM in PC.

5.1.4 X-Ray Powder Diffraction

PANalytical X'Pert Pro Multipurpose Diffractometer (MPD).

5.1.5 Single Crystal X-Ray Diffraction Analysis

Crystal structure data for all samples were collected on a Xcalibur, Atlas, Gemini ultra-diffractometer equipped with a fine-focus sealed X-ray tube ($\lambda_{\text{MoK}\alpha} = 0.71073 \text{ \AA}$ for $(\text{TBA})_2[\text{PMo}_{12}\text{O}_{40}\text{Sb}_2]$, $(\text{TBA})_3[\text{PMo}_{12}\text{O}_{40}\text{Sb}_2]$ and $(\text{TBA})_3[\text{PMo}_{12}\text{O}_{40}\text{Zn}(\text{dmsO})_2]$); $\lambda_{\text{CuK}\alpha} = 1.54184 \text{ \AA}$ for $(\text{TBA})_3[\text{PMo}_{12}\text{O}_{40}\text{Bi}(\text{dmsO})_4]$) and an Oxford Cryosystems CryostreamPlus open-flow N_2 cooling device. Cell refinement, data collection and data reduction were undertaken via software CrysAlisPro.¹ Intensities were corrected for absorption using the CrysAlisPro software.¹ Analytical numeric absorption correction using a multifaceted crystal model based on expressions derived by R.C. Clark & J.S. Reid.² Empirical absorption correction using spherical harmonics, implemented in SCALE3 ABSPACK scaling algorithm. Using Olex2,³ the structure was solved using ShelXT,⁴ and refined by XL.⁵

5.1.6 Thermogravimetric Analysis

Perkin Elmer TGA 4000. Nitrogen gas flow 40.0 mL/min. Sample loaded into crucible. Temperature held at 30.0 °C for 5 min. The sample was then heated from 30.0 °C to 800.0 °C at a rate of 10.0 °C /min. The temperature was then held at 800.0 °C for 5 min.

5.1.7 Scanning Electron Microscopy

The instrument used was a Tescan Vega 3LMU. The samples were dry loaded on to the mounts then gold coated.

5.1.8 Solution Cyclic Voltammetry

Cyclic voltammetry was measured using Ivium A25356. 100 mM electrolyte solution of $(\text{TBA})(\text{BF}_4)$ in dry MeCN. Ag wire RE, GC disc WE and Pt wire CE. All analytes were 1 mM solutions dissolved in the electrolyte solution.

Biologic SP-300 potentiostat and an Autolab PGSTAT204 potentiostat. The concentration of the V_{10} solution used was 1 mM in a 0.4 M CH_3COONa and acetic acid buffer at pH 5.0. GC disc WE, Pt wire CE and Ag/AgCl in 3 M NaCl aqueous solution RE.

5.1.9 Solid State Electrochemistry

Autolab PGSTAT204 potentiostat. For three electrode experiments: 1 M LiClO_4 in PC electrolyte, Ag/AgNO₃ non-aqueous RE (1 mM AgNO₃ in 100 mM $(\text{TBA})(\text{BF}_4)$ MeCN), Pt CE. WE as described in Section 5.4.4. CV were recorded at 5 mV.s⁻¹ scan

rate, voltage range -1.0 to $+0.7$ V vs Ag/AgNO₃. Chronopotentiometry were recorded at 0.5 A.g⁻¹ current density, voltage range -1.0 to $+0.7$ V vs Ag/NO₃. Two electrode experiments: two 18 mm disc electrodes with separator and 250 μ L 1 M LiClO₄ PC electrolyte in EL-Cell. CV were recorded at scan rates; 20 mV.s⁻¹, 0 to $+1.7$ V voltage range. GCD at current densities; 1.0 A.g⁻¹, 1.0 - 3.0 V voltage range.

5.2 Chapter 2

5.2.1 Materials

Materials were purchased from suppliers as listed below in Table 5.1.

Chemical	Supplier
Na ₂ MoO ₄ .2H ₂ O	Fisher Scientific
85% H ₃ PO ₄	Sigma Aldrich
1,4-dioxane	Fisher Scientific
Conc. HNO ₃	Fisher Scientific
(TBA)(Br)	Fisher Scientific
IMS	Fisher Scientific
Diethyl ether	Fisher Scientific
MeCN	Fisher Scientific
Na	Fisher Scientific
PC	Sigma Aldrich
PhCN	Alfa Aesar
99.8% CD ₃ CN	Goss Scientific
Li pellets	Fisher Scientific
Toluene	Sigma Aldrich
Na ₃ VO ₄	Sigma Aldrich
37% HCl	Fisher Scientific
Potassium	Fisher Scientific
Graphite flakes	Sigma Aldrich

Table 5.1 Materials used in Chapter 2 and their suppliers.

The mercury used in the experiments was recycled Hg cleaned by filtration and successive washing with dilute HNO₃, water and ethanol then dried under vacuum.

Solvents used in reactions where air/moisture sensitive compounds were used and prepared, were dried before use. This was done by firstly adding sodium wire to the solvent bottle to remove water. Secondly the solvent was transferred to the still and the relevant drying agent was added to the solvent and the solvent is then refluxed under N₂. The distilled solvent is then transferred to a storage ampoule containing another drying agent. The drying agents required for specific solvents are shown in

Chapter 5 Experimental

Table 5.2. DMSO, PC and PhCN were dried o/n three times over sieves before use. The boiling points of these solvents are too high for stills.

Solvent	Stills	Ampoule
MeCN	Calcium hydride	4 Å molecular sieves
Ether	Sodium wire and benzophenone	4 Å molecular sieves
DMSO		4 Å molecular sieves (x3)
PC		4 Å molecular sieves (x3)
PhCN		4 Å molecular sieves (x3)

Table 5.2 Solvents and their specific drying agents for use in stills and ampoules.

The 4 Å molecular sieves were activated by heating at 300 °C under vacuum for 24 hours. Deuterated solvents were dried over 4 Å molecular sieves for at least one week before use.

5.2.2 Synthesis

5.2.2.1 $(TBA)_3[PMo_{12}O_{40}]$ ⁶

$Na_2MoO_4 \cdot 2H_2O$ (29.0 g, 120 mmol) was dissolved in water (120 mL) to give a 1 M colourless solution. 1 M H_3PO_4 solution was made up by adding 85% H_3PO_4 (0.68 mL) to water (9.3 mL) and this was then added to the molybdate solution. 1,4-dioxane (100 mL) was added and the solution changed from colourless to cloudy. Concentrated HNO_3 (15 mL) was added to the molybdate solution which turned the solution orange and then yellow after stirring for five min. $(TBA)(Br)$ (10.2 g, 31.6 mmol) was dissolved in water (10 mL) which required heating to give a colourless solution which was then added to the yellow solution to give a yellow solid. The solid was filtered, washed with water and then boiled in water (100 mL). The solid was filtered using a Buchner funnel and washed with water, IMS and ether. The solid was dried under vacuum over a weekend. The solid was dissolved in MeCN (500 mL) with heating and then left overnight to recrystallize. The next day yellow crystals had formed and were filtered using a Buchner funnel. The crystals were transferred to a Schlenk flask and pumped dry under vacuum for one hour, which gave a yield of 19.8 g (78%).

FTIR (cm^{-1}): 2961.1 (m), 2932.8 (m), 2873.2 (w), 1461.4 (m), 1379.8 (w), 1169.4 (w), 1108.3 (w), 1060.0 (s, sh), 950.4 (s), 873.8 (s), 785.4 (s, br), 615.7 (w), 499.5 (m), 462.4 (s)

$^{31}\text{P}\{\text{H}\}$ NMR in CD_3CN : -3.8 ppm (0.9 Hz); in PC: -3.7 ppm (4.3 Hz); in PhCN : -3.0 ppm (12.5 Hz)

5.2.2.2 0.35 wt.% Na|Hg Amalgam

Na was weighed out into a beaker of toluene then transferred to a Schlenk flask and pumped dry. Hg was then added under nitrogen and a glass rod was used to initiate the solvation; this gave a 0.35 wt.% amalgam.

5.2.2.3 The Reaction Between $(\text{TBA})_3[\text{PMo}_{12}\text{O}_{40}]$ and Na|Hg Amalgam in MeCN

0.35 wt.% Na|Hg amalgam (x g) was added to a Schlenk flask under N_2 .

$(\text{TBA})_3[\text{PMo}_{12}\text{O}_{40}]$ (y g) and MeCN (5 mL) were added to the Schlenk flask under N_2 . The reaction was then stirred over the weekend and then a sample was taken for ^{31}P NMR. The NMR sample was put back in to the flask and the reaction mixture was separated from Hg in the glovebox and then pumped dry. The solid was scratched with ether and pumped dry under vacuum, until no residual MeCN remained and a dry powder was obtained. FTIR was then recorded of the solid.

<i>n</i>	x Na Hg/ g (mmol)	y PMo_{12} / g (mmol)	Yield/ %	Colour
1	1.76 (0.27)	0.62 (0.24)	46	Dark green
2	3.07 (0.47)	0.54 (0.21)	89	Dark blue
3	4.19 (0.64)	0.49 (0.19)	89	Dark blue
4	6.13 (0.93)	0.54 (0.21)	78	Dark blue
5	7.18 (1.08)	0.50 (0.20)	92	Dark blue
6	8.94 (1.36)	0.53 (0.21)	86	Dark blue

Table 5.3 The reactions between PMo_{12} and *n* mole-equivalents of Na|Hg amalgam in MeCN.

<i>n</i>	δ_{P} / ppm	LW1/2/ Hz	Reaction mixture/ %
1	-0.0	3.5	100
2	-7.0	2.4	100
3	-2.7, -6.3, -7.0	6.1, 2.5, 1.0	80.8, 10.6, 8.6
4	-2.7, -6.9	5.1, 1.5	27.3, 72.7
5	-3.1, -6.1	5.0, 1.3	95.5, 4.5
6	-2.5, -3.1, -3.9, -4.6	13.7, 14.8, 20.1, 13.1	12.2, 40.5, 11.5, 35.8

Table 5.4 Peaks in $^{31}\text{P}\{\text{H}\}$ NMR spectra for the reactions between PMo_{12} and *n* mole-equivalents of Na|Hg amalgam in MeCN.

Chapter 5 Experimental

<i>n</i>	Wavenumber/ cm ⁻¹
0	2961.1 (m), 2932.8 (m), 2873.2 (w), 1461.4 (m), 1379.8 (w), 1169.4 (w), 1108.3 (w), 1060.0 (s, sh), 950.4 (s), 873.8 (s), 785.4 (s, br), 615.7 (w), 499.5 (m), 462.4 (s)
1	2958.5 (m), 2933.1 (m), 2871.5 (m), 1480.3 (s), 1379.7 (w), 1151.8 (w), 1056.5 (s, sh), 1027.4 (w), 938.0 (s, sh), 768.3 (s, br), 592.4 (w), 494.7 (w)
2	3488.4 (w, br), 2958.6 (w), 2929.3 (w), 2870.6 (w), 1617.0 (w), 1479.5 (m), 1379.2 (w), 1361.4 (w), 1151.8 (w), 1056.2 (m, sh), 935.7 (s, sh), 748.7 (s, br), 590.3 (w), 486.9 (w)
3	3381.2 (w, br), 2958.3 (w), 2929.7 (w), 2870.6 (w), 1479.7 (m), 1379.3 (w), 1361.6 (w), 1151.4 (w), 1056.4 (m, sh), 936.2 (s, sh), 749.1 (s, br), 590.5 (w), 487.3 (w)
4	3325.2 (w, br), 2958.7 (w), 2928.9 (w), 2870.8 (w), 1627.5 (w), 1479.4 (m), 1379.4 (w), 1361.1 (w), 1151.4 (w), 1056.5 (m, sh), 935.6 (s, sh), 744.8 (s, br), 590.0 (w), 484.1 (w)
5	3320.5 (w, br), 2958.3 (w), 2931.6 (w), 2871.0 (w), 1634.1 (w), 1480.2 (m), 1379.5 (w), 1150.7 (w), 1056.5 (m, sh), 937.1 (s, sh), 751.2 (s, br), 590.4 (w), 493.0 (w)
6	3383.4 (w, br), 2958.3 (w), 2932.5 (w), 2871.3 (w), 1480.5 (m), 1379.2 (w), 1151.1 (w), 1056.4 (m, sh), 938.2 (s), 732.3 (s, br), 590.4 (w), 489.5 (w)

Table 5.5 Bands in FTIR spectra for solids isolated from the reactions between PMo_{12} and *n* mole-equivalents of Na|Hg amalgam in MeCN.

5.2.2.4 The Reaction Between $(\text{TBA})_3[\text{PMo}_{12}\text{O}_{40}]$ and Na|Hg Amalgam in PC

0.35 wt.% Na|Hg amalgam (x g) was added to a Schlenk flask under N_2 .

$(\text{TBA})_3[\text{PMo}_{12}\text{O}_{40}]$ (y) and PC (3 mL) were added to the Schlenk flask under N_2 . The reaction was then stirred over the weekend and then a sample was taken for ^{31}P NMR. The NMR sample was put back in to the flask and the solution was separated from Hg in the glovebox. Ether (60 mL) was added to the solution, shook together and left to separate o/n. The next day the ether layer was filtered off and the remaining oil was scratched with ether until a free flowing powder was obtained. This powder was pumped dry and FTIR was recorded.

<i>n</i>	x NaHg/ g (mmol)	y PMo_{12} / g (mmol)	Yield/ %	Colour
1	0.78 (0.12)	0.30 (0.12)	51	Dark green
2	0.80 (0.12)	0.15 (0.07)	89	Dark blue
3	0.41 (0.063)	0.12 (0.05)	95	Dark blue
4	0.93 (0.14)	0.09 (0.04)	92	Dark blue
5	1.28 (0.2)	0.10 (0.04)	88	Dark blue
6	1.11 (0.17)	0.07 (0.03)	96	Dark blue
12	17.35 (2.64)	0.56 (0.22)	98	Dark brown
24	43.58 (6.63)	0.64 (0.25)	97	Dark brown

Table 5.6 The reactions between PMo_{12} and *n* mole-equivalents of Na|Hg amalgam in PC.

<i>n</i>	δ_P/ ppm	LW1/2/ Hz	Reaction mixture/ %
0	-3.7	4.5	100.0
1	0.2	3.0	100.0
2	-6.6	1.2	100.0
3	-6.7	1.9	100.0
4	-2.7, -3.3, -5.8	35.3, 1.4, 2.4	58.7, 7.2, 34.1
5	-0.1	15.2	100.0
6	-2.7, -3.7, -5.5, -6.1	1.6, 2.2, 4.7, 6.9	10.8, 39.6, 7.5, 42.1
12	-6.5	2.3	100
24	No peaks		

Table 5.7 Peaks in $^{31}\text{P}\{^1\text{H}\}$ NMR spectra for the reactions between PMo_{12} and n mole-equivalents of $\text{Na}|\text{Hg}$ amalgam in PC.

<i>n</i>	δ_P/ ppm	LW1/2/ Hz	Reaction mixture/ %	Parameters
0	-3.4, -3.6	59.9	100	$\text{D1} = 80\text{ s, P1} = 3.8\text{ }\mu\text{s, RG} = 64,$ $\text{NS} = 128$
1	0.1	47.4	100	$\text{D1} = 35\text{ s, P1} = 3.8\text{ }\mu\text{s, RG} = 4,$ $\text{NS} = 40$
2	-0.1, -6.8	42.0, 25.6	11.3, 88.7	$\text{D1} = 35\text{ s, P1} = 3.8\text{ }\mu\text{s, RG} = 64,$ $\text{NS} = 16$
24	8.4	2063.5	100	$\text{D1} = 35\text{ s, P1} = 3.8\text{ }\mu\text{s, RG} = 64,$ $\text{NS} = 240$

Table 5.8 Peaks in the ^{31}P MAS NMR spectra for the reactions between PMo_{12} and n mole-equivalents of $\text{Na}|\text{Hg}$ amalgam in PC. Abbreviations: D1 = recycle delay, P1 = pulse speed, RG = receiver gain, NS = number of scans.

<i>n</i>	δ_{Na}/ ppm	LW1/2/ Hz	Reaction mixture/ %	Parameters
1	6.8, -3.4, -10.9, -11.6, -22.0	4551.4	100	$\text{D1} = 10\text{ s, P1} = 2.5\text{ }\mu\text{s, RG} = 128, \text{NS} = 12320$
2	-13.8, -21.4	1996.4	100	$\text{D1} = 0.5\text{ s, P1} = 2.5\text{ }\mu\text{s, RG} = 128, \text{NS} = 128$
24	-7.7	2076.3	100	$\text{D1} = 0.5\text{ s, P1} = 2.5\text{ }\mu\text{s, RG} = 128, \text{NS} = 128$

Table 5.9 Peaks in the ^{23}Na MAS NMR spectra for the reactions between PMo_{12} and n mole-equivalents of $\text{Na}|\text{Hg}$ amalgam in PC. Abbreviations: D1 = recycle delay, P1 = pulse speed, RG = receiver gain, NS = number of scans.

Chapter 5 Experimental

<i>n</i>	Wavenumber/ cm⁻¹
1	2961.4 (m), 2933.6 (m), 2873.6 (m), 1789.9 (s), 1561.1 (w), 1481.1 (m, sh), 1383.6 (m), 1353.5 (m), 1180.5 (m), 1117.3 (w) 1054.6 (s, sh), 941.6 (s, sh), 871.5 (w), 768.7 (s, br), 591.5 (w), 499.0 (w)
2	2960.8 (m), 2933.4 (m), 2872.9 (m), 1778.4 (m), 1481.0 (m), 1383.6 (w), 1353.9 (w), 1183.7 (w), 1116.0(w), 1054.2 (m, sh), 938.0 (s, sh), 749.8 (s, br), 715.3 (w), 590.6 (w), 490.8 (w)
3	3487.4 (w, br), 2961.7 (m), 2934.0 (m), 2873.4 (m), 1899.7 (w), 1776.0 (s), 1557.3 (w), 1481.0 (m), 1460.0 (w), 1423.8 (w), 1385.1 (m), 1353.6 (w), 1181.0 (m), 1115.8 (w), 1052.6 (m), 935.8 (s, sh), 745.1 (s, br), 709.5 (w), 590.2 (w), 487.6 (w)
4	3398.9 (w, br), 2960.4 (m), 2931.6 (m), 2872.4 (m), 1772.1 (s), 1665.0 (w), 1480.0 (m), 1381.3 (m), 1351.8 (w), 1180.7 (w), 1112.8 (w), 1055.4 (m), 934.9 (s), 742.0 (s, br), 709.6 (w), 589.0 (w), 481.1 (w)
5	2960.8 (m), 2932.8 (m), 2872.9 (m), 1772.9 (s), 1662.3 (m), 1480.3 (m), 1458.7 (w), 1381.6 (m), 1331.9 (w), 1181.2 (w), 1114.2 (w), 1054.1 (s), 936.8 (s, sh), 751.5 (s, br), 710.5 (w), 590.3 (w), 491.8 (w)
6	3353.0 (w, br), 2960.5 (m), 2931.4 (m), 2872.1 (m), 1782.0 (s), 1672.9 (m), 1556.4 (w), 1480.0 (m), 1457.7 (m), 1380.0 (w), 1350.2 (w), 1172.8 (w), 1115.3 (w), 1045.3 (m), 927.4 (s, br), 777.9 (w), 736.6 (w), 706.7 (w), 628.0 (w), 577.6 (w), 515.0 (w), 478.1 (w), 461.8 (w)
12	3236.3 (w, br), 2961.9 (w), 2930.6 (w), 2873.1 (w), 1785.7 (m), 1656.7 (m), 1457.6 (m), 1372.4 (m), 1297.6 (m), 1180.3 (w), 1116.5 (w), 1047.0 (s), 934.7 (w), 821.9 (s), 775.1 (w), 742.0 (w), 709.5 (w), 612.4 (w), 481.1 (w), 408.9 (w)
24	3171.5 (w, br), 2965.0 (w), 2932.3 (w), 2875.1 (w), 1786.7 (s, sh), 1651.8 (s), 1540.9 (w), 1448.9 (w), 1327.6 (s), 1290.0 (s), 1177.6 (w), 1143.4 (w), 1117.2 (w), 1045.0 (s), 937.7 (m), 852.3 (w), 818.7 (m), 775.4 (w, sh), 708.6 (m), 618.2 (w), 575.1 (w), 486.0 (w)

Table 5.10 Bands in FTIR spectra for solids isolated from the reactions between PMo_{12} and n mole-equivalents of $\text{Na}|\text{Hg}$ amalgam in PC.

5.2.2.5 The Reaction Between $(\text{TBA})_3[\text{PMo}_{12}\text{O}_{40}]$ and $\text{Na}|\text{Hg}$ Amalgam in PhCN

0.35 wt.% $\text{Na}|\text{Hg}$ amalgam (x g) was added to a Schlenk flask under N_2 .

$(\text{TBA})_3[\text{PMo}_{12}\text{O}_{40}]$ (y) and PhCN (3 mL) were added to the Schlenk flask under N_2 .

The reaction was then stirred over the weekend and then a sample was taken for ^{31}P NMR. For 1:1 the reaction mixture was dark green and for two to six mole-equivalents of Na the reaction mixture was dark blue.

<i>n</i>	x $\text{Na} \text{Hg}$ / g (mmol)	y PMo_{12} / g (mmol)	Colour
1	0.78 (0.12)	0.30 (0.12)	Dark green
2	0.80 (0.12)	0.15 (0.07)	Dark blue
3	0.91 (0.139)	0.12 (0.05)	Dark blue
4	0.93 (0.14)	0.09 (0.04)	Dark blue
5	1.28 (0.20)	0.10 (0.04)	Dark blue
6	1.11 (0.17)	0.07 (0.03)	Dark blue

Table 5.11 The reactions between PMo_{12} and n mole-equivalents of $\text{Na}|\text{Hg}$ amalgam in PhCN.

<i>n</i>	δ_P / ppm	LW1/2/ Hz	Reaction mixture/ %
1	1.6, -2.6, -5.6	19.4, 31.8, 21.4	65.8, 25.0, 9.2
2	1.1, -5.8	7.4, 8.4	25.1, 74.9
3	-0.7, -5.8	47.5, 10.0	18.7, 81.3
4	-6.1	1.7	100.0
5	-1.6, -4.7, -5.9	3.6, 3.6, 1.8	11.6, 7.7, 80.7
6	-5.8	2.0	100.0

Table 5.12 Peaks in the $^{31}P\{^1H\}$ NMR spectra for the reactions between PMo_{12} and *n* mole-equivalents of $Na|Hg$ amalgam in PhCN.

5.2.2.6 0.03 wt.% Li|Hg Amalgam

In an argon glovebox Li was weighed out, then Hg was weighed out in to a clean Schlenk flask under nitrogen. The flask was then put under vacuum before transferring into the argon glovebox. In the glovebox the Li was added to the Hg and a glass rod was used to initiate the solvation by scratching the surface of the Li. 0.03 wt.% amalgam.

5.2.2.7 The Reaction Between $(TBA)_3[PMo_{12}O_{40}]$ and Li|Hg Amalgam in MeCN

0.03 wt.% Li|Hg amalgam (x g) was added to a Schlenk flask under N_2 .

$(TBA)_3[PMo_{12}O_{40}]$ (y g) and MeCN (3 mL) was added to the Schlenk flask under N_2 . The reaction was then stirred over the weekend and then a sample was taken for ^{31}P NMR. For 1:1 the reaction mixture was dark green and for two to six equivalents of Na the reaction mixture was dark blue.

<i>n</i>	x Li Hg/ g (mmol)	y PMo_{12} / g (mmol)	Yield/ %	Colour
1	14 (1.0)	2.55 (1.0)	54	Dark green
2	9.1 (0.4)	0.50 (0.20)	55	Dark blue
4	20.01 (0.87)	0.55 (0.22)	98	Dark blue
6	23.5 (1.0)	0.43 (0.17)	88	Dark blue
12	20.1 (0.87)	0.17 (0.07)	97	Dark brown
24	23.5 (1.0)	0.11 (0.04)	86	Dark brown

Table 5.13 The reactions between PMo_{12} and *n* mole-equivalents of Li|Hg amalgam in MeCN

<i>n</i>	δ_P / ppm	LW1/2/ Hz	Reaction mixture/ %
1	-0.1	4.2	100.0
2	-7.0	3.5	100.0
4	-2.3, -5.9, -6.9	5.8, 1.4, 2.6	30.3, 63.9, 5.8
6	-2.3, -5.9, -6.9	6.5, 1.9, 2.2	41.6, 21.5, 36.9
12	1.1, -2.5, -5.4	20.9, 36.4, 45.6	41.1, 28.2, 30.7
24	-2.4	109.1	100.0

Table 5.14 Peaks in $^{31}P\{^1H\}$ NMR spectra for the reactions between PMo_{12} and *n* mole-equivalents of Li|Hg amalgam in MeCN.

Chapter 5 Experimental

<i>n</i>	Bands in FTIR/ cm ⁻¹
1	2958.1 (m), 2933.3 (m), 2871.0 (m), 2038.6 (w), 1978.1 (w), 1634.2 (w), 1480.2 (m), 1379.7 (w), 1151.7 (w), 1105.0 (w), 1056.6 (m, sh), 937.7 (s), 851.4 (s), 765.2 (s), 590.7 (s), 497.6 (s)
2	2959.3 (m), 2934.1 (m), 2872.4 (m), 2273.6 (w), 2047.6 (w), 1988.6 (w), 1480.6 (m), 1380.2 (w), 1362.8 (w), 1150.4 (w), 1105.2 (w), 1057.5 (m), 934.4 (s), 746.3 (s), 590.8 (s), 486.9 (s)
4	2959.1 (m), 2932.8 (m), 2871.9 (m), 2269.9 (w), 2206.7 (w), 2042.8 (w), 1980.3 (w), 1636.2 (w), 1480.5 (m), 1379.2 (w), 1363.3 (w), 1151.8 (w), 1106.4 (w), 1057.3 (m), 937.5 (s), 790.0 (s), 735.1 (s), 591.2 (s), 468.6 (s)
6	2957.9 (m), 2932.4 (m), 2871.0 (m), 2270.7 (w), 2045.8 (w), 1665.7 (w), 1480.0 (m), 1379.5 (w), 1362.1 (w), 1151.2 (w), 1057.4 (m), 936.6 (s, sh), 748.4 (s), 591.2 (s), 485.2 (s)
12	3338.0 (w), 3210.2 (w), 2961.4 (m), 2932.7 (m), 2871.9 (m), 2192.3 (m), 1630.4 (m), 1591.4 (m), 1518.7 (w), 1480.3 (m), 1380.7 (w), 1344.0 (w), 1271.5 (w), 1150.6 (w), 1058.2 (m), 937.6 (s, sh), 744.8 (s), 591.0 (s), 499.5 (s), 461.9 (s)
24	3337.9 (w), 3205.5 (w), 2960.3 (m), 2933.9 (m), 2872.6 (m), 2181.9 (m), 1674.5 (w), 1630.2 (m), 1592.4 (m), 1480.9 (m), 1379.3 (w), 1310.0 (w), 1151.2 (w), 1106.2 (w), 1057.5 (w), 1021.3 (w), 931.2 (s, sh), 735.9 (s), 590.4 (s), 481.7 (s)

Table 5.15 Bands in the FTIR spectra for solids isolated from the reactions between PMo_{12} and *n* mole-equivalents of Li|Hg amalgam in MeCN.

5.2.2.8 The Reaction Between $(\text{TBA})_3[\text{PMo}_{12}\text{O}_{40}]$ and Li|Hg Amalgam in PC

0.03 wt.% Li|Hg amalgam (x g) was added to a Schlenk flask under N_2 .

$(\text{TBA})_3[\text{PMo}_{12}\text{O}_{40}]$ (y g) and PC (3 mL) was added to the Schlenk flask under N_2 . The reaction was then stirred over the weekend and a sample was taken for ^{31}P NMR.

The NMR sample was put back in to the flask and the solution was separated from Hg in the glovebox. Ether (60 mL) was added to the solution, shook together and left to separate o/n. The next day the ether layer was filtered off and the remaining oil was scratched with ether until a free flowing powder was obtained. This powder was pumped dry and FTIR was recorded.

<i>n</i>	x Li Hg/ g (mmol)	y PMo_{12} / g (mmol)	Yield/ %	Colour
1	6.6 (0.29)	0.67 (0.26)	77	Dark green
2	10.0 (0.43)	0.50 (0.20)	95	Dark blue
3	13.3 (0.58)	0.45 (0.18)	83	Dark blue
4	16.6 (0.72)	0.42 (0.16)	81	Dark blue
5	23.3 (1.0)	0.47 (0.18)	80	Dark blue
6	26.6 (1.15)	0.45 (0.18)	80	Dark blue
8	40.0 (1.7)	0.50 (0.20)	86	Dark blue
10	47.0 (2.0)	0.47 (0.18)	93	Dark blue
12	50.0 (2.2)	0.42 (0.16)	79	Dark brown
24	54.5 (2.36)	0.23 (0.09)	82	Dark brown

Table 5.16 The reactions between PMo_{12} and *n* mole-equivalents of Li|Hg amalgam in PC.

<i>n</i>	δ_P / ppm	LW1/2/ Hz	Reaction mixture/ %
1	0.1, -3.5	5.5, 12.1	83.4, 16.6
2	-2.2, -6.7	5.8, 1.0	15.6, 84.4
3	-0.0, -7.0	12.9, 1.8	6.2, 93.8
4	-0.1, -6.7	5.0, 3.6	40.5, 59.5
5	-2.3, -5.8, -6.7	16.0, 6.9, 4.3	40.5, 50.6, 8.9
6	-2.2, -5.8, -6.8	23.5, 25.6, 23.5	44.1, 44.1, 11.8
8	2.1, -0.8, -4.4	46.3, 22.0, 315.2	32.5, 47.1, 20.4
10	2.3, -0.8, -4.3	21.2, 18.4, 239.8	41.8, 31.4, 26.8
12	15.5, -1.2, -5.0	7.9, 11.3, 359.8	35.3, 33.2, 31.5
24	+20 to -20	3188.7	100.0

Table 5.17 Peaks in the $^{31}P\{^1H\}$ NMR spectra for the reactions between PMo_{12} and *n* mole-equivalents of Li|Hg amalgam in PC.

<i>n</i>	δ_P / ppm	LW1/2/ Hz	Reaction mixture/ %	Parameters
0	-3.4, -3.6	59.9	100	D1 = 80 s, P1 = 3.8 μ s, RG = 64, NS = 128
1	-0.1	43.4	100	D1 = 1.2 s, P1 = 3.8 μ s, RG = 64, NS = 1408
2	0.1, -6.6, -7.3	61.6, 82.5, 49.5	46.7, 41.3, 12.0	D1 = 1.2 s, P1 = 3.8 μ s, RG = 64, NS = 4096
12	0.0, -6.6, -6.8, -7.6	55.6, 71.5, 54.3	36.1, 53.9, 10.0	D1 = 1.2 s, P1 = 3.8 μ s, RG = 64, NS = 2408
24	5.7	2432.2	100	D1 = 1.2 s, P1 = 3.8 μ s, RG = 64, NS = 3968

Table 5.18 Peaks in the ^{31}P MAS NMR spectra for solids isolated from the reactions between PMo_{12} and *n* mole-equivalents of Li|Hg amalgam in PC. Abbreviations: D1 = recycle delay, P1 = pulse speed, RG = receiver gain, NS = number of scans.

<i>n</i>	δ_{Li} / ppm	LW1/2/ Hz	Reaction mixture/ %	Parameters
1	-1.7	75.2	100	D1 = 2.5 s, P1 = 3.0 μ s, RG = 128, NS = 408
2	-0.6	111.3	100	D1 = 2.5 s, P1 = 3.0 μ s, RG = 128, NS = 12474
12	-0.6	450.0	100	D1 = 2.5 s, P1 = 3.0 μ s, RG = 128, NS = 12474
24	-0.2	792.2	100	D1 = 1.2 s, P1 = 3.0 μ s, RG = 128, NS = 16

Table 5.19 Peaks in the 7Li MAS NMR spectra for solids isolated from the reactions between PMo_{12} and *n* mole-equivalents of Li|Hg amalgam in PC. Abbreviations: D1 = recycle delay, P1 = pulse speed, RG = receiver gain, NS = number of scans.

Chapter 5 Experimental

<i>n</i>	Wavenumber/ cm ⁻¹
1	2960.9 (m), 2932.2 (m), 2872.7 (m), 2345.1 (w), 1793.1 (m), 1753.2 (m), 1481.4 (m), 1461.1 (m), 1403.2 (w), 1381.2 (m), 1357.4 (w), 1200.0 (w), 1117.5 (w), 1059.8 (s), 945.8 (s), 874.6 (s), 783.4 (s), 591.0 (s), 496.9 (s), 462.2 (s)
2	3384.7 (w, br), 2960.9 (m), 2933.0 (m), 2872.7 (m), 2174.3 (w), 2014.5 (w), 1754.1 (m), 1480.8 (m), 1403.3 (m), 1381.7 (w), 1356.3 (w), 1198.6 (w), 1117.2 (w), 1055.2 (m), 942.3 (s), 742.8 (s), 716.1 (s), 591.0 (s), 491.2 (s)
3	3445.5 (w, br), 2960.1 (m), 2934.0 (m), 2872.2 (m), 2201.8 (w), 2040.0 (w), 1766.0 (m), 1480.5 (m), 1380.7 (w), 1359.3 (w), 1203.0 (w), 1151.5 (w), 1117.3 (w), 1057.3 (m), 939.9 (s), 765.1 (s), 592.0 (s), 488.3 (s), 428.1 (s)
4	3396.5 (w, br), 2960.5 (m), 2931.7 (m), 2872.1 (m), 2322.1 (w), 1967.9 (w), 1766.7 (m), 1480.2 (m), 1380.7 (w), 1356.3 (w), 1197.7 (w), 1116.6 (w), 1057.1 (m), 940.6 (s, sh), 782.9 (s), 591.6 (s), 493.0 (s), 444.1 (s), 423.0 (s)
5	3281.7 (w, br), 2960.6 (m), 2872.6 (m), 2167.0 (m), 2048.4 (w), 1954.6 (w), 1780.7 (m), 1618.3 (w), 1480.3 (m), 1380.8 (w), 1180.2 (w), 1114.4 (w), 1055.5 (m), 939.3 (s), 772.8 (s), 591.4 (s), 480.1 (s), 464.8 (s), 443.7 (s), 430.6 (s)
6	3286.6 (w, br), 2960.1 (m), 2934.1 (m), 2872.6 (m), 2181.9 (w), 2015.5 (w), 1780.9 (w), 1632.8 (w), 1480.4 (m), 1381.0 (w), 1057.6 (m), 938.1 (s, sh), 779.9 (s), 752.5 (s), 591.1 (s)
8	3292.0 (w, br), 2961.5 (m), 2933.3 (m), 2873.4 (m), 2322.3 (w), 1786.9 (s), 1616.6 (w), 1481.0 (m), 1381.8 (m), 1351.5 (w), 1179.2 (w), 1116.8 (w), 1052.0 (s, 937.3 (s), 773.1 (s), 591.0 (s)
10	3346.4 (w, br), 2961.7 (m), 2932.3 (m), 2873.1 (m), 2324.4 (w), 1981.2 (w), 1784.2 (s), 1654.7 (w), 1480.4 (m), 1457.8 (m), 1382.8 (m), 1351.8 (m), 1178.7 (w), 1145.1 (m), 1115.6 (m), 1048.2 (m), 934.0 (s), 733.4 (s, br), 588.0 (w), 427.3 (m)
12	3260.8 (w, br), 2960.6 (m), 2931.9 (m), 2872.3 (m), 2111.4 (w), 1982.4 (w), 1784.2 (m), 1648.8 (m), 1480.9 (m), 1456.2 (m), 1380.3 (m), 1300.8 (m), 1051.4 (m), 932.8 (s), 869.6 (s), 778.3 (s), 730.7 (s), 586.1 (s)
24	2965.3 (m), 2933.5 (m), 2876.2 (m), 2119.8 (w), 1783.2 (s), 1655.5 (m), 1482.6 (m), 1449.8 (m), 1385.6 (s), 1351.8 (s), 1224.1 (s), 1177.0 (s), 1145.4 (s), 1116.4 (s), 1044.4 (s), 939.3 (s), 868.8 (s), 775.5 (s), 707.2 (s)

Table 5.20 Bands in the FTIR spectra for solids isolated from the reactions between PMo_{12} and *n* mole-equivalents of Li|Hg amalgam in PC.

5.2.2.9 $(\text{TBA})_3[\text{V}_{13}\text{O}_{34}]$ ⁷

$(\text{TBA})_3[\text{V}_{10}\text{O}_{28}\text{H}_3]$ (1.77 g, 1.05 mmol) and $\text{VO}(\text{O}^t\text{Bu})_3$ (0.90 g, 3.14 mmol) were added to a Schlenk flask under N_2 and dry MeCN (25 mL) was added. The mixture was stirred vigorously to give an orange suspension. Distilled water (58 μL , 3.14 mmol) was added with stirring and the solution instantly turned deep red-brown. After further stirring (ca. 10 min) a yellow solid formed. The mixture was stirred o/n at RT. The solvent was removed to give a sticky yellow-gold solid, which was then washed with dry ether (2 x 20 mL) to give a yellow-gold solid. Hot dry MeCN (25 mL) was added to the solid and it all dissolved with the help of heating with a heat gun. The solution was left to cool to RT, some crystals formed, the flask was placed in the

freezer o/n. Filtered the mother liquor from the orange crystals and pumped dry the crystals (1.89 g, 93% yield).

$^{51}\text{V}\{\text{H}\}$ NMR in D_2O / ppm: $-331.3, -451.0, -496.4, -500.2$

FTIR/ cm^{-1} : 2960.8 (m), 2932.5 (m), 2872.9 (m), 1480.5 (m), 1468.0 (m), 1379.1 (w), 1316.1 (w), 1153.0 (w), 1060.9 (w), 1031.2 (w), 984.1 (s, sh), 926.7 (w), 851.0 (s, br), 814.5 (m, br), 767.7 (s, br), 737.8 (m), 588.4 (s, br), 512.1 (s, br), 451.8 (s, br), 415.9 (s)

5.2.2.10 $(\text{TBA})_3[\text{H}_3\text{V}_{10}\text{O}_{28}]$ ⁸

Na_3VO_4 (7.5 g, 40.8 mmol) was dissolved in water (55 mL) with heating. 3 M HCl (35.5 mL, 106.5 mmol) added at RT, at a rate of 2 drops s^{-1} from a burette. The colourless solution turned dark orange. The acidified solution was added in 2 mL portions to a stirred solution of $(\text{TBA})(\text{Br})$ (30 g, 93 mmol) in water (30 mL) and an orange precipitate formed. The mixture was stirred for a further 15 min. The solid was filtered under vacuum and washed with water (30 mL), ethanol (30 mL) and ether (150 mL). The orange solid was filtered under vacuum overnight to dry. The crude product was collected and weighed (6.00 g). The solid was transferred to a Schlenk flask and pumped dry under vacuum for 6.5 hours which reduced the weight of the solid (5.96 g). The crude dried product was added to MeCN (75 mL) and stirred for 10 min. The solution was gravity filtered to remove insoluble yellow material. The dark orange solution was placed in a vacuum desiccator with a beaker of ether to crystallize. The orange-red crystals were filtered and dried on a Buchner funnel, crude mass 3.78 g. the crystals were transferred to a Schlenk flask and pumped dry (3.72 g).

$^{51}\text{V}\{\text{H}\}$ NMR in D_2O / ppm (Hz): -397.5 (1048.7), -430.6 (1048.7), -505.7 (605.6), -524.3 (384.0)

FTIR/ cm^{-1} : 3262.3 (m, br), 2958.5 (m), 2930.8 (m), 2870.8 (m), 1479.7 (m), 1378.3 (m), 1152.4 (w), 1107.1 (w), 1062.2 (w), 963.6 (s), 881.2 (w), 835.5 (s), 800.3 (s), 764.6 (s), 715.7 (s), 599.8 (s, br), 548.5 (s, br), 505.9 (m), 488.5 (m, br), 440.4 (m)

5.2.2.11 The Reaction Between $(\text{TBA})_3[\text{V}_{13}\text{O}_{34}]$ and $\text{Na}|\text{Hg}$ Amalgam in MeCN

To a pre-weighed Schlenk flask a few drops of 0.35 wt.% $\text{Na}|\text{Hg}$ amalgam (x g) was added under N_2 . $(\text{TBA})_3[\text{V}_{13}\text{O}_{34}]$ (y g) was added to a Schlenk flask and dissolved in

Chapter 5 Experimental

MeCN (10 mL), with a little heating to give an orange solution. The vanadium solution was cannula transferred to the Na|Hg amalgam containing flask and stirred. After a few minutes of stirring the mixture turned green. Reaction stirred o/n and then took a sample for ^{51}V NMR. NMR sample put back in to the flask and then the solution was separated from Hg in glovebox. Solution pumped dry and scratched with ether (10 mL). FTIR taken of the solid.

<i>n</i>	<i>x</i> Na Hg/ g (mmol)	<i>y</i> V_{13}/ g (mmol)	Yield/ %	Colour
1	0.22 (0.03)	0.06 (0.03)	-	Dark green
2	0.92 (0.14)	0.13 (0.07)	-	Dark green
3	0.88 (0.13)	0.09 (0.04)	-	Dark green
4	0.39 (0.06)	0.03 (0.02)	-	Dark green
5	0.60 (0.09)	0.04 (0.02)	-	Dark green
6	1.05 (0.16)	0.05 (0.03)	-	Dark green
13	5.41 (0.82)	0.11 (0.06)	93	Dark brown

Table 5.21 The reactions between $(\text{TBA})_3[\text{V}_{13}\text{O}_{34}]$ and *n* mole-equivalents of Na|Hg in MeCN.

<i>n</i>	δv/ ppm	LW1/2/ Hz	Reaction mixture/ %
1	-293.0, -330.8, -450.6, -496.1, -499.9	1661.1, 194.1, 322.7, 480.7	12.1, 6.6, 17.0, 64.3
2	-230.7, -300.8	1323.1, 2039.7	80.0, 20.0
3	-229.7, -302.8, -500.3	1281.3, 2062.6, 20.1	79.0, 20.6, 0.4
4	-229.5	985.4	100.0
5	-239.0	2260.2	100.0
6	-227.5	1075.0	100.0
13	-496.7, -501.1, -518.3, -523.2, -528.2, -544.9, -552.2, -569.1	285.6, 109.8, 40.8, 53.4, 244.8, 244.8, 48.3	72.0, 0.7, 2.9, 1.4, 3.6, 3.6, 15.8

Table 5.22 Peaks in the $^{51}\text{V}\{^1\text{H}\}$ NMR spectra for the reactions between $(\text{TBA})_3[\text{V}_{13}\text{O}_{34}]$ and *n* mole-equivalents of Na|Hg in MeCN.

<i>n</i>	Bands in FTIR/ cm⁻¹
1	3354.7 (w, br), 2959.3 (m), 2931.2 (m), 2871.5 (m), 2170.7 (w), 2078.6 (w), 1657.1 (w), 1478.8 (s), 1377.7 (m), 1151.8 (w), 1106.5 (w), 1064.5 (w), 974.4 (s), 851.0 (s), 815.1 (s), 753.7 (s), 586.6 (s), 558.2 (s), 515.5 (s), 445.4 (s)
2	3385.5 (w, br), 2959.2 (m), 2931.8 (m), 2871.2 (m), 2050.2 (w), 1727.9 (w), 1627.4 (w), 1478.6 (s), 1377.9 (m), 1284.2 (w), 1151.6 (w), 1069.6 (w), 987.4 (s), 970.1 (s), 850.3 (s), 820.3 (s), 749.2 (s), 587.1 (s), 555.4 (s), 524.4 (s), 433.1 (s)
3	3359.1 (w, br), 2958.9 (m), 2930.8 (m), 2870.8 (m), 2210.0 (w), 2177.9 (w), 1478.6 (s), 1377.8 (m), 1152.0 (w), 987.2 (s), 969.0 (s), 850.4 (s), 816.6 (s), 751.6 (s), 590.2 (s), 555.8 (s), 522.6 (s), 436.2 (s)
4	2959.1 (m), 2930.9 (m), 2870.9 (m), 2030.5 (w), 1989.2 (w), 1738.4 (w), 1478.4 (m), 1377.7 (m), 1151.6 (w), 1106.1 (w), 1066.1 (w), 1027.1 (w), 986.4 (s), 967.5 (s), 850.6 (s), 817.2 (s), 741.3 (s), 587.7 (s), 555.1 (s), 524.3 (s), 428.4 (s), 408.9 (s)
5	3307.1 (w, br), 2958.3 (m), 2932.2 (m), 2869.4 (m), 2323.4 (w), 2196.2 (w), 2095.6 (w), 2013.4 (w), 2000.6 (w), 1705.7 (w), 1668.4 (w), 1478.5 (s), 1377.3 (m), 1152.5 (w), 1106.6 (w), 1065.8 (w), 1031.1 (w), 962.5 (s), 884.8 (s), 808.4 (s), 737.1 (s), 585.8 (s), 553.0 (s), 533.0 (s), 533.4 (s), 508.3 (s), 432.0 (s), 414.9 (s)
6	3355.4 (m), 2958.4 (m), 2931.8 (m), 2870.6 (m), 1478.5 (s), 1377.7 (m), 1151.7 (m), 1106.0 (w), 1067.3 (w), 1027.4 (w), 965.8 (s), 852.4 (s), 813.2 (s), 737.4 (s), 587.3 (s), 527.6 (s), 427.0 (s)
13	3270.2 (w, br), 2962.5 (m), 2874.7 (m), 2185.4 (w), 2113.1 (w), 2056.8 (w), 1988.3 (w), 1784.1 (s), 1609.2 (m, br), 1458.0 (w), 1383.7 (m), 1350.0 (m), 1223.1 (w), 1177.5 (m), 1117.6 (m), 1047.1 (m), 894.3 (s, br), 643.8 (s), 558.1 (s), 440.8 (s), 426.6 (s)

Table 5.23 Bands in the FTIR spectra for solids isolated from the reactions between (TBA)₃[V₁₃O₃₄] and *n* mole-equivalents of Na|Hg in MeCN.

5.2.2.12 The Reaction Between (TBA)₃[V₁₃O₃₄] and Na|Hg Amalgam in PC

0.35 wt.% Na|Hg amalgam (x g) was weighed out under N₂ in to a Schlenk flask. (TBA)₃[V₁₃O₃₄] (y g) was weighed out in glovebox and dissolved in PC to give an orange solution before being added to amalgam flask. Reaction stirred o/n and then a sample was taken for ⁵¹V NMR. NMR sample was put back into the flask and then the solution was separated from Hg in glovebox. Ether (60 mL) was added to the solution, scratched and then the solid was pumped dry. FTIR was taken of the solid.

<i>n</i>	x of Na Hg/ g (mmol)	y of V₁₃/ g (mmol)	Yield/ %	Colour
1	1.38 (0.21)	0.37 (0.19)	95	Dark green
2	3.39 (0.52)	0.45 (0.23)	95	Dark green
3	4.32 (0.66)	0.39 (0.20)	100	Dark green
4	1.49 (0.23)	0.10 (0.05)	95	Bronze
5	1.89 (0.29)	0.10 (0.05)	61	Blue-green
6	2.20 (0.34)	0.10 (0.05)	54	Blue-green
13	5.08 (0.77)	0.10 (0.05)	20	Blue-green

Table 5.24 The reactions between (TBA)₃[V₁₃O₃₄] and *n* mole-equivalents of Na|Hg in PC.

Chapter 5 Experimental

<i>n</i>	δv/ ppm	LW1/2/ Hz	Reaction mixture/ %
1	-224.1, -297.8, -485.9, -517.5	1301.4, 2552.8, 2602.8, 750.8	76.5, 7.8, 15.6, 0.1
2	-24.5, -219.3, -284.4, -494.4	2675.7, 1373.1, 2816.5, 3291.8	3.1, 58.4, 9.2, 29.3
3	4.9, -502.1	2573.5, 2983.8	11.1, 88.9
4	-10.1, -498.6, -513.2, -577.0	564.5, 1780.4, 2062.7, 2909.4	23.3, 6.1, 52.0, 18.6
5	-12.8, -494.9, -496.9, -499.3	907.7, 260.8	70.9, 29.1
6	-10.3, -495.2, -497.2, -499.5	709.1, 223.6	24.5, 76.5
13	-496.4, -518.8, -523.6	315.2, 94.2, 108.7	94.3, 1.9, 3.8

Table 5.25 Peaks in the $^{51}\text{V}\{\text{H}\}$ NMR spectra for the reactions between $(\text{TBA})_3[\text{V}_{13}\text{O}_{34}]$ and n mole-equivalents of $\text{Na}|\text{Hg}$ in PC.

<i>n</i>	Bands in FTIR/ cm^{-1}
1	2960.54 (m), 2932.73 (m), 2871.87 (m), 1785.66 (m), 1478.92 (m, sh), 1379.14 (w, sh), 1351.47 (w), 1167.87 (w), 1112.65 (w), 1051.33 (w), 988.38 (w), 971.76 (s), 850.25 (s), 814.99 (w), 753.02 (s, br), 588.56 (s), 556.29 (s), 526.57 (s), 426.11 (s)
2	3282.11 (w, br), 2960.31 (m), 2932.48 (m), 2872.16 (m), 1781.62 (s), 1478.79 (s), 1379.21 (w), 1351.48 (w), 1154.14 (w), 1112.03 (w), 1048.56 (w), 987.20 (s), 964.38 (s), 850.73 (s), 816.43 (s), 739.03 (s), 592.28 (s), 533.30 (s), 426.97 (s), 408.64 (s)
3	2960.25 (m), 2933.45 (m), 2872.35 (m), 1781.70 (m, sh), 1480.45 (m), 1380.43 (w), 1351.66 (w), 1167.58 (w), 1112.42 (w), 1046.40 (w), 948.14 (s, sh), 922.41 (w), 890.86 (w), 797.52 (s), 737.10 (s), 661.55 (m), 583.98 (s), 540.95 (s), 424.13 (s)
4	3202.99 (w, br), 2959.97 (m), 2932.56 (m), 2872.60 (m), 1786.97 (m), 1642.41 (w), 1482.09 (m), 1379.97 (w), 1152.79 (w), 1112.00 (w), 1047.41 (w), 953.17 (s), 924.27 (s), 887.31 (s), 833.14 (s), 685.82 (s), 655.25 (s), 524.14 (s), 448.13 (s)
5	3272.46 (w, br), 2960.59 (m), 2930.60 (m), 2872.13 (m), 1781.86 (m), 1605.43 (w, br), 1478.94 (m), 1379.33 (m), 1351.63 (w), 1167.11 (w), 1112.44 (w), 1044.84 (w), 948.68 (s, br), 809.71 (s), 738.27 (s), 585.68 (s), 565.58 (s), 541.25 (s)
6	3267.48 (w, br), 2960.26 (m), 2931.52 (m), 2871.63 (m), 1781.63 (s), 1556.87 (w), 1459.28 (m), 1378.45 (m), 1351.33 (m), 1167.81 (w), 1112.21 (w), 1044.72 (m), 942.97 (s, br), 807.31 (s), 736.89 (s), 562.75 (s), 410.73 (s)
13	3256.00 (w, br), 2960.93 (m), 2872.56 (m), 1784.20 (w), 1666.47 (m, br), 1447.24 (s), 1378.20 (s), 1139.93 (w), 1057.94 (m), 940.37 (s), 879.30 (m), 810.71 (s), 739.28 (s), 564.58 (s), 441.07 (s), 409.81 (s)

Table 5.26 Bands in the FTIR spectra for solids isolated from the reactions between $(\text{TBA})_3[\text{V}_{13}\text{O}_{34}]$ and n mole-equivalents of $\text{Na}|\text{Hg}$ in PC.

5.2.2.13 The Reaction Between $(\text{TBA})_3[\text{V}_{13}\text{O}_{34}]$ and $\text{Li}|\text{Hg}$ Amalgam in MeCN

0.03 wt.% $\text{Li}|\text{Hg}$ amalgam (x g) was weighed out in an Argon glovebox in to a Schlenk flask. $(\text{TBA})_3[\text{V}_{13}\text{O}_{34}]$ (y g) was weighed out in glovebox and dissolved in MeCN to give an orange solution before being added to amalgam flask. Reaction stirred overnight and then took a sample for ^{51}V NMR. The NMR sample put back in

flask then the solution was separated from Hg in glovebox. Solution pumped dry and scratched with ether (10 mL). FTIR taken of the solid.

<i>n</i>	<i>x</i> Li Hg / g (mmol)	<i>y</i> V₁₃ / g (mmol)	Yield/ %	Colour
1	1.81 (0.08)	0.14 (0.07)	161	Khaki green
2	2.66 (0.11)	0.10 (0.05)	90	Khaki green
3	3.82 (0.17)	0.10 (0.05)	80	Blue green
4	5.35 (0.23)	0.10 (0.05)	67	Blue green
5	6.62 (0.29)	0.10 (0.05)	89	Dark blue
6	8.12 (0.35)	0.10 (0.05)	124	Blue green
13	17.01 (0.72)	0.10 (0.05)	100	Dark brown

Table 5.27 The reactions between (TBA)₃[V₁₃O₃₄] and *n* mole-equivalents of Li|Hg in MeCN.

<i>n</i>	δv/ ppm	LW1/2/ Hz	Reaction mixture/ %
1	–232.2, –306.3, –450.0, –485.8, –495.7, –499.5	3038.2, 3413.7, 375.5, 597.4	81.3, 10.7, 0.9, 7.1
2	–225.0, –291.4, –480.7, –510.5	1323.1, 2370.5, 336.3, 482.9	77.2, 22.2, 0.2, 0.4
3	–30.5, –225.5, –290.6, –500.0	957.6, 1333.9, 1846.9, 3334.6	10.8, 64.9, 19.0, 5.3
4	–33.2	2287.8	100.0
5	–530.7, –613.0	2976.9, 2039.7	89.3, 10.7
6	–545.2	2332.7	100.0
13	–565.5	4881.1	100.0

Table 5.28 Peaks in the ⁵¹V{¹H} NMR spectra for the reactions between (TBA)₃[V₁₃O₃₄] and *n* mole-equivalents of Li|Hg in MeCN.

Chapter 5 Experimental

<i>n</i>	Bands in FTIR/ cm⁻¹
1	3420.4 (w, br), 2959.8 (m), 2932.6 (m), 2871.8 (m), 2175.0 (w), 2160.6 (w), 2110.0 (w), 1787.2 (w), 1659.9 (w), 1478.9 (m), 1378.0 (m), 1152.1 (w), 1066.3 (w), 974.3 (s), 850.8 (s), 815.6 (s), 753.1 (s), 557.4 (s), 512.3 (s), 442.8 (s), 417.3 (s)
2	3419.7 (w, br), 2958.7 (m), 2932.1 (m), 2871.2 (m), 2178.2 (w), 2030.2 (w), 1785.4 (w), 1626.8 (w), 1478.6 (w), 1377.7 (w), 1151.4 (w), 1106.7 (w), 1064.9 (w), 986.9 (s), 971.8 (s), 850.9 (s), 816.2 (s), 751.1 (s), 556.0 (s), 514.4 (s), 435.0 (s)
3	3406.5 (w, br), 2959.2 (m), 2931.0 (m), 2870.6 (m), 2322.5 (w), 2160.5 (w), 1994.8 (w), 1626.6 (w), 1478.9 (s), 1378.1 (m), 1153.1 (w), 1107.1 (w), 1066.0 (w), 1026.6 (w), 976.2 (s), 943.5 (s), 892.2 (s), 855.4 (s), 814.4 (s), 739.0 (s), 575.8 (s), 529.0 (s), 496.6 (s), 463.5 (s), 432.3 (s)
4	3369.2 (w, br), 2958.6 (m), 2931.3 (m), 2869.8 (m), 2179.8 (w), 2114.7 (w), 1634.5 (w), 1478.8 (s), 1377.8 (m), 1152.2 (w), 1106.8 (w), 1065.9 (w), 1028.3 (w), 974.8 (s), 942.5 (s), 812.3 (s), 764.3 (s), 735.9 (s), 630.2 (s), 563.9 (s), 529.5 (s), 495.6 (s)
5	3321.3 (w, br), 2958.6 (m), 2930.0 (m), 2869.2 (m), 2169.4 (w), 2040.8 (w), 1635.5 (w), 1591.1 (w), 1478.3 (s), 1377.6 (m), 1151.7 (w), 1106.9 (w), 1065.9 (w), 1028.4 (w), 974.7 (s), 941.1 (s), 811.8 (s), 766.5 (s), 735.0 (s), 631.1 (s), 563.1 (s), 528.1 (s), 495.3 (s), 434.7 (s)
6	3398.4 (w, br), 2958.1 (m), 2932.0 (m), 2869.0 (m), 2167.6 (w), 2033.2 (w), 1636.0 (w), 1478.5 (m), 1377.7 (w), 1152.1 (w), 1106.9 (w), 1066.9 (w), 974.7 (s), 941.2 (s), 811.1 (s), 735.2 (s), 629.8 (s), 565.4 (s), 530.3 (s), 495.2 (s), 423.6 (s), 412.2 (s)
13	3331.0 (w), 3211.2 (w), 2960.9 (m), 2933.1 (m), 2873.1 (m), 2181.1 (m), 1636.2 (m), 1591.9 (m), 1461.7 (m), 1420.9 (m), 1379.0 (m), 1307.9 (m), 1151.2 (w), 1107.1 (w), 1059.1 (w), 1029.2 (w), 875.1 (s), 812.2 (s), 735.4 (s)

Table 5.29 Bands in the FTIR spectra for solids isolated from the reactions between (TBA)₃[V₁₃O₃₄] and *n* mole-equivalents of Li|Hg in MeCN.

5.2.2.14 The Reaction Between (TBA)₃[V₁₃O₃₄] and Li|Hg Amalgam in PC

0.03 wt.% Li|Hg amalgam (x g) was weighed out in Argon glovebox in to a Schlenk flask. (TBA)₃[V₁₃O₃₄] (y g) was weighed out in glovebox and dissolved in PC to give an orange solution before being added to amalgam flask. Reaction stirred o/n and then a sample was taken for ⁵¹V NMR. The NMR sample was put back into the flask and then the solution was separated from Hg in glovebox. Ether (60 mL) was added to the solution, scratched and then the solid was pumped dry. FTIR was taken of the solid.

<i>n</i>	x Li Hg/ g (mmol)	y V₁₃/ g (mmol)	Yield/ %	Colour
1	1.8 (0.08)	0.13 (0.07)	103	Khaki green
2	2.7 (0.11)	0.10 (0.05)	95	Khaki green
3	4.1 (0.18)	0.10 (0.05)	89	Dark green
4	5.4 (0.24)	0.10 (0.05)	24	Blue green
5	6.6 (0.29)	0.10 (0.05)	64	Blue green
6	8.0 (0.35)	0.10 (0.05)	12	Blue green
13	20.0 (0.86)	0.10 (0.05)	90	Dark blue

Table 5.30 The reactions between (TBA)₃[V₁₃O₃₄] and *n* mole-equivalents of Li|Hg in PC.

<i>n</i>	δ/ ppm	LW1/2/ Hz	Reaction mixture/ %
1	-57.1, -232.6, -297.6, -395.5, -428.6, -505.1, -524.4	1323.1, 2508.3, 4189.7, 2646.1	1.1, 70.1, 2.5, 26.4
2	-54.4, -225.5, -291.4, -506.1	1433.3, 1543.6, 2012.2, 3335.2	3.0, 73.3, 20.2, 3.5
3	-29.4, -225.7, -292.6, -509.1	1075.2, 1141.4, 2365.4, 2233.1	4.6, 71.0, 20.5, 3.9
4	-29.1, -225.7, -290.6, -495.2	990.4, 1127.5, 2316.0, 2696.9	22.0, 45.8, 15.4, 16.7
5	-27.1, -494.1, -511.5, -519.3, -523.7	1210.9, 3747.2	5.9, 94.1
6	-395.6, -496.8, -518.9, -523.8	1802.3, 3746.8	2.9, 97.1
13	-524.2	3831.4	100.0

Table 5.31 Peaks in the $^{51}\text{V}\{^1\text{H}\}$ NMR spectra for the reactions between $(\text{TBA})_3[\text{V}_{13}\text{O}_{34}]$ and *n* mole-equivalents of Li|Hg in PC.

<i>n</i>	Bands in FTIR/ cm^{-1}
1	3307.0 (w, br), 2959.9 (m), 2933.1 (m), 2872.1 (m), 2216.7 (m), 1784.2 (m), 1478.9 (m), 1379.3 (m), 1351.6 (w), 1167.2 (w), 1113.4 (w), 1050.9 (w), 987.5 (s), 970.6 (s), 850.5 (s), 814.9 (s), 753.8 (s), 590.6 (s), 556.6 (s), 521.7 (s), 431.6 (s)
2	3345.3 (w, br), 2960.0 (m), 2932.7 (m), 2872.0 (m), 2018.4 (w), 1785.5 (m), 1624.4 (w), 1479.0 (m), 1379.1 (m), 1351.1 (w), 1167.0 (w), 1112.2 (w), 1048.7 (w), 987.6 (s), 971.1 (s), 851.3 (s), 816.5 (s), 750.1 (s), 555.6 (s), 523.5 (s), 425.8 (s)
3	3387.6 (w, br), 2960.4 (m), 2931.3 (m), 2872.0 (m), 2020.6 (w), 1783.3 (m), 1478.7 (m), 1379.5 (m), 1351.4 (w), 1164.7 (w), 1112.8 (w), 1046.2 (w), 973.1 (s), 945.5 (s), 853.7 (s), 814.9 (s), 757.4 (s), 578.3 (s), 526.9 (s), 422.4 (s), 411.2 (s)
4	3362.5 (w, br), 2958.2 (m), 2928.8 (m), 2869.6 (m), 2323.0 (w), 1988.1 (w), 1782.5 (w), 1628.0 (w), 1477.8 (m), 1377.5 (w), 1150.5 (w), 1106.9 (w), 1067.0 (w), 975.5 (s), 942.5 (s), 856.5 (s), 813.8 (s), 738.5 (s), 632.8 (s), 566.1 (s), 531.7 (s), 495.5 (s), 466.8 (s), 418.8 (s)
5	3388.6 (w, br), 2960.3 (m), 2871.5 (m), 2161.0 (w), 2004.0 (w), 1783.2 (w), 1627.6 (w), 1479.6 (m), 1379.0 (w), 1148.0 (w), 1061.6 (w), 977.0 (s), 936.1 (s), 814.9 (s), 578.4 (s), 533.3 (s)
6	3691.8 (w), 3334.4 (w, br), 2959.7 (m), 2931.4 (m), 2871.2 (m), 2181.8 (w), 1995.4 (w), 1782.5 (w), 1629.7 (w), 1479.5 (m), 1459.7 (m), 1378.7 (w), 1146.5 (w), 1032.4 (w), 977.0 (s), 933.2 (s), 814.2 (s), 574.5 (s), 533.4 (s), 424.4 (s)
13	3341.3 (w, br), 2960.7 (m), 2932.1 (m), 2872.1 (m), 2181.3 (w), 1979.5 (w), 1782.3 (m), 1635.7 (w), 1478.0 (m), 1381.7 (m), 1164.7 (w), 1112.1 (w), 1046.3 (w), 977.5 (s), 937.8 (s), 873.1 (m), 812.5 (s), 778.6 (m), 737.4 (m), 632.3 (m), 569.8 (s), 495.8 (s), 437.9 (s)

Table 5.32 Bands in the FTIR spectra for solids isolated from the reactions between $(\text{TBA})_3[\text{V}_{13}\text{O}_{34}]$ and *n* mole-equivalents of Li|Hg in PC.

5.2.2.15 The Reaction Between $(\text{TBA})_3[\text{PMo}_{12}\text{O}_{40}]$ and KC_8 in MeCN

Potassium (0.50 g, 12.7 mmol) was weighed out in to toluene and then transferred to a Schlenk flask and pumped dry. Graphite flake (1.23 g, 102 mmol) was weighed out, transferred to a Schlenk flask and pumped dry with heating. The potassium was

Chapter 5 Experimental

transferred in to the graphite containing flask under N₂. The flask was put under vacuum then heated whilst agitating the graphite until all the potassium had vaporised and all the graphite had turned bronze in colour.

(TBA)₃[PMo₁₂O₄₀] (1.00 g, 0.39 mmol) was pumped dry then dissolved in dry MeCN (15 mL). The POM solution was taken into the glovebox and KC₈ (0.05 g, 0.39 mmol) was added, the solution immediately changed from yellow to dark green. The reaction mixture was stirred o/n, and a sample was taken for ³¹P NMR. KC₈ (0.05 g, 0.39 mmol) was added to the reaction and stirred o/n, and ³¹P NMR recorded and this was repeated until ten mole-equivalents were added.

<i>n</i>	x KC ₈ / g (mmol)	y PMo ₁₂ /g (mmol)
1	0.05 (0.39)	1.00 (0.39)
2	0.11 (0.78)	1.00 (0.39)
3	0.16 (1.17)	1.00 (0.39)
4	0.21 (1.56)	1.00 (0.39)
5	0.27 (1.95)	1.00 (0.39)
6	0.32 (2.34)	1.00 (0.39)
7	0.37 (2.73)	1.00 (0.39)
8	0.42 (3.12)	1.00 (0.39)
9	0.48 (3.51)	1.00 (0.39)
10	0.53 (3.90)	1.00 (0.39)

Table 5.33 The reactions between (TBA)₃[PMo₁₂O₄₀] and *n* mole-equivalents of KC₈ in MeCN.

<i>n</i>	δ_{P} / ppm	LW1/2 / Hz	Reaction mixture/ %
1	-0.0	15.8	100.0
2	-6.8	17.5	100.0
3	-6.8	3.8	100.0
4	-6.8	3.9	100.0
5	-6.8	4.7	100.0
6	-4.0, -5.8, -6.8	7.8, 11.1, 6.5	15.4, 29.8, 54.8
7	-4.1, -5.9, -6.8	10.7, 9.1, 4.3	22.1, 42.3, 35.6
8	-4.1, -5.9, -6.8	10.8, 12.4, 5.4	12.2, 51.5, 36.3
9	-5.8	12.6	100.0
10	NO PEAKS		

Table 5.34 Peaks in the ³¹P{¹H} NMR spectra for the reactions between (TBA)₃[PMo₁₂O₄₀] and *n* mole-equivalents of KC₈ in MeCN.

5.2.2.16 The Reaction Between (TBA)₃[PMo₁₂O₄₀] and K⁺PhCN^{-•} in PhCN

K (x g) was weighed out into toluene then pumped dry. PhCN (5 mL) was then added to the flask and heated to dissolve K, this gave a dark red solution. Some K remained undissolved so more PhCN (5 mL) was added and heated further. (TBA)₃[PMo₁₂O₄₀]

(y g) was added and the reaction mixture was stirred, the colour changed from red to purple and then to dark green for 1:1 and dark blue for two, four and six mole-equivalents. The reaction was stirred o/n and then a sample was taken for ^{31}P NMR the next day.

<i>n</i>	<i>x</i> K/ g (mmol)	<i>y</i> PMo₁₂ /g (mmol)	Colour
1	0.02 (0.44)	1.11 (0.44)	Dark green
2	0.01 (0.36)	0.44 (0.17)	Dark blue
4	0.01 (0.36)	0.23 (0.09)	Dark blue
6	0.02 (0.46)	0.20 (0.08)	Dark blue

Table 5.35 The reactions between $(\text{TBA})_3[\text{PMo}_{12}\text{O}_{40}]$ and *n* mole-equivalents of $\text{K}^+\text{PhCN}^{\bullet-}$ in PhCN.

<i>n</i>	δ_{P} / ppm	LW1/2 / Hz	Reaction mixture/ %
1	0.4	15.8	100
2	1.2	4.8	100
4	0.3, -6.4	46.3, 30.8	55.2, 44.8
6	-6.9	3.1	100

Table 5.36 Peaks in the $^{31}\text{P}\{^1\text{H}\}$ NMR spectra for the reactions between $(\text{TBA})_3[\text{PMo}_{12}\text{O}_{40}]$ and *n* mole-equivalents of $\text{K}^+\text{PhCN}^{\bullet-}$.

5.3 Chapter 3

5.3.1 Materials

Materials were purchased from suppliers as listed below in Table 5.37.

Chemical	Supplier
Na	Fisher Scientific
SbCl_3	Sigma Aldrich
MeCN	Fisher Scientific
CD_3CN	Goss Scientific
Bi metal	Acros
DMSO	Sigma Aldrich
99.9% DMSO- d^6	Goss Scientific
Diethyl ether	Fisher Scientific
Zn dust	Sigma Aldrich

Table 5.37 Materials used in Chapter 3 and their suppliers.

The mercury used in the experiments was recycled Hg cleaned by filtration and successive washing with dilute HNO_3 , water and ethanol then dried under vacuum.

Solvents used were dried in the same methods as described in Section 5.2.1.

5.3.2 Synthesis

5.3.2.1 $(TBA)_3[PMo_{12}O_{40}Sb_2]$

Literature procedure.⁹ 0.35 wt.% Na/Hg amalgam was made by weighing out sodium (0.03 g, 1.48 mmol) in to toluene. This was then transferred to a Schlenk flask and pumped dry. Hg (8.5 g) was added and the sodium was squashed with a glass rod to activate. $(TBA)_3[PMo_{12}O_{40}]$ (0.63 g, 0.25 mmol) was dissolved in dry MeCN (30 mL) with heating to give a yellow solution. The $(TBA)_3[PMo_{12}O_{40}]$ solution was transferred into the flask containing Na|Hg amalgam, and the POM flask was rinsed with MeCN (5 mL). The reaction was stirred, which gave a dark blue solution. A sample of the solution after 1 hour of stirring was taken for ^{31}P NMR spectroscopy, this gave a peak at -6.5 ppm. $SbCl_3$ (0.11 g, 0.49 mmol) was weighed out in the glovebox and dissolved in dry MeCN (5 mL), then transferred into the reaction flask, the flask was rinsed with MeCN (5 mL) and the dark blue reaction mixture was stirred overnight. ^{31}P NMR spectrum was recorded the next day and contained one peak at -5.8 ppm. The blue reaction mixture was filtered and the blue solution was vacuum dried to obtain a blue solid. The solid was then re-dissolved in the minimum amount of MeCN, with heating and allowed to cool, then placed in freezer over the weekend. Crystals had formed in the flask and so were sent to crystallography.

$^{31}P\{^1H\}$ NMR, CD_3CN (ppm): -6.5 (after the addition of 6 Na|Hg)

-5.8 (after the addition of 2 $SbCl_3$)

-5.8 (isolated crystals)

FTIR (cm^{-1}): 2959.2 (m), 2931.9 (m), 2871.2 (m), 2247.8 (w), 1701.6 (w), 1480.0 (m), 1463.2 (m), 1378.4 (m), 1152.2 (w), 1107.7 (w), 1065.7 (w), 1028.7 (m), 940.9 (s, sh), 726.5 (m), 635.9 (m), 602.4 (m), 588.8 (m), 574.8 (m), 511.8 (m), 478.6 (m), 439.8 (m)

5.3.2.2 $(TBA)_3[PMo_{12}O_{40}\{Bi(dmsO)_4\}_2]$

$(TBA)_3[PMo_{12}O_{40}]$ (0.30 g, 0.12 mmol) was dissolved in dry DMSO (10 mL) to give a yellow-orange solution. Bi (0.05 g, 0.24 mmol) was added and the reaction stirred, with the temperature increased to 60 °C. After 10 minutes the reaction had changed to pale green in colour. After 2.5 hr the solution had changed to a dark blue colour. The reaction was stirred overnight at 60 °C. ^{31}P NMR was recorded the next day;

three peaks were present, -0.3 , -2.2 and -4.1 ppm. The reaction was stirred for a further 5 hr at $60\text{ }^{\circ}\text{C}$ and another ^{31}P NMR was recorded; four peaks were present;

$^{31}\text{P}\{^1\text{H}\}$ NMR, $\text{d}^6\text{-dmsO}$ (ppm): -0.3 , -2.2 and -4.1 (o/n stir)

-0.3 , -2.2 and -4.1 and -6.8 (further 5 hr)

-0.3 and -6.9 (isolated crystals)

FTIR (cm^{-1}): 2958.4 (m), 2930.1 (m), 2870.5 (m), 2162.5 (w), 2050.6 (w), 1980.2 (w), 1479.6 (m), 1459.5 (m), 1378.1 (w), 1151.2 (w), 1106.8 (w), 1054.8 (m), 938.1 (s), 884.8 (s), 755.1 (s, br), 687.9 (s, br), 579.5 (m), 513.1 (m), 464.0 (m)

5.3.2.3 $(\text{TBA})_3[\text{PMo}_{12}\text{O}_{40}\{\text{Zn}(\text{dmsO})_2\}]$

5.3.2.3.1 One Mole-equivalent of Zn

DMSO (2 mL) was added to a Schlenk flask charged with $(\text{TBA})_3[\text{PMo}_{12}\text{O}_{40}]$ (0.50 g, 0.2 mmol) and Zn dust (0.01 g, 0.22 mmol) and the mixture was heated to dissolve the PMo_{12} . The reaction solution changed from orange to green to dark blue after several minutes of stirring with no further heating. The reaction was stirred o/n at RT, the next day took a sample for ^{31}P NMR, and there were three peaks present; -0.3 , -6.9 and -7.8 ppm. The reaction mixture was filtered in to a clean flask and ether added to precipitate the product as a dark blue solid. The solid was then dissolved in the minimum amount of MeCN with heating and some of this was transferred to a crystallisation tube and surrounded with ether. After several days crystals formed and these crystals were taken to crystallography.

$^{31}\text{P}\{^1\text{H}\}$ NMR, CD_3CN (ppm): -0.3 , -6.9 and -7.8 (o/n stir)

-8.1 (isolated crystals)

FTIR (cm^{-1}): 2958.2 (m), 2931.6 (m), 2871.2 (m), 2176.7 (w), 2114.8 (w), 1951.8 (w), 1480.7 (m), 1378.1 (w), 1316.8 (w), 1152.2 (w), 1105.9 (w), 1052.7 (w), 1033.4 (w), 982.1 (w), 941.6 (s, sh), 873.9 (m), 777.9 (s, br), 590.7 (m), 511.0 (m), 479.4 (m), 450.0 (m)

5.3.2.3.2 Two Mole-equivalents of Zn

DMSO (2 mL) was added to a Schlenk flask charged with $(\text{TBA})_3[\text{PMo}_{12}\text{O}_{40}]$ (0.50 g, 0.2 mmol) and Zn dust (0.03 g, 0.43 mmol) and the mixture was heated to dissolve the PMo_{12} . The reaction solution changed from orange to green to dark blue after several minutes of stirring with no further heating. The reaction was stirred o/n at RT,

Chapter 5 Experimental

the next day took a sample for ^{31}P NMR, and there were three peaks present; -0.2 , -6.8 and -8.2 ppm. The reaction mixture was filtered in to a clean flask and ether added to precipitate the product as a dark blue solid. The solid was then dissolved in the minimum amount of MeCN with heating and some of this was transferred to a crystallisation tube and surrounded with ether. After several days crystals formed and these crystals were taken to crystallography.

$^{31}\text{P}\{\text{H}\}$ NMR, CD_3CN (ppm): -0.2 , -6.8 and -8.2 (o/n stir)

-8.1 (isolated crystals)

FTIR (cm^{-1}): 2959.0 (m), 2933.1 (m), 2871.6 (m), 2235.7 (w), 2145.3 (w), 2048.9 (w), 1975.0 (w), 1939.7 (w), 1899.9 (w), 1791.1 (w), 1480.9 (m), 1379.2 (m), 1309.2 (w), 1238.1 (m), 1151.1 (w), 1054.2 (m, sh), 1002.8 (w), 982.8 (w), 940.4 (s, sh), 857.0 (m, br), 775.7 (s, br), 591.5 (m), 494.4 (m), 454.1 (m)

5.4 Chapter 4

5.4.1 Materials

Materials were purchased from suppliers as listed below in Table 5.38.

Chemical	Supplier
Na_3VO_4	Sigma Aldrich
Acetic acid	Sigma Aldrich
Acetone	Fisher Scientific
Ethanol	Fisher Scientific
NaVO_3	Sigma Aldrich
37% HCl	Fisher Scientific
D_2O	Fluorochem
Super P	Fisher Scientific
PVDF	Sigma Aldrich
NMP	Sigma Aldrich
Activated carbon YP-80F (μm)	Kuraray
LiClO_4	Alfa Aesar
PC	Sigma Aldrich

Table 5.38 Materials used in Chapter 4 and their suppliers.

Five different current collectors were used as part of this research as listed in Table 5.39.

Current collector	Manufacturer	Purchased from
TGP-H-030	Toray™	Fuel cell earth
2050A-0550	Spectracarb™	Fuel cell store
2050A-0850	Spectracarb™	Fuel cell store
2050L-0850	Spectracarb™	Fuel cell store
2050A-1550	Spectracarb™	Fuel cell store

Table 5.39 Current collectors.

5.4.2 Synthesis

5.4.2.1 Johnson and Murmann Method.¹⁰

Na₃VO₄ (6.7 g, 36.4 mmol) was dissolved in water (20 mL) at approx. 30 °C with stirring which gave a cloudy solution. Glacial acetic acid (10 mL, 228.4 mmol) was added dropwise over 15 mins with vigorous stirring, keeping the temperature between 30-35 °C, the solution turned orange and then an orange solid fell out of the solution. The mixture was stirred for 1 hr at approximately 25 °C. The mixture was filtered using a Buchner funnel and washed with acetone (4 x 10 mL) and air dried o/n. Crude product (4.1 g). A yellow solid had formed o/n and the mixture was filtered and the solid allowed to air dry after washing with acetone. The solid was dissolved in water (20 mL) with minimal heating and filtered using coarse fibre-glass paper (Whatman GF/A) which gave a red-orange solution. This red-orange solution was then placed in an ice bath to recrystallize. The red crystals obtained were filtered and air dried.

Yield: 3.4 g, 65%.

⁵¹V{¹H} NMR, D₂O (ppm): -420.9, -495.0, -511.7, -550.7, -569.6 and -575.7

FTIR (cm⁻¹): 3473.5 (s, br), 2095.1 (w, br), 1625.4 (m), 1397.5 (w), 977.3 (s, sh), 949.1 (s), 934.4 (s), 816.7 (s), 735.0 (m, br), 559.6 (w)

5.4.2.2 Yerra Method.¹¹

NaVO₃ (2.0 g, 16.4 mmol) was dissolved in water (100 mL) and heated to 70 °C for 2 hrs. Acetic acid was added dropwise until pH 5 (using a pre-calibrated pH meter). Ice cold acetonitrile (60 mL) was added to the rapidly stirring vanadate solution and a yellow-orange precipitate formed. The precipitate was collected on a filter and air dried o/n.

Yield: 2.0 g, 84%.

⁵¹V{¹H} NMR, D₂O (ppm): -421.8, -496.9, -512.8, -557.1, -571.2, 575.8 and 584.3

Chapter 5 Experimental

FTIR (cm⁻¹): 3311.2 (m, br), 1625.1 (m), 977.2 (m, sh), 935.1 (s), 813.1 (m), 736.4 (m, br), 493.2 (m, br), 447.2 (m)

5.4.2.3 Chen Method + Ethanol.¹²

NaVO₃ (3.0 g, 24.6 mmol) was dissolved in water (100 mL) with heating. 4 M HCl added until the pH was 4.8 (using a pre-calibrated pH meter). The solution was filtered and 4 M HCl added dropwise to adjust pH to 4.5. Ice cold 95% ethanol (200 mL) was added to the rapidly stirring vanadate solution to give a yellow-orange solid, collected on a filter and air dried o/n.

Yield: 2.6 g, 75%.

⁵¹V{¹H} NMR, D₂O (ppm): -421.7, -498.8, -514.1, -558.7, -571.5 and 575.8

FTIR (cm⁻¹): 3354.2 (m, br), 2162.9 (w), 2051.3 (w), 1623.5 (m), 974.1 (w), 949.4 (s), 816.2 (m), 739.3 (m, br), 492.8 (m, br)

5.4.2.4 Chen Method + Acetone.¹²

This was a modified literature procedure. ¹² NaVO₃ (3.0 g, 24.6 mmol) was dissolved in water (100 mL) with heating. 4 M HCl added until the pH was 4.8 (using pH meter). The solution was filtered and 4 M HCl added dropwise to adjust pH to 4.5. Ice cold acetone (200 mL) was added to the rapidly stirring vanadate solution to give a yellow-orange solid collected on a filter and air dried o/n.

Yield: 1.8 g, 52%.

⁵¹V{¹H} NMR, D₂O (ppm): -422.5, -499.0, -514.2, -558.8, -571.5 and 575.8

FTIR (cm⁻¹): 3362.0 (m, br), 2160.9 (w), 1624.1 (m), 1025.9 (w), 973.1 (s, sh), 949.9 (s), 817.1 (m), 740.9 (m, br), 499.3 (m, br)

5.4.3 V₁₀ Processing

5.4.3.1 Sonoprecipitation

A sonics & materials inc. sonication horn was put into a test tube to a depth of 1 cm from the bottom with the test tube in an ice bath. The test tube contained 10 mL of anti-solvent (MeCN, EtOH or Acetone). A syringe containing 5 mL of aqueous vanadate solution (from the Yerra *et al.* or Chen *et al.* preparations) was added to the continuously sonicating anti-solvent to give V₁₀ powder. Output control was set to 4 and the pulser was switched off.

5.4.3.2 Grinding

V_{10} was ground using a ceramic pestle and mortar for 15 mins.

5.4.3.3 Sonofragmentation



Figure 5.1 Control panel of sonication probe.

A sonication horn was put into a test tube that contained a suspension of V_{10} (50 mg) in anti-solvent (10 mL) and sonicated with the pulser switched on and set to a 10% duty cycle, output control 4 for ten mins as shown in the photo of the control panel of the sonicator in Figure 5.1.

5.4.3.4 Ball Mill

A Fisherbrand™ mini vortex mixer, plastic test tube and two 5 mm stainless steel ball bearings were used to make a ball mill.

5.4.3.5 HEBM

Retsch E_{max} was used with 1 mm ZrO₂ beads and a 50 mL ZrO₂ jar. The grinding jar was 1/3 filled with V_{10} powder, 1/3 beads and then topped up with propan-2-ol with a slight gap at the top of the jar. T = 20 °C. 10 minutes at 2000 rpm up until 60 mins taking an aliquot of sample after each time interval, t = 0-60 mins.

5.4.4 Working Electrode Preparation

5.4.4.1 Current Collector Experiment

Series Q, R, S and U: V_{10} was prepared following the prep detailed in Section 5.4.2.3. V_{10} was dried in oven o/n at 80 °C, ground for 15 mins using a pestle and mortar, sonicated 50 mg portions for 10 mins in EtOH (10 mL) using a 30% duty cycle, dried in an oven at 80 °C o/n and then ball milled for 5 mins. The V_{10} was then ground together with Super P for 15 mins then transferred to a vial, PVDF added and

Chapter 5 Experimental

then NMP added until slurry stirred smoothly. 75:10:15 V₁₀: Super P: PVDF. The current collectors were then coated using a spatula and oven dried at 80 °C o/n.

Q Spectracarb 2050A-0550

R Spectracarb 2050A-0850

S Spectracarb 2050L-0850

U TGP-H-030

5.4.4.2 Conducting Carbon Experiment

Series AL: V₁₀ was prepared following the prep detailed in Section 5.4.2.3. V₁₀ was dried in oven o/n at 80 °C, ground for 15 mins using a pestle and mortar, sonicated 50 mg portions for 10 mins in EtOH (10 mL) using a 30% duty cycle, dried in an oven at 80 °C o/n and then ball milled o/n. The V₁₀ was then sonicated with Super P for 10 mins in EtOH (10 mL) using a 30% duty cycle, dried in oven o/n at 80 °C then transferred to a vial, PVDF added and then NMP added until slurry stirred smoothly. 75:10:15 V₁₀: Super P: PVDF. The Spectracarb 2050A-1550 current collector was then coated using a spatula and oven dried at 80 °C o/n.

Series AR: V₁₀ was prepared following the prep detailed in Section 5.4.2.3. V₁₀ was dried in oven o/n at 80 °C, ground for 15 mins using a pestle and mortar, sonicated 50 mg portions for 10 mins in EtOH (10 mL) using a 30% duty cycle and dried in an oven at 80 °C o/n. The V₁₀ was then ground together with Denka black for 15 mins then transferred to a vial, PVDF added and then NMP added until slurry stirred smoothly. 75:10:15 V₁₀: Denka black: PVDF. The Spectracarb 2050A-1550 current collector was then coated using a spatula and oven dried at 80 °C o/n.

5.4.4.3 Loading Experiment

Series AH: V₁₀ was prepared following the prep detailed in Section 5.4.2.3. V₁₀ was dried in oven o/n at 80 °C, ground for 15 mins using a pestle and mortar, sonicated 50 mg portions for 10 mins in EtOH (10 mL) using a 30% duty cycle, dried in an oven at 80 °C o/n and then ball milled for 5 mins. The V₁₀ was then sonicated with Super P for 10 mins in EtOH (10 mL) using a 30% duty cycle, dried in oven o/n at 80 °C then transferred to a vial, PVDF added and then NMP added until slurry stirred smoothly. 75:15:10 V₁₀: Super P: PVDF. The Spectracarb 2050A-1550 current collector was then coated using a spatula and oven dried at 80 °C o/n.

Series AK: V_{10} was prepared following the prep detailed in Section 5.4.2.3. V_{10} was dried in oven o/n at 80 °C, ground for 15 mins using a pestle and mortar, sonicated 50 mg portions for 10 mins in EtOH (10 mL) using a 30% duty cycle, dried in an oven at 80 °C o/n and then ball milled for 5 mins. The V_{10} was then ground together with Super P for 10 mins, transferred to a vial, PVDF added and then NMP added until slurry stirred smoothly. 75:15:10 V_{10} : Super P: PVDF. The Spectracarb 2050A-1550 current collector was then coated using a spatula and oven dried at 80 °C o/n.

Series AL: As described in Section 5.4.4.2

Series AU: V_{10} was prepared following the prep detailed in Section 5.4.2.1. V_{10} was dried in oven o/n at 80 °C then ball milled using a Retsch HEBM set at 2000 rpm for 60 mins, then separated from propan-2-ol by centrifuging and decanting of the liquid. V_{10} was dried in oven o/n at 80 °C. The V_{10} was then ground together with Super P for 10 mins using a pestle and mortar then transferred to a vial, PVDF added and then NMP added until slurry stirred smoothly. V_{10} : Super P: PVDF, 75:15:10. The Spectracarb 2050A-1550 current collector was then coated using a spatula and oven dried at 80 °C o/n.

5.4.4.4 CP Dwell Experiment

Series AK: As described Section 5.4.4.3.

5.4.4.5 Asymmetric Supercapacitor

V_{10} slurry: V_{10} was prepared following the prep detailed in Section 5.4.2.1. V_{10} was dried in oven o/n at 80 °C then ball milled using a Retsch HEBM set at 2000 rpm for 60 mins, then separated from propan-2-ol by centrifuging and decanting of the liquid. V_{10} was dried in oven o/n at 80 °C. The V_{10} was then ground together with Super P for 10 mins using a pestle and mortar then transferred to a vial, PVDF added and then NMP added until slurry stirred smoothly. V_{10} : Super P: PVDF, 75:15:10. The Spectracarb 2050A-1550 2.54 cm² area disc current collector was then coated using a spatula and oven dried at 80 °C o/n.

AC slurry: The slurry was prepared by first grinding AC (Kuraray 80F- 6u) using a pestle and mortar, then transferred to a vial, PVDF added and then NMP added until slurry stirred smoothly. AC: PVDF, 88:12. The Spectracarb 2050A-1550 2.54 cm² area disc current collector was then coated using a spatula and oven dried at 80 °C o/n.

5.5 References

1. CrysAlisPro, *Rigaku, Oxford Diffraction*, 2015.
2. R. C. Clark and J. S. Reid, *Acta Cryst.*, 1995, **A51**, 887.
3. O. V. Dolomanov, L. J. Bourhis, R. J. Gildea, J. A. K. Howard and H. Puschmann, *J. Appl. Cryst.*, 2009, **42**, 339.
4. G. M. Sheldrick, *Acta Cryst.*, 2015, **A71**, 3.
5. G. M. Sheldrick, *Acta Cryst.*, 2008, **A64**, 112.
6. J. L. C. Sanchez, J. P. Launay, M. Fournier, Y. Jeannin, *J. Am. Chem. Soc.*, 1982, **104**, 3194.
7. R. Bakri, Newcastle University, 1998.
8. W. G. Klemperer and O. M. Yaghi, *Inorg. Synth.*, 1990, **27**.
9. R. Bakri, A. Booth, G. Harle, P. S. Middleton, C. Wills, W. Clegg, R. W. Harrington and R. J. Errington, *Chem. Commun.*, 2012, **48**, 2779.
10. G. K. Johnson and R. K. Murmann, *Inorg. Synth.*, 1979, **19**, 142.
11. S. Yerra, B. K. Tripuramallu and S. K. Das, *Polyhedron*, 2014, **81**, 147.
12. H.-Y. Chen, G. Wee, R. Al-Oweini, J. Friedl, K. S. Tan, Y. Wang, C. L. Wong, U. Kortz, U. Stimming and M. Srinivasan, *ChemPhysChem*, 2014, **15**, 2162.

A1 Appendix

A1. Appendix

A1.1 Crystal data for $(\text{TBA})_2[\text{PMo}_{12}\text{O}_{40}\text{Sb}_2]$

Empirical formula	$\text{C}_{32}\text{H}_{72}\text{Mo}_{12}\text{N}_2\text{O}_{40}\text{PSb}_{1.98}$
Formula weight	2548.23
Temperature/K	150.0(2)
Crystal system	cubic
Space group	Fm-3m
$a/\text{\AA}$	18.7381(5)
$b/\text{\AA}$	18.7381(5)
$c/\text{\AA}$	18.7381(5)
$\alpha/^\circ$	90
$\beta/^\circ$	90
$\gamma/^\circ$	90
Volume/ \AA^3	6579.3(5)
Z	4
$\rho_{\text{calc}}/\text{cm}^3$	2.573
μ/mm^{-1}	3.117
$F(000)$	4872.0
Crystal size/ mm^3	0.17 \times 0.14 \times 0.11
Radiation	MoK α ($\lambda = 0.71073$)
2 Θ range for data collection/ $^\circ$	7.212 to 57.538
Index ranges	-19 \leq h \leq 21, -17 \leq k \leq 23, -21 \leq l \leq 23
Reflections collected	3454
Independent reflections	452 [$R_{\text{int}} = 0.0226$, $R_{\text{sigma}} = 0.0116$]
Data/restraints/parameters	452/27/59
Goodness-of-fit on F^2	1.143
Final R indexes [$I \geq 2\sigma(I)$]	$R_1 = 0.0434$, $wR_2 = 0.0951$
Final R indexes [all data]	$R_1 = 0.0589$, $wR_2 = 0.1048$
Largest diff. peak/hole / e \AA^{-3}	0.40/-0.67

Table A1.1 Crystal data and structure refinement for $(\text{TBA})_2[\text{PMo}_{12}\text{O}_{40}\text{Sb}_2]$.

Atom x	y	z	U(eq)
Sb1 5000	5000	2707.9(14)	93.3(11)
Mo1 3645.2(3)	5000	3645.2(3)	96.4(6)
P1 5000	5000	5000	30.9(12)
O1 3029(3)	5000	3029(3)	164(5)
O2 4313(3)	5687(3)	3298(4)	125(2)
O3 4527(4)	5473(4)	4527(4)	43(3)
N1 2500	7500	2500	51(4)
C1 2934(15)	7707(17)	3146(15)	58(13)
C2 3500(20)	8290(20)	3042(12)	82(13)
C3 3720(30)	8513(18)	3820(30)	102(13)
C4 4349(19)	9010(20)	3635(18)	126(17)

Table A1.2 Fractional Atomic Coordinates ($\times 10^4$) and Equivalent Isotropic Displacement Parameters ($\text{\AA}^2 \times 10^3$). U_{eq} is defined as 1/3 of the trace of the orthogonalised U_{ij} tensor, for $(\text{TBA})_2[\text{PMo}_{12}\text{O}_{40}\text{Sb}_2]$.

A1 Appendix

Atom	U_{11}	U_{22}	U_{33}	U_{23}	U_{13}	U_{12}
Sb1	127.7(18)	127.7(18)	24.4(14)	0	0	0
Mo1	83.8(6)	121.6(10)	83.8(6)	0	-53.5(6)	0
P1	30.9(12)	30.9(12)	30.9(12)	0	0	0
O1	124(6)	244(14)	124(6)	0	-90(7)	0
O2	136(4)	136(4)	103(5)	-15(3)	15(3)	-32(5)
O3	43(3)	43(3)	43(3)	4(3)	-4(3)	4(3)
N1	51(4)	51(4)	51(4)	0	0	0
C1	80(30)	53(14)	46(12)	8(10)	0(16)	-9(17)
C2	90(20)	70(20)	82(17)	6(16)	-12(13)	-10(20)
C3	120(30)	71(16)	110(30)	-10(30)	-69(18)	20(30)
C4	110(30)	150(40)	120(30)	10(20)	-30(20)	20(30)

Table A1.3 Anisotropic Displacement Parameters ($\text{\AA}^2 \times 10^3$). The Anisotropic displacement factor exponent takes the form: $-2\pi^2[h^2a^*{}^2U_{11} + 2hka^*b^*U_{12} + \dots]$, for $(\text{TBA})_2[\text{PMo}_{12}\text{O}_{40}\text{Sb}_2]$.

Atom Atom Length/Å			Atom Atom Length/Å		
Sb1	Mo1	3.0870(15)	P1	O3 ³	1.534(12)
Sb1	Mo1 ¹	3.0870(15)	P1	O3 ⁹	1.534(12)
Sb1	Mo1 ²	3.0870(15)	P1	O3 ¹⁰	1.534(12)
Sb1	Mo1 ³	3.0870(15)	P1	O3 ⁴	1.534(12)
Sb1	O2	2.130(7)	P1	O3 ⁵	1.534(12)
Sb1	O2 ³	2.130(7)	P1	O3 ¹¹	1.534(12)
Sb1	O2 ⁴	2.130(7)	P1	O3 ¹²	1.534(12)
Sb1	O2 ⁵	2.130(7)	O2	Mo1 ¹	1.910(2)
Mo1	Sb1 ⁶	3.0870(15)	O3	Mo1 ⁸	2.500(7)
Mo1	O1	1.633(7)	O3	Mo1 ¹	2.500(7)
Mo1	O2 ⁴	1.910(2)	O3	O3 ⁵	1.771(13)
Mo1	O2 ⁷	1.910(2)	O3	O3 ⁴	1.771(13)
Mo1	O2	1.910(2)	O3	O3 ¹¹	1.771(13)
Mo1	O2 ⁸	1.910(2)	N1	C1	1.51(2)
Mo1	O3 ⁴	2.500(7)	C1	C2	1.54(3)
Mo1	O3	2.500(7)	C2	C3	1.56(3)
P1	O3	1.534(12)	C3	C4	1.55(4)

Table A1.4 Bond lengths for $(\text{TBA})_2[\text{PMo}_{12}\text{O}_{40}\text{Sb}_2]$.

Atom	Atom	Atom	Angle/°	Atom	Atom	Atom	Angle/°
Mo1	Sb1	Mo1 ¹	71.11(4)	O3 ⁴	Mo1	Sb1 ⁶	80.35(4)
Mo1	Sb1	Mo1 ²	71.11(4)	O3	Mo1	Sb1 ⁶	80.35(4)
Mo1 ³	Sb1	Mo1 ²	71.12(4)	O3	Mo1	Sb1	80.35(4)
Mo1	Sb1	Mo1 ³	110.65(9)	O3	Mo1	O3 ⁴	41.5(4)
Mo1 ¹	Sb1	Mo1 ³	71.12(4)	O3 ⁹	P1	O3 ³	109.471(4)
Mo1 ¹	Sb1	Mo1 ²	110.65(9)	O3 ⁹	P1	O3 ¹⁰	109.471(1)
O2 ³	Sb1	Mo1 ²	37.60(6)	O3 ¹¹	P1	O3 ¹⁰	70.528(4)
O2 ⁴	Sb1	Mo1 ¹	101.66(18)	O3 ¹⁰	P1	O3	109.5
O2 ⁴	Sb1	Mo1	37.60(6)	O3 ³	P1	O3 ¹⁰	109.472(1)
O2 ⁵	Sb1	Mo1 ³	37.60(6)	O3 ⁴	P1	O3 ¹⁰	70.529(3)
O2 ⁵	Sb1	Mo1 ¹	37.60(6)	O3 ¹²	P1	O3	180.0(4)
O2	Sb1	Mo1 ³	101.66(18)	O3 ⁴	P1	O3 ¹¹	109.471(1)

O2 ³	Sb1	Mo1	101.66(18)	O3 ⁹	P1	O3 ¹²	70.528(2)
O2 ⁵	Sb1	Mo1 ²	101.66(18)	O3 ³	P1	O3 ¹²	70.529(1)
O2 ⁴	Sb1	Mo1 ³	101.66(18)	O3 ⁹	P1	O3	109.471(2)
O2 ⁵	Sb1	Mo1	101.66(18)	O3 ⁴	P1	O3 ⁵	109.471(2)
O2 ⁴	Sb1	Mo1 ²	37.60(6)	O3 ⁵	P1	O3 ¹¹	109.472(2)
O2 ³	Sb1	Mo1 ¹	101.66(18)	O3 ⁴	P1	O3	70.529(2)
O2	Sb1	Mo1	37.60(6)	O3 ⁵	P1	O3 ¹²	109.471(3)
O2	Sb1	Mo1 ²	101.66(18)	O3 ⁵	P1	O3	70.529(1)
O2 ³	Sb1	Mo1 ³	37.60(6)	O3 ³	P1	O3 ¹¹	180.0(4)
O2	Sb1	Mo1 ¹	37.60(6)	O3 ¹¹	P1	O3	70.529(2)
O2	Sb1	O2 ³	117.5(4)	O3 ⁵	P1	O3 ¹⁰	180.0(4)
O2 ⁴	Sb1	O2 ³	74.40(19)	O3 ⁴	P1	O3 ³	70.529(1)
O2 ⁵	Sb1	O2 ⁴	117.5(4)	O3 ³	P1	O3	109.471(1)
O2	Sb1	O2 ⁵	74.39(19)	O3 ⁵	P1	O3 ³	70.528(1)
O2	Sb1	O2 ⁴	74.39(19)	O3 ⁴	P1	O3 ¹²	109.472(1)
O2 ⁵	Sb1	O2 ³	74.40(19)	O3 ¹²	P1	O3 ¹⁰	70.529(3)
Sb1	Mo1	Sb1 ⁶	159.35(9)	O3 ⁹	P1	O3 ⁵	70.529(1)
O1	Mo1	Sb1 ⁶	100.32(4)	O3 ⁹	P1	O3 ¹¹	70.529(1)
O1	Mo1	Sb1	100.32(4)	O3 ¹¹	P1	O3 ¹²	109.471(1)
O1	Mo1	O2 ⁴	102.8(2)	O3 ⁴	P1	O3 ⁹	180.0(4)
O1	Mo1	O2 ⁷	102.8(2)	Mo1	O2	Sb1	99.5(2)
O1	Mo1	O2 ⁸	102.8(2)	Mo1 ¹	O2	Sb1	99.5(2)
O1	Mo1	O2	102.8(2)	Mo1	O2	Mo1 ¹	140.1(4)
O1	Mo1	O3 ⁴	159.3(2)	Mo1	O3	Mo1 ⁷	91.8(3)
O1	Mo1	O3	159.3(2)	Mo1	O3	Mo1 ¹	91.8(3)
O2 ⁷	Mo1	Sb1 ⁶	42.9(2)	Mo1 ¹	O3	Mo1 ⁷	91.8(3)
O2 ⁸	Mo1	Sb1	130.8(2)	P1	O3	Mo1	124.0(2)
O2	Mo1	Sb1	42.9(2)	P1	O3	Mo1 ⁷	124.0(2)
O2 ⁴	Mo1	Sb1	42.9(2)	P1	O3	Mo1 ¹	124.0(2)
O2 ⁷	Mo1	Sb1	130.8(2)	P1	O3	O3 ⁵	54.733(1)
O2 ⁴	Mo1	Sb1 ⁶	130.8(2)	P1	O3	O3 ⁴	54.733(1)
O2	Mo1	Sb1 ⁶	130.8(2)	P1	O3	O3 ¹¹	54.733(1)
O2 ⁸	Mo1	Sb1 ⁶	42.9(2)	O3 ⁴	O3	Mo1 ⁷	131.40(8)
O2 ⁸	Mo1	O2 ⁴	89.5(4)	O3 ⁴	O3	Mo1 ¹	131.40(7)
O2 ⁷	Mo1	O2 ⁸	84.8(4)	O3 ⁵	O3	Mo1 ⁷	131.40(7)
O2	Mo1	O2 ⁴	84.8(4)	O3 ⁴	O3	Mo1	69.3(2)
O2	Mo1	O2 ⁷	89.5(4)	O3 ¹¹	O3	Mo1	131.40(7)
O2	Mo1	O2 ⁸	154.4(4)	O3 ¹¹	O3	Mo1 ¹	131.40(8)
O2 ⁷	Mo1	O2 ⁴	154.4(4)	O3 ⁵	O3	Mo1	131.40(7)
O2 ⁸	Mo1	O3	91.8(3)	O3 ¹¹	O3	Mo1 ⁷	69.3(2)
O2	Mo1	O3	63.5(2)	O3 ⁵	O3	Mo1 ¹	69.3(2)
O2 ⁴	Mo1	O3	91.8(3)	O3 ⁵	O3	O3 ⁴	89.996(1)
O2 ⁴	Mo1	O3 ⁴	63.5(2)	O3 ⁵	O3	O3 ¹¹	89.996(1)
O2	Mo1	O3 ⁴	91.8(3)	O3 ¹¹	O3	O3 ⁴	89.996(1)
O2 ⁸	Mo1	O3 ⁴	63.5(2)	N1	C1	C2	117(2)
O2 ⁷	Mo1	O3	63.5(2)	C1	C2	C3	104(3)
O2 ⁷	Mo1	O3 ⁴	91.8(3)	C4	C3	C2	99(4)

A1 Appendix

O3⁴ Mo1 Sb1 80.35(4)

Table A1.5 Bond Angles for (TBA)₂[PMo₁₂O₄₀Sb₂].

¹+Y,1-Z,+X;²+Y,+Z,+X;³1-X,1-Y,+Z;⁴+X,1-Y,+Z;⁵1-X,+Y,+Z;⁶+Z,+X,+Y;⁷+Z,1-X,1-Y; ⁸+Z,+X,1-Y;⁹1-X,+Y,1-Z;¹⁰+X,1-Y,1-Z;¹¹+X,+Y,1-Z;¹²1-X,1-Y,1-Z

Atom	x	y	z	U(eq)
H1A	3177	7274	3326	70
H1B	2600	7867	3523	70
H2A	3301	8706	2779	98
H2B	3918	8108	2776	98
H3A	3329	8769	4068	122
H3B	3871	8098	4106	122
H4A	4554	9204	4077	189
H4B	4714	8744	3376	189
H4C	4178	9407	3338	189

Table A1.6 Hydrogen Atom Coordinates (Å×10⁴) and Isotropic Displacement Parameters (Å²×10³) for (TBA)₂[PMo₁₂O₄₀Sb₂].

Atom	Occupancy	Atom	Occupancy	Atom	Occupancy
Sb1	0.33	O3	0.5	C1	0.1667
H1A	0.1667	H1B	0.1667	C2	0.1667
H2A	0.1667	H2B	0.1667	C3	0.1667
H3A	0.1667	H3B	0.1667	C4	0.1667
H4A	0.1667	H4B	0.1667	H4C	0.1667

Table A1.7 Atomic Occupancy for (TBA)₂[PMo₁₂O₄₀Sb₂].

A1.2 Crystal Data for (TBA)₃[PMo₁₂O₄₀Sb₂]

Empirical formula	C _{50.85} H ₁₀₇ Mo ₁₂ N _{4.42} O ₄₀ PSb ₂
Formula weight	2846.27
Temperature/K	150.0(2)
Crystal system	monoclinic
Space group	C2/c
a/Å	33.6711(9)
b/Å	13.9959(3)
c/Å	37.6117(8)
α/°	90
β/°	97.375(2)
γ/°	90
Volume/Å ³	17578.2(8)
Z	8
ρ _{calc} g/cm ³	2.151
μ/mm ⁻¹	2.352
F(000)	11072.0
Crystal size/mm ³	0.32 × 0.21 × 0.15
Radiation	MoKα (λ = 0.71073)
2Θ range for data collection/°	6.46 to 56.61
Index ranges	-41 ≤ h ≤ 44, -18 ≤ k ≤ 18, -49 ≤ l ≤ 50
Reflections collected	70625
Independent reflections	18961 [R _{int} = 0.0364, R _{sigma} = 0.0346]

Data/restraints/parameters	18961/2992/1376
Goodness-of-fit on F^2	1.283
Final R indexes [$ I >= 2\sigma (I)$]	$R_1 = 0.1207$, $wR_2 = 0.2274$
Final R indexes [all data]	$R_1 = 0.1312$, $wR_2 = 0.2314$
Largest diff. peak/hole / e \AA^{-3}	2.27/-2.04

Table A1.8 Crystal data and structure refinement for $(\text{TBA})_3[\text{PMo}_{12}\text{O}_{40}\text{Sb}_2]$.

Atom x	y	z	U(eq)
Sb1 5281.4(3)	2462.2(8)	3659.6(3)	23.8(2)
Mo1 5937.4(4)	2391.5(11)	3091.2(3)	24.6(3)
Mo2 5126.9(4)	4349.7(10)	3146.7(3)	23.7(3)
Mo3 4381.6(4)	2522.3(10)	3202.9(3)	22.2(3)
Mo4 5179.7(4)	572.3(10)	3145.5(3)	25.4(3)
Mo5 4244.9(4)	4306.8(10)	2575.1(4)	24.6(3)
Mo6 4243.5(4)	605.3(10)	2537.4(4)	24.8(3)
P1 5000	2454(3)	2500	13.1(9)
P2 2500	7500	5000	21.2(10)
O42 2318(6)	6890(14)	5274(5)	19(3)
O20 4795(3)	3080(8)	2755(3)	24.1(19)
O19 5315(3)	1800(8)	2722(3)	26(2)
O1 6353(4)	2549(10)	3392(3)	37(3)
O41 2814(6)	8201(14)	5192(5)	19(3)
O2 5276(4)	5177(9)	3464(3)	39(3)
O3 4128(4)	2365(9)	3551(3)	34(3)
O4 5175(4)	-232(9)	3477(3)	41(3)
O40 2175(6)	8091(15)	4790(6)	22(3)
O5 5522(3)	3248(9)	3305(3)	30(2)
O6 4824(3)	3429(9)	3444(3)	31(2)
O7 4877(3)	1665(8)	3342(3)	28(2)
O39 2724(7)	6875(16)	4761(6)	26(2)
O8 5616(3)	1509(9)	3392(3)	30(2)
O9 5956(4)	3282(9)	2750(3)	33(2)
O10 5417(3)	4599(9)	2784(3)	32(2)
O11 4652(4)	4871(9)	2941(3)	34(2)
O12 4103(3)	3534(9)	2982(3)	33(2)
O13 4195(3)	1605(9)	2882(3)	31(2)
O14 4735(4)	302(8)	2834(3)	31(2)
O15 6090(4)	1354(10)	2826(3)	35(2)
O16 3891(4)	5136(10)	2539(4)	41(3)
O17 3923(4)	-234(9)	2629(4)	42(3)
O18 4454(4)	12(9)	2132(3)	37(3)
N1 4204(5)	5275(12)	4055(4)	39(3)
N2 3259(6)	346(14)	3416(5)	54(3)
N3A 6155(8)	8562(19)	3887(7)	74(5)
N4 6955(15)	6380(30)	3222(13)	131(18)
N5 5582(10)	6100(30)	4299(10)	85(9)
C1 4389(6)	4329(15)	4135(5)	43(4)

A1 Appendix

C2	4215(8)	3753(19)	4434(6)	61(6)
C3	4394(8)	2748(19)	4458(7)	62(6)
C4	4273(11)	2130(30)	4759(9)	103(11)
C5	3765(6)	5216(14)	3932(5)	38(4)
C6	3648(8)	4590(20)	3613(7)	73(7)
C7	3207(9)	4620(20)	3478(8)	85(7)
C9	4422(7)	5707(16)	3768(6)	50(4)
C10	4283(7)	6682(17)	3626(7)	58(6)
C11	4573(8)	7095(17)	3374(7)	59(6)
C12	4464(8)	8035(18)	3245(8)	68(7)
C13	4247(6)	5925(16)	4394(5)	46(4)
C14	4657(8)	6210(20)	4534(8)	80(7)
C17	3025(7)	826(18)	3690(7)	60(5)
C18	3185(9)	1790(20)	3826(9)	87(8)
C19	2920(11)	2210(30)	4076(10)	102(9)
C20A	3110(20)	2910(50)	4260(20)	114(12)
C21	3697(7)	274(17)	3567(6)	54(4)
C22	3794(6)	-301(16)	3905(6)	51(5)
C23	4239(7)	-192(19)	4057(7)	64(6)
C24	4345(8)	-870(20)	4386(8)	71(7)
C25	3070(7)	-631(17)	3339(6)	55(4)
C26	3246(9)	-1270(20)	3072(8)	74(7)
C27	3033(9)	-2240(20)	3014(8)	77(7)
C28	3221(10)	-2730(30)	2730(9)	94(9)
C29	3255(8)	900(20)	3088(7)	73(6)
C30	2862(10)	1070(30)	2884(9)	98(9)
C33A	6290(13)	7590(20)	4056(10)	88(5)
C34A	6517(14)	7690(30)	4397(10)	88(5)
C35A	6745(13)	7050(30)	4632(9)	88(5)
C36A	6828(13)	7190(30)	5006(9)	88(5)
C37A	5853(10)	8200(30)	3575(9)	82(6)
C38B	5870(30)	7910(60)	3292(11)	91(10)
C39B	5700(30)	7720(60)	2937(12)	105(12)
C40A	5419(17)	7370(40)	2740(13)	125(14)
C41A	5956(10)	9340(30)	4097(10)	78(6)
C42A	5657(10)	8950(30)	4283(10)	75(7)
C43A	5526(12)	9680(20)	4501(10)	77(7)
C44A	5410(11)	10620(20)	4415(13)	80(10)
C45A	6438(12)	9090(30)	3667(11)	86(7)
C46A	6446(11)	9870(30)	3439(11)	78(7)
C47A	6797(17)	10030(30)	3278(14)	79(8)
C48A	6901(13)	9350(30)	3026(12)	85(10)
C49	6813(15)	5630(30)	3198(13)	104(16)
C50	6679(18)	4780(30)	3221(12)	120(20)
C51	5763(10)	5460(30)	4217(10)	73(10)
C52	5988(12)	4810(30)	4104(10)	91(13)
Sb2B	2208(4)	7490(6)	3847(3)	40(2)

Mo9B 2357(3)	9373(8)	4344(4)	33.6(19)
Mo3B 3267(3)	9302(8)	4928(4)	37.3(19)
Mo1B 1558(3)	7541(6)	4422(3)	38.1(19)
Mo2B 3242(3)	5614(8)	4945(4)	36(2)
Mo7B 2324(3)	5597(9)	4366(4)	38.7(19)
Mo8B 3113(5)	7446(10)	4287(5)	28.8(18)
O33B 2068(10)	9680(20)	4704(8)	30(3)
O21B 2251(11)	4790(20)	4045(9)	36(5)
O24B 1141(8)	7560(30)	4142(9)	32(5)
O36B 3587(9)	4790(20)	4900(10)	35(5)
O32B 2823(7)	9762(16)	4581(7)	35(3)
O38B 3539(7)	8420(20)	5279(8)	38(4)
O35B 1958(11)	5260(20)	4622(11)	38(3)
O29B 2781(8)	5175(17)	4632(8)	37(3)
O37B 3612(9)	10130(20)	4897(10)	36(5)
O27B 1922(7)	8380(18)	4153(9)	33(3)
O26B 2658(6)	8356(15)	4080(7)	37(3)
O28B 1907(6)	6580(17)	4165(8)	32(3)
O23B 2275(10)	10197(18)	4034(8)	33(5)
O22B 3367(10)	7410(30)	3932(8)	31(4)
O25B 2632(6)	6590(14)	4109(7)	34(3)
O30B 3331(7)	6441(18)	4554(7)	31(2)
O34B 1489(8)	8510(30)	4719(10)	39(4)
O31B 3362(7)	8387(17)	4565(7)	34(3)
C16B 4475(17)	7260(50)	5044(17)	71(8)
C15B 4690(20)	6160(60)	4979(11)	79(7)
C8A 3076(17)	5470(40)	3299(15)	87(10)
C31 2933(14)	1720(40)	2508(11)	143(14)
C32 3052(16)	2730(40)	2556(15)	180(20)
Sb2A 2214.7(14)	7262(2)	3843.8(11)	19.0(5)
Mo7A 2414.3(13)	5483(3)	4405.6(13)	24.9(7)
Mo8A 3115(2)	7509(4)	4293(2)	23.9(8)
Mo9A 2277.4(12)	9254(3)	4303.9(13)	18.9(7)
Mo2A 3316.1(11)	5799(3)	4988.2(13)	19.2(7)
Mo1A 1563.8(11)	7213(2)	4416.0(11)	21.0(6)
Mo3A 3192.3(11)	9480(3)	4890.3(12)	19.0(6)
O28A 1955(5)	6328(12)	4184(5)	35(3)
O25A 2681(4)	6514(10)	4127(4)	35(2)
O31A 3319(5)	8563(11)	4538(4)	33(2)
O33A 1928(5)	9691(12)	4596(4)	31(2)
O34A 1447(4)	8204(14)	4691(5)	36(3)
O36A 3693(5)	5047(12)	4996(5)	33(4)
O32A 2712(5)	9759(11)	4549(4)	34(2)
O38A 3489(5)	8728(13)	5262(5)	38(3)
O29A 2901(5)	5198(11)	4661(5)	37(2)
O21A 2372(6)	4619(12)	4105(4)	32(3)
O35A 2090(6)	5083(12)	4730(5)	40(3)

A1 Appendix

O24A 1146(4)	7144(12)	4136(4)	23(3)
O23A 2182(5)	9990(11)	3959(4)	29(3)
O22A 3374(5)	7497(14)	3940(4)	30(3)
O30A 3381(5)	6636(11)	4597(4)	32(2)
O37A 3494(5)	10378(12)	4822(5)	35(3)
O27A 1894(5)	8123(12)	4139(5)	34(2)
O26A 2619(4)	8264(11)	4075(5)	36(2)
C15A 4607(16)	6950(40)	4870(13)	79(7)
C16A 4567(13)	6320(40)	5191(13)	71(8)
C8B 3152(18)	4330(50)	3113(14)	87(10)
C20B 2554(18)	2400(50)	3920(20)	114(12)
C42B 5737(19)	8990(50)	4110(17)	82(8)
N3B 6274(13)	8310(30)	3833(10)	84(6)
C33B 6396(19)	7690(40)	4168(14)	88(5)
C37B 6120(20)	7490(40)	3577(14)	85(8)
C41B 5956(19)	9100(50)	3817(15)	86(7)
C45B 6597(16)	8670(50)	3611(17)	85(8)
C34B 6680(30)	8140(50)	4423(18)	88(5)
C38A 5898(17)	7490(30)	3317(9)	97(9)
C46B 6560(20)	9200(70)	3288(19)	85(9)
C35B 6900(20)	7840(50)	4750(15)	88(5)
C39A 5715(15)	7030(30)	3009(10)	98(10)
C43B 5810(30)	9850(50)	4307(15)	86(10)
C47B 6820(40)	9980(50)	3270(30)	85(10)
C36B 7150(30)	7030(60)	4780(20)	88(5)
C40B 5700(40)	6990(70)	2680(18)	125(14)
C44B 5950(30)	9990(70)	4671(18)	110(20)
C48B 7060(30)	9980(80)	2990(20)	95(17)

Table A1.9 Fractional Atomic Coordinates ($\times 10^4$) and Equivalent Isotropic Displacement Parameters ($\text{\AA}^2 \times 10^3$). U_{eq} is defined as 1/3 of the trace of the orthogonalised U_{ij} tensor, for $(\text{TBA})_3[\text{PMo}_{12}\text{O}_{40}\text{Sb}_2]$.

Atom	U_{11}	U_{22}	U_{33}	U_{23}	U_{13}	U_{12}
Sb1	23.4(5)	34.9(6)	14.0(4)	-0.8(4)	5.7(4)	-2.0(4)
Mo1	18.4(6)	41.1(8)	14.8(6)	2.2(5)	4.0(5)	2.4(5)
Mo2	27.8(7)	22.6(6)	21.1(6)	-5.8(5)	4.8(5)	0.7(5)
Mo3	18.1(6)	34.3(7)	15.7(6)	-3.5(5)	8.2(5)	-3.0(5)
Mo4	34.3(7)	23.5(6)	18.6(6)	5.0(5)	4.6(5)	-3.2(6)
Mo5	20.1(6)	28.9(7)	25.3(6)	-4.4(5)	5.3(5)	6.2(5)
Mo6	26.2(7)	27.6(7)	21.8(6)	-1.5(5)	7.5(5)	-9.6(5)
P1	18(2)	16(2)	7.8(19)	0	10.2(17)	0
P2	20(2)	23(2)	20(2)	0.2(19)	1.3(18)	0.8(19)
O42	20(6)	19(6)	18(5)	-1(5)	5(5)	1(5)
O20	24(4)	31(4)	18(4)	-2(3)	6(3)	1(3)
O19	28(4)	35(5)	16(4)	6(3)	7(3)	3(3)
O1	29(5)	57(7)	24(5)	1(5)	-1(4)	0(4)
O41	18(5)	19(5)	19(5)	2(4)	4(4)	3(4)
O2	47(7)	34(5)	34(5)	-6(4)	2(5)	-7(5)

O3	29(5)	53(7)	22(4)	-4(4)	9(4)	-5(5)
O4	64(8)	37(5)	23(5)	7(4)	8(5)	-2(5)
O40	22(5)	22(5)	23(4)	1(4)	5(3)	0(4)
O5	32(4)	36(4)	23(4)	6(3)	9(3)	0(3)
O6	28(4)	34(4)	29(4)	2(3)	2(3)	-3(3)
O7	27(4)	34(4)	24(4)	-5(3)	3(3)	-4(3)
O39	27(4)	26(4)	24(4)	0(3)	6(3)	1(3)
O8	35(4)	37(4)	19(4)	-3(3)	10(3)	-5(3)
O9	33(6)	45(5)	22(5)	5(4)	9(4)	3(4)
O10	31(5)	35(6)	30(5)	5(4)	6(4)	0(4)
O11	35(4)	32(5)	34(5)	5(4)	1(4)	-2(4)
O12	27(5)	42(5)	29(5)	-1(4)	4(4)	-1(4)
O13	28(5)	38(5)	27(5)	-4(4)	3(4)	-2(4)
O14	37(4)	28(5)	28(4)	-7(4)	5(3)	-1(4)
O15	30(5)	48(6)	29(5)	-1(4)	14(4)	5(4)
O16	39(6)	40(6)	45(7)	-6(5)	8(5)	15(5)
O17	42(6)	37(6)	47(7)	-2(5)	11(5)	-17(5)
O18	48(7)	35(6)	30(5)	-4(4)	10(5)	-3(5)
N1	36(6)	50(6)	34(5)	-3(4)	19(4)	4(5)
N2	48(7)	59(7)	61(7)	6(5)	27(5)	-7(5)
N3A	51(10)	91(10)	73(9)	17(7)	-19(7)	9(7)
N4	150(40)	90(20)	130(30)	20(20)	-80(30)	-30(20)
N5	60(18)	100(20)	90(20)	8(17)	2(16)	-11(14)
C1	45(8)	53(7)	33(7)	0(5)	17(6)	8(6)
C2	64(13)	72(9)	51(10)	14(8)	26(10)	2(8)
C3	63(14)	69(9)	52(11)	12(8)	5(10)	0(9)
C4	130(30)	100(16)	85(18)	40(15)	35(19)	2(16)
C5	38(6)	41(8)	39(7)	0(6)	17(5)	4(5)
C6	62(10)	85(14)	71(11)	-37(11)	-2(8)	19(9)
C7	63(10)	96(16)	89(14)	-41(12)	-12(9)	19(9)
C9	49(9)	58(8)	49(8)	2(6)	30(7)	5(6)
C10	62(12)	58(9)	61(12)	6(8)	33(10)	8(8)
C11	65(12)	53(9)	64(12)	5(9)	35(11)	10(8)
C12	72(16)	54(10)	83(16)	9(10)	36(13)	8(9)
C13	45(8)	54(9)	42(7)	-7(6)	20(6)	-1(6)
C14	56(9)	112(16)	72(10)	-30(11)	12(7)	-13(9)
C17	55(10)	63(9)	67(10)	7(7)	29(8)	-3(7)
C18	83(14)	77(11)	112(18)	-20(12)	58(13)	-16(10)
C19	100(16)	98(15)	124(19)	-26(14)	71(15)	-9(13)
C20A	101(17)	107(17)	150(20)	-38(17)	62(16)	-5(13)
C21	48(7)	51(10)	67(9)	3(7)	26(6)	-6(6)
C22	43(8)	43(10)	69(9)	0(8)	18(7)	-13(7)
C23	45(8)	65(13)	83(12)	1(10)	11(8)	-10(8)
C24	69(14)	65(14)	80(12)	-7(11)	6(10)	-1(11)
C25	55(10)	61(8)	51(9)	10(6)	17(8)	-9(6)
C26	75(15)	78(10)	75(14)	-10(10)	32(12)	-16(10)
C27	77(16)	76(11)	79(15)	-8(10)	12(13)	-16(10)

A1 Appendix

C28	90(20)	95(16)	93(18)	-21(14)	17(16)	-9(14)
C29	70(10)	84(12)	72(8)	22(8)	32(7)	6(9)
C30	83(12)	130(20)	83(13)	14(14)	18(10)	21(12)
C33A	67(11)	99(10)	87(9)	23(8)	-28(7)	10(8)
C34A	67(11)	99(10)	87(9)	23(8)	-28(7)	10(8)
C35A	67(11)	99(10)	87(9)	23(8)	-28(7)	10(8)
C36A	67(11)	99(10)	87(9)	23(8)	-28(7)	10(8)
C37A	67(11)	98(13)	74(10)	20(9)	-19(9)	3(9)
C38B	81(18)	101(18)	82(12)	24(12)	-25(12)	3(15)
C39B	110(20)	110(20)	84(13)	23(13)	-32(14)	-1(19)
C40A	140(30)	130(20)	92(14)	15(14)	-29(16)	0(20)
C41A	59(12)	94(12)	73(11)	23(9)	-18(9)	13(9)
C42A	60(12)	87(13)	71(14)	15(11)	-17(10)	9(10)
C43A	54(14)	83(14)	89(14)	8(12)	-5(11)	-6(11)
C44A	46(18)	82(15)	110(30)	16(13)	16(18)	-6(12)
C45A	73(11)	101(13)	81(12)	13(10)	-8(9)	-1(9)
C46A	60(12)	96(14)	70(13)	9(11)	-16(10)	-3(11)
C47A	60(13)	100(16)	71(14)	12(12)	-15(11)	-2(12)
C48A	65(18)	110(20)	79(17)	3(17)	-11(14)	-5(16)
C49	110(30)	76(19)	100(30)	21(19)	-80(20)	-12(19)
C50	170(40)	80(20)	70(30)	20(20)	-90(30)	-40(20)
C51	48(17)	100(20)	70(20)	5(17)	-17(15)	-12(14)
C52	70(20)	130(30)	60(20)	-10(20)	-35(17)	17(19)
Sb2B	38(3)	47(4)	34(3)	3(3)	2(2)	2(3)
Mo9B	39(4)	33(3)	28(3)	7(2)	3(3)	4(3)
Mo3B	35(4)	35(4)	43(3)	4(3)	11(3)	-6(3)
Mo1B	27(3)	52(4)	35(3)	0(4)	1(2)	-2(3)
Mo2B	40(4)	34(4)	34(3)	-1(3)	6(3)	11(3)
Mo7B	49(4)	35(3)	33(3)	-5(3)	6(3)	2(3)
Mo8B	28(3)	34(3)	26(3)	0(3)	9(3)	-2(3)
O33B	32(6)	33(6)	23(5)	4(5)	0(5)	1(5)
O21B	42(9)	34(7)	31(7)	-2(6)	3(7)	1(6)
O24B	26(6)	43(10)	27(8)	3(8)	6(5)	-3(6)
O36B	36(8)	31(8)	37(10)	-3(8)	5(7)	8(7)
O32B	35(4)	34(5)	36(5)	1(4)	4(4)	3(4)
O38B	39(6)	39(7)	40(6)	7(6)	15(5)	7(6)
O35B	48(6)	37(6)	29(5)	2(5)	5(5)	7(5)
O29B	44(5)	33(5)	35(5)	2(4)	2(4)	2(4)
O37B	32(8)	34(8)	41(9)	6(7)	6(7)	-2(6)
O27B	33(5)	37(5)	30(5)	0(4)	6(4)	-2(4)
O26B	33(5)	37(5)	42(6)	-1(4)	4(4)	2(4)
O28B	35(4)	36(4)	28(5)	3(4)	8(4)	1(4)
O23B	38(9)	33(7)	27(7)	4(6)	1(6)	0(6)
O22B	31(7)	38(9)	27(6)	3(6)	9(6)	3(7)
O25B	35(5)	36(5)	30(5)	2(4)	2(4)	-1(4)
O30B	32(4)	33(4)	28(4)	-1(4)	3(4)	0(4)
O34B	31(6)	50(7)	38(6)	-6(6)	10(5)	-7(6)

O31B 31(5)	35(4)	36(4)	0(4)	7(4)	-1(4)
C16B 44(15)	101(16)	68(12)	-28(11)	4(10)	-13(13)
C15B 67(15)	101(16)	68(10)	-27(10)	9(8)	-7(12)
C8A 73(17)	94(16)	88(14)	-40(13)	-12(11)	23(12)
C31 110(30)	200(30)	112(16)	70(20)	13(15)	10(20)
C32 140(40)	200(30)	190(40)	70(20)	20(30)	0(20)
Sb2A 25.7(10)	20.6(12)	11.7(8)	0.6(9)	6.6(7)	-2.1(10)
Mo7A 44(2)	16.4(12)	14.0(12)	-0.9(9)	2.6(13)	6.4(12)
Mo8A 22.6(14)	32.3(16)	19.0(14)	-1.3(13)	11.5(12)	-2.8(13)
Mo9A 23.1(15)	19.8(12)	13.6(12)	2.3(9)	1.3(10)	-3.8(10)
Mo2A 18.1(13)	17.9(14)	22.4(14)	0.0(11)	6.3(10)	1.5(10)
Mo1A 15.7(10)	31.2(16)	16.7(10)	-0.8(13)	4.0(8)	1.1(12)
Mo3A 19.5(14)	17.3(13)	21.3(12)	5.5(10)	6.7(10)	1.0(10)
O28A 40(4)	36(5)	33(5)	8(4)	15(4)	6(4)
O25A 37(4)	36(4)	33(5)	7(4)	0(4)	-2(3)
O31A 30(4)	33(4)	36(4)	-3(3)	5(3)	3(3)
O33A 34(5)	34(5)	24(5)	-5(4)	7(4)	-5(4)
O34A 31(5)	45(6)	34(5)	-8(5)	16(4)	-13(5)
O36A 24(6)	27(6)	48(8)	-1(6)	7(5)	7(5)
O32A 33(4)	33(4)	34(4)	-3(4)	1(3)	4(3)
O38A 42(5)	39(6)	36(5)	9(4)	16(4)	16(5)
O29A 42(4)	31(4)	36(4)	6(4)	-3(4)	-2(3)
O21A 40(7)	29(6)	26(6)	-4(5)	5(5)	2(5)
O35A 52(5)	40(5)	28(5)	12(4)	11(4)	12(4)
O24A 20(5)	27(7)	22(5)	7(5)	5(4)	0(5)
O23A 45(7)	24(6)	17(5)	1(4)	-1(5)	-3(5)
O22A 30(6)	37(7)	24(5)	2(5)	14(4)	5(5)
O30A 33(4)	34(4)	29(4)	4(3)	0(3)	-5(3)
O37A 33(7)	28(6)	44(7)	6(5)	5(6)	-2(5)
O27A 34(4)	37(4)	32(4)	-4(4)	12(3)	-6(3)
O26A 31(4)	35(4)	40(5)	-5(4)	5(3)	1(3)
C15A 67(15)	101(16)	68(10)	-27(10)	9(8)	-7(12)
C16A 44(15)	101(16)	68(12)	-28(11)	4(10)	-13(13)
C8B 73(17)	94(16)	88(14)	-40(13)	-12(11)	23(12)
C20B 101(17)	107(17)	150(20)	-38(17)	62(16)	-5(13)
C42B 60(14)	92(15)	84(14)	22(12)	-25(12)	4(12)
N3B 61(12)	97(12)	83(10)	21(8)	-25(8)	4(9)
C33B 67(11)	99(10)	87(9)	23(8)	-28(7)	10(8)
C37B 68(15)	98(13)	81(12)	23(10)	-20(10)	-1(11)
C41B 65(13)	100(13)	85(13)	22(10)	-23(10)	6(10)
C45B 64(13)	96(15)	85(13)	20(11)	-23(10)	2(11)
C34B 67(11)	99(10)	87(9)	23(8)	-28(7)	10(8)
C38A 96(16)	109(16)	80(12)	11(12)	-8(12)	-4(14)
C46B 70(16)	94(17)	84(13)	19(12)	-16(12)	7(14)
C35B 67(11)	99(10)	87(9)	23(8)	-28(7)	10(8)
C39A 110(20)	102(17)	72(13)	20(12)	-8(13)	-16(16)
C43B 68(19)	96(16)	90(15)	16(13)	-10(14)	-7(14)

A1 Appendix

C47B	69(19)	97(17)	81(18)	18(14)	-16(15)	4(15)
C36B	67(11)	99(10)	87(9)	23(8)	-28(7)	10(8)
C40B	140(30)	130(20)	92(14)	15(14)	-29(16)	0(20)
C44B	110(50)	110(30)	92(17)	17(18)	-20(20)	-20(30)
C48B	80(30)	110(30)	90(20)	20(20)	0(20)	0(20)

Table A1.10 Anisotropic Displacement Parameters ($\text{\AA}^2 \times 10^3$). The Anisotropic displacement factor exponent takes the form: $-2\pi^2[h^2a^*a^*U_{11} + 2hka^*b^*U_{12} + \dots]$ for $(\text{TBA})_3[\text{PMo}_{12}\text{O}_{40}\text{Sb}_2]$.

Atom	Atom	Length/ \AA	Atom	Atom	Length/ \AA
Sb1	Mo1	3.2668(17)	C30	C31	1.72(5)
Sb1	Mo4	3.2685(17)	C33A	C34A	1.412(18)
Sb1	O5	1.979(11)	C34A	C35A	1.412(18)
Sb1	O6	2.131(12)	C35A	C36A	1.413(18)
Sb1	O7	2.027(11)	C37A	C38A	1.405(18)
Sb1	O8	2.087(12)	C38B	C39B	1.405(18)
Mo1	O19	2.501(11)	C38B	C37B	1.408(18)
Mo1	O1	1.698(12)	C39B	C40B	1.408(19)
Mo1	O5	2.081(12)	C40A	C39A	1.409(18)
Mo1	O8	2.070(11)	C41A	C42A	1.408(18)
Mo1	O9	1.797(12)	C42A	C43A	1.412(18)
Mo1	O15	1.870(12)	C43A	C44A	1.409(18)
Mo2	O20	2.481(11)	C45A	C46A	1.395(18)
Mo2	O2	1.693(12)	C46A	C47A	1.412(18)
Mo2	O5	2.074(12)	C47A	C48A	1.415(18)
Mo2	O6	2.059(12)	C49	C50	1.29(4)
Mo2	O10	1.812(12)	C51	C52	1.29(4)
Mo2	O11	1.836(12)	Sb2B	Mo9B	3.230(13)
Mo3	O20	2.447(10)	Sb2B	Mo1B	3.269(17)
Mo3	O3	1.668(11)	Sb2B	O27B	2.02(2)
Mo3	O6	2.075(12)	Sb2B	O26B	2.05(2)
Mo3	O7	2.066(12)	Sb2B	O28B	2.096(19)
Mo3	O12	1.838(12)	Sb2B	O25B	2.056(18)
Mo3	O13	1.818(12)	Mo9B	O42 ²	2.45(2)
Mo4	O19	2.427(11)	Mo9B	O33B	1.817(19)
Mo4	O4	1.682(12)	Mo9B	O32B	1.789(19)
Mo4	O7	2.030(12)	Mo9B	O27B	2.08(2)
Mo4	O8	2.094(12)	Mo9B	O26B	2.07(2)
Mo4	O14	1.820(11)	Mo9B	O23B	1.638(18)
Mo4	O18 ¹	1.886(13)	Mo3B	O32B	1.962(19)
Mo5	O9 ¹	1.948(12)	Mo3B	O38B	1.94(2)
Mo5	O10 ¹	1.918(12)	Mo3B	O35B ²	2.03(5)
Mo5	O11	1.978(12)	Mo3B	O37B	1.655(19)
Mo5	O12	1.983(12)	Mo3B	O31B	1.928(18)
Mo5	O16	1.656(12)	Mo1B	O24B	1.646(19)
Mo6	O19 ¹	2.515(11)	Mo1B	O38B ²	1.81(3)
Mo6	O13	1.928(12)	Mo1B	O27B	2.05(3)
Mo6	O14	1.920(12)	Mo1B	O28B	2.10(3)
Mo6	O15 ¹	1.958(13)	Mo1B	O34B	1.79(2)

Mo6	O17	1.661(12)	Mo2B O33B ² 1.83(3)
Mo6	O18	1.949(12)	Mo2B O36B 1.659(19)
P1	O20 ¹	1.527(11)	Mo2B O29B 1.92(2)
P1	O20	1.527(11)	Mo2B O30B 1.925(18)
P1	O19	1.559(11)	Mo2B O34B ² 1.90(3)
P1	O19 ¹	1.559(11)	Mo7B O41 ² 2.45(2)
P2	O42 ²	1.527(19)	Mo7B O21B 1.643(19)
P2	O42	1.527(19)	Mo7B O35B 1.72(4)
P2	O41 ²	1.55(2)	Mo7B O29B 1.83(2)
P2	O41	1.55(2)	Mo7B O28B 2.04(2)
P2	O40	1.51(2)	Mo7B O25B 2.051(18)
P2	O40 ²	1.51(2)	Mo8B O42 ² 2.51(3)
P2	O39 ²	1.52(2)	Mo8B O26B 2.066(17)
P2	O39	1.52(2)	Mo8B O22B 1.678(17)
O42	O41 ²	1.76(3)	Mo8B O25B 2.055(17)
O42	O40 ²	1.75(3)	Mo8B O30B 1.827(17)
O42	O39 ²	1.74(3)	Mo8B O31B 1.819(18)
O42	Mo9B ²	2.45(2)	O33B Mo2B ² 1.83(3)
O42	Mo8B ²	2.51(3)	O38B Mo1B ² 1.82(3)
O42	Mo8A ²	2.47(2)	O35B Mo3B ² 2.03(5)
O19	Mo6 ¹	2.515(11)	O34B Mo2B ² 1.90(3)
O41	O42 ²	1.76(3)	C16B C15B 1.73(10)
O41	O40 ²	1.81(3)	C31 C32 1.48(7)
O41	Mo3B	2.47(2)	Sb2A Mo1A 3.264(6)
O41	Mo7B ²	2.45(2)	Sb2A O28A 2.097(15)
O41	Mo1A ²	2.47(2)	Sb2A O25A 2.066(14)
O40	O42 ²	1.75(3)	Sb2A O27A 2.041(16)
O40	O41 ²	1.81(3)	Sb2A O26A 2.066(15)
O40	O39 ²	1.68(3)	Mo7A O28A 2.037(16)
O40	Mo1B	2.47(2)	Mo7A O25A 2.057(14)
O40	Mo9A	2.50(2)	Mo7A O29A 1.835(16)
O40	Mo2A ²	2.49(2)	Mo7A O21A 1.649(14)
O39	O42 ²	1.74(3)	Mo7A O35A 1.825(19)
O39	O40 ²	1.68(3)	Mo8A O42 ² 2.47(2)
O39	Mo2B	2.52(2)	Mo8A O25A 2.056(14)
O39	Mo8B	2.47(3)	Mo8A O31A 1.827(14)
O39	Mo7A	2.51(2)	Mo8A O22A 1.678(12)
O39	Mo8A	2.49(2)	Mo8A O30A 1.827(14)
O9	Mo5 ¹	1.948(12)	Mo8A O26A 2.057(14)
O10	Mo5 ¹	1.917(12)	Mo9A O33A 1.817(14)
O15	Mo6 ¹	1.958(13)	Mo9A O32A 1.772(16)
O18	Mo4 ¹	1.886(13)	Mo9A O23A 1.656(13)
N1	C1	1.48(3)	Mo9A O27A 2.086(16)
N1	C5	1.49(2)	Mo9A O26A 2.059(14)
N1	C9	1.51(2)	Mo2A O40 ² 2.49(2)
N1	C13	1.56(2)	Mo2A O33A ² 1.979(17)
N2	C17	1.53(3)	Mo2A O34A ² 1.947(18)

A1 Appendix

N2	C21	1.52(3)	Mo2A O36A	1.646(14)
N2	C25	1.52(3)	Mo2A O29A	1.931(16)
N2	C29	1.46(3)	Mo2A O30A	1.916(14)
N3A	C33A	1.54(2)	Mo1A O41 ²	2.47(2)
N3A	C37A	1.54(2)	Mo1A O28A	2.081(17)
N3A	C41A	1.55(2)	Mo1A O34A	1.805(17)
N3A	C45A	1.53(2)	Mo1A O38A ²	1.815(18)
N4	C49	1.15(4)	Mo1A O24A	1.650(13)
N5	C51	1.15(4)	Mo1A O27A	2.058(17)
C1	C2	1.56(3)	Mo3A O31A	1.931(14)
C2	C3	1.53(3)	Mo3A O32A	1.971(15)
C3	C4	1.52(3)	Mo3A O38A	1.923(17)
C5	C6	1.50(3)	Mo3A O35A ²	1.92(2)
C6	C7	1.51(3)	Mo3A O37A	1.656(15)
C7	C8A	1.41(5)	O33A Mo2A ²	1.980(17)
C7	C8B	1.42(5)	O34A Mo1A ²	1.947(17)
C9	C10	1.52(3)	O38A Mo1A ²	1.815(18)
C10	C11	1.56(3)	O35A Mo3A ²	1.92(2)
C11	C12	1.43(3)	C15A C16A	1.51(8)
C13	C14	1.47(3)	C42B C41B	1.412(19)
C14	C15B	1.66(4)	C42B C43B	1.410(19)
C14	C15A	1.66(4)	N3B C33B	1.54(2)
C17	C18	1.52(4)	N3B C37B	1.54(2)
C18	C19	1.50(4)	N3B C41B	1.54(2)
C19	C20A	1.32(5)	N3B C45B	1.54(2)
C19	C20B	1.32(5)	C33B C34B	1.405(19)
C21	C22	1.50(3)	C45B C46B	1.411(18)
C22	C23	1.54(3)	C34B C35B	1.409(18)
C23	C24	1.56(4)	C38A C39A	1.398(18)
C25	C26	1.52(3)	C46B C47B	1.411(18)
C26	C27	1.55(4)	C35B C36B	1.407(19)
C27	C28	1.48(4)	C43B C44B	1.409(19)
C29	C30	1.46(4)	C47B C48B	1.410(19)

Table A1.11 Bond Lengths for $(\text{TBA})_3[\text{PMo}_{12}\text{O}_{40}\text{Sb}_2]$.

¹1-X,+Y,1/2-Z;²1/2-X,3/2-Y,1-Z

Atom	Atom	Atom	Angle/ ^o	Atom	Atom	Atom	Angle/ ^o
Mo1	Sb1	Mo4	67.45(4)	C45A	C46A	C47A	118(3)
O5	Sb1	Mo1	37.5(3)	C46A	C47A	C48A	118(4)
O5	Sb1	Mo4	94.1(3)	N4	C49	C50	171(5)
O5	Sb1	O6	74.3(5)	N5	C51	C52	174(5)
O5	Sb1	O7	102.2(5)	Mo9B	Sb2B	Mo1B	70.6(4)
O5	Sb1	O8	74.7(5)	O27B	Sb2B	Mo9B	38.7(7)
O6	Sb1	Mo1	106.6(3)	O27B	Sb2B	Mo1B	37.0(8)
O6	Sb1	Mo4	105.8(3)	O27B	Sb2B	O26B	76.9(9)
O7	Sb1	Mo1	93.3(3)	O27B	Sb2B	O28B	75.4(10)

O7	Sb1	Mo4	36.4(3)	O27B	Sb2B	O25B	117.2(12)
O7	Sb1	O6	74.1(5)	O26B	Sb2B	Mo9B	38.6(6)
O7	Sb1	O8	74.2(5)	O26B	Sb2B	Mo1B	103.1(8)
O8	Sb1	Mo1	38.0(3)	O26B	Sb2B	O28B	120.2(11)
O8	Sb1	Mo4	38.7(3)	O26B	Sb2B	O25B	74.3(8)
O8	Sb1	O6	129.1(4)	O28B	Sb2B	Mo9B	102.5(9)
O19	Mo1	Sb1	77.6(2)	O28B	Sb2B	Mo1B	38.9(7)
O1	Mo1	Sb1	97.4(4)	O25B	Sb2B	Mo9B	100.2(7)
O1	Mo1	O19	166.8(5)	O25B	Sb2B	Mo1B	100.4(8)
O1	Mo1	O5	101.8(5)	O25B	Sb2B	O28B	73.3(8)
O1	Mo1	O8	99.1(5)	O42 ²	Mo9B	Sb2B	77.0(6)
O1	Mo1	O9	106.5(6)	O33B	Mo9B	O42 ²	88.5(13)
O1	Mo1	O15	101.4(6)	O33B	Mo9B	Sb2B	124.3(10)
O5	Mo1	Sb1	35.4(3)	O33B	Mo9B	O27B	89.6(12)
O5	Mo1	O19	81.3(4)	O33B	Mo9B	O26B	149.3(13)
O8	Mo1	Sb1	38.4(3)	O32B	Mo9B	O42 ²	68.2(9)
O8	Mo1	O19	69.3(4)	O32B	Mo9B	Sb2B	126.7(9)
O8	Mo1	O5	73.0(5)	O32B	Mo9B	O33B	94.4(13)
O9	Mo1	Sb1	122.4(4)	O32B	Mo9B	O27B	155.6(12)
O9	Mo1	O19	86.3(5)	O32B	Mo9B	O26B	89.8(10)
O9	Mo1	O5	87.9(5)	O27B	Mo9B	O42 ²	87.8(10)
O9	Mo1	O8	150.8(5)	O27B	Mo9B	Sb2B	37.4(7)
O9	Mo1	O15	96.9(5)	O26B	Mo9B	O42 ²	64.9(9)
O15	Mo1	Sb1	128.8(4)	O26B	Mo9B	Sb2B	38.0(6)
O15	Mo1	O19	73.4(5)	O26B	Mo9B	O27B	75.1(9)
O15	Mo1	O5	153.8(5)	O23B	Mo9B	O42 ²	161.6(14)
O15	Mo1	O8	91.5(5)	O23B	Mo9B	Sb2B	99.5(11)
O2	Mo2	O20	168.3(5)	O23B	Mo9B	O33B	107.9(15)
O2	Mo2	O5	100.6(6)	O23B	Mo9B	O32B	101.4(14)
O2	Mo2	O6	99.7(6)	O23B	Mo9B	O27B	100.3(14)
O2	Mo2	O10	105.0(6)	O23B	Mo9B	O26B	101.0(13)
O2	Mo2	O11	100.9(6)	O32B	Mo3B	O41	90.8(10)
O5	Mo2	O20	82.0(4)	O32B	Mo3B	O35B ²	96.9(16)
O6	Mo2	O20	70.0(4)	O38B	Mo3B	O41	66.0(9)
O6	Mo2	O5	73.9(4)	O38B	Mo3B	O32B	155.6(11)
O10	Mo2	O20	86.3(5)	O38B	Mo3B	O35B ²	79.6(16)
O10	Mo2	O5	88.4(5)	O35B ²	Mo3B	O41	62.4(9)
O10	Mo2	O6	151.9(5)	O37B	Mo3B	O41	160.4(14)
O10	Mo2	O11	97.5(5)	O37B	Mo3B	O32B	101.8(14)
O11	Mo2	O20	74.5(5)	O37B	Mo3B	O38B	102.6(14)
O11	Mo2	O5	155.3(5)	O37B	Mo3B	O35B ²	100.9(16)
O11	Mo2	O6	90.7(5)	O37B	Mo3B	O31B	103.5(15)
O3	Mo3	O20	167.7(5)	O31B	Mo3B	O41	92.1(10)
O3	Mo3	O6	98.6(5)	O31B	Mo3B	O32B	85.9(11)
O3	Mo3	O7	101.6(5)	O31B	Mo3B	O38B	87.4(12)
O3	Mo3	O12	100.0(6)	O31B	Mo3B	O35B ²	154.3(12)
O3	Mo3	O13	105.1(6)	O40	Mo1B	Sb2B	77.9(6)

A1 Appendix

O6	Mo3	O20	70.4(4)	O24B	Mo1B	O40	160.4(17)
O7	Mo3	O20	81.2(4)	O24B	Mo1B	Sb2B	99.5(15)
O7	Mo3	O6	74.5(5)	O24B	Mo1B	O38B ²	101.8(18)
O12	Mo3	O20	75.3(4)	O24B	Mo1B	O27B	100.8(18)
O12	Mo3	O6	91.3(5)	O24B	Mo1B	O28B	101.5(16)
O12	Mo3	O7	155.6(5)	O24B	Mo1B	O34B	102.5(15)
O13	Mo3	O20	86.9(4)	O38B ²	Mo1B	O40	95.2(10)
O13	Mo3	O6	152.8(5)	O38B ²	Mo1B	Sb2B	125.7(13)
O13	Mo3	O7	87.6(5)	O38B ²	Mo1B	O27B	153.8(13)
O13	Mo3	O12	97.5(5)	O38B ²	Mo1B	O28B	88.0(14)
O19	Mo4	Sb1	78.5(3)	O27B	Mo1B	O40	65.5(10)
O4	Mo4	Sb1	96.5(4)	O27B	Mo1B	Sb2B	36.3(7)
O4	Mo4	O19	168.9(6)	O27B	Mo1B	O28B	74.7(9)
O4	Mo4	O7	100.4(6)	O28B	Mo1B	O40	88.8(9)
O4	Mo4	O8	99.4(6)	O28B	Mo1B	Sb2B	38.8(6)
O4	Mo4	O14	104.7(6)	O34B	Mo1B	O40	65.2(9)
O4	Mo4	O18 ¹	101.6(6)	O34B	Mo1B	Sb2B	125.4(15)
O7	Mo4	Sb1	36.3(3)	O34B	Mo1B	O38B ²	97(2)
O7	Mo4	O19	81.5(4)	O34B	Mo1B	O27B	90.4(17)
O7	Mo4	O8	74.0(4)	O34B	Mo1B	O28B	153.7(12)
O8	Mo4	Sb1	38.5(3)	O33B ²	Mo2B	O39	85.2(13)
O8	Mo4	O19	70.5(4)	O33B ²	Mo2B	O29B	83.2(15)
O14	Mo4	Sb1	124.4(4)	O33B ²	Mo2B	O30B	147.5(14)
O14	Mo4	O19	86.2(5)	O33B ²	Mo2B	O34B ²	86.1(17)
O14	Mo4	O7	88.9(5)	O36B	Mo2B	O39	158.1(15)
O14	Mo4	O8	152.6(5)	O36B	Mo2B	O33B ²	113.0(18)
O14	Mo4	O18 ¹	95.8(5)	O36B	Mo2B	O29B	103.6(16)
O18 ¹	Mo4	Sb1	129.6(4)	O36B	Mo2B	O30B	99.1(14)
O18 ¹	Mo4	O19	74.9(5)	O36B	Mo2B	O34B ²	103.6(16)
O18 ¹	Mo4	O7	155.5(5)	O29B	Mo2B	O39	65.1(9)
O18 ¹	Mo4	O8	91.9(5)	O29B	Mo2B	O30B	85.2(11)
O9 ¹	Mo5	O11	152.2(5)	O30B	Mo2B	O39	62.5(9)
O9 ¹	Mo5	O12	89.1(5)	O34B ²	Mo2B	O39	89.1(11)
O10 ¹	Mo5	O9 ¹	84.5(5)	O34B ²	Mo2B	O29B	152.8(12)
O10 ¹	Mo5	O11	89.1(5)	O34B ²	Mo2B	O30B	90.7(19)
O10 ¹	Mo5	O12	152.1(5)	O21B	Mo7B	O41 ²	160.7(15)
O11	Mo5	O12	84.0(5)	O21B	Mo7B	O35B	100.0(19)
O16	Mo5	O9 ¹	106.1(6)	O21B	Mo7B	O29B	102.5(15)
O16	Mo5	O10 ¹	106.2(6)	O21B	Mo7B	O28B	99.2(14)
O16	Mo5	O11	101.7(6)	O21B	Mo7B	O25B	98.9(15)
O16	Mo5	O12	101.7(6)	O35B	Mo7B	O41 ²	66.2(12)
O13	Mo6	O19 ¹	83.3(4)	O35B	Mo7B	O29B	102.6(18)
O13	Mo6	O15 ¹	89.5(5)	O35B	Mo7B	O28B	83.4(16)
O13	Mo6	O18	155.0(5)	O35B	Mo7B	O25B	152.9(15)
O14	Mo6	O19 ¹	82.2(4)	O29B	Mo7B	O41 ²	94.0(11)
O14	Mo6	O13	84.9(5)	O29B	Mo7B	O28B	156.0(13)
O14	Mo6	O15 ¹	153.9(5)	O29B	Mo7B	O25B	92.0(11)

O14	Mo6	O18	89.3(5)	O28B	Mo7B	O41 ²	66.9(11)
O15 ¹	Mo6	O19 ¹	71.8(4)	O28B	Mo7B	O25B	74.6(8)
O17	Mo6	O19 ¹	169.2(5)	O25B	Mo7B	O41 ²	90.3(10)
O17	Mo6	O13	105.1(6)	O39	Mo8B	O42 ²	40.8(8)
O17	Mo6	O14	105.0(6)	O26B	Mo8B	O42 ²	63.7(10)
O17	Mo6	O15 ¹	101.2(6)	O26B	Mo8B	O39	92.1(11)
O17	Mo6	O18	99.9(6)	O22B	Mo8B	O42 ²	158.7(14)
O18	Mo6	O19 ¹	71.8(4)	O22B	Mo8B	O39	159.2(15)
O18	Mo6	O15 ¹	85.1(5)	O22B	Mo8B	O26B	98.4(13)
O20	P1	O20 ¹	110.0(9)	O22B	Mo8B	O25B	100.5(13)
O20	P1	O19 ¹	109.9(6)	O22B	Mo8B	O30B	101.8(14)
O20	P1	O19	109.4(5)	O22B	Mo8B	O31B	103.6(14)
O20 ¹	P1	O19	109.9(6)	O25B	Mo8B	O42 ²	86.2(10)
O20 ¹	P1	O19 ¹	109.4(5)	O25B	Mo8B	O39	65.2(10)
O19 ¹	P1	O19	108.2(9)	O25B	Mo8B	O26B	73.9(9)
O42 ²	P2	O42	180.0	O30B	Mo8B	O42 ²	98.6(12)
O42	P2	O41 ²	69.7(10)	O30B	Mo8B	O39	64.4(10)
O42 ²	P2	O41	69.7(10)	O30B	Mo8B	O26B	155.3(13)
O42 ²	P2	O41 ²	110.3(10)	O30B	Mo8B	O25B	88.6(11)
O42	P2	O41	110.3(10)	O31B	Mo8B	O42 ²	67.5(10)
O41	P2	O41 ²	180.0	O31B	Mo8B	O39	93.9(12)
O40	P2	O42	109.5(11)	O31B	Mo8B	O26B	92.0(11)
O40	P2	O42 ²	70.5(11)	O31B	Mo8B	O25B	153.6(13)
O40 ²	P2	O42 ²	109.5(11)	O31B	Mo8B	O30B	96.8(13)
O40 ²	P2	O42	70.5(11)	Mo9B	O33B	Mo2B ²	153.5(19)
O40	P2	O41 ²	72.5(11)	Mo9B	O32B	Mo3B	141.0(14)
O40 ²	P2	O41	72.5(11)	Mo1B ²	O38B	Mo3B	141.7(15)
O40 ²	P2	O41 ²	107.5(11)	Mo7B	O35B	Mo3B ²	138.8(16)
O40	P2	O41	107.5(11)	Mo7B	O29B	Mo2B	142.2(14)
O40 ²	P2	O40	180.0	Sb2B	O27B	Mo9B	103.9(11)
O40 ²	P2	O39	67.2(11)	Sb2B	O27B	Mo1B	106.7(12)
O40 ²	P2	O39 ²	112.8(11)	Mo1B	O27B	Mo9B	130.6(17)
O40	P2	O39 ²	67.2(11)	Sb2B	O26B	Mo9B	103.3(9)
O40	P2	O39	112.8(11)	Sb2B	O26B	Mo8B	105.5(10)
O39 ²	P2	O42 ²	110.5(11)	Mo8B	O26B	Mo9B	128.8(13)
O39 ²	P2	O42	69.5(11)	Sb2B	O28B	Mo1B	102.3(11)
O39	P2	O42	110.5(11)	Mo7B	O28B	Sb2B	105.1(10)
O39	P2	O42 ²	69.5(11)	Mo7B	O28B	Mo1B	131.3(15)
O39	P2	O41	106.2(11)	Mo7B	O25B	Sb2B	106.2(9)
O39 ²	P2	O41	73.8(11)	Mo7B	O25B	Mo8B	131.8(13)
O39 ²	P2	O41 ²	106.2(11)	Mo8B	O25B	Sb2B	105.5(9)
O39	P2	O41 ²	73.8(11)	Mo8B	O30B	Mo2B	142.4(15)
O39	P2	O39 ²	180.0(13)	Mo1B	O34B	Mo2B ²	144.4(15)
P2	O42	O41 ²	55.8(9)	Mo8B	O31B	Mo3B	141.4(15)
P2	O42	O40 ²	54.3(9)	C14	C15B	C16B	98(4)
P2	O42	O39 ²	55.1(10)	C32	C31	C30	118(4)
P2	O42	Mo9B ²	127.8(11)	O28A	Sb2A	Mo1A	38.4(5)

A1 Appendix

P2	O42	Mo8B ²	123.5(11)	O25A	Sb2A	Mo1A	100.4(5)
P2	O42	Mo8A ²	125.2(11)	O25A	Sb2A	O28A	73.7(6)
O41 ²	O42	Mo9B ²	124.8(12)	O25A	Sb2A	O26A	73.2(6)
O41 ²	O42	Mo8B ²	126.1(12)	O27A	Sb2A	Mo1A	37.4(5)
O41 ²	O42	Mo8A ²	126.0(12)	O27A	Sb2A	O28A	75.2(7)
O40 ²	O42	O41 ²	89.4(13)	O27A	Sb2A	O25A	116.1(7)
O40 ²	O42	Mo9B ²	73.9(10)	O27A	Sb2A	O26A	74.7(6)
O40 ²	O42	Mo8B ²	137.7(13)	O26A	Sb2A	Mo1A	101.5(5)
O40 ²	O42	Mo8A ²	138.9(12)	O26A	Sb2A	O28A	118.1(7)
O39 ²	O42	O41 ²	89.3(13)	O28A	Mo7A	O39	90.5(7)
O39 ²	O42	O40 ²	92.6(14)	O28A	Mo7A	O25A	75.1(6)
O39 ²	O42	Mo9B ²	142.1(13)	O25A	Mo7A	O39	63.2(7)
O39 ²	O42	Mo8B ²	68.5(10)	O29A	Mo7A	O39	66.9(7)
O39 ²	O42	Mo8A ²	70.2(10)	O29A	Mo7A	O28A	157.0(7)
Mo9B ²	O42	Mo8B ²	97.7(8)	O29A	Mo7A	O25A	90.0(7)
Mo3	O20	Mo2	94.2(3)	O21A	Mo7A	O39	157.9(8)
P1	O20	Mo2	125.4(6)	O21A	Mo7A	O28A	98.7(8)
P1	O20	Mo3	126.3(6)	O21A	Mo7A	O25A	99.7(8)
Mo1	O19	Mo6 ¹	86.6(3)	O21A	Mo7A	O29A	101.1(8)
Mo4	O19	Mo1	94.8(4)	O21A	Mo7A	O35A	103.1(9)
Mo4	O19	Mo6 ¹	87.3(4)	O35A	Mo7A	O39	97.2(8)
P1	O19	Mo1	124.6(6)	O35A	Mo7A	O28A	87.9(8)
P1	O19	Mo4	126.4(6)	O35A	Mo7A	O25A	153.3(8)
P1	O19	Mo6 ¹	125.3(6)	O35A	Mo7A	O29A	98.9(9)
P2	O41	O42 ²	54.5(9)	O42 ²	Mo8A	O39	41.0(7)
P2	O41	O40 ²	52.7(9)	O25A	Mo8A	O42 ²	88.5(7)
P2	O41	Mo3B	128.9(11)	O25A	Mo8A	O39	63.5(7)
P2	O41	Mo7B ²	125.0(11)	O25A	Mo8A	O26A	73.6(6)
P2	O41	Mo1A ²	127.2(11)	O31A	Mo8A	O42 ²	66.9(7)
O42 ²	O41	O40 ²	88.0(13)	O31A	Mo8A	O39	97.4(8)
O42 ²	O41	Mo3B	74.6(10)	O31A	Mo8A	O25A	155.0(7)
O42 ²	O41	Mo7B ²	132.9(12)	O31A	Mo8A	O30A	95.8(7)
O42 ²	O41	Mo1A ²	131.7(12)	O31A	Mo8A	O26A	91.1(7)
O40 ²	O41	Mo3B	128.9(12)	O22A	Mo8A	O42 ²	159.2(8)
O40 ²	O41	Mo7B ²	131.7(12)	O22A	Mo8A	O39	158.4(9)
O40 ²	O41	Mo1A ²	74.4(9)	O22A	Mo8A	O25A	100.1(8)
Mo7B ²	O41	Mo3B	91.4(8)	O22A	Mo8A	O31A	102.0(8)
P2	O40	O42 ²	55.1(9)	O22A	Mo8A	O30A	103.0(8)
P2	O40	O41 ²	54.8(9)	O22A	Mo8A	O26A	99.6(8)
P2	O40	O39 ²	56.7(10)	O30A	Mo8A	O42 ²	95.7(7)
P2	O40	Mo1B	128.5(12)	O30A	Mo8A	O39	65.2(7)
P2	O40	Mo9A	125.4(11)	O30A	Mo8A	O25A	90.5(7)
P2	O40	Mo2A ²	129.4(12)	O30A	Mo8A	O26A	154.3(8)
O42 ²	O40	O41 ²	90.2(13)	O26A	Mo8A	O42 ²	64.5(7)
O42 ²	O40	Mo1B	133.7(13)	O26A	Mo8A	O39	89.4(7)
O42 ²	O40	Mo9A	70.3(9)	O33A	Mo9A	O40	67.4(7)
O42 ²	O40	Mo2A ²	137.4(13)	O33A	Mo9A	O27A	90.6(7)

O41 ²	O40	Mo1B	73.8(10)	O33A	Mo9A O26A	156.9(7)
O41 ²	O40	Mo9A	132.2(12)	O32A	Mo9A O40	93.5(7)
O41 ²	O40	Mo2A ²	128.5(12)	O32A	Mo9A O33A	96.1(8)
O39 ²	O40	O42 ²	93.6(14)	O32A	Mo9A O27A	153.5(7)
O39 ²	O40	O41 ²	89.4(14)	O32A	Mo9A O26A	91.1(7)
O39 ²	O40	Mo1B	128.3(13)	O23A	Mo9A O40	161.0(8)
O39 ²	O40	Mo9A	133.3(13)	O23A	Mo9A O33A	101.0(8)
O39 ²	O40	Mo2A ²	72.7(10)	O23A	Mo9A O32A	102.9(8)
Mo2A ² O40		Mo9A	89.9(7)	O23A	Mo9A O27A	100.9(8)
Sb1	O5	Mo1	107.1(5)	O23A	Mo9A O26A	98.8(7)
Sb1	O5	Mo2	107.7(5)	O27A	Mo9A O40	65.5(7)
Mo2	O5	Mo1	139.0(5)	O26A	Mo9A O40	90.3(7)
Mo2	O6	Sb1	102.7(5)	O26A	Mo9A O27A	73.9(6)
Mo2	O6	Mo3	121.6(5)	O33A ² Mo2A O40 ²	65.8(7)	
Mo3	O6	Sb1	102.8(5)	O34A ² Mo2A O40 ²	65.3(7)	
Sb1	O7	Mo3	106.8(5)	O34A ² Mo2A O33A ²	86.4(8)	
Sb1	O7	Mo4	107.3(5)	O36A	Mo2A O40 ²	159.5(9)
Mo4	O7	Mo3	140.5(6)	O36A	Mo2A O33A ²	99.3(8)
P2	O39	O42 ²	55.4(10)	O36A	Mo2A O34A ²	101.2(9)
P2	O39	O40 ²	56.1(10)	O36A	Mo2A O29A	103.1(9)
P2	O39	Mo2B	128.3(12)	O36A	Mo2A O30A	103.9(8)
P2	O39	Mo8B	126.0(12)	O29A	Mo2A O40 ²	91.6(7)
P2	O39	Mo7A	123.8(12)	O29A	Mo2A O33A ²	90.7(8)
P2	O39	Mo8A	124.0(12)	O29A	Mo2A O34A ²	155.7(7)
O42 ²	O39	Mo2B	140.0(14)	O30A	Mo2A O40 ²	91.3(7)
O42 ²	O39	Mo8B	70.7(10)	O30A	Mo2A O33A ²	156.7(7)
O42 ²	O39	Mo7A	134.9(13)	O30A	Mo2A O34A ²	87.6(8)
O42 ²	O39	Mo8A	68.8(10)	O30A	Mo2A O29A	85.5(7)
O40 ²	O39	O42 ²	93.0(14)	O41 ²	Mo1A Sb2A	79.0(5)
O40 ²	O39	Mo2B	72.5(11)	O28A	Mo1A O41 ²	64.9(7)
O40 ²	O39	Mo8B	131.1(14)	O28A	Mo1A Sb2A	38.8(4)
O40 ²	O39	Mo7A	125.0(13)	O34A	Mo1A O41 ²	93.9(7)
O40 ²	O39	Mo8A	130.0(13)	O34A	Mo1A Sb2A	125.2(6)
Mo8B	O39	Mo2B	90.8(8)	O34A	Mo1A O28A	153.5(7)
Mo8A	O39	Mo7A	96.9(8)	O34A	Mo1A O38A ²	97.3(9)
Sb1	O8	Mo4	102.8(5)	O34A	Mo1A O27A	89.2(8)
Mo1	O8	Sb1	103.6(5)	O38A ² Mo1A O41 ²	65.1(7)	
Mo1	O8	Mo4	121.2(5)	O38A ² Mo1A Sb2A	126.0(6)	
Mo1	O9	Mo5 ¹	156.6(7)	O38A ² Mo1A O28A	88.2(7)	
Mo2	O10	Mo5 ¹	156.3(7)	O38A ² Mo1A O27A	153.2(8)	
Mo2	O11	Mo5	128.5(7)	O24A	Mo1A O41 ²	163.0(8)
Mo3	O12	Mo5	127.5(6)	O24A	Mo1A Sb2A	99.8(6)
Mo3	O13	Mo6	155.1(7)	O24A	Mo1A O28A	103.4(8)
Mo4	O14	Mo6	154.8(7)	O24A	Mo1A O34A	100.4(8)
Mo1	O15	Mo6 ¹	128.0(6)	O24A	Mo1A O38A ²	103.6(8)
Mo4 ¹	O18	Mo6	125.8(7)	O24A	Mo1A O27A	100.7(8)
C1	N1	C5	112.9(16)	O27A	Mo1A O41 ²	88.6(7)

A1 Appendix

C1	N1	C9	105.9(14)	O27A	Mo1A	Sb2A	37.0(4)
C1	N1	C13	111.5(15)	O27A	Mo1A	O28A	75.2(6)
C5	N1	C9	110.6(15)	O31A	Mo3A	O32A	85.4(6)
C5	N1	C13	105.8(14)	O38A	Mo3A	O31A	89.7(7)
C9	N1	C13	110.4(16)	O38A	Mo3A	O32A	152.6(7)
C21	N2	C17	109.7(19)	O35A ²	Mo3A	O31A	154.0(7)
C21	N2	C25	112.0(18)	O35A ²	Mo3A	O32A	88.8(8)
C25	N2	C17	106.5(16)	O35A ²	Mo3A	O38A	83.9(8)
C29	N2	C17	113(2)	O37A	Mo3A	O31A	101.8(8)
C29	N2	C21	105.0(18)	O37A	Mo3A	O32A	102.5(8)
C29	N2	C25	111(2)	O37A	Mo3A	O38A	104.9(8)
C33A	N3A	C41A	122(3)	O37A	Mo3A	O35A ²	104.2(9)
C37A	N3A	C33A	99(2)	Mo7A	O28A	Sb2A	104.9(7)
C37A	N3A	C41A	110(2)	Mo7A	O28A	Mo1A	131.5(9)
C45A	N3A	C33A	118(3)	Mo1A	O28A	Sb2A	102.7(7)
C45A	N3A	C37A	98(3)	Mo7A	O25A	Sb2A	105.3(6)
C45A	N3A	C41A	106(3)	Mo8A	O25A	Sb2A	106.1(6)
N1	C1	C2	114.9(16)	Mo8A	O25A	Mo7A	131.3(8)
C3	C2	C1	109.7(19)	Mo8A	O31A	Mo3A	141.4(9)
C4	C3	C2	115(2)	Mo9A	O33A	Mo2A ²	136.7(10)
N1	C5	C6	115.5(16)	Mo1A	O34A	Mo2A ²	143.5(9)
C5	C6	C7	114(2)	Mo9A	O32A	Mo3A	144.4(9)
C8A	C7	C6	115(4)	Mo1A ²	O38A	Mo3A	142.8(10)
C8B	C7	C6	109(3)	Mo7A	O29A	Mo2A	139.8(9)
N1	C9	C10	117.2(17)	Mo7A	O35A	Mo3A ²	142.8(10)
C9	C10	C11	111.0(18)	Mo8A	O30A	Mo2A	142.6(9)
C12	C11	C10	113(2)	Sb2A	O27A	Mo9A	105.0(7)
C14	C13	N1	115.9(18)	Sb2A	O27A	Mo1A	105.5(8)
C13	C14	C15B	107(3)	Mo1A	O27A	Mo9A	132.3(9)
C13	C14	C15A	105(3)	Mo8A	O26A	Sb2A	106.0(7)
C18	C17	N2	115.3(19)	Mo8A	O26A	Mo9A	130.4(8)
C19	C18	C17	110(2)	Mo9A	O26A	Sb2A	105.1(6)
C20A	C19	C18	110(4)	C16A	C15A	C14	106(4)
C20B	C19	C18	113(4)	C43B	C42B	C41B	105(4)
C22	C21	N2	116.6(17)	C33B	N3B	C37B	97(3)
C21	C22	C23	110.8(18)	C33B	N3B	C41B	123(3)
C22	C23	C24	110(2)	C33B	N3B	C45B	120(3)
C26	C25	N2	117.7(19)	C37B	N3B	C45B	96(3)
C25	C26	C27	113(2)	C41B	N3B	C37B	110(3)
C28	C27	C26	106(2)	C41B	N3B	C45B	106(3)
N2	C29	C30	116(2)	C34B	C33B	N3B	113(3)
C29	C30	C31	108(3)	C38B	C37B	N3B	107(4)
C34A	C33A	N3A	113(3)	C42B	C41B	N3B	109(4)
C33A	C34A	C35A	134(4)	C46B	C45B	N3B	131(4)
C34A	C35A	C36A	124(4)	C33B	C34B	C35B	134(5)
C38A	C37A	N3A	130(3)	C39A	C38A	C37A	145(5)
C39B	C38B	C37B	141(7)	C47B	C46B	C45B	117(4)

C38B	C39B	C40B	139(8)	C36B	C35B	C34B	124(4)
C42A	C41A	N3A	111(3)	C38A	C39A	C40A	130(5)
C41A	C42A	C43A	108(3)	C44B	C43B	C42B	130(5)
C44A	C43A	C42A	130(4)	C48B	C47B	C46B	117(5)
C46A	C45A	N3A	141(4)				

Table A1.12 Bond Angles for $(\text{TBA})_3[\text{PMo}_{12}\text{O}_{40}\text{Sb}_2]$. $^11\text{-X, +Y, 1/2-Z}; ^21/2\text{-X, 3/2-Y, 1-Z}$

Atom x	y	z	U(eq)
H1A	4680	4420	51
H1B	4357	3945	51
H2A	4280	4083	73
H2B	3920	3714	73
H3A	4313	2418	74
H3B	4689	2804	74
H4A	3981	2063	154
H4B	4367	2420	154
H4C	4394	1491	154
H5A	3665	5869	46
H5B	3629	4981	46
H6A	3724	3919	88
H6B	3800	4782	88
H7A	3031	4105	102
H7B	3000	4799	102
H9A	4401	5257	60
H9B	4709	5756	60
H10A	4269	7124	70
H10B	4010	6626	70
H11A	4847	7115	70
H11B	4576	6662	70
H12A	4260	7988	101
H12B	4701	8363	101
H12C	4356	8397	101
H13A	4089	6513	55
H13B	4129	5588	55
H14A	4714	6861	96
H14B	4853	5763	96
H14C	4790	6528	96
H14D	4818	5640	96
H17A	2744	909	72
H17B	3024	392	72
H18A	3460	1715	104
H18B	3198	2229	104
H19A	2672	2459	123
H19B	2843	1708	123
H19C	2902	1759	123

A1 Appendix

H19D 3043	2808	4179	123
H20A 2928	3176	4426	171
H20B 3348	2661	4405	171
H20C 3177	3409	4102	171
H21A 3844	-8	3381	65
H21B 3801	929	3615	65
H22A 3734	-983	3853	61
H22B 3624	-84	4085	61
H23A 4293	479	4132	77
H23B 4409	-349	3869	77
H24A 4446	-1477	4305	107
H24B 4105	-985	4502	107
H24C 4552	-569	4558	107
H25A 3085	-982	3569	66
H25B 2783	-534	3251	66
H26A 3533	-1376	3158	89
H26B 3229	-928	2839	89
H27A 3069	-2622	3237	92
H27B 2743	-2151	2939	92
H28A 3014	-3047	2565	140
H28B 3414	-3199	2838	140
H28C 3359	-2253	2597	140
H29A 3423	566	2930	88
H29B 3381	1527	3150	88
H30A 2690	1430	3031	118
H30B 2729	454	2814	118
H33A 6051	7199	4080	105
H33B 6452	7253	3895	105
H34A 6326	7975	4546	105
H34B 6709	8210	4362	105
H35A 7007	6987	4542	105
H35B 6611	6424	4598	105
H36A 6989	6660	5114	132
H36B 6975	7792	5054	132
H36C 6576	7223	5110	132
H37A 5617	7993	3688	99
H37B 5767	8776	3434	99
H38C 5626	8053	3407	109
H38D 5998	8534	3269	109
H39C 5796	8274	2807	127
H39D 5415	7838	2944	127
H40A 5354	6870	2559	187
H40B 5177	7537	2847	187
H40C 5518	7936	2627	187
H41A 6162	9652	4269	93
H41B 5835	9832	3927	93
H42A 5767	8404	4433	90

H42B 5431	8712	4112	90
H43A 5295	9394	4602	92
H43B 5743	9733	4704	92
H44A 5336	10941	4629	120
H44B 5634	10966	4331	120
H44C 5181	10622	4227	120
H45A 6670	9220	3851	104
H45B 6529	8564	3520	104
H46A 6395	10451	3576	93
H46B 6220	9802	3244	93
H47A 7025	10074	3473	95
H47B 6771	10659	3158	95
H48A 7150	9553	2937	128
H48B 6940	8726	3141	128
H48C 6686	9314	2825	128
H16A 4469	7359	5301	107
H16B 4633	7764	4950	107
H16C 4202	7268	4919	107
H15A 4973	6126	5093	94
H15B 4536	5625	5063	94
H8AA 2788	5433	3220	130
H8AB 3132	6015	3462	130
H8AC 3219	5558	3090	130
H31A 3140	1386	2389	171
H31B 2681	1693	2341	171
H32A 3060	3023	2321	264
H32B 3318	2765	2697	264
H32C 2857	3064	2683	264
H15C 4845	7368	4918	94
H15D 4367	7354	4812	94
H16D 4536	6726	5399	107
H16E 4331	5912	5138	107
H16F 4807	5926	5244	107
H8BA 2866	4349	3022	130
H8BB 3298	4768	2973	130
H8BC 3254	3680	3093	130
H20D 2396	2672	4097	171
H20E 2568	2860	3725	171
H20F 2428	1810	3822	171
H42C 5448	8914	4027	98
H42D 5833	8434	4257	98
H33C 6154	7537	4281	105
H33D 6510	7081	4094	105
H37C 6348	7160	3486	102
H37D 5971	7015	3703	102
H41C 6088	9734	3826	103
H41D 5774	9055	3589	103

A1 Appendix

H45C 6780	9057	3781	101
H45D 6751	8094	3561	101
H34C 6538	8721	4488	105
H34D 6887	8361	4281	105
H38A 6153	7698	3236	116
H38B 5974	6936	3474	116
H46C 6604	8751	3092	102
H46D 6283	9434	3239	102
H35C 7066	8392	4839	105
H35D 6698	7754	4920	105
H39A 5603	6436	3097	117
H39B 5939	6830	2880	117
H43C 5992	10219	4174	104
H43D 5550	10193	4271	104
H47C 6658	10571	3251	102
H47D 7000	10015	3502	102
H36D 7266	6968	5035	132
H36E 6987	6461	4713	132
H36F 7357	7104	4631	132
H40D 5533	7187	2457	187
H40E 5970	6852	2631	187
H40F 5580	6407	2771	187
H44D 5969	10676	4723	163
H44E 5774	9682	4821	163
H44F 6222	9709	4723	163
H48D 7230	10553	3008	143
H48E 7234	9410	3013	143
H48F 6891	9968	2761	143

Table A1.13 Hydrogen Atom Coordinates ($\text{\AA} \times 10^4$) and Isotropic Displacement Parameters ($\text{\AA}^2 \times 10^3$) for $(\text{TBA})_3[\text{PMo}_{12}\text{O}_{40}\text{Sb}_2]$.

Atom Occupancy	Atom	Occupancy	Atom Occupancy
O42 0.5	O41	0.5	O40 0.5
O39 0.5	N3A	0.6737	N4 0.6744
N5 0.75	H7A	0.5182	H7B 0.4818
H14A 0.4374	H14B	0.4374	H14C 0.5626
H14D 0.5626	H19A	0.4889	H19B 0.4889
H19C 0.5111	H19D	0.5111	C20A 0.4889
H20A 0.4889	H20B	0.4889	H20C 0.4889
C33A 0.6737	H33A	0.6737	H33B 0.6737
C34A 0.6737	H34A	0.6737	H34B 0.6737
C35A 0.6737	H35A	0.6737	H35B 0.6737
C36A 0.6737	H36A	0.6737	H36B 0.6737
H36C 0.6737	C37A	0.6737	H37A 0.6737
H37B 0.6737	C38B	0.3263	H38C 0.3263
H38D 0.3263	C39B	0.3263	H39C 0.3263
H39D 0.3263	C40A	0.6737	H40A 0.6737
H40B 0.6737	H40C	0.6737	C41A 0.6737

H41A 0.6737	H41B	0.6737	C42A 0.6737
H42A 0.6737	H42B	0.6737	C43A 0.6737
H43A 0.6737	H43B	0.6737	C44A 0.6737
H44A 0.6737	H44B	0.6737	H44C 0.6737
C45A 0.6737	H45A	0.6737	H45B 0.6737
C46A 0.6737	H46A	0.6737	H46B 0.6737
C47A 0.6737	H47A	0.6737	H47B 0.6737
C48A 0.6737	H48A	0.6737	H48B 0.6737
H48C 0.6737	C49	0.6744	C50 0.6744
C51 0.75	C52	0.75	Sb2B 0.3143
Mo9B 0.3143	Mo3B	0.3143	Mo1B 0.3143
Mo2B 0.3143	Mo7B	0.3143	Mo8B 0.3143
O33B 0.3143	O21B	0.3143	O24B 0.3143
O36B 0.3143	O32B	0.3143	O38B 0.3143
O35B 0.3143	O29B	0.3143	O37B 0.3143
O27B 0.3143	O26B	0.3143	O28B 0.3143
O23B 0.3143	O22B	0.3143	O25B 0.3143
O30B 0.3143	O34B	0.3143	O31B 0.3143
C16B 0.4374	H16A	0.4374	H16B 0.4374
H16C 0.4374	C15B	0.4374	H15A 0.4374
H15B 0.4374	C8A	0.5182	H8AA 0.5182
H8AB 0.5182	H8AC	0.5182	Sb2A 0.6857
Mo7A 0.6857	Mo8A	0.6857	Mo9A 0.6857
Mo2A 0.6857	Mo1A	0.6857	Mo3A 0.6857
O28A 0.6857	O25A	0.6857	O31A 0.6857
O33A 0.6857	O34A	0.6857	O36A 0.6857
O32A 0.6857	O38A	0.6857	O29A 0.6857
O21A 0.6857	O35A	0.6857	O24A 0.6857
O23A 0.6857	O22A	0.6857	O30A 0.6857
O37A 0.6857	O27A	0.6857	O26A 0.6857
C15A 0.5626	H15C	0.5626	H15D 0.5626
C16A 0.5626	H16D	0.5626	H16E 0.5626
H16F 0.5626	C8B	0.4818	H8BA 0.4818
H8BB 0.4818	H8BC	0.4818	C20B 0.5111
H20D 0.5111	H20E	0.5111	H20F 0.5111
C42B 0.3263	H42C	0.3263	H42D 0.3263
N3B 0.3263	C33B	0.3263	H33C 0.3263
H33D 0.3263	C37B	0.3263	H37C 0.3263
H37D 0.3263	C41B	0.3263	H41C 0.3263
H41D 0.3263	C45B	0.3263	H45C 0.3263
H45D 0.3263	C34B	0.3263	H34C 0.3263
H34D 0.3263	C38A	0.6737	H38A 0.6737
H38B 0.6737	C46B	0.3263	H46C 0.3263
H46D 0.3263	C35B	0.3263	H35C 0.3263
H35D 0.3263	C39A	0.6737	H39A 0.6737
H39B 0.6737	C43B	0.3263	H43C 0.3263
H43D 0.3263	C47B	0.3263	H47C 0.3263

A1 Appendix

H47D 0.3263	C36B 0.3263	H36D 0.3263
H36E 0.3263	H36F 0.3263	C40B 0.3263
H40D 0.3263	H40E 0.3263	H40F 0.3263
C44B 0.3263	H44D 0.3263	H44E 0.3263
H44F 0.3263	C48B 0.3263	H48D 0.3263
H48E 0.3263	H48F 0.3263	

Table A1.14 Atomic Occupancy for $(\text{TBA})_3[\text{PMo}_{12}\text{O}_{40}\text{Sb}_2]$.

A1.3 Crystal Data for $(\text{TBA})_3[\text{PMo}_{12}\text{O}_{40}\{\text{Bi}(\text{dmso})_4\}_2]$

Empirical formula	$\text{C}_{24}\text{H}_{72}\text{Bi}_2\text{Mo}_{12}\text{O}_{52}\text{PS}_{12}$
Formula weight	3177.74
Temperature/K	150.0(2)
Crystal system	monoclinic
Space group	$\text{I}2/\text{m}$
$a/\text{\AA}$	14.4984(2)
$b/\text{\AA}$	22.5625(3)
$c/\text{\AA}$	18.0666(3)
$\alpha/^\circ$	90
$\beta/^\circ$	113.2454(19)
$\gamma/^\circ$	90
Volume/ \AA^3	5430.21(16)
Z	2
$\rho_{\text{calc}}/\text{g/cm}^3$	1.943
μ/mm^{-1}	20.085
$F(000)$	3018.0
Crystal size/ mm^3	0.22 \times 0.09 \times 0.04
Radiation	$\text{CuK}\alpha$ ($\lambda = 1.54184$)
2 Θ range for data collection/°	6.61 to 134.172
Index ranges	-12 \leq h \leq 16, -26 \leq k \leq 26, -21 \leq l \leq 21
Reflections collected	39158
Independent reflections	4953 [$R_{\text{int}} = 0.0461$, $R_{\text{sigma}} = 0.0224$]
Data/restraints/parameters	4953/378/290
Goodness-of-fit on F^2	1.049
Final R indexes [$ I >= 2\sigma (I)$]	$R_1 = 0.0294$, $wR_2 = 0.0760$
Final R indexes [all data]	$R_1 = 0.0352$, $wR_2 = 0.0795$
Largest diff. peak/hole / e \AA^{-3}	0.96/-0.96

Table A1.15 Crystal data and structure refinement for $(\text{TBA})_3[\text{PMo}_{12}\text{O}_{40}\{\text{Bi}(\text{dmso})_4\}_2]$.

Atom	x	y	z	U(eq)
Bi1	5000	7133.0(2)	5000	28.33(9)
Mo1	5587.9(3)	6096.6(2)	6551.4(2)	27.95(11)
Mo2	6850.0(3)	6092.4(2)	5151.4(2)	28.87(11)
Mo3	7405.9(4)	5000	6678.7(3)	25.97(13)
Mo4	6237.5(4)	5000	3621.7(3)	33.79(14)
S1	7054.8(12)	7832.6(6)	4638.3(9)	45.9(3)
S2	6444.1(13)	7921.7(8)	6815.1(10)	59.4(5)
P1	5000	5000	5000	18.6(4)
O1	6535(3)	7739.5(17)	5214(2)	41.7(9)

O2	5378(3)	7724.1(18)	6276(2)	45.9(9)
O3	6186(3)	6443.0(17)	5830(2)	45.3(10)
O4	5618(3)	6444(2)	4319(2)	58.9(12)
O5	5882(3)	6609.3(17)	7273(2)	44.9(9)
O6	7702(3)	6605.0(17)	5227(3)	45.7(10)
O7	6674(4)	5593.9(18)	6974(3)	56.0(12)
O8	7576(4)	5592(2)	5984(3)	61.6(13)
O9	6965(3)	5595(2)	4387(3)	74.1(16)
O10	5231(3)	5598(2)	3176(3)	77.0(18)
O11	8503(4)	5000	7446(3)	58.0(17)
O12	6811(4)	5000	2991(3)	44.1(13)
C1	8320(5)	8001(3)	5293(4)	59.5(17)
C2	6690(6)	8546(3)	4215(5)	70(2)
C3	6525(6)	8665(4)	6556(5)	76(2)
C4	6400(7)	8053(4)	7777(4)	88(3)
S3A	6098.7(19)	6823.5(13)	1998.1(16)	77.5(7)
O13A	5838(4)	5372(3)	5583(4)	23.0(12)
O14A	6686(7)	6954(5)	1508(5)	102(3)
C5A	5806(11)	7517(7)	2355(8)	119(4)
C6A	6960(9)	6624(5)	2981(6)	91(3)
S3B	6906(12)	6469(8)	2240(10)	97(3)
O14B	7220(30)	6863(18)	1740(20)	97(6)
C5B	6400(40)	6900(20)	2810(30)	96(5)
C6B	5690(20)	6157(18)	1638(19)	60(6)
O13B	5423(4)	5415(3)	4518(3)	21.2(12)

Table A1.16 Fractional Atomic Coordinates ($\times 10^4$) and Equivalent Isotropic Displacement Parameters ($\text{\AA}^2 \times 10^3$). U_{eq} is defined as 1/3 of the trace of the orthogonalised U_{ij} tensor, for $(\text{TBA})_3[\text{PMo}_{12}\text{O}_{40}\{\text{Bi}(\text{dmsO})_4\}_2]$.

Atom	U_{11}	U_{22}	U_{33}	U_{23}	U_{13}	U_{12}
Bi1	28.62(14)	25.78(14)	26.28(15)	0	6.20(11)	0
Mo1	32.3(2)	26.9(2)	21.0(2)	-2.25(14)	6.55(17)	-4.75(14)
Mo2	20.18(19)	27.9(2)	37.7(2)	-5.28(16)	10.49(17)	-5.26(14)
Mo3	18.5(2)	26.6(3)	25.2(3)	0	0.5(2)	0
Mo4	27.4(3)	51.2(4)	27.1(3)	0	15.4(2)	0
S1	50.8(8)	40.8(8)	46.1(8)	3.0(6)	19.0(7)	-10.8(6)
S2	61.3(10)	57.7(10)	37.9(8)	-15.3(7)	-3.3(7)	13.6(8)
P1	14.1(9)	21.5(10)	18.4(10)	0	4.5(8)	0
O1	42(2)	39(2)	43(2)	-3.2(17)	15.9(17)	-13.5(16)
O2	54(2)	41(2)	33(2)	-7.7(17)	6.4(17)	5.1(18)
O3	57(2)	38(2)	54(2)	16.5(17)	36(2)	19.8(17)
O4	38(2)	74(3)	45(2)	-30(2)	-5.6(18)	22.1(19)
O5	63(3)	36(2)	27.7(19)	-3.3(16)	9.2(18)	10.4(18)
O6	31.6(19)	36(2)	71(3)	8.0(19)	22.6(19)	-5.2(15)
O7	82(3)	41(2)	70(3)	29(2)	57(2)	30(2)
O8	88(3)	51(2)	72(3)	27(2)	60(2)	38(2)
O9	39(2)	92(3)	60(3)	-40(3)	-14.0(19)	34(2)
O10	42(2)	91(4)	64(3)	-53(3)	-16(2)	27(2)

A1 Appendix

O11	24(3)	105(5)	34(3)	0	1(2)	0
O12	41(3)	62(4)	36(3)	0	23(2)	0
C1	47(3)	61(4)	71(4)	5(3)	24(3)	-14(3)
C2	68(4)	57(4)	79(5)	20(4)	23(4)	-7(3)
C3	75(5)	67(4)	66(5)	-30(4)	7(4)	-14(4)
C4	124(7)	83(6)	35(3)	-17(4)	9(4)	20(5)
S3A	71.7(14)	94.4(18)	74.5(15)	-4.4(14)	37.5(12)	-11.2(13)
O13A	18(3)	25(3)	27(3)	1(2)	9(2)	1(2)
O14A	109(5)	128(6)	90(5)	2(4)	61(4)	-5(5)
C5A	120(8)	130(7)	115(8)	-3(6)	54(7)	-1(6)
C6A	95(6)	87(6)	84(5)	6(5)	30(5)	-26(5)
S3B	97(6)	98(6)	92(6)	-1(5)	32(5)	-11(5)
O14B	96(10)	102(10)	93(9)	-2(8)	39(8)	-14(9)
C5B	98(9)	103(10)	86(8)	-6(8)	34(8)	-12(8)
C6B	80(10)	71(11)	38(10)	14(9)	32(8)	-5(9)
O13B	19(3)	21(3)	22(3)	-3(2)	7(2)	3(2)

Table A1.17 Anisotropic Displacement Parameters ($\text{\AA}^2 \times 10^3$). The Anisotropic displacement factor exponent takes the form: $-2\pi^2[h^2a^*a^*U_{11} + 2hka^*b^*U_{12} + \dots]$, for $(\text{TBA})_3[\text{PMo}_{12}\text{O}_{40}\{\text{Bi}(\text{dmsO})_4\}_2]$.

Atom	Atom	Length/ \AA	Atom	Atom	Length/ \AA
Bi1	O1 ¹	2.510(4)	Mo4	O9 ²	1.916(5)
Bi1	O1	2.510(4)	Mo4	O10 ²	1.915(4)
Bi1	O2	2.530(4)	Mo4	O10	1.915(4)
Bi1	O2 ¹	2.530(4)	Mo4	O12	1.653(5)
Bi1	O3	2.365(4)	S1	O1	1.520(4)
Bi1	O3 ¹	2.365(4)	S1	C1	1.788(7)
Bi1	O4	2.367(4)	S1	C2	1.770(7)
Bi1	O4 ¹	2.367(4)	S2	O2	1.533(4)
Mo1	O3	1.988(4)	S2	C3	1.758(9)
Mo1	O4 ¹	1.993(4)	S2	C4	1.789(8)
Mo1	O5	1.668(4)	P1	O13A	1.509(6)
Mo1	O7	1.844(4)	P1	O13A ²	1.509(6)
Mo1	O10 ¹	1.839(4)	P1	O13A ³	1.509(6)
Mo1	O13B ¹	2.452(6)	P1	O13A ¹	1.509(6)
Mo2	O3	1.997(4)	P1	O13B ¹	1.560(6)
Mo2	O4	1.990(4)	P1	O13B	1.560(6)
Mo2	O6	1.658(4)	P1	O13B ²	1.560(6)
Mo2	O8	1.843(4)	P1	O13B ³	1.560(6)
Mo2	O9	1.838(4)	O4	Mo1 ¹	1.993(4)
Mo2	O13A	2.513(6)	O10	Mo1 ¹	1.839(4)
Mo2	O13B	2.461(6)	S3A	O14A	1.480(7)
Mo3	O7 ²	1.911(4)	S3A	C5A	1.805(14)
Mo3	O7	1.911(4)	S3A	C6A	1.779(10)
Mo3	O8	1.913(4)	S3B	O14B	1.462(18)
Mo3	O8 ²	1.913(4)	S3B	C5B	1.77(2)
Mo3	O11	1.647(5)	S3B	C6B	1.81(2)
Mo3	O13A	2.497(6)	O13B	Mo1 ¹	2.452(6)
Mo3	O13A ²	2.497(6)	O13B	O13A ¹	1.767(8)

Mo4 O9 1.916(5)

Table A1.18 Bond Lengths for $(TBA)_3[PMo_{12}O_{40}\{Bi(dmso)_4\}_2]$. $^{11}X, +Y, 1-Z; ^2+X, 1-Y, +Z; ^31-X, 1-Y, 1-Z$

Atom	Atom	Atom	Angle/ $^{\circ}$	Atom	Atom	Atom	Angle/ $^{\circ}$
O1 ¹	Bi1	O1	113.91(19)	O11	Mo3	O7	102.9(2)
O1	Bi1	O2	73.29(14)	O11	Mo3	O7 ²	102.9(2)
O1 ¹	Bi1	O2 ¹	73.29(14)	O11	Mo3	O8 ²	102.7(2)
O1	Bi1	O2 ¹	73.29(13)	O11	Mo3	O8	102.7(2)
O1 ¹	Bi1	O2	73.29(13)	O11	Mo3	O13A ²	160.39(14)
O2	Bi1	O2 ¹	116.36(19)	O11	Mo3	O13A	160.39(14)
O3 ¹	Bi1	O1	146.65(12)	O13A ²	Mo3	O13A	39.2(3)
O3	Bi1	O1 ¹	146.65(12)	O9	Mo4	O9 ²	88.9(3)
O3 ¹	Bi1	O1 ¹	83.25(14)	O10 ²	Mo4	O9 ²	85.47(18)
O3	Bi1	O1	83.25(14)	O10	Mo4	O9 ²	155.1(3)
O3 ¹	Bi1	O2	140.04(13)	O10	Mo4	O9	85.47(18)
O3 ¹	Bi1	O2 ¹	85.84(13)	O10 ²	Mo4	O9	155.1(3)
O3	Bi1	O2	85.84(13)	O10 ²	Mo4	O10	89.5(3)
O3	Bi1	O2 ¹	140.04(13)	O12	Mo4	O9 ²	102.3(2)
O3 ¹	Bi1	O3	97.7(2)	O12	Mo4	O9	102.3(2)
O3	Bi1	O4 ¹	64.40(14)	O12	Mo4	O10	102.5(2)
O3 ¹	Bi1	O4	64.40(14)	O12	Mo4	O10 ²	102.5(2)
O3 ¹	Bi1	O4 ¹	64.38(14)	O1	S1	C1	103.5(3)
O3	Bi1	O4	64.38(14)	O1	S1	C2	106.1(3)
O4	Bi1	O1 ¹	140.60(13)	C2	S1	C1	98.5(3)
O4 ¹	Bi1	O1	140.60(13)	O2	S2	C3	105.4(3)
O4	Bi1	O1	86.76(15)	O2	S2	C4	104.6(4)
O4 ¹	Bi1	O1 ¹	86.76(15)	C3	S2	C4	97.6(4)
O4 ¹	Bi1	O2	82.10(16)	O13A	P1	O13A ¹	112.5(4)
O4	Bi1	O2	146.09(13)	O13A ²	P1	O13A ¹	180.0(4)
O4 ¹	Bi1	O2 ¹	146.09(13)	O13A	P1	O13A ²	67.5(4)
O4	Bi1	O2 ¹	82.10(16)	O13A	P1	O13A ³	180.0
O4 ¹	Bi1	O4	97.9(3)	O13A ³	P1	O13A ¹	67.5(4)
O3	Mo1	O4 ¹	78.60(16)	O13A ²	P1	O13A ³	112.5(4)
O3	Mo1	O13B ¹	90.57(18)	O13A	P1	O13B ¹	70.3(3)
O4 ¹	Mo1	O13B ¹	63.9(2)	O13A ³	P1	O13B ²	70.3(3)
O5	Mo1	O3	101.3(2)	O13A ¹	P1	O13B ²	109.2(3)
O5	Mo1	O4 ¹	102.6(2)	O13A	P1	O13B	70.8(3)
O5	Mo1	O7	100.9(2)	O13A ¹	P1	O13B	70.3(3)
O5	Mo1	O10 ¹	102.0(2)	O13A ¹	P1	O13B ³	109.7(3)
O5	Mo1	O13B ¹	160.1(2)	O13A ³	P1	O13B ¹	109.7(3)
O7	Mo1	O3	89.49(16)	O13A ²	P1	O13B ²	70.8(3)
O7	Mo1	O4 ¹	155.3(2)	O13A	P1	O13B ³	109.2(3)
O7	Mo1	O13B ¹	95.1(2)	O13A ³	P1	O13B ³	70.8(3)
O10 ¹	Mo1	O3	155.6(2)	O13A ¹	P1	O13B ¹	70.8(3)
O10 ¹	Mo1	O4 ¹	89.64(17)	O13A ³	P1	O13B	109.2(3)

A1 Appendix

O10 ¹	Mo1	O7	92.8(2)	O13A ² P1	O13B ¹	109.2(3)	
O10 ¹	Mo1	O13B ¹	65.1(2)	O13A ² P1	O13B	109.7(3)	
O3	Mo2	O13A	65.38(18)	O13A P1	O13B ²	109.7(3)	
O3	Mo2	O13B	90.64(18)	O13A ² P1	O13B ³	70.3(3)	
O4	Mo2	O3	78.45(16)	O13B ¹ P1	O13B ²	180.0(3)	
O4	Mo2	O13A	91.9(2)	O13B ² P1	O13B ³	106.2(4)	
O4	Mo2	O13B	63.7(2)	O13B ¹ P1	O13B ³	73.8(4)	
O6	Mo2	O3	101.37(19)	O13B P1	O13B ²	73.8(4)	
O6	Mo2	O4	101.6(2)	O13B ¹ P1	O13B	106.2(4)	
O6	Mo2	O8	101.2(2)	O13B P1	O13B ³	180.0(5)	
O6	Mo2	O9	101.7(2)	S1	O1	Bi1	128.2(2)
O6	Mo2	O13A	159.0(2)	S2	O2	Bi1	122.2(2)
O6	Mo2	O13B	159.0(2)	Mo1	O3	Bi1	106.14(16)
O8	Mo2	O3	89.97(16)	Mo1	O3	Mo2	133.4(2)
O8	Mo2	O4	156.1(2)	Mo2	O3	Bi1	106.11(16)
O8	Mo2	O13A	64.2(2)	Mo1 ¹	O4	Bi1	105.91(16)
O8	Mo2	O13B	95.9(2)	Mo2	O4	Bi1	106.26(16)
O9	Mo2	O3	155.8(2)	Mo2	O4	Mo1 ¹	133.3(3)
O9	Mo2	O4	89.77(17)	Mo1	O7	Mo3	142.5(3)
O9	Mo2	O8	92.7(2)	Mo2	O8	Mo3	141.6(3)
O9	Mo2	O13A	94.3(2)	Mo2	O9	Mo4	141.5(3)
O9	Mo2	O13B	65.2(2)	Mo1 ¹	O10	Mo4	141.6(3)
O13B	Mo2	O13A	41.88(19)	O14A	S3A	C5A	108.2(6)
O7 ²	Mo3	O7	89.0(3)	O14A	S3A	C6A	107.7(5)
O7	Mo3	O8 ²	154.4(2)	C6A	S3A	C5A	92.0(6)
O7	Mo3	O8	85.59(16)	Mo3	O13A	Mo2	90.15(18)
O7 ²	Mo3	O8 ²	85.59(16)	P1	O13A	Mo2	123.4(3)
O7 ²	Mo3	O8	154.4(2)	P1	O13A	Mo3	126.7(3)
O7	Mo3	O13A ²	91.4(2)	O14B	S3B	C5B	109.1(16)
O7	Mo3	O13A	63.5(2)	O14B	S3B	C6B	109.5(16)
O7 ²	Mo3	O13A	91.4(2)	C5B	S3B	C6B	92.1(13)
O7 ²	Mo3	O13A ²	63.5(2)	Mo1 ¹	O13B	Mo2	96.2(2)
O8 ²	Mo3	O8	88.5(3)	P1	O13B	Mo1 ¹	124.9(3)
O8 ²	Mo3	O13A	91.6(2)	P1	O13B	Mo2	123.9(3)
O8	Mo3	O13A	63.8(2)	P1	O13B	O13A ¹	53.5(3)
O8	Mo3	O13A ²	91.6(2)	O13A ¹	O13B	Mo1 ¹	71.4(3)
O8 ²	Mo3	O13A ²	63.8(2)	O13A ¹	O13B	Mo2	136.8(4)

Table A1.19 Bond Angles for (TBA)₃[PMo₁₂O₄₀{Bi(dmso)₄}₂].

¹1-X,+Y,1-Z;²+X,1-Y,+Z;³1-X,1-Y,1-Z

A	B	C	D	Angle/°	A	B	C	D	Angle/°
O3	Mo1	O7	Mo3	-56.7(4)	O13A ² P1	O13B	Mo1 ¹		177.7(3)
O3	Mo2	O8	Mo3	56.4(4)	O13A ³ P1	O13B	Mo2		-177.3(3)
O3	Mo2	O9	Mo4	3.0(9)	O13A P1	O13B	Mo2		2.7(3)
O4 ¹	Mo1	O7	Mo3	3.8(7)	O13A ² P1	O13B	Mo2		-53.5(4)
O4	Mo2	O8	Mo3	-3.9(8)	O13A ¹ P1	O13B	Mo2		126.5(4)

O4	Mo2 O9	Mo4	-57.2(5)	O13A ² P1	O13B O13A ¹	179.998(1)
O5	Mo1 O7	Mo3	-158.2(4)	O13A ³ P1	O13B O13A ¹	56.2(4)
O6	Mo2 O8	Mo3	158.0(4)	O13A P1	O13B O13A ¹	-123.8(4)
O6	Mo2 O9	Mo4	-159.0(5)	O13B ¹ Mo1 O7	Mo3	33.8(4)
O8	Mo2 O9	Mo4	99.0(5)	O13B Mo2 O8	Mo3	-34.2(4)
O9	Mo2 O8	Mo3	-99.5(4)	O13B Mo2 O9	Mo4	3.7(4)
O10 ¹	Mo1 O7	Mo3	99.0(4)	O13B ² P1	O13A Mo2	61.3(4)
C1	S1 O1	Bi1	-154.5(3)	O13B ¹ P1	O13A Mo2	-118.7(4)
C2	S1 O1	Bi1	102.4(4)	O13B P1	O13A Mo2	-2.6(3)
C3	S2 O2	Bi1	99.3(4)	O13B ³ P1	O13A Mo2	177.4(3)
C4	S2 O2	Bi1	-158.4(3)	O13B ¹ P1	O13A Mo3	121.7(4)
O13A Mo2 O8	Mo3	-6.0(4)	O13B ³ P1	O13A Mo3	57.7(4)	
O13A Mo2 O9	Mo4	34.7(5)	O13B ² P1	O13A Mo3	-58.3(4)	
O13A ¹ P1	O13A Mo2	-60.5(3)	O13B P1	O13A Mo3	-122.3(4)	
O13A ² P1	O13A Mo2	119.5(3)	O13B ¹ P1	O13B Mo1 ¹	-64.4(3)	
O13A ¹ P1	O13A Mo3	179.9(5)	O13B ² P1	O13B Mo1 ¹	115.6(3)	
O13A ² P1	O13A Mo3	-0.1(5)	O13B ¹ P1	O13B Mo2	64.4(3)	
O13A P1	O13B Mo1 ¹	-126.1(4)	O13B ² P1	O13B Mo2	-115.6(3)	
O13A ¹ P1	O13B Mo1 ¹	-2.3(3)	O13B ¹ P1	O13B O13A ¹	-62.1(3)	
O13A ³ P1	O13B Mo1 ¹	53.9(4)	O13B ² P1	O13B O13A ¹	117.9(3)	

Table A1.20 Torsion Angles for (TBA)₃[PMo₁₂O₄₀{Bi(dmso)₄}₂].
$$^{11}\text{-X, +Y, 1-Z}; ^{2+}\text{X, 1-Y, +Z}; ^{31}\text{-X, 1-Y, 1-Z}$$

Atom x	y	z	U(eq)
H1A 8322	8309	5676	89
H1B 8687	8142	4974	89
H1C 8645	7643	5589	89
H2A 5970	8546	3876	105
H2B 7067	8648	3886	105
H2C 6831	8838	4647	105
H3A 6493	8685	6005	114
H3B 7162	8835	6928	114
H3C 5966	8890	6591	114
H4A 5864	8337	7718	132
H4B 7045	8215	8147	132
H4C 6268	7679	7994	132
H5AA 5416	7439	2681	179
H5AB 6430	7722	2683	179
H5AC 5412	7766	1893	179
H6AA 6591	6535	3319	136
H6AB 7342	6274	2947	136
H6AC 7423	6954	3217	136
H5BA 6191	6640	3149	145
H5BB 6918	7176	3158	145
H5BC 5825	7127	2449	145
H6BA 5478	5893	1973	90

A1 Appendix

H6BB 5198	6477	1426	90
H6BC 5733	5931	1189	90

Table A1.21 Hydrogen Atom Coordinates ($\text{\AA} \times 10^4$) and Isotropic Displacement Parameters ($\text{\AA}^2 \times 10^3$) for $(\text{TBA})_3[\text{PMo}_{12}\text{O}_{40}\{\text{Bi}(\text{dmso})_4\}_2]$.

Atom Occupancy	Atom	Occupancy	Atom	Occupancy
S3A 0.8406	O13A	0.5	O14A	0.8406
C5A 0.8406	H5AA	0.8406	H5AB	0.8406
H5AC 0.8406	C6A	0.8406	H6AA	0.8406
H6AB 0.8406	H6AC	0.8406	S3B	0.1594
O14B 0.1594	C5B	0.1594	H5BA	0.1594
H5BB 0.1594	H5BC	0.1594	C6B	0.1594
H6BA 0.1594	H6BB	0.1594	H6BC	0.1594
O13B 0.5				

Table A1.22 Atomic Occupancy for $(\text{TBA})_3[\text{PMo}_{12}\text{O}_{40}\{\text{Bi}(\text{dmso})_4\}_2]$.

Number	X	Y	Z	Volume	Electron count	Content
1	-0.328	0.000	-0.877	853.5	217.3	?
2	-0.422	0.500	-0.132	853.5	217.3	?

Table A1.23 Solvent masks information for $(\text{TBA})_3[\text{PMo}_{12}\text{O}_{40}\{\text{Bi}(\text{dmso})_4\}_2]$.

A1.4 Crystal Data for $(\text{TBA})_3[\text{PMo}_{12}\text{O}_{40}\{\text{Zn}(\text{dmso})_2\}]$

Empirical formula	$\text{C}_{54}\text{H}_{123}\text{Mo}_{12}\text{N}_4\text{O}_{42}\text{PS}_2\text{Zn}$
Formula weight	2812.30
Temperature/K	150.0(2)
Crystal system	monoclinic
Space group	$\text{P}2_1/\text{c}$
a/ \AA	25.5150(6)
b/ \AA	14.5574(3)
c/ \AA	27.1152(7)
$\alpha/^\circ$	90
$\beta/^\circ$	109.441(3)
$\gamma/^\circ$	90
Volume/ \AA^3	9497.2(4)
Z	4
$\rho_{\text{calc}}/\text{g/cm}^3$	1.967
μ/mm^{-1}	1.915
F(000)	5568.0
Crystal size/mm ³	0.43 \times 0.26 \times 0.06
Radiation	$\text{MoK}\alpha$ ($\lambda = 0.71073$)
2 Θ range for data collection/ $^\circ$	6.644 to 57.678
Index ranges	-34 \leq h \leq 34, -18 \leq k \leq 19, -32 \leq l \leq 32
Reflections collected	78428
Independent reflections	21518 [$R_{\text{int}} = 0.0489$, $R_{\text{sigma}} = 0.0573$]
Data/restraints/parameters	21518/3421/1468
Goodness-of-fit on F^2	1.056
Final R indexes [$ I \geq 2\sigma(I)$]	$R_1 = 0.0512$, $wR_2 = 0.1099$

Final R indexes [all data] $R_1 = 0.0940$, $wR_2 = 0.1347$ Largest diff. peak/hole / e Å⁻³ 1.92/-1.19Table A1.24 Crystal data and structure refinement for (TBA)₃[PMo₁₂O₄₀{Zn(dmso)₂}].

Atom x	y	z	U(eq)
Mo2	6179.4(2)	3792.5(4)	3027.4(2)
P1	7255.9(6)	3869.2(10)	4262.2(6)
O2	5686.7(18)	3512(3)	2454.7(18)
O14	5699.9(17)	4395(3)	3376.4(17)
O18	6815.5(18)	3187(3)	2990.6(17)
O19	6417.1(18)	4926(3)	2867.9(16)
O26	6802.0(16)	4409(3)	3848.4(15)
O27	7666.5(17)	3490(3)	4010.7(16)
O28	7554.1(16)	4521(3)	4713.9(16)
N2	9820(3)	6452(5)	6332(3)
N4	9911(7)	1397(16)	6904(7)
C1	7195(5)	-411(6)	3411(4)
C2	6675(4)	-844(6)	3037(4)
C3	6357(4)	-131(6)	2627(4)
C4	5801(4)	-461(7)	2290(4)
C17	9596(5)	6620(8)	5716(4)
C18	9920(5)	6397(9)	5410(4)
C19	9709(5)	6613(14)	4854(5)
C20	9944(7)	6442(12)	4464(6)
C21	10351(4)	6969(7)	6566(4)
C22	10380(4)	7935(7)	6442(4)
C23	10890(5)	8388(7)	6783(5)
C24	10967(7)	9331(8)	6642(7)
C25	9927(5)	5436(7)	6394(5)
C26	10094(5)	5081(8)	6936(5)
C27	10241(7)	4093(9)	6980(6)
C28	10421(8)	3714(13)	7511(6)
C29	9392(5)	6756(9)	6544(6)
C53	9609(7)	1552(12)	6519(7)
C54	9236(7)	1757(9)	6023(6)
Mo1A	6437.4(15)	1830(3)	3978.9(19)
Mo3A	6023(3)	5273(4)	3977(3)
Mo4A	6299.7(13)	3297.8(16)	4936.5(14)
Mo5A	7436(3)	2400(6)	3294(3)
Mo6A	6947(4)	5761(8)	3357(4)
Mo7A	7129(3)	5425(4)	5256(3)
Mo8A	7474.2(11)	1995(3)	5161.6(14)
Mo9A	8211(4)	4366(5)	3618(4)
Mo10	8052(4)	5890(5)	4635(3)
Mo11	8300(3)	4123(5)	5509(3)
Mo12	8460.9(18)	2551(3)	4480.9(18)
Zn1A	5435(3)	3295(4)	3754(3)

A1 Appendix

S1	5060(8)	1905(15)	2801(8)	43.9(19)
S2	4771(4)	4287(4)	4411(3)	43.9(15)
O1A	6027(4)	933(8)	3701(5)	31(2)
O3A	5449(5)	5858(8)	3974(7)	30(2)
O4A	5803(4)	3258(7)	5219(5)	32(2)
O5A	7398(8)	1643(10)	2816(5)	34(2)
O6A	6932(8)	6663(12)	2968(7)	29(2)
O7A	6939(6)	6089(7)	5673(5)	35(3)
O8A	7701(4)	1161(7)	5607(4)	33(2)
O9A	8662(7)	4778(9)	3341(7)	33(2)
O10A	8435(7)	6854(9)	4685(8)	30(2)
O11A	8820(5)	3973(13)	6078(5)	34(2)
O12A	9033(4)	1901(8)	4714(5)	31(2)
O13A	6099(5)	2838(8)	3493(4)	26.5(11)
O15A	5960(4)	4137(5)	4340(3)	26.0(12)
O16A	5983(3)	2395(6)	4363(3)	26.5(13)
O17A	6983(5)	1826(9)	3659(5)	28.1(12)
O20A	6314(5)	6025(10)	3577(6)	24.3(12)
O21A	6553(4)	5636(8)	4610(4)	24.8(16)
O22A	6728(4)	4284(6)	5261(4)	27.4(16)
O23A	6802(3)	2419(6)	5310(4)	26.3(14)
O24A	6907(3)	1328(6)	4593(3)	25.6(18)
O25A	6976(3)	3108(5)	4488(3)	22.5(11)
O29A	8067(4)	1931(8)	3844(3)	28.6(19)
O30A	7909(6)	3321(7)	3176(5)	30.1(14)
O31A	7556(6)	5035(13)	3297(6)	25.6(11)
O32A	7451(6)	6114(11)	4017(4)	25.2(13)
O33A	7621(5)	6214(7)	5057(5)	27.5(11)
O34A	7791(4)	4812(9)	5718(4)	31.3(13)
O35A	7846(4)	3029(6)	5505(4)	28.3(18)
O36A	7955(4)	1920(7)	4779(4)	27.3(13)
O37A	8344(6)	5089(10)	4221(5)	27.4(12)
O38A	8534(5)	5187(8)	5239(5)	31.5(10)
O39A	8540(6)	3396(8)	5032(5)	28(3)
O40A	8695(5)	3433(7)	4092(5)	27.0(13)
O41A	4920(5)	2479(11)	3213(6)	41(3)
O42A	4782(4)	3627(8)	3979(5)	39(2)
N1A	7483(6)	-1018(9)	3888(5)	60(3)
N3A	6583(4)	470(8)	6336(4)	57(3)
C5A	7798(9)	-1751(12)	3684(8)	63(4)
C6A	8189(12)	-1356(15)	3424(12)	81(4)
C7A	8545(11)	-2143(18)	3282(12)	95(5)
C8A	8232(15)	-2830(20)	2897(13)	91(6)
C9A	7882(8)	-369(11)	4284(6)	60(4)
C10A	8303(8)	-830(11)	4743(7)	69(6)
C11A	8708(9)	-158(13)	5092(9)	93(8)
C12A	9148(12)	-610(19)	5535(10)	131(13)

C13A 7128(8)	-1536(12)	4120(7)	57(3)
C14A 6824(10)	-1002(15)	4419(10)	75(4)
C15A 6459(10)	-1670(19)	4632(10)	84(4)
C16A 5940(11)	-1930(30)	4213(13)	100(6)
C30A 8901(8)	6180(20)	6514(12)	122(6)
C31A 8630(17)	6160(30)	6932(18)	131(6)
C32A 8256(17)	5430(30)	7010(20)	149(7)
C33A 6335(5)	561(10)	5751(4)	60(3)
C34A 5731(6)	830(14)	5524(6)	86(5)
C35A 5564(5)	577(14)	4892(5)	95(5)
C36A 5079(6)	1113(15)	4544(8)	145(9)
C37A 6390(8)	1272(10)	6596(7)	64(4)
C38A 6564(7)	2224(10)	6494(6)	71(3)
C39A 6265(6)	2976(12)	6712(6)	78(4)
C40A 5644(6)	2958(13)	6466(6)	86(5)
C41A 6384(6)	-417(9)	6540(5)	68(3)
C42A 6507(8)	-1258(11)	6391(7)	91(5)
C43A 6319(9)	-2025(12)	6669(10)	80(5)
C44A 6668(11)	-2818(15)	6631(11)	105(8)
C45A 7209(5)	470(11)	6485(5)	58(3)
C46A 7571(7)	556(18)	6991(7)	78(4)
C47A 8223(7)	508(15)	7064(10)	109(6)
C48A 8366(7)	1506(14)	7057(6)	84(5)
C49A 4595(15)	2327(18)	2196(8)	51(2)
C50A 4745(8)	818(14)	2810(9)	51(2)
C51A 4443(9)	3670(12)	4791(8)	56(4)
C52A 4224(8)	5056(13)	4093(8)	56(3)
Mo1 8020(5)	5929(7)	4657(4)	24.5(5)
Mo1B 6542(2)	1733(4)	3936(3)	24.2(5)
Mo3 8350(4)	4084(7)	5472(4)	27.7(6)
Mo3B 6017(4)	5115(5)	4030(4)	22.5(6)
Mo4 8537(2)	2633(4)	4404(2)	23.3(5)
Mo4B 6387.2(19)	3056(2)	4935.4(19)	23.9(4)
Mo5B 7497(4)	2481(7)	3247(4)	26.1(7)
Mo6B 6901(5)	5768(10)	3388(5)	22.5(6)
Mo7B 7142(4)	5255(5)	5297(3)	27.9(7)
Mo8B 7593.2(16)	1895(3)	5102.5(19)	26.3(4)
Mo9B 8200(5)	4500(7)	3606(5)	25.0(6)
Zn1B 5504(4)	3111(6)	3761(4)	27.2(7)
S1B 5111(10)	1790(20)	2777(10)	43.9(19)
S2B 4820(5)	3941(5)	4456(5)	43.9(15)
O1B 6156(6)	815(10)	3637(7)	31(2)
O3B 5421(6)	5605(11)	4037(9)	30(2)
O4B 5898(6)	2940(9)	5226(6)	32(2)
O5B 7451(11)	1809(13)	2730(7)	34(2)
O6B 6852(11)	6724(16)	3030(10)	29(2)
O7B 6947(9)	5814(11)	5748(6)	35(3)

A1 Appendix

O8B	7860(5)	1023(9)	5525(5)	33(2)
O9B	8623(9)	5005(13)	3320(9)	33(2)
O10B	8366(10)	6931(11)	4729(10)	30(2)
O11B	8895(7)	3918(17)	6019(6)	34(2)
O12B	9131(5)	2032(11)	4626(7)	31(2)
O13B	6160(6)	2741(10)	3474(5)	26.5(11)
O15B	6009(5)	3928(7)	4366(4)	26.0(12)
O16B	6085(4)	2195(7)	4341(4)	26.5(13)
O17B	7072(6)	1817(11)	3600(6)	28.1(12)
O20B	6280(7)	5941(13)	3644(8)	24.3(12)
O21B	6535(6)	5483(11)	4673(5)	24.8(16)
O22B	6789(6)	4059(7)	5278(5)	27.4(16)
O23B	6914(4)	2189(8)	5276(5)	26.3(14)
O24B	7037(4)	1211(8)	4528(4)	25.6(18)
O25B	7045(4)	3009(6)	4464(4)	22.5(11)
O29B	8157(5)	2021(10)	3762(4)	28.6(19)
O30B	7922(8)	3484(10)	3135(6)	30.1(14)
O31B	7524(8)	5125(16)	3302(8)	25.6(11)
O32B	7406(7)	6139(14)	4050(6)	25.2(13)
O33B	7594(7)	6138(9)	5103(7)	27.5(11)
O34B	7833(6)	4657(11)	5724(5)	31.3(13)
O35B	7937(6)	2930(8)	5455(6)	28.3(18)
O36B	8054(5)	1918(9)	4700(6)	27.3(13)
O37B	8319(8)	5193(12)	4217(6)	27.4(12)
O38B	8536(6)	5216(10)	5235(7)	31.5(10)
O39B	8583(7)	3461(10)	4956(6)	27(3)
O40B	8732(6)	3581(9)	4028(6)	27.0(13)
O41B	4993(7)	2281(15)	3226(8)	41(3)
O42B	4853(6)	3327(11)	4015(6)	39(2)
N1B	7643(6)	-1025(10)	3791(6)	60(3)
N5A	7385(15)	5290(20)	7045(13)	84(7)
C5B	7886(10)	-1768(13)	3540(10)	63(4)
C6B	8313(13)	-1502(17)	3291(13)	81(4)
C7B	8560(12)	-2410(20)	3122(13)	95(5)
C8B	8169(16)	-3010(20)	2724(15)	91(6)
C9B	8086(8)	-385(12)	4142(8)	60(4)
C10B	8556(9)	-876(13)	4550(8)	69(6)
C11B	8985(10)	-202(15)	4870(10)	93(8)
C12B	9466(12)	-630(20)	5274(12)	131(13)
C13B	7360(8)	-1554(13)	4104(8)	57(3)
C14B	7047(11)	-942(17)	4360(12)	75(4)
C15B	6662(11)	-1520(20)	4594(12)	84(4)
C16B	6167(12)	-1850(30)	4173(15)	100(6)
C30B	8834(7)	6340(18)	6353(11)	122(6)
C31B	8399(9)	6850(18)	6526(11)	131(6)
C32B	8158(10)	7692(19)	6201(12)	149(7)
C49B	4579(19)	2160(20)	2200(10)	51(2)

C50B 4856(10)	652(19)	2801(12)	51(2)
C51B 4495(12)	3232(16)	4809(10)	56(4)
C52B 4253(10)	4691(16)	4173(10)	56(3)
C55A 7599(17)	4700(30)	6943(18)	74(6)
C56A 7729(15)	3890(20)	6735(12)	69(6)
N5B 7251(18)	4020(30)	6601(14)	68(7)
C55B 7550(20)	4540(40)	6830(20)	74(7)
C56B 7790(30)	5240(30)	7182(18)	81(8)
N3B 7044(8)	228(15)	6576(7)	59(4)
C33B 7238(9)	-121(17)	6134(8)	55(5)
C34B 7741(12)	-720(20)	6314(10)	80(7)
C35B 7745(13)	-1260(20)	5782(10)	82(8)
C36B 8239(17)	-1810(30)	5840(13)	125(15)
C37B 6627(11)	976(19)	6335(9)	61(5)
C38B 6425(13)	1490(20)	6722(10)	56(6)
C39B 5990(9)	2244(18)	6453(10)	66(5)
C40B 5436(10)	1870(20)	6150(11)	78(9)
C41B 6847(9)	-579(16)	6835(8)	52(4)
C42B 6777(16)	-1355(18)	6535(13)	83(7)
C43B 6460(19)	-2110(20)	6710(20)	86(8)
C44B 6830(20)	-2920(30)	6830(20)	97(12)
C45B 7507(13)	410(30)	7069(11)	81(6)
C46B 8009(12)	680(30)	7058(18)	110(8)
C47B 7933(14)	1660(30)	6775(15)	113(9)
C48B 8485(15)	2140(30)	6948(17)	121(11)

Table A1.25 Fractional Atomic Coordinates ($\times 10^4$) and Equivalent Isotropic Displacement Parameters ($\text{\AA}^2 \times 10^3$). U_{eq} is defined as 1/3 of the trace of the orthogonalised U_{ij} tensor, for $(\text{TBA})_3[\text{PMo}_{12}\text{O}_{40}\{\text{Zn}(\text{dmso})_2\}]$.

Atom	U₁₁	U₂₂	U₃₃	U₂₃	U₁₃	U₁₂
Mo2	24.6(3)	25.3(3)	19.5(3)	-2.0(2)	3.1(2)	-1.9(2)
P1	15.4(7)	16.9(7)	12.9(7)	0.6(5)	3.1(5)	-0.5(6)
O2	29(2)	37(3)	26(2)	-4.5(19)	0.3(18)	-2(2)
O14	23(2)	34(2)	24(2)	-5.3(16)	2.5(16)	0.1(17)
O18	30(2)	27(2)	26(2)	-3.9(17)	6.9(17)	0.1(17)
O19	28(2)	29(2)	21(2)	0.5(16)	1.5(17)	1.2(17)
O26	23.1(18)	22.6(18)	18.9(19)	-0.5(14)	4.3(15)	-0.6(15)
O27	22.8(18)	19.3(18)	26(2)	2.0(15)	4.6(15)	2.3(15)
O28	21.3(18)	23.6(18)	20.1(19)	-1.0(14)	3.2(15)	-0.6(15)
N2	37(3)	56(4)	74(4)	-17(3)	20(3)	-6(3)
N4	61(9)	155(19)	58(8)	54(10)	-16(7)	-23(11)
C1	98(6)	28(4)	74(5)	7(3)	-17(4)	0(4)
C2	83(6)	35(4)	67(5)	5(4)	-10(4)	3(4)
C3	89(6)	43(5)	53(5)	5(4)	-2(4)	11(4)
C4	79(6)	74(7)	54(6)	13(5)	10(4)	10(5)
C17	75(6)	77(7)	83(5)	-22(4)	19(4)	-23(5)
C18	69(6)	109(9)	77(6)	-19(6)	18(5)	-23(6)
C19	61(7)	280(20)	78(6)	-22(7)	15(5)	-28(10)

A1 Appendix

C20	154(14)	166(15)	103(9)	-15(9)	63(9)	-41(12)
C21	58(5)	65(5)	81(6)	-21(4)	12(4)	-13(4)
C22	82(6)	61(5)	92(7)	-27(5)	41(5)	-14(4)
C23	76(7)	81(6)	132(10)	-44(6)	40(6)	-30(5)
C24	152(14)	80(7)	190(16)	-35(8)	66(12)	-39(8)
C25	79(7)	70(5)	98(7)	-8(4)	37(5)	-4(4)
C26	88(8)	86(6)	87(7)	9(5)	37(6)	0(6)
C27	136(12)	99(8)	162(12)	43(7)	73(10)	13(7)
C28	207(19)	169(15)	167(13)	88(11)	96(12)	64(14)
C29	63(5)	109(8)	129(9)	-31(7)	52(6)	-9(5)
C53	43(8)	60(10)	44(7)	26(7)	-9(6)	-16(8)
C54	60(9)	22(7)	36(7)	7(5)	-23(6)	-1(7)
Mo1A	21.5(13)	20.8(9)	30.9(8)	-0.7(6)	9.6(7)	-1.1(9)
Mo3A	18.5(3)	25.3(18)	21.9(12)	0.2(10)	4.2(6)	1.4(10)
Mo4A	22.1(10)	28.0(13)	22.6(3)	1.2(9)	8.8(6)	2.2(8)
Mo5A	28.7(14)	23.3(12)	28.4(12)	-2.7(9)	12.1(7)	1.4(9)
Mo6A	21.4(12)	20.2(3)	23.3(10)	3.3(6)	3.9(7)	1.9(8)
Mo7A	25.1(4)	35.6(19)	20.4(9)	-4.7(11)	4.0(6)	-1.3(11)
Mo8A	22.3(12)	30.6(8)	27.4(8)	9.5(6)	10.1(6)	2.2(8)
Mo9A	24.6(4)	21.6(18)	30.0(5)	5.1(11)	10.7(4)	3.2(11)
Mo10	19.7(8)	19.6(6)	29.6(6)	-0.7(4)	2.1(4)	0.5(5)
Mo11	23.1(10)	34.8(6)	21.1(8)	4.3(5)	1.8(7)	0.6(6)
Mo12	23.1(11)	21.5(8)	28.7(13)	9.8(7)	13.4(6)	4.7(7)
Zn1A	21.9(14)	31(2)	27.7(5)	-6.6(13)	6.4(8)	0.2(12)
S1	37(3)	48(5)	42.8(18)	-18.9(18)	8.1(16)	-14(3)
S2	29.6(18)	64(4)	39.7(19)	-18(3)	13.5(16)	-3(3)
O1A	26(5)	26(3)	43(4)	-3(2)	15(3)	-2(3)
O3A	24(2)	30(6)	32(4)	-2(4)	6(2)	-1(3)
O4A	27(4)	40(6)	31(3)	1(4)	12(3)	3(4)
O5A	47(4)	24(5)	34(4)	-4(4)	19(3)	-3(4)
O6A	24(5)	27(3)	33(4)	10(3)	6(3)	5(3)
O7A	34(3)	44(6)	25(4)	-6(4)	8(3)	1(4)
O8A	29(5)	38(4)	37(4)	15(3)	17(3)	6(3)
O9A	34(3)	24(6)	43(3)	9(4)	17(3)	6(4)
O10A	24(4)	21(3)	39(4)	-1(2)	2(3)	2(3)
O11A	29(4)	41(3)	26(3)	6(3)	1(3)	0(3)
O12A	27(4)	26(4)	44(5)	15(3)	16(3)	5(3)
O13A	25(3)	28(3)	26(2)	-3.0(18)	7.9(18)	0.0(18)
O15A	20(2)	29(3)	26(2)	1(2)	4.3(17)	2(2)
O16A	21(3)	30(3)	27(2)	-3(2)	7.1(19)	0(2)
O17A	28(3)	24(2)	34(3)	-1(2)	13(2)	0(2)
O20A	23(2)	24(3)	24(3)	-1(2)	5.8(19)	1.2(19)
O21A	23(2)	30(4)	22(3)	-3(2)	7.7(18)	-3(2)
O22A	28(3)	30(3)	24(2)	-1(2)	8(2)	-1(3)
O23A	23(3)	31(4)	25(3)	4(2)	9(2)	3(2)
O24A	22(3)	24(3)	34(3)	4(2)	14(2)	3(2)
O25A	22(2)	23(2)	22(2)	0.8(16)	7.9(16)	-0.5(17)

O29A 33(3)	24(3)	33(3)	5(2)	17(2)	3(2)
O30A 35(2)	26(3)	31(3)	2(2)	14(2)	2(2)
O31A 27(2)	22(3)	27(2)	1.2(19)	7.5(17)	3.5(18)
O32A 23(2)	20(2)	29(2)	0.5(17)	4.6(18)	3.2(19)
O33A 21(2)	29(2)	28(3)	-3(2)	2.5(18)	-0.5(19)
O34A 25(2)	40(4)	24(2)	-3(2)	1.1(18)	-3(2)
O35A 25(3)	34(3)	25(3)	7.2(19)	7(2)	0(2)
O36A 26(3)	27(2)	31(3)	7(2)	12(2)	1(2)
O37A 25(2)	23(3)	34(2)	0.1(19)	8.6(18)	-1(2)
O38A 25(2)	32(2)	32(2)	4.0(17)	1.2(17)	-1.5(17)
O39A 28(5)	26(4)	28(4)	9(3)	8(4)	4(3)
O40A 25(2)	23(3)	36(3)	8(2)	14(2)	3(2)
O41A 31(4)	49(6)	41(3)	-17(3)	9(3)	-9(4)
O42A 24(3)	53(6)	37(3)	-12(4)	9(3)	0(3)
N1A 77(6)	21(3)	61(5)	3(3)	-8(4)	-4(4)
N3A 51(5)	75(5)	46(5)	1(4)	15(4)	-3(4)
C5A 81(6)	29(4)	55(8)	4(4)	-8(5)	-2(4)
C6A 102(9)	43(7)	89(10)	-12(7)	21(7)	-19(6)
C7A 102(8)	60(11)	110(14)	-23(8)	18(9)	-10(7)
C8A 101(10)	67(10)	107(16)	-21(9)	38(11)	-26(8)
C9A 76(8)	25(4)	61(7)	-1(4)	-4(5)	-10(5)
C10A 87(9)	30(5)	64(8)	-4(6)	-10(7)	-3(6)
C11A 96(11)	43(6)	92(13)	-7(7)	-31(10)	-1(8)
C12A 134(16)	60(8)	120(17)	-13(12)	-61(15)	15(13)
C13A 62(8)	25(4)	58(5)	5(3)	-16(6)	0(6)
C14A 84(10)	43(6)	83(7)	1(5)	6(7)	4(8)
C15A 98(11)	49(8)	95(8)	-8(6)	20(8)	-7(8)
C16A 101(13)	87(10)	106(10)	-23(8)	26(10)	-15(11)
C30A 76(6)	145(11)	170(14)	-76(10)	75(8)	-33(7)
C31A 88(9)	154(14)	184(16)	-86(10)	90(11)	-34(8)
C32A 102(11)	167(14)	215(19)	-69(12)	104(12)	-25(9)
C33A 60(6)	74(8)	42(5)	-2(5)	12(4)	-20(6)
C34A 58(7)	126(12)	63(7)	31(7)	4(5)	-13(7)
C35A 51(7)	185(15)	41(6)	32(7)	6(5)	-53(8)
C36A 70(9)	187(17)	132(13)	86(12)	-28(8)	-89(9)
C37A 66(8)	79(6)	46(8)	4(5)	19(6)	8(5)
C38A 76(8)	76(6)	58(8)	3(5)	18(6)	2(6)
C39A 78(8)	82(8)	66(9)	-7(7)	12(7)	10(7)
C40A 81(8)	107(13)	67(10)	29(9)	23(7)	11(7)
C41A 70(8)	94(6)	41(7)	3(5)	19(6)	-6(5)
C42A 86(11)	99(7)	70(9)	2(6)	3(8)	-8(6)
C43A 62(11)	102(8)	53(9)	2(7)	-11(8)	-25(7)
C44A 79(15)	119(10)	99(18)	-4(9)	6(12)	-13(9)
C45A 52(5)	81(8)	38(6)	-12(5)	12(4)	-3(5)
C46A 49(6)	143(12)	40(6)	-16(7)	12(5)	-13(6)
C47A 63(7)	176(13)	82(11)	15(9)	14(7)	-4(7)
C48A 56(8)	160(13)	33(8)	25(8)	13(6)	-16(8)

A1 Appendix

C49A 41(4)	53(6)	51(3)	-16(3)	5(3)	-16(4)
C50A 41(4)	53(6)	51(3)	-16(3)	5(3)	-16(4)
C51A 44(6)	80(10)	48(5)	-12(7)	20(4)	-3(8)
C52A 41(5)	74(9)	56(6)	-11(6)	21(4)	9(6)
Mo1 19.7(8)	19.6(6)	29.6(6)	-0.7(4)	2.1(4)	0.5(5)
Mo1B 21.5(13)	20.8(9)	30.9(8)	-0.7(6)	9.6(7)	-1.1(9)
Mo3 23.1(10)	34.8(6)	21.1(8)	4.3(5)	1.8(7)	0.6(6)
Mo3B 18.5(3)	25.3(18)	21.9(12)	0.2(10)	4.2(6)	1.4(10)
Mo4 23.1(11)	21.5(8)	28.7(13)	9.8(7)	13.4(6)	4.7(7)
Mo4B 22.1(10)	28.0(13)	22.6(3)	1.2(9)	8.8(6)	2.2(8)
Mo5B 28.7(14)	23.3(12)	28.4(12)	-2.7(9)	12.1(7)	1.4(9)
Mo6B 21.4(12)	20.2(3)	23.3(10)	3.3(6)	3.9(7)	1.9(8)
Mo7B 25.1(4)	35.6(19)	20.4(9)	-4.7(11)	4.0(6)	-1.3(11)
Mo8B 22.3(12)	30.6(8)	27.4(8)	9.5(6)	10.1(6)	2.2(8)
Mo9B 24.6(4)	21.6(18)	30.0(5)	5.1(11)	10.7(4)	3.2(11)
Zn1B 21.9(14)	31(2)	27.7(5)	-6.6(13)	6.4(8)	0.2(12)
S1B 37(3)	48(5)	42.8(18)	-18.9(18)	8.1(16)	-14(3)
S2B 29.6(18)	64(4)	39.7(19)	-18(3)	13.5(16)	-3(3)
O1B 26(5)	26(3)	43(4)	-3(2)	15(3)	-2(3)
O3B 24(2)	30(6)	32(4)	-2(4)	6(2)	-1(3)
O4B 27(4)	40(6)	31(3)	1(4)	12(3)	3(4)
O5B 47(4)	24(5)	34(4)	-4(4)	19(3)	-3(4)
O6B 24(5)	27(3)	33(4)	10(3)	6(3)	5(3)
O7B 34(3)	44(6)	25(4)	-6(4)	8(3)	1(4)
O8B 29(5)	38(4)	37(4)	15(3)	17(3)	6(3)
O9B 34(3)	24(6)	43(3)	9(4)	17(3)	6(4)
O10B 24(4)	21(3)	39(4)	-1(2)	2(3)	2(3)
O11B 29(4)	41(3)	26(3)	6(3)	1(3)	0(3)
O12B 27(4)	26(4)	44(5)	15(3)	16(3)	5(3)
O13B 25(3)	28(3)	26(2)	-3.0(18)	7.9(18)	0.0(18)
O15B 20(2)	29(3)	26(2)	1(2)	4.3(17)	2(2)
O16B 21(3)	30(3)	27(2)	-3(2)	7.1(19)	0(2)
O17B 28(3)	24(2)	34(3)	-1(2)	13(2)	0(2)
O20B 23(2)	24(3)	24(3)	-1(2)	5.8(19)	1.2(19)
O21B 23(2)	30(4)	22(3)	-3(2)	7.7(18)	-3(2)
O22B 28(3)	30(3)	24(2)	-1(2)	8(2)	-1(3)
O23B 23(3)	31(4)	25(3)	4(2)	9(2)	3(2)
O24B 22(3)	24(3)	34(3)	4(2)	14(2)	3(2)
O25B 22(2)	23(2)	22(2)	0.8(16)	7.9(16)	-0.5(17)
O29B 33(3)	24(3)	33(3)	5(2)	17(2)	3(2)
O30B 35(2)	26(3)	31(3)	2(2)	14(2)	2(2)
O31B 27(2)	22(3)	27(2)	1.2(19)	7.5(17)	3.5(18)
O32B 23(2)	20(2)	29(2)	0.5(17)	4.6(18)	3.2(19)
O33B 21(2)	29(2)	28(3)	-3(2)	2.5(18)	-0.5(19)
O34B 25(2)	40(4)	24(2)	-3(2)	1.1(18)	-3(2)
O35B 25(3)	34(3)	25(3)	7.2(19)	7(2)	0(2)
O36B 26(3)	27(2)	31(3)	7(2)	12(2)	1(2)

O37B 25(2)	23(3)	34(2)	0.1(19)	8.6(18)	-1(2)
O38B 25(2)	32(2)	32(2)	4.0(17)	1.2(17)	-1.5(17)
O39B 23(6)	30(5)	26(5)	7(4)	6(4)	4(4)
O40B 25(2)	23(3)	36(3)	8(2)	14(2)	3(2)
O41B 31(4)	49(6)	41(3)	-17(3)	9(3)	-9(4)
O42B 24(3)	53(6)	37(3)	-12(4)	9(3)	0(3)
N1B 77(6)	21(3)	61(5)	3(3)	-8(4)	-4(4)
N5A 98(15)	89(13)	62(13)	25(11)	23(12)	-18(12)
C5B 81(6)	29(4)	55(8)	4(4)	-8(5)	-2(4)
C6B 102(9)	43(7)	89(10)	-12(7)	21(7)	-19(6)
C7B 102(8)	60(11)	110(14)	-23(8)	18(9)	-10(7)
C8B 101(10)	67(10)	107(16)	-21(9)	38(11)	-26(8)
C9B 76(8)	25(4)	61(7)	-1(4)	-4(5)	-10(5)
C10B 87(9)	30(5)	64(8)	-4(6)	-10(7)	-3(6)
C11B 96(11)	43(6)	92(13)	-7(7)	-31(10)	-1(8)
C12B 134(16)	60(8)	120(17)	-13(12)	-61(15)	15(13)
C13B 62(8)	25(4)	58(5)	5(3)	-16(6)	0(6)
C14B 84(10)	43(6)	83(7)	1(5)	6(7)	4(8)
C15B 98(11)	49(8)	95(8)	-8(6)	20(8)	-7(8)
C16B 101(13)	87(10)	106(10)	-23(8)	26(10)	-15(11)
C30B 76(6)	145(11)	170(14)	-76(10)	75(8)	-33(7)
C31B 88(9)	154(14)	184(16)	-86(10)	90(11)	-34(8)
C32B 102(11)	167(14)	215(19)	-69(12)	104(12)	-25(9)
C49B 41(4)	53(6)	51(3)	-16(3)	5(3)	-16(4)
C50B 41(4)	53(6)	51(3)	-16(3)	5(3)	-16(4)
C51B 44(6)	80(10)	48(5)	-12(7)	20(4)	-3(8)
C52B 41(5)	74(9)	56(6)	-11(6)	21(4)	9(6)
C55A 95(13)	78(13)	48(13)	31(10)	22(11)	-22(12)
C56A 89(14)	77(13)	48(13)	33(11)	31(12)	-31(12)
N5B 87(15)	74(14)	44(13)	32(11)	24(12)	-11(13)
C55B 95(14)	78(13)	47(13)	32(10)	24(11)	-19(12)
C56B 101(17)	83(14)	54(14)	28(12)	19(14)	-21(14)
N3B 52(7)	103(8)	26(7)	-6(6)	18(5)	0(6)
C33B 59(10)	81(11)	36(8)	-13(7)	31(7)	-22(8)
C34B 78(12)	110(15)	66(12)	-14(10)	41(10)	-3(11)
C35B 123(18)	87(16)	58(13)	2(11)	58(13)	2(14)
C36B 160(20)	170(30)	53(18)	2(19)	55(18)	60(20)
C37B 53(9)	99(9)	31(8)	-5(7)	16(7)	-2(8)
C38B 63(10)	86(11)	27(9)	7(8)	24(8)	3(9)
C39B 64(9)	87(11)	54(11)	16(9)	31(8)	8(8)
C40B 69(10)	91(17)	65(15)	52(13)	9(10)	-1(11)
C41B 32(9)	103(8)	25(8)	0(6)	14(7)	7(7)
C42B 82(15)	112(9)	64(12)	-14(8)	36(11)	-9(9)
C43B 75(17)	116(11)	67(16)	-6(10)	25(14)	-17(10)
C44B 80(20)	119(13)	100(30)	2(15)	40(20)	-14(14)
C45B 70(9)	133(12)	34(8)	-10(8)	8(7)	-1(8)
C46B 82(10)	172(16)	71(14)	-10(12)	18(9)	-5(10)

A1 Appendix

C47B 108(15)	160(16)	68(16)	-1(13)	25(13)	6(12)
C48B 105(18)	170(20)	90(20)	-31(18)	33(16)	12(15)

Table A1.26 Anisotropic Displacement Parameters ($\text{\AA}^2 \times 10^3$). The Anisotropic displacement factor exponent takes the form: $-2\pi^2[h^2a^*{}^2U_{11}+2hka^*b^*U_{12}+\dots]$ for $(\text{TBA})_3[\text{PMo}_{12}\text{O}_{40}\{\text{Zn}(\text{dmso})_2\}]$

Atom	Atom	Length/ \AA	Atom	Atom	Length/ \AA
Mo2	O2	1.691(4)	N3A	C37A	1.527(13)
Mo2	O14	1.983(4)	N3A	C41A	1.556(12)
Mo2	O18	1.878(4)	N3A	C45A	1.511(12)
Mo2	O19	1.858(4)	C5A	C6A	1.51(2)
Mo2	O26	2.435(4)	C6A	C7A	1.59(2)
Mo2	O13A	1.935(10)	C7A	C8A	1.474(14)
Mo2	O13B	1.963(13)	C9A	C10A	1.504(16)
P1	O26	1.534(4)	C10A	C11A	1.508(17)
P1	O27	1.531(4)	C11A	C12A	1.495(14)
P1	O28	1.536(4)	C13A	C14A	1.51(2)
P1	O25A	1.550(7)	C14A	C15A	1.58(2)
P1	O25B	1.534(8)	C15A	C16A	1.481(14)
O14	Mo3A	2.017(9)	C30A	C31A	1.511(17)
O14	Zn1A	2.129(9)	C31A	C32A	1.486(16)
O14	Mo3B	1.985(11)	C33A	C34A	1.510(18)
O14	Zn1B	2.276(11)	C34A	C35A	1.66(2)
O18	Mo5A	1.906(10)	C35A	C36A	1.501(14)
O18	Mo5B	1.939(12)	C37A	C38A	1.51(2)
O19	Mo6A	1.966(12)	C38A	C39A	1.561(19)
O19	Mo6B	1.964(16)	C39A	C40A	1.499(13)
O26	Mo3A	2.473(9)	C41A	C42A	1.360(18)
O26	Mo6A	2.473(11)	C42A	C43A	1.512(19)
O26	Mo3B	2.444(11)	C43A	C44A	1.483(14)
O26	Mo6B	2.397(14)	C45A	C46A	1.38(2)
O27	Mo5A	2.425(9)	C46A	C47A	1.61(2)
O27	Mo9A	2.381(9)	C47A	C48A	1.498(14)
O27	Mo12	2.426(6)	Mo1	O10B	1.682(11)
O27	Mo4	2.459(7)	Mo1	O32B	1.881(10)
O27	Mo5B	2.457(11)	Mo1	O33B	1.902(10)
O27	Mo9B	2.492(12)	Mo1	O37B	1.937(10)
O28	Mo7A	2.476(7)	Mo1	O38B	1.973(11)
O28	Mo10	2.410(8)	Mo1B	O1B	1.697(10)
O28	Mo11	2.425(8)	Mo1B	O13B	1.964(10)
O28	Mo1	2.400(10)	Mo1B	O16B	1.966(10)
O28	Mo3	2.443(9)	Mo1B	O17B	1.869(9)
O28	Mo7B	2.421(9)	Mo1B	O24B	1.844(10)
N2	C17	1.594(13)	Mo1B	O25B	2.434(10)
N2	C21	1.494(11)	Mo3	O11B	1.681(10)
N2	C25	1.504(13)	Mo3	O34B	1.872(11)
N2	C29	1.462(12)	Mo3	O35B	1.974(10)
N4	C53	1.094(19)	Mo3	O38B	1.886(11)
C1	C2	1.512(13)	Mo3	O39B	1.920(10)

C1	N1A	1.538(14)	Mo3B Zn1B 3.180(11)
C1	N1B	1.544(14)	Mo3B O3B 1.685(11)
C2	C3	1.541(12)	Mo3B O15B 1.956(9)
C3	C4	1.487(10)	Mo3B O20B 1.862(10)
C17	C18	1.389(15)	Mo3B O21B 1.882(10)
C18	C19	1.457(13)	Mo4 O12B 1.680(10)
C19	C20	1.402(12)	Mo4 O29B 1.907(10)
C21	C22	1.455(14)	Mo4 O36B 1.975(9)
C22	C23	1.477(12)	Mo4 O39B 1.894(10)
C23	C24	1.455(12)	Mo4 O40B 1.879(10)
C25	C26	1.481(15)	Mo4B O4B 1.692(10)
C26	C27	1.481(13)	Mo4B O15B 1.983(9)
C27	C28	1.465(13)	Mo4B O16B 1.984(9)
C29	C30A	1.48(2)	Mo4B O22B 1.848(9)
C29	C30B	1.472(17)	Mo4B O23B 1.851(10)
C53	C54	1.398(19)	Mo4B O25B 2.425(9)
Mo1A	O1A	1.686(8)	Mo5B O5B 1.681(11)
Mo1A	O13A	1.969(8)	Mo5B O17B 1.930(10)
Mo1A	O16A	1.978(7)	Mo5B O29B 1.916(11)
Mo1A	O17A	1.869(7)	Mo5B O30B 1.903(10)
Mo1A	O24A	1.848(8)	Mo6B O6B 1.678(11)
Mo1A	O25A	2.448(8)	Mo6B O20B 1.944(10)
Mo3A	O3A	1.690(9)	Mo6B O31B 1.926(10)
Mo3A	O15A	1.958(8)	Mo6B O32B 1.905(11)
Mo3A	O20A	1.860(8)	Mo7B O7B 1.674(10)
Mo3A	O21A	1.873(8)	Mo7B O21B 1.904(10)
Mo4A	O4A	1.686(8)	Mo7B O22B 1.953(10)
Mo4A	O15A	1.981(7)	Mo7B O33B 1.914(10)
Mo4A	O16A	1.989(8)	Mo7B O34B 1.962(10)
Mo4A	O22A	1.841(8)	Mo8B O8B 1.693(11)
Mo4A	O23A	1.855(8)	Mo8B O23B 1.989(9)
Mo4A	O25A	2.436(7)	Mo8B O24B 1.990(10)
Mo5A	O5A	1.679(9)	Mo8B O25B 2.443(9)
Mo5A	O17A	1.944(8)	Mo8B O35B 1.843(11)
Mo5A	O29A	1.918(9)	Mo8B O36B 1.851(10)
Mo5A	O30A	1.900(9)	Mo9B O9B 1.692(11)
Mo6A	O6A	1.676(9)	Mo9B O30B 1.928(11)
Mo6A	O20A	1.939(9)	Mo9B O31B 1.881(10)
Mo6A	O31A	1.931(8)	Mo9B O37B 1.878(10)
Mo6A	O32A	1.896(9)	Mo9B O40B 1.977(10)
Mo7A	O7A	1.677(8)	Zn1B O13B 2.138(10)
Mo7A	O21A	1.900(8)	Zn1B O15B 2.087(10)
Mo7A	O22A	1.953(8)	Zn1B O16B 2.213(10)
Mo7A	O33A	1.907(8)	Zn1B O41B 2.002(11)
Mo7A	O34A	1.953(8)	Zn1B O42B 2.024(11)
Mo8A	O8A	1.675(9)	S1B O41B 1.527(12)
Mo8A	O23A	1.986(7)	S1B C49B 1.780(15)

A1 Appendix

Mo8A O24A 1.982(8)	S1B C50B 1.785(14)
Mo8A O25A 2.456(8)	S2B O42B 1.518(11)
Mo8A O35A 1.856(9)	S2B C51B 1.788(15)
Mo8A O36A 1.855(8)	S2B C52B 1.771(16)
Mo9A O9A 1.681(9)	N1B C5B 1.517(18)
Mo9A O30A 1.931(9)	N1B C9B 1.529(15)
Mo9A O31A 1.878(8)	N1B C13B 1.497(18)
Mo9A O37A 1.878(8)	N5A C55A 1.10(2)
Mo9A O40A 1.992(8)	C5B C6B 1.51(2)
Mo10 O10A 1.690(9)	C6B C7B 1.60(2)
Mo10 O32A 1.884(8)	C7B C8B 1.485(15)
Mo10 O33A 1.892(9)	C9B C10B 1.514(17)
Mo10 O37A 1.931(8)	C10B C11B 1.510(18)
Mo10 O38A 1.976(9)	C11B C12B 1.483(14)
Mo11 O11A 1.680(8)	C13B C14B 1.51(2)
Mo11 O34A 1.871(8)	C14B C15B 1.58(2)
Mo11 O35A 1.967(8)	C15B C16B 1.472(14)
Mo11 O38A 1.894(9)	C30B C31B 1.531(16)
Mo11 O39A 1.923(9)	C31B C32B 1.515(15)
Mo12 O12A 1.677(8)	C55A C56A 1.39(2)
Mo12 O29A 1.911(8)	N5B C55B 1.10(2)
Mo12 O36A 1.964(7)	C55B C56B 1.40(3)
Mo12 O39A 1.894(8)	N3B C33B 1.527(14)
Mo12 O40A 1.880(8)	N3B C37B 1.511(15)
Zn1A O13A 2.147(8)	N3B C41B 1.54(2)
Zn1A O15A 2.100(8)	N3B C45B 1.48(3)
Zn1A O16A 2.207(8)	C33B C34B 1.49(2)
Zn1A O41A 2.000(8)	C34B C35B 1.65(2)
Zn1A O42A 2.014(8)	C35B C36B 1.457(15)
S1 O41A 1.529(10)	C37B C38B 1.51(2)
S1 C49A 1.783(12)	C38B C39B 1.56(2)
S1 C50A 1.779(12)	C39B C40B 1.480(15)
S2 O42A 1.523(9)	C41B C42B 1.37(2)
S2 C51A 1.775(13)	C42B C43B 1.52(2)
S2 C52A 1.773(14)	C43B C44B 1.483(15)
N1A C5A 1.544(17)	C45B C46B 1.35(3)
N1A C9A 1.535(14)	C46B C47B 1.60(3)
N1A C13A 1.470(18)	C47B C48B 1.501(15)
N3A C33A 1.507(12)	

Table A1.27 Bond Lengths for $(TBA)_3[PMo_{12}O_{40}\{Zn(dmso)_2\}]$.

Atom	Atom	Atom	Angle/ $^{\circ}$	Atom	Atom	Atom	Angle/ $^{\circ}$
O2	Mo2	O14	99.0(2)	Mo9A	O37A	Mo10	148.3(8)
O2	Mo2	O18	103.3(2)	Mo11	O38A	Mo10	123.7(6)
O2	Mo2	O19	101.6(2)	Mo12	O39A	Mo11	156.1(8)
O2	Mo2	O26	171.07(19)	Mo12	O40A	Mo9A	125.7(6)
O2	Mo2	O13A	102.6(4)	S1	O41A	Zn1A	127.2(9)

O2	Mo2	O13B	102.4(5)	S2	O42A	Zn1A	127.8(7)
O14	Mo2	O26	73.68(15)	C1	N1A	C5A	104.8(12)
O18	Mo2	O14	156.08(18)	C9A	N1A	C1	104.8(10)
O18	Mo2	O26	84.79(16)	C9A	N1A	C5A	111.9(13)
O18	Mo2	O13A	88.8(3)	C13A	N1A	C1	117.6(13)
O18	Mo2	O13B	82.3(4)	C13A	N1A	C5A	105.5(11)
O19	Mo2	O14	91.09(19)	C13A	N1A	C9A	112.1(12)
O19	Mo2	O18	92.83(19)	C33A	N3A	C37A	109.4(10)
O19	Mo2	O26	73.82(16)	C33A	N3A	C41A	112.0(10)
O19	Mo2	O13A	154.7(4)	C33A	N3A	C45A	108.4(9)
O19	Mo2	O13B	156.0(5)	C37A	N3A	C41A	106.0(10)
O13A	Mo2	O14	77.9(3)	C45A	N3A	C37A	110.6(11)
O13A	Mo2	O26	81.2(4)	C45A	N3A	C41A	110.3(11)
O13B	Mo2	O14	84.6(4)	C6A	C5A	N1A	114.0(12)
O13B	Mo2	O26	82.3(5)	C5A	C6A	C7A	111.0(15)
O26	P1	O28	108.7(2)	C8A	C7A	C6A	116.3(17)
O26	P1	O25A	108.7(3)	C10A	C9A	N1A	115.3(11)
O26	P1	O25B	114.2(4)	C9A	C10A	C11A	112.4(12)
O27	P1	O26	108.7(2)	C12A	C11A	C10A	113.1(15)
O27	P1	O28	110.3(2)	N1A	C13A	C14A	117.8(12)
O27	P1	O25A	113.0(3)	C13A	C14A	C15A	110.5(14)
O27	P1	O25B	103.8(4)	C16A	C15A	C14A	111.3(17)
O28	P1	O25A	107.4(4)	C29	C30A	C31A	124(3)
O25B	P1	O28	111.0(4)	C32A	C31A	C30A	126(3)
Mo2	O14	Mo3A	121.0(3)	N3A	C33A	C34A	117.7(11)
Mo2	O14	Zn1A	104.0(2)	C33A	C34A	C35A	103.8(12)
Mo2	O14	Mo3B	121.8(4)	C36A	C35A	C34A	114.1(16)
Mo2	O14	Zn1B	96.9(3)	C38A	C37A	N3A	117.2(13)
Mo3A	O14	Zn1A	101.4(3)	C37A	C38A	C39A	111.3(13)
Mo3B	O14	Zn1B	96.3(3)	C40A	C39A	C38A	113.3(14)
Mo2	O18	Mo5A	150.2(3)	C42A	C41A	N3A	120.4(12)
Mo2	O18	Mo5B	156.6(4)	C41A	C42A	C43A	111.9(15)
Mo2	O19	Mo6A	126.6(4)	C44A	C43A	C42A	104.0(16)
Mo2	O19	Mo6B	124.2(4)	C46A	C45A	N3A	124.2(12)
Mo2	O26	Mo3A	90.3(2)	C45A	C46A	C47A	116.1(14)
Mo2	O26	Mo6A	88.2(3)	C48A	C47A	C46A	101.6(16)
Mo2	O26	Mo3B	90.6(3)	O10B	Mo1	O28	170.0(9)
P1	O26	Mo2	125.7(2)	O10B	Mo1	O32B	102.3(10)
P1	O26	Mo3A	127.2(3)	O10B	Mo1	O33B	100.2(9)
P1	O26	Mo6A	126.2(3)	O10B	Mo1	O37B	104.6(9)
P1	O26	Mo3B	122.5(3)	O10B	Mo1	O38B	100.3(9)
P1	O26	Mo6B	128.3(4)	O32B	Mo1	O28	84.8(7)
Mo6A	O26	Mo3A	86.7(3)	O32B	Mo1	O33B	92.6(8)
Mo6B	O26	Mo2	88.7(4)	O32B	Mo1	O37B	86.3(8)
Mo6B	O26	Mo3B	89.6(3)	O32B	Mo1	O38B	157.1(8)
P1	O27	Mo5A	125.0(3)	O33B	Mo1	O28	72.3(5)
P1	O27	Mo9A	126.4(3)	O33B	Mo1	O37B	154.9(8)

A1 Appendix

P1	O27	Mo12	123.0(2)	O33B	Mo1	O38B	87.1(8)
P1	O27	Mo4	130.0(3)	O37B	Mo1	O28	82.7(7)
P1	O27	Mo5B	129.5(3)	O37B	Mo1	O38B	84.4(7)
P1	O27	Mo9B	122.6(3)	O38B	Mo1	O28	73.3(5)
Mo5A	O27	Mo12	89.4(3)	O1B	Mo1B	O13B	101.4(8)
Mo9A	O27	Mo5A	90.8(3)	O1B	Mo1B	O16B	100.3(6)
Mo9A	O27	Mo12	91.6(2)	O1B	Mo1B	O17B	102.5(7)
Mo4	O27	Mo9B	86.8(3)	O1B	Mo1B	O24B	102.2(8)
Mo5B	O27	Mo4	86.7(3)	O1B	Mo1B	O25B	172.1(7)
Mo5B	O27	Mo9B	87.1(3)	O13B	Mo1B	O16B	80.9(5)
P1	O28	Mo7A	127.1(3)	O13B	Mo1B	O25B	81.9(6)
P1	O28	Mo10	125.1(3)	O16B	Mo1B	O25B	72.9(4)
P1	O28	Mo11	126.6(3)	O17B	Mo1B	O13B	85.7(6)
P1	O28	Mo1	126.9(4)	O17B	Mo1B	O16B	155.4(6)
P1	O28	Mo3	124.2(3)	O17B	Mo1B	O25B	84.9(5)
P1	O28	Mo7B	125.9(3)	O24B	Mo1B	O13B	156.0(7)
Mo10	O28	Mo7A	87.8(3)	O24B	Mo1B	O16B	91.0(5)
Mo10	O28	Mo11	89.8(3)	O24B	Mo1B	O17B	93.0(6)
Mo11	O28	Mo7A	88.2(2)	O24B	Mo1B	O25B	74.2(4)
Mo1	O28	Mo3	89.2(4)	O11B	Mo3	O28	172.8(9)
Mo1	O28	Mo7B	89.9(3)	O11B	Mo3	O34B	102.5(9)
Mo7B	O28	Mo3	89.2(3)	O11B	Mo3	O35B	100.1(9)
C21	N2	C17	109.0(8)	O11B	Mo3	O38B	101.4(9)
C21	N2	C25	110.0(8)	O11B	Mo3	O39B	102.1(9)
C25	N2	C17	104.8(8)	O34B	Mo3	O28	72.7(5)
C29	N2	C17	108.2(9)	O34B	Mo3	O35B	87.3(7)
C29	N2	C21	111.8(8)	O34B	Mo3	O38B	91.3(8)
C29	N2	C25	112.7(9)	O34B	Mo3	O39B	154.7(8)
C2	C1	N1A	113.0(9)	O35B	Mo3	O28	85.1(5)
C2	C1	N1B	119.6(9)	O38B	Mo3	O28	73.7(5)
C1	C2	C3	109.6(7)	O38B	Mo3	O35B	158.2(7)
C4	C3	C2	113.0(8)	O38B	Mo3	O39B	89.4(8)
C18	C17	N2	120.8(10)	O39B	Mo3	O28	83.2(6)
C17	C18	C19	118.7(11)	O39B	Mo3	O35B	82.8(7)
C20	C19	C18	129.9(14)	O14	Mo3B	O26	73.5(4)
C22	C21	N2	119.8(9)	O14	Mo3B	Zn1B	45.4(3)
C21	C22	C23	112.9(10)	O26	Mo3B	Zn1B	82.6(3)
C24	C23	C22	115.1(12)	O3B	Mo3B	O14	97.6(9)
C26	C25	N2	115.8(9)	O3B	Mo3B	O26	169.6(9)
C25	C26	C27	113.6(11)	O3B	Mo3B	Zn1B	95.0(7)
C28	C27	C26	115.7(14)	O3B	Mo3B	O15B	102.7(7)
N2	C29	C30A	122.3(18)	O3B	Mo3B	O20B	103.2(8)
N2	C29	C30B	119.9(12)	O3B	Mo3B	O21B	103.2(10)
N4	C53	C54	178(2)	O15B	Mo3B	O14	83.5(5)
O1A	Mo1A	O13A	102.0(6)	O15B	Mo3B	O26	81.9(5)
O1A	Mo1A	O16A	99.9(4)	O15B	Mo3B	Zn1B	39.6(3)
O1A	Mo1A	O17A	103.8(5)	O20B	Mo3B	O14	87.3(8)

O1A	Mo1A O24A	102.6(6)	O20B	Mo3B O26	71.6(6)
O1A	Mo1A O25A	171.5(5)	O20B	Mo3B Zn1B	131.4(8)
O13A	Mo1A O16A	80.7(4)	O20B	Mo3B O15B	153.4(8)
O13A	Mo1A O25A	81.3(4)	O20B	Mo3B O21B	93.6(8)
O16A	Mo1A O25A	72.8(3)	O21B	Mo3B O14	158.4(7)
O17A	Mo1A O13A	85.5(5)	O21B	Mo3B O26	86.3(6)
O17A	Mo1A O16A	154.6(5)	O21B	Mo3B Zn1B	125.6(6)
O17A	Mo1A O25A	84.1(4)	O21B	Mo3B O15B	86.2(6)
O24A	Mo1A O13A	154.9(5)	O12B	Mo4 O27	175.6(7)
O24A	Mo1A O16A	90.4(4)	O12B	Mo4 O29B	102.0(8)
O24A	Mo1A O17A	93.3(5)	O12B	Mo4 O36B	101.0(7)
O24A	Mo1A O25A	73.6(3)	O12B	Mo4 O39B	103.7(8)
O14	Mo3A O26	72.3(3)	O12B	Mo4 O40B	101.9(7)
O3A	Mo3A O14	101.2(7)	O29B	Mo4 O27	74.3(5)
O3A	Mo3A O26	172.1(7)	O29B	Mo4 O36B	85.9(6)
O3A	Mo3A O15A	102.3(5)	O36B	Mo4 O27	81.3(5)
O3A	Mo3A O20A	102.3(6)	O39B	Mo4 O27	80.2(6)
O3A	Mo3A O21A	102.8(7)	O39B	Mo4 O29B	153.8(7)
O15A	Mo3A O14	78.0(4)	O39B	Mo4 O36B	84.2(6)
O15A	Mo3A O26	81.1(4)	O40B	Mo4 O27	75.8(5)
O20A	Mo3A O14	92.1(6)	O40B	Mo4 O29B	89.6(6)
O20A	Mo3A O26	73.9(5)	O40B	Mo4 O36B	157.1(7)
O20A	Mo3A O15A	154.8(6)	O40B	Mo4 O39B	90.1(7)
O20A	Mo3A O21A	93.5(6)	O4B	Mo4B O15B	100.5(6)
O21A	Mo3A O14	153.4(5)	O4B	Mo4B O16B	99.7(6)
O21A	Mo3A O26	84.4(5)	O4B	Mo4B O22B	102.5(7)
O21A	Mo3A O15A	86.1(5)	O4B	Mo4B O23B	103.0(6)
O4A	Mo4A O15A	101.6(5)	O4B	Mo4B O25B	171.8(6)
O4A	Mo4A O16A	99.2(5)	O15B	Mo4B O16B	79.4(5)
O4A	Mo4A O22A	103.1(5)	O15B	Mo4B O25B	81.4(5)
O4A	Mo4A O23A	102.4(5)	O16B	Mo4B O25B	72.8(4)
O4A	Mo4A O25A	171.0(4)	O22B	Mo4B O15B	86.0(5)
O15A	Mo4A O16A	79.4(4)	O22B	Mo4B O16B	155.3(6)
O15A	Mo4A O25A	81.5(4)	O22B	Mo4B O23B	95.7(6)
O16A	Mo4A O25A	72.9(3)	O22B	Mo4B O25B	85.6(5)
O22A	Mo4A O15A	86.4(4)	O23B	Mo4B O15B	155.5(6)
O22A	Mo4A O16A	155.6(4)	O23B	Mo4B O16B	89.8(5)
O22A	Mo4A O23A	94.8(5)	O23B	Mo4B O25B	74.3(4)
O22A	Mo4A O25A	85.5(4)	O18	Mo5B O27	82.5(4)
O23A	Mo4A O15A	155.0(4)	O5B	Mo5B O18	101.7(10)
O23A	Mo4A O16A	89.9(4)	O5B	Mo5B O27	174.1(9)
O23A	Mo4A O25A	73.7(3)	O5B	Mo5B O17B	103.1(8)
O18	Mo5A O27	84.1(3)	O5B	Mo5B O29B	101.9(10)
O18	Mo5A O17A	85.9(5)	O5B	Mo5B O30B	101.5(8)
O18	Mo5A O29A	155.6(6)	O17B	Mo5B O18	81.8(6)
O5A	Mo5A O18	103.6(8)	O17B	Mo5B O27	81.5(6)
O5A	Mo5A O27	169.9(7)	O29B	Mo5B O18	155.8(7)

A1 Appendix

O5A Mo5A O17A 102.7(6)	O29B Mo5B O27 74.3(5)
O5A Mo5A O29A 100.6(7)	O29B Mo5B O17B 88.0(7)
O5A Mo5A O30A 102.1(6)	O30B Mo5B O18 91.6(8)
O17A Mo5A O27 84.2(4)	O30B Mo5B O27 74.1(6)
O29A Mo5A O27 72.1(4)	O30B Mo5B O17B 155.3(8)
O29A Mo5A O17A 86.4(5)	O30B Mo5B O29B 88.6(7)
O30A Mo5A O18 89.2(6)	O19 Mo6B O26 73.1(5)
O30A Mo5A O27 71.1(4)	O6B Mo6B O19 101.1(12)
O30A Mo5A O17A 155.2(6)	O6B Mo6B O26 170.3(10)
O30A Mo5A O29A 88.2(5)	O6B Mo6B O20B 100.8(9)
O19 Mo6A O26 71.3(4)	O6B Mo6B O31B 103.7(10)
O6A Mo6A O19 101.2(9)	O6B Mo6B O32B 102.0(11)
O6A Mo6A O26 170.5(8)	O20B Mo6B O19 86.9(9)
O6A Mo6A O20A 101.0(7)	O20B Mo6B O26 71.5(7)
O6A Mo6A O31A 103.1(7)	O31B Mo6B O19 87.4(9)
O6A Mo6A O32A 104.4(9)	O31B Mo6B O26 84.0(9)
O20A Mo6A O19 82.7(6)	O31B Mo6B O20B 155.5(10)
O20A Mo6A O26 72.7(5)	O32B Mo6B O19 156.8(9)
O31A Mo6A O19 89.8(7)	O32B Mo6B O26 84.2(8)
O31A Mo6A O26 83.0(7)	O32B Mo6B O20B 90.3(8)
O31A Mo6A O20A 155.7(8)	O32B Mo6B O31B 85.7(8)
O32A Mo6A O19 154.5(7)	O7B Mo7B O28 171.9(8)
O32A Mo6A O26 83.2(6)	O7B Mo7B O21B 102.3(8)
O32A Mo6A O20A 91.6(6)	O7B Mo7B O22B 101.9(8)
O32A Mo6A O31A 85.2(6)	O7B Mo7B O33B 103.1(8)
O7A Mo7A O28 171.3(6)	O7B Mo7B O34B 102.2(8)
O7A Mo7A O21A 102.7(6)	O21B Mo7B O28 84.1(6)
O7A Mo7A O22A 102.5(6)	O21B Mo7B O22B 84.3(6)
O7A Mo7A O33A 102.0(6)	O21B Mo7B O33B 91.4(7)
O7A Mo7A O34A 102.3(6)	O21B Mo7B O34B 155.0(8)
O21A Mo7A O28 84.1(5)	O22B Mo7B O28 83.5(5)
O21A Mo7A O22A 84.1(5)	O22B Mo7B O34B 86.4(6)
O21A Mo7A O33A 91.3(5)	O33B Mo7B O28 71.6(5)
O21A Mo7A O34A 154.8(6)	O33B Mo7B O22B 155.0(7)
O22A Mo7A O28 83.5(4)	O33B Mo7B O34B 87.4(7)
O33A Mo7A O28 72.1(4)	O34B Mo7B O28 71.9(5)
O33A Mo7A O22A 155.5(5)	O8B Mo8B O23B 100.8(5)
O33A Mo7A O34A 86.9(6)	O8B Mo8B O24B 100.1(7)
O34A Mo7A O28 71.4(4)	O8B Mo8B O25B 169.5(6)
O34A Mo7A O22A 87.1(5)	O8B Mo8B O35B 104.3(7)
O8A Mo8A O23A 101.2(4)	O8B Mo8B O36B 102.8(6)
O8A Mo8A O24A 101.1(5)	O23B Mo8B O24B 80.9(5)
O8A Mo8A O25A 169.8(4)	O23B Mo8B O25B 71.7(4)
O8A Mo8A O35A 103.3(5)	O24B Mo8B O25B 71.7(4)
O8A Mo8A O36A 103.1(4)	O35B Mo8B O23B 90.2(6)
O23A Mo8A O25A 71.2(3)	O35B Mo8B O24B 155.1(6)
O24A Mo8A O23A 81.6(4)	O35B Mo8B O25B 83.4(5)

O24A Mo8A O25A 71.4(3)	O35B Mo8B O36B 90.3(6)
O35A Mo8A O23A 88.7(4)	O36B Mo8B O23B 155.6(6)
O35A Mo8A O24A 155.0(5)	O36B Mo8B O24B 88.6(6)
O35A Mo8A O25A 83.7(4)	O36B Mo8B O25B 84.1(5)
O36A Mo8A O23A 155.3(5)	O9B Mo9B O27 169.4(8)
O36A Mo8A O24A 89.1(4)	O9B Mo9B O30B 100.4(9)
O36A Mo8A O25A 84.1(4)	O9B Mo9B O31B 102.8(10)
O36A Mo8A O35A 90.4(5)	O9B Mo9B O37B 103.3(9)
O9A Mo9A O27 168.2(6)	O9B Mo9B O40B 98.0(8)
O9A Mo9A O30A 101.2(7)	O30B Mo9B O27 72.9(6)
O9A Mo9A O31A 104.1(7)	O30B Mo9B O40B 84.0(7)
O9A Mo9A O37A 103.7(7)	O31B Mo9B O27 85.6(9)
O9A Mo9A O40A 99.3(6)	O31B Mo9B O30B 90.0(8)
O30A Mo9A O27 71.6(5)	O31B Mo9B O40B 159.1(10)
O30A Mo9A O40A 84.1(5)	O37B Mo9B O27 83.1(7)
O31A Mo9A O27 85.6(7)	O37B Mo9B O30B 155.9(9)
O31A Mo9A O30A 90.6(6)	O37B Mo9B O31B 89.0(8)
O31A Mo9A O37A 89.3(6)	O37B Mo9B O40B 88.5(7)
O31A Mo9A O40A 156.6(8)	O40B Mo9B O27 73.5(5)
O37A Mo9A O27 82.8(6)	O14 Zn1B Mo3B 38.4(2)
O37A Mo9A O30A 154.3(7)	O13B Zn1B O14 73.9(5)
O37A Mo9A O40A 85.8(6)	O13B Zn1B Mo3B 90.2(6)
O40A Mo9A O27 71.0(4)	O13B Zn1B O16B 71.7(4)
O10A Mo10 O28 170.8(7)	O15B Zn1B O14 73.8(4)
O10A Mo10 O32A 101.8(7)	O15B Zn1B Mo3B 36.7(3)
O10A Mo10 O33A 100.4(7)	O15B Zn1B O13B 94.4(6)
O10A Mo10 O37A 102.9(7)	O15B Zn1B O16B 72.1(4)
O10A Mo10 O38A 100.3(7)	O16B Zn1B O14 128.6(5)
O32A Mo10 O28 85.7(5)	O16B Zn1B Mo3B 105.2(4)
O32A Mo10 O33A 91.7(6)	O41B Zn1B O14 110.6(9)
O32A Mo10 O37A 86.9(6)	O41B Zn1B Mo3B 147.0(9)
O32A Mo10 O38A 157.6(7)	O41B Zn1B O13B 89.0(6)
O33A Mo10 O28 73.9(4)	O41B Zn1B O15B 175.1(9)
O33A Mo10 O37A 156.4(6)	O41B Zn1B O16B 105.8(8)
O33A Mo10 O38A 87.4(6)	O41B Zn1B O42B 86.0(7)
O37A Mo10 O28 82.5(5)	O42B Zn1B O14 111.0(6)
O37A Mo10 O38A 85.1(6)	O42B Zn1B Mo3B 95.8(5)
O38A Mo10 O28 72.5(4)	O42B Zn1B O13B 174.0(7)
O11A Mo11 O28 173.5(7)	O42B Zn1B O15B 90.3(6)
O11A Mo11 O34A 102.0(7)	O42B Zn1B O16B 106.5(7)
O11A Mo11 O35A 100.6(7)	O41B S1B C49B 105.3(14)
O11A Mo11 O38A 101.9(7)	O41B S1B C50B 103.6(13)
O11A Mo11 O39A 102.4(7)	C49B S1B C50B 97.6(11)
O34A Mo11 O28 73.9(4)	O42B S2B C51B 103.8(10)
O34A Mo11 O35A 88.2(5)	O42B S2B C52B 105.8(11)
O34A Mo11 O38A 91.1(6)	C52B S2B C51B 97.4(11)
O34A Mo11 O39A 155.1(6)	Mo2 O13B Mo1B 150.2(8)

A1 Appendix

O35A Mo11 O28	84.4(4)	Mo2	O13B Zn1B	102.2(6)
O38A Mo11 O28	73.4(4)	Mo1B	O13B Zn1B	103.7(5)
O38A Mo11 O35A	157.1(6)	Mo3B	O15B Mo4B	148.2(7)
O38A Mo11 O39A	88.7(6)	Mo3B	O15B Zn1B	103.7(6)
O39A Mo11 O28	82.2(5)	Mo4B	O15B Zn1B	105.1(5)
O39A Mo11 O35A	82.6(5)	Mo1B	O16B Mo4B	121.8(6)
O12A Mo12 O27	170.6(5)	Mo1B	O16B Zn1B	101.0(5)
O12A Mo12 O29A	101.8(6)	Mo4B	O16B Zn1B	100.6(5)
O12A Mo12 O36A	100.9(5)	Mo1B	O17B Mo5B	153.2(10)
O12A Mo12 O39A	102.6(6)	Mo3B	O20B Mo6B	127.3(10)
O12A Mo12 O40A	101.4(5)	Mo3B	O21B Mo7B	152.4(10)
O29A Mo12 O27	72.2(4)	Mo4B	O22B Mo7B	153.1(8)
O29A Mo12 O36A	86.0(4)	Mo4B	O23B Mo8B	125.0(6)
O36A Mo12 O27	86.1(4)	Mo1B	O24B Mo8B	125.4(6)
O39A Mo12 O27	84.2(5)	P1	O25B Mo1B	126.3(6)
O39A Mo12 O29A	154.9(6)	P1	O25B Mo4B	123.5(5)
O39A Mo12 O36A	83.8(5)	P1	O25B Mo8B	127.5(6)
O40A Mo12 O27	71.7(4)	Mo1B	O25B Mo8B	88.6(3)
O40A Mo12 O29A	89.2(5)	Mo4B	O25B Mo1B	90.5(3)
O40A Mo12 O36A	157.7(5)	Mo4B	O25B Mo8B	88.8(3)
O40A Mo12 O39A	91.6(5)	Mo4	O29B Mo5B	124.0(8)
O14 Zn1A O13A	70.3(4)	Mo5B	O30B Mo9B	125.9(9)
O14 Zn1A O16A	125.7(4)	Mo9B	O31B Mo6B	148.9(11)
O13A Zn1A O16A	71.9(3)	Mo1	O32B Mo6B	152.0(11)
O15A Zn1A O14	72.5(3)	Mo1	O33B Mo7B	126.3(8)
O15A Zn1A O13A	93.2(5)	Mo3	O34B Mo7B	125.9(8)
O15A Zn1A O16A	72.2(3)	Mo8B	O35B Mo3	149.9(9)
O41A Zn1A O14	109.3(7)	Mo8B	O36B Mo4	148.5(8)
O41A Zn1A O13A	88.4(5)	Mo9B	O37B Mo1	149.2(10)
O41A Zn1A O15A	178.0(7)	Mo3	O38B Mo1	123.6(8)
O41A Zn1A O16A	107.1(6)	Mo4	O39B Mo3	157.3(10)
O41A Zn1A O42A	87.6(5)	Mo4	O40B Mo9B	123.8(8)
O42A Zn1A O14	113.1(4)	S1B	O41B Zn1B	127.5(12)
O42A Zn1A O13A	175.4(5)	S2B	O42B Zn1B	128.7(10)
O42A Zn1A O15A	90.9(4)	C5B	N1B C1	115.9(14)
O42A Zn1A O16A	107.3(5)	C5B	N1B C9B	112.6(14)
O41A S1	C49A 103.8(10)	C9B	N1B C1	107.0(11)
O41A S1	C50A 105.1(10)	C13B	N1B C1	106.7(13)
C50A S1	C49A 98.8(9)	C13B	N1B C5B	103.5(12)
O42A S2	C51A 105.1(8)	C13B	N1B C9B	110.9(14)
O42A S2	C52A 103.7(8)	C6B	C5B N1B	118.8(14)
C52A S2	C51A 98.9(9)	C5B	C6B C7B	109.2(16)
Mo2 O13A Mo1A	148.6(6)	C8B	C7B C6B	117.4(19)
Mo2 O13A Zn1A	105.0(5)	C10B	C9B N1B	114.1(12)
Mo1A O13A Zn1A	103.3(4)	C11B	C10B C9B	111.0(13)
Mo3A O15A Mo4A	147.7(5)	C12B	C11B C10B	114.5(16)
Mo3A O15A Zn1A	104.5(4)	N1B	C13B C14B	112.7(13)

Mo4A O15A Zn1A	104.7(4)	C13B C14B C15B	111.2(15)
Mo1A O16A Mo4A	122.0(4)	C16B C15B C14B	110.6(18)
Mo1A O16A Zn1A	100.9(4)	C29 C30B C31B	114.0(17)
Mo4A O16A Zn1A	100.6(4)	C32B C31B C30B	114(2)
Mo1A O17A Mo5A	153.7(7)	N5A C55A C56A	165(5)
Mo3A O20A Mo6A	126.7(8)	N5B C55B C56B	161(6)
Mo3A O21A Mo7A	154.2(7)	C33B N3B C41B	110.2(16)
Mo4A O22A Mo7A	152.7(6)	C37B N3B C33B	105.6(15)
Mo4A O23A Mo8A	126.1(5)	C37B N3B C41B	117.2(18)
Mo1A O24A Mo8A	126.4(5)	C45B N3B C33B	113.3(18)
P1 O25A Mo1A	124.6(4)	C45B N3B C37B	120(2)
P1 O25A Mo4A	127.7(4)	C45B N3B C41B	90.4(15)
P1 O25A Mo8A	124.9(4)	C34B C33B N3B	114.0(16)
Mo1A O25A Mo8A	88.4(3)	C33B C34B C35B	104.4(18)
Mo4A O25A Mo1A	90.6(3)	C36B C35B C34B	115(2)
Mo4A O25A Mo8A	88.9(2)	C38B C37B N3B	114.3(18)
Mo12 O29A Mo5A	126.0(6)	C37B C38B C39B	112.2(19)
Mo5A O30A Mo9A	126.5(7)	C40B C39B C38B	114(2)
Mo9A O31A Mo6A	149.5(9)	C42B C41B N3B	110.8(17)
Mo10 O32A Mo6A	152.6(8)	C41B C42B C43B	113(2)
Mo10 O33A Mo7A	126.2(6)	C44B C43B C42B	106(2)
Mo11 O34A Mo7A	126.1(6)	C46B C45B N3B	121(3)
Mo8A O35A Mo11	149.4(6)	C45B C46B C47B	108(2)
Mo8A O36A Mo12	148.2(6)	C48B C47B C46B	108(3)

Table A1.28 Bond Angles for (TBA)₃[PMo₁₂O₄₀{Zn(dmso)₂}].

Atom x	y	z	U(eq)
H1AA 7096	185	3533	94
H1AB 7458	-286	3221	94
H1BC 7076	43	3624	94
H1BD 7376	-63	3198	94
H2A 6435	-1067	3234	84
H2B 6777	-1377	2861	84
H3A 6309	437	2808	81
H3B 6581	26	2402	81
H4A 5618	18	2038	108
H4B 5846	-1015	2103	108
H4C 5574	-604	2509	108
H17A 9243	6276	5573	96
H17B 9503	7280	5659	96
H18A 9993	5729	5445	104
H18B 10282	6711	5563	104
H19A 9337	6323	4724	169
H19B 9641	7284	4839	169
H20A 9696	6675	4128	204
H20B 10304	6753	4553	204
H20C 9996	5779	4437	204

A1 Appendix

H21A 10456	6918	6950	85
H21B 10641	6644	6465	85
H22A 10052	8257	6477	91
H22B 10364	7992	6073	91
H23A 10885	8381	7146	114
H23B 11215	8022	6776	114
H24A 11313	9575	6888	207
H24B 10984	9347	6287	207
H24C 10654	9707	6658	207
H25A 9585	5110	6183	97
H25B 10222	5280	6246	97
H26A 9785	5180	7074	102
H26B 10418	5438	7156	102
H27A 9914	3740	6763	152
H27B 10542	3996	6831	152
H28A 10508	3061	7499	259
H28B 10752	4043	7729	259
H28C 10122	3786	7660	259
H29A 9247	7347	6373	114
H29B 9583	6893	6919	114
H29C 9345	7426	6485	114
H29D 9539	6661	6928	114
H54A 9415	1651	5759	74
H54B 9122	2402	6012	74
H54C 8908	1361	5949	74
H5AA 8014	-2142	3980	75
H5AB 7523	-2148	3430	75
H6AA 8441	-909	3663	97
H6AB 7971	-1026	3102	97
H7AA 8819	-1850	3146	114
H7AB 8756	-2469	3608	114
H8AA 8491	-3281	2839	136
H8AB 7967	-3145	3031	136
H8AC 8031	-2525	2567	136
H9AA 8083	4	4099	73
H9AB 7659	58	4419	73
H10A 8511	-1291	4613	83
H10B 8107	-1159	4950	83
H11A 8888	195	4880	111
H11B 8502	283	5237	111
H12A 9398	-141	5747	196
H12B 8974	-948	5752	196
H12C 9361	-1036	5395	196
H13A 7362	-2001	4359	69
H13B 6848	-1871	3834	69
H14A 6581	-537	4186	90
H14B 7096	-678	4715	90

H15A 6677	-2229	4778	101
H15B 6366	-1362	4918	101
H16A 5723	-2347	4357	150
H16B 5721	-1382	4073	150
H16C 6031	-2248	3932	150
H30A 9006	5539	6471	146
H30B 8606	6351	6184	146
H31A 8938	6210	7269	157
H31B 8418	6744	6892	157
H32A 8138	5589	7304	223
H32B 7928	5385	6689	223
H32C 8454	4845	7071	223
H33A 6383	-35	5594	72
H33B 6556	1022	5636	72
H34A 5681	1493	5575	103
H34B 5502	474	5688	103
H35A 5891	692	4782	114
H35B 5476	-87	4844	114
H36A 5006	928	4180	218
H36B 4750	991	4643	218
H36C 5166	1771	4581	218
H37A 5979	1257	6480	77
H37B 6528	1168	6978	77
H38A 6475	2314	6113	86
H38B 6972	2289	6661	86
H39A 6362	2890	7095	94
H39B 6403	3588	6654	94
H40A 5481	3443	6619	128
H40B 5544	3058	6089	128
H40C 5503	2359	6530	128
H41A 6534	-397	6927	82
H41B 5974	-379	6440	82
H42A 6914	-1305	6468	109
H42B 6325	-1328	6009	109
H43A 6381	-1863	7038	96
H43B 5920	-2162	6494	96
H44A 6572	-3353	6804	157
H44B 6603	-2962	6262	157
H44C 7061	-2665	6803	157
H45A 7309	-111	6347	70
H45B 7302	972	6282	70
H46A 7487	64	7205	94
H46B 7497	1150	7133	94
H47A 8438	216	7400	131
H47B 8289	170	6773	131
H48A 8761	1569	7099	125
H48B 8141	1778	6723	125

A1 Appendix

H48C 8289	1823	7344	125
H49A 4214	2310	2204	76
H49B 4621	1942	1909	76
H49C 4694	2961	2144	76
H50A 4759	451	2511	76
H50B 4356	907	2787	76
H50C 4945	497	3136	76
H51A 4110	3363	4559	84
H51B 4337	4096	5021	84
H51C 4700	3209	5003	84
H52A 4334	5438	3846	84
H52B 4147	5450	4354	84
H52C 3890	4706	3904	84
H5BA 8057	-2235	3811	75
H5BB 7574	-2070	3268	75
H6BA 8615	-1146	3543	97
H6BB 8138	-1113	2980	97
H7BA 8861	-2224	2988	114
H7BB 8733	-2783	3441	114
H8BA 8370	-3540	2655	136
H8BB 7875	-3222	2855	136
H8BC 8003	-2661	2400	136
H9BA 8244	-13	3919	73
H9BB 7907	43	4321	73
H10C 8405	-1231	4784	83
H10D 8734	-1315	4376	83
H11C 9124	161	4631	111
H11D 8802	228	5045	111
H12D 9724	-150	5463	196
H12E 9336	-978	5520	196
H12F 9658	-1045	5105	196
H13C 7642	-1909	4377	69
H13D 7097	-1997	3872	69
H14C 6816	-502	4099	90
H14D 7315	-585	4644	90
H15C 6873	-2056	4790	101
H15D 6545	-1141	4841	101
H16D 5933	-2214	4325	150
H16E 5955	-1328	3983	150
H16F 6282	-2241	3932	150
H30C 8859	5699	6480	146
H30D 8707	6322	5966	146
H31C 8093	6421	6508	157
H31D 8572	7040	6895	157
H32D 7885	7980	6334	223
H32E 8457	8130	6223	223
H32F 7977	7511	5835	223

H49D 4219	2139	2256	76
H49E 4568	1751	1908	76
H49F 4656	2788	2116	76
H50D 4823	330	2474	76
H50E 4491	685	2845	76
H50F 5115	319	3096	76
H51D 4187	2893	4562	84
H51E 4353	3617	5033	84
H51F 4768	2796	5027	84
H52D 4346	5118	3936	84
H52E 4173	5038	4450	84
H52F 3925	4331	3978	84
H56A 8132	3793	6872	104
H56B 7540	3375	6835	104
H56C 7607	3939	6353	104
H56D 8160	5386	7159	121
H56E 7557	5783	7098	121
H56F 7837	5031	7537	121
H33C 6932	-470	5883	65
H33D 7320	414	5946	65
H34C 7714	-1162	6582	97
H34D 8082	-348	6462	97
H35C 7416	-1666	5663	99
H35D 7708	-799	5503	99
H36D 8205	-2105	5505	188
H36E 8568	-1415	5946	188
H36F 8276	-2284	6106	188
H37C 6798	1422	6159	73
H37D 6303	699	6065	73
H38C 6746	1778	6989	68
H38D 6255	1046	6902	68
H39C 5949	2665	6725	79
H39D 6132	2607	6216	79
H40D 5184	2379	5992	117
H40E 5470	1466	5874	117
H40F 5288	1524	6384	117
H41C 7123	-698	7184	62
H41D 6490	-416	6884	62
H42C 7147	-1594	6554	99
H42D 6574	-1194	6166	99
H43C 6372	-1908	7020	103
H43D 6107	-2247	6423	103
H44D 6641	-3428	6941	145
H44E 6911	-3108	6514	145
H44F 7174	-2771	7108	145
H45C 7378	884	7262	97
H45D 7565	-161	7280	97

A1 Appendix

H46C 8154	222	6864	132
H46D 8275	722	7419	132
H47C 7799	1576	6391	136
H47D 7656	2028	6871	136
H48D 8447	2738	6778	181
H48E 8613	2215	7328	181
H48F 8756	1765	6849	181

Table A1.29 Hydrogen Atom Coordinates ($\text{\AA} \times 10^4$) and Isotropic Displacement Parameters ($\text{\AA}^2 \times 10^3$) for $(\text{TBA})_3[\text{PMo}_{12}\text{O}_{40}\{\text{Zn}(\text{dmso})_2\}]$.

Atom Occupancy	Atom Occupancy	Atom Occupancy
N4 0.5	H1AA 0.5258	H1AB 0.5258
H1BC 0.4742	H1BD 0.4742	H29A 0.3616
H29B 0.3616	H29C 0.6384	H29D 0.6384
C53 0.5	C54 0.5	H54A 0.5
H54B 0.5	H54C 0.5	Mo1A 0.5633
Mo3A 0.5633	Mo4A 0.5633	Mo5A 0.5633
Mo6A 0.5633	Mo7A 0.5633	Mo8A 0.5633
Mo9A 0.5633	Mo10 0.5633	Mo11 0.5633
Mo12 0.5633	Zn1A 0.5633	S1 0.5633
S2 0.5633	O1A 0.5633	O3A 0.5633
O4A 0.5633	O5A 0.5633	O6A 0.5633
O7A 0.5633	O8A 0.5633	O9A 0.5633
O10A 0.5633	O11A 0.5633	O12A 0.5633
O13A 0.5633	O15A 0.5633	O16A 0.5633
O17A 0.5633	O20A 0.5633	O21A 0.5633
O22A 0.5633	O23A 0.5633	O24A 0.5633
O25A 0.5633	O29A 0.5633	O30A 0.5633
O31A 0.5633	O32A 0.5633	O33A 0.5633
O34A 0.5633	O35A 0.5633	O36A 0.5633
O37A 0.5633	O38A 0.5633	O39A 0.5633
O40A 0.5633	O41A 0.5633	O42A 0.5633
N1A 0.5258	N3A 0.666	C5A 0.5258
H5AA 0.5258	H5AB 0.5258	C6A 0.5258
H6AA 0.5258	H6AB 0.5258	C7A 0.5258
H7AA 0.5258	H7AB 0.5258	C8A 0.5258
H8AA 0.5258	H8AB 0.5258	H8AC 0.5258
C9A 0.5258	H9AA 0.5258	H9AB 0.5258
C10A 0.5258	H10A 0.5258	H10B 0.5258
C11A 0.5258	H11A 0.5258	H11B 0.5258
C12A 0.5258	H12A 0.5258	H12B 0.5258
H12C 0.5258	C13A 0.5258	H13A 0.5258
H13B 0.5258	C14A 0.5258	H14A 0.5258
H14B 0.5258	C15A 0.5258	H15A 0.5258
H15B 0.5258	C16A 0.5258	H16A 0.5258
H16B 0.5258	H16C 0.5258	C30A 0.3616
H30A 0.3616	H30B 0.3616	C31A 0.3616
H31A 0.3616	H31B 0.3616	C32A 0.3616

H32A 0.3616	H32B 0.3616	H32C 0.3616
C33A 0.666	H33A 0.666	H33B 0.666
C34A 0.666	H34A 0.666	H34B 0.666
C35A 0.666	H35A 0.666	H35B 0.666
C36A 0.666	H36A 0.666	H36B 0.666
H36C 0.666	C37A 0.666	H37A 0.666
H37B 0.666	C38A 0.666	H38A 0.666
H38B 0.666	C39A 0.666	H39A 0.666
H39B 0.666	C40A 0.666	H40A 0.666
H40B 0.666	H40C 0.666	C41A 0.666
H41A 0.666	H41B 0.666	C42A 0.666
H42A 0.666	H42B 0.666	C43A 0.666
H43A 0.666	H43B 0.666	C44A 0.666
H44A 0.666	H44B 0.666	H44C 0.666
C45A 0.666	H45A 0.666	H45B 0.666
C46A 0.666	H46A 0.666	H46B 0.666
C47A 0.666	H47A 0.666	H47B 0.666
C48A 0.666	H48A 0.666	H48B 0.666
H48C 0.666	C49A 0.5633	H49A 0.5633
H49B 0.5633	H49C 0.5633	C50A 0.5633
H50A 0.5633	H50B 0.5633	H50C 0.5633
C51A 0.5633	H51A 0.5633	H51B 0.5633
H51C 0.5633	C52A 0.5633	H52A 0.5633
H52B 0.5633	H52C 0.5633	Mo1 0.4367
Mo1B 0.4367	Mo3 0.4367	Mo3B 0.4367
Mo4 0.4367	Mo4B 0.4367	Mo5B 0.4367
Mo6B 0.4367	Mo7B 0.4367	Mo8B 0.4367
Mo9B 0.4367	Zn1B 0.4367	S1B 0.4367
S2B 0.4367	O1B 0.4367	O3B 0.4367
O4B 0.4367	O5B 0.4367	O6B 0.4367
O7B 0.4367	O8B 0.4367	O9B 0.4367
O10B 0.4367	O11B 0.4367	O12B 0.4367
O13B 0.4367	O15B 0.4367	O16B 0.4367
O17B 0.4367	O20B 0.4367	O21B 0.4367
O22B 0.4367	O23B 0.4367	O24B 0.4367
O25B 0.4367	O29B 0.4367	O30B 0.4367
O31B 0.4367	O32B 0.4367	O33B 0.4367
O34B 0.4367	O35B 0.4367	O36B 0.4367
O37B 0.4367	O38B 0.4367	O39B 0.4367
O40B 0.4367	O41B 0.4367	O42B 0.4367
N1B 0.4742	N5A 0.2994	C5B 0.4742
H5BA 0.4742	H5BB 0.4742	C6B 0.4742
H6BA 0.4742	H6BB 0.4742	C7B 0.4742
H7BA 0.4742	H7BB 0.4742	C8B 0.4742
H8BA 0.4742	H8BB 0.4742	H8BC 0.4742
C9B 0.4742	H9BA 0.4742	H9BB 0.4742
C10B 0.4742	H10C 0.4742	H10D 0.4742

A1 Appendix

C11B 0.4742	H11C 0.4742	H11D 0.4742
C12B 0.4742	H12D 0.4742	H12E 0.4742
H12F 0.4742	C13B 0.4742	H13C 0.4742
H13D 0.4742	C14B 0.4742	H14C 0.4742
H14D 0.4742	C15B 0.4742	H15C 0.4742
H15D 0.4742	C16B 0.4742	H16D 0.4742
H16E 0.4742	H16F 0.4742	C30B 0.6384
H30C 0.6384	H30D 0.6384	C31B 0.6384
H31C 0.6384	H31D 0.6384	C32B 0.6384
H32D 0.6384	H32E 0.6384	H32F 0.6384
C49B 0.4367	H49D 0.4367	H49E 0.4367
H49F 0.4367	C50B 0.4367	H50D 0.4367
H50E 0.4367	H50F 0.4367	C51B 0.4367
H51D 0.4367	H51E 0.4367	H51F 0.4367
C52B 0.4367	H52D 0.4367	H52E 0.4367
H52F 0.4367	C55A 0.2994	C56A 0.2994
H56A 0.2994	H56B 0.2994	H56C 0.2994
N5B 0.2006	C55B 0.2006	C56B 0.2006
H56D 0.2006	H56E 0.2006	H56F 0.2006
N3B 0.334	C33B 0.334	H33C 0.334
H33D 0.334	C34B 0.334	H34C 0.334
H34D 0.334	C35B 0.334	H35C 0.334
H35D 0.334	C36B 0.334	H36D 0.334
H36E 0.334	H36F 0.334	C37B 0.334
H37C 0.334	H37D 0.334	C38B 0.334
H38C 0.334	H38D 0.334	C39B 0.334
H39C 0.334	H39D 0.334	C40B 0.334
H40D 0.334	H40E 0.334	H40F 0.334
C41B 0.334	H41C 0.334	H41D 0.334
C42B 0.334	H42C 0.334	H42D 0.334
C43B 0.334	H43C 0.334	H43D 0.334
C44B 0.334	H44D 0.334	H44E 0.334
H44F 0.334	C45B 0.334	H45C 0.334
H45D 0.334	C46B 0.334	H46C 0.334
H46D 0.334	C47B 0.334	H47C 0.334
H47D 0.334	C48B 0.334	H48D 0.334
H48E 0.334	H48F 0.334	

Table A1.30 Atomic Occupancy for $(TBA)_3[PMo_{12}O_{40}\{Zn(dmso)_2\}]$.